NGU REPORT 2017.027

Ramså Basin, Northern Norway: an Integrated Study

GEOLOGY FOR SOCIETY

SINCE 1858

GEOLOGICAL SURVEY OF NORWAY

- NGU -

NORGES GEOLOGISKE UNDERSØKELSE
- NGU -

REPORT

Geological Survey of Norway
P.O.Box 6315 Torgard
NO-7491 TRONDHEIM
Tel.: 47 73 90 40 00

Report no.: 2017.027

ISSN: 0800-3416 (print)
ISSN: 2387-3515 (online)

Grading: Open

Title: Ramså Basin, Northern Norway: an integrated study,

Authors:
M. Brönner, T.A. Johansen, V. Baranwal, A. Črne, B. Davidsen, H. Elvebakk, A. Engvik, T. Forthun, J. Gellein, T. Henningsen, O. Lutro, A. Margreth, P. Midbøe, B.O. Ruud, H. Rueslåtten, A. Ryseth, J.S. Rønning, H. Schiellerup, J. Schöneberger, M. Smelror, E. Tveten

Client:
AkerBP, Lundin Norway, NGU, Mærsk Oil, Statoil, Wintershall Norge and NPD

County:
Nordland

Commune:
Andenes

Map-sheet name (M=1:250.000)
Andøya

Map-sheet no. and -name (M=1:50.000)

Deposit name and grid-reference:
WGS 84 UTM 33

Number of pages: 290 **Price (NOK): 2000,-**
Map enclosures:

Fieldwork carried out:	Date of report:	Project no.:	Person responsible:
2012, 2013, 2014, 2015, 2016	31.08.2017	346800	Tom Arne Rydland

Summary:

The Ramså Basin in the northeast of the island of Andøya combines both a Mesozoic sedimentary succession and a subjacent deeply weathered basement. The basin must be considered as the only easily accessible analogue for the setting and development of the offshore Mesozoic basins. The aim of this study was first of all to study deep weathering and gain additional knowledge about weathering processes and the settings of weathering products underneath sedimentary strata potentially underlying the sedimentary basins on the Norwegian shelf and to develop a methodology to image these deep weathering remains with geophysics. Secondly, the delineation of structural geometries, depth-to-basement and fracture and fault systems of the Ramså Basin and the adjacent Andfjorden can provide important information about the tectonic evolution of the region and the development of the margin as an important link between the south-western Barents Sea and the Norwegian Sea. For this purpose, airborne and ground geophysical data were acquired for a comprehensive onshore-offshore study. Airborne gravity, magnetic and EM data were used to delineate the Ramså Basin extension and identified different basement domains and tectonic elements onshore and for the adjacent Andfjorden as well as additional sub-basins or a basin extension south of the Ramså Basin. Onshore and offshore seismic data secured structural information, which were interpreted jointly with the airborne data to derive a tectonic evolution model for the area. Bedrock mapping onshore Andøya, as part of the MINN project, and four new core drillings contributed to an updated bedrock map for northern Andøya. Geochemical and mineralogical analyses of samples from new and existing core material and from the surface revealed the weathering to be much less extensive than expected and disclosed a hardly observable weathering type, which to a large extent resemble the petrophysical parameters of compacted sediments or even basement.

Keywords:	Geology	Geophysics
Mapping	Analytical methods	Scientific report
Minerology	Geochemistry	

Content

1. INTRODUCTION

Marco Brönner

The Lofoten-Vesterålen area represents the narrowest part of the Norwegian shelf and is situated in the transition zone between the Mid-Norwegian passive continental margin and the sheared southwestern Barents Sea margin. The eventful past of the Norwegian margin with continent collision and thrusting in the Silurian/Devonian and subsequent extension and final continental breakup during the Eocene is still a matter of discussion.

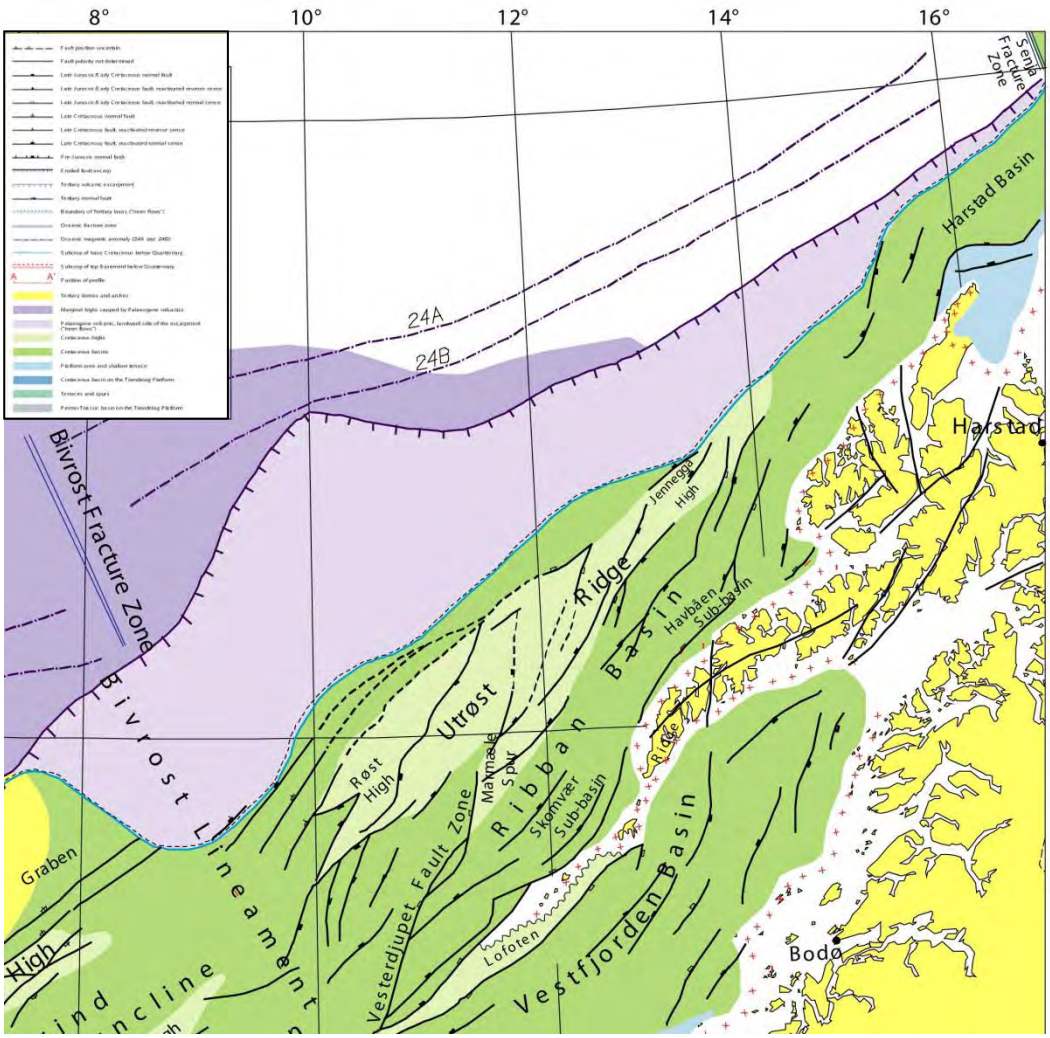

Figure 1.1 Structural element map of the Lofoten-Vesterålen segment of the Norwegian passive continental margin. Modified after Blystad et al. (1995).

The region constitutes a key area in the face of the varying tectonic conditions and the structural development of the continental margin. It is characterised by a complex system of uplifted and rotated basement blocks, where the various islands represent the exposed part of a basement high, which is well adapted to study both tectonic evolution and deep weathering as an analogue for different basement highs offshore on the Norwegian shelf.

The islands are flanked by a network of steep faults, where deep Mesozoic basins still exist offshore between the islands and the mainland but the structural settings are barely understood. Various basement types and a noticeable variation in crustal thickness within a relatively small area reflect the genesis of the Norwegian continental margin between 66° N and 71° N.

Andøya is the northernmost island of the Lofoten-Vesterålen archipelago and the Ramså Basin in the northeast of the island combines both a Mesozoic sedimentary succession and a subjacent by deeply weathered basement. The basin must be considered as the only easily accessible analogue for the setting and development of the offshore Mesozoic basins. The Mesozoic basin of Ramså has been the object of geological investigations since its discovery at the end of the 19th century. Coal mining and hydrocarbon potentials attracted the attention of both geologists and industry to this little field and resulted in a number of intensive geological studies including shallow drillings (Friis 1903, Vogt 1905) and four deep wells, drilled by Norminol in 1972 and 1973 to explore for hydrocarbons and investigate the underlying basement. The surface observations and local depth profiles from wells and refraction seismic profiling were used to map the basin's lateral extensions and to interpret its structural settings and historical evolution (Dalland 1975, 1973, Sturt et al. 1979).

Geophysical observations, however, were lacking in the very early years and consequently a detailed picture of the structures and geometries within the sedimentary succession was missing and the tectonic history consequently remained unsure. Furthermore very little is known about the adjacent Andfjorden and its impact for the development of the Harstad and Tromsø basins.

More recently, from well cores, resistivity profiling (Brönner et al. 2012) and surface observations in and around the Ramså Basin, fractured basement and deep weathering have been recorded and might indicate a significant impact of these phenomenon also for large parts of the Norwegian shelf. Consequently a better knowledge of these features and the evolution of the deep basins is therefore crucial to better understand and possibly map deep weathering on the Norwegian continental shelf.

As a particular challenge, the Fennoscandian Shield was exposed to several ice ages and significant glaciations, where almost the entire sedimentary strata and most likely large amounts of deeply weathered basement were eroded and at least partly deposited on the Norwegian shelf. The onshore weathering remains, as known so far, are mainly observed in joints and fractures, but at a few locations –especially in Nordland– we can observe tens of metres of deeply weathered bedrock with a noticeable lateral extent, indicating possible thick or formerly thick layers with weathered material, originally overlain by Mesozoic sediments. Observations from other parts of the world like Ukraine and Australia confirm the existence of thick layers of weathered material and demonstrate the potential for possible mineral and HC exploration, which might also apply for Norway. Recent reservoir findings on the Norwegian shelf in or/and in the vicinity of deeply weathered basement confirm the direct link and also the importance of this phenomenon for the Norwegian shelf. Furthermore, the

existence of deep weathering in joints and fractures has an important impact for various construction projects onshore Norway and along the Norwegian coast.

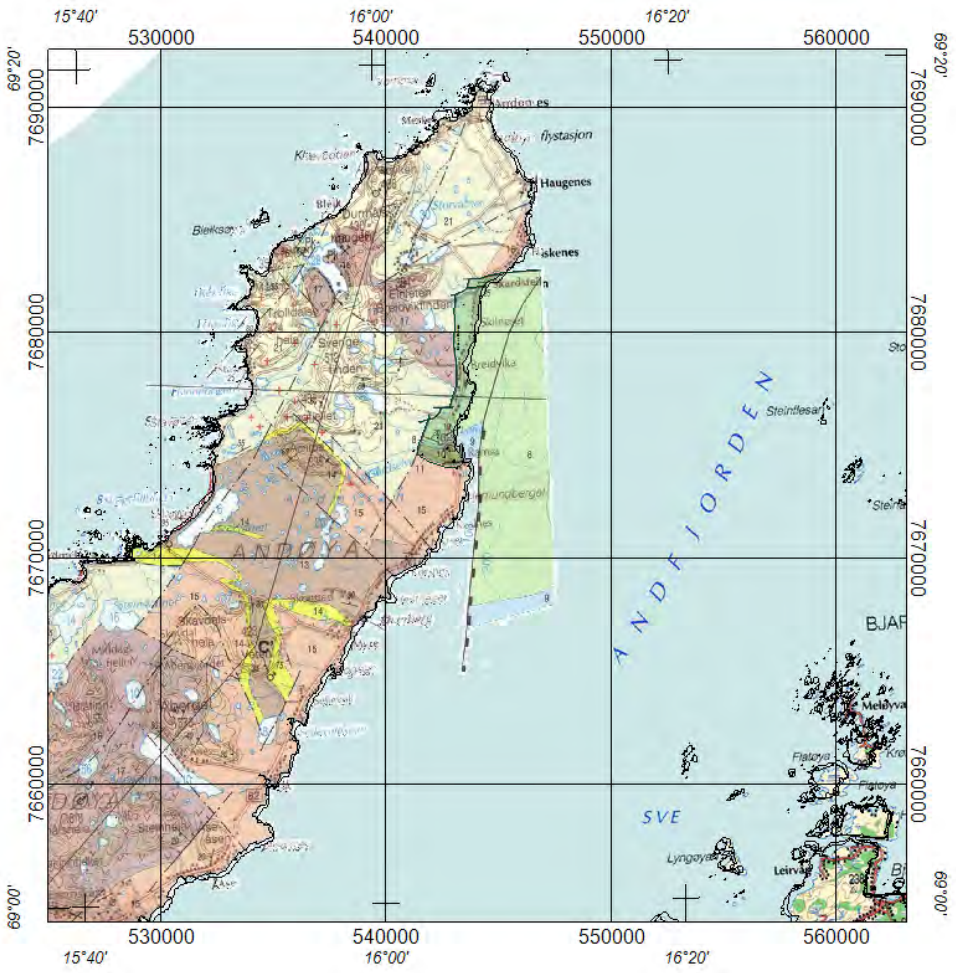

Figure 1.2. Geological map of Andøya (Henningsen & Tveten, 1998) with the Ramså Basin in the east, the only known Mesozoic sedimentary basin onshore Norway.

This research project addresses some of the questions concerning deep weathering on- and offshore Norway and has the prime aim to map deep weathering and attempt to correlate tectonic events and weathering. The Ramså area on Andøya, northern Norway, with a small Mesozoic basin and a c. 30 m wide zone with exposed deeply weathered basement can be considered as an easily accessible analogue for the development of the Lofoten-Vesterålen margin with a potential to demonstrate the interaction between weathered and unweathered basement rocks and structures and the overlying sedimentary succession.

The delineation of structural geometries, depth-to-basement and fracture and fault systems of the Ramså Basin and the adjacent Andfjorden can provide important information to gain a better knowledge of paleo-stress regimes and the uplift and erosion history of the region through time. It is of importance to understand and determine whether the finds of weathering remains are just limited to joints and fractures as observed onshore or if there exist possibly continuous layers of saprolite?

2. AN INTRODUCTION TO THE RAMSÅ BASIN

Peter Midbøe

2.1 Location

Mesozoic rocks of Mid Jurassic to Early Cretaceous age are preserved in downfaulted blocks on land on the island Andøya, northern Norway. The area containing Mesozoic sediments covers about 10 km^2 along the northeastern coast of Andøya, and represents the western margin of the Andfjorden sedimentary basin (Andfjorden Graben). The basin continues to the north into the Harstad Basin. The Jurassic-Cretaceous sedimentary succession onshore occurs within a flat coastal plain area (strandflat), and is generally covered by peat swamps, beach ridges and Quaternary moraine. The exposures are small, and are restricted mainly along the Ramså river (Gårdselva) and to the shoreline immediately north of the river mouth (Figure 2.1). Black Cretaceous shales belonging to the Nordelva Member are exposed in the lower part of Nordelva and a few minor exposures along the beach just south of Skarstein. The quality of all the exposures along the beach may vary seasonally due to movement of beach sand, and are not accessible during high tide.

Figure 2.1. Exposed Mesozoic sedimentary rocks on the beach in Ramså with a view to the north. Most of the basin is covered by Quaternary sands and/or peat. Mesozoic exposures on the beach are mostly only accessible at low tide (photo by P. Midbøe).

These sediments are the youngest onshore exposures of sedimentary rocks in Norway. The sediments are associated with a structural fault system of half-grabens stretching from the offshore area eastward into the mainland. The easternmost known sediment fill in these basins lies in the recently discovered Sortlandssundet Basin. This basin was located by shallow seismic following the discovery of Mesozoic erratic blocks along the Sortlanssundet in the summer 2000 (Davidsen et al. 2001a).

The Andøya succession shows structural and lithological similarities to the time-equivalent sections in East Greenland and in the offshore Lofoten/Vesterålen area where IKU has carried out shallow drilling projects (Hansen et al. 1991).

The limited thickness of the Mesozoic succession on Andøya indicates a very marginal position compared to the central Upper Jurassic-Lower Cretaceous sedimentary basin.

2.2 **Exploration history**

The existence of the Mesozoic field of Andøya was first detected by Tellef Dahll in 1867 when he investigated an outcrop of coal on the island, previous known to, and on a moderate scale also utilised, by the local farmers (Dahll 1891). Fossil plants were described as early as 1877 (Heer 1877), but it was the occurrence of Jurassic coal seams that attracted serious geological exploration by means of boreholes in 1869-1873 and in the 1890s'. Data from this prospecting and from limited shore and river bed exposures were put together by Friis (1903) and Vogt (1905) to produce the first fundamental account of stratigraphy and structure of the Ramså field.

During the following years fossils were collected on various occasions, and of these, the invertibrates were dealt with especially by Sokolov (1912) and the plants by Johansson (1920) and Bose (1960). Syntheses that draw upon all this work and new investigations were published by Øvrig (1953, 1960). Manum (1968) later added another plant species to the record.

The University of Bergen started geological and geophysical investigations on the island in 1969 (Dalland 1979). Refraction seismic, gravimetric and magnetic measurements were performed. Extensive excavations were carried out to establish a continuous geological section across the greater part of the Jurassic sequence in the southern part of the basin (Dalland et al. 1973, Dalland 1975).

Arne Dalland carried out extensive fieldwork during the summer season in 1969, 1970 and 1971. His detailed lithological results (Dalland 1974, unpublished thesis) were published in summary in 1975 and followed up with two further publications (Dalland 1979, 1981). Palaeontological material sampled during this work was studied by Vigran & Thusu (1975) and Birkelund et al. (1978).

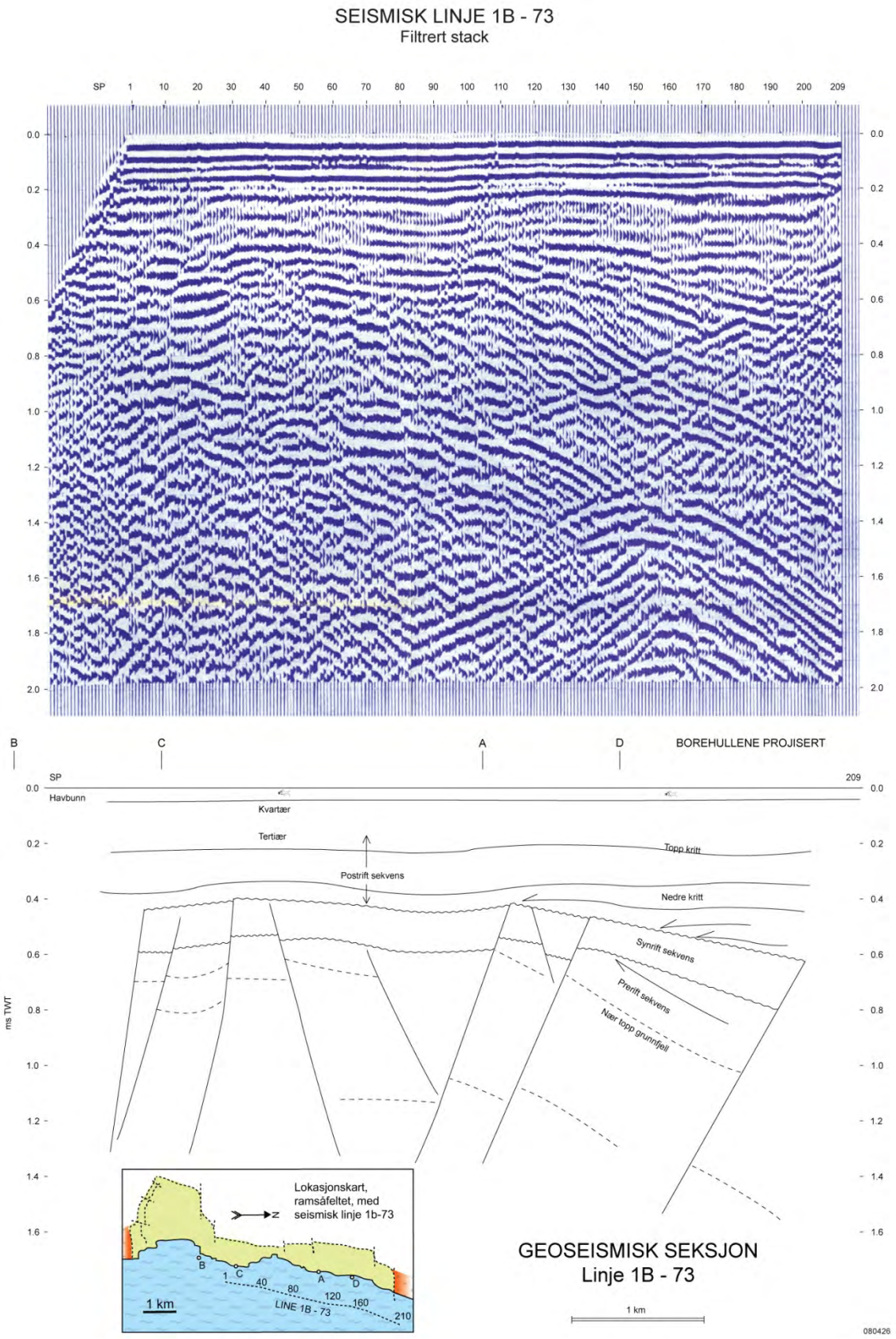

Figure 2.2. Seismic line 1B-73, acquired and processed by Geco offshore the Ramså Basin. The interpretation shows a north-dipping rotated block with possibly onlapping Cretaceous sediments.

Four shallow wells were drilled during the years 1972-1974 by the Andenes based oil company Norminol. The drilling was partly based on the result of four seismic refraction lines shot by Geoteam in 1971/1972 and one single reflection seismic line acquired by Geco in 1973 (line B1-73). This 5,5 km line was shot in shallow water offshore (0,5 – 1 km) the coast of the Ramså field with a 1200 m cable, 4 air guns and digital recording. The data received from this drilling contributed with new information that to some extent modified our geological understanding of Andøya.

The wells A, B and C were continuously cored (3.5 cm diameter) down to TD at 530 m, 527 m and 238 m, respectively, and were logged with the slim hole tools of Terratest AB of Sweden (natural radioactivity, seismic velocity, magnetic intensity and self potential). The cores were described lithologically and various analyses of the core material (palynology, porosity, source potential, etc.) from the wells were carried out.

Figure 2.3. Drilling rigg for well D in Skarstein in 1974.

Well D, however, was drilled with a conventional oil rig (Figure 2.3). The well was drilled with a 6 3/4 inch bit down to TD at 836 m. Cutting descriptions were carried out by Exploration Logging, and Schlumberger performed a full log suite from 350 m to TD.

In 1984, Norminol offered a data package with all the information from the drilling activity for sale to oil companies.

Based on these data, well D was dated by Stratlab exdusively for Norsk Hydro (Bell 1985) and a completion log was constructed (Rasmussen 1985) from 350 m to TD.

Based on well data, the lower part of the Andøya sequence was interpreted to onlap the basement to the north. This was based on the fact that the Ramså Formation is missing in well D and the well going directly into basement from the Dragneset Formation (Taumhølet Member). Recent investigation of the core from the bottom of Well D, however, indicates that the well was terminated in a rock containing large basement clasts and more stratigraphy (300+ m?) remains undrilled in this position. From interpretation of the seismic line B1-73 it can be seen that the basin deepens to the north and an estimated thickness of Mesozoic sediments in the Ramså Basin of around 1500 m is likely (Figure 2.2).

In 1986, Norminol A/S and READ Production Geology Services A/S established an agreement to jointly offer a reorganised and interpreted data package based on cores and logs from the 4 wells (READ 1987).

Since this time little work has been carried out before the inception of this project.

3. GEOLOGY

Tore Forthun, Peter Midbøe & Marco Brönner

The Lofoten-Vesterålen margin extends over a distance of c. 400 km from the Senja Fracture Zone in the north to the Bivrost Fracture Zone in the south (Figure 1.1). It is dominated by the Lofoten-Vesterålen archipelago, a NNE-SSW and NE-SW-oriented basement high (Åm 1975, Blystad et al. 1995, Løseth & Tveten 1996, Olesen et al. 1997, Tsikalas et al. 2001), which is situated between 67°24'N and 69°20'N latitude at the narrowest part of the Norwegian continental shelf. The basement onshore the Lofoten-Vesterålen islands is dominated by Palaeoproterozoic and Archaean polymetamorphic migmatitic gneisses and intrusions of mangeritic to charnockitic composition (Figure 3.1, Heier & Compston 1969).

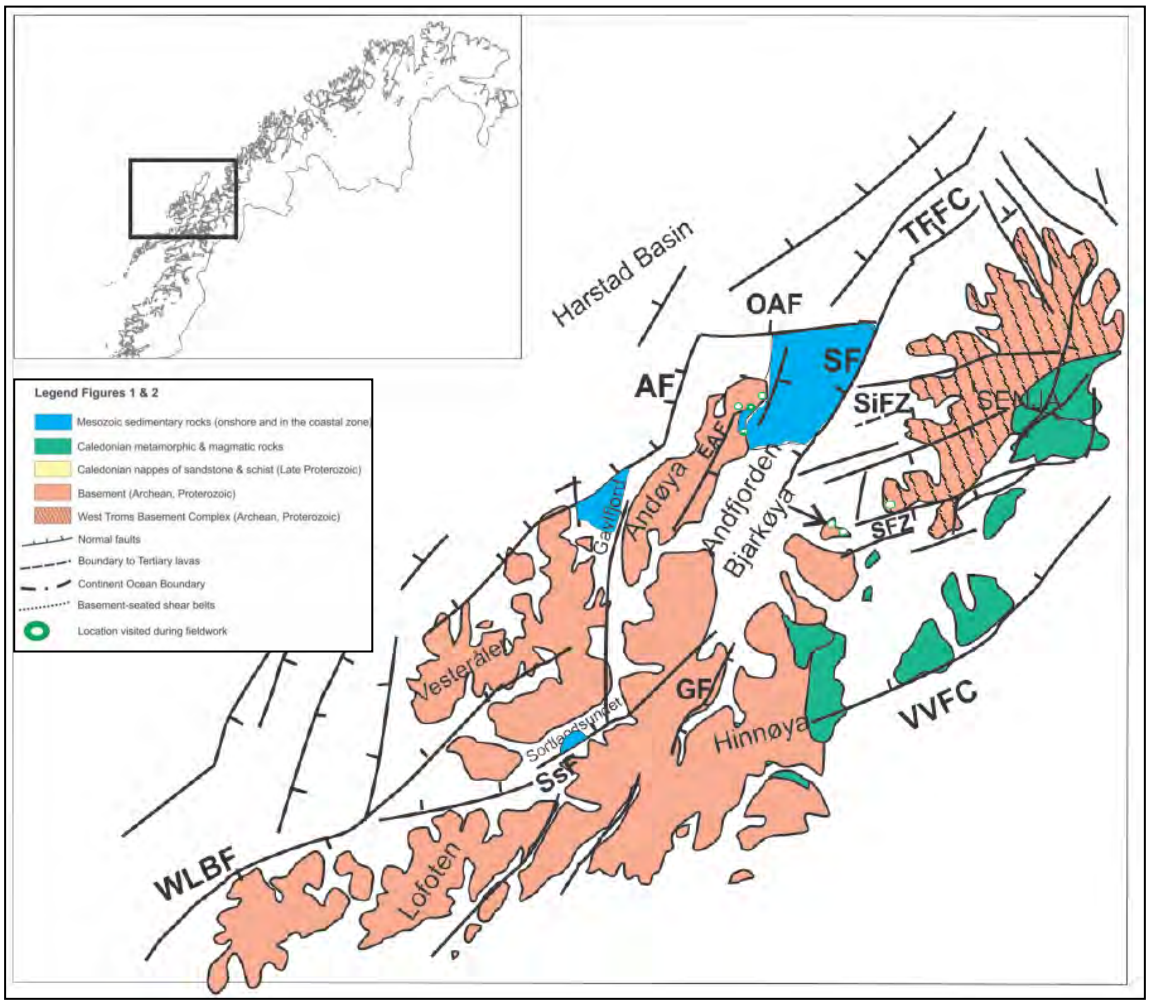

Figure 3.1. Simplified geological and structural map of the study area showing Precambrian basement rocks, Caledonian nappes and Mesozoic sedimentary rocks. From Forthun, (2014), modified after Indrevær et al. (2014). AF = Andøya fault, SF = Senja fault, AB = Andfjorden basin, SFZ = Stonglandseidet Fault Zone, EAF = East Andøya Fault Zone, SiFZ = Sifjorden fault zone, ELBF = East Lofoten Border Fault SsF = Sortlandsundet fault, GF = Gullesfjorden Fault, TFFC = Troms-Finnmark Fault Complex, HB = Harstad Basin, VVFC = Vestfjorden-Vanna Fault Complex, OAF = Outer Andfjorden fault, WLBF = West Lofoten Border Fault

The landscape of Lofoten-Vesterålen reflects the complex tectonic history of the area, which is mainly characterised by normal faulting, extensional structures and block-wise vertical movements (Griffin et al. 1978, Peulvast 1986), which were particularly active during Mesozoic and Cenozoic times (Løseth & Tveten 1996, Hendriks et al. 2010). Rotated and tilted fault-bounded blocks form a diversified landscape which shows both an alpine-type morphology with mountainous ridges and steep cliffs rising up from sea level to more than 1200 m (west Hinnøya, Moskenesøya) and paleic surfaces of smooth hill shapes (Langøya), wide valleys (Vestvågøya) and extensive strandflats at sea level. Peulvast (1986) described the main morphostructural features as NE-SW-oriented "*mountains or plateau ridges* a*rranged 'en echelon' between longitudinal fjords, sounds and basins',* which are cross-cut by "*oblique or perpendicular features',* splitting the islands into smaller blocks.

Fault structures mapped offshore are in principal orientated NNE-SSW to NE-SW, with a few in NNW-SSE to NW-SE orientations referred to as transfer zones to give lateral segmentation (Eldholm et al. 1979, Mokhtari & Pegrum 1992, Myhre et al. 1992, Løseth & Tveten 1996, Olesen et al. 1997, 2002, Tsikalas et al. 2001, 2005, Wilson et al. 2006) and are in good correlation with a fault and thrust system onshore Lofoten (Bergh et al. 2007). However, the evolution of the margin is still debated and various models have been proposed (Wilson et al., 2006, Bergh et al. 2007, Davids et al. 2010, Eig & Bergh, 2011, Hansen & Bergh, 2012; Hansen et al. 2012). Wilson et al. (2006) proposed a different model, where the margin is segmented in distinct domains, each domain deforming differently with regard to an extension direction constantly oriented WNW-ESE. Plate reconstructions by Mosar et al. (2002) indicate that the regional extension direction changed from WNW-ESE to NW-SE during the Late Cretaceous, and the latest Cretaceous to Palaeogene oblique-normal to strike-slip fault zones are interpreted to reflect NW-SE trending extension (e.g. Bergh et al. 2007, Hansen et al. 2012).

From the indirect timing of sedimentary strata and faulting events in offshore basins, Eig (2008) believed that the main fault patterns formed during three discrete tectonic events. The first took place in the Permian-Jurassic and was responsible for the development of the right-stepping *en échelon*, NNE-SSW-trending faults due to WNW-ESE orthogonal extension. A shift in the extension direction from WNW-ESE to NNW-SSE was supposed to have occurred in the Mid/Late Jurassic-Early Cretaceous, in order to enable the development of the ENE-WSW striking faults. Hansen & Bergh (2012), however, argued for simultaneous formation of the ENE-WSW and NNE-SSW trending faults. The ENE-WSW-striking faults potentially acted as sinistral strike-slip soft- and hard-linked transfer faults to the NNE-SSW-striking faults, resulting in the zigzag pattern described by Bergh et al. (2007). The fault-segment linkage also caused the development of major boundary faults, establishing the Lofoten Ridge as a prominent structural element at this time (Hansen et al. 2012).

The timing and nature of the uplift and exhumation of the basement ridges in Lofoten, Vesterålen, Andøya and western Troms is still much debated (cf. Olesen et al. 1997, Mosar et al. 2002, Eig, 2008, Hendriks et al. 2010, Osmundsen et al. 2010, Redfield & Osmundsen,

2013, Indrevær et al. 2014). Various causes of uplift have been proposed, e.g. rapid switches in the regional strain and stress fields (Bergh et al. 2007, Eig et al. 2008), stress perturbations within transfer zones (Eig & Bergh, 2011), passive margin exhumation due to NW-SE directed ridge-push forces (cf. Grønlie et al. 1991, Doré et al. 2002, Gabrielsen et al. 2002, Mosar et al. 2002) and asthenospheric diapiric rise due to emplacement of the Iceland Plume and later climate deterioration with increased erosion (e.g. Rohrman & van der Beek, 1996, Nielsen et al. 2002, Pascal & Olesen, 2009). Recent work has suggested that the nature of the uplift has been controlled by the hyper-extended character of the Norwegian passive margin (Osmundsen & Redfield, 2011, Redfield & Osmundsen, 2013). The contrast in geometry between the listric Troms-Finnmark Fault Complex and the planar Vestfjorden-Vanna Fault Complex is believed to have resulted in the formation of a short-tapered, hyper-extended margin after final break-up in the Palaeocene/Eocene (c. 55 Ma), uplifting and exhuming the West Troms Basement Complex as a short-tapered margin due to unloading and crustal flexure with continued uplift and erosion to the present stage level (Indrevær et al. 2014).

The strandflat along the Norwegian coast was recently related to deep weathering and a Late Palaeozoic to Early Mesozoic weathering front (Olesen et al. 2013). From Hadseløya and Leknes (Vestvågøya) some of the most significant locations with deeply weathered basement remains onshore the Lofoten-Vesterålen archipelago have been reported (Paasche et al. 2006, Olesen et al. 2010) and underline the importance of this phenomenon for the development of the landscape here.

The islands are flanked by a system of deep Late Palaeozoic/Early Mesozoic grabens and half-grabens (Tsikalas et al. 2005, 2008, Olesen et al. 2003, Mjelde et al. 1993) which experienced major extensional phases during the Cretaceous to Tertiary. Two major graben or half-graben systems, the Vestfjorden and the Andfjorden, separate the Lofoten and Vesterålen islands from the mainland, whilst to the east the Ribban Basin with sub-basins isolates the Lofoten islands from the Utrøst Ridge. From the gravity, but even more so from the magnetic data the Utrøst Ridge has a similar shape as the Lofoten island chain running quite parallel to this outcropping basement high. The basement drilled on the Utrøst Ridge (6710/03-U-03) however, was of Caledonian age (Hansen et al. 1992, Børre Davidsen, pers. comm. 2008).

3.1 **Timing of faulting**

Timing of offshore fault activity can be indirectly dated from sedimentary successions in the basins (cf. Bergh et al. 2007). Mesozoic rifting on the Lofoten-Vesterålen Margin occurred during the Early Triassic, Mid/Late Jurassic (Bajocian to Volgian), Early Cretaceous (Valanginian to Albian) and latest Cretaceous to breakup (Campanian/Maastrichtian to Eocene) (Hansen et al. 2012). The timing of main fault activity in the Harstad Basin is more difficult to infer due to the quality of the seismic data and lack of geological information, but it would seem that the main fault activity ceased at the Jurassic/Cretaceous boundary in the south and in the Late Cretaceous farther north (Brekke & Riis, 1987). The Harstad Basin is

bordered to the east by the Troms-Finnmark Fault Complex, which is most likely an old (Precambrian?) zone of weakness that has been reactivated several times until the Eocene (Gabrielsen et al. 1990). It has been proposed that extensional faulting (in the basin) started in the Mid Jurassic and continued during a period of major subsidence in the Early Cretaceous and that renewed normal faulting, combined with inversion along some major faults, took place in the Late Cretaceous (Gabrielsen et al. 1990). As there is little published literature from the area, the timing of fault activity in the offshore Andfjorden basin remains even more equivocal. However, Late Jurassic - Early Cretaceous extension on the shelf has been correlated with contemporaneous faults on Andøya (Tsikalas et al. 2001).

Absolute dating of onshore brittle fault rocks in the area between Lofoten and Western Troms have been undertaken recently (Olesen et al. 1997, Hendriks, 2003, Davids et al. 2010, 2012a, 2012b, 2013, Hendriks et al. 2010, Steltenpohl et al. 2011). K-Ar illite ages (Davids et al. 2010, 2012a, 2012b, 2013), apatite fission-track analysis (AFT, Hendriks, 2003, Hendriks et al. 2010) and $^{40}Ar/^{39}Ar$ K-feldspar data (Steltenpohl et al. 2011) show a contrast in the timing of fault activity and exhumation between the Troms and Vesterålen regions. K-Ar illite data from fault gouge indicate that the onshore brittle faulting may have initiated as early as in the Devonian with faulting along both N-S and NE-SW-trending faults on Andøya and farther inland in Central Troms (Davids et al. 2013). Carboniferous rifting events have been demonstrated in the Nordkapp Basin northeast of Finnmark, which was simultaneous with the initiation of the offshore Troms-Finnmark Fault Complex that bounded the Hammerfest and Tromsø basins to the south (Davids et al. 2013). While faulting continued at least into the Cretaceous and possibly into the Cenozoic (Hendriks, 2003, Hendriks et al. 2010) in the Lofoten-Vesterålen part of the margin, major faulting on the onshore Troms margin appears to have ceased after the Permian faulting event. Most of the post-Permian rifting in northern Norway must therefore have occurred either offshore west of Troms or farther southwest onshore and offshore adjacent to the Lofoten-Vesterålen and Andøya basement horst (Davids et al. 2013).

On Andøya, Sturt et al. (1979) reported normal faults parallel to the East Andøya Fault Zone (trending NNE-SSW) in sedimentary rocks of Aptian age near Ramså. K-Ar dating of samples from semi-brittle/mylonitic fault zones in the weathering profile yielded Late Cretaceous-Early Cenozoic ages, while Dalland (1981) also inferred movement to have occurred in Mid Jurassic (Bajocian-Bathonian), Ryazanian and Turonian times. AFT ages from Andøya document the overall exhumation of the island to have occurred between 127 ±11 Ma and 142 ±14 Ma (Hendriks, 2003).

3.2 **Sedimentary deposits**

Mesozoic rocks occur in very near-shore positions in Andfjorden, Sortlandsundet between Langøya and Hinnøya and in Gavlfjorden between Andøya and Langøya (Davidsen et al. 2001, Figure 3.1), and in similar half-graben systems in fjords farther south (Bøe et al. 2010).

These rocks are interpreted to represent the remains of a much more extensive Jurassic-Cretaceous sedimentary succession that covered large parts of coastal Norway (Sturt et al. 1979, Bøe et al. 2010) prior to the Late Cenozoic to Quaternary uplift and erosion (Bøe et al. 2010).

The offshore basins are all bounded by normal faults and filled with predominantly Lower to Upper Cretaceous sedimentary rocks that are locally near 7 km in thickness (Bergh et al. 2007). Jurassic units have a constant thickness or increase in thickness when approaching the Vesterålen islands. Since no pronounced boundary faults seem to separate the offshore basins from onshore areas this indicates that large parts, if not all, of the now exposed and denudated basement rocks onshore Vesterålen were covered by Middle and Upper Jurassic sedimentary sequences (Hansen et al. 2012). This is supported by the preserved Mesozoic rift basin on Andøya (Dalland 1974, 1975, 1979, 1981), erratic blocks found in coastal areas (Fürsich & Thomsen, 2005), the presence of fault-bounded Mesozoic basins in shallow fjord areas in Vesterålen (Davidsen et al. 2001, Bøe et al. 2010) and inferred Mesozoic faults onshore (Sturt et al. 1979, Dalland 1981, Bartley, 1982, Løseth & Tveten 1996, Bergh et al. 2007). The Vesterålen margin thus could resemble the western flank of a graben that probably covered the entire islands of Vesterålen (Hansen et al. 2012).

Pre-Cretaceous (possibly Permo-Jurassic) sedimentary strata have also been identified offshore, in the Træna Basin and the Vestfjorden Basin, and they were also inferred to lie beneath the Cretaceous sequence in the Harstad Basin, located at 5 s TWT or more on seismic data (Brekke & Riis 1987). Palaeozoic and Early-Mid Mesozoic sedimentary rocks are also known from the Loppa High and Finnmark Platform (Gabrielsen et al. 1990) as well as the Wandel Sea basin in Northeast Greenland (cf. Stemmerik et al. 1998), which, according to paleogeographic reconstructions, was located near this study area before the development of the transform Barents Sea margin in the Cenozoic (Mosar et al. 2002)

3.3 **Ramså Basin**

The Ramså field is generally considered as two smaller deep basins separated by a WNW-ESE-striking gabbro dyke (Figure 3.2 and Figurea, Dalland et al. 1973, Ørvig, 1960), which is exposed west of the basin and buried by a relatively thin cover of Mid Cretaceous sedimentary rocks within the field. A N-S-trending well-correlation profile shows the internal structuring of the basin as interpreted by Rasmussen (1985) (Figure 3.2). The two sub-basins represent down-faulted blocks, where the northern one is bounded by sharp and steep faults to the surrounding exposed basement blocks in the north and west. The sedimentary rocks are likely located in a half-graben to the south and another graben to the north, separated by a gabbroic basement horst (Figure 3.2Figure 3.6). Exposed layers of Cretaceous sedimentary rocks show a southwards dip of more than 20 degrees (Dalland 1975), indicating a rotation of the submerged blocks. The southern basin, however, is thought to be a northward-tilted block with onlapping Mesozoic strata, dipping at c. 15 to 30 degrees.

The architecture and basin filling pattern is largely controlled by several normal faults dipping to the south and north (Dalland 1981). While the contact between sedimentary strata and crystalline basement rocks appears to be faulted in the north (Skarstein), a possible onlap is indicated in the south (Ramså) (Figure 3.6).

Here, the exposed units show older ages towards the south from Lower Cretaceous to Mid Jurassic sedimentary rocks consisting of shales, sandstones, claystones and Jurassic coal.

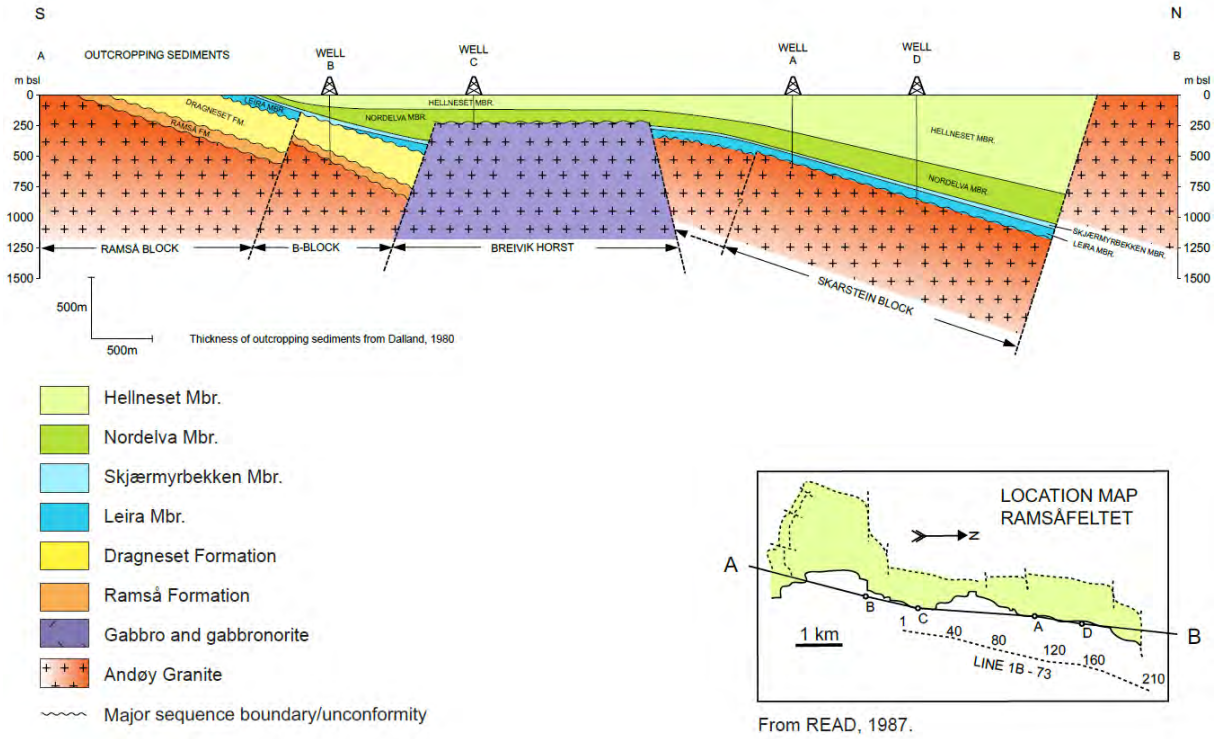

Figure 3.2. Structural cross-section through wells A, B, C, and D based on well logs shown in Figure 3.4 (from P. Midbøe 2013). The dip of the fault blocks towards north is illustrated, but these blocks also have dips towards the east.

The Jurassic to Upper Cretaceous sediments on Andøya occur in an up to c. 1km-wide and 4 km-long fault-bounded basin extending along part of the northeast coast of the island (Figure 3.4). The sediments rest unconformably on weathered basement, have an estimated total stratigraphic thickness, from well data and seismic data, of around 1500 m and define two major fining-upward sequences (Figure 3.3) of Bajocian/Bathonian to Ryazanian and Valanginian to Cenomanian age, respectively (Dalland et al. 1973, Dalland 1975, 1981, Bell 1985).

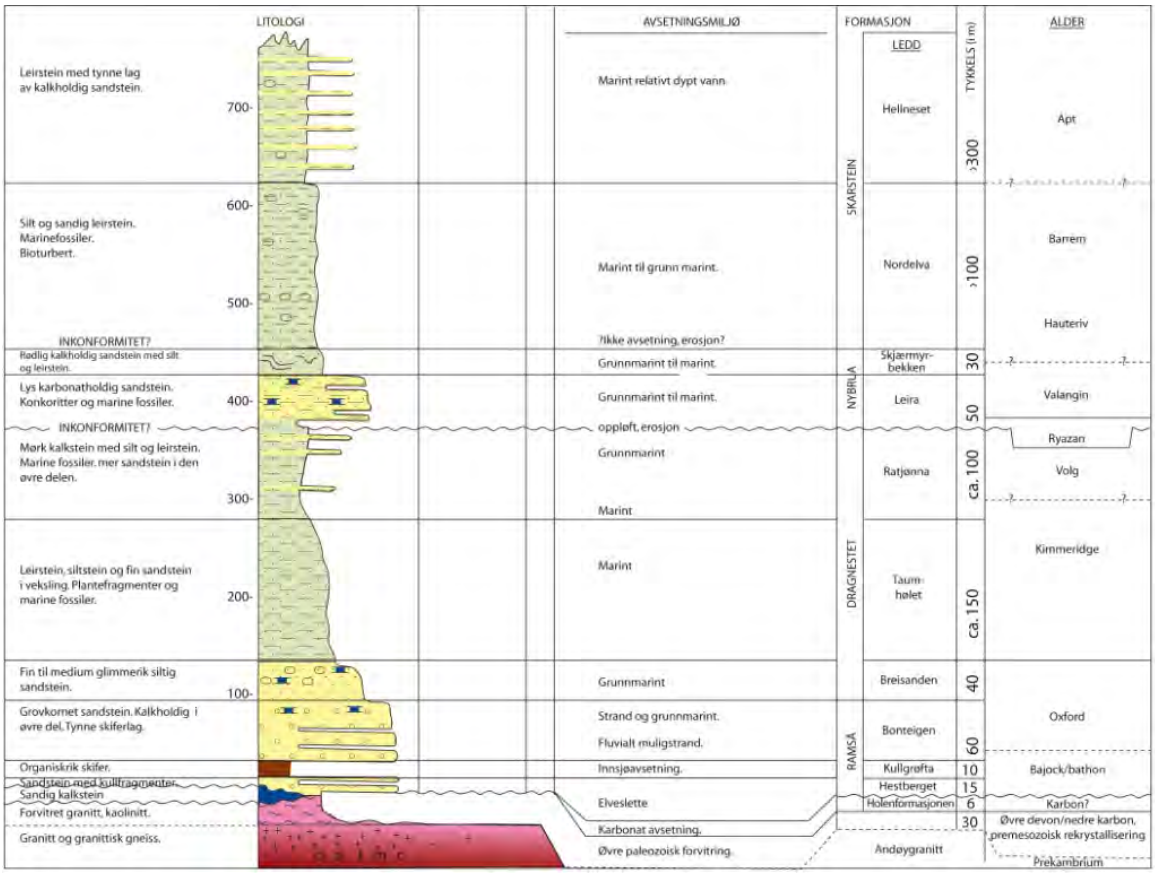

Figure 3.3. Stratigraphy of the Ramså Basin, Andøya (after Dalland et al. 1981)

The lower fining-upwards sequence comprise Mid Jurassic non-marine sediments of the Ramså Formation which grade upwards into Upper Jurassic marginal marine and marine sediments belonging to the Dragneset Formation. The younger fining-upward sequence consists of a lower shallow-marine unit of Ryazanian to Hauterivian and Cenomanian age (Bell 1985), the Skarstein Formation (Dalland 1975, 1981). The two fining-upward sequences are separated by an unconformity (BCU) of probable Ryazanian age coursed by Late Kimmerian/Volgian tectonic activity (rift climax).

The lowermost Ramså Formation is about 100 m thick and was deposited on a weathered surface of granitic basement rocks and basic dykes in a terrain with some topography. The deep tropical weathering profile present below the Mesozoic sediments has been dated by palynomorphs to be of Upper Triassic – Lower Jurassic age (J. Os-Vigran pers. comm. to Rasmussen 1985) but also Late Palaeozoic ages were occured from K-Ar dating (Sturt et al. 1979).

The Ramså Formation shows an overall transgressive trend starting in the Bajocian with deposition of continental fluvial coarse-grained sandstones interbedded with coal layers and organic-rich shales. The upper part consists of medium-grained sandstones of Bathonian to Oxfordian age deposited in a shallow-marine environment (Dalland 1981).

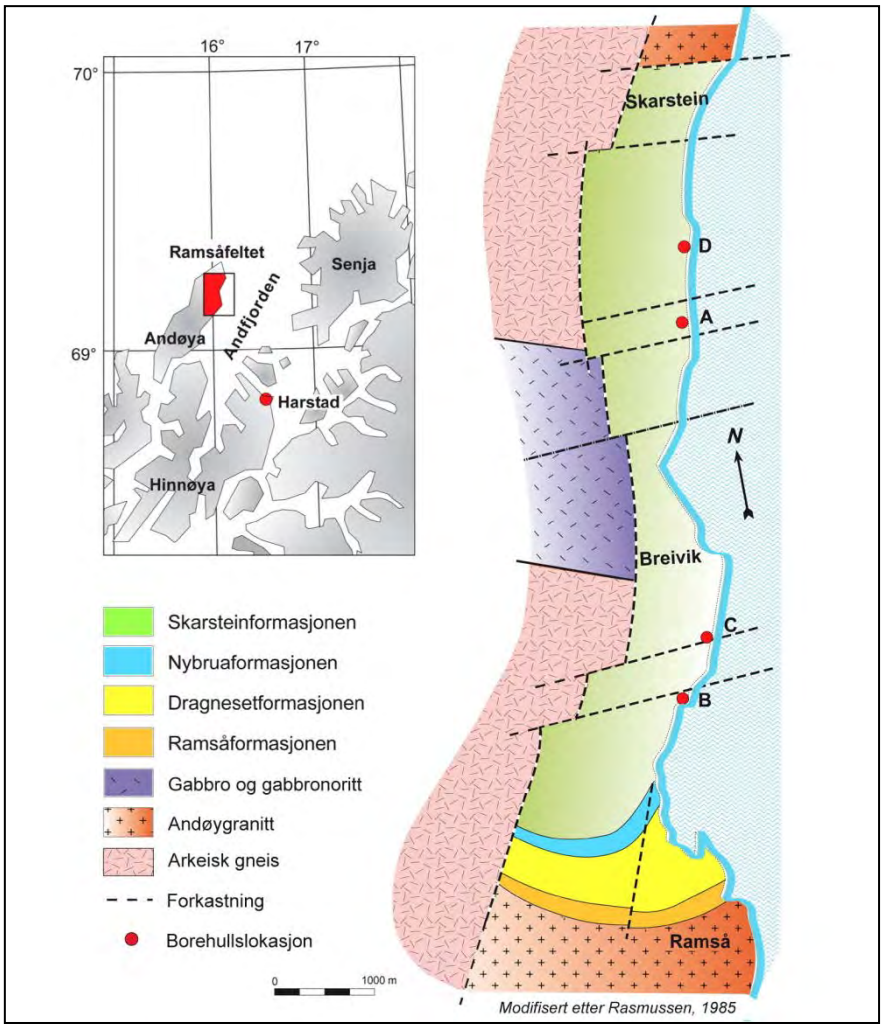

Figure 3.4. Schematic geological map of the Ramså Basin (after Rasmussen 1985, from Midbøe 2013)

The Ramså Formation is subdivided into three members. The basal Hestberget Member is 15 m thick and comprises fluvial sandstones with subordinate shales and coals whereas the overlying Kullgrøfta Member is 10 m in thickness and is dominated by bituminous shale thought to be a lake or lagoonal deposit. The uppermost up to 60 m Bonteigen Member comprises point-bar sandstones with a few layers of shaly micaceous siltstone and thin bituminous shales and coals in its lower part, whereas the upper part comprises calcareous beach and shallow-marine sandstones (Dalland 1975, 1981).

The Upper Jurassic Dragneset Formation is approximately 290 m thick. Its lower member, the 40 m-thick Breisanden Member, comprises mainly fine to medium-grained micaceous sandstones with interspersed calcite concretions and common marine fossils. The overlying Taumhølet Member is around 150 m thick and comrprises fine-grained micaceous sandstones with some marine fossils and plant remains plus more silty and shaly beds. The uppermost member of the Dragneset Formation, the Ratjønna Member, has a thickness of approximately 100m and consists of siltstones and shales with common marine fossils and plant remains. Dalland (1975, 1981) interprets the Dragneset Formation as a shallow-marine unit deposited in a gradually deepening marine basin and its very rapid sedimentation rate reflects deposition

during the rift climax with a regional high waterstand and proximity to the provenance area of the sediments.

The Nybrua Formation rests unconformably on the Dragneset Formation and has given a Valanginian age (Birkelund et. al. 1978, Løfaldli et. al. 1979). The formation's thickness is approximately 80 m, with a lower 50 m-thick Leira Member made up of calcareous sandstone, siltstone and marl containing abundant marine fossils, and an upper 30 m-thick Skjermyrbekken Member comprising red and slightly calcareous siltstones with numerous marine fossils. Dalland (1975, 1981) considered the Nybrua Formation to have been deposited in a shallow marine environment around and below wave base and the deposition of the formation is probably related to the Early Cretaceous regional subsidence and sea-level rise during the late rift stage in Valaginian time.

The Skarstein Formation is by far the thickest unit on Andøya reaching a thickness of 720 m in well D. The 100 m-thick lower Nordelva Member of Hauterivian – Barremian age (Bell 1985) consists of bioturbated silty and sandy mudstone with sideritic concretions. The overlying Hellneset Member with a minimum thickness of 550 m is dated as Lower Aptian to upper Cenomanian (Bell 1985) and consists of mudstones and shales with numerous thin beds of calcareous sandstone and a few sideritic concretions. Both members contain marine fossils such as ammonites, belemnites and bivalves.

The deposition of the Skarstein Formation signals a change to a quiet tectonic regime with rapid subsidence and deposition of open marine shales with thin dolomitic stringers and turbiditic sands deposited in intermediate and deep-marine settings.

A thick package of Cretaceous sediments (more than 3 km based on geochemical maturation studies and sonic velocities) was probably deposited in the Andøya area before the onset of faulting and erosion in Late Cretaceous – Paleocene time.

The transition to the bedrock at the southern rim of the Ramså Basin marks a c. 30 m wide zone with weathered basement (Sturt et al. 1979), which is locally exposed along the Gårdselv River and is apparently underlying the Mid Jurassic unit. Friis (1903) published the well cores, drilled at the end of the 19th century where he described a greenschist unit in the deeper wells which rests on top of the basement. His description with the greenish colour and high mica content, appears similar to what is observed at the surface as weathered basement and indicates a continuation of weathered basement underneath the Mesozoic sedimentary rocks to the north although with a significantly smaller thickness of 2-3 m which pinches out until it is no longer observed farther north. The mineralogy of the exposed or near-surface weathered basement was already studied by Dalland et al. (1974) and revisited during this study (Chapter 10) with focus on the origin and development. Dalland (1974, 1975, 1979, 1981) also observed an enigmatic sandy limestone layer, which rests on top of the basement and was introduced as the Holen Formation. The Holen Formation consists of an up to 6 metres thick sandy limestone that has not been observed in outcrop, but is known from boreholes I, II and V (cf. Friis 1903, Dalland 1974; Dalland 1981, Aslagsen 1981). Its age depends on the

disputed age of the deep weathering. K/Ar dating of the weathering profile indicate that weathering occurred in the Late Palaeozoic (Sturt et al. 1979), but this has also been correlated to Jurassic weathering profiles offshore (Smelror et al., 2001). The Holen Formation may thus represent either the lowermost unit of the Mesozoic succession (Dalland 1974, Smelror et al. 2001) or the last remnants of a previously very thick Palaeozoic sedimentary cover that was uplifted and eroded in the Triassic (Sturt et al. 1979, Dalland, 1981, Manum et al. 1991). This unit has also been suggested to belong to the basement rocks (Vogt 1905). The total thickness of the *confirmed* Mesozoic succession is more than 500 metres consisting of two major fining-upwards sequences: (i) A lower unit of Middle Jurassic (Bajocian/Bathonian-Ryazanian) non-marine sedimentary rocks that gradually grade into marine deposits, which again are truncated by an unconformity or a hiatus, and (ii) a Lower Cretaceous fining-upward sequence grading from shallow to deep-marine facies upwards in the stratigraphy (Dalland 1974, 1975, 1979, 1981). On a larger scale, the basin sequence is bounded by NNE-SSW-striking faults that probably follow lines of weakness from, e.g., older brittle faults of Late Palaeozoic to Mesozoic age (Dalland 1975). On the landward side, this basin succession is believed to be separated from the crystalline basement by the East Andøya Fault Zone (Løseth & Tveten, 1996; Henningsen & Tveten 1998, Figure 3.1) but maps from high-resolution magnetic data do not confirm the presence of such a fault, and rather indicate an onlap sequence on basement rocks to the west and south, along with sedimentary rocks farther inland (Brönner et al. 2008).

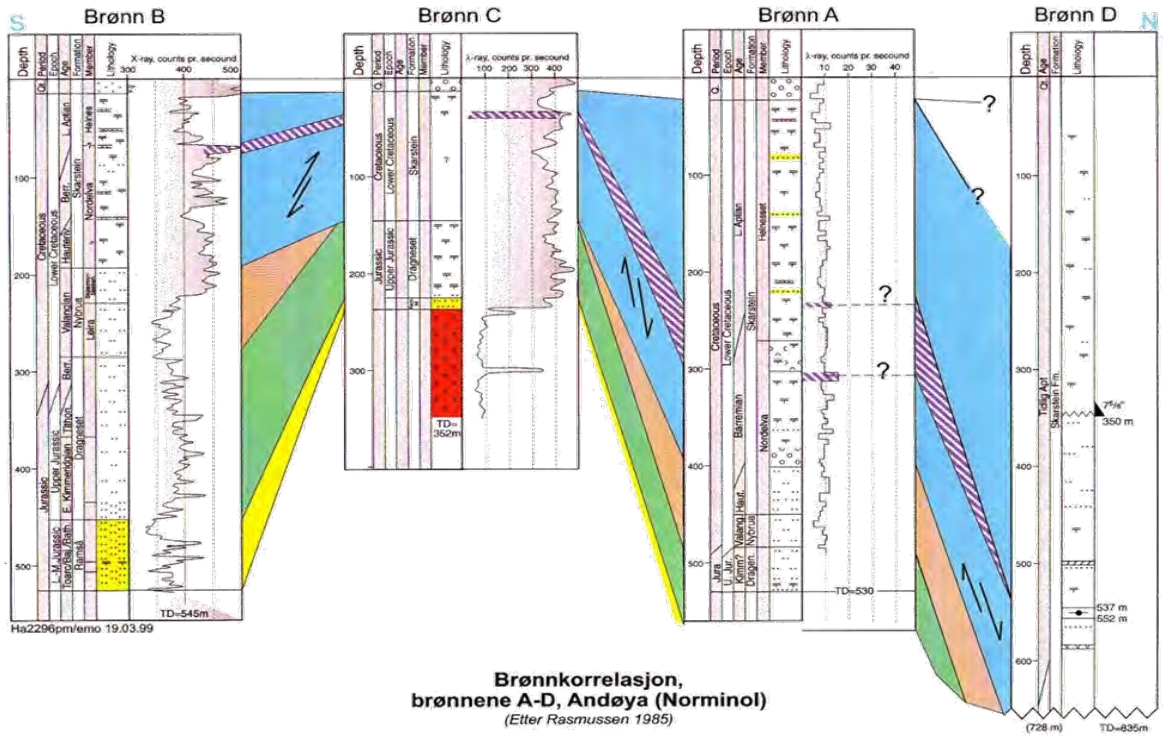

Figure 3.5. Stratigraphy and well logs for the four wells drilled by Norminol in the early 1970's, numbered A, B, C, and D (see Figure 3.4 for locations) (from P. Midbøe 2013).

Little information has been published from the offshore Andfjorden basin, but it is believed to be a downfaulted graben representing the continuation of the basin onshore and likely reflects the same tectonic and depositional events (Dalland 1981). It is bounded by the NNE-SSW-striking Senja fault in the east (Zwaan & Grogan 1998; Tsikalas et al. 2001, Hansen et al. 2012) and is believed to continue into the deep Harstad Basin to the north (Dalland 1981, Henningsen & Tveten 1998, Zwaan & Grogan 1998). This is also supported by lithostratigraphic correlations between Nordland VII, Andøya and Troms III (Smelror et al. 2001, Bøe et al. 2010). No data on the kinematic history of the Ramså and Andfjorden basins have yet been published, but is it likely that the kinematics reflect those depicted from nearby areas and the shelf as a whole.

Apart from the split of the basin into northern and southern sub-basins by the gabbro horst, Vogt (1903) and Dalland (1975) introduced a c. N-S-striking segmentation, which appears to have a strike-slip character and horizontal displacement. The suggested faults are parallel to the strike of the Ramså Basin and sub-parallel to a major fault, which is exposed at a mountain slope in Skarstein and indicates also an E-W structural segmentation of the basin. North and south of the basin along the coast, faulting is observed with a striking NE-SW, which is in good correlation with the direction of faults introduced by Dalland (1975) along the western boundary of the Ramså Basin.

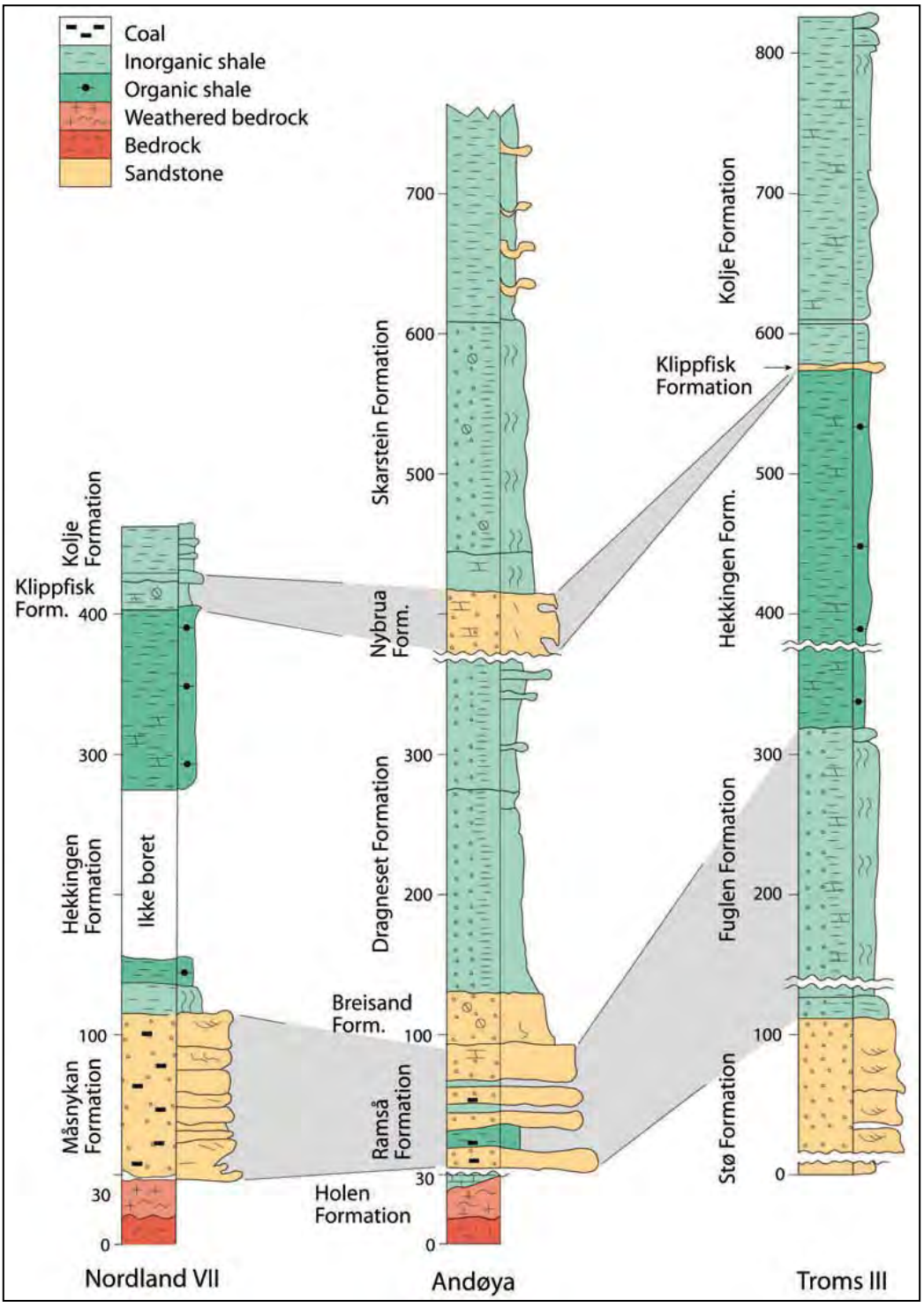

Figure 3.6. Lithostratigraphic and sequence stratigraphic correlation of cored successions in Nordland VII, Andøya and Troms III. From Bøe et al. (2010), modified from Smelror et al. (2001) and Henningsen (2006).

4. APPROACH

Marco Brönner

Hitherto, the Ramså Basin on Andøya, its lateral extension and depth, the basins sedimentary and structural settings have been based mostly on geological observations from a shallow but comprehensive excavation surveys (Dalland et al. 1973, Dalland 1974), a few wells (Midbøe 2015, Vogt 1905, Friis 1903) and surface outcrops. Refraction seismic profiling was carried out along short lines onshore Andøya and offshore in Andfjorden in 1969-1971 (Dalland et al. 1973) and the profiles were related to each other. Seismic velocities were applied to correlate stratigraphic units in the Ramså Basin and in Andfjorden. The concepts are poorly constrained or extrapolated by the use of geophysical data. As described above, the two main objectives were to test and evaluate the potential to map deeply weathered basement from geophysical data and to develop a geotectonic model of the Ramså Basin to contribute to a better understanding of the regional geology of Andfjorden and the Lofoten-Vesterålen archipelago.

The combined observations and interpretation of faulting and basement surfaces as well as a better knowledge of the different basement types now allow a more accurate and differentiated interpretation of the tectonic setting and evolution of the region. Therefore, we acquired a variety of geophysical data and combined them with surface observations from revised bedrock mapping on Andøya.

4.1 **Airborne geophysics**

We acquired airborne magnetic and gravity data over the Ramså Basin and surrounding areas (Figure). The data were collected with an aircraft by Fugro airborne services, South Africa in 2013. In an area of 450 km^2, c. 2000 line km were collected and subsequently processed. The line direction was N-S with a line spacing of 200 m and flight altitude 60 m. The resolution of the resulting grids was 50 m. In addition, further magnetic data were collected during the helicopter EM survey in the mountainous areas (Figurea). The helicopter data were solely acquired onshore and do not expand into the adjacent Andfjorden. Flight altitude was 56 m and line direction was E-W. The line spacing was 200 m.

Aeromagnetic and airborne gravity data have the potential to map quickly and economically very large areas. They are particularly adapted to indicate fault structures and lithological boundaries. They also indicate variations in basement depth as well as helping to identify different types of basement.

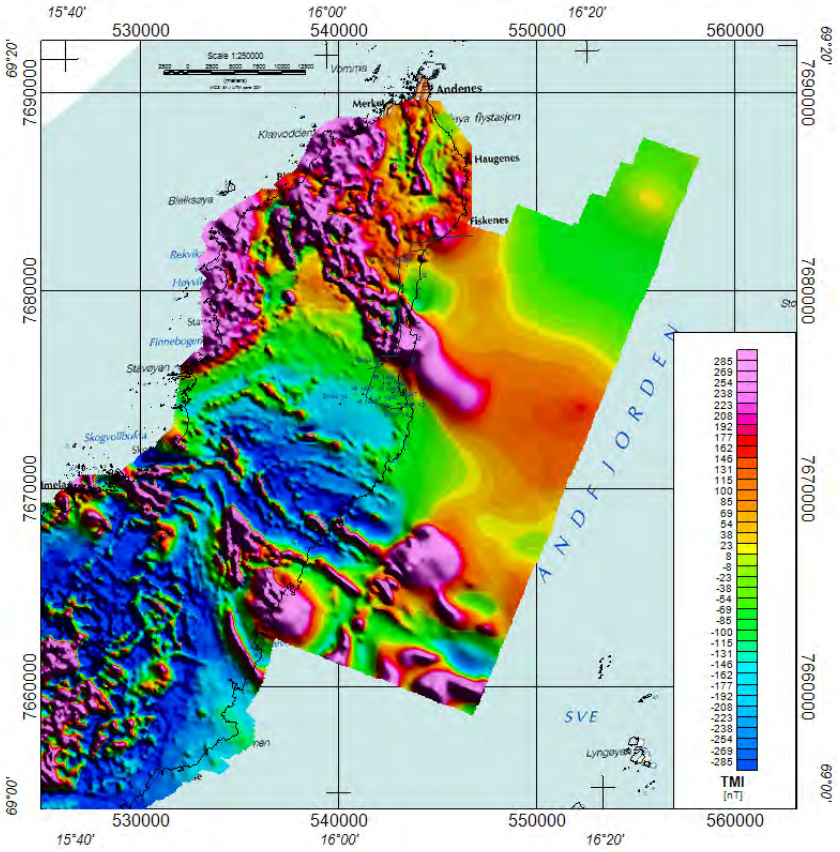

a)

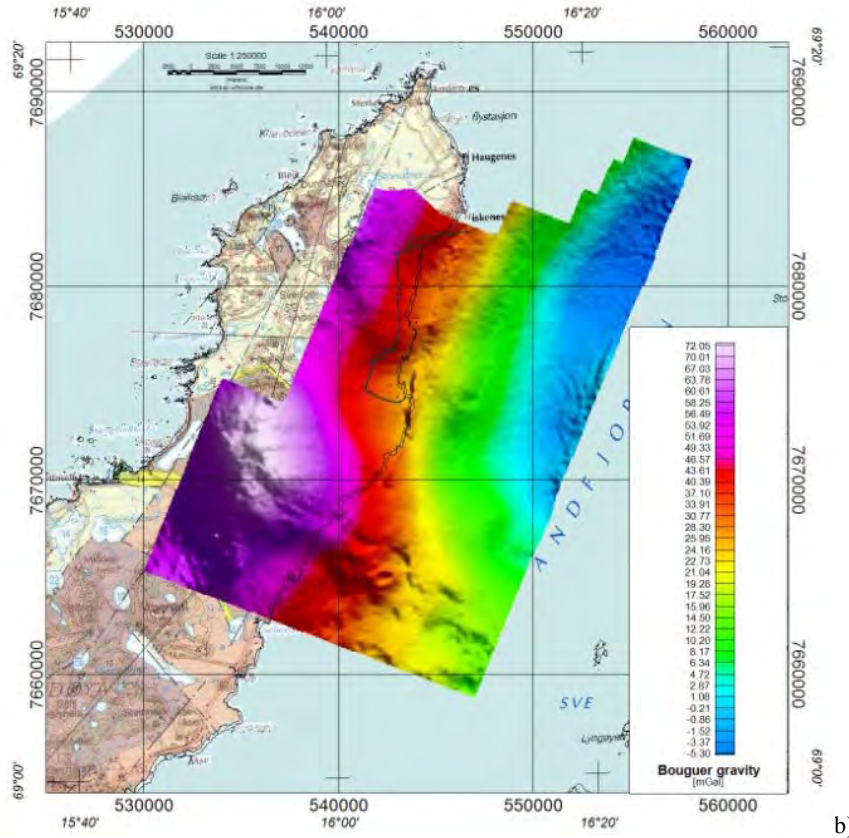

b)

Figure 4.1. Airborne data a) Total magnetic intensity, b) Total gravity field, c) Vertical gravity gradient Gzz and d) a 5 km highpass filter of the gravity field

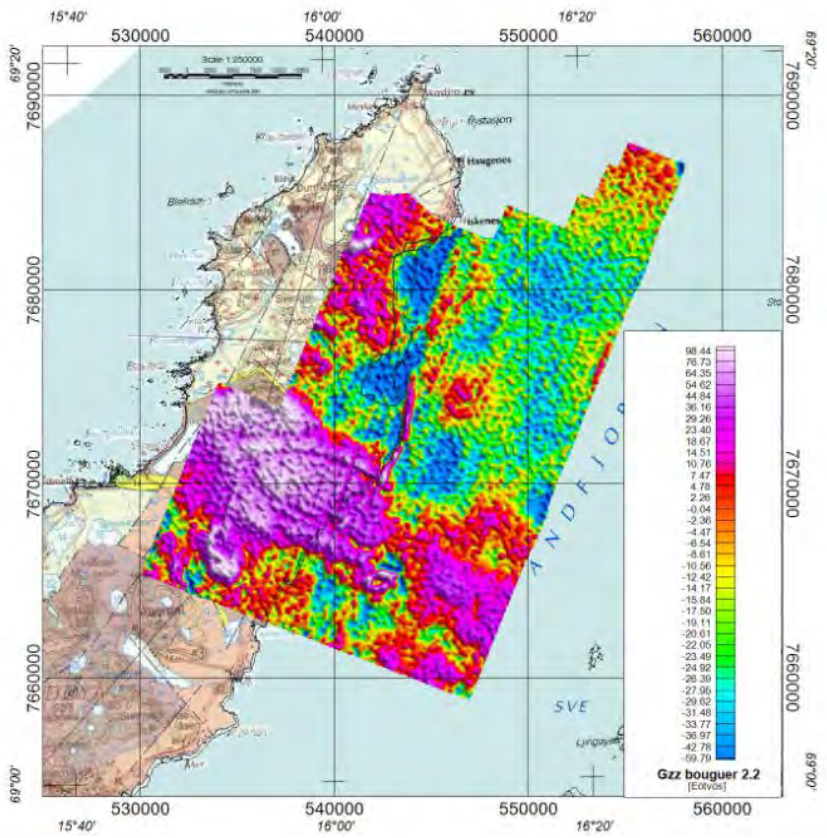

c)

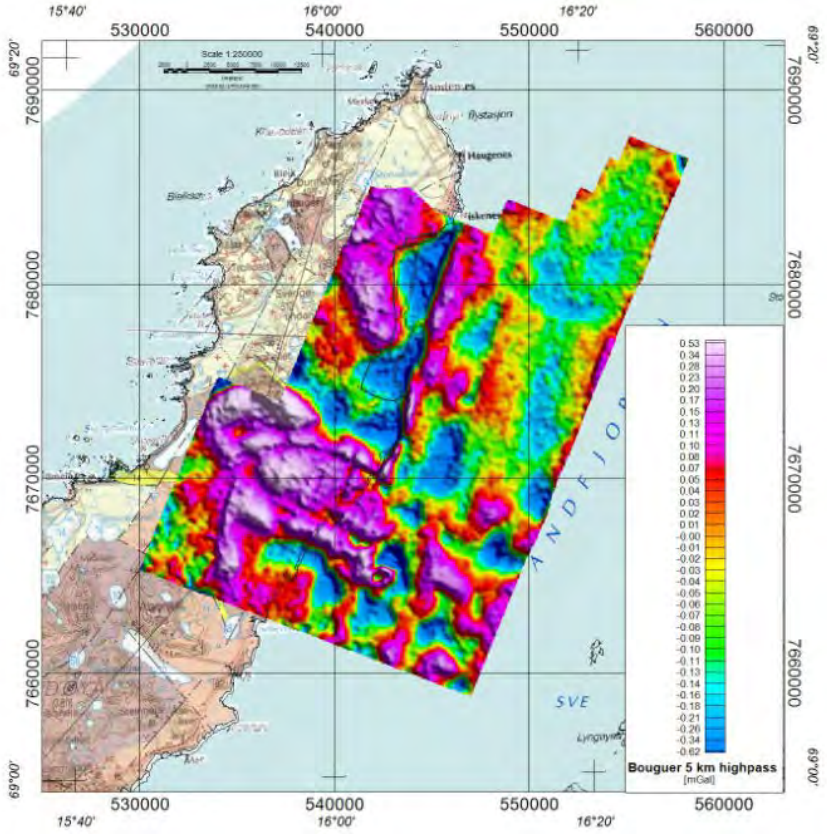

d)

Figure 4.1. cont. Airborne data a) Total magnetic intensity, b) Total gravity field, c) Vertical gravity gradient Gzz and d) a 5 km highpass filter of the gravity field

The data highlight the different geological domains and settings. From the magnetic data (Figurea) an elongated NW-SE-striking magnetic high is noticeable which can be correlated onshore with exposed gabbro. The Ramså Basin appears as a magnetic low north and south of this gabbro belt. South of the basin, another magnetic low is clearly seen followed to the south by a complete domain change with a distinct magnetic low, imprintedby a set of horseshoe-shaped high-magnetic bands which terminate offshore abruptly at a NNE-SSW lineament. This pattern can be related to supracrustal metasedimentary rocks of the Skogsvoll group (Chapter 7.2.2). The gravity data appear much smoother with a maximum in the area of the Skogsvoll group and with a gentle decrease in gravity towards the east into Andfjorden (Figureb).

However, the vertical gravity gradient or a simple highpass filter of 5 km wavelength reveal many more details and highlight the Ramså Basin as a gravity low which extends to the west into the Andfjorden, where it is terminated along a NNE-SSW oriented narrow gravity high. The horseshoe-features of the Skogsvoll group are also noticeable from density contrast but not in the same detail as with the magnetics (Figurec and d). Furthermore, from the magnetic data a prominent low is observed south of the Ramså Basin which appears in the gravity filterings as two predominant gravity lows between the Ramså Basin and the Skogsvoll group. Both gravity lows show a similar characteristic as the deep basins in the Ramså Basin.

The magnetic data from the helicopter survey covered other than the fixed wing survey the entire island with its mountaneous areas in the west (Figurea). The data show nicely the continuation of the gabbro towards NW.

4.2 **Seismic**

The seismic data acquisition and the processing were done under the aegis of the University of Bergen and are extensively presented in Chapter 5. During the project, six seismic lines were acquired onshore Andøya, which were aligned along both N-S and E-W trends. Furthermore, c. 10 marine seismic lines were shot with two different pairs of seismic sources. During the acquisition of four of the marine lines, which were prolongations of the E-W-oriented land profiles, the marine shots were registered also onshore. The interpretation of the seismic data was carried out in conjunction with a reprocessed version of the two existing NPD seismic profiles in Andfjorden from 1988.

4.3 **Airborne EM**

Airborne AEM data were collected with NGUs helicopter-borne system for entire the Andøya. The system records for different frequencies conductivity changes in the subsurface, and is commonly applied to detect mineral deposits such as graphite or iron ore in the subsurface.

Form the Ramså Basin, the porosity and permeability of the Mesozoic sedimentary rocks is supposed to be significantly higher than in the basement which when filled with water and in particular with saline seawater, increases their conductivity by far and produces a high contrast to the basement. The acquisition and results are discussed in more detail in Chapter 6.

4.4 **Petrophysics**

In Order too understand and reach a correct interpretation of the geophysical data a profound knowledge of the petrophyics is crucial. For the Ramså Project we therefore extracted relevant samples from NGUs extensive petrophysical database and collected additional petrophysical data from both surface samples and core samples from the four Norminol cores, which are stored at NPD in Stavanger. All samples were analysed for density and susceptibility, whilst for the core samples we also measured seismic P-wave velocity.

The Mesozoic strata drilled in the Ramså Basin are of Mid Jurassic to Early Cretaceous age. The youngest sediments were recorded from polymorphs of Aptian-Albian age (Chapter 9).

The densities and velocities (Figure 4.2 &Figure 4.3) are generally low to intermediate and vary on average between 2.4-2.6 g/cm^3 and 2800 to 4300 m/s, respectively. Densities and velocities in well A increase fairly linearly with depth until the Base Cretaceous Unconformity (BCU), whilst in Well B both parameters on average are increasing down to 100-150 m before they become more stable or even decrease slightly with depth. Well C actually shows a negative gradient within the sedimentary strata for both density and velocity and a significant jump to 2.9-3.0 g/cm^3 and 5000- 6000 m/s, respectively, for the basement at c. 240 m depth. However, densities and velocities are not only a function of depth but also lithology due to grain and mineral size and porosity. Claystones and sandstones are dominating in all three wells and for the sandstones higher porosity can be assumed, which could at least partly explain densities and velocities to be slightly lower in these units.

The BCU is a significant marker in seismic data on the Norwegian continental shelf which reflects an impedance contrast and consequently a density/velocity contrast between Cretaceous and Jurassic units.

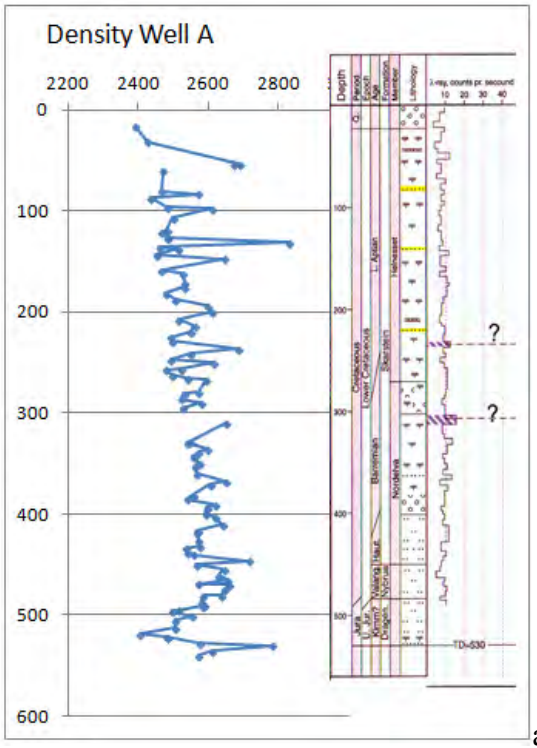

a)

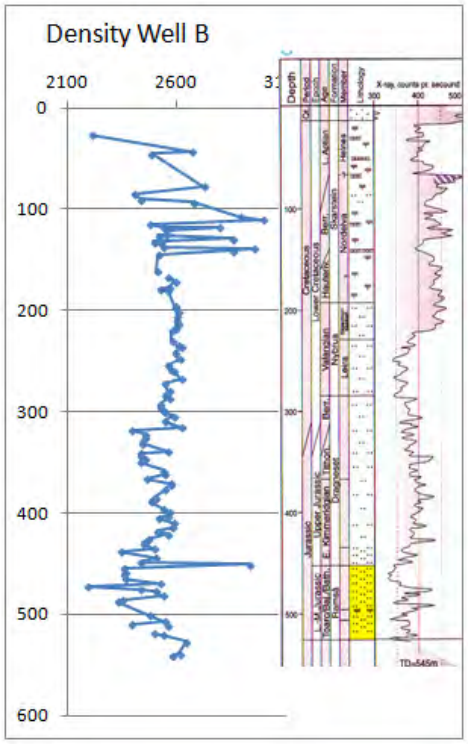

b)

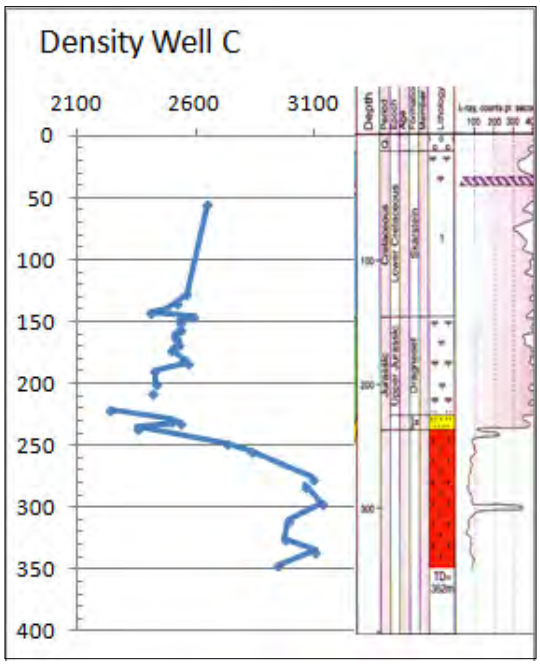

c)

Figure 4.2. Density measurements (kg/m^3) on core samples from the Norminol cores A, B and C. The stratigraphic interpretation is from Midbøe (2015) after a report from Rasmussen (1985, confidential)

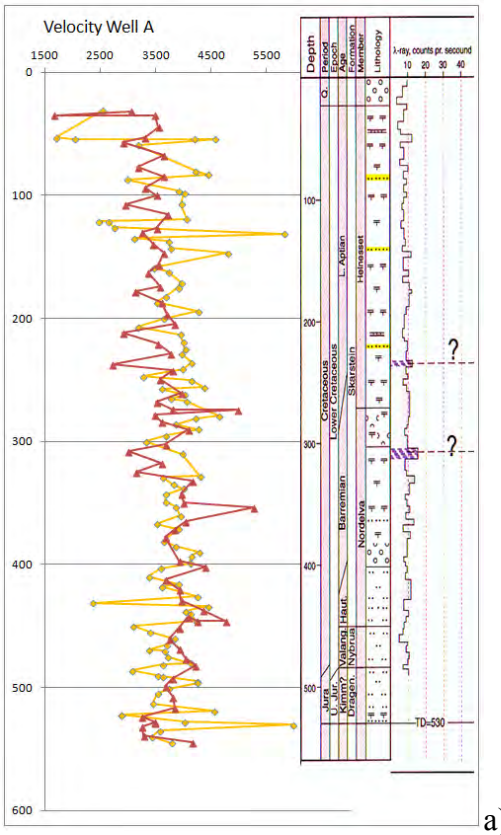

a)

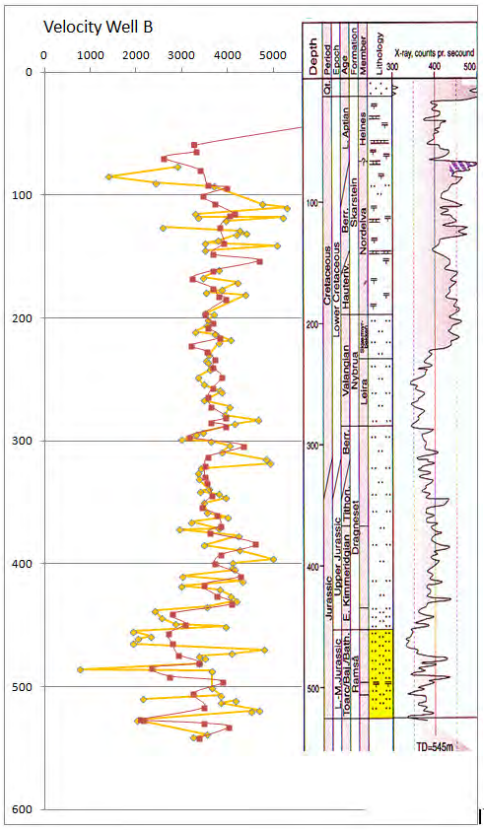

b)

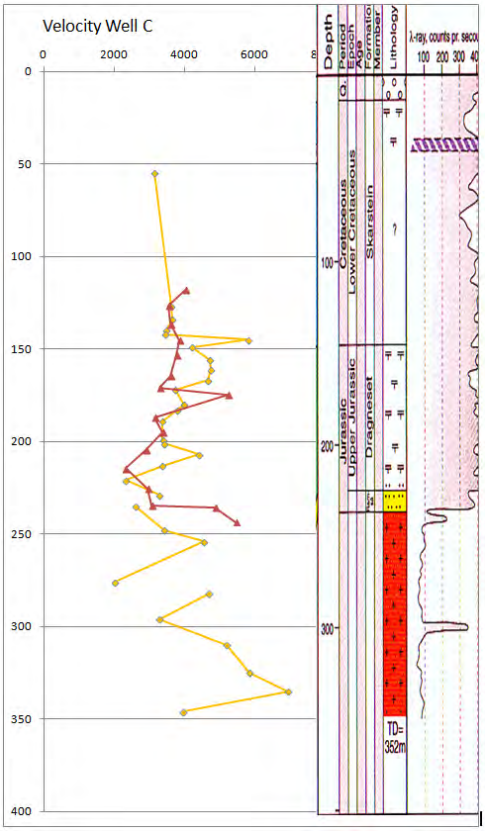

c)

Figure 4.3. P-wave velocity measurements (m/s) on core samples from the Norminol cores A, B and C (yellow by NGU) and on selected depth on the cores (red by NPD). The stratigraphic interpretation is from Midbøe (2015) after a report from Rasmussen (1985, confidential)

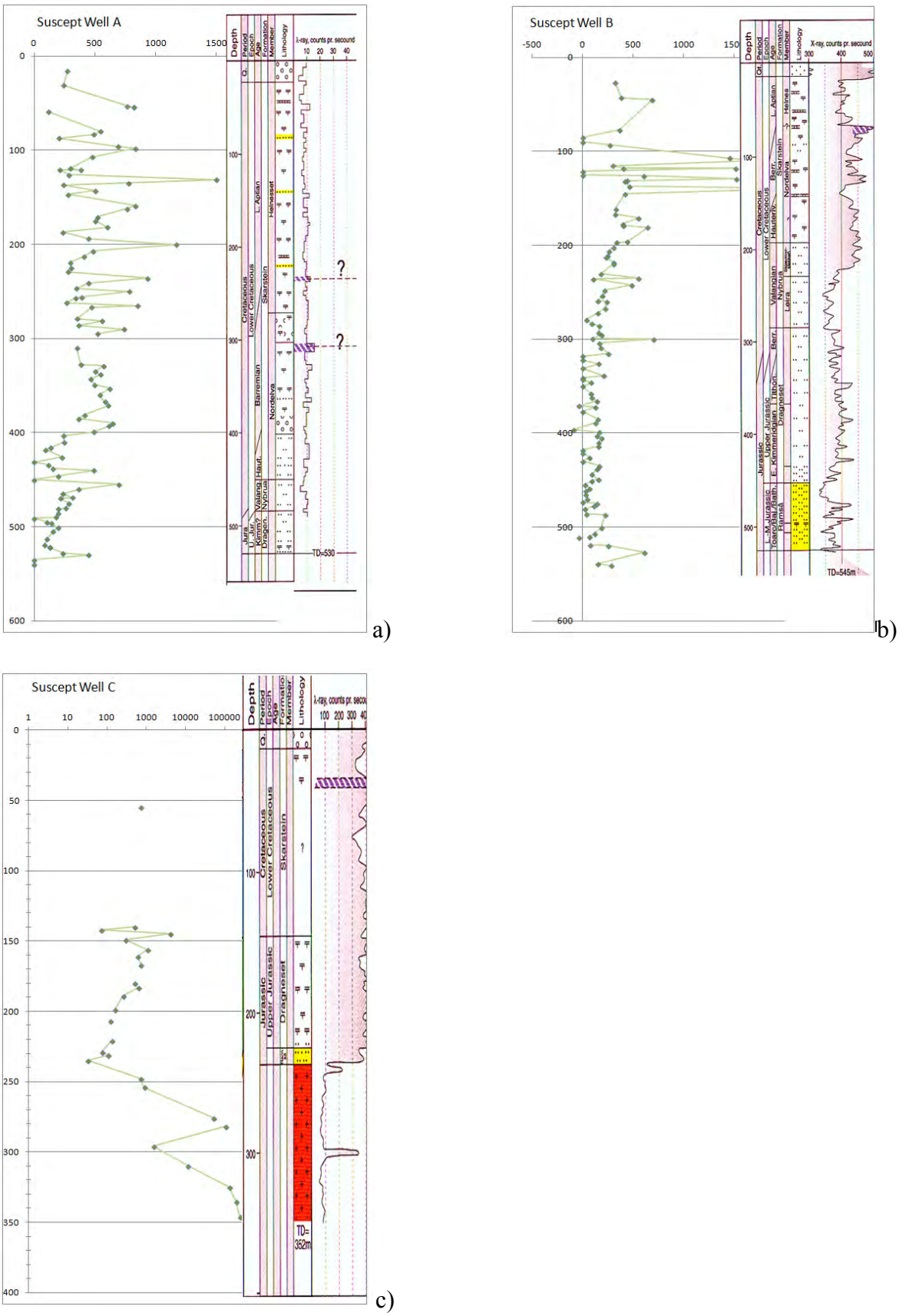

Figure 4.4. Susceptibility measurements (10^{-6} SI) on core samples from the Norminol cores A, B and C. The stratigraphic interpretation is from Midbøe (2015) after a report from Rasmussen (1985, confidential)

However, regarding the interpretation of Rasmussen (1985), the measured densities and velocities from the wells indicate only a slight change with a sudden decrease in density and velocity at the observed Jurassic-Cretaceous boundary even though it does not appear to be very predominant. Also from the seismic data (Chapter 5) the BCU marker is difficult to identify if at all, which helps to underline our observation. The new wells, drilled in 2015 and 2016 (Chapter 8), did not penetrate the BCU but instead either Cretaceous (BH 2) or Jurassic sedimentary rocks (BH 1 and BH 3), and it therefore remains difficult to retrieve more information on the BCU from the new data. However, the P-wave velocity logs from the new wells (Table 8.9) show slightly lower velocities compared to the one measured from the Norminol cores, which can partly be explained with burial depth. But a direct comparison has to be handled with care since the measurements on core material produce different results as logged data. Pore fluids and pressure conditions are different and yield different values for both density and velocity. In this regard, the bulk density measured at the core samples was carried out at dry or semi wet samples since the material dissolved quite fast when exposed to water. However, it is noticeable that both, velocities from cores and logged velocities show a jump and lower velocities at the measured bottom Cretaceous and measured top Jurassic. Although with the new cores the BCU was not drilled and consequently not logged, the similar appearance compared to the measurements from the Norminol core samples confirm the BCU as a negative velocity jump.

The magnetisation of the sedimentary rocks is generally low (Figure 4.4). Sandstones and claystones do not contain any significant amount of iron-bearing minerals, which is quite common and characteristic for the Mesozoic sedimentary units on the Norwegian shelf (Mørk et al. 1996). From well B (Figure 4.4b) we can observe some higher magnetisation in the Cretaceous at c. 100 to 150 m depth, but the data from Well C (Figure 4.4c) show that the underlying basement is still one to two magnitudes higher than the sedimentary strata, which can be used to identify the basement depth from the magnetic data.

However, basement samples from Andøya show that there can be significant differences in the magnetisation of the basement rocks and even for one bedrock type, too. The gabbro, which was drilled in Well C is generally of high magnetisation and even shows some remanence, which is also well expressed in the magnetic maps (Figurea). The surrounding bedrock, however, is on average much less magnetic and shows a large range for the different bedrock types, which not only indicates a complex basement composition for the study area, but also can point to a measure of uncertainty for a depth-to-basement estimation from the magnetic data only.

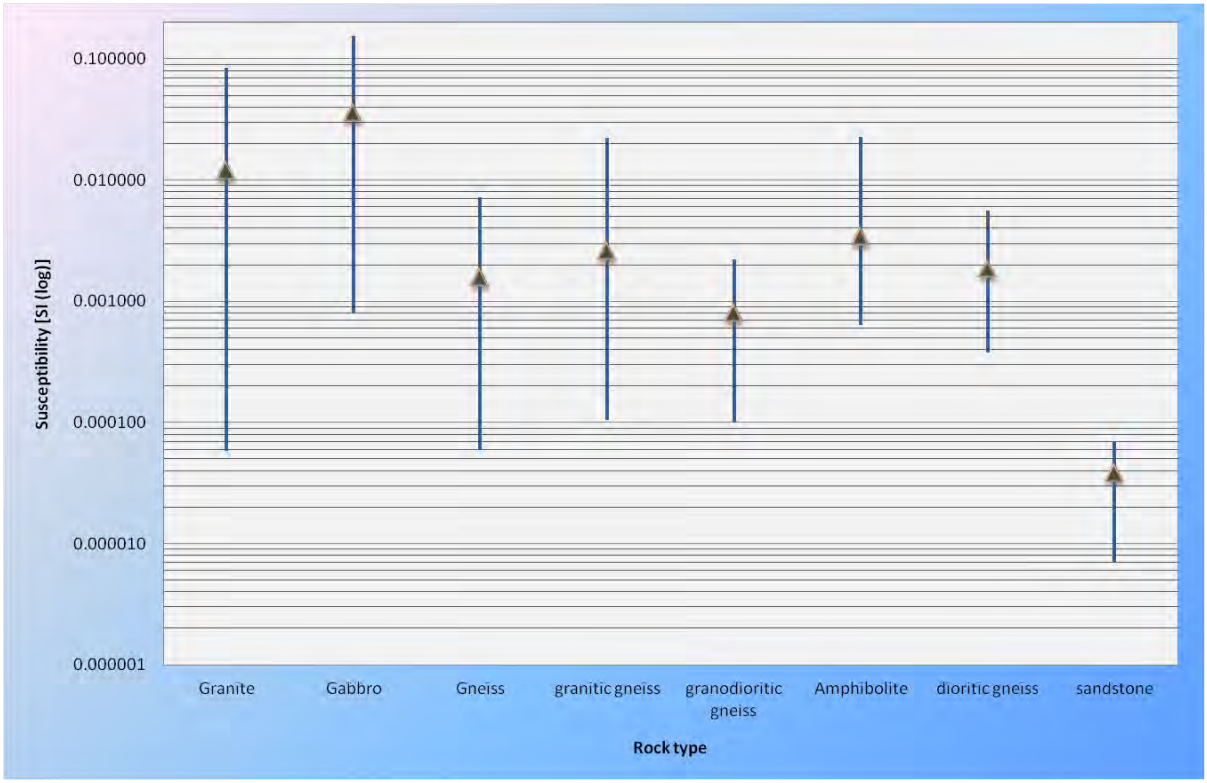

Figure 4.5. Susceptibility variation of bedrock samples from Andøya around the Ramså Basin (on a half-logarithmic scale).The bedrock shows a significantly higher magnetisation than the sedimentary rocks, but the magnetisation for one bedrock type can vary by up to ±1-2 magnitudes.

5. 2D SEISMIC SURVEYING OF THE RAMSÅ BASIN AND THE ANDFJORDEN

Tor Arne Johansen, Bent Ole Ruud, Tormod Henningsen & Marco Brönner

5.1 Introduction

Andøya is an island in the north of Norway that on its eastern side provides an exclusive area for studying Mesozoic sediments onshore. Mesozoic sediments above the present sea level were regionally removed during glacial periods and transported seawards, towards the northwest. Some remains of these sediments have been sheltered from glacial erosion in a down-faulted complex on the eastern side of Andøya, ranging from a couple of kilometres west of the shoreline and eastwards into Andfjorden. See Figure 3.2 for a conceptual overview. Midbøe at al. (2011) reported on the geological mapping of this area (Chapter 2). The Mesozoic sediment column here is mainly of Mid Jurassic age or younger, partly resting on Devonian sedimentare rocks (Holen formation) and partly on weathered Precambrian rocks. According to Sturt et al. (1979) the older Mesozoic sediments were most likely eroded because of a transgression in Late Triassic Early Jurassic.

Due to its geological manifold, this part of Andøya has received particular attention for more than 150 years. It started in the 1860s as outcropping coal was found at the Ramså location. During the following century, several geological surveys were undertaken to delineate the coal prospects.

From the motivation that Mesozoic sediments provide the main source of hydrocarbons exploited by the gas and oil industry in the North Sea, four wells were drilled in the early 1970s along the shoreline of the Ramså Basin (Figure 3.5) to delineate possible source and reservoir units.. Furthermore, weathered Precambrian basement rocks have been revealed by a hydrocarbon discovery on the Utsira High in the northern North Sea to occur as a potential reservoir rock. As Andøya and eastern Greenland in Mesozoic time, and before the opening of the North Atlantic Ocean, were close neighbours within the same geological province, derivation of geological and geophysical analogues is important for revealing a piece of the geological history before the opening of the Atlantic Ocean. Finally, the presence of weathered Precambrian bedrock potentially presents a serious problem for the construction of subsea tunnels beneath fjords where such unstable zones might be encountered.

To better understand the extent and geometries of the Mesozoic sediment successions and possible seismic reflection signatures from weathered Precambrian rocks in this area, a rather extensive geo-scientific acquisition campaign was carried out in 2013 and 2014. This included land, marine and marine-to-land seismic, and, magnetic and gravimetric airborne surveying. Furthermore, several shallow wells were drilled on land also in order to aid the correlation of geological and seismic data. The main objective of this chapter is to review the seismic acquisition, processing and present the main seismic sections and an analysis of this work. Chapter 11 presents an integrated geo-scientific interpretation of all the data in this report.

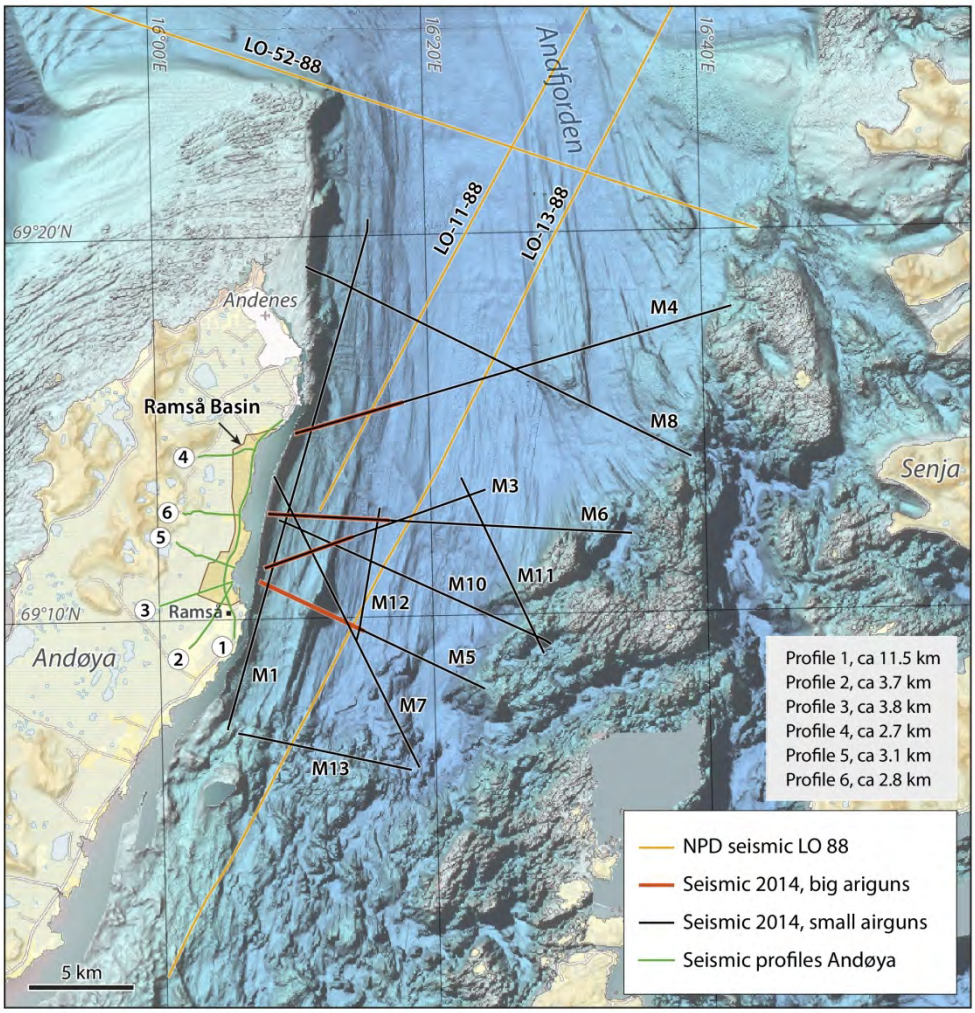

Figure 5.1. Map of the study area showing the 6 land seismic lines (1 – 6) and the 10 shallow marine seismic lines (M2, M3, M4, M5, M6, M7, M8, M10, M11 and M12), which were acquired during the project period. Also, two seismic lines shot in 1988 using both a 0.5 km and a 3 km streamer are indicated (LO11-88 and LO13-88).

5.2 The seismic lines, acquisition set-ups and data preparation

The lines defined for the seismic study are shown in Figure 5.1 and data were acquired during three different time periods: early autumn of 2013, winter of 2014 and early autumn of 2014. Lines 1, 4 and 6 are along existing roads and were acquired during the first autumn. Lines 2, 3 and 5 are on soft, wet marshland and had, accordingly, to be acquired during winter when the wet soil was frozen. The profiles were mainly planned along existing roads or trails, which gave a representive coverage of the basin. However, Line 2 and 3 were positioned based on the interpretation of the gravity and magentic data to test the indication of a basin extension to the south and southwest.

In the second autumn, ten marine lines were acquired using a 50 m-long marine mini-streamer, and, because of environmental restrictions, partly using a single airgun, and partly using an array of airguns. For the geophysical study, two seismic lines LO88-11 and LO88-13 from 1988 were made available from the Norwegian Petroleum Directorate.

Table 5.1. Acquisition parameters for all seismic lines discussed in this report. The 1988 survey was performed by GECO for NPD and includes two lines, LO-11-88 and LO-13-88, from Andfjorden. Except for these two lines, the acquisition was performed as collaboration between the University of Bergen and NGU.

Date of acquisition	Recording		Receivers / Marine streamers / Geophones groups					Sources / Airgun array			
	Instrument	Sampling interval	Streamer / Land lines	Total active length	Number of groups	Group interval	Streamer depth	Shot interval	Total volume	Pressure	Depth
July 1988	DFS-V	2 ms	Main streamer	3,000 m	120	25.0 m	9 m	25 m	5946 cu.in.	2000 psi	6 m
			Mini-streamer	500 m	40	12.5 m	3 m	25 m	500 cu.in.	2000 psi	3 m
Sept. 2013	Sercel Unite nodes (RAU3)	2 ms	Line 1 Line 4 Line 6	11,475 m 2,737 m 2.850 m	918 219 228	12.5 m	-	25 m	Swept Impact Seismic Tech. (VIBSIST 3000)		
March 2014	Sercel Unite nodes (RAU3)	2 ms	Line 2 Line 3 Line 5	3,687 m 3,750 m 3,112 m	295 300 249	12.5 m	-	25 m	Detonating cord: 25 m (1 kg)		
Sept. 2014	Sercel Unite	2 ms	Lines 3,4,5,6	1,500 m	120	12.5 m	-	50 m	766 cu.in.	2000 psi	8 m
	Geometrics Geode	1 ms	Mini-streamer	50 m	8	6.25 m	3 m	15 m	90 cu.in.	2000 psi	3 m

These were acquired using both a 3 km-long conventional streamer, and, simultaneously, using a shorter 500 m-long streamer (see Table 5.1 for the acquisition parameters).

Two alternating airgun arrays were used, both firing at 25 m intervals, with the smaller and shallower source fired 2 seconds before the larger and deeper source. To our knowledge, the data from the 500 m streamer have not been processed or published before now.

The experimental set up for acquiring data along roads during autumn time (lines 1, 4 and 6) is schematically shown in Figure 5.2. Strings with 4 Sercel 10 Hz spike geophones were planted along the shoulder of the road with both group length and group distance of 12.5 m. For recording, 3-channel nodes (Unite RAU3 from Sercel), each serving 3 successive geophone strings, were placed out on average every 37.5 m along the spread. The nodes were set to sample continuously at a rate of 2 ms during the operation time of the spread. 120 nodes were available, resulting in a possible maximum spread length of 4.5 km. Thus, all lines, except Line 1, could be recorded without moving any geophones. For Line 1, 50-60% of the geophones were moved from the back to the front of the spread three times as the shooting proceeded along the line. This resulted in a fold of more than 80 for most part of Line 1. For the other lines, the fold increased linearly from the end points of the line and reached a value of half the number of geophone groups at the mid-point of the line (see Table 5.1).

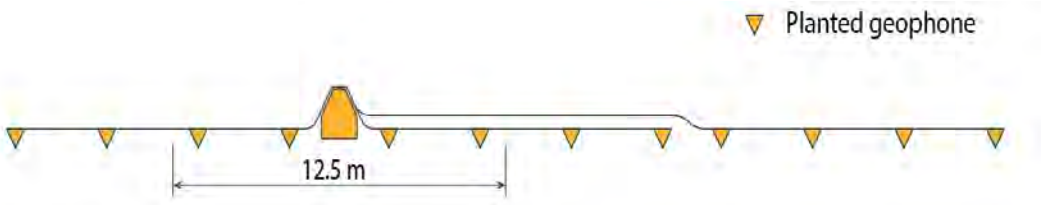

Figure 5.2. Schematics of recording set up during autumn (planted geophones) and during winter (gimballed geophones).

To generate seismic energy along roads we applied the swept impact seismic technique (SIST) (Park et al. 1996) using Vibsist-3000 from Vibrometric. The source consists of a hydraulic hammer impacting a quadratic steel plate of approximately 50 cm x 50 cm coupled to the ground using the weight of the truck, see Figure 5.3. The source point interval was 25 m and for line 1 three sweeps where run at each source point. For lines 4 and 6 two to three sweeps were run. Each sweep counted around 110 impacts over 30 seconds where the time interval between impacts started at 1 second and linearly decreased to about 0.14 second. An advantage of this technique is that it is relative fast, non-destructive and according to Park et al. (1996) adequate in retaining a relative high-frequency source also in areas with much traffic. However, seismic surveying along congested roads was challenging both from a logistical point of view and, indeed, also due to the extra noise generated in the data. Figure 5.4a shows an example of data from one sweep along line 1 where several vehicles are driving parallel to the spread in both directions at the same time. To suppress noise from vehicles moving along the spread, we used a method similar to a diversity stack before decoding.

a) *b)*

Figure 5.3. Picture of truck carrying the Vibsist-3000 seismic source, including a close-up of the hydraulic hammer and steel plate (b).

In this method the average power in a moving time window is computed, like for AGC (automatic gain control) amplitude scaling, but instead of scaling with the inverse square root of the power (as done with AGC), the amplitudes are scaled with the inverse power. Thus, the amplitudes in time intervals with high power is heavily reduced, and by choosing a moving time window larger than the intervals between impacts, this method will suppress noise burst which is stronger than the source generated signals without removing much of the signals. Originally, diversity stack was a method which was typically applied when stacking repeated vibroseis sweeps after correlation (e.g. Klemperer, 1987), but with the increased computing and storage capacity available today, it is possible to improve the results by suppressing noise before correlation (e.g. Lambrecht et al., 2004) or, as shown here, before decoding SIST data. Figure 5.4b shows how the traffic noise identified in Figure 4a has been relatively effectively muted. Miller et al. (2016) reported similar results in a study for seismic surveying of a water aquifer using a vibrator.

Another pre-decoding noise suppression method we applied was spectral whitening. While the diversity stack is efficient for removing transient noise, spectral whitening will suppress time-stationary, monochromatic noise, such as the low-frequency noise from waves breaking at the shore, noise from heavy machinery, or noise from high-voltage power lines.

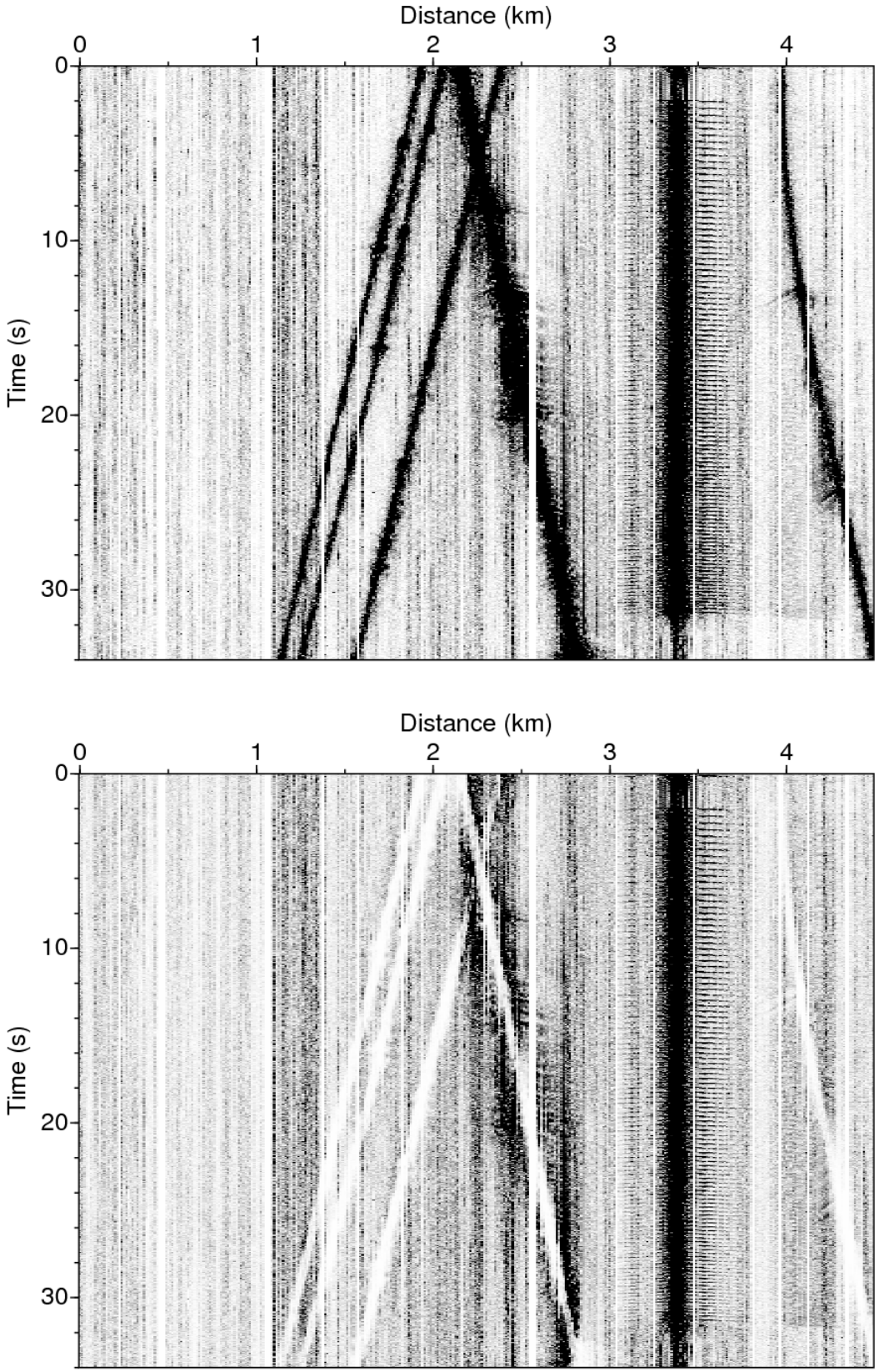

Figure 5.4. ***a)*** *Raw data acquired during one sweep along line 1. The strong vertical energetic event at point S is caused by the Vibsist, while the oblique events labelled A, B, C, D and E are noise bursts caused by vehicles driving parallel and close to the spread during one recording.* ***b)*** *Raw data subsequent to reduction of noise caused by passing vehicles using the diversity stack procedure described in Rückemann (2012).*

After noise suppression, a decoding of the data was performed to transform each sweep to become a single impact gather, i.e. similar to a shot gather. The decoding implies a time shift and stacking operation so that the energies from all the individual impacts in one sweep are coherently summed together. The times of the impacts were found from the pilot trace recorded by a geophone at the hydraulic hammer. The time shift and stack procedure was performed in the Fourier domain for increased accuracy and speed of computation. For details of the SIST methodology, see Park et al. (1996). Finally, the decoded traces for each sweep in the same position were stacked to increase the signal to noise ratio of the shot gather.

The total recording time used for each sweep was 34 sec, which after decoding results in a shot record of 4 sec. The effects of the noise reduction and decoding process are further displayed in Figure 5.5. In Figure 5.5a a close-up of the first 1.5 sec of the raw data including traffic noise is shown. We can clearly identify the single impacts. Figure 5.5b and c show results of decoding the signal without and with prior traffic noise mute, respectively. Figure 5.5c shows how the signal-to-noise ratio particularly has been improved for the far offset traces.

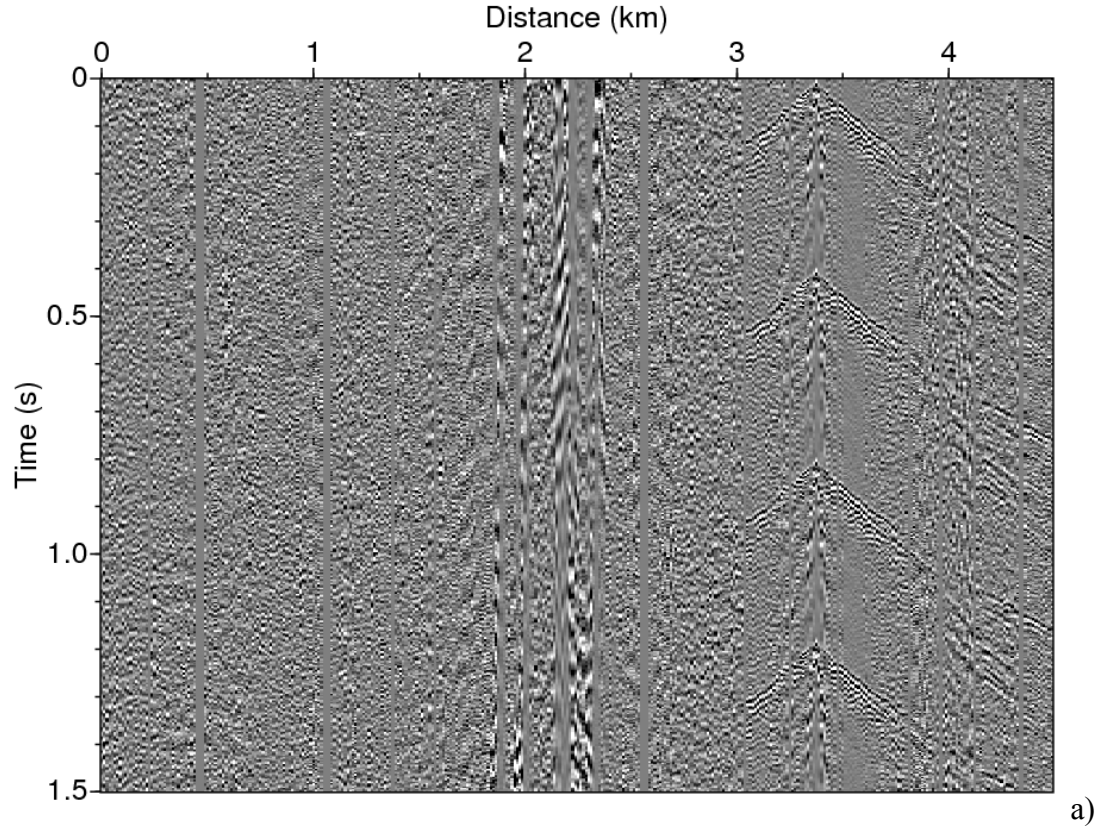

Figure 5.5. ***a)*** *Close-up of the first 1.5 sec of the raw data. The distinct impacts of the hydraulic hammer are easily visible and noise bands caused by passing vehicles are profound.*

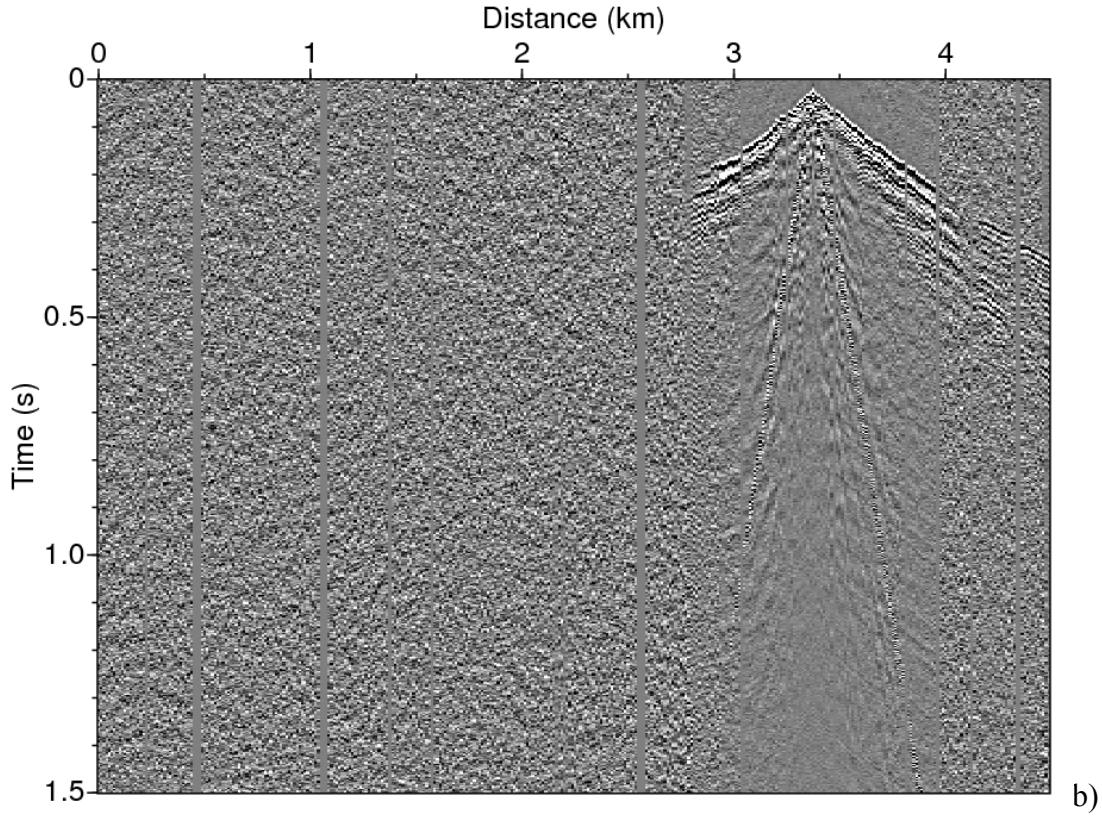

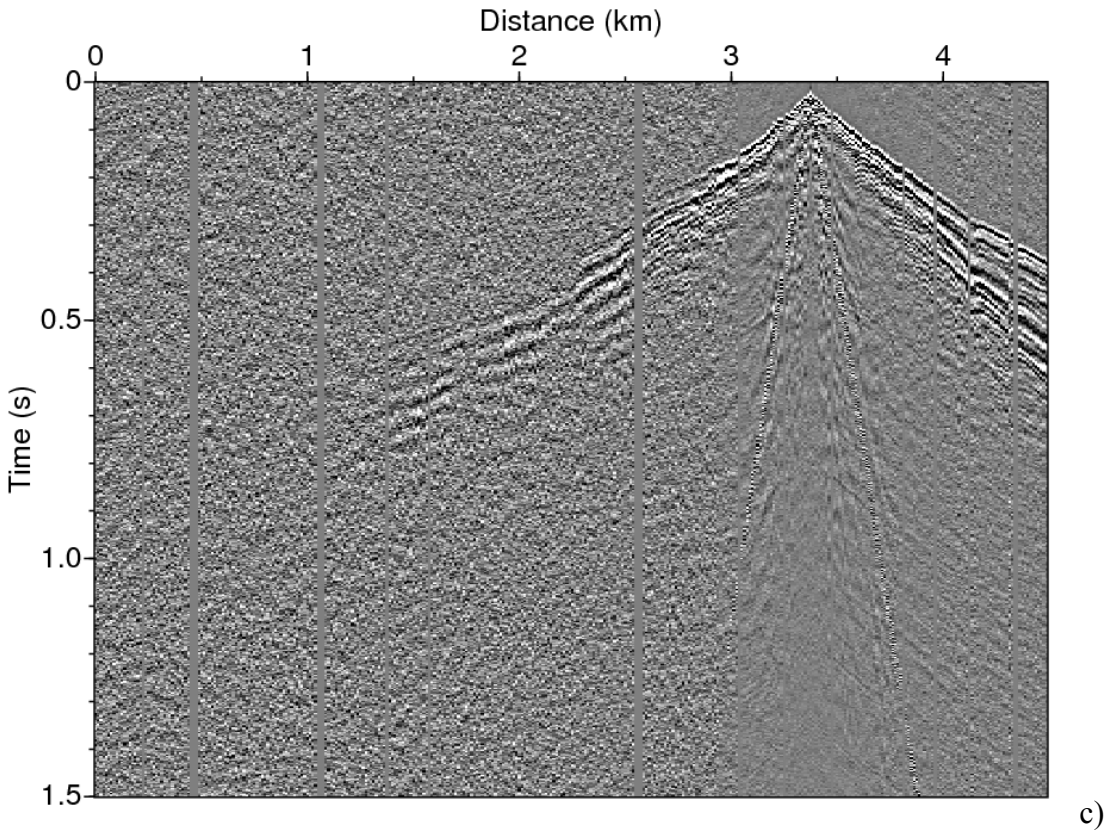

Figure 5.5 (cont). ***b)*** *Same data window subsequent to decoding/stacking the raw data into a single high energetic impact, or seismic shot-like appearance.* ***c)*** *Same data window as in b) but prior to the decoding the noise bursts caused by vehicles were suppressed.*

Lines 2, 3 and 5 were acquired during March 2014 using the same recording set up as for the 2013 acquisition, but the source was now detonating cord, an explosive burning with a velocity of 7000 m/s. Each shot was of 25 m length, equivalent to 1 kg of TNT, placed along the ground in the direction of the spread and with the ignition point such that the cords burned in the survey direction, which for all lines were from the shore and into the island. Figure 5.6a shows the detonating cord laid out and Figure 5.6b when a shot is fired. Due to snowfall the geophone strings were at times buried in snow sheltering them for weather noise as shown in Figure 5.6c

Figure 5.6. Seismic acquisition during wintertime. ***a)*** *Detonating cord laid out.* ***b****) A shot fired, and* ***c)*** *Geophone strings were partly buried in snow, sheltering them from weather noise.*

All the marine lines acquired in the autumn of 2014 were recorded by a mini-streamer with a 50 m-long active section consisting of 8 hydrophone groups. For most lines a single airgun was used in order to reduce environmental effects; see Table 5.1 for details about the acquisition. The four marine seismic lines M3, M4, M5 and M6 are eastward continuations of the land seismic lines 3, 4, 5 and 6, respectively. The first 5 km (western part, marked with red in Figure 5.1) of these marine lines were also shot with a larger source because we made a simultaneous recording of the shots on land. The land recordings were made with spreads of 1.5 km (starting near the shore) and with the same group length and recording parameters as for the other land lines (see Table 5.1).

5.3 Seismic processing and data analysis

Due to the complex and heterogeneous geology in this area, seismic imaging is challenging. In particular, the varying geometrical shape of the geological layers and fault complexes near the surface makes reflected events difficult to interpret and locate both in space and two-way travel time. Moreover, the seismic 2D lines are acquired on a truly varying 3D structure. Effects of the near surface heterogeneities, for instance sand dunes and wet marsh, are clearly visible in the shot gathers and must be adjusted for. In Figure 5.7a this is seen as the first break event is buckled and deviates from a smooth (curved) line. The first breaks within the near offset interval are mainly caused by P-waves refracted close to the surface, and, where variations in velocities above the refractor cause the increment in travel time between succeeding geophone stations to vary. To compensate for the near-surface heterogeneities, a static correction was performed based on first breaks in the offset range 70 to 400 m, as briefly explained in Appendix I. Figure 5.7b shows the data in Figure 5.7a after static correction. Figure 5.8 shows the estimated P-wave velocity profile near the surface along line 1 and the inferred time shifts for the source and receiver positions.

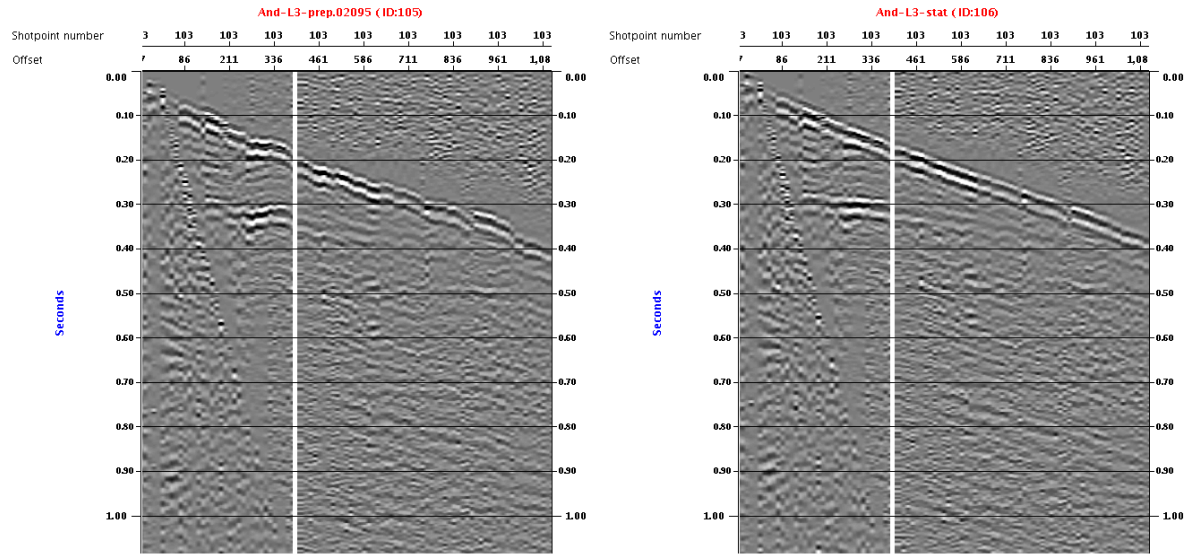

Figure 5.7. ***a)*** *One common receiver gather along line 1 displaying the problems caused by a heterogeneous surface (appearance of sand dunes and wet mire) causing the first break to appear buckled.* ***b)*** *Same data as in a) after static corrections based on inferring horizontal velocity variations along the near surface causing an oblique alignment of the first breaks.*

The general workflow for the processing of the land seismic lines is outlined in Table 5.2a Processing of land lines. Conventional velocity analysis to retrieve stacking or normal move-out velocities, subsequent to static correction, became difficult due to a lack of clear reflection events in the common midpoint gathers. Instead, for velocity estimation we applied the 2D seismic tomography inversion technique based on first breaks as described by Korenaga et al. (2000). The method assumes that the velocity field is smooth and that velocities increase with depth.

Table 5.2a Processing of land lines

1. Decoding (only for SIST acquisition) consisting of:
-Scaling with inverse power of a moving time window
-Spectral whitening
-Determine impact times from pilot trace
-Time shift and stack impacts
2. Stacking repeated sweeps (only for SIST acquisition)
3. Trace editing
4. Set geometry
5. Pick first breaks (FB)
-FBs in the offset interval 70-400 m were used to determine refraction statics
-All FBs where used to in a tomographic inversion to make an initial velocity model
6. Compute and apply surface consistent refraction statics
7. Mute air-wave and first breaks
8. Amplitude recovery
9. Surface consistent deconvolution
10. FK-filtering of shot gathers
11. Sort traces to receiver gathers
12. FK-filtering of receiver gathers
13. Sort traces to CMP gathers
14. Velocity analysis
15. NMO and stack, or Kirchhoff pre-stack time migration

Table 5.2b Processing of new mini-streamer lines acquired in September 2014)

1. Set geometry
2. Deconvolution (two passes):
-with gap corresponding to bubble pulse
-with gap corresponding to water depth
3. Amplitude recovery
4. Bandpass filter
5. Generate NMO velocity model from water depth
6. Kirchhoff pre-stack time migration
7. Zero-phasing
8. Bandpass filter (Ormsby 25-60-200-400 Hz)

Table 5.2c Processing of old NPD lines (LO-88)

Main streamer (3000 m):

1. Trace editing
2. Set geometry
3. Source statics
4. Resample to 4 ms
5. Amplitude recovery
6. FK-filter to remove low velocity water waves
7. Spiking deconvolution
8. Bandpass filter
9. Sort to CMP gathers (12.5 m interval)
10. Creation of water bottom multiple model
-NMO correction with water velocities
-FK-filter which pass only multiples
11. Adaptive subtraction of velocity model
12. Velocity analysis every 1.5 km
13. Multiple suppression by parabolic Radon transform
14. Mute incidence angles > 35 degrees
15. Time variant bandpass filter
16. Kirchhoff pre-stack time migration
17. Amplitude scaling

Mini-streamer (500 m):

1. Trace editing
2. Set geometry
3. Source statics
4. Amplitude recovery
5. FK-filter to remove low velocity water waves
6. Spiking deconvolution
7. Bandpass filter
8. Sort to CMP gathers (6.25 m interval)
9. Velocity analysis every 1.5 km
10. Mute incidence angles > 35 degrees
11. Amplitude scaling
12. Kirchhoff pre-stack time migration
13. FK-filter to remove steep events

Figure 5.9a shows the velocity distribution for line 1 obtained using the tomographic inversion, while Figure 5.9b displays estimated ray paths associated with the first break events. For comparison, Figure 5.8a verifies that the near surface velocities estimated for the static correction are consistent with the estimated shallow velocities obtained from the tomographic inversion.

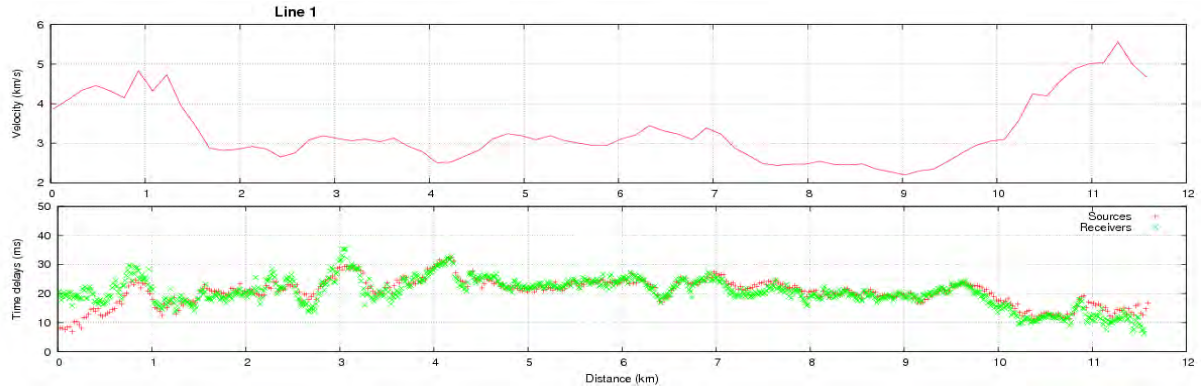

Figure 5.8 ***a)*** *Near surface velocity profile along line 1 as inferred by the static correction, and* ***b)*** *the corresponding time shifts of the source and receiver positions.*

This velocity model was then used to time migrate the data resulting in the identification of more coherent reflection events. Hence, a new velocity model was made by a conventional velocity analysis, and, finally, based on this, a second seismic migration was performed. The final results of the processing of the land seismic data are shown in Figure 5.10 and Figure 5.12. As the geometry of the basin is rather complex, interpretation of the seismic data also become challenging. One can expect a strong event seen in the seismic sections to represent the boundary between the basement and the overlying and dipping Mesozoic sedimentary rocks of the Ramså Basin. However, some of the strong reflectors can also be linked to the BCU, which is a very strong marker on the Norwegian shelf or as we interpreted the shallowest strong events, an intra-Cretaceous event due to an observed unconformity in the Nybrua formation (Dalland et al. 1981, Figure 3.6). Any structures aside from this sedimentary package are most likely not visible due to the very high velocities (low seismic resolution) and low impedance contrasts. Figure 5.10 represents the processed seismic data along line 1 overlain with the interpretation of pronounced reflectors. The geometry from the seismic data is similar to that derived from geological information (Figure 3.2) and a seismic profile (Figure 2.2), but the new data reveal much more detail and a more complex top-basement geometry. As has already been shown by earlier geological and geophysical observations (Read 1987, Rasmussen 1985, Dalland, 1981), the new seismic data along line 1 clearly shows the bifid character of the Ramså Basin with a deeper basin in the north and a horst in the central part. The visible reflectors north and south of this horst are tilted northwards, whilst they appear fairly flat-lying on top of the horst. The horst can be related to a gabbro, which was drilled in Well C (Figure 3.5) and is outcropping west of the basin (Figure 1.2). Buckles and interpretation of the interpreted events infer faults and fractures, which indicate the strong tectonisation and down-faulting character of the basin.

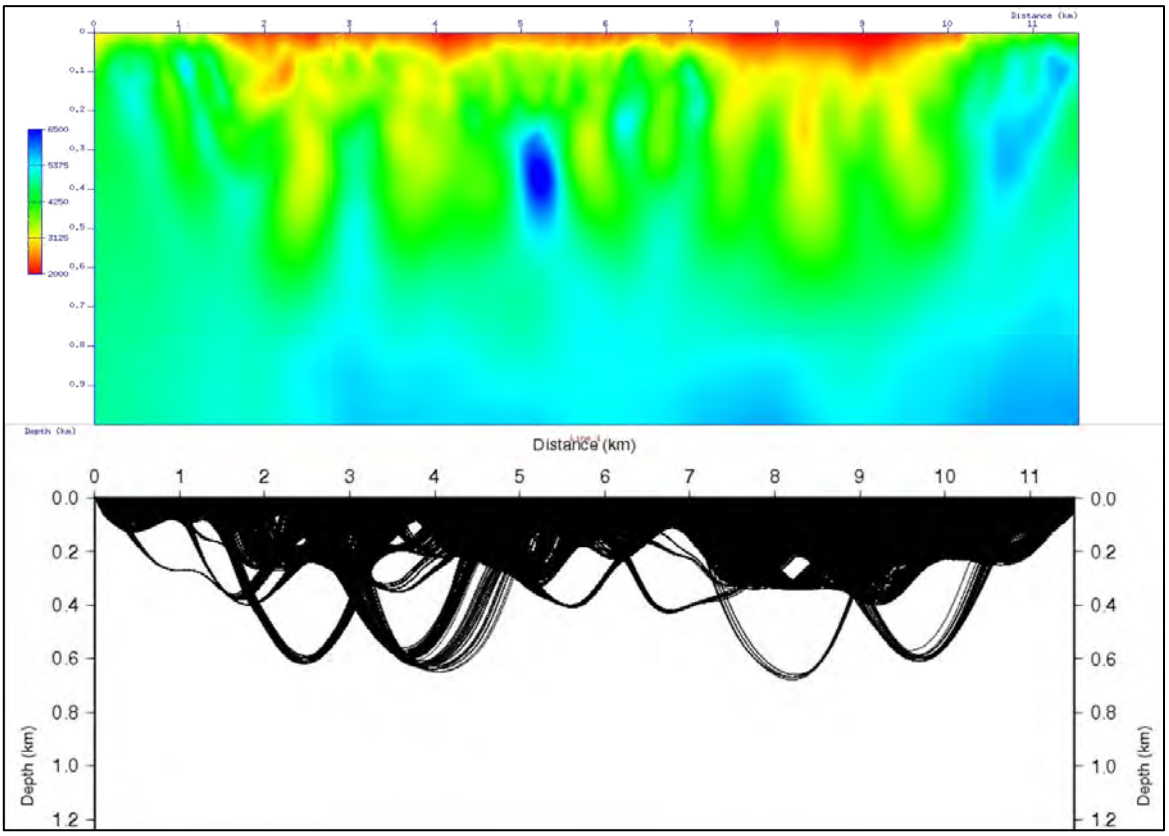

Figure 5.9. ***a)*** *Estimated P-wave velocity profile obtained using the seismic tomography method based on first break events as outlined by Korenaga et al. (2000).* ***b)*** *Modelled seismic rays as imposed by the estimated velocity model displayed in a).*

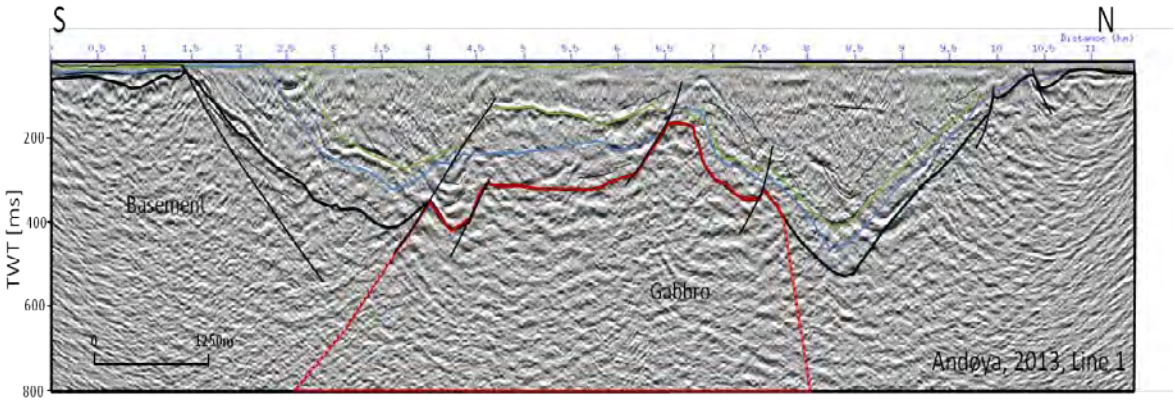

Figure 5.10. The processed land seismic line 1 including the most profound interfaces indicated.

The other land seismic lines were significantly shorter but also indicate the complexity and possibly high degree of tectonisation (Figure 5.12) within the sedimentary strata and consequently limited imaging regarding the geometry of the sedimentary layers. The strongest reflector was related to the top basement, and was actually in good correlation in the crossing points with line 1. Lines 4 and 6 are basement dominated since the Ramså Basin is fairly narrow, but show a lot of intra-basement reflectors which can indicate fracturing and/or possible weathering, a feature that is in good correlation with the low resistivities observed by the EM data (Chapter 6).

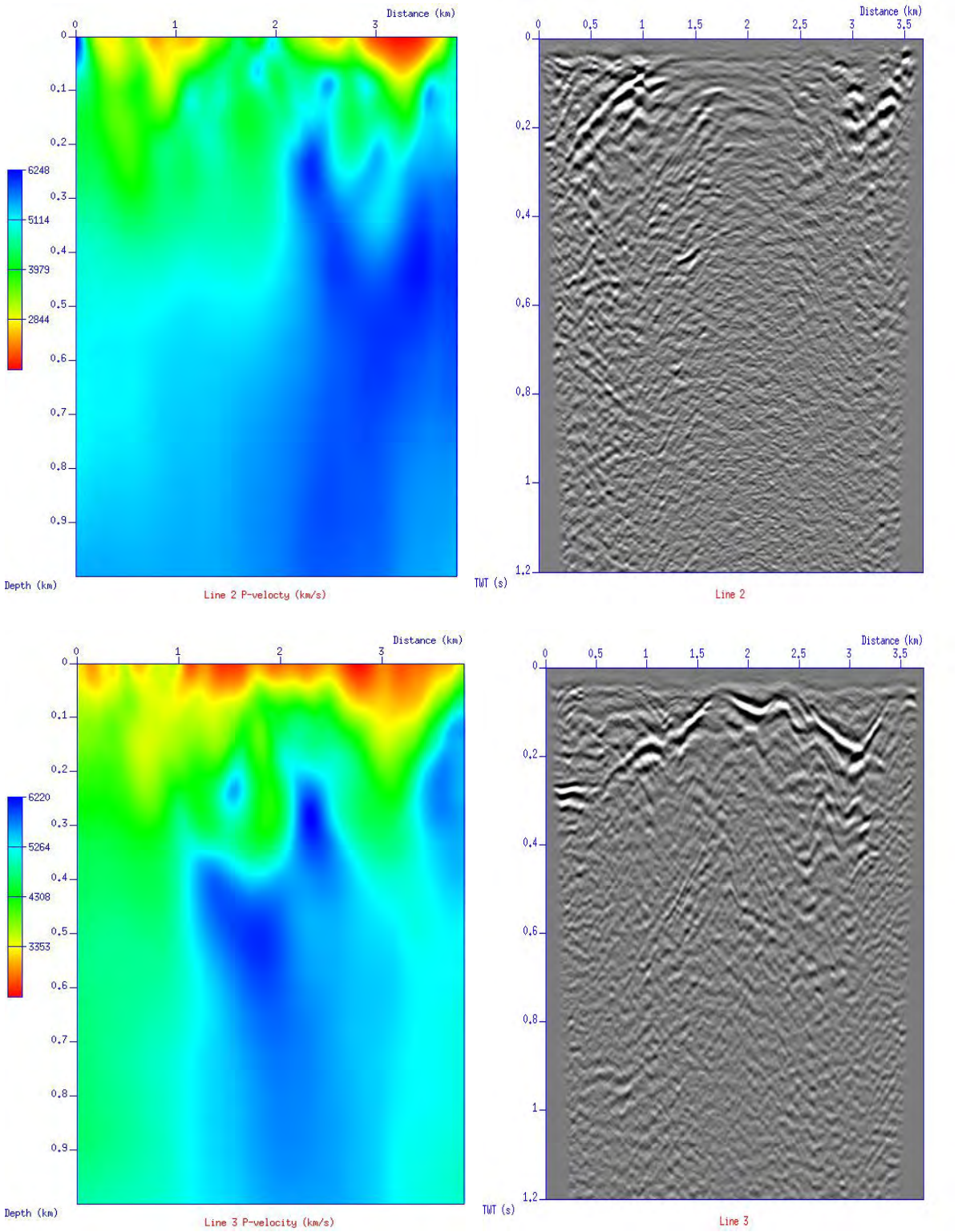

Figure 5.11. Velocities and seismic images for lines a) 2, b) 3, c) 4, d) 5, e) 6. The velocities are obtained from tomographic inversion of the first breaks. The rays of the first breaks does not penetrate deeper than a few hundred meters, so deeper velocites are based on the a priori (input) velocity model.

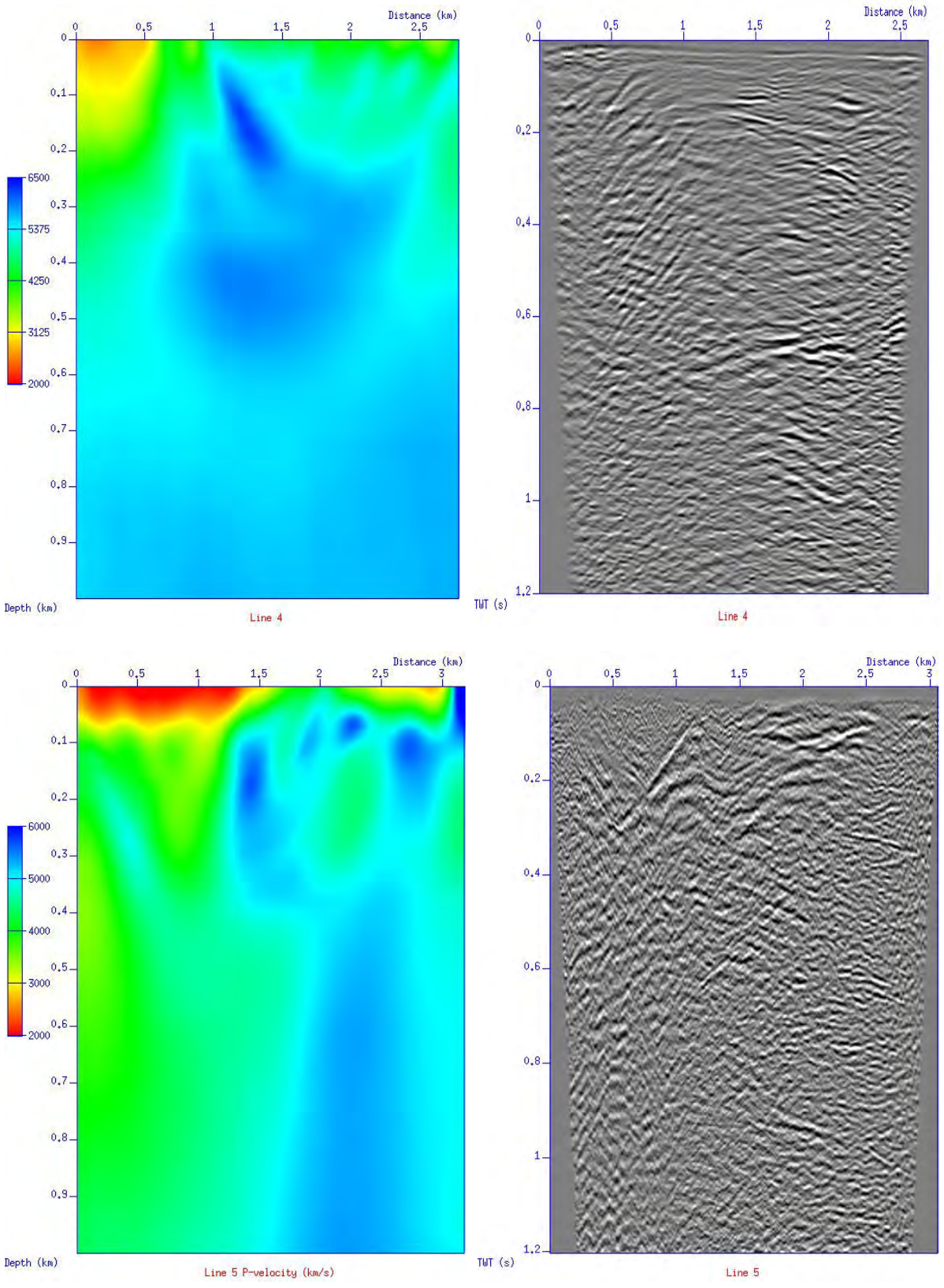

Figure 5.11. cont. Velocities and seismic images for lines a) 2, b) 3, c) 4, d) 5, e) 6. *The velocities are obtained from tomographic inversion of the first breaks. The rays of the first breaks does not penetrate deeper than a few hundred meters, so deeper velocites are based on the a priori (input) velocity model.*

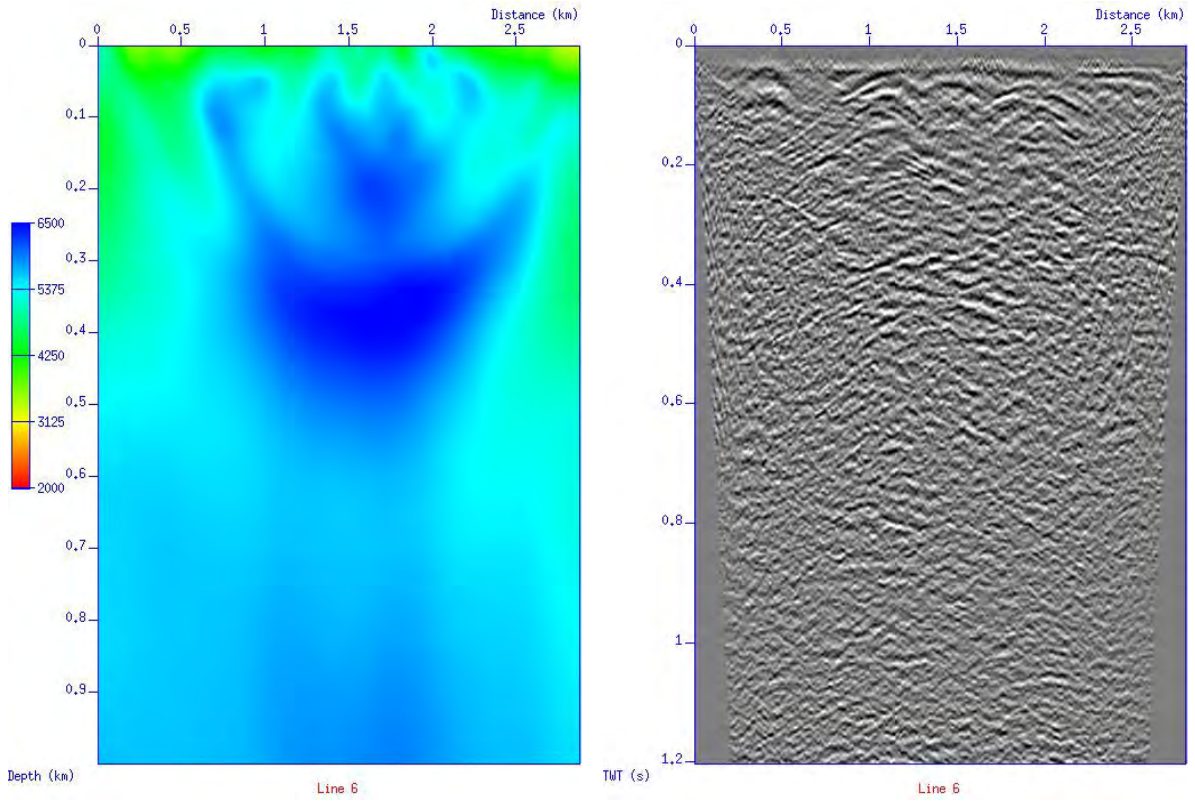

Figure 5.12. cont. Velocities and seismic images for lines a) 2, b) 3, c) 4, d) 5, e) 6. *The velocities are obtained from tomographic inversion of the first breaks. The rays of the first breaks does not penetrate deeper than a few hundred meters, so deeper velocites are based on the a priori (input) velocity model.*

However, lines 2 and 3 (Figure 5.13) cross the gravity and magnetic low south of the Ramså Basin and actually observe an extension or sub-basins in this area of which the one on line 3 was confirmed from drilling (Chapter 8) to be filled with Mesozoic sedimentary rocks of Jurassic age (Chapter 9).

The processing sequence applied for the marine seismic lines acquired with 50 m-long streamer is outlined in Table 5.1. Acquisition parameters for all seismic lines discussed in this report. The 1988 survey was performed by GECO for NPD and includes two lines, LO-11-88 and LO-13-88, from Andfjorden. Except for these two lines, the acquisition was performed as collaboration between the University of Bergen and NGU. and the acquisistion parameters are summarized in Table 5.1. Due to the short offset window, velocity analysis was not possible, and besides, the seismic velocities have hardly affected the final seismic images. For the migration, we computed a stacking velocity model from the water depth and an assumed interval velocity of 3500 m/s below the seafloor. The small offset window also makes it difficult to remove multiples, and the data from these lines suffer from the water bottom multiple, which due to the strong bathymetry also makes it difficult to interpret events deeper than the double two-way travel time for the sea-bottom reflection.

Interpretation of the marine lines is partly uncertain but within the shallower Mesozoic sedimentary succession, reflections indicating various dips of the sedimentary strata and faulting and folding were observed and are indicated in Figure 5.14a-c. Rather continuous seismic signals were interpreted as stratigraphic boundaries and accorded to Mesozoic ages in accordance with existing knowledge and experience from the Lofoten-Vesterålen margin (Chapters 2 and 3). The depth to the basement interpretation is strongly linked to the long NPD lines (Figures 5.15 & 5.16) where the top basement is visible as a strong and continous seismic signal. For the new seismic lines the basement reflection is much weaker and often overprinted or close to a water bottom multiple, which hampered an exact identification of this horizon. In addition, some interesting remains of probable Quaternary sediments can be seen in some of the seismic sections (Figure 5.14c).

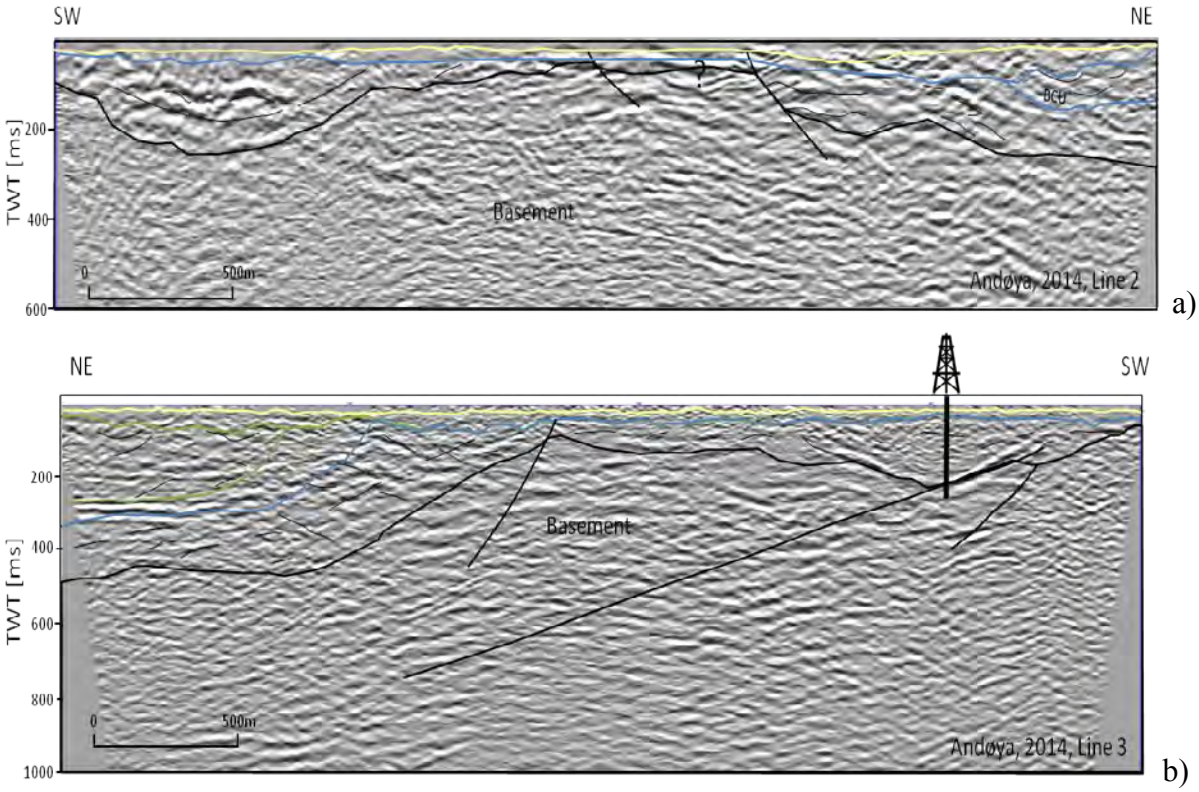

Figure 5.13. Land seismic line 2(a) and 3(b) with interpretation of the most profound interfaces.

As on aid for the seismic interpretation, results from re-processing of two conventional marine seismic lines acquired in 1988 are included. The processing sequence is defined in Table 5.2c. The re-processed data particularly have less energy associated with the water bottom multiple, but some details in parts of the image shallower than the two-way travel time of the water bottom multiple may have been lost. This is evident from comparing the two sections of Figure 5.14a and b. However, along with the acquisition of the two conventional lines LO-88-11 and LO-88-13, data were simultaneously acquired using a short streamer, 500 m-long (see Table 5.1 for acquisition details).

Data from the short streamer were processed for details. Finally, the datasets from the 3000 m and 500 m-long streamers were merged applying a weighting procedure producing a seismic

section where data down to two times the travel time of the water bottom multiple displays results from the 500 m-long streamer, while further increasing travel time display results from the 3000 m-long streamer. The merged sections are shown in Figure 5.15a and b.

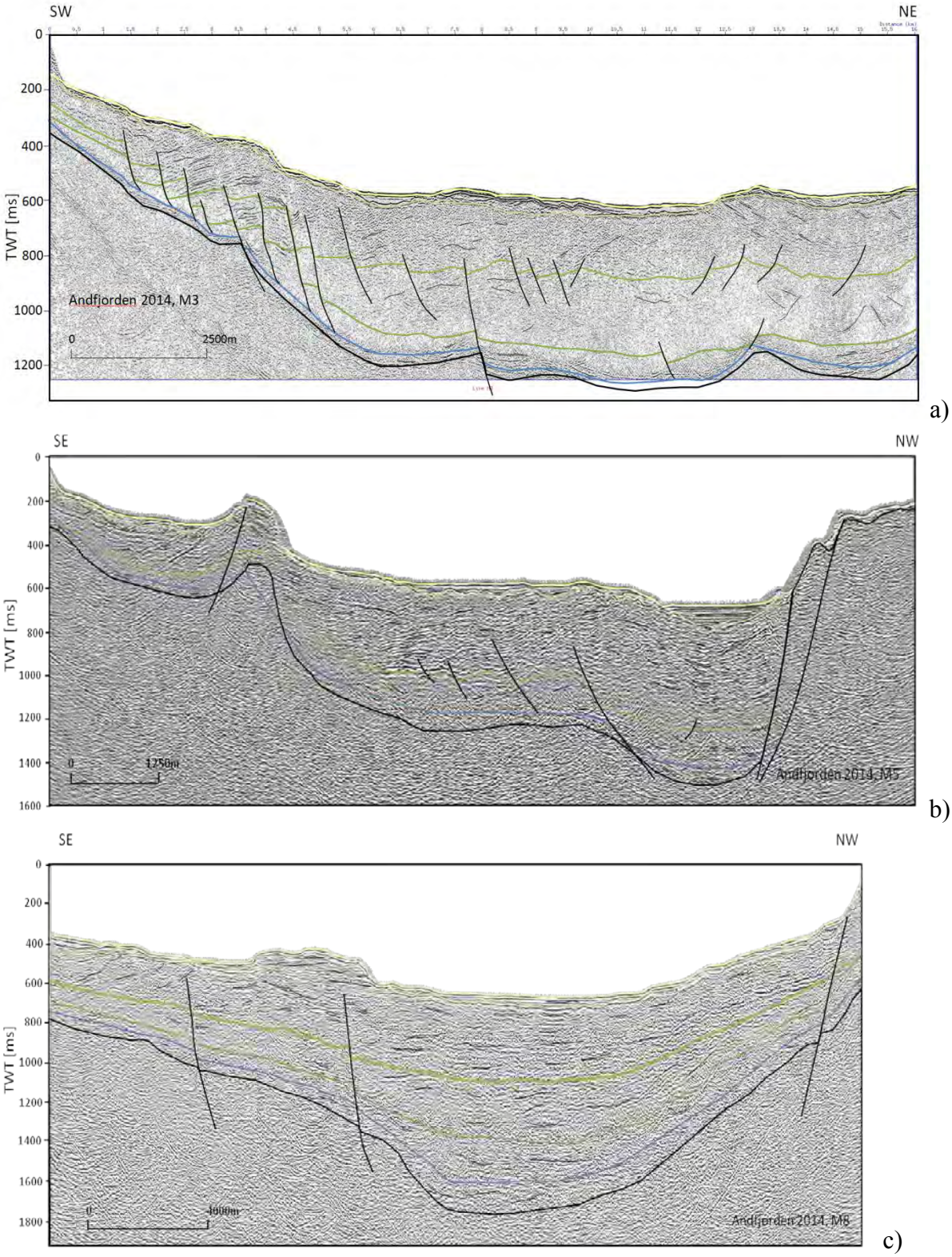

Figure 5.14. Processed marine seismic lines including the most profound interfaces indicated: a) M3, b) M5, c) M8

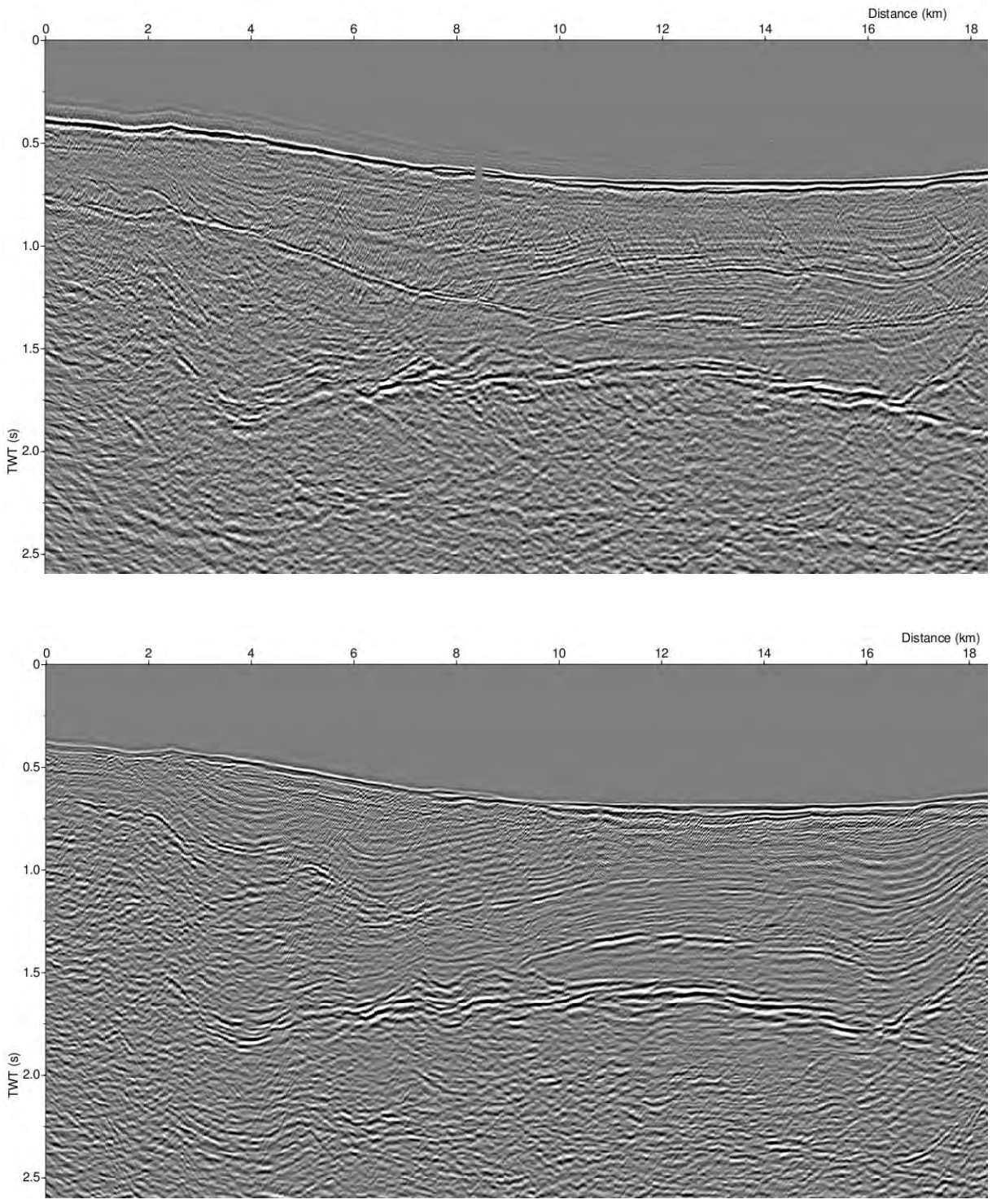

Figure 5.15. Seismic line LO-88-11 original processing (a) and re-processed by UiB (b).

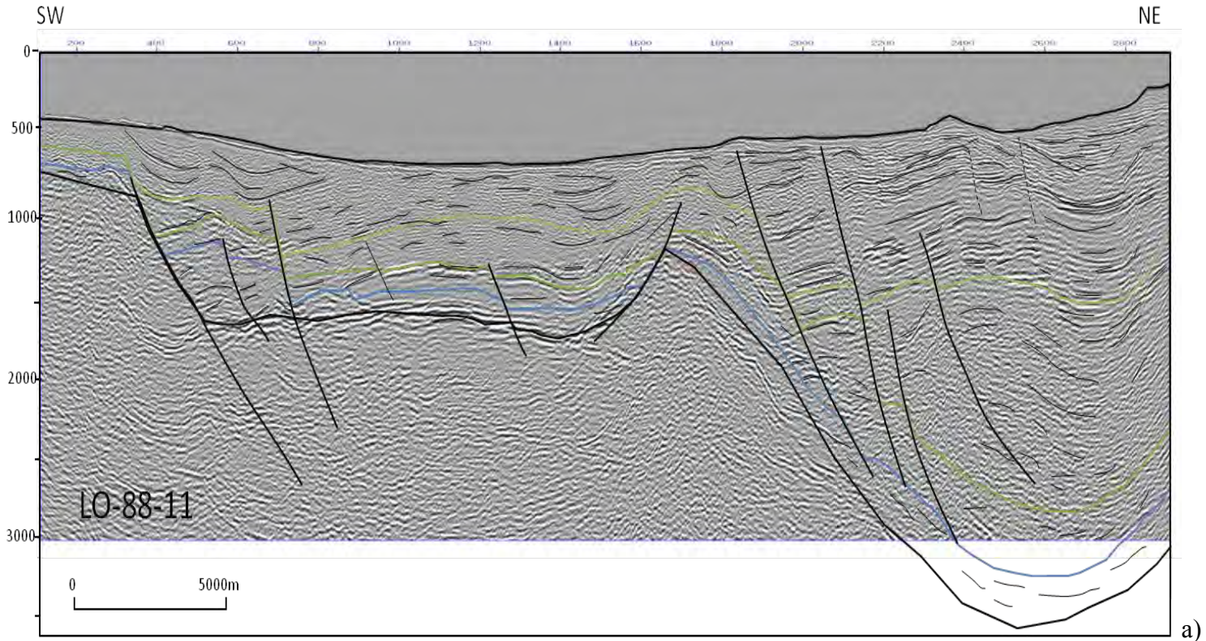

a)

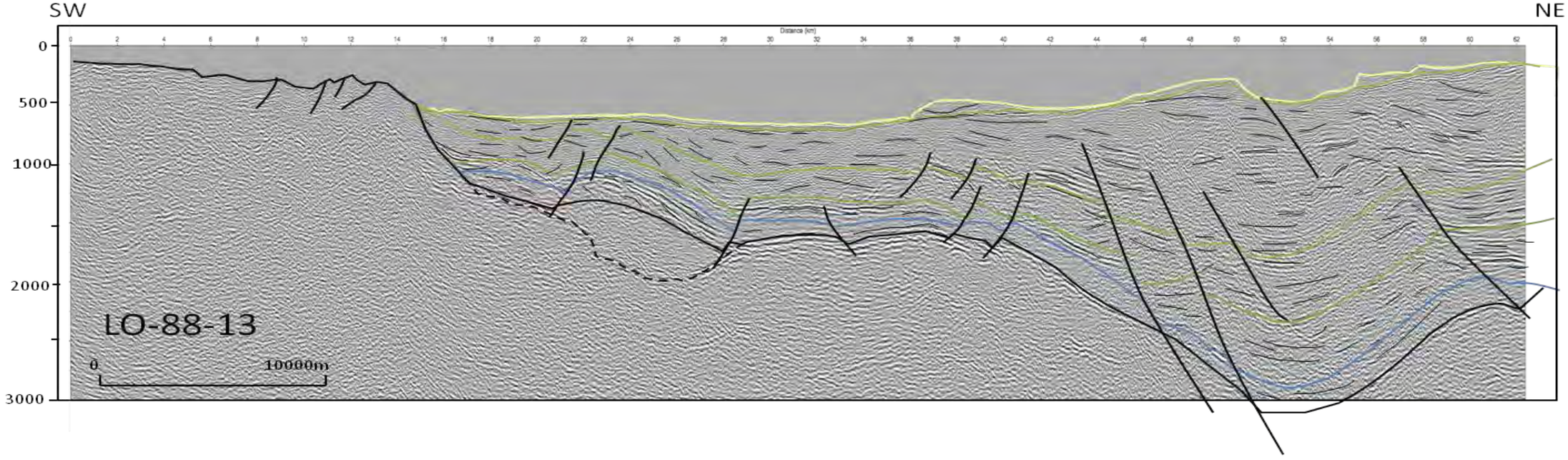

b)

Figure 5.16. Seismic line LO-88-11 (a) and LO-88-13 (b) re-processed where processed mini-streamer data are merged within the time interval starting with the seafloor arrival time and ending at the arrival time of the first water bottom multiple (i.e. two times the seafloor arrival time).

In particular for the deeper part and the top-basement interpretation of the depth-to-basement horizon from the long NPD lines was applied as an important link to identify a top-basement reflector in the new seismic lines (Figure 5.14a,b & c). The interpreted geometries identify the Andfjorden basin as a complex half-graben, with a major border fault or rather a border fault complex in the west. Sturt et al. (1979) and Dalland (1981) suggested a similar setting as '*tentative model*' and with these lines the model can be confirmed and refined for the first time. However, several faults are observed with possible N-S trends and are related to the E-W extensional opening of the Andfjorden. Steep-dipping seismic reflectors (Figure 5.14a) and horst structures, which locally can even be observed in the bathymetry (Figure 5.14), indicate a more complex setting of the Andfjorden. The comparison with the long N-S-striking NPD lines (Figure 5.16a & b) shows a deepening of Andfjorden northwards and an abrupt fault-controlled transition into the Harstad Basin with an extensional setting and a significant increase in the thickness of the sedimentary strata. The high-resolution data from the short streamer on this line, however, reveal folding (Figure 5.15b and Figure 5.16) in southern Andfjorden and in front of the Ramså Basin, which indicates compression and underlines the complexity of the Andfjorden setting.

5.4 **Discussion and conclusions**

In this report we have reviewed acquisition and processing of both land and marine seismic data aimed for the study of the extent and seismic signature of Mesozoic sediments in the Ramså Basin in the northeastern part of Andøya. A major obstacle for doing this kind of surveying in this area is the strong constraints put on the logistics of the operation. An optimal survey designed for seismic imaging cannot be followed because of the existing infrastructure. To a major extent, the land seismic lines had to follow existing roads and trails. The complex geometry of the target reflector also makes this challenging, as the seismic 2D lines cannot be defined to minimise out-of-plane reflections (3D effects) which will cause errors in the seismic processing, imaging and interpretation. Furthermore, the strength of the seismic source has to be kept as gentle as possible since humans, cattles and other animals are living here. Except for the Mesozoic sediments of the Ramså Basin, the geology is basically consisting of older and rigid basement rocks, which implies high seismic velocities (low seismic resolution) and low impedance contrasts. The subsurface structures of such basement rocks are therefore generally very difficult to image seismically.

The marine seismic surveying also had to be carried out with great caution. As coastal fishery was ongoing, the survey time had to be kept to a minimum. Consequently, an easy to operate short streamer was used. Also, the size of the airguns had to be kept moderate. With a short streamer, it is difficult to remove multiples due to the lack of difference in reflection move-out times of the primaries and multiples. The strongly varying bathymetry in the Andfjorden, as revealed in Figure 5.1, makes the extent of the ocean-bottom multiples to overprint events occurring deeper. As such, interpretation of events in the seismic sections from the arrival time of the ocean bottom multiple and below is difficult. However, we also discussed an

interpretation of selected lines where we identified depth-to-basement and derived intra-sedimentary structures and fault systems onshore and offshore. The onshore seismic confirmed the settings earlier proposed, but could reveal more structural details and in addition an extension of the basin to the south. Furthermore, we could confirm the Andfjorden Basin as a half-graben basin in a obviously complex 3D setting with the adjacent deep Harstad Basin to the north. The link between the onshore and the offshore domain and consequently the role of the Ramså Basin in regard to Andforden remains difficult and is investigated further in Chapter 11 applying an integrated interpretation.

However, seismic processing of the wide-angle seismic lines (Figure 5.17), which are those recorded on land while the shooting is performed along the seaward extensions of the lines (3 – M3, 4 – M4, 5– M5, 6 – M6) have the potential to bridge the gap. A comparison of the marine seismic data (near trace) along M5 is shown in Figure 5.17 together with data recorder on one geophone receiver (station 11) on line 5, and underline the importance of considering the effects of the bathymetry on seismic wave propagation and the strong interference of both reflected and refracted waves.

Processing and modelling of these wide angle lines is outside the scope of this paper spite of constraints of geological and technical matter, the seismic surveying and data have given promising results which can unveil further details about the marine extension of the Ramså Basin and that further can be used to study the foundation of these sediments when Andøya and Greenland were closely bounded.

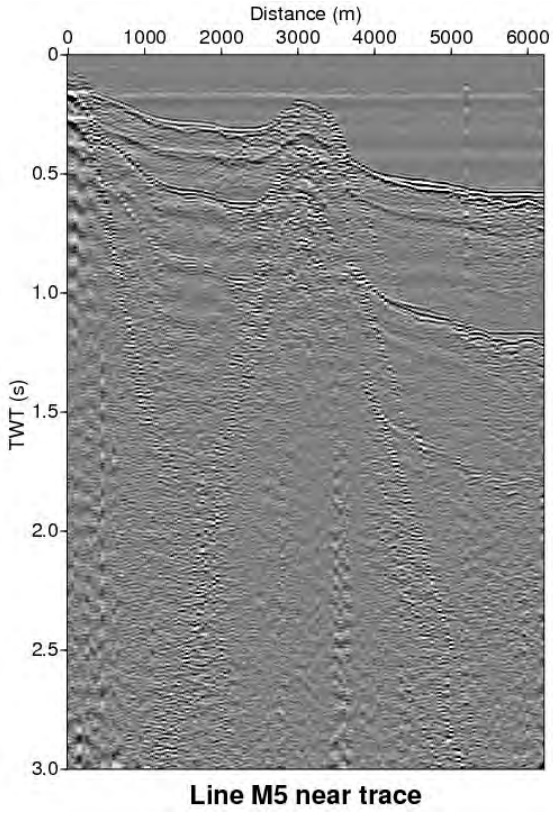

a)

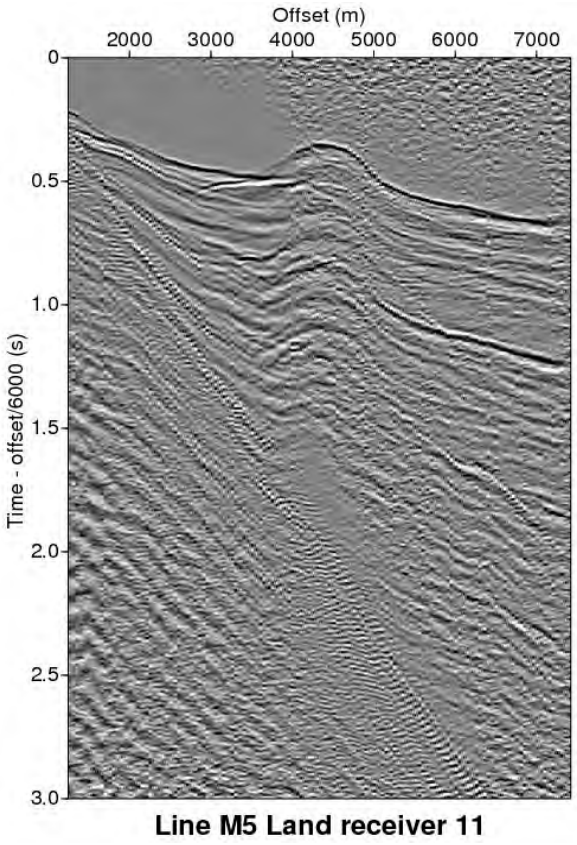

b)

Figure 5.17. ***a)*** *Common receiver seismic data recorded on station A on line 5 with shooting performed along the seaward extended marine line M5.* ***b)*** *Near trace seismic data obtained along marine seismic line M5.*

6. 3D RESISTIVITY INTERPRETATION OF HELICOPTER-BORNE FREQUENCY EM (HEM) DATA FROM RAMSÅ BASIN AND AROUND IN ANDØYA, NORWAY

Vikas C. Baranwal, Einar Dalsegg, Harald Elvebakk, Jan-Steinar Rønning and Marco Brönner

6.1 Introduction

The Ramså Basin on Andøya, Northern Norway is the only known Mesozoic basin onshore Norway. It is situated along the strandflat on the north-eastern side of Andøya between Ramså and Skarstein. The thickness of the sedimentary basin is reported to be more than 650 m (Dalland 1975). Deeply weathered materials are exposed at the surface (Brönner et al., 2012) and were also observed in well cores drilled in the Ramså Basin (Vogt 1903, Dalland 1975). The weathered bedrock is overlain by mid Jurassic to Cretaceous sedimentary rocks.

Six 2D electrical resistivity tomography (ERT) profiles were collected in 2010 (Brönner et al. 2012) and followed by an airborne EM helicopter survey in 2012 (Rodionov et al. 2012) to map the basin boundary and to investigate the appearance of weathered and fractured basement. DC resistivity and electromagnetic (EM) methods map resistivity to identify different rock types, conductive minerals and weathered and fractured bedrock. Later, four boreholes were drilled and logged in 2015 and 2016. Locations of these boreholes were chosen on the basis of initial interpretation of airborne geophysical data and seismic profiling (Chapter 4).

A quasi-3D inversion result of helicopter-borne frequency-domain EM (HEM) data for the area of the Ramså Basin is presented in this paper. The inverted resistivity obtained from this HEM data inversion was subsequently compared with borehole resistivity logs from the four recently drilled wells and 2D ERT profiles acquired during the TWIN project (Brönner et al. 2012) to cross-check its validity. The inversion result is correlated to bedrock, possible bedrock alteration, boundary between sedimentary rocks and basement since these different rock units show distinct resistivity ranges.

6.2 Geology of the area

The existing bedrock map of Andøya is shown in Figure 6.1. The primary basement rocks in the area are mainly granodiorite (Chapter 7) granite and gabbro. The sedimentary rocks in the Ramså Basin consist of sandstone and different variation with clay and shales of mid Jurassic to early Cretaceous age (Dalland 1974, Midbøe 2015, Chapter 9). Few bands of quartzite are also observed as part of supra crustal metasedimentary rocks in the Skogsvoll group south of the Ramså Basin.

Most of Andøya is covered by quaternary marine deposits, moraine and bog. The cover varies from a few meters to tenth of meters at different locations. The original boundary of the

Ramså sedimentary basin is derived from Henningsen & Tveten (1998) which was refined on the base of shallow drilling (Fries 1903, Vogt 1903) and is shown by a green line (Figure 6.1).

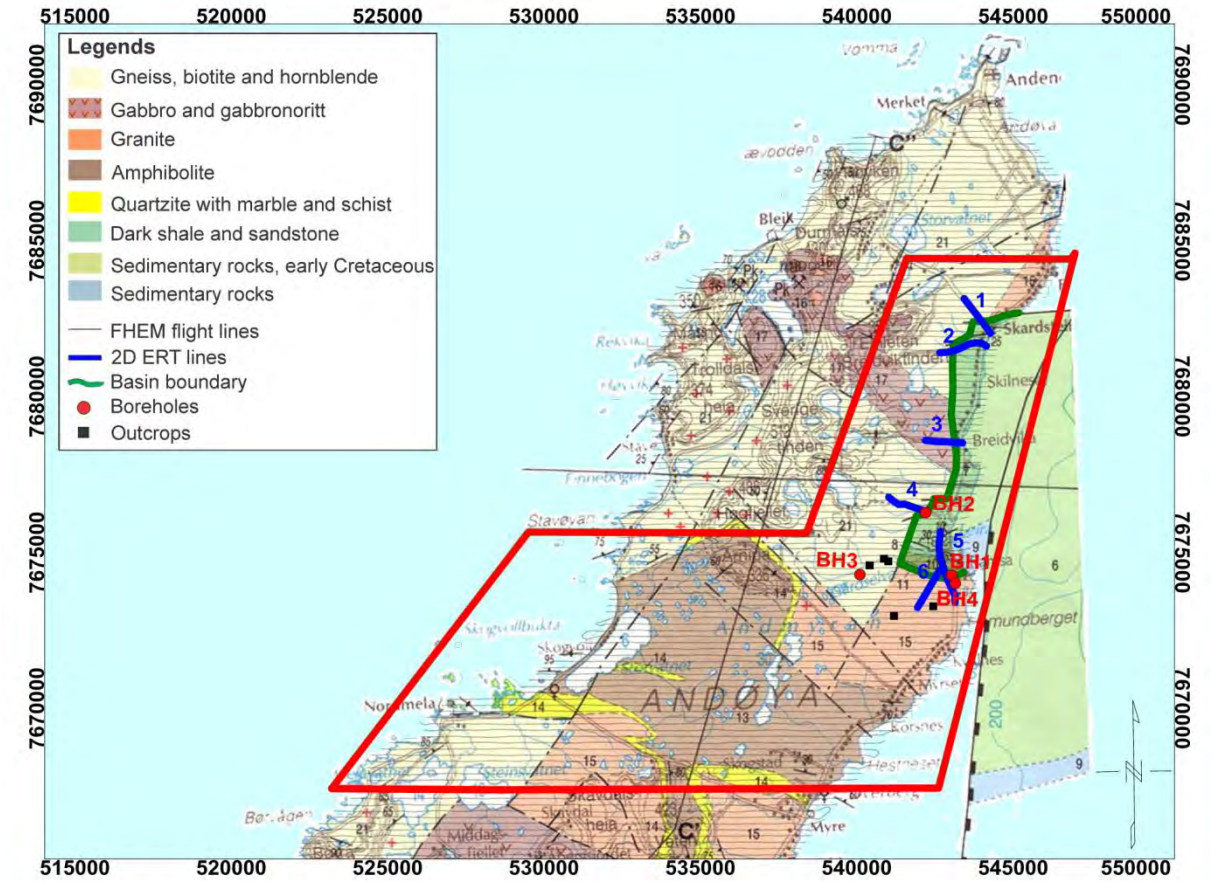

Figure 6.1. Bedrock map of Andøya (Henningsen & Tveten, 1998) and location of geophysical surveys. Previously assumed geological Ramså Basin boundary is shown by green line. Location of the geophysical surveys and basement outcrops are also marked. Red polygon shows a part of HEM data chosen for quasi-3D inversion.

6.3 **HEM and other geophysical surveys**

Airborne EM (AEM) surveys using various types of EM transmitter and receiver coils deployed on fixed wing aircraft or helicopter have been used successfully for various geological and hydro-geological investigations e.g. river clay mapping (Asch et al. 2008), groundwater exploration (Ley-Cooper et al. 2008, Siemon et al. 2011), tunnel construction (Okazaki et al. 2011), depth to bedrock mapping (Christensen et al. 2015) , 3D geological modelling (Høyer et al. 2015) and mineral exploration (Roach et al. 2014). The measurements are performed by different AEM systems either in time or in frequency domain. A good review of various AEM systems can be found in Siemon et al. (2009) and Anschutz et al. (2014).

A common interpretation of AEM data is done using homogeneous half-space, 1D and 3D inversions. 2D modelling of AEM data is not very common though some codes can be found in the literature (Li et al., 2016). Recently, full 3D inversion codes were developed to invert

AEM data (Cox et al. 2012, Liu and Yen 2016, Scheunert et al. 2016). Quasi-3D inversion using 1D forward modelling and spatially constrained inversion is extensively used to invert AEM data for groundwater and mineral exploration applications (Anshutz et al. 2014, Høyer et al. 2015). Quasi-3D inversion produces results similar to full 3D inversion when sufficiently long horizontal layers of a few hundred meters are present in the area justifying the use of 1D forward modelling in the inversion (Viezzoli et al. 2010**).**

6.3.1 Data acquisition

The HEM data presented here were collected at five different frequencies using a Hummingbird system (Geotech 1979), where three of them (34133, 6600 and 880 Hz) were in a horizontal coplanar setting and two of them (7001 and 980 Hz) were in a vertical coaxial setting. A 7.5 m long bird containing transmitter and receiver coils for all five frequencies was fastened with a 30 m long wire below the helicopter. Terrain clearance was measured with a radar altimeter fixed at the helicopter. Average terrain clearance of the bird was c. 56 m. HEM data was recorded at every 0.1 sec to give c. 3 m data interval. The location of the airborne survey is shown by thin black lines in Figure 6.1. A quasi-3D inversion was performed for the HEM data within the red colored polygon which covers the Ramså sedimentary basin area. The positions of six ERT profiles collected in 2010 are shown by blue lines. Four boreholes used for resistivity and other geophysical logging in 2015 and 2016 are shown by red circles. Black squares show observed locations with outcropping bedrock.

6.3.2 Processing of HEM data

Before starting the airborne survey, the HEM system was calibrated following the standard procedure adapted at NGU for phasing using a ferrite bar and for gain using a calibration coil as recommended by manufacturer (Geotech 1997). The calibration process set correct sign and gain to the system with help of known signal and made sure that correct recording of in-phase (real part) and quadrature (imaginary part) components is done by the HEM system.

The HEM data was processed using the HEM module of the Geosoft Oasis Montaj software (Geosoft 2005) and details of data processing are reported by Rodionov et al. (2012). In-phase and quadrature data were non-linearly filtered for 3 fiducials and low-pass filtered for 20 fiducials to suppress high frequency components from instrumental and the cultural noise. The bird was raised to an altitude of approximately 1200 ft above the topographic surface to obtain a background zero level of the system avoiding any electromagnetic responses in the measurements from the ground. The background levels were recorded at 20-30 minutes intervals and instrumental drift of the system was removed from the data by resetting these points to the initial zero level of the system assuming the drift to be linear (Valleau, 2000). Later, residual instrumental and non-linear drift were manually removed on line-to-line basis after splitting the data in the flight lines.

After levelling of the HEM data, apparent resistivity was calculated from in-phase and quadrature data using a homogeneous half-space model of the Earth (Valleau 2000,

Whitehead 2005) for five frequencies separately. Threshold of 5 ppm was set for inversion of three higher frequencies of 6606, 7001 and 34133 Hz and 3 ppm for lower frequencies of 880 and 980 Hz. Higher frequencies provide resistivity information from shallower depth and lower frequencies provide resistivity information from greater depth respectively. The sensor height is used in the calculation of the apparent resistivity therefore gridded apparent resistivity images were subsequently used to look for some along-line errors in the levelled EM data and to re-level them accordingly as needed. Apparent resistivity images at frequencies 6 kHz (for coplanar coils) and 7 kHz (for coaxial coils) from the whole survey area are shown in Figure 6.2 and Figure 6.3. Half-space inversion is a very quick and easy approach to locate the conductors but it cannot reveal correct resistivity and depth of the anomalous regions. They are helpful in a qualitative interpretation of the HEM data but not precise in a quantitative interpretation. Detailed inversion is needed for quantitative interpretation of the data. A small area covering the sedimentary basin and a conductive area south of the basin (shown by a black polygon in Figure 6.2 and Figure 6.3) was selected on the basis of apparent resistivity images to invert it using quasi-3D inversion.

6.3.3 Quasi-3D inversion of HEM data

Quasi-3D inversion is a spatially constrained inversion approach developed by the Hydro geophysics group of University of Aarhus, Denmark, (Viezzoli et al. 2008, AarhusInv 2013). In the quasi-3D inversion approach, the whole area is discredited in a 3D triangular mesh. Forward response is computed in 1D in z-direction. Cells in x- and y- directions are connected with each other by spatial constraints and conductivity/resistivity of each cell is iteratively optimized till a good fitting between observed and computed data is reached or other stopping criteria of the inversion are satisfied. There could be errors in altitude measurements due to canopy effects and quick ascending and descending of the helicopter. Therefore, the altitude of the sensor is also inverted during initial iterations (e.g. five). The inverted altitude is used in the following iterations of the inversion. Laterally constrained inversion (LCI) is a quasi-2D inversion with similar settings as spatially constrained inversion (SCI) (Auken & Christiansen 2004). First, few flight lines were inverted individually using LCI for all five frequencies with 10 and 100 Ωm starting models. This was done to get appropriate inversion parameters, e.g. noise floor, lateral and vertical constraints etc. to be used in SCI. Though LCI results are not shown here, it was observed that coaxial data (at 980 and 7001 Hz) did not fit well and showed a higher mismatch than coplanar data (at 880, 6606 and 34133 Hz). The LCI inversion result with 100 Ωm starting model produced many artefacts and recovered higher resistivity of the seawater in comparison to the starting model with 10 Ωm. Therefore, 10 Ωm starting model was used to invert three frequencies coplanar data from black polygon area (Figure 6.2 &Figure 6.3) using SCI.

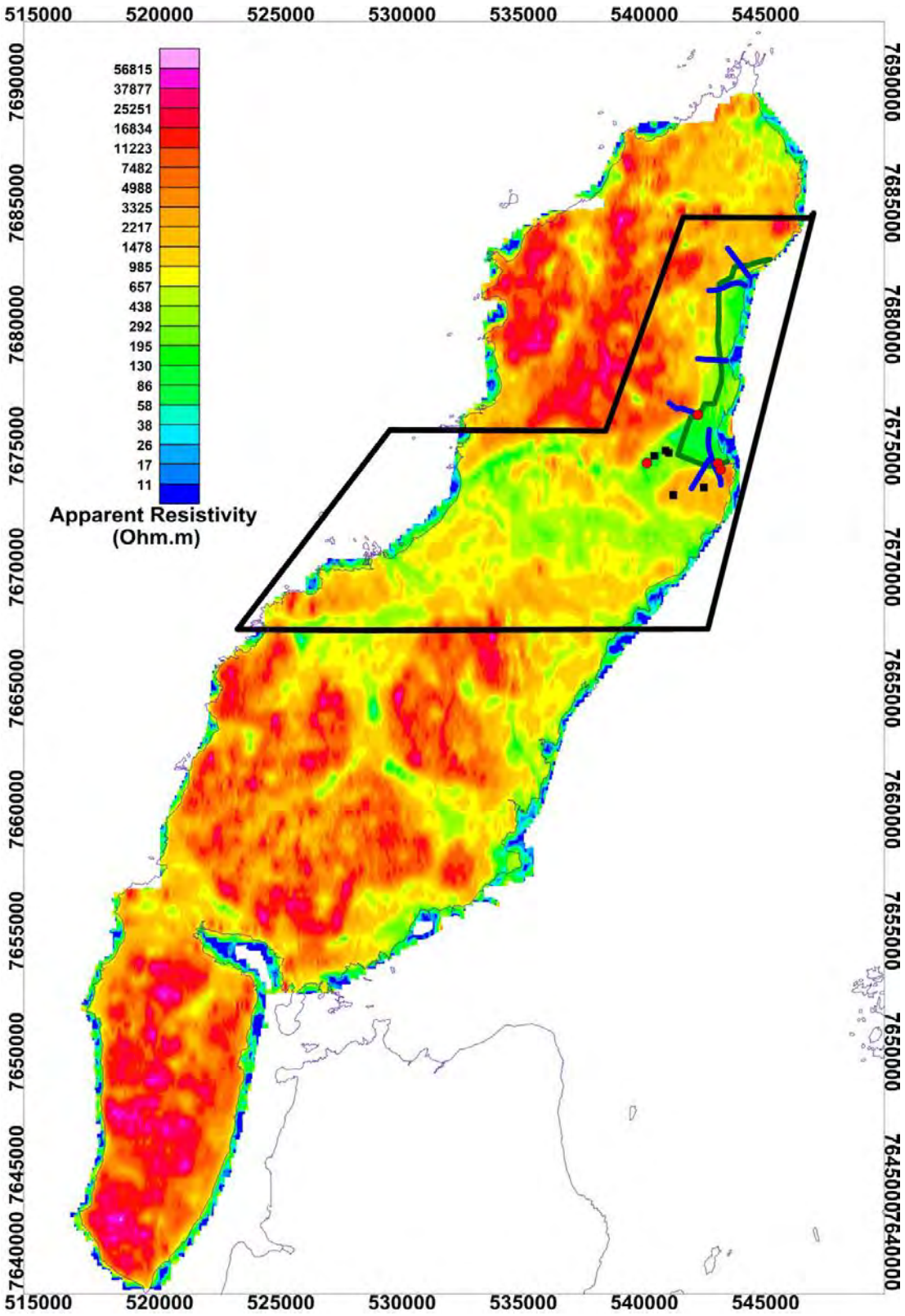

Figure 6.2. Apparent resistivity image of Andøya from homogeneous half-space inversion of 6606 Hz coplanar data. The legend is shown in Figure 6.1.Black polygon covers the area used for quasi-3D inversion.

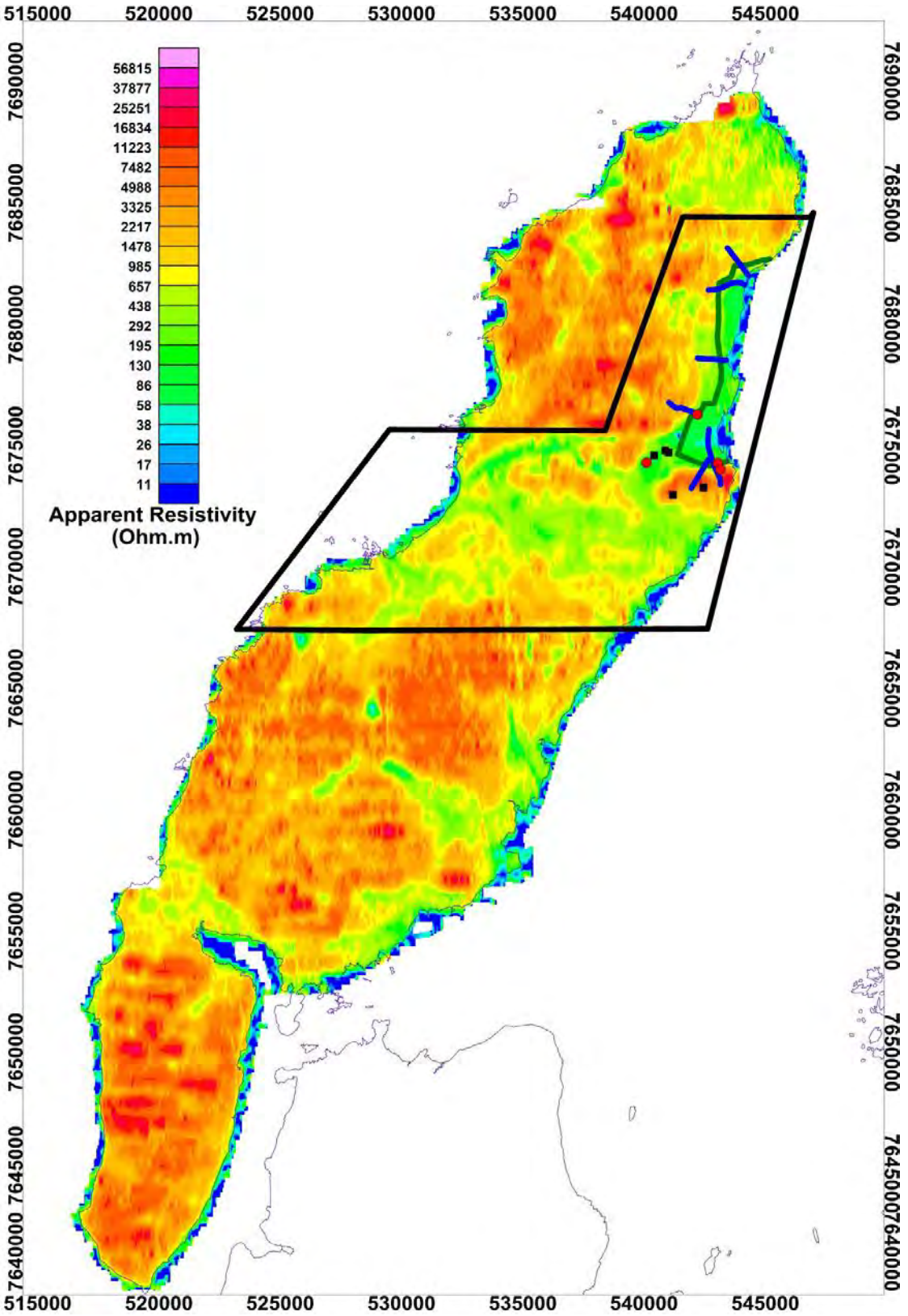

Figure 6.3. Apparent resistivity image of Andøya from homogeneous half-space inversion of 7001 Hz coaxial data. The legend is shown in Figure 6.1. Black polygon covers the area used for quasi-3D inversion.

6.4 **Results**

In this section, resistivity obtained from quasi-3D inversion of coplanar data at three frequencies (880, 6606 and 34133 Hz) using SCI is discussed together with its correlation with resistivity obtained from borehole and 2D ERT. First we discuss comparison of resistivity values obtained from HEM, borehole and ERT. Later, we discuss 3D resistivity images and detailed interpretation.

6.4.1 Comparison of HEM resistivity with 2D ERT and borehole resistivity

Six ERT profiles and geophysical logging data from four boreholes were collected to map the boundary of the Ramså Basin. All the four boreholes were located at different flight lines. We extracted HEM resistivity from quasi-3D inversion result to compare it with ERT and borehole resistivity and present it in Figure 6.4. A formation log is also shown in the figure for each borehole (Chapter 8). All the formations except the basement belong to sedimentary rock types and they are part of the sedimentary basin. ERT data was available only at BH 2. We see a very good correlation between HEM, borehole and ERT resistivity at all the four borehole locations with a varying range of resistivity from c. 10 Ωm to 2000 Ωm. Borehole resistivity of the sedimentary basin varies between 10 Ωm to 600 Ωm at different depths. It becomes less than 300 Ωm after 30 m depth. The conductivity of the water in the boreholes was also measured and plotted in Figure 6.4. Resistivity variations within the boreholes correlate with the water resistivity variation in the borehole. Water resistivity measured in the boreholes 1 to 3 is found very close to seawater resistivity. The water resistivity of c. 0.2 Ωm is observed from boreholes 2 and 3. This very high conductive water is assumed to be fossil seawater (Chapter 8). Borehole resistivity logs and core samples from boreholes 1 to 3 indicate that the basement was reached at c. 200 m at these locations. Fresh basement was observed at the boreholes 1 and 2 but basement at borehole 3 was weathered and highly compacted (Børre Davidsen, pers. Comm. 2017). The borehole resistivity in boreholes 2 and 3 indicates a significant increase when the basement is reached but still it is less than 100 Ωm at the transition to the basement. The borehole resistivity varies between 100 Ωm – 500 Ωm within the basement rock most likely due to the presence of very conductive pore water in the fresh bedrock and the weathered bedrock. BH 2 did not show significant amounts of weathered bedrock, which might indicate fairly fractured basement. The resistivity range of 100 Ωm -500 Ωm is also depicted by the sedimentary basin at the surface where it is likely to be saturated with fresh pore water as seen in BH 1 and 3. BH 4 drilled only basement and confirmed that this location was outside the Ramså Basin.

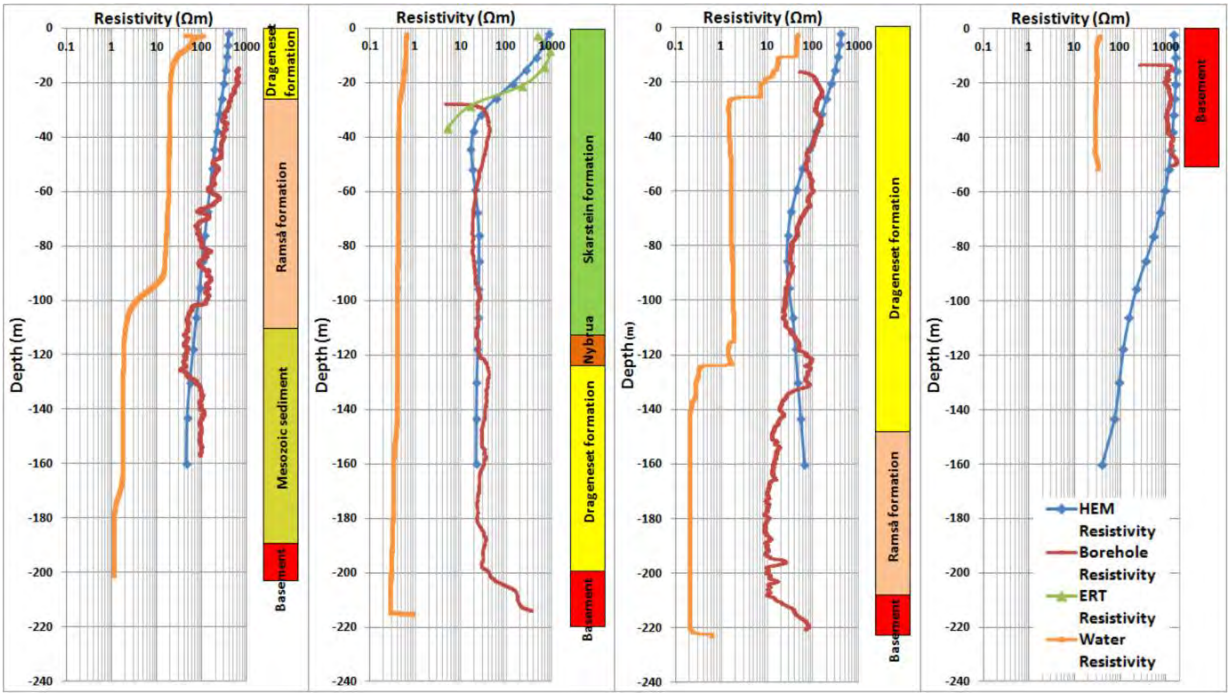

Figure 6.4. Resistivity obtained from HEM, borehole logging and ERT at four borehole locations from left to right for boreholes 1, 2, 3 and 4.

(a)

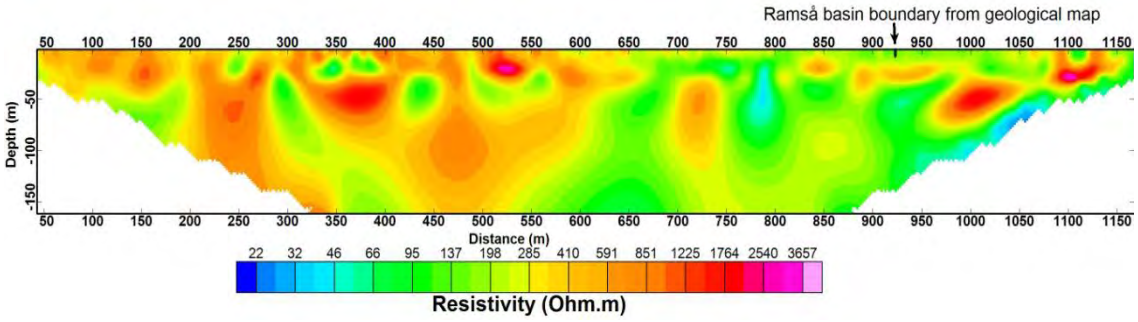

(b)

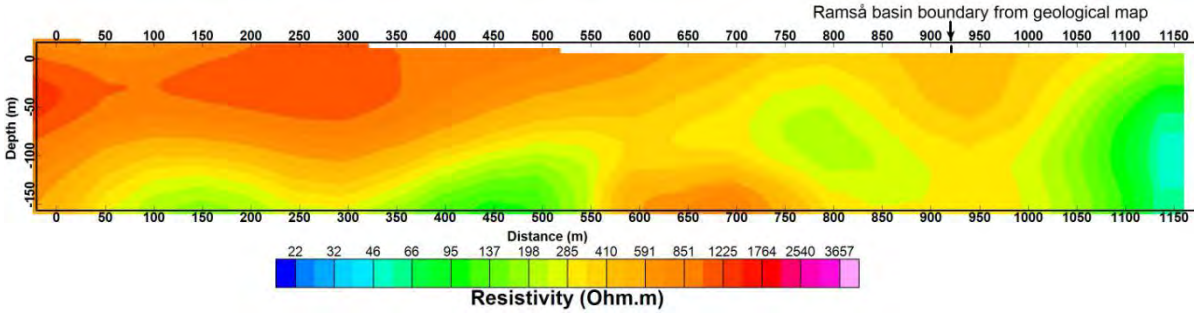

Figure 6.5. Resistivity cross-section in E-W direction (a) from 2D inversion of ERT data (Brönner et al. 2012) and (b) extracted from quasi-3D inversion of HEM data along the ERT line 3.

The ERT line 3 (see Figure 6.1 for position) is parallel to the HEM flight line 570. The resistivity cross-section along ERT line 3 from 2D inversion of ERT data (Brönner et al., 2012) and quasi-3D inversion of HEM data are shown in Figure 6.5. The resistivity cross-sections are plotted with a different colour scale than the resistivity images in Figure 6.2 and Figure 6.3 to adapt a full resistivity range of the grids.

We see similar resistivity ranges along line 3 from both ERT and HEM interpretation but ERT resistivity is more detailed. The western boundary of the Ramså Basin from the geological map is at c. 930 m on the ERT profile (Henningsen and Tveten, 1998) whilst both ERT and HEM inversion indicate higher resistive rocks further west at c. 650 m.

6.4.2 3D HEM resistivity images

Vertical 2D resistivity images along few of the flight lines after quasi-3D inversion of a subset of HEM data is shown in Figure 6.6. Highly conductive seawater and possible marine sedimentary rocks are seen in the east and west. The basement rock in the study area seems to be highly fractured as moderate to high conductive areas (green and blue colored) show up below and in the middle of highly resistive basement (yellow to red collared). The resistivity does not show a regular increase with depth, to indicate the transition from fractured to fresh bedrock. Rather, it shows an opposite behaviour of showing higher conductivity with depth. HEM inversion could not resolve deeper than c. 150m and consequently does not resolve the basin base to show an expected more pronounced contrast of resistivity between basin and weathered/fresh bedrock.

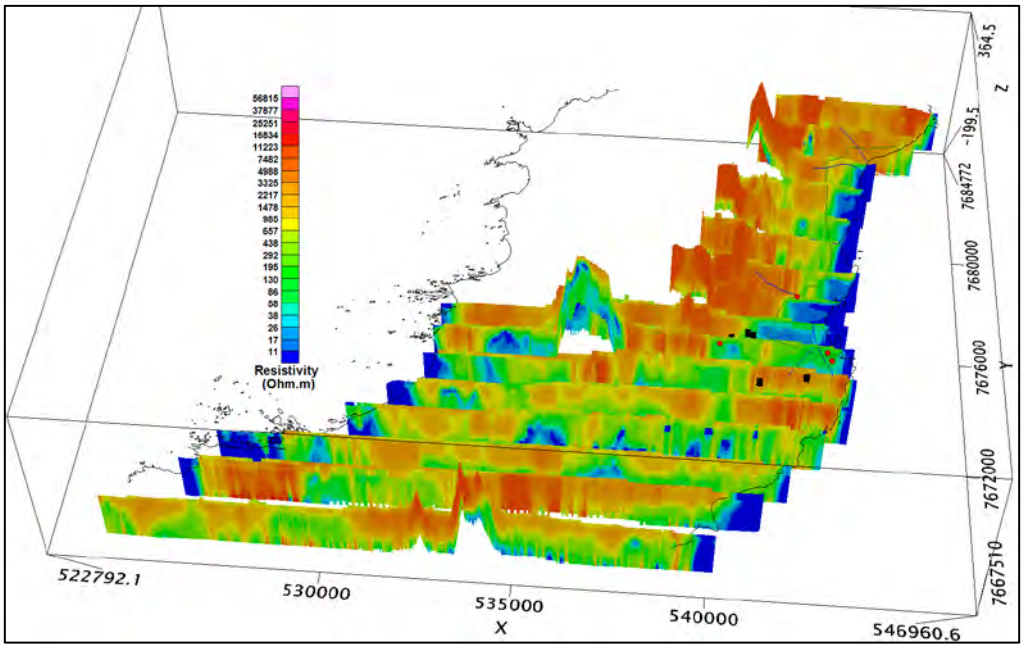

Figure 6.6. Resistivity sections along selected flight lines from quasi-3D inversion results. The existing Ramså geological basin boundary and the coast line are shown by green and black lines, respectively.

The HEM resistivity variation could be driven by a variation in the conductivity of the seawater present there as seen from boreholes. Borehole logging reported generally a lower conductivity of the borehole water at shallower depth and higher conductivity at greater depth at all the four borehole locations (Figure 6.4 and Chapter 8). The 3D resistivity model shows a conductive structure at the very bottom of the resistivity sections which could be an artefact generated to fit the data.

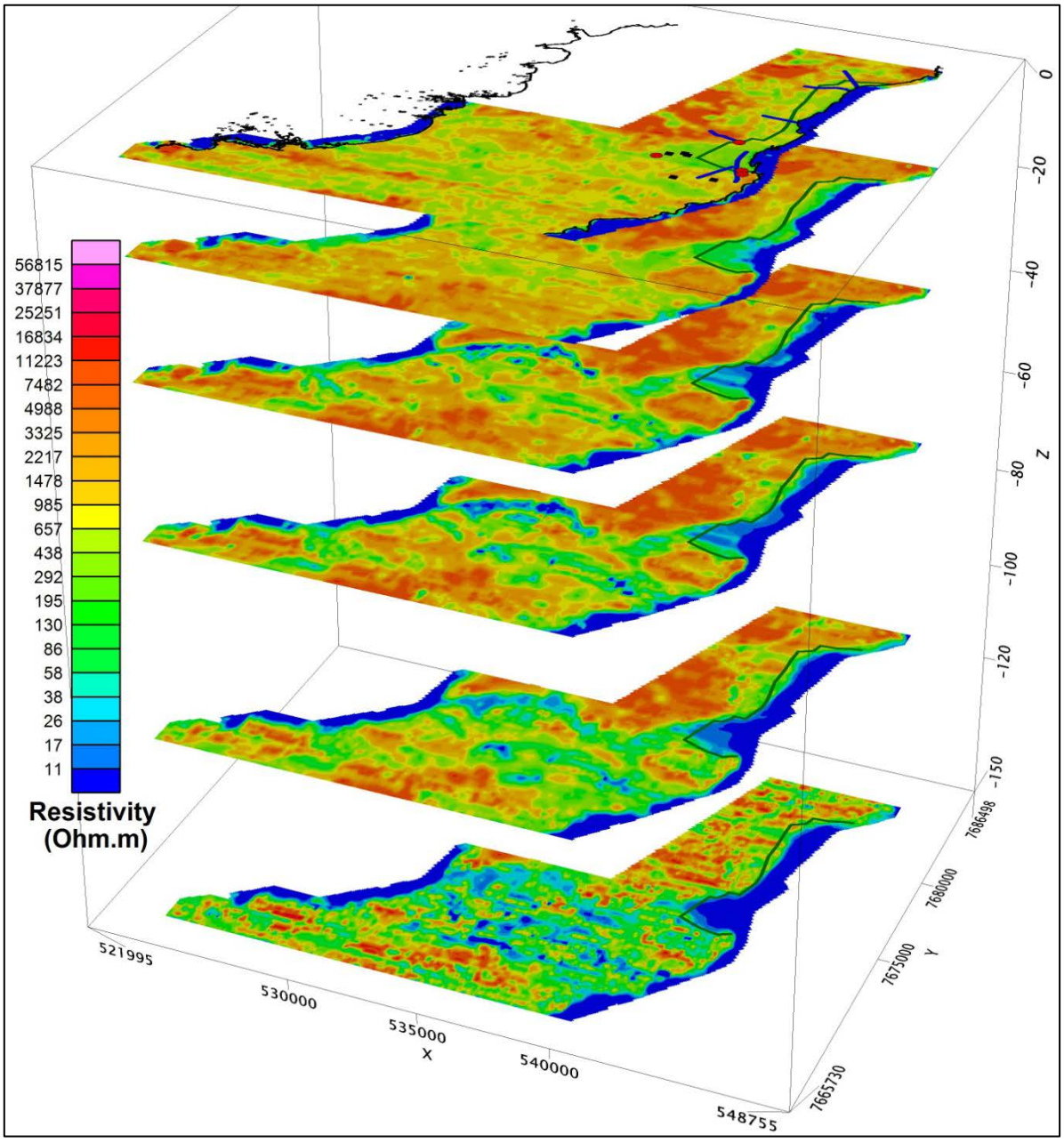

Figure 6.7. HEM resistivity slices at 2, 20, 45, 76, 118 and 160 m depth below the surface. Ramså Basin boundary is plotted by green line.

The horizontal HEM resistivity slices are also shown at 2, 20, 45, 76, 118 and 160 m depths below the surface in Figure 6.7. The Ramså Basin area in the top slices (down to 20 m depth) is relatively resistive (500-600 Ωm) compared to the resistivity of the basin from the greater depth (<300 Ωm). New high conductive areas are observed in the southern part of the image, and they become more conductive at greater depth. One of the conductive zones is confirmed with graphite and sulphide minerals (Børre Davidsen, pers. Communication 2017). The basin is more conductive at depth and it could be filled with conductive seawater. Figure 6.7 also reveals that the basin boundary and its resistivity vary at different depths, which could reflect the significant fracturing of the basement. The significant fracturing of the basement rocks are obvious in the mountainous areas on Andøya and is made responsible in 2015 for the destruction of a radar station on one of the mountains west of Ramså by a lightning due to insufficient grounding.

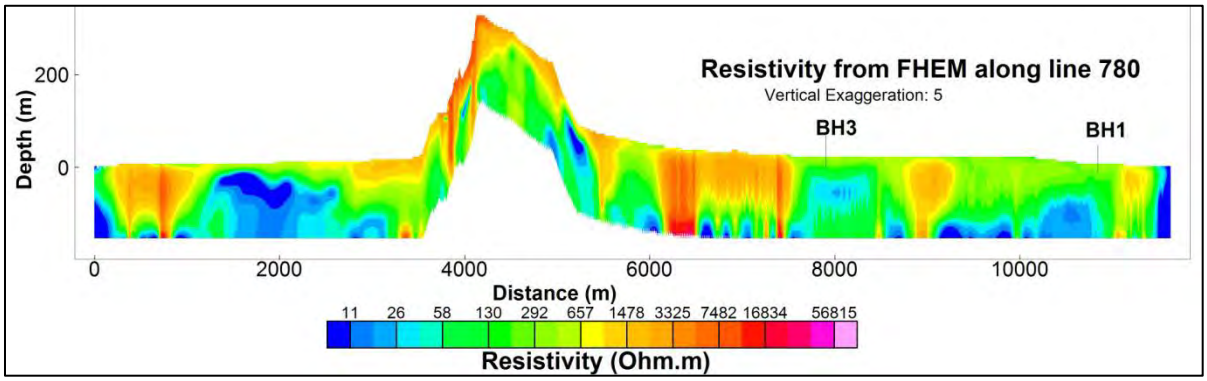

Figure 6.8. Resistivity section along HEM line 780 with locations of boreholes 1 and 3.

Figure 6.8 shows a resistivity section along HEM line 780 on which BH 1 and 3 are located. This resistivity cross-section also shows that the area is very much fractured and there are high conductive areas present below the high elevated region at c. 5000 m location. Small conductive regions at the bottom of the image at c. 500 m and at 7000 m locations could be artefacts generated to fit the data. However, conductive areas at c. 2000 m, 5000 m and near BH 3 and 1 are real (see Figure 6.4 for borehole resistivity). The Ramså Basin was not thought to be stretching till BH 3 on the geological map.

HEM resistivity from quasi-3D inversion was three-dimensionally interpolated using a kriging method available in Geosoft (Geosoft, 2012). The data interval along and across the flight lines were 30 m and 200 m, respectively. Some of the small conductive areas seen in individual EM inverted lines were lost in the interpolation due to a less accurate interpolation method.

Three different geological units can be extracted from the interpolated resistivity assuming different HEM resistivity ranges to these units e.g. (1) basement rock (Resistivity > 1000 Ωm), (2) Ramså Basin together with other fractured and weathered zones (10 - 600 Ωm) and (3) marine sedimentary rocks, conductive minerals and seawater (< 10 Ωm). These three

different units are plotted with 50% transparency with yellow, green and blue colours, respectively as shown in Figure 6.9. The original Ramså Basin geological boundary, ERT lines, borehole locations and basement outcrop locations are shown by black line, blue lines, red circles and black squares, respectively. The green area is in good correlation with low-density-low-magnetization data from the gravity and magnetic maps and shows a possible extent of the Ramså Basin which is large than expected so far (Figure 6.9). However, the resistivity range of the Ramså Basin (10-600 Ωm) can also be attributed to other fractures and weathered zones and therefore it does not show the Ramså Basin area alone but other moderate conductive zones as well, as observed in the southern part of the image. Some regions with resistivity <10 Ωm can be related to sulphide and graphite minerals and are present below the green layer but not visible well in this image.

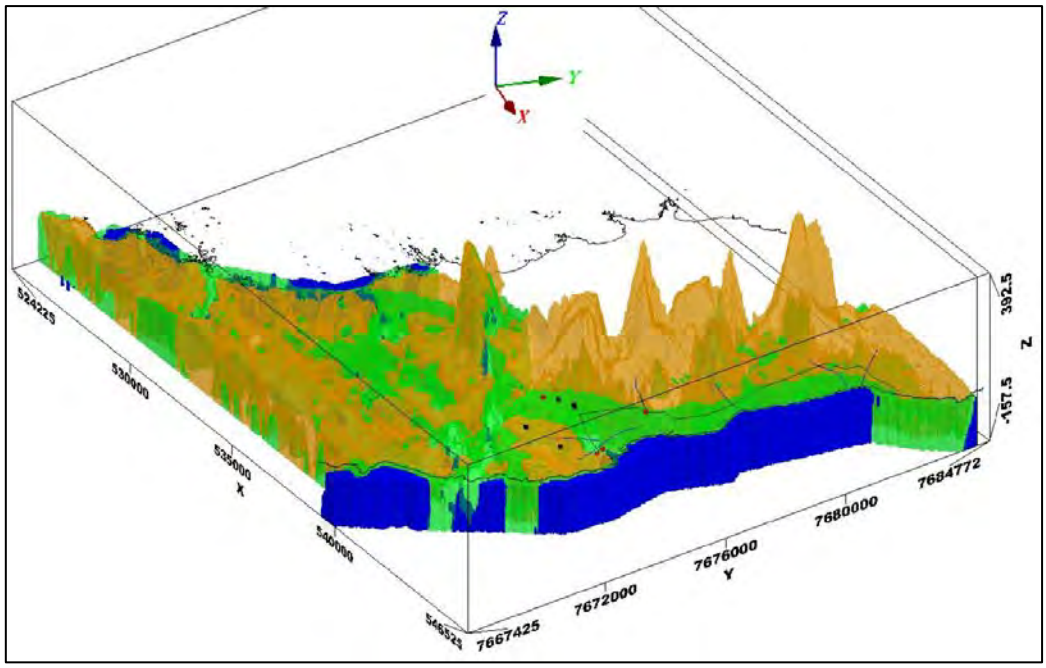

Figure 6.9. Three different geological units are shown with 50 % transparency and by different resistivity ranges as (1) basement (yellow, > 1000 Ωm), (2) Ramså Basin together with other fractured and weathered zones (green, 10 - 600 Ωm) (3) marine sediments, conductive minerals and seawater (blue, < 10 Ωm). Black line shows presently assumed Ramså Basin geological boundary.

6.4.3 Detailed HEM resistivity interpretation

A HEM resistivity slice at 76 m depth is shown in Figure 6.10. We focus on detail interpretation of this image to check the boundary of the Ramså Basin at this depth. The resistivity image is plotted with a new colour scale to adapt full resistivity range of the grid. HEM, borehole logging and ERT profiles in the area suggested a resistivity range of c. 10-300 Ωm for the Ramså Basin below 30 m depth. Therefore contour lines of 100 and 300 Ωm are plotted in Figure 6.10 with thin black lines to locate the boundary of the Ramså Basin on the basis of HEM resistivity. The contoured regions show weathered rocks, mineral zones, and the sedimentary basin all together. Basement outcrops observed near BH 3 are either outside

or at the 300 Ωm contour at this depth. A discontinuity of 100 – 300 Ωm resistivity around the outcrop observations at BH 3 is also observed in this image. High resistivity area of greater than 1000 Ωm (yellow to red colour around BH 4 in Figure 6.10) is confirmed as a part of basement rock by outcrop observations and borehole core samples. The Resistivity slices (Figure 6.7) interpret this part of the basement rock to be fractured at greater depth because relatively conductive areas of less than 100 Ωm (green to blue colour regions) show up at the greater depth. Two high conductive areas (P1 and P2) having resistivities less than 10 Ωm are marked in Figure 6.10. Figure 6.7 depicts a relatively high resistivity at these locations near the surface and lower resistivity started to appear deeper than 20-30 m depth. These conductive zones are not visible in Figure 6.9 because they are concealed below higher resistive regions. P1 is confirmed containing graphite and sulphide minerals (Børre Davidsen, pers. Comm. 2017). A number of sulphide and graphite bearing units are observed at many places throughout the area (Børre Davidsen, pers. Comm. 2017), and this can cause the low resistivity. However, small pockets of blue and green regions can be interpreted either as fractured rock containing seawater or conductive minerals or a combination of both.

The conductive area P1 containing graphite and sulphide is situated in a high elevated area (c. 100 m above m.s.l.) and c. 76 m below the surface. However, the conductive area P2 is situated in a relatively flat land, and could contain low resistive saline water.

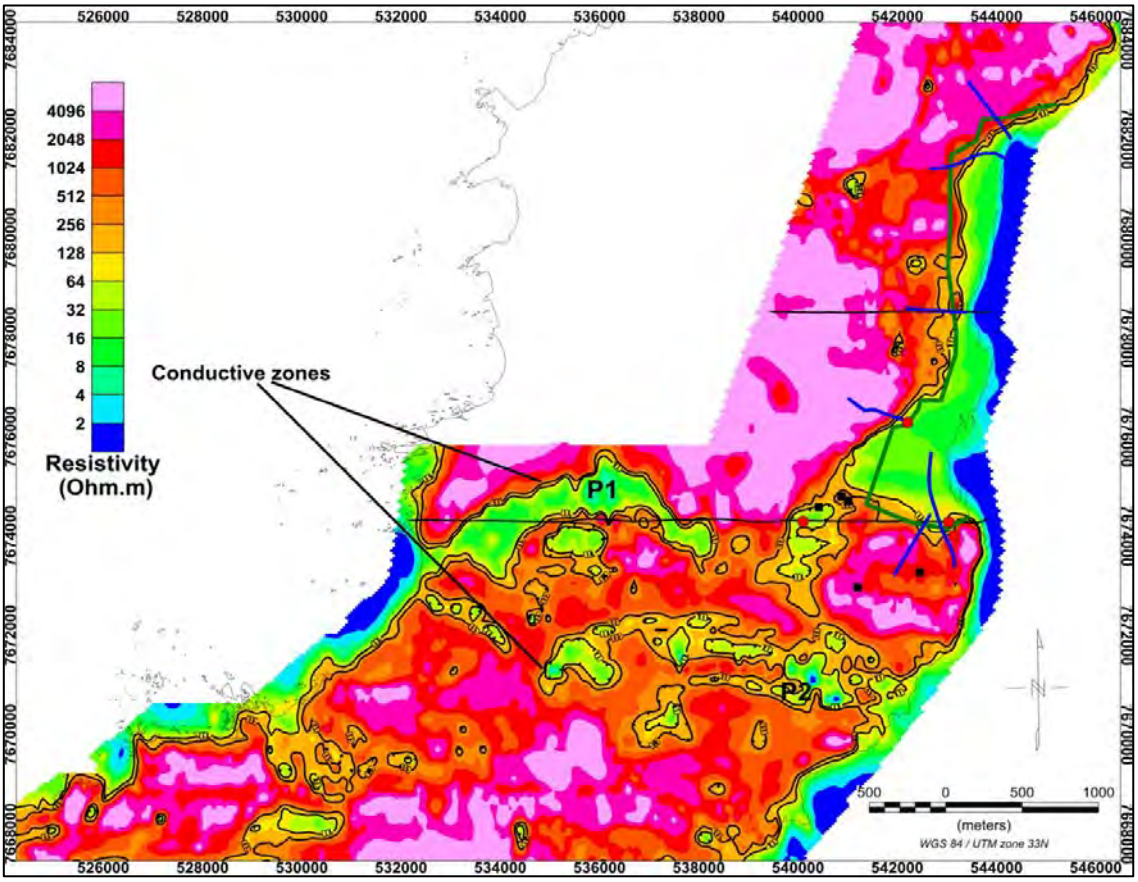

Figure 6.10. Interpretation of HEM Resistivity slice at 76 m depth below the surface with 100 and 300 Ωm resistivity contours (thin black lines). Borehole locations (red circles), outcrop observations (black squares) and ERT lines (blue lines) are also shown.

6.5 **Discussion**

A sedimentary basin may have resistivities around a few tens to thousand Ωm depending on the porosity, water filling and the fluid conductivity (Dobrin, 1960). In general, there should be a clear contrast between the resistivity of the basement rock (few thousands Ωm) and the sedimentary rocks (few tens to few hundred Ωm). Basement rocks can show similar range of resistivity as sedimentary rocks if the basement is fractured or filled with conductive pore water as we have seen at the bottom of BH 2 when fresh basement is reached (Figure 6.4). Similar resistivities as for sedimentary rocks can also be attributed to the weathered basement as observed at the bottom of the BH 3 (Figure 6.4). Conductive minerals like graphite and sulphide have resistivity as low as 1 Ωm in the same range of seawater resistivity. Consequently resistivity and EM methods alone cannot per se distinguish between such geological domains. Additional information about the area from other geophysical or geological observations is necessary to make a certain interpretation in such cases.

Half-space inversion of HEM data yields apparent resistivity and locates conductors but fails to interpret the depth and correct resistivity. Still, it shows sea water saturated sedimentary rocks and exposed basement rock areas quite well and provides an insight in extension of the Ramså Basin, which is in good correlation with the observed extension from gravity and magnetic data. The apparent resistivity image obtained from coplanar data at 6606 Hz shows the basin boundary at c. 700 m on ERT line 3 (Figure 6.2), as shown by ERT and quasi-3D inversion result (Figure 6.5a and b), however, apparent resistivity image obtained from coaxial data at 7001 Hz doesn't show the boundary around that location very well (Figure 6.3). 3D inversion is required to get the correct depth and correct resistivity estimation.

ERT and borehole resistivity data were available from previous surveys. The three resistivity measurement methods as HEM, borehole resistivity and ERT vary in the resolution of the measurements but they provide a similar resistivity range of the area. Borehole resistivity gives a very local variation of the resistivity and has a resolution of few centimetres. ERT data was collected at 10 m electrode spacing and resistivity structures obtained from inversion of ERT data would have c. 10 m or less resolution. HEM data was measured by EM coils at c. 50 m height and then inverted with data spacing of 30 m along the line and 200 m across the flight lines. The HEM interpretation results in resolution of c. 70 m (Smith et al. 2011) depending on sensor height and average speed of flying.

The spatially constrained inversion of HEM data produces a rather smooth image of the subsurface in comparison to a robust inversion of 2D ERT data. With all these constraints, similar resistivity values at four borehole locations shown by the HEM survey and borehole logging establish the validity of the HEM inversion results for this area (Figure 6.4). One ERT line along part of a HEM line also shows a good agreement with each other (Figure 6.5). Water conductivity varied with depth in four boreholes in the area and showed a direct correlation with formation resistivity obtained by the borehole logging. HEM resistivity at these locations correlated well with the borehole resistivity for a range of 10 – 2000 Ωm. A

resistivity range of 10 - 600 Ωm is attributed to the Ramså Basin according to the borehole observations.

Both, Figure 6.6 and Figure 6.7 show the Ramså Basin extension in green colour according to the HEM resistivity. The apparent resistivity images in Figure 6.2 and Figure 6.3 also show similar extension of the basin as seen in Figure 6.6 and Figure 6.7. In general different resistivity ranges can be used to delineate different geological units using HEM or any other resistivity survey. The HEM interpretation in this study constructs three distinct zones as shown in Figure 6.9: (1) higher resistive areas (> 1000 Ωm) representing basement rocks with Gabbro and Amphibolites shown in yellow, (2) Moderate resistive areas (10 - 600 Ωm) around the Ramså Basin boundary representing Ramså Basin, weathered zones and fractures shown in green and (3) low resistive areas (< 10 Ωm) representing marine sedimentary rocks, conductive minerals and seawater shown in blue colour. However, as discussed earlier, the resistivity range of the Ramså Basin (10 - 600 Ωm) can also be attributed to different settings like fractures and weathered zones, therefore the HEM interpretations alone cannot define the Ramså Basin area. However, the extension of the basin from the HEM inversion shows a correlation with what is observed for other data like gravity and magnetics and confirms an extension of the basin towards SW, which was also confirmed from seismic (Chapter 5). The lateral extent of the sedimentary basin beyond BH 3 location should be confirmed by additional borehole and geological observations. Conductive zones with conductivity < 10 Ωm containing sulphide and graphite minerals reported from the area are masked below the resistive green layer in Figure 6.9.

Figure 6.10 depicts the resistivity distribution down to 76 m depth below the surface. It clearly indicates that the geologically mapped Ramså Basin boundary at this depth does not match with the resistivity contrast observed in the area. Two new highly conductive areas P1 and P2 (Figure 6.10) are identified by HEM data in southern part of the inverted area. They can be interpreted as due to presence of conductive minerals or seawater saturated fractured basement. The first conductive area P1 is found embedded under a high elevated region and transportation of seawater to such high elevated areas (100-200 m above m.s.l.) is very less likely. Later, conductive area P1 is confirmed with presence of graphite and sulphide minerals. The other area P2 is situated in flat land and it could reflect either minerals or fractured bedrock filled with seawater which needs to be further investigated.

The presently assumed Ramså Basin extension was drawn mainly on the basis of earlier geological surface observations and shallow drillings. There were only a few geophysical data available before. Recent airborne magnetic, HEM, gravity, ERT and 2D seismic surveys helped to re-explore the area and to redraw the Ramså Basin boundary. BH 3 was considered outside the sedimentary basin according to the earlier geological interpretation but recent geophysical survey results suggest that the basin extends to this location and it is confirmed by core samples obtained from BH 3 (Chapter 8). Quasi-3D inversion results of the area around the Ramså Basin show that the Ramså Basin's extension also match with the HEM interpretation.

Core samples from BH 1, 2 and 3 (Chapter 9) confirm that basement is at c. 200 m depth at these locations. HEM could not interpret deeper than 150 m due to limited depth of investigation of the applied EM frequencies. Fresh and weathered basement is observed at borehole locations 2 and 3, respectively with low resistivity (100-500 Ωm) (Chapter 8). Borehole water resistivity from locations 1 to 3 confirmed presence of saline water in deeper parts of the boreholes. Very high conductive seawater (c. 0.2 Ωm) was reported from different depths at borehole locations 2 and 3 and it is suspected to be ancient seawater trapped in troughs (Chapter 8). We observe low resistivity in the Ramså Basin area at several locations from HEM interpretation as well and that could be due to the presence of saline water or sulphide veins.

Resistivity cross-section and magnetic data (Brönner et al., 2012) had interpreted the basin boundary around 200 m far in NW direction from the boundary shown by the geological map along the ERT line 1 (Figure 6.1). This location was interpreted as a local fault from ERT data (Brönner et al. 2012). HEM interpretation could not resolve the basin boundary at this location rather shows the basin boundary around 200 m far in the SE direction along ERT line 1 (Figure 6.7 &Figure 6.9). The western boundary of the Ramså Basin as observed from the geological map is supposed to be at c. 930 m on the ERT line 3 (Figure 6.5, Henningsen & Tveten 1998). However, resistivity cross-sections from ERT line 3 and HEM data along the same line suggest a resistive boundary of 300-500 Ωm at c. 650 m location. This could be the actual western boundary of the basin. Furthermore, the shallow part of the basement seems weathered or fractured from 0 to 600 m along this line (Figure 6.5a) because the resistivity is not as high up to a few thousands Ωm as it should be for a fresh basement rock. A rather higher contrast in the resistivity images from HEM data exists at the beginning of the ERT line 3 where bedrock could be fresher without fracturing and weathering (Figure 6.5b).

We note that a few of the basement outcrops and basement extension are observed near BH 3. Magnetic and gravity data interpreted this part of basement outcrop to be a horst (Chapter 11). HEM data interprets this area with 300-600 Ωm resistivity down to 30 m depth and <300 Ωm after 20 m depth. Resistivity based geophysical methods will interpret this area (black rectangles in Figure 6.10) either to be a part of the basin or bedrock filled with conductive pore water and weathered bedrock instead of fresh bedrock due to its low resistivity. BH 3 (inside sedimentary boundary) and outcrop observations near BH 3 (outside of the sedimentary basin) could be separated by c. 400 Ωm resistivity boundary at the surface. If the basement is continued to be present at greater depths then this part of basement shows a low resistivity of c. 200 Ωm. A discontinuity of 100 – 300 Ωm resistivity around the outcrop observations near borehole 3 with rest of the basin depicting resistivity <100 Ωm is observed in this resistivity image (Figure 6.10). The 100 Ωm contour lines could separate the extended basin in two parts at basement outcrop observations to match with other geophysical and outcrop observations. Therefore c. 100 Ωm resistivity seems to be appropriate for this part of the Ramså Basin at 76 m depth. The low resistivity observed at the outcrop location could be due to fractured or weathered basement filled with water or conductive materials.

6.6 Conclusions

Helicopter EM survey is a fast and economic tool to explore subsurface resistivity of a large area. Half-space inversion of HEM data yields apparent resistivity and locates conductors but fails to interpret the depth and correct resistivity. 3D inversion of HEM data, however, interprets the correct depth and correct resistivity of the subsurface. A part of the whole HEM data around the Ramså Basin is inverted using spatially constrained inversion (SCI), a quasi-3D inversion approach. 3D resistivity obtained from quasi-3D inversion of HEM data establishes its validity and usefulness by showing good correlation with borehole logging and ERT resistivity. HEM interpretation presents a continuous 3D subsurface resistivity image of a larger area in comparison to what could have been drawn from few ERT lines and borehole logging. The Ramså sedimentary basin shows a rather wide range of resistivity variation between c. 10 Ωm to 600 Ωm at different depths and therefore EM and resistivity methods alone cannot distinguish between fractured and weathered basement and sedimentary basin with similar resistivity ranges.

The basement in BH 2 and BH 3 also shows a significantly low resistivity due to presence of very conductive pore water and weathered basement. Conductivity of pore water or water in the fractures plays a significant role in deciding the overall resistivity of the sedimentary basin and the basement rock in Andøya.

The HEM interpretation result in agreement to other geophysical data indicates an extension of the Ramså Basin boundary beyond the presently mapped boundary. However, an extension of the Ramså Basin beyond BH 3 shown by HEM interpretation needs to be confirmed.

Three different units are drawn using HEM inversion results representing basement rocks, sedimentary basin with weathered and fractured rocks; and marine sediments with conductive minerals and seawater.

New highly conductive areas are identified by HEM data interpretation and one of the areas is confirmed with presence of graphite and sulphide minerals by geological observations. Other areas showing similar range of high conductivity except coastal regions with seawater may contain such conductive minerals which need to be further investigated with ground truth and drilling.

7. BEDROCK GEOLOGY OF NORTHERN ANDØYA

Børre Davidsen, Marco Brönner, Ane K. Engvik, Ole Lutro, Henrik Schiellerup & Einar Tveten

The bedrock geology of the northern part of Andøya is dominated by the Archaean Hinnøya granodiorite pluton. In the central part of Andøya the Hinnøya granodiorite is unconformably overlain by supracrustal rocks of the Skogvoll group, inferred to be of Early Proterozoic age. The Skogvoll group forms a volcano-sedimentary sequence with an estimated thickness of 3 km, which has been exposed to amphibolite facies metamorphism. Early Proterozoic plutons considered being part of the anorthosite-gabbro-mangerite-charnockite-granite suite of Lofoten and Vesterålen intrude both the Hinnøya granodiorite and the Skogvoll group.

The Mesozoic Ramså Basin rests upon a basement composed of the Hinnøya granodiorite and an Early Proterozoic gabbro, partially subjected to deep weathering. The Ramså Basin is constrained by faults, with a newly discovered subsidiary basin in the southwest, and possibly another satellite basin in the south.

7.1 **Introduction**

The Lofoten-Vesterålen area in northern Norway is generally considered to be a part of the Baltic Shield, belonging to a Precambrian domain comprising Lofoten, Vesterålen and the western islands of Troms County (Figure 7.1)

The general outline of the geology was established in the 1960s and 70s, following the work of Heier (1960) and Griffin with co-workers (Griffin et al. 1978, references therein). The mapping also resulted in the publication of the 1:250 000 Svolvær map sheet, covering the Lofoten and Vesterålen area (Tveten 1978), Figure 7.2

In broad terms, the area is composed of an Archaean to possibly Early Proterozoic basement of magmatic and metasedimentary rocks, intruded by an Early Proterozoic magmatic suite composed of anorthosite-mangerite-charnockite-granite (AMCG) rocks. Subsequent radiometric dating has confirmed the presence of Archaean and Early Proterozoic rocks (Corfu 2004a, 2007, Davidsen & Skår 2004), with most of the AMCG suite emplaced into the basement within a narrow time interval; 1800 to 1790 Ma (Corfu 2004a).

The supracrustal sequences are distributed as patches and bands intermingled with the Archaean domains, and comprise graphite-bearing rocks, marbles, quartzites, banded iron formations, and presumed felsic and mafic volcanic rocks. Polyphase high-grade metamorphism and deformation have obliterated most of the primary supracrustal features, and the sequence is now represented by various shists, gneisses and migmatites (Griffin et al. 1978, references therein). The metamorphic event(s) reached peak conditions at P= 0.8-0.9 GPa and T= 860-880 °C (Engvik et al. 2016). The metasedimentary rocks were previously

considered to be of Early Proterozoic age (Griffin et al. 1978), but results from the ongoing studies are less conclusive and an Archaean age cannot be excluded.

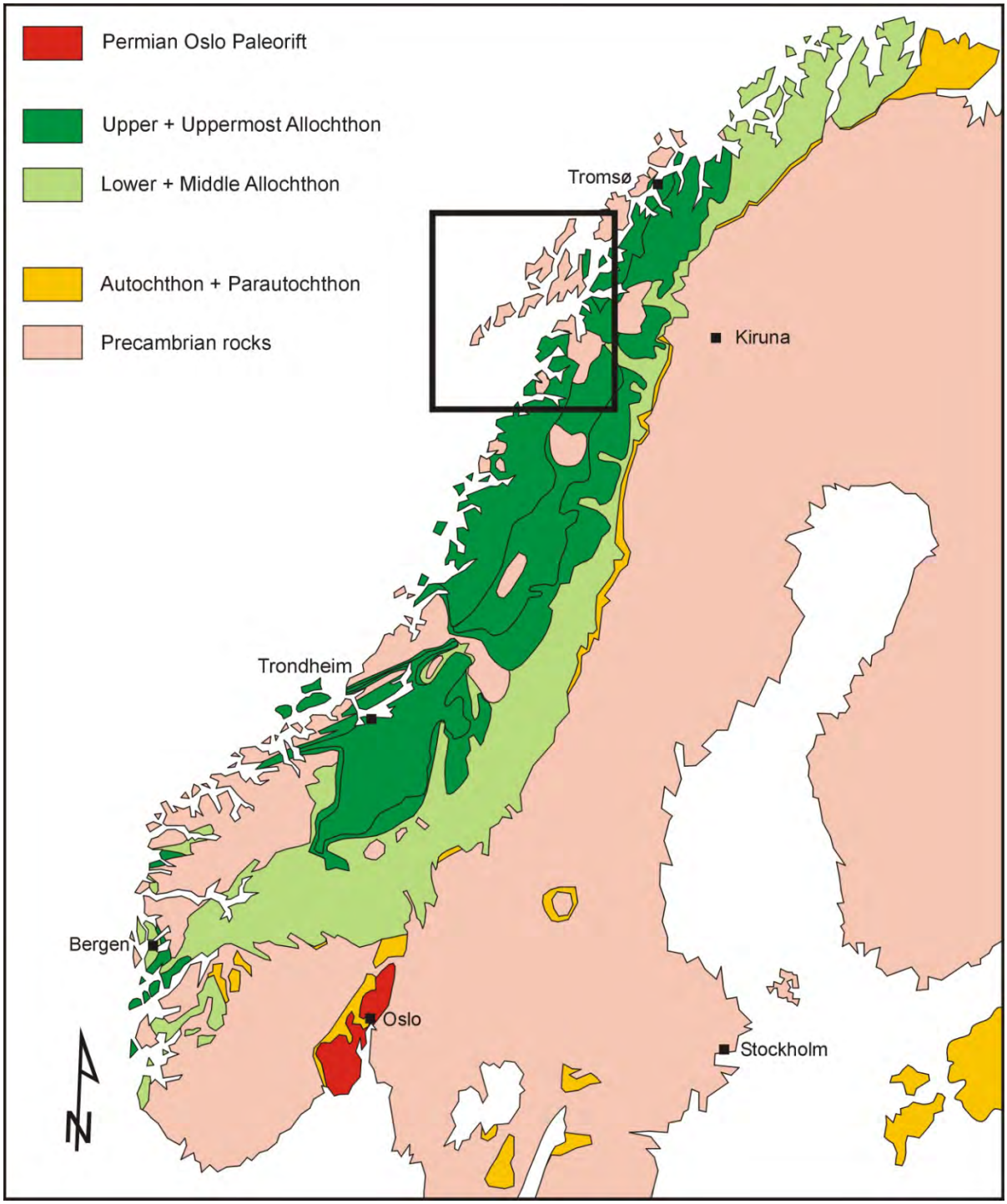

Figure 7.1. Location of the described area

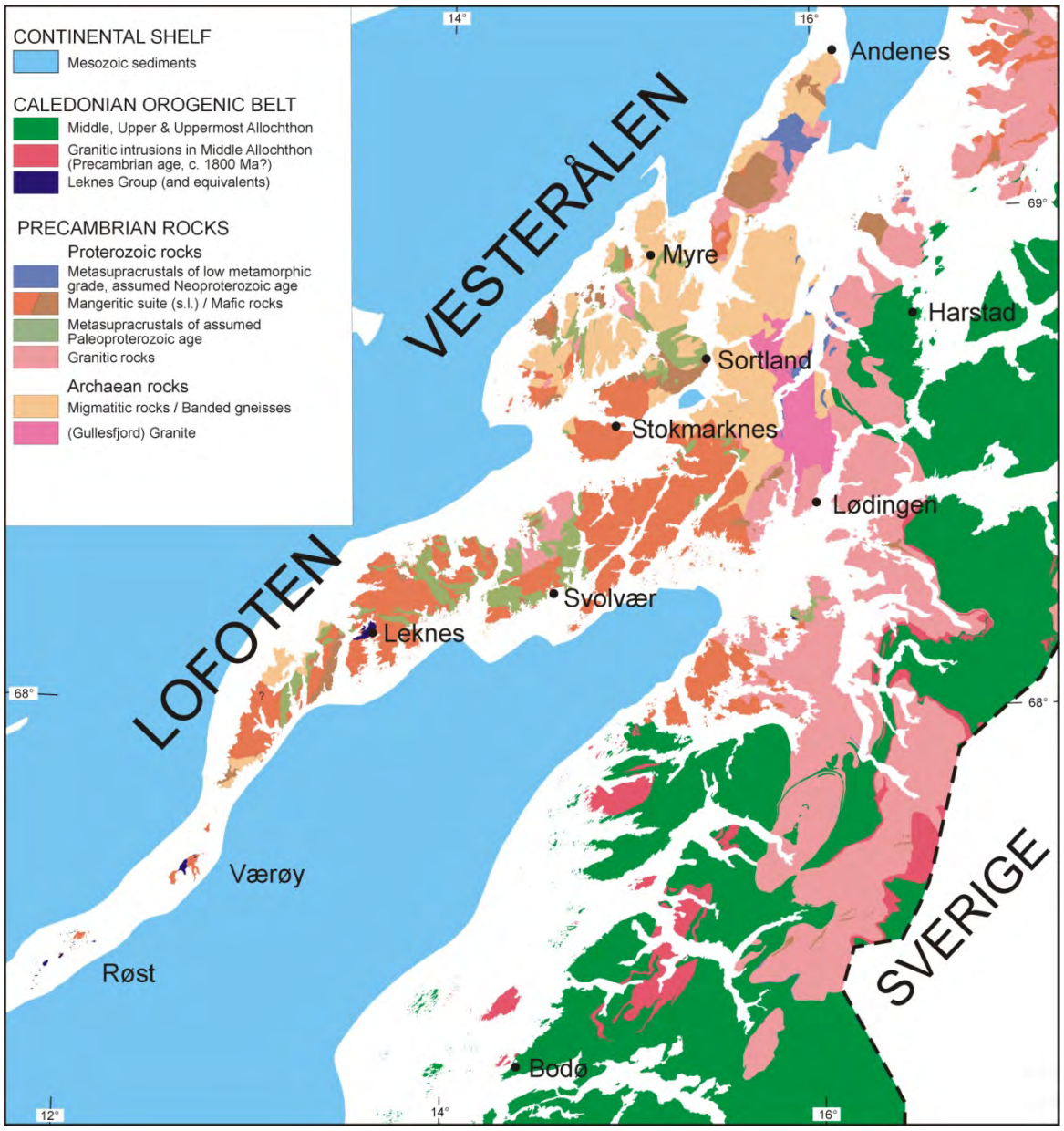

Figure 7.2. Geological map over the bedrock of Vesterålen and Lofoten. The map is based on presently published databases from NGU. Recent mapping results from Vesterålen are not implemented in this compilation.

The youngest bedrock assemblage within the Lofoten-Vesterålen region is the supracrustal Leknes group, covering an area of about 20 km^2 around Leknes in Lofoten (Tull 1977). The Leknes group includes amphibolites, mica schists, calc-silicate gneisses, quartzites and marbles, and has been metamorphosed to amphibolite facies (Tull 1977, Klein et al. 1999). The Leknes group is probably allocthoneous, and is currently considered to represent a Caledonian nappe (Corfu 2004b). Similar rocks are also found at Værøy and Røst.

Similarly, the supracrustal Skogvoll group on Andøya was previously interpreted to be of Cambro-Silurian age (e.g. Often 1980), while Henningsen and Tveten (1998) considered it to be Early Proterozoic. Only recently, however, has the Early Proterozoic age been further constrained (se later).

The only onshore site with Mesozoic rocks on the Norwegian mainland is found on Andøya (Dalland 1975, 1979, 1981), the northernmost island of the Vesterålen archipelago. The occurrence has been known since the 19th century and was first described by Tellef Dahll after a visit in 1867, initiated by rumours about findings of coal. This fault-bounded sedimentary succession is estimated to be more than 650 m thick onshore and consists of Middle Jurassic to Lower Cretaceous sequences (Dalland 1975, 1981), which were deposited in continental and shallow marine to open shelf environments. According to Dalland (1981), the sediments rest with a marked unconformity on Precambrian basement, in part with deeply weathered, kaolinitic granite at the top. To the east, the Mesozoic sedimentary succession extends into Andfjorden, where the up to 5 km thick sedimentary succession is segmented into several basins separated by basement ridges (Sundvor & Sellevold 1969).

In recent times, Mesozoic rocks have also been found in a fault-bounded basin beneath the sea just south of Sortland, between Hinnøya and Langøya (Davidsen & Smelror 2000, Davidsen et al. 2001a, b, Fürsich & Thomsen 2005).

Subsequent to the studies of Griffin and co-workers, NGU continued the mapping activities, leading to the publication of the preliminary 1:50.000 map sheet Sortland (Tveten 1990) and the 1:250.000 map sheet Andøy (Henningsen & Tveten 1998).

Since 2011 revived activity in the Vesterålen area have been conducted under the MINN programme at NGU (**M**ineral resources **I**n **N**orthern **N**orway), comprising general bedrock mapping and research, air-borne geophysics (Rodionov et al. 2012, 2013a,b, Stampolidis et al. 2014), and targeted mineral exploration. In addition, the Mesozoic sequence at Andøya has been targeted for dedicated geophysical surveys, sampling and drilling in the project 'An integrated study of the Ramså Basin on Andøya, northern Norway'.

7.2 Geological outline of Andøya

Ongoing mapping and geochronology have brought new data and considerably modified our understanding of the geology of Andøya. The bedrock of Andøya can be subdivided into an Archaean granodiorite, supracrustal rocks of the Skogvoll group, Early Proterozoic AMCG-intrusives, and finally, the Mesozoic sedimentary rocks of the Ramså Basin (*Figure* 7.3).

7.2.1 Archaean basement

The main rock unit on Andøya is a medium to coarse-grained granodioritic pluton, informally named the Hinnøya granodiorite (HGD). Unpublished radiometric dating yields an Archaean age of about 2.65 Ga. The pluton is very large, and is found on both Andøya, Hinnøya west of Gullesfjorden, and the north-eastern parts of Langøya. The total length is about 90 km, with a maximum width of 25 km, giving it batholithic proportions.

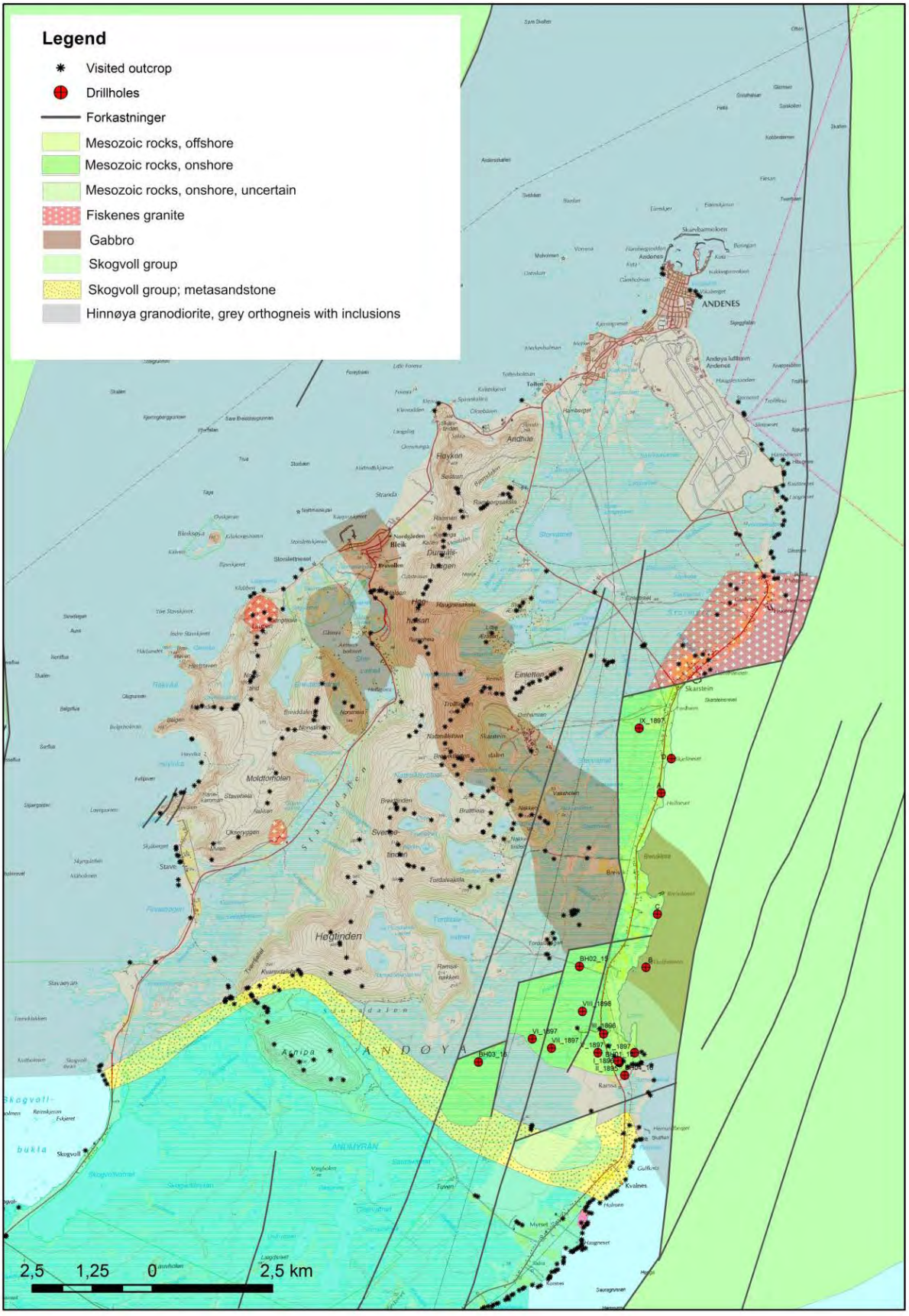

Figure 7.3. Geological map over the northern part of Andøya. The map is based on the results from the ongoing mapping.

In its most characteristic form, the HGD is medium to coarse grained with 0.5-1 cm rounded white feldspar phenochrysts in a biotite-rich matrix which gives it a spotted appearance (Figure 7.4a and b). The quartz content is low to moderate, and it may contain some hornblende. Muscovite is rare, and only occurs in minor amounts, if present at all. However, other textural types can also be found, amongst these more coarse-grained varieties with pink to reddish feldspar. Deformation is heterogeneous, and the textures range from almost undeformed magmatic textures to mylonitic varieties. High-strained, foliated and schistose rocks are widespread on the north-western side of Andøya.

a)

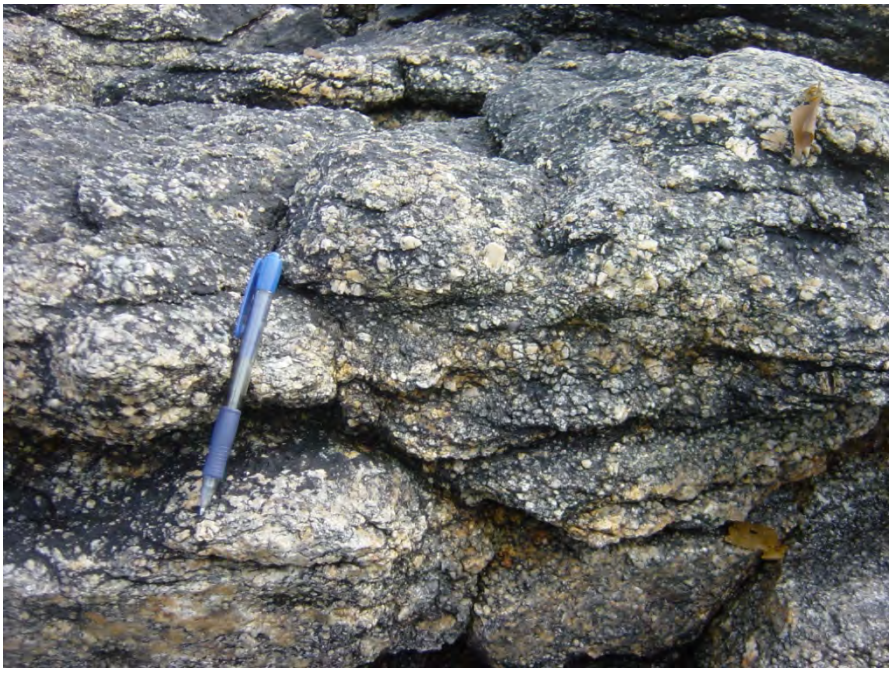

b)

Figure 7.4. Hinnøy granodiorite, slightly porphyritic with rounded feldspars giving a spotted appearance.

The HGD contains variable amounts, but in places numerous xenoliths of older rocks. One of the most common is a fine- to medium grained mesocratic gneiss with biotite and amphibole. Radiometric dating of the xenoliths yields ages considerably older than 2.65 Ga, although the isotopic compositions may have been disturbed. As the oldest, major unit on Andøya, the Hinnøya granodiorite is the host for several younger intrusions.

7.2.2 The Skogvoll group

The Skogvoll group (Henningsen & Tveten 1998) occurs as a 6-15 km wide belt extending across the central part of Andøya, from Dverberg in the east to Skogvoll in the west. The zone is widest in the east. The sequence appears to form an eastward plunging synform that has an estimated thickness of about 3 km on the north-eastern flank. The Skogvoll group rests unconformably on the Hinnøya granodiorite, and has a 250-800 m thick unit of arkosic to quartzitic sandstone at the base. In places a thin basal conglomerate with quartz pebbles is resting on the Hinnøya granodiorite.

The remaining part of the Skogvoll group is composed of a wide range of supracrustal rocks, comprising minor metasandstones, conglomerates, marbles, mica schists, carbonaceous schists, calc-silicate rocks, banded iron formations and metabasalts. The rocks have been metamorphosed to amphibolite facies. The general deformation is moderate, and primary features, such as layering, cross-bedding, mud cracks and soft sediment slump-structures are preserved locally. The group also contains numerous sulphide mineralisations (mainly iron sulphides) that have been investigated by drilling and coring (Lindahl 1978, Often 1980) and is also noticeable from the airborne EM measurements (Chapter 6).

The age of the Skogvoll group has not been directly determined, but is supposed to be Early Proterozoic. The age is constrained by the age of the Hinnøya granodiorite (2.65 Ga) forming the basement, and the 1.87 Ga old felsic rocks intruding the group.

7.2.3 Early Proterozoic intrusives

A number of post Archaean plutons occur on Andøya, ranging in composition from gabbro to mangerite/monzonite and charnockite/granite. On the southern part of the island they make up almost half of the exposed bedrock. The majority is considered to belong to the anorthosite-mangerite-charnockite-granite suite (AMCG) found elsewhere in Vesterålen and Lofoten (Corfu 2004a, Markl et al. 1998), but gabbroic intrusions are also abundant. However, the distinction between mangerite - monzonite and charnockite - granite is not straight forward, because diagnostic orthopyroxene in mangerite and charnockite may be consumed during subsequent amphibolite facies metamorphism. The intrusions vary in size from a few tens of meters to several km across, with gabbros being the largest. Felsic rocks are sometimes intimately associated with the Hinnøya granodiorite forming numerous thin dikes, which are not easily separated on a map scale. The gabbros themselves are also hosts for granitic dikes.

Unpublished geochronology suggests an age of 1800 Ma for the majority of these intrusions, but some smaller granitic to granodioritic intrusives give ages around 1870 Ma.

An orthopyroxene-bearing 1800 Ma mangeritic pluton also intrudes the Skogvoll group on the eastern coast of Andøya.

In the northern part of Andøya, north of the Skogvoll group, several map-scale plutons of Early Proterozoic age have been identified. Towards north-west a 1-3 km wide gabbroic pluton is underlying the middle part of the Mesozoic Ramså Basin. The rocks generally vary from fine to coarse grained, and have a subofittic texture with plagioclase laths. Pyroxene is variably replaced by secondary amphibole, and locally secondary garnet and biotite are present. Close to Bleik, on the western side of Andøya, the intrusion contains troctolitic (olivine-bearing) parts. The pluton appears to continue to the east, beneath the sedimentary rocks of Andfjorden, indicating a relationship with gabbros and peridotites at Steinavær on the eastern side of Andfjorden. Unpublished preliminary results from radiometric dating give an age of c. 1800 Ma both for the gabbro and the granitic dykes in the gabbro. These are considered to represent emplacement ages.

Figure 7.5. Fiskenes granite.

At Fiskenes on the eastern coast of Andøya, a coarse-grained, pink to reddish granite, about 1.5 x 2.5 km in size is found. Its texture is almost pristine magmatic, and slightly porphyritic with tabular feldspar laths (Figure 7.5). It is generally known as the Fiskenes granite. Unpublished geochronological studies give an age about 1800 Ma. On the map (*Figure* 7.3),

two small granitic plutons are indicated on the western coast of Andøy, between Stave and Bleik. These are considered to belong to the Fiskenes granite, but neither their outlines, nor their ages, have been confirmed.

7.2.4 The Mesozoic Ramså Basin

The Mesozoic rocks on Andøya occur on the eastern coast of the island in a fault-bounded, NS-trending basin between Ramså and Skarstein, about 8 km long and 400 m - 2.5 km wide.

Geophysical studies within this project (Chapters 5 and 11) have documented a subsidiary basin at the south-western margin of the main basin, and a probably isolated basin just south of Ramså. At the southern margin of these basins, the arkosic rocks of the Skogvoll group form the basement. The main basin is underlain by the Archaean Hinnøya granodiorite, and the Early Proterozoic gabbro (see above) along a 4 km wide belt in its middle part. At the outlet of the Ramså river deeply weathered and kaolinized Hinnøya granodiorite is exposed, yielding an Archaean U-Pb zircon age of c. 2.65 Ga, as for the rest of this pluton. The weathered basement is investigated in detail in Chapter 10. The northern margin of the Ramså Basin is in fault contact with the 1.8 Ga Fiskenes granite.

The Mesozoic Ramså Basin, including its subsidiary basins in the south, is interpreted to be mainly bounded by post deposition faults. This is conceptually founded, as the actual faults are rarely exposed in this bog-covered terrain. However, there is support for this interpretation, both from the geophysical maps covering the Skogvoll group, and from several outcrops around the Ramså Basin itself. Numerous small faults are also observed in drill cores, and have been inferred by previous studies of the area (e.g. Vogt 1905, Dalland 1975).

The Mesozoic sedimentary rocks of Andøya are presented in Chapter 9.

7.3 **Conclusions**

The bedrock geology of the northern part of Andøya is dominated by the Archaean Hinnøya granodiorite pluton. In the central part of Andøya the Hinnøya granodiorite is unconformably overlain by supracrustal rocks of the Skogvoll group, inferred to be of Early Proterozoic age. The Skogvoll group forms a volcano-sedimentary sequence with an estimated thickness of 3 km, which has been exposed to amphibolite facies metamorphism. Early Proterozoic plutons considered being part of the anorthosite-gabbro-mangerite-charnockite-granite suite of Lofoten and Vesterålen intrude both the Hinnøya granodiorite and the Skogvoll group. In northern Andøya, this group has a NW-SE trend, which is also observed from the magnetic data sub-parallel to the gabbro (Chapter 11) and can be considered as an old predominant trend.

The Mesozoic Ramså Basin rests upon a basement composed of the Hinnøya granodiorite and an Early Proterozoic gabbro, partially subjected to deep weathering. The Ramså Basin is constrained by faults, with a newly discovered subsidiary basin in the southwest, and possibly another satellite basin in the south. The observed fall of the sedimentary rocks in the south is northwards, whilst for the sediments north of the gabbro a southwards fall is reported (Dalland 1973).

The underlying basement within the basin, however, appears to be complex. It is likely to be predominated by the Hinnøy granodiorite, but the central gabbro horst and the drilled ultramafic gang at the southern rim (Chapter 8, BH1) indicate significant crustal-scale tectonic activity combined with magmatic intrusion of the crust in the Proterozoic.

Observed faults with N-S and NE-SW orientation (Vogt 1905, Dalland 1973, 1981, this study) are obviously younger and related to the opening of the Andfjorden during Late Palaeozoic to Mid(?) Mesozoic times. NE-SW faults confine the Ramså Basin in the north and possibly an N-S segmentation of the basin is controlled by faults of the same orientation.

N-S striking faults are obvious from both geophysics and surface observations and seem to interact with the NE-SW trending fractures. The N-S trend is fairly sub-parallel to the axis of the Ramså Basin and the Andfjorden Basin in general and can be assumed to be the overall principal structural setting for the interaction of the Ramså Basin with the Andfjorden Basin.

8. DRILLING AND BOREHOLE LOGGING IN THE RAMSÅ BASIN, ANDØYA, NORDLAND

Harald Elvebakk, Jan Steinar Rønning & Jomar Gellein

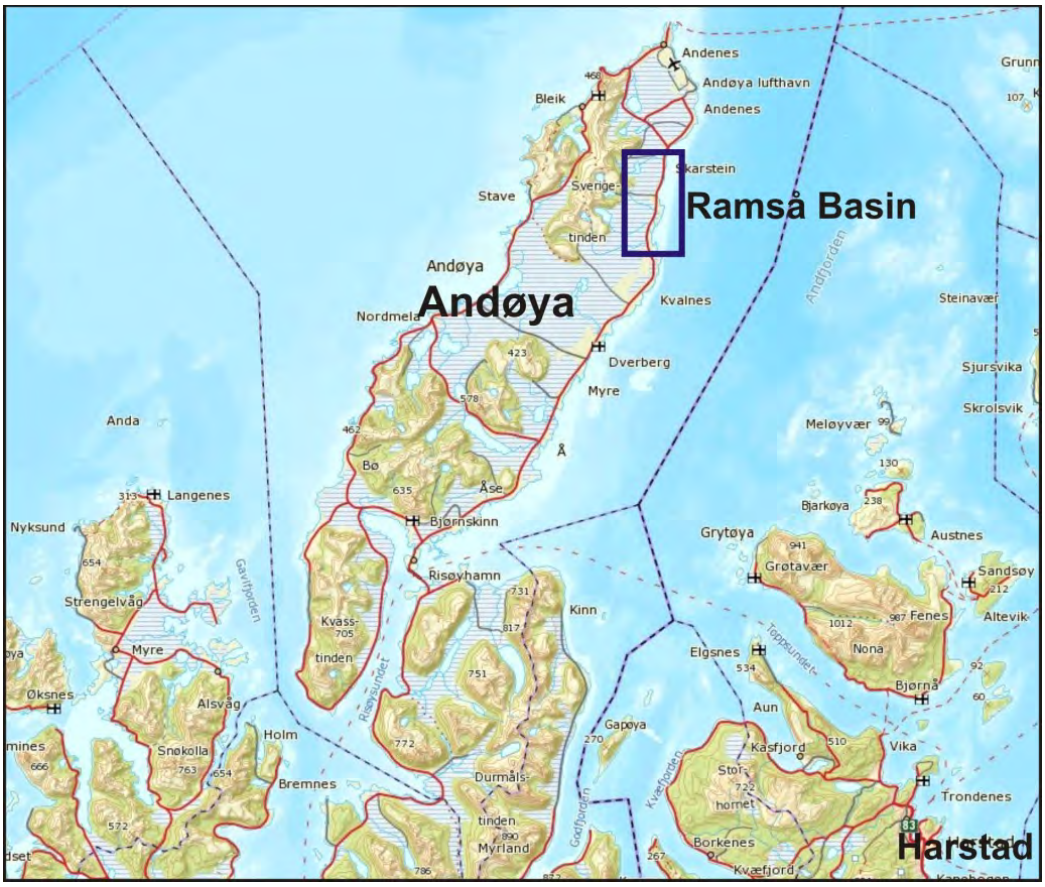

Figure 8.1. Geographic map of Andøya with the position of the Ramså Basin (blue box)

8.1 Introduction

The Ramså Basin is situated between Ramså and Skarstein on the north-eastern side of Andøya in northern Norway (Figure 8.1). This well developed strandflat consists of Mesozoic rocks in a 6 km-wide and 8.4 km-long area known as the only Mesozoic basin onshore Norway. As a part of this, four boreholes were drilled in the basin during the summer 2015 and the winter 2016. Follow-up borehole logging was performed in the autumn 2015 and winter 2016 by NGU.

The main goals were to get a more detailed geological map of the basin, study its tectonic development and to study deep weathering in the basement rocks below the sedimentary succession. Near-surface deeply weathered rocks can be found on the beach and also in old wells drilled through the sediments.

Weathering of rocks and particularly deep weathering is an important issue in preliminary investigations for tunnel construction. Geophysical parameters such as seismic velocity, resistivity, magnetic susceptibility and induced polarisation (IP) are commonly influenced by weathering processes. To gain a better understanding as to how these properties vary in weathered rock, geophysical logging was performed in all four boreholes. In situ measurements in boreholes would make it possible to characterise the lithological formations and members. By doing acoustic logs (acoustic televiewer), azimuth and dip angles in the sediments were mapped. Altogether, including core analysis from the drilling, this would make for a better understanding of the evolution of the Ramså Basin.

Borehole geophysical parameters and methods employed were: seismic velocity, resistivity, temperature, fluid electric conductivity, total natural gamma radiation, gamma spectroscopy, magnetic susceptibility, induced polarisation, self potential and acoustic televiewer.

Several geophysical investigations have been performed in the latest years such as airborne magnetic, electromagnetic and radiometric (Rodinov et al 2012). More detailed gravity measurements, reflection seismic (on-and offshore), 2D resistivity profiling (Olesen et al 2012) and georadar have also been carried out.

8.2 **Drilling**

Figure 8.2 shows the locations of the four boreholes in the Ramså Basin.

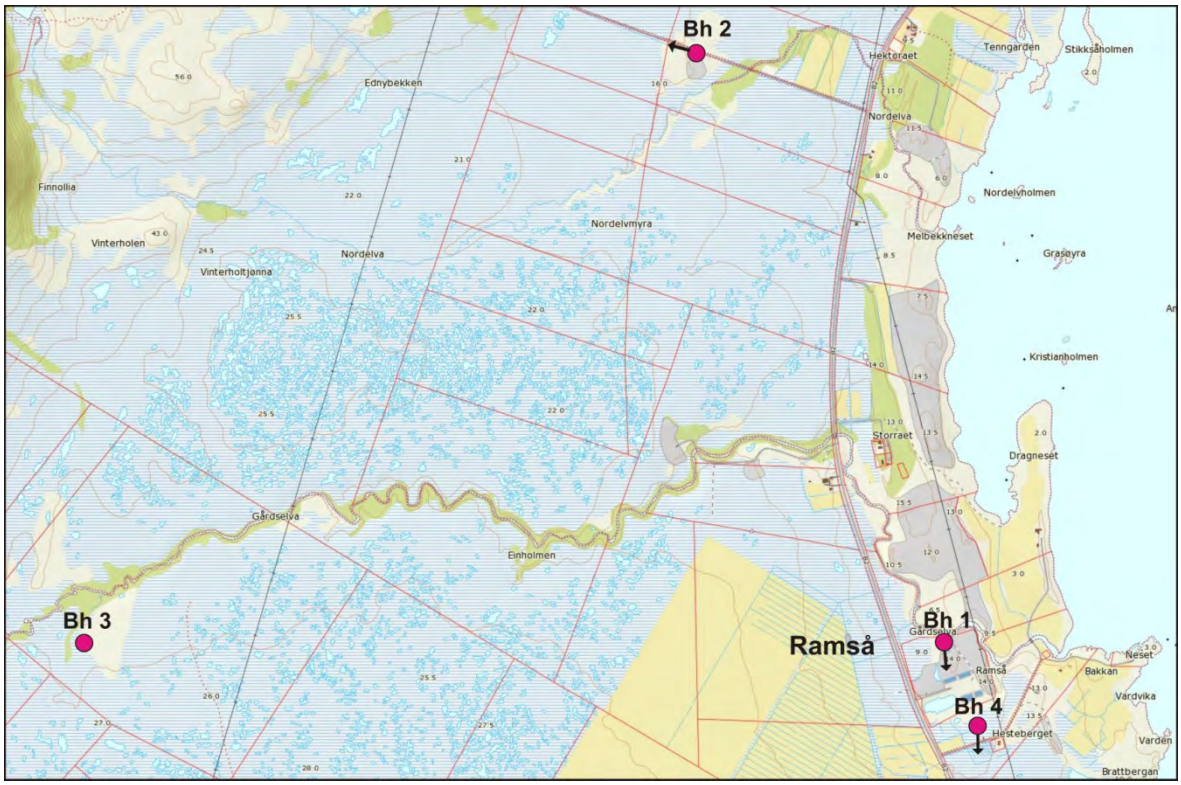

Figure 8.2. Locations of the four new boreholes at Ramså.

BH 1 and BH 2 were drilled during the summer 2015 and BH 3 and BH 4 in the winter 2016. Because of the heavy drilling equipment BH 3 and BH 4 had to be drilled in winter time when the ground surface (moor) was frozen. BH 3 was drilled to the southwest outside the area which until now has been defined as the basin. New airborne magnetic- and electromagnetic data and new gravity measurements indicated that the basin area was bigger than the former geological mapping had shown (Chapters 5 and 11).

The drilling was performed by the Norwegian company Geodrilling AS. The drilling rig was a Diamec U-4 APC using a drillbit NQ-3 (76 mm). Icy and slippery small roads made access to the drilling sites somewhat challenging. The drilling operation was successful and reached the depth expected in the plan. Figure 8.3 shows the Diamec U-4 APC, diesel generator and a vehicle for transport of the drilling equipment.

Figure 8.3. Drilling rig Diamec U-4 APC at location BH 4.

Table 8.1 shows technical data and coordinates for all 4 boreholes. Not all sondes reached the bottom of the boreholes. Rock breakouts at about 150 m depth in BH 1 blocked the borehole and only one sonde reached the bottom. In BH 4 the resistivity sonde got stuck at 52 m depth and it was lost when trying to pull it out.

Table 8.1. Borehole data, coordinates in WGS84, UTM zone 33W.

Borehole	East	North	m.a.s.l.	Depth	Dip	Azimuth	Diam	Logged depth
BH 1	543036	7674280	10 m	203.5 m	66	N180	76 mm	142-157 m
BH 2	542206	7676280	15 m	217.5 m	60	N290	76 mm	201-215 m
BH 3	540102	7674290	26 m	225 m	90	Vertical	76 mm	220-223 m
BH 4	543149	7674013	9 m	53.7 m	65	N 180	76 mm	51.5 m

8.3 Borehole logging

NGU has been doing borehole logging onshore since 1999. The amount of sondes has increased since then and NGU can now measure the most important geophysical parameters in slim boreholes. All logging equipment including two winches is produced by Robertson Geologging ltd, Wales (http://www.geologging.com).

8.3.1 Sondes and logging parameters.

Table 8.2 gives an overview of all measured parameters in the Ramså boreholes.

Table 8.2. Logging parameters, logging speed and sampling interval.

Measured parameters	Logging speed	Sampling interval
Temperature	3 m/min	1 cm
Water conductivity	3 m/min	1 cm
Natural total gamma radiation	3 m/min	1 cm
Gamma spectrometry, U, Th, K	1 m/min	1 cm
Rock resistivity	5 m/min	1 cm
Self Potential, SP	5 m/min	1 cm
Seismic velocity (P- and S-wave)	4 m/min	1 cm
Magnetic susceptibility	5 m/min	1 cm
Induced Polarisation	5 m/min	1 cm
Acoustic televiewer (HIRAT)	3 m/min	1 mm
Deviation (OPTV, HIRAT)	1 – 3 m/min	1 cm

Temperature

To measure exact temperature the measurements should ideally be performed some time after the drilling stops, since the energy from the drilling process (hot drilling fluid, rock crushing, and friction) will increase the temperature in the borehole. From the temperature log the temperature gradient (^{o}C/km) can be calculated. Local changes in the gradient may indicate fractures and related inflow (or outflow) of water. A change in thermal conductivity will also influence the gradient.

Fluid conductivity

The fluid conductivity (µS/cm) depends on the salinity of the fluid. The conductivity measurements can identify zones of water inflow/outflow and locate zones of different water quality. The measured values are temperature-compensated to a reference temperature of 25 ^{o}C.

Natural Gamma

The natural gamma log (API) is useful for geological mapping along walls of a borehole. All rocks contain small quantities of radioactive material, in that certain minerals contain trace amounts of Uranium and Thorium. Potassium-bearing minerals (most common) will include traces of a radioactive isotope of Potassium (K_{40}). Natural gamma measurements are useful because the radioactive elements are concentrated in certain rock types, e.g., claystone, shale and granite, and depleted in others, e.g. sandstone and coal. The unit is in API standard units which means that data can be compared to other measurements performed with the same standard.

Gamma spectroscopy

The natural gamma spectroscopy probe analyses the energy spectrum of gamma radiation from naturally occurring or man-made isotopes in the rock formation surrounding a borehole. By doing gamma spectroscopy measurements the content of U (ppm), Th (ppm) and K (%) can be determined in situ. Log applications are shale/clay typing, lithology determination, correlations in complex mineral situations and radioactive waste pollution measurements. Continuous logs or single energy spectra can be made.

Seismic velocity

The sonic probe has one transmitter and three receivers separated by 20.0 cm that records the full sonic wave-train at both receivers simultaneously and also the velocity of the first arrival. Both P-velocity (compression) and S-velocity (shear wave) are calculated at every cm. Data can be filtered using a running average filter over e.g. 0.4 m. The first arrival of the P-wave is quite easy to pick while the arrival of the S-wave is more indistinct. P-velocity (formation velocity) is used for lithological identification and fracture mapping. Data processing is carried out by using software from ALT (ALT 2006).

Resistivity

Resistivity logging in boreholes is extensively used in hydrocarbon exploration of sedimentary rocks both to identify lithological boundaries and to estimate the rock porosity. The resistivity depends on porosity and fractures (water content), content of electronic conductive minerals such as sulphides, oxides, and graphite and clay. Saline pore-water will also influence the apparent resistivity. The resistivity is measured using two configurations, Short Normal (SN) and Long Normal (LN). The resistivity data are processed by using a program that corrects borehole resistivity logging data for the influence of the borehole liquid salinity, borehole diameter and probe size (Thunehed & Olsson 2004). The porosity is calculated using the measured resistivity and Archie's law (Archie 1942). Archie's law was

found to be correct for porous sandstones with uniform grain size. If there are parameters other than the porosity (e.g., electronic-conductive minerals, fractures) that influence the resistivity, the calculated porosity using Archie's law will be wrong.

Self Potential, SP

SP is measured as an integrated part of the resistivity measurements. SP is a natural potential in the ground which can be measured when crossing electric-conducting minerals (sulphides, graphite). Clay and water flow in the ground can also create quite small SP anomalies.

Induced Polarisation, IP

IP is an electrical method which is primarily used for detecting disseminated sulphide, and copper ores. Current pulses (e.g., 110 ms) are applied to the ground by two electrodes. When the current is turned off, an induced voltage can be measured if there are conducting minerals present in the ground. The size of the voltage increases with the amount of conducting minerals.

Deviation

The borehole deviation is measured by a deviation probe or as an integrated part of the acoustic televiewer. Borehole azimuth and dip angle are measured by magnetometers and accelerometers.

Acoustic televiewer

The HIRAT (High Resolution Acoustic Televiewer), also named BHTV (Bore Hole Tele Viewer) sonde uses a fixed acoustic transducer and rotating mirror system to acquire 2-way travel-time and amplitude of the acoustic signal reflected back to the transducer from a spiral trajectory on the borehole wall. From this an image of the borehole wall is constructed using both the travel-time and amplitude signal. The pixel size at the borehole wall depends on the borehole diameter but is approximately 1 x 1 mm, or better, using the highest resolution (360 shots per revolution).

A study of fractures during processing aims to identify geometric sets of fractures/veins, and then estimate variations in mean dip and frequency within the sets and lines of intersection among the sets, with depth. In sedimentary rocks, the structural interpretation aims to extract formation dip and to identify geological structures such as unconformities, folds and faults from the distribution and orientation of dips assigned to bedding. Digitalising the observed features on the well bore image creates strike and dip of identified structures which can be

presented in fracture stereograms, rose diagrams, fracture frequency histograms, and thickness calculations of beds, bands and fractures. The deviation of the borehole is also calculated.

From the recorded acoustic televiewer data it is possible to make a breakout/ovalisation log. The ratio between maximum and minimum diameter (alpha/beta) in the borehole is calculated continuously (ovalisation log). The azimuth to alpha (max diameter) is also calculated. Using the breakout log it is possible to look at borehole cross-sections at selected depths showing breakout sections in the borehole. Such breakouts can be related to rock stress, and the main horizontal stress orientation can be estimated.

8.4 **Geology and deep weathering**

The Ramså Basin is situated between Ramså and Skarstein on the north-eastern side of Andøya in northern Norway. This well developed strandflat consists of the Skarstein Formation (Lower Cretaceous) in the north and the Ramså Formation (Middle/Upper Jurassic) (Dalland 1975). The Mesozoic basin area is about 1-2 km wide and 8.4 km long and known as the only Mesozoic basin onshore Norway. Figure 3.4 shows a geological map with defined sedimentary formations. The boreholes on the map were drilled in the 1970s by Norminol, a company prospecting for oil. No oil was ever found (Nilssen 2005). Coal was found for the first time in 1867 and was mined in several periods, but no large deposits were ever found and the mining activity was terminated after some years (see Chapter 2 for more details).

In the southernmost part of the Ramså Basin, a 30 m-wide outcrop of weathered basement is exposed on the beach (Chapter 10.3). Weathered basement is also found below the sediments in the old boreholes. Weathering of rocks and particularly deep weathering is an important issue in preliminary investigations for tunnel construction. Many problems during constructing tunnels have been associated with deep weathering.

Deep weathering of basement rocks is mostly known to occur in a sub-tropical climate in equatorial areas and is strongly related to fractures and openings within the rock, where fluids can circulate. During the Mesozoic, Norway had a sub-tropical climate and deep weathering processes probably had been going on for a long time. Acidic water was probably penetrating the crystalline basement in existing fractures commencing weathering processes. Gravel and clay were formed as a result. During the course of time, the weathered rocks were overlain by sedimentary rocks. Later, uplift followed by erosion and several glacial periods, led to removal of the sedimentary cover down to the weathering horizon. Today, deep-weathered basement can be observed both at the surface and in deeper parts of the crust. On the surface, weathered zones can be observed as depressions (valleys) and they are often correlated to low-magnetic zones. By disintegration of silicates the magnetic properties are changed in the way that magnetite and hematite are transformed to oxides (Olesen & Rønning 2008).

Geophysical parameters in the weathered basement will have changed compared with the original basement: lower density and magnetisation, reduced seismic velocity and particularly lower resistivity. Th highest grade of weathering is observed close to the surface, (Figure 8.4) and thus the geophysical parameters will vary from the near surface to increasing depth.

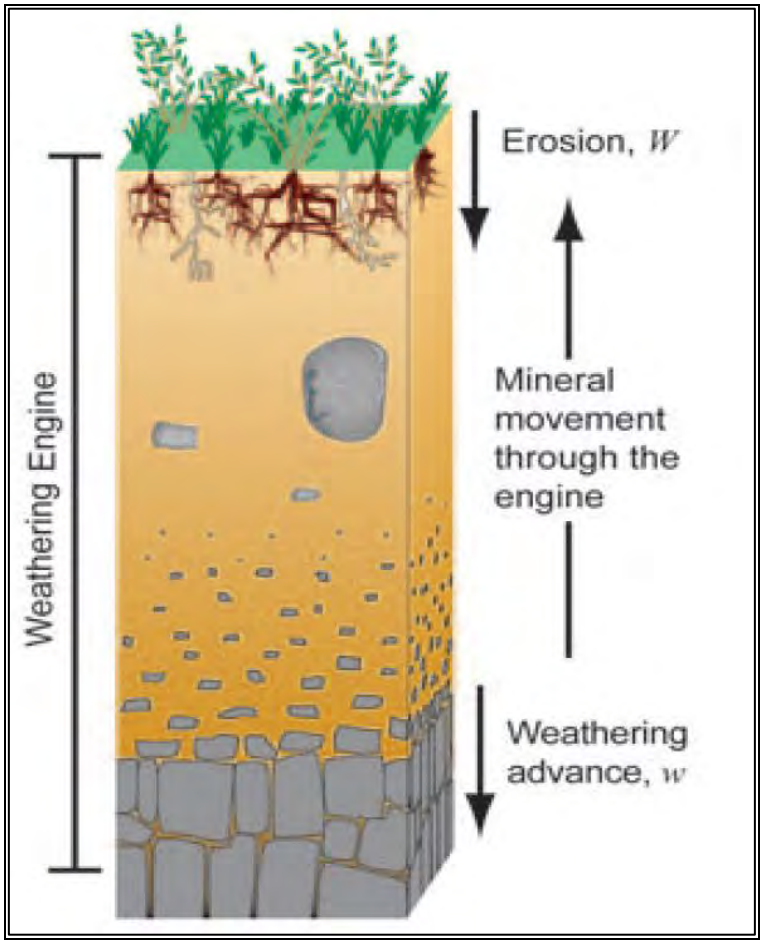

Figure 8.4. Principle of the weathering process (Brantley et al 2007).

8.5 **Logging results**

A geological map of the Ramså Basin is shown in Figure 8.5 including locations of the boreholes and 2D resistivity profiles. BH 1 and BH 4 are located in the southernmost part of the basin, BH 2 on the western boundary of the basin and BH 3 about 1.5 km to the southwest of the basin.

Logs are presented for each borehole showing all measured parameters. From the acoustic televiewer log all observed fractures are digitised. Azimuth and dip angles for each fracture are calculated. Azimuth and dip angles for bedding (in the sediments) are also calculated. In some parts of the borehole the bedding is clearly seen on the acoustic image, but in other parts it is indistinct.

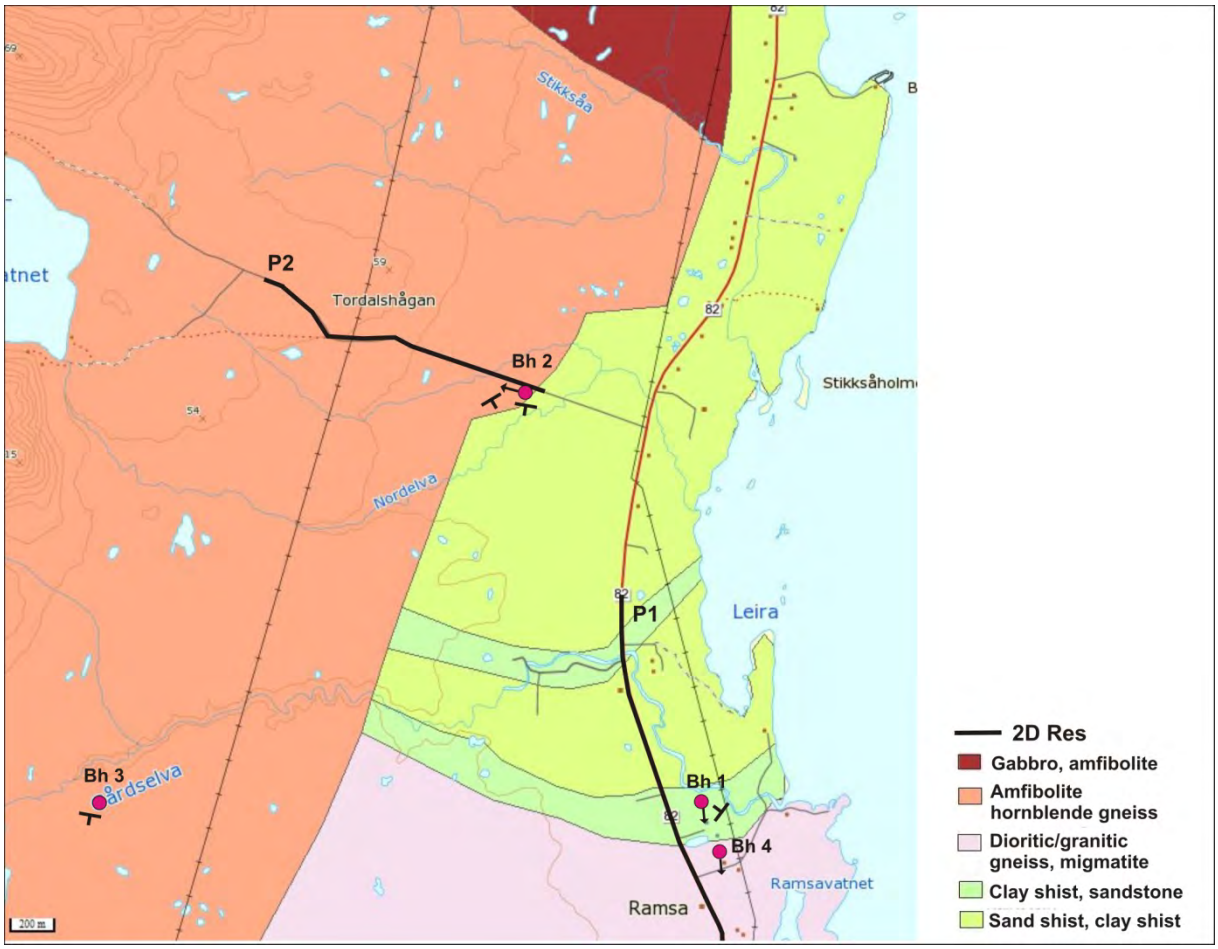

Figure 8.5. Geological map including locations of boreholes and 2D resistivity profiles.

Stratigraphic and lithological logs of the cores have been made by Alf Ryseth (Chapter 9). Data from these logs are used to make stratigraphic logs which are presented together with the borehole parameter logs. BH 1, BH 2 and BH 3 cut the sediments and reached the underlying basement. Mineralogical and chemical analyses have been carried out at NGU to see if deep weathering can be observed in the basement. Clay minerals are a product of the weathering process and geophysical parameters such as IP and resistivity might indicate the presence of clay.

The measured resistivity is an apparent resistivity. The rock is not homogeneous and the apparent resistivity is a kind of average value of the influenced area between the electrodes.

8.5.1 Results BH 1 Temperature, electric conductivity in water and total natural gamma radiation in BH 1.

A rock breakout between 140 and 150 m in BH 1 caused problems for the logging operations. Only one sonde (temperature, conductivity and gamma) reached the bottom of the borehole. The resistivity sonde got stuck in the borehole at 150 m depth. The sonde was saved by using a tractor to pull it up, but 150 m of wire was lost (Figure 8.6. Logging in BH 1 (left) and rescue action to save the resistivity sonde (right).).

Figure 8.6. Logging in BH 1 (left) and rescue action to save the resistivity sonde (right).

Figure 8.7 shows logs of temperature, conductivity in water, natural total gamma and the calculated thermal gradient. The dip angle is 66°, but the gradient is calculated using the vertical depth. Average thermal gradient is about 25°C/km which is quite high. The bottom borehole temperature is 8.4°C at a vertical depth of 187.4 m. The average thermal gradient in eastern Norway is close to 20°C/km.

Electric conductivity in water varies in two steps down the borehole. From the surface to 90 m the water is fresh, 500 – 600 µS/cm. From 90 m-170 m it increases to 5700 µS/cm and below that depth it increases further to 9000 µS/cm. This means that the salt (NaCl) content increases with depth. This will be discussed further in the chapter describing BH 2 and BH 3.

Natural total gamma radiation is varying down to 120 m, 50 – 200 API. Below 120 m the radiation is more or less constant, about 50 API. This might indicate a different rock type. On the stratigraphic log metamorphic basement is mapped below 114 m.

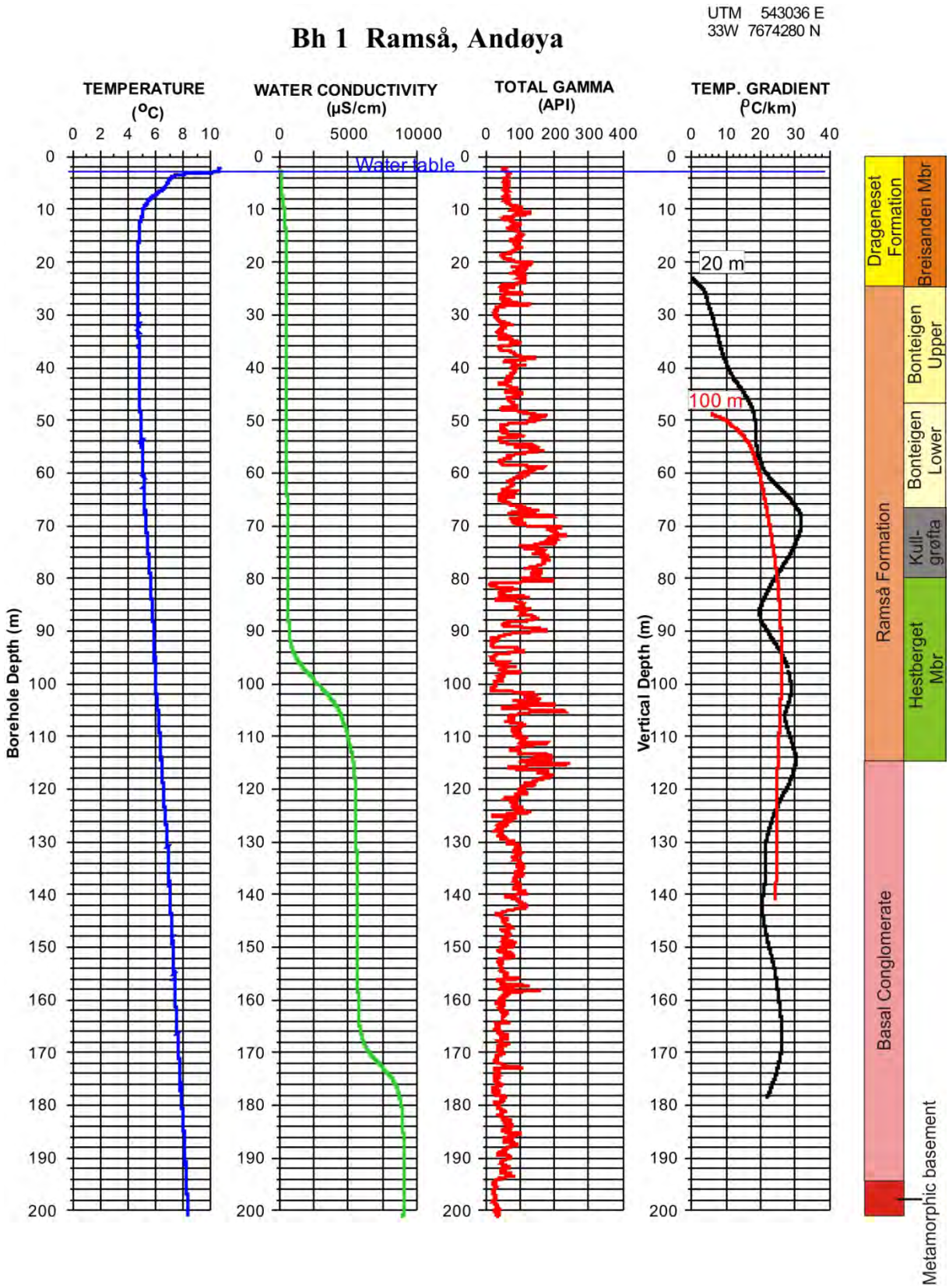

Figure 8.7. BH 1, logs of temperature, water conductivity, total gamma and thermal gradient.

8.5.1.1 Gamma spectroscopy

Figure 8.8 shows the result from the gamma spectroscopy measurements in BH 1. The logs are continuous logs measured with a constant speed of 1 m/min. Total gamma, U (ppm), Th (ppm) and K (%) are measured in situ along the borehole. Measurements are taken every cm which might cause some uncertainty. Stationary measurements for several minutes can be taken to analyze the complete energy spectrum which will give a more accurate content of U, Th and K.

NGU has done correlations between continuous logs and stationary measurements (Elvebakk 2013) and found the correlation to be acceptable.

Table 8.3 shows total gamma and average content of the elements U, Th and K in each stratigraphic member. As can be seen on the logs and Table 8.3, the U content is almost constant (2.1-2.9 ppm) and low in all members except Kullgrøfta where the average value is 6.8 ppm. Th is low and constant in the Breisanden and Bonteigen members (4.7 – 4.8 ppm) except in the lower part of Bonteigen with values up to 10 -15 ppm. Kullgrøfta member has 10.0 ppm and the Hestberget member 7.5 ppm Th. The lower part of the Hestberget member has a Th-content up to 25 ppm, and also in the upper part of the Basal Conglomerate the Th-content is quite high. The K-content is mostly below 2 % except in the Basal Conglomerate, locally up to 4 – 6 %. The Hestberget member has a very low K-content (0.24 %) which confirms Dalland's observation of surprisingly little feldspar (Dalland 1975).

The core logging of BH 1 (Chapter 9) shows that the southernmost boundary of the Dragneset formation is farther to the south of the boundary shown on the geological map in Figure 8.5. On the map, The location of BH 1 is in the Ramså Formation whereas the cores show that the BH 1 starts is in the Dragneset Formation.

Table 8.3. Stratigraphy and lithology (Dalland 1975) in BH 1 and average content of U, Th and K.

Stratigraphic formation BH 1	**Lithology**	**Total Gamma (API)**	**U (ppm)**	**Th (ppm)**	**K (%)**
Dragneset formation Breisanden member	Micaceous sandstone	122	2.4	4.7	1.8
Ramså formation Bonteigen member	Sandstone, siltstone, thin layers of coal	107	2.4	4.8	1.2
Ramså formation Kullgrøfta member	Bituminous shale (oil shale)	208	6.8	10.0	1.1
Ramså formation Hestberget member	Coarse-grained sandstone	116	3.3	7.5	0.24
Metamorphic basement	granite	140	2.1	7.5	2.0

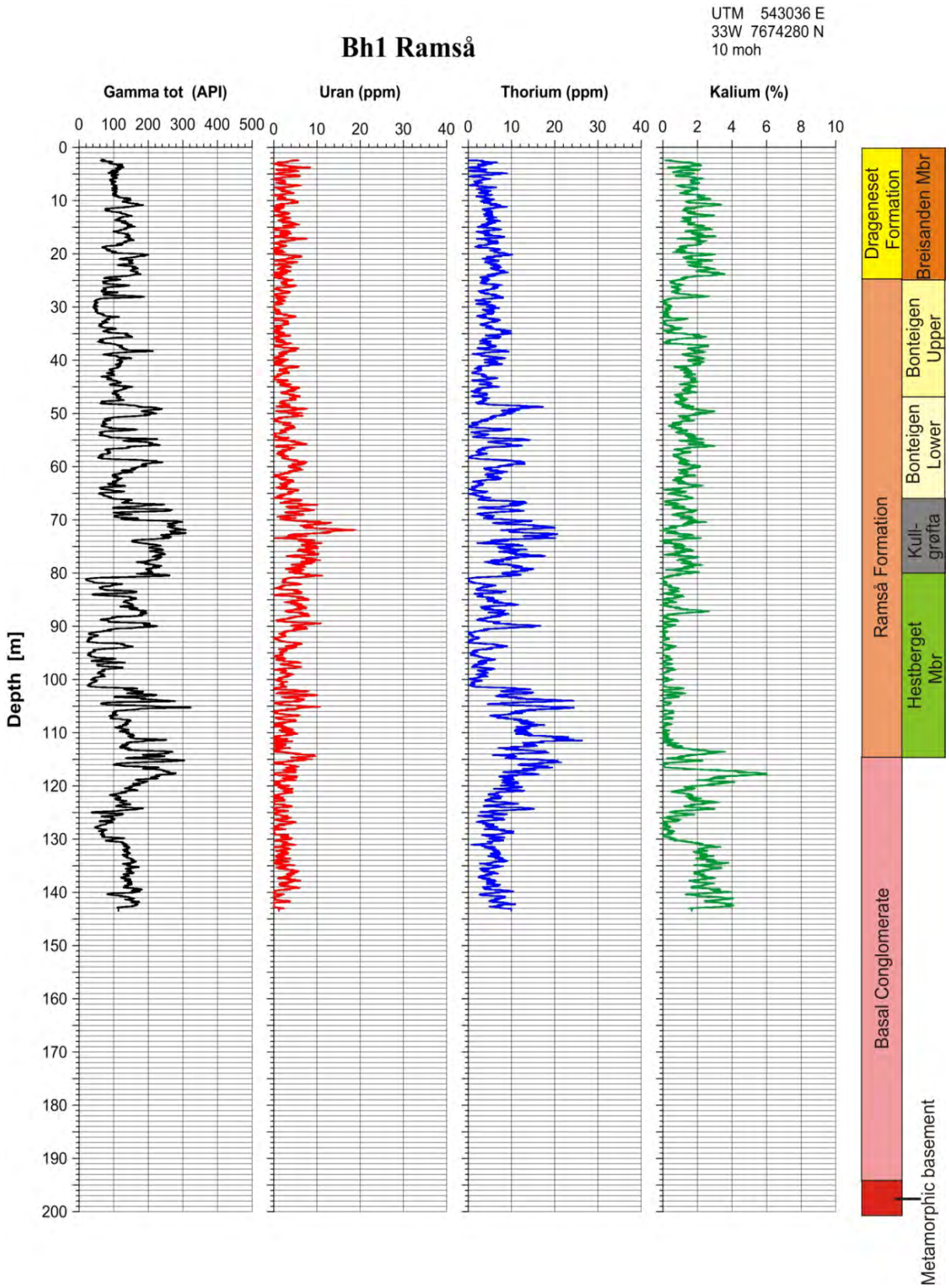

Figure 8.8. BH 1, gamma spectroscopy showing total gamma, U (ppm), Th (ppm) and K (%)

8.5.1.2 Seismic velocity, resistivity, magnetic susceptibility, induced polarisation and self potential, BH 1.

Figure 8.9 shows logs for seismic velocity, total gamma radiation, formation resistivity, magnetic susceptibility, IP and SP. The gamma radiation log is described in the previous chapter. Because of rock breakouts into the borehole at about 150 m depths all logs, except temperature/gamma, stopped at this depth. Average values of measured parameters for each member are shown in Table 8.4. The formation resistivity is very low. This is not only because of heavily fractured rocks. The high electric conductivity in the borehole water will have a strong influence on the formation resistivity. The pore-water and water in fractures will have the same high conductivity and the measured resistivity will be too low. However, variations in the resistivity may indicate fractures and conducting minerals (sulphides).

Table 8.4. Average values of geophysical parameters in stratigraphic formations/members BH 1.

Stratigraphic Formation/ member	P-velocity (m/s)	Resistivity (ohmm) SN	LN	MagSus (SI 10^{-5})	IP (%)	Total Gamma (API)	U (ppm)	Th (ppm)	K (%)
Dragneset formation Breisanden member	2800	365	580	224	1.8	122	2.4	4.7	1.8
Ramså formation Bonteigen member	2965	230	262	224	2.1	107	2.4	4.8	1.2
Ramså formation Kullgrøfta member	2880	71	95	269	3.0	208	6.1	8.2	1.1
Ramså formation Hestberget member	3290	108	96	197	1.2	116	3.3	8.3	0.24
Metamorphic basement	4000	80	76	231	0.6	140	2.1	7.5	2.0

The seismic velocity log (P-wave) is somewhat inaccurate. Problems with the counter wheel on the winch led to inaccurate depth registration. Data are therefore missing in some parts on the log. The seismic velocity (P-wave) increases with depth from 2800 m/s in the Dragneset formation to 4000 m/s in the basement, see Table 8.4. Both the sediment and basement granite velocities are lower than in sandstone and granite in other parts of Norway (Elvebakk 2011). The reason for this could be highly fractured rocks, but also the fact that rocks outside the Mesozoic basin are older and more consolidated will increase the P-velocity.

As mentioned above the formation resistivity is wrong because of the salty pore-water. Local variations on the resistivity log are real. Several thin low-resistivity zones are observed in the sediments. Many of these zones correlate with high IP-effect in Breisanden and Kullgrøfta members. This could be caused by clay minerals, but IP-effects in the range of 5 -10 % most probably are caused by sulphide minerals (pyrite, pyrrhotite). Small increases in magnetic susceptibility correlate with both resistivity and IP and could be caused by pyrrhotite. The magnetic susceptibility is generally very low both in the sediments and in the basement. As mentioned, the IP-effect varies quite considerably in the sediments (sulphides?), but in the basement below 114 m depth the IP-effect is low throughout. The SP data provide no information.

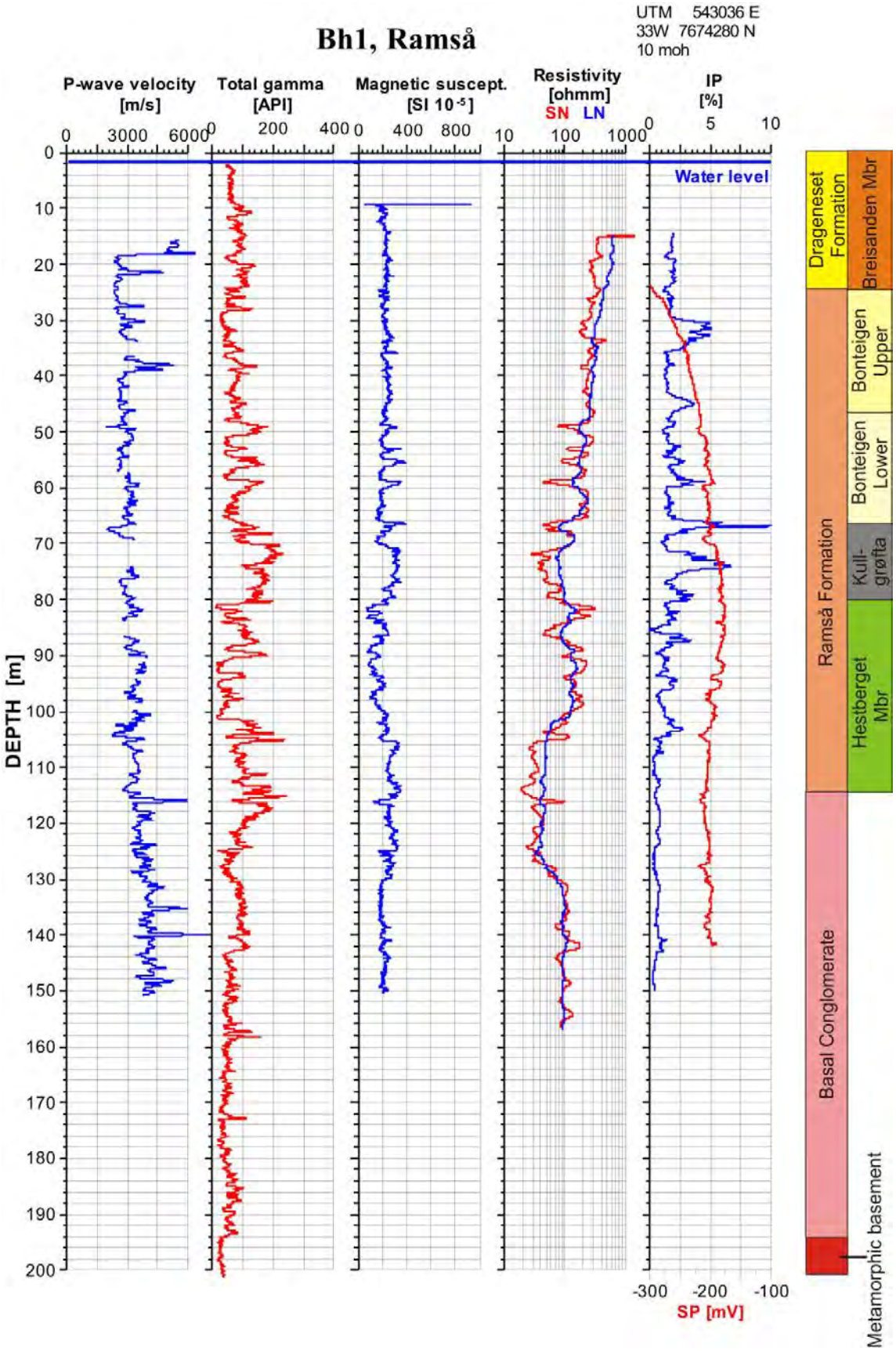

Figure 8.9. BH 1, logs of seismic velocity, total gamma, resistivity, magnetic susceptibility, induced polarisation and SP.

8.5.1.3 Acoustic televiewer, fracture mapping and calculation of bedding azimuth and dip, BH 1.

BH 1 was logged with the acoustic televiewer down to 141 m depth. Because of a dipping borehole (66^{o}) the probe is a bit decentralised in the borehole. This will reduce the quality of the recorded images but observed fractures may well be digitised. In BH 1 all observed fractures are digitised with calculation of azimuth and dip angle. The same is done for the observed bedding in the sediments. It is more difficult to observe layered rocks in the basement. The digitised data are used to make fracture frequency histograms and rose diagrams.

Figure 8.10 and Figure 8.11 show fracture frequency histograms, resistivity, apparent porosity and seismic velocity (P-wave). Every observed fracture is shown to the left as a needle showing the azimuth (north is up). The borehole is heavily fractured down to 70 m and particularly in the upper 35 m with a fracture frequency of 8-9 fractures/metre. This is in the sediments (Breisanden and Bonteigen members). The borehole is also heavily fractured from 105 to 140 m (lower Hestberget member and basement).

Figure 8.12 shows a rose diagram of fracture azimuth and angle of dip. The average azimuth is NW and average dip angle is about 30^{o}.

In most parts of the borehole bedding can be observed on the acoustic image. By digitalising the bedding (in the same way as for fractures) azimuth and dip angle can be calculated. In Figure 8.14bedding azimuth and dip angle are plotted versus depth. Azimuth is almost constantly to the NW down to 100 m depth. Below 100 m there are large variations. Dip angle is between 15 and 40^{o}. Borehole deviation, bedding dip angle, borehole azimuth and bedding azimuth are also shown in Figure 8.14.

Figure 8.14 shows acoustic images from two sections in the borehole. Section 68 - 72 m depth is from the Kullgrøfta member showing some fractures. Bedding can clearly be seen. The vertical dark/light bands are caused by decentralisation of the sonde. Between 127 and 131 m depth the basement (transition zone) is heavily fractured as seen on the image.

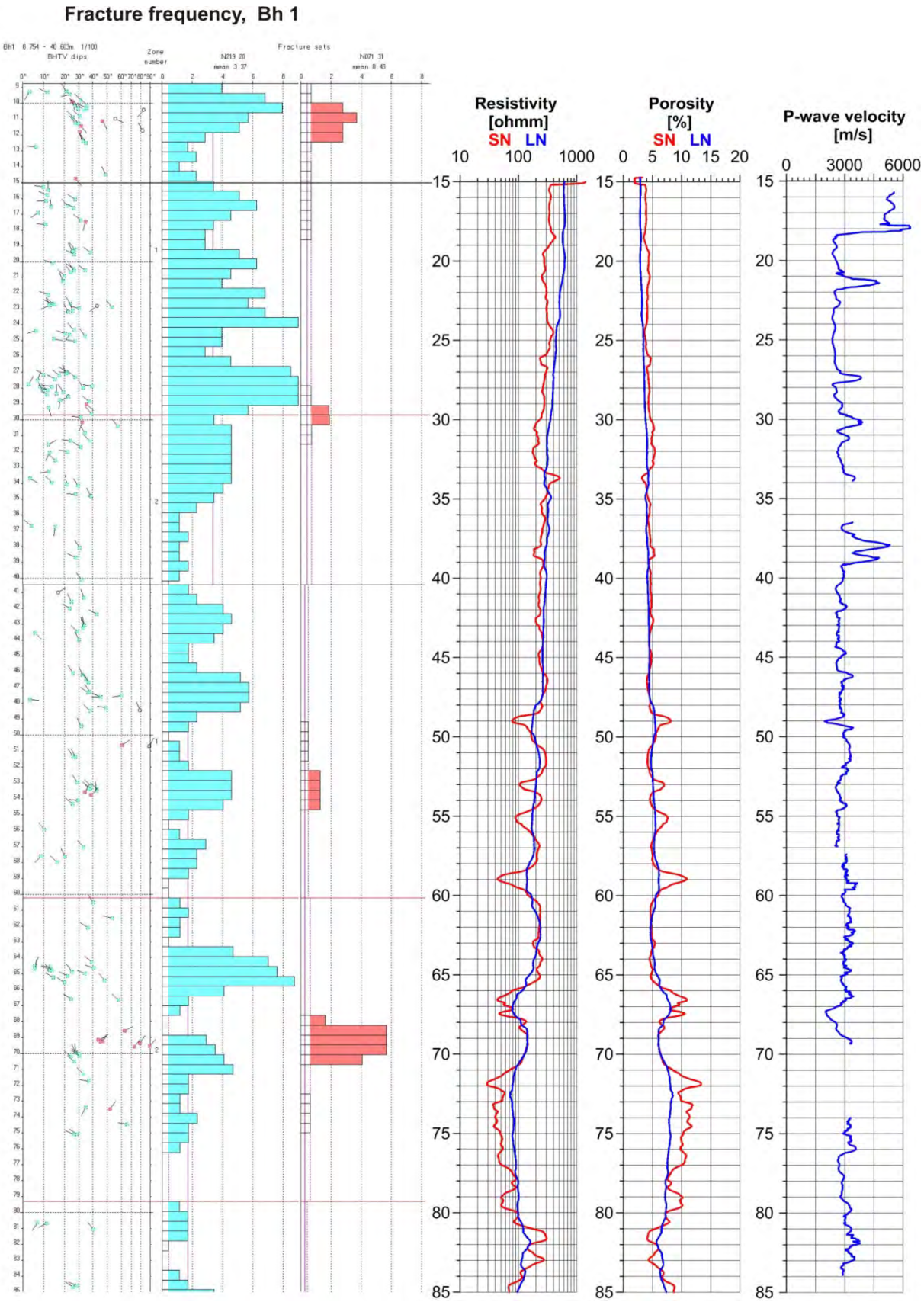

Figure 8.10. BH 1, 15 – 85 m. Fracture frequency, resistivity, porosity and P-wave velocity.

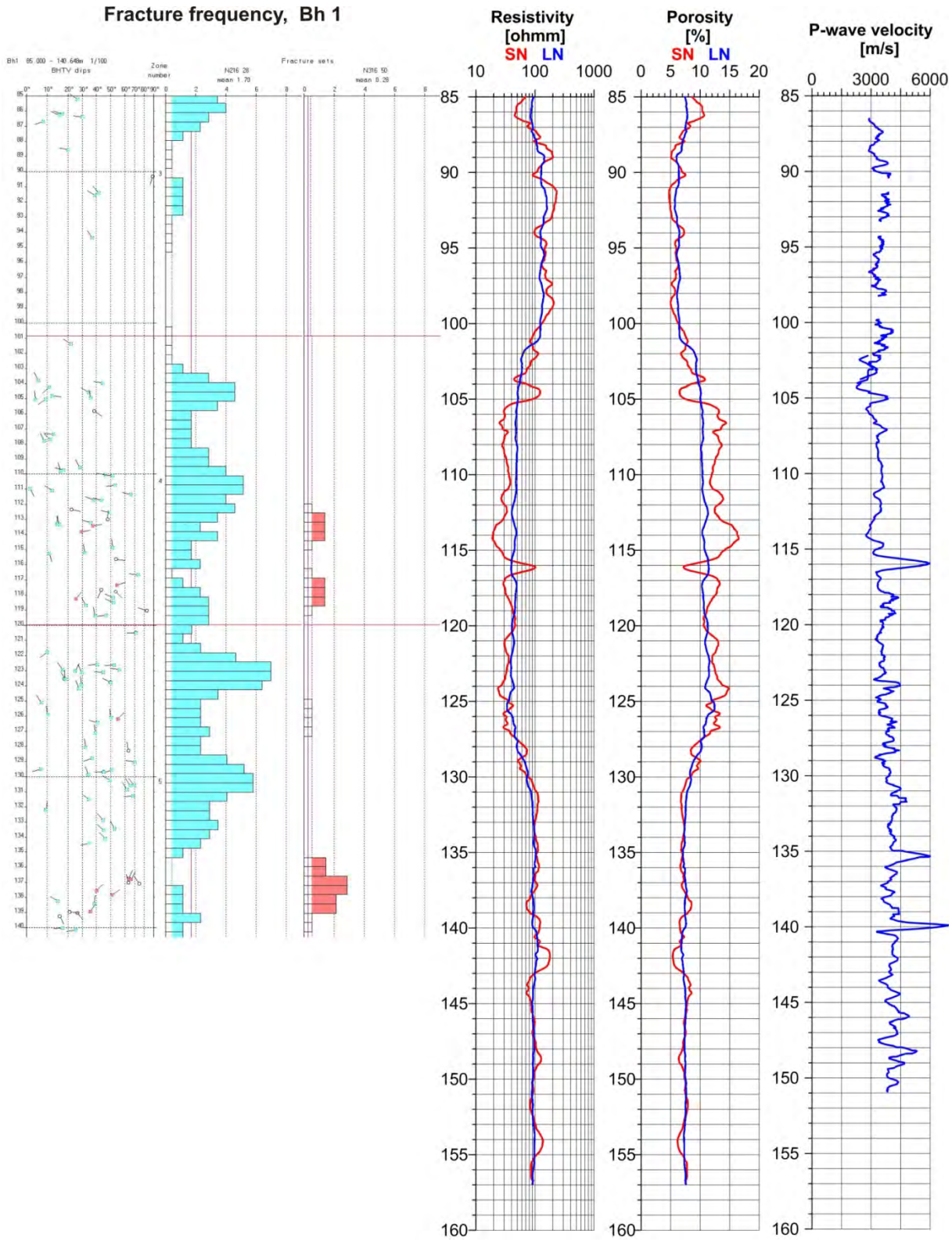

Figure 8.11. BH 1, 85 – 140 m. Fracture frequency, resistivity, porosity and P-wave velocity.

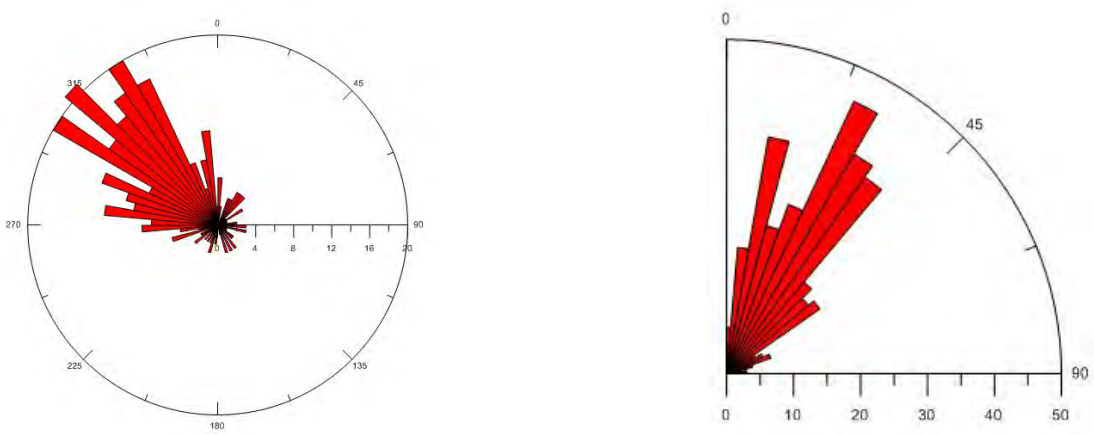

Figure 8.12. BH 1, fracture azimuth (left) and fracture dip angle (right).

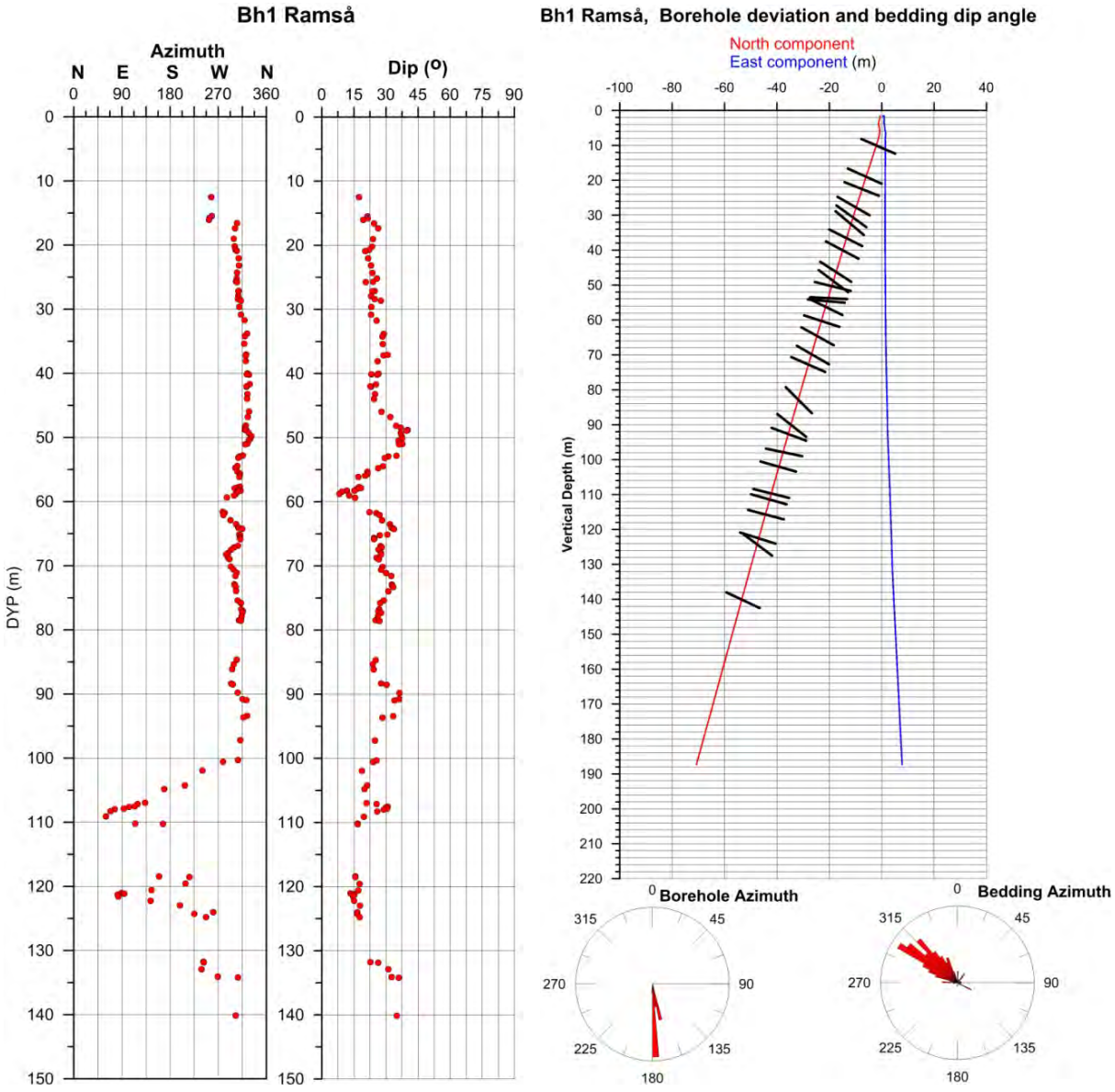

Figure 8.13. BH 1, Azimuth and dip angle of bedding (left), borehole deviation, borehole azimuth and bedding azimuth (right).

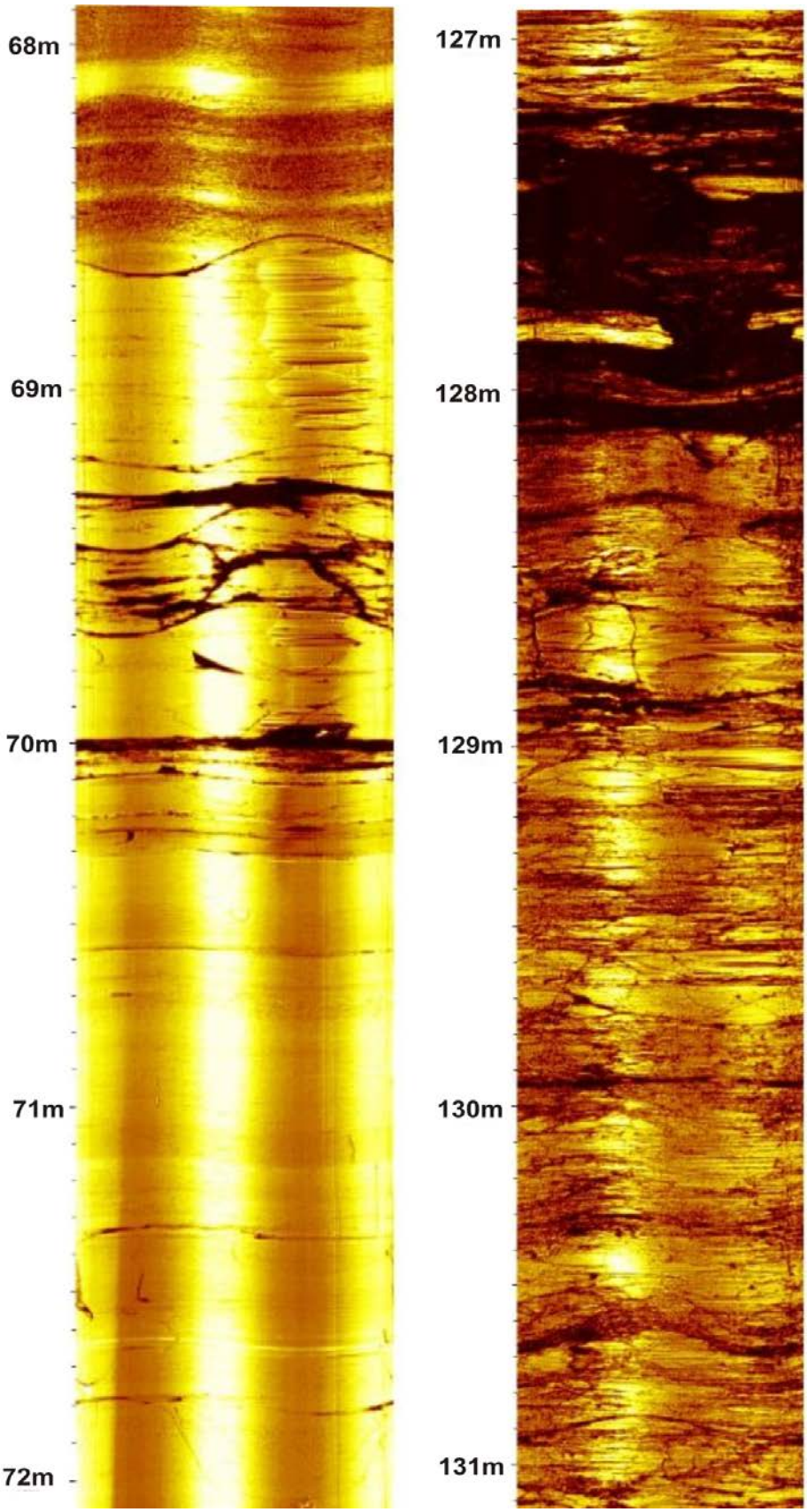

Figure 8.14. BH 1, acoustic televiewer image, 68-72 m (left), 127-131 m (right).

8.5.2 Results BH 2

BH 2 was drilled about 1 km west of the Andfjorden shore as shown in Figure 8.2. The borehole direction was WNW, dip angle 60°. Drilling stopped at 217 m and the deepest log was at 215 m. The location was along "Fjellveien' as shown in Figure 8.15.

Figure 8.15. Location of BH 2 along "Fjellveien', 1 km west of the Andfjorden shore.

According to the geological map, Figure 8.5 , the BH 2 location was close to the western boundary of the Ramså Basin. However, 2D resistivity profiling (Brönner et al., 2012) along "Fjellveien' shows that the BH 2 location is about 300 m from the basement boundary. On the resistivity profile P2, Figure 8.16, the boundary between high-resistive granite (red, brown) and the low-resistive sediments (blue, green) is clearly seen. Depth to basement in BH 2 was 200 m and fits well with the boundary on the 2D resistivity profile and the indicated dip of the sediments.

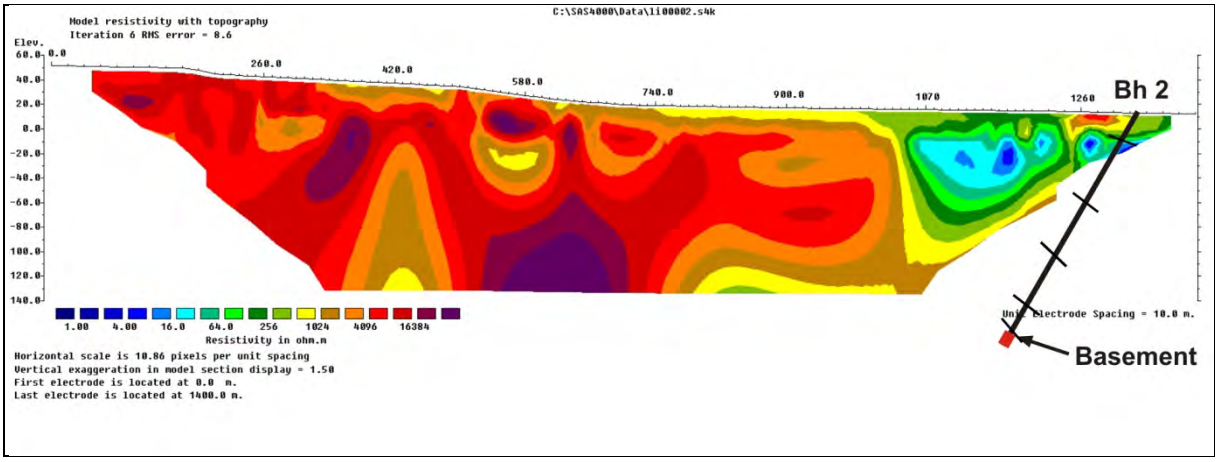

Figure 8.16. 2D resistivity profile along "Fjellveien' close to the BH 2 location.

8.5.2.1 Temperature, electric conductivity in water and total natural gamma radiation in BH 2.

Figure 8.17 shows logs of temperature, conductivity in water, natural total gamma and calculated thermal gradient. The dip angle is 60°, but the gradient is calculated using the vertical depth. Average thermal gradient is about 30°C/km in the upper part of the borehole and 25 °C/km in the deepest part. This is higher than in the central parts of southern Norway. The bottom borehole temperature is 9.1°C at a vertical depth of 186.9 m. The average thermal gradient in eastern Norway is close to 20°C/km.

Electric conductivity in water varies in two steps downwards in the borehole. Even at the surface the water conductivity is high, 16000 µS/cm. Further down it increases to 25000 µS/cm and 30000 µS/cm in the deepest part. This is close to seawater (c. 45,000 µS/cm). Observed water in small ponds on the surface was fresh (by tasting). The reason for the salty water at depth has been discussed and most probably it is fossil water. Dalland (1975) described faults that have created two small troughs in the basin. Salty water could have been trapped in these troughs.

Natural total gamma radiation is quite constant in the sediments, 150 – 200 API. In the upper 26 m, the gamma radiation is attenuated because of the steel casing. Below 200 m depth the gamma radiation rises up to 500 API in the basement. Gamma radiation can be quite high in granites.

Table 8.5. Stratigraphy and lithology (Dalland 1975) in BH 2 and average content of U, Th , K.

Stratigraphic Formation/member	Lithology	Total Gamma	U (ppm)	Th (ppm)	K (%)
Skarstein formation Nordelva/Helnesset mbr	Mudstone, sandstone	227	4.8	13.5	2.0
Nybrua formation	Sandstone, siltstone marls	226	3.9	14.7	2.2
Dragneset formation Ratjønna member	Laminated siltstone	219	6.0	8.4	2.3
Basement > 200 m	granite	327	8.7	9.2	2.8

8.5.2.2 Gamma spectroscopy, BH 2.

Figure 8.18 shows the result from the gamma spectroscopy measurements in BH 2. The logs are continuous logs measured with a constant speed of 1 m/min. Table 8.5 shows total gamma and average contents of the elements U, Th and K in each stratigraphic formation. The U-content is 4-5 ppm in the Skarstein and Nybrua formations. It increases to 6 ppm in the Dragneset formation and 8.7 ppm in the underlying basement. Only two metres were logged in the basement (sonde stopped). Th content is 13 – 15 ppm in the Skarstein and Nybrua

formations. In the upper Nybrua formation the Th-content is up to 20 – 25 ppm. In the underlying Dragneset formation the average Th-content is 6 ppm. The K content is 2 – 3 % in the entire borehole.

The temperature/conductivity/gamma sonde reached 215 m and showed an increase in total gamma radiation of 300 API (Figure 8.17). The U log using the spectroscopy sonde shows a similar behaviour as the total gamma log (Figure 8.18) but it stopped at 202 m depth. The high radiation below is perhaps caused by increased U-content.

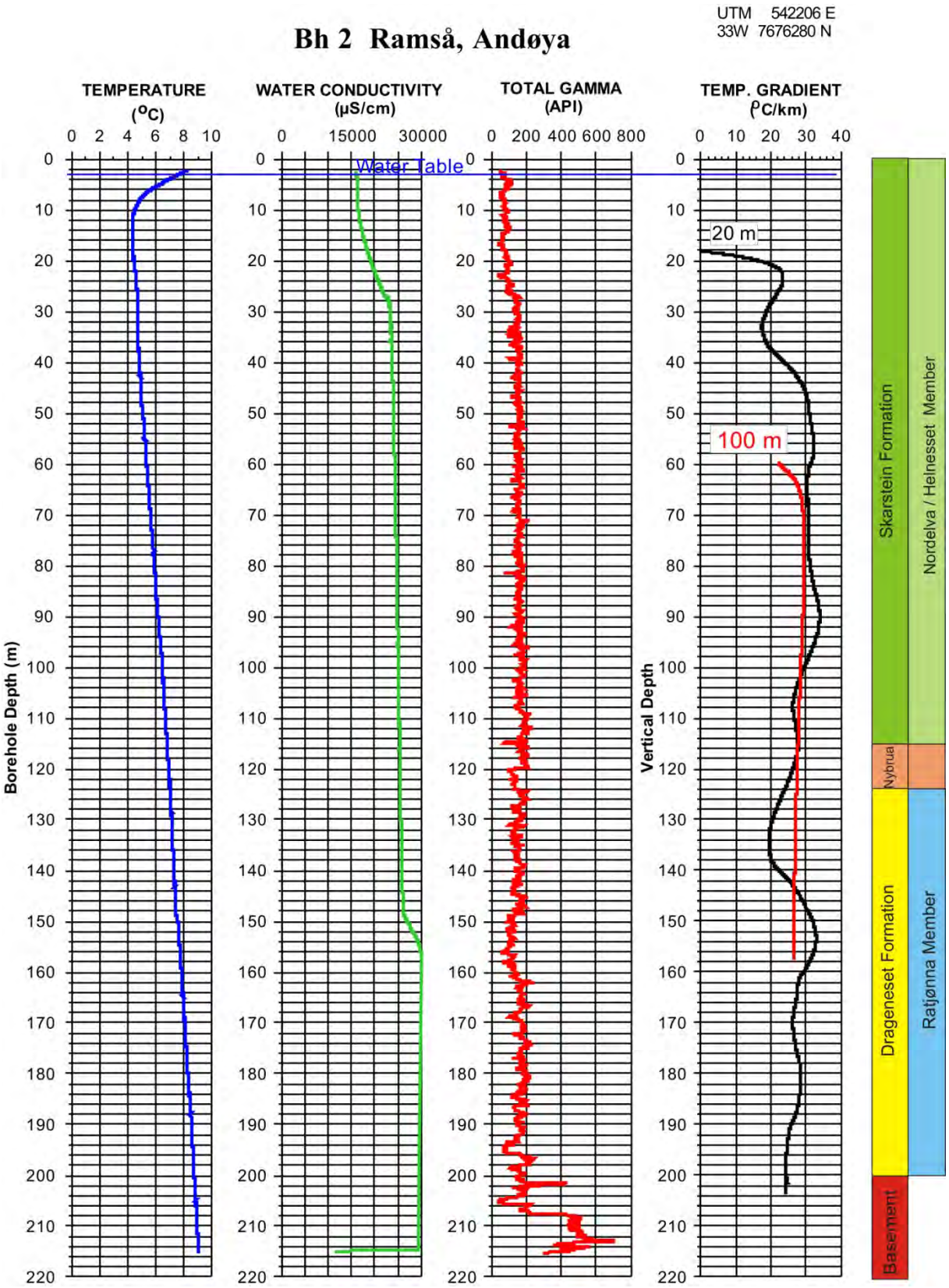

Figure 8.17. BH 2, logs of temperature, water conductivity, total gamma and thermal gradient.

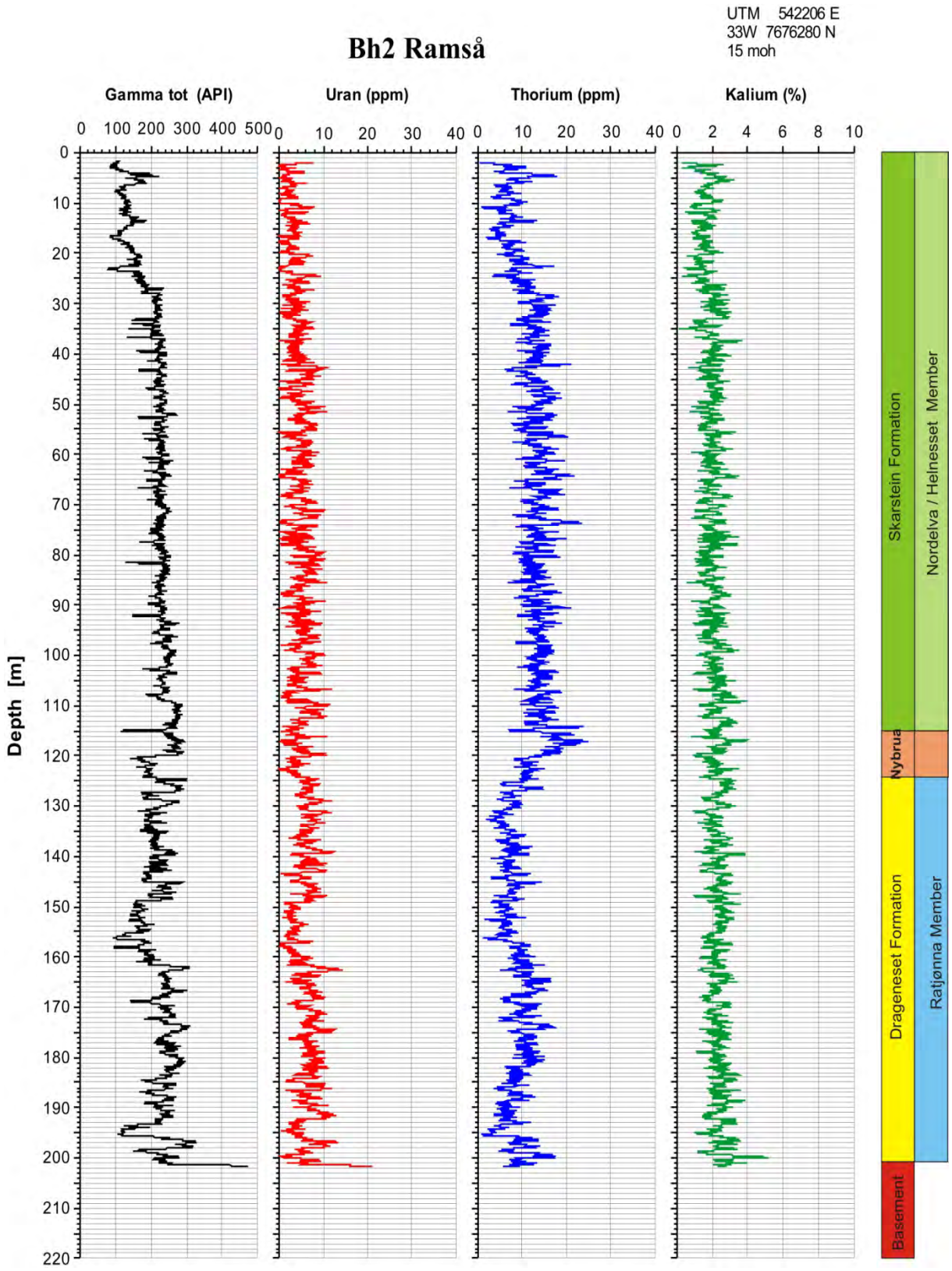

Figure 8.18. BH 2, gamma spectroscopy showing total gamma, U (ppm), Th (ppm) and K (%).

8.5.2.3 Seismic velocity, resistivity, magnetic susceptibility, induced polarisation and self potential, BH 2.

Figure 8.19 shows logs for seismic velocity, total gamma radiation, formation resistivity, magnetic susceptibility, IP and SP. The gamma radiation log is described in the previous chapter. Average values of measured parameters for each formation are shown in Table 8.6. The formation resistivity is very low (20 – 30 ohmm), even lower than in BH 1. However, the entire borehole was highly fractured as indicated by the acoustic televiewer, see later. The resistivity increases clearly below 200 m depth in the basement. The basement was also heavily fractured, but in general granite has a higher resistivity than sediments. Based on mineralogical and chemical analyses there is no deep weathering in the basement in BH 2.

Table 8.6. Average values of geophysical parameters in stratigraphic formations/members BH 2.

Stratigraphic Formation/member	**P-velocity (m/s)**	**Resistivity (ohmm) SN LN**	**MagSus (SI 10^{-5})**	**IP (%)**	**Total Gamma (API)**	**U (ppm)**	**Th (ppm)**	**K (%)**
Skarstein formation Nordelva/Helnesset m	3060	19 29	911	1.09	227	4.8	13.5	2.0
Nybrua Formation	3380	25 27	777	0.14	226	3.9	14.7	2.2
Dragneset Formation Ratjønna member	3300	27 30	679	0.3	219	6.0	8.4	2.3
Basement > 200 m	3400	114 142	685	0.2	327	8.7	9.2	2.8

The seismic velocity sonde stopped at 202 m depth, measuring only 2 m in basement rocks. In general, the P-velocity is constant in the entire borehole, 3000 – 3400 m/s. Some high value peaks are probably caused by calcite veins (A. Ryseth, pers. comm. 2016). The low P-velocity is mainly caused by high porosity and fractured rocks.

The magnetic susceptibility decreases with depth. Skarstein and Nybrua formation have stronger magnetic properties than the underlying Dragneset formation. The IP measurements clearly show the highest values in the Skarstein formation, 1 - 2 %. This can be caused by the presence of clay minerals. It is difficult to say if it is caused by sulphides because the resistivity in general is very low. The SP log does not seem to indicate the presence of sulphide minerals.

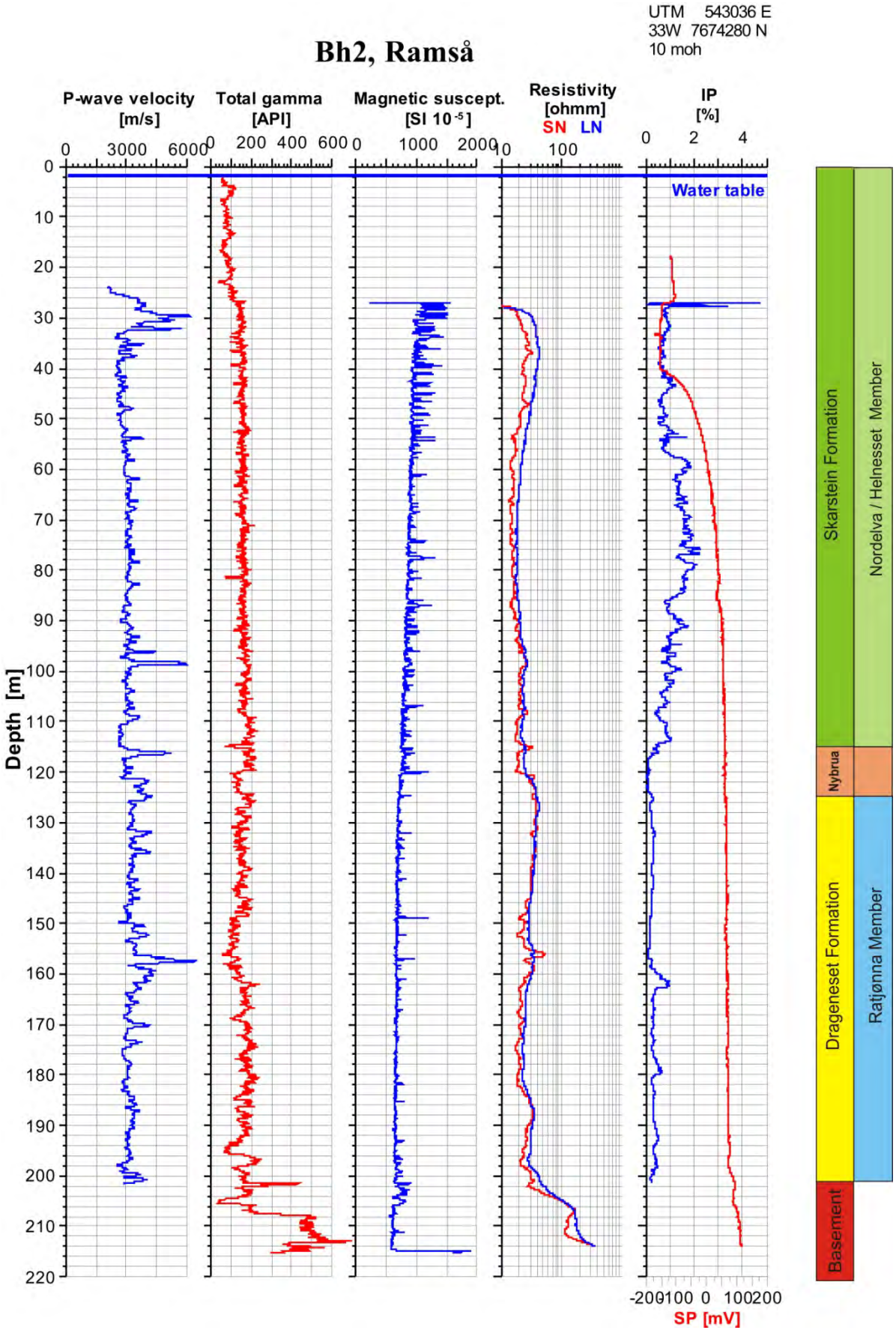

Figure 8.19. BH 2, logs of seismic velocity, total gamma, resistivity, magnetic susceptibility, induced polarization and SP.

8.5.2.4 Acoustic televiewer, fracture mapping and calculation of bedding azimuth and dip angle, BH 2.

BH 2 was logged with an acoustic televiewer down to 207 m depth. Because of a dipping borehole (66 ^{o}) the probe is a bit decentralized in the borehole. This will reduce the quality of the recorded images but observed fractures may well be digitised. In BH 2 all observed fractures are digitised with calculation of azimuth and dip angle. The same is done for the observed bedding in the sediments. It is more difficult to observe layered rock in the basement. The digitised data are used to make fracture frequency histograms and rose diagrams.

Figure 8.20, Figure 8.21 and Figure 8.22 show fracture frequency histograms, resistivity, apparent porosity and seismic velocity (P-wave). Every observed fracture is shown to the left as a needle showing the azimuth (north is up). The entire borehole is highly fractured with a fracture frequency up to 8-12 fractures/metre in the sediments. Fracture frequency in the basement is 4 – 8 fractures/metre.

Figure 8.23 shows a rose diagram of fracture azimuth and dip angle. The average azimuth is SSE and the average dip angle is about 30^{o}.

In most parts of the borehole, bedding can be observed on the acoustic image. By digitising the bedding (in the same way as for fractures), azimuth and dip angle can be calculated. In Figure 8.24 bedding azimuth and dip angle are plotted versus depth. The bedding azimuth is close to S, but rather more SSE below 130 m depth. Dip angle is 15 -25 ^{o} in the upper 90 m and 40 – 50^{o} in the lower part of the borehole. Borehole deviation, bedding dip angle, borehole azimuth and bedding azimuth are also shown in Figure 8.24.

Figure 8.25 shows acoustic images from two sections in the borehole, at 112-115 m (fractured sediments) and 201-204 m (fractured basement). The vertical dark/light bands are caused by decentralisation of the sonde. Between 201 and 204 m depth the basement is highly fractured as can be seen on the image.

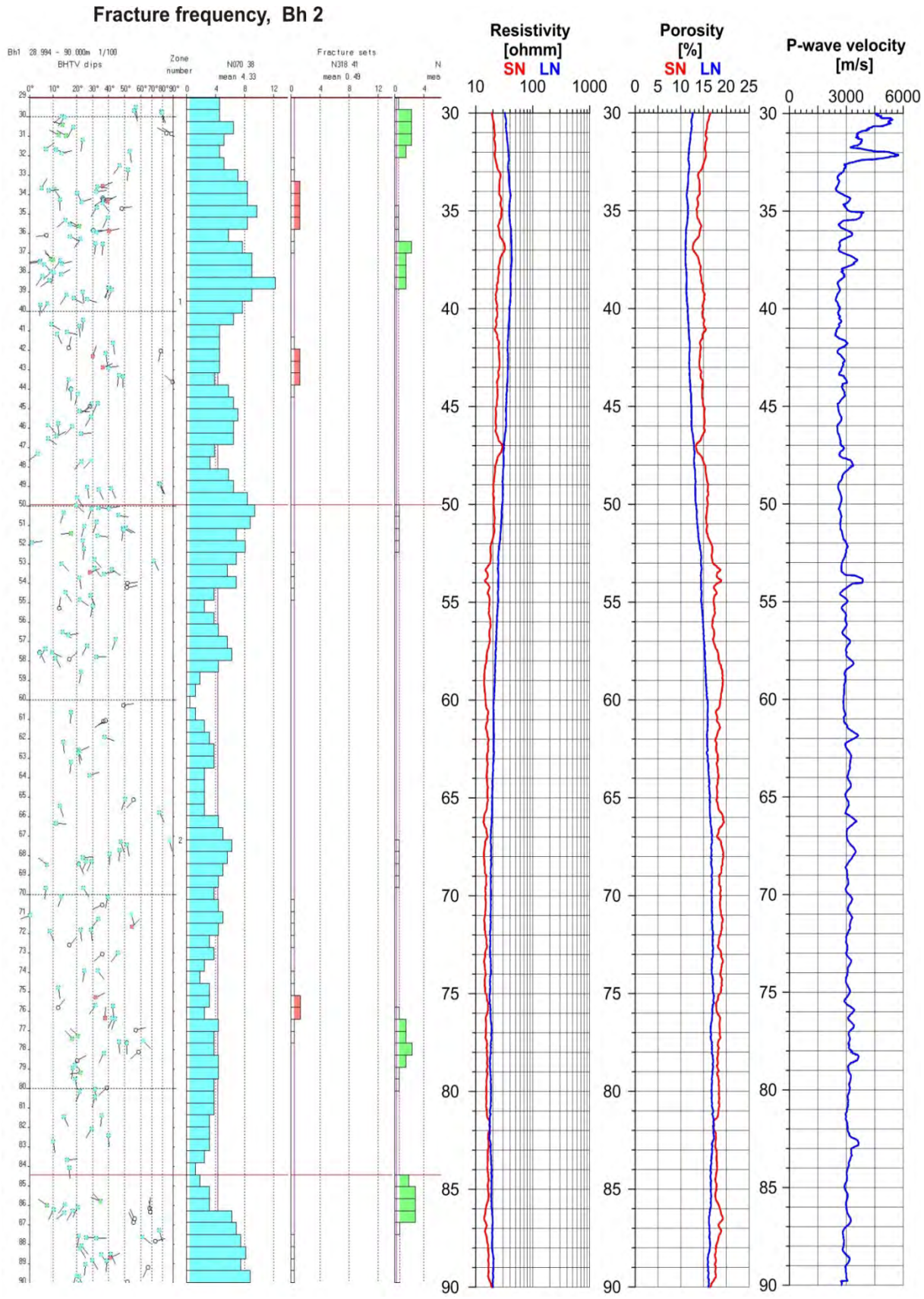

Figure 8.20. BH 2, 30 – 90 m. Fracture frequency, resistivity, porosity and P-wave velocity.

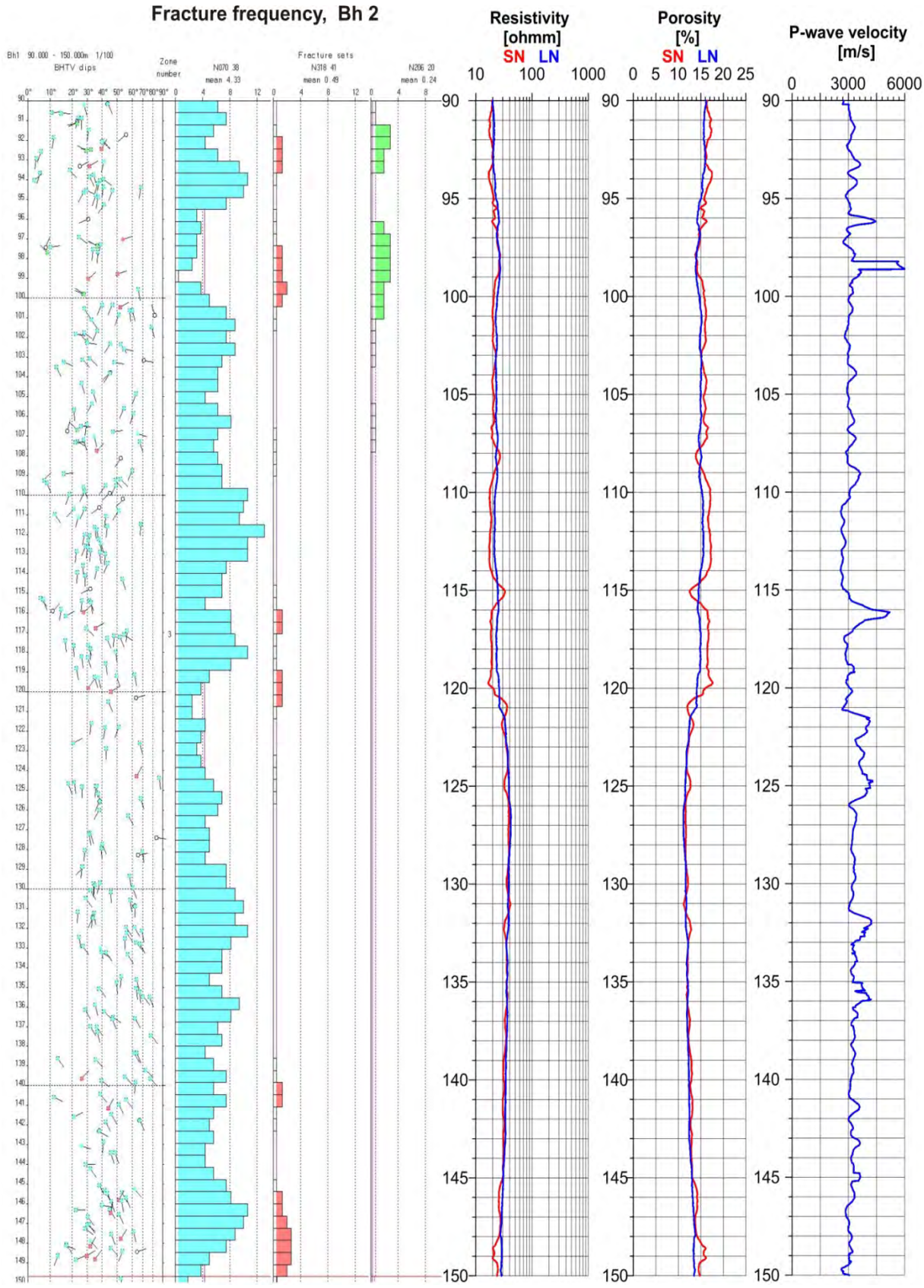

Figure 8.21. BH 2, 90 – 150 m. Fracture frequency, resistivity, porosity and P-wave velocity.

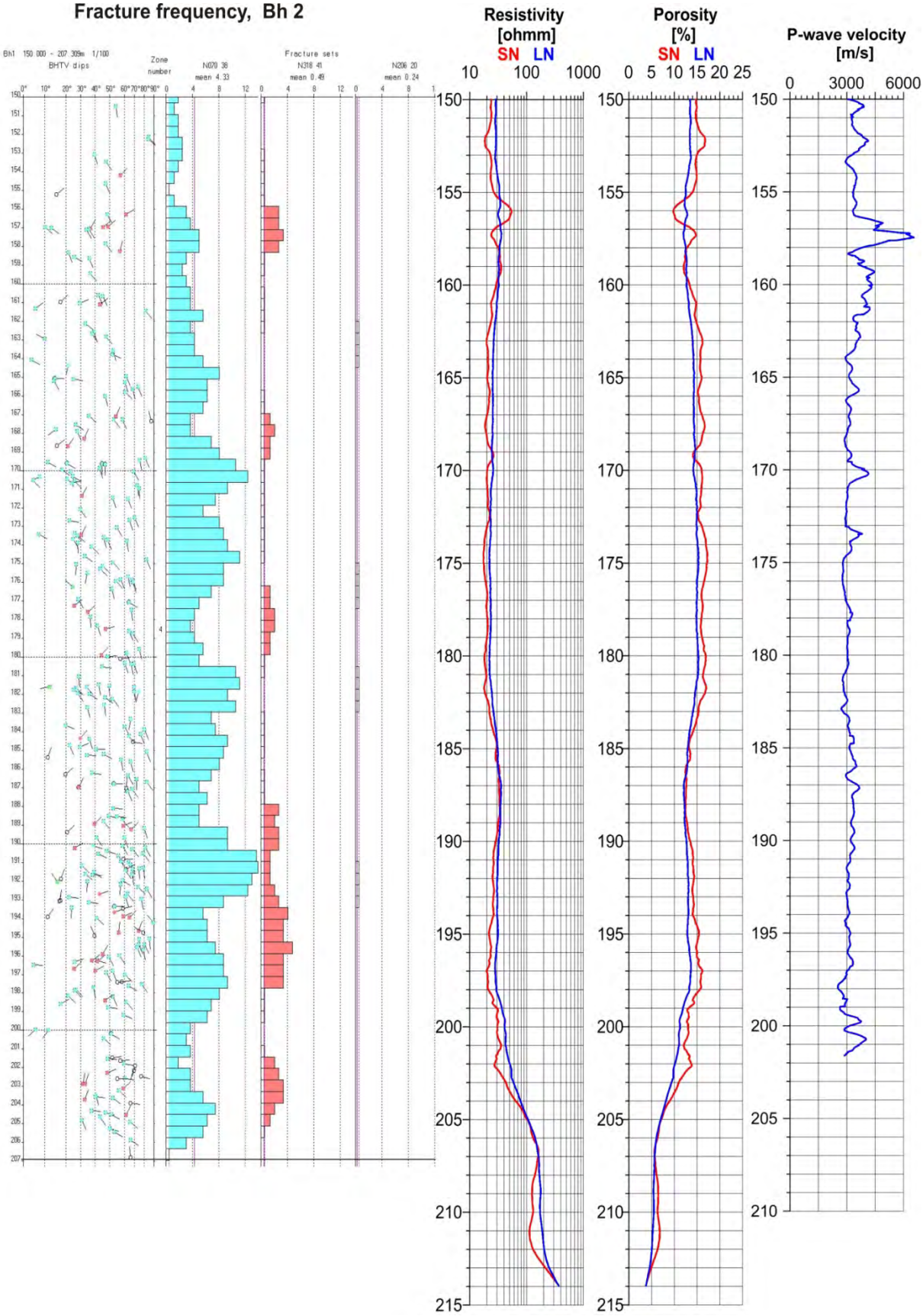

Figure 8.22. BH 2, 150 – 214 m. Fracture frequency, resistivity, porosity and P-wave velocity.

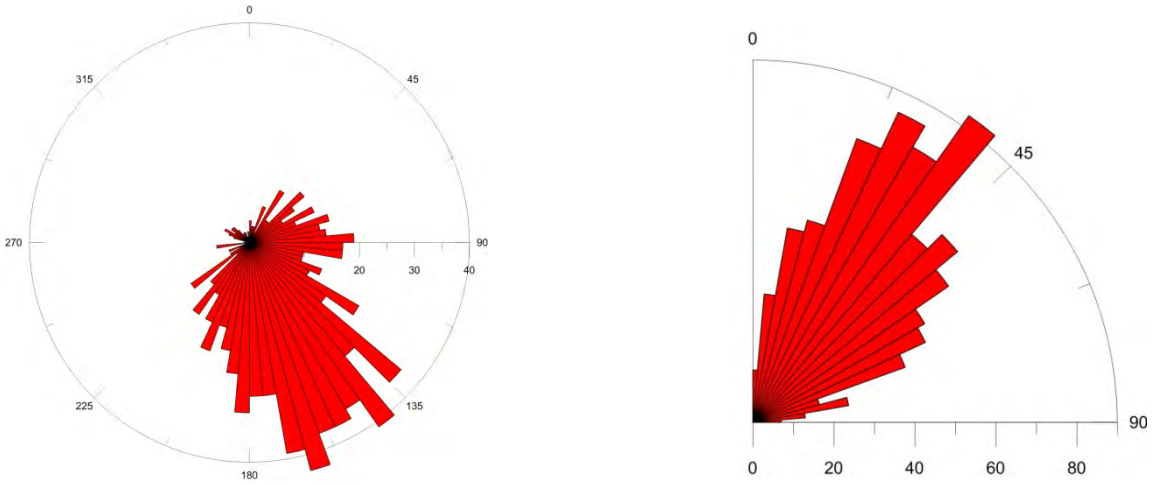

Figure 8.23. BH 2, fracture azimuth (left) and fracture dip angle (right).

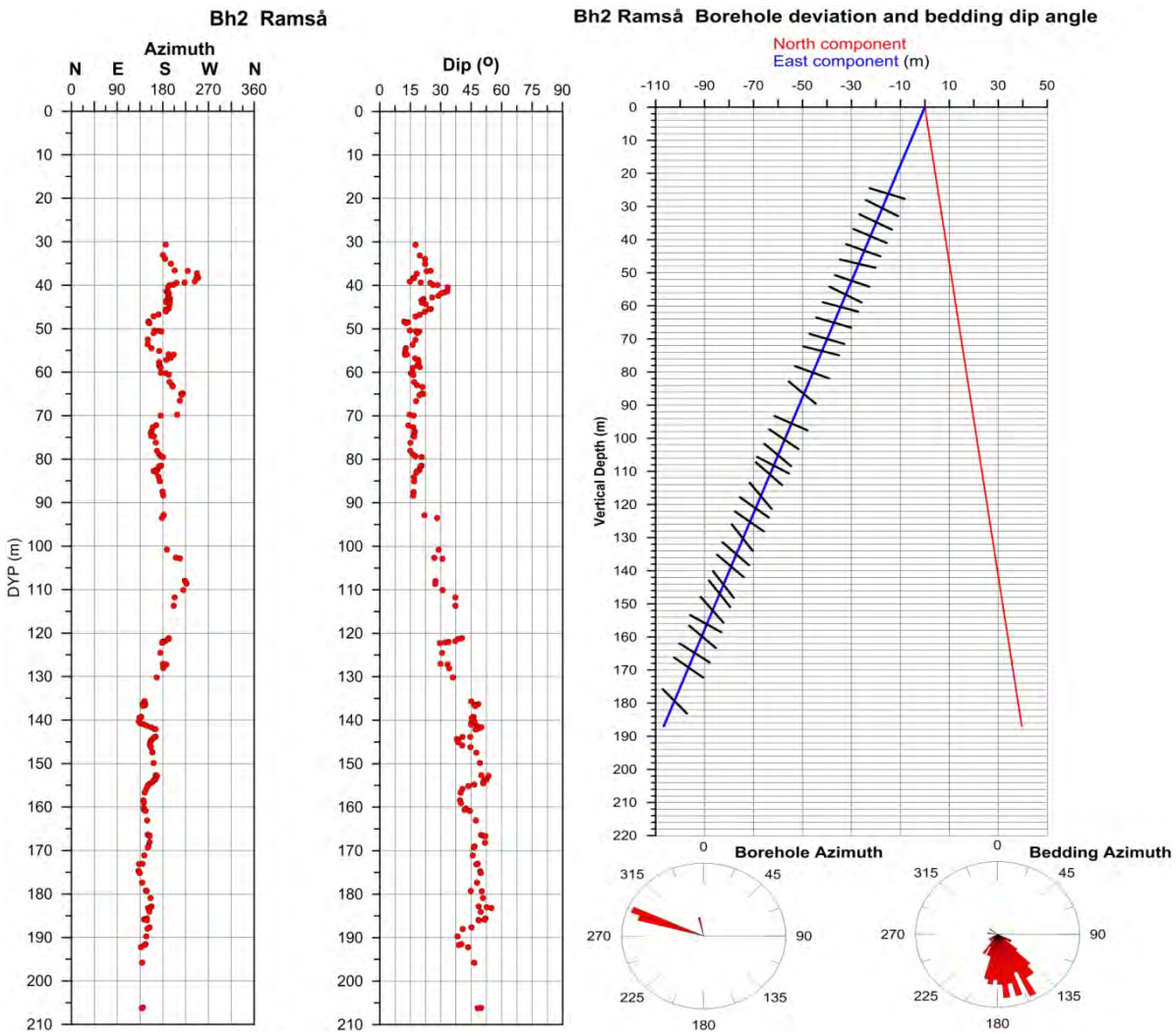

Figure 8.24. BH 2, Azimuth and dip angle of bedding (left), borehole deviation, borehole azimuth and bedding azimuth (right).

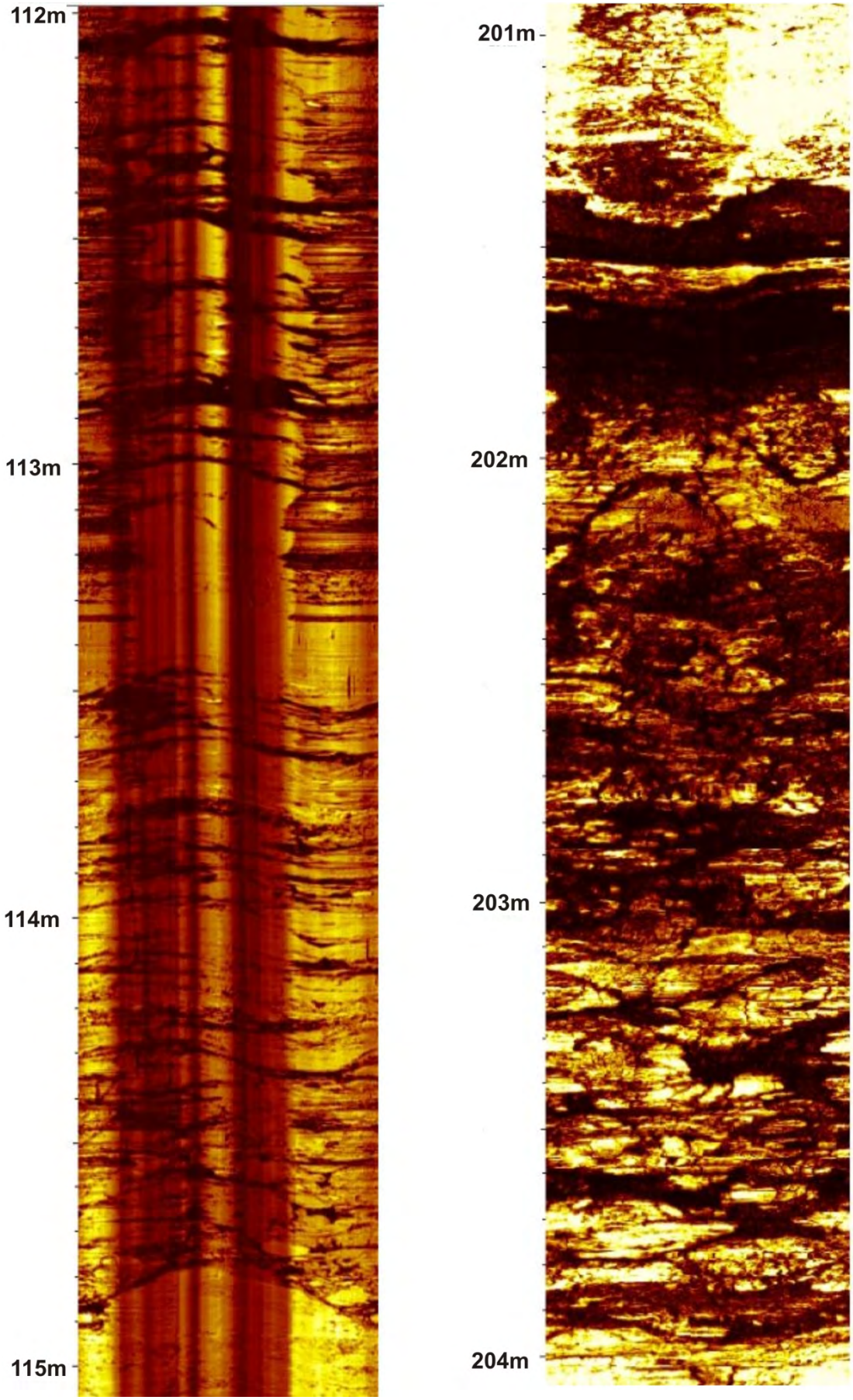

Figure 8.25. BH 2, acoustic televiewer image, 112-115 m (left), 201-204 m (right).

8.5.3 Results BH 3

BH 3 was drilled and logged in February 2016. The borehole location is to the southwest of the Ramså Basin at Kvalnesmyra about 3.5 km from the shore. The drilling and logging operations had to be done while the surface (moor) was frozen in order to transport the heavy drilling equipment. The Ramså Basin is inferred to have a further extension to the southwest based on interpretation of new magnetic, gravity and seismic data. Figure 8.26 shows logging at the BH 3 location at Kvalnesmyra.

Figure 8.26. BH 3 location at Kvalnesmyra southwest of the Ramså Basin.

8.5.3.1 Temperature, electric conductivity in water and total natural gamma radiation in BH 3.

Figure 8.27 shows logs of temperature, conductivity in water, natural total gamma and calculated thermal gradient. The borehole is vertical. The average thermal gradient is about 20 ^{o}C/km. which is less than in BH 1 and BH 2. The bottom borehole temperature is 8.2^{o}C at 223 m depth.

Electric conductivity in water varies in several steps downwards in the borehole. Fresh water is observed in the upper 15 m. The conductivity increases strongly from 124 m depth and below 140 m it is 50,000 µS/cm. This is even higher than in seawater. The reason for the salty water at depth has been discussed and most probably represents fossil water (Dalland 1975) considered that faults had created two small troughs in the basin.

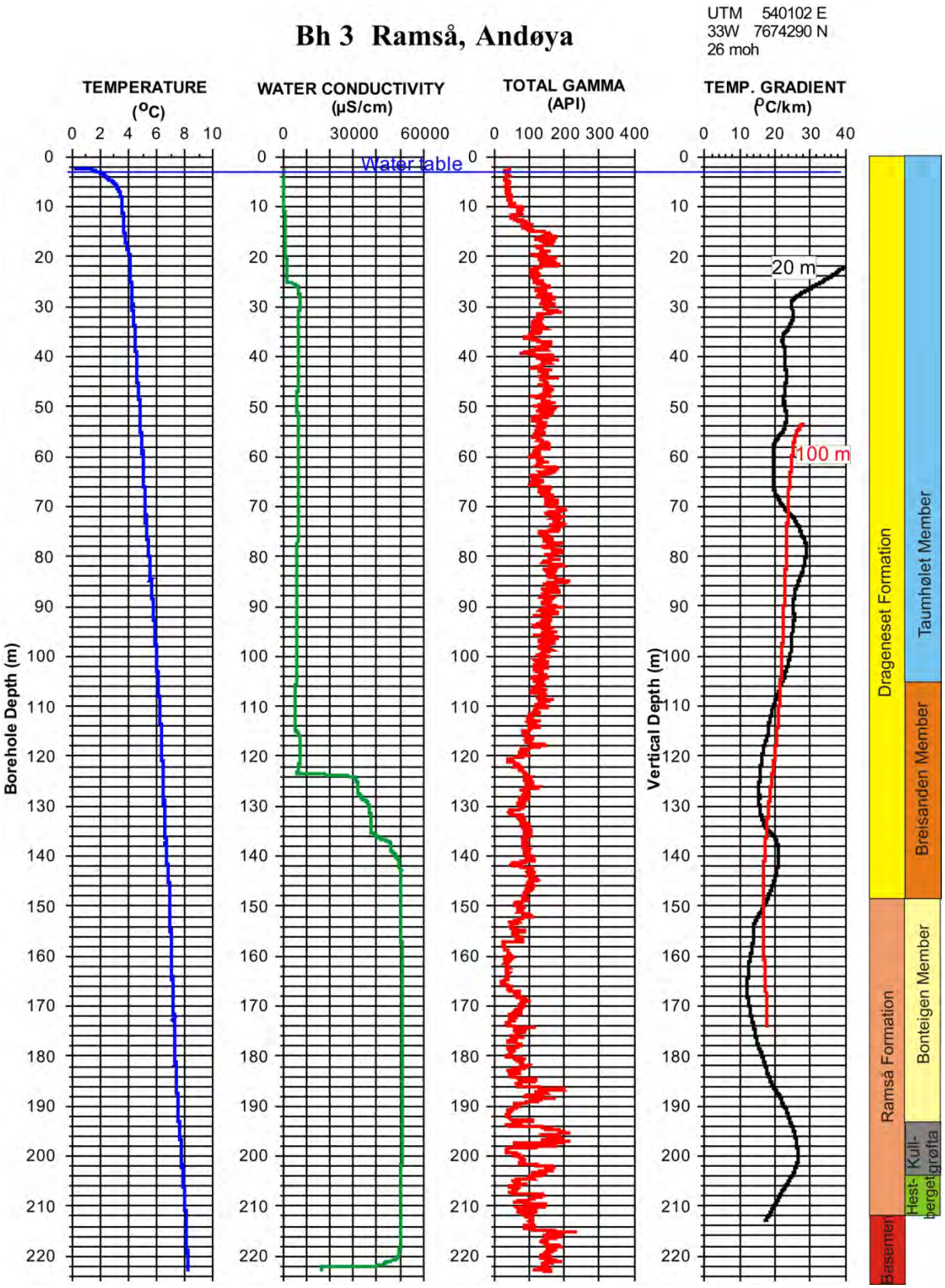

Figure 8.27. BH 3, logs of temperature, water conductivity, total gamma and thermal gradient.

Saline water could have been trapped in these troughs. A ten litres sample was collected at 145 m depth for analysis.

Above 120 m depth natural total gamma radiation is 100 – 200 API. Below this depth it varies from 30 to 200 API with the highest values in the Kullgrøfta member. In the basement below 212 m depth the gamma radiation is about 150 API.

8.5.3.2 Gamma spectroscopy, BH 3.

Figure 8.28 shows the result from the gamma spectroscopy measurements in BH 3. The logs are continuous and measured with a constant speed of 1 m/min.

Table 8.7 shows total gamma and average contents of the elements U, Th and K in each stratigraphic member. The U content is highest in the Taumhølet member with an average of 4.7 ppm. The Kullgrøfta member has an average U content of 4.1 ppm with up to 10 ppm locally. The same can be seen in the basement.

The highest values of Th are measured in the Kullgrøfta member (22 ppm) and in basement (26 ppm). Also the lower Taumhølet member has a high content of Th (15 – 18 ppm). Average values are shown in Table 8.7.

The highest K values are measured in the Taumhølet member (2.5 ppm). The very low K content (0.3 %) in the Hestberget member found in BH 1 does not seem to be repeated in Hestberget BH 3 (1.8 %).

Table 8.7. Stratigraphy and lithology (Dalland 1975) in BH 3 and average content of U, Th and K.

Stratigraphic Members	**Lithology**	**Total Gamma (API)**	**U (ppm)**	**Th (ppm)**	**K (%)**
Taumhølet mbr.	Fine-grained sandstone	195	4.7	7.3	2.5
Breisanden mbr.	Micaceous sandstone	145	2.8	4.6	2.3
Bonteigen mbr.	Coarse-grained sandstone Siltstone, thin coal layers	95	1.9	4.2	1.2
Kullgrøfta mbr.	Bituminous shale, oil shale	170	4.1	8.7	1.5
Hestberget mbr	Coarse-grained sandstone	130	2.0	6.0	1.9
Basement	Andøy granite	200	4.5	13.8	0.6

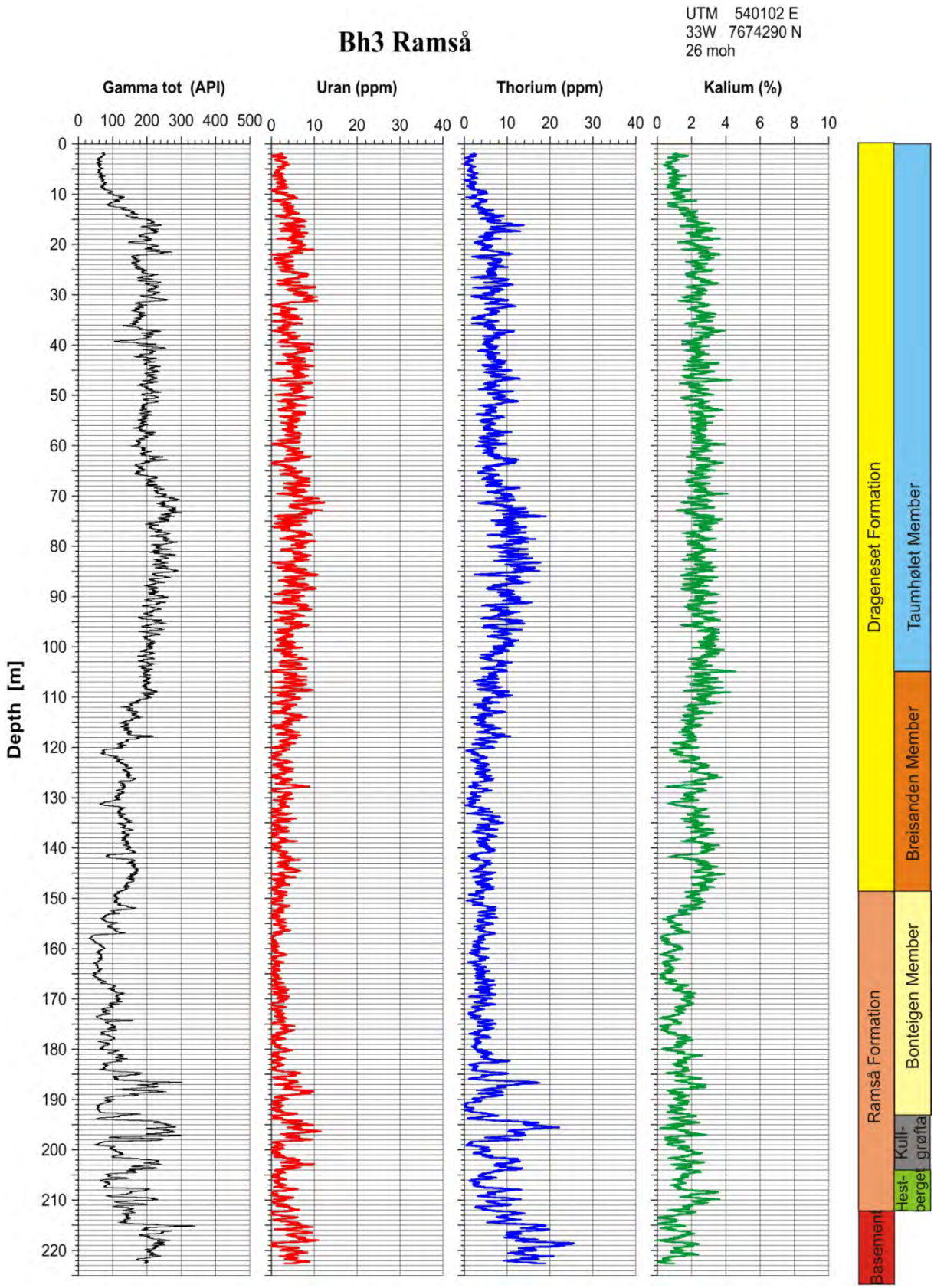

Figure 8.28. BH 3, gamma spectroscopy showing total gamma, U (ppm), Th (ppm) and K (%).

8.5.3.3 Seismic velocity, resistivity, magnetic susceptibility, induced polarisation and self potential, BH 3.

Figure 8.29 shows logs for seismic velocity, total gamma radiation, formation resistivity, magnetic susceptibility, IP and SP. The gamma radiation log is described in the previous chapter. Average values of measured parameters for each formation are shown in Table 8.8.

The formation resistivity is low (10 – 100 ohmm) mainly because of the high-conductive pore-water. However, the upper 100 m of the borehole (Taumhølet member) was highly fractured as mapped by the acoustic televiewer; see later. Despite that, the highest resistivity is measured in the upper 60 m. The lowest resistivity is measured in the Ramså formation (10 ohmm). The water conductivity increases markedly from about 125 m depth (Figure 8.28) which leads to low resistivity in the formation. In the basement (from 212 m) the resistivity increases which confirms the basement boundary. In BH 3, deep weathering has been indicated in the basement rock (Chapter 10).

The P-wave velocity is lowest (2700 m/s) in the Taumhølet member. This fits well with the highly fractured rock in this part of the borehole. The P-velocity increases slightly to the bottom of the borehole, especially in the basement (4500 m/s). Several high-velocity peaks can be observed below 120 m depth (up to 6000 m/s). These peaks correlate well with high-resistivity peaks (SN resistivity) and are caused by the presence of calcite veins (A. Ryseth, pers. comm. 2016). Such veins can also be observed on the acoustic televiewer image log.

Magnetic susceptibility is highest in the upper Taumhølet formation (15 – 60 m depth) with values 10 – 150 10^{-5} SI. In the rest of the borehole the magnetic susceptibility is low and especially in the basement.

Table 8.8. Average values of geophysical parameters in stratigraphic formations/members BH 3.

Stratigraphic member	**P-velocity (m/s)**	**Resistivity SN**	**Resistivity LN**	**MagSus (SI 10^{-5})**	**IP (%)**	**Total Gamma**	**U (ppm)**	**Th (ppm)**	**K (%)**
Taumhølet mbr.	2700	60	74	49.9	0.58	195	4.7	7.3	2.5
Breisanden mbr.	3025	48	43	24.4	0.51	145	2.8	4.6	2.3
Bonteigen mbr.	3210	8	12	29.3	0.79	95	1.9	4.2	1.2
Kullgrøfta mbr.	3335	15	14	2.5	0.64	170	4.1	8.7	1.5
Hestberget mbr	3515	11	14	7.2	0.55	130	2.0	6.0	1.9
Basement	4350	58	55	4.3	0.46	200	4.5	13.8	0.6

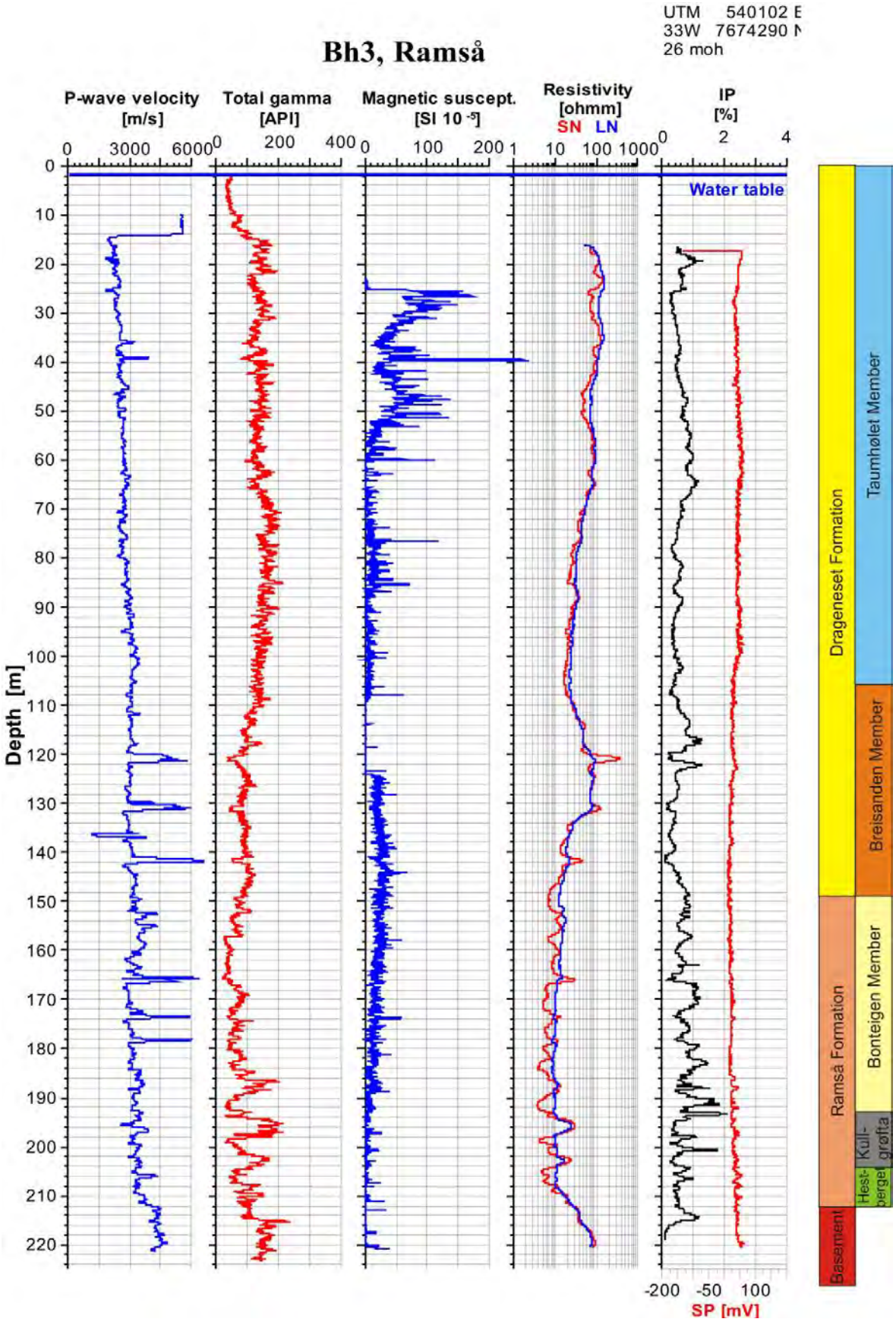

Figure 8.29. BH 3, logs of seismic velocity, total gamma, resistivity, magnetic susceptibility, induced polarization and SP.

The average IP is low (below 1 %) in the entire borehole. Some increased values (up to 2 %) can be observed in the Bonteigen and Kullgrøfta members and in the basement. Deep weathering has been observed in the basement and clay might give a weak IP-effect. Pyrite has also been observed (A. Ryseth oral information).

8.5.3.4 Acoustic televiewer, fracture mapping, bedding azimuth and dip angle, BH 3.

BH 3 was logged with an acoustic televiewer down to 221.8 m depth. The borehole was drilled vertical. In BH 3, all observed fractures are digitised with calculation of azimuth and dip angle. The same is done for the observed bedding in the sediments. It is more difficult to observe layered rock in the basement. The digitised data are used to make fracture frequency histograms and rose diagrams.

Figure 8.30 - Figure 8.32 show fracture frequency histograms, resistivity, apparent porosity and seismic velocity (P-wave). Every observed fracture is shown to the left as a needle showing the azimuth (north is up). The upper 100 m of the borehole (Taumhølet member) is highly fractured with a calculated fracture frequency up to 8 fractures/metre (see Figure 8.30). Below this depth the maximum fracture frequency is 1 – 2 fractures/metre.

Figure 8.33 shows a rose diagram of fracture azimuth and dip angle. Fracture azimuth varies from SW to SE. The dip angle is 10 - 30^{o}.

In most parts of the borehole bedding can be observed on the acoustic image. By digitising the bedding (in the same way as for fractures) the azimuth and dip angle can be calculated. The borehole deviation, bedding dip angle, borehole azimuth and bedding azimuth are shown in Figure 8.34. The dip angle is 10 – 30^{o} in the upper 70 m and 7 – 10^{o} below this depth. It should be mentioned that the bedding is dipping slightly opposite to the bedding azimuth in BH 1 but close to the dip direction in BH 2. The same stratigraphic members are found in BH 3 as in BH 1 but at a deeper level.

Figure 8.35 shows acoustic images from three sections in the borehole, 36 -39 m (fractured sediments), 77 - 80 m (fractured sediments) and 129 – 132 m (unfractured sediments including a 1 m-thick calcite vein).

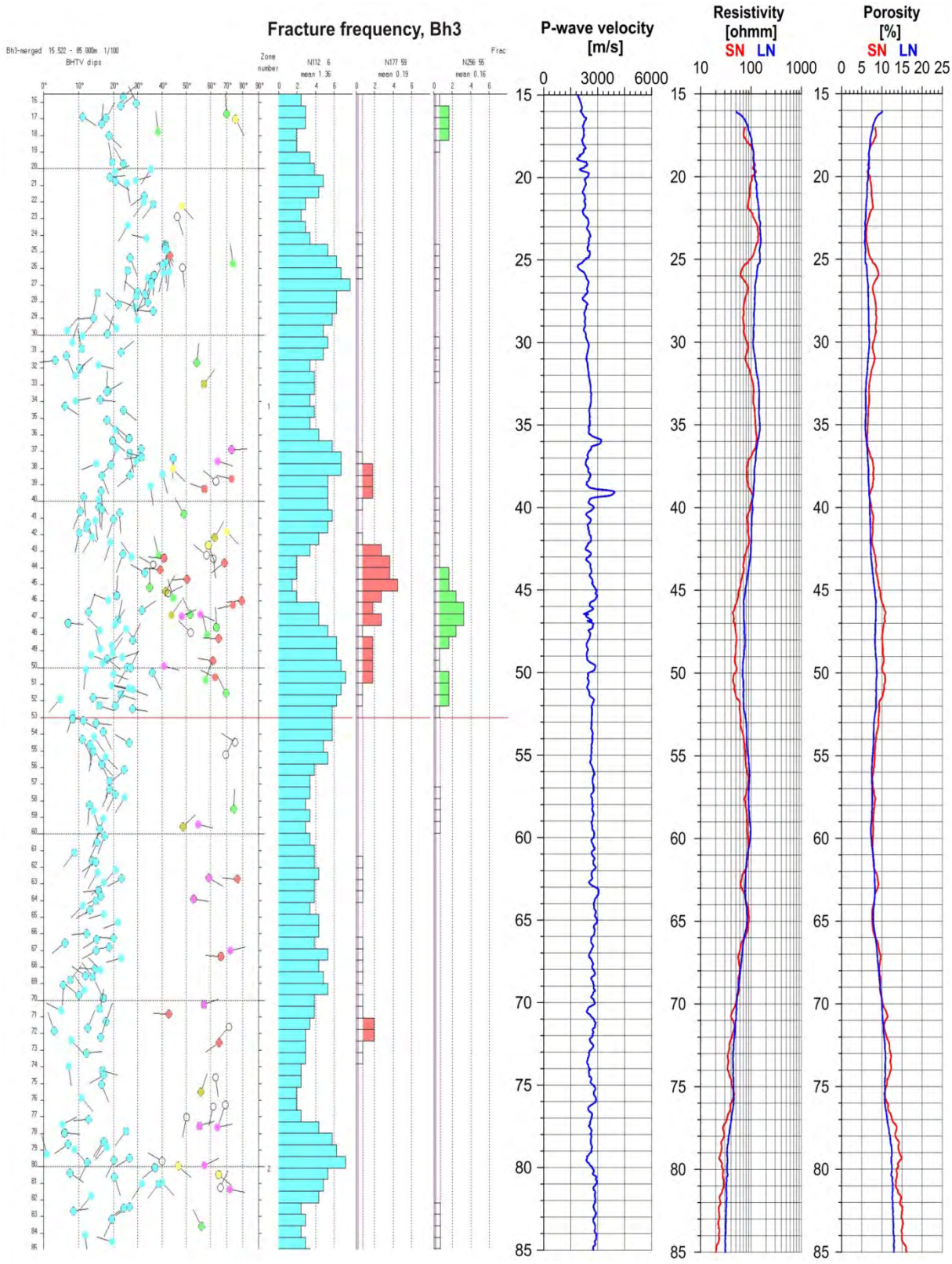

Figure 8.30. BH 3, 15 – 85 m. Fracture frequency, resistivity, porosity and P-wave velocity.

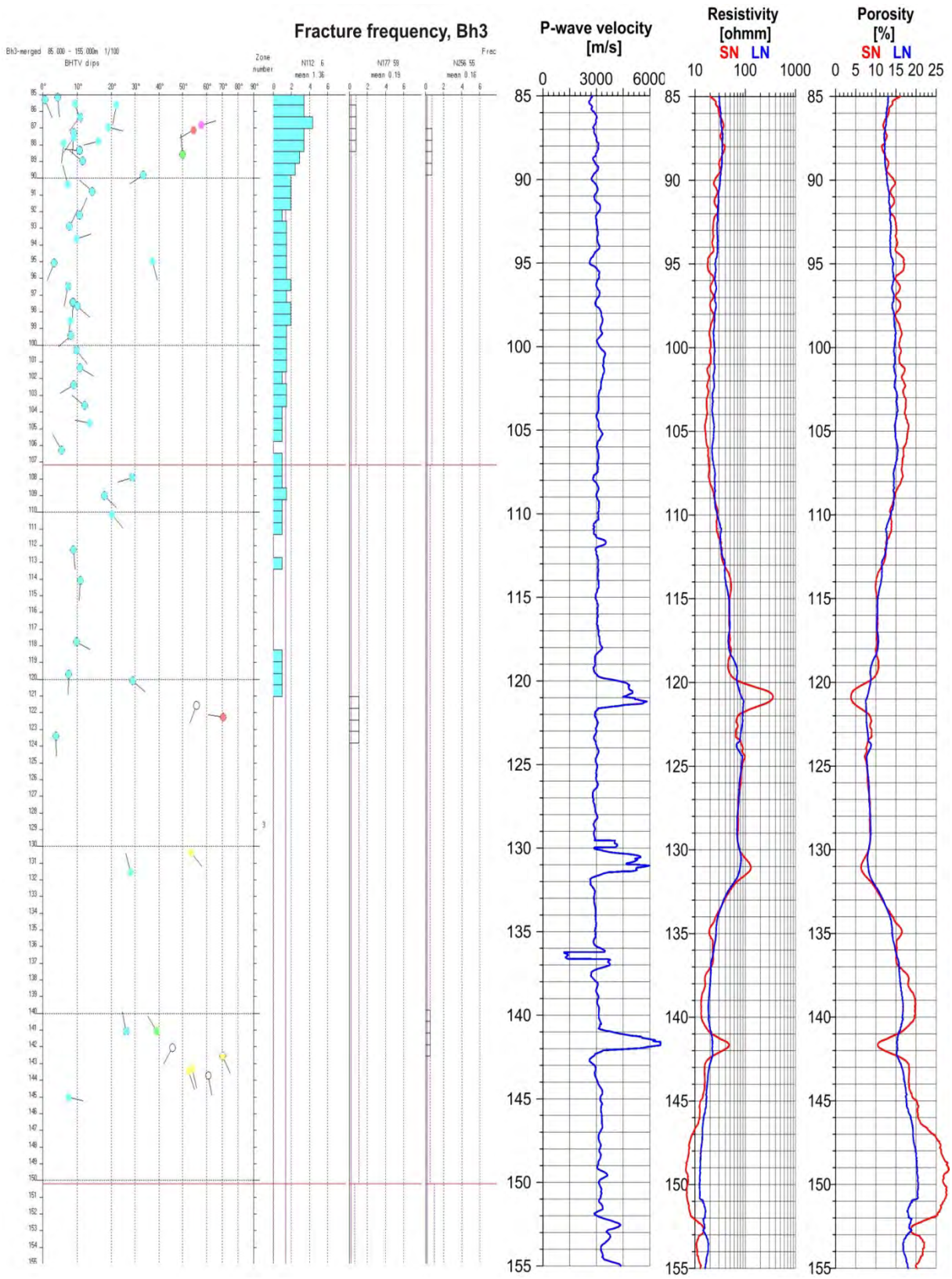

Figure 8.31. BH 3, 85 – 155 m. Fracture frequency, resistivity, porosity and P-wave velocity.

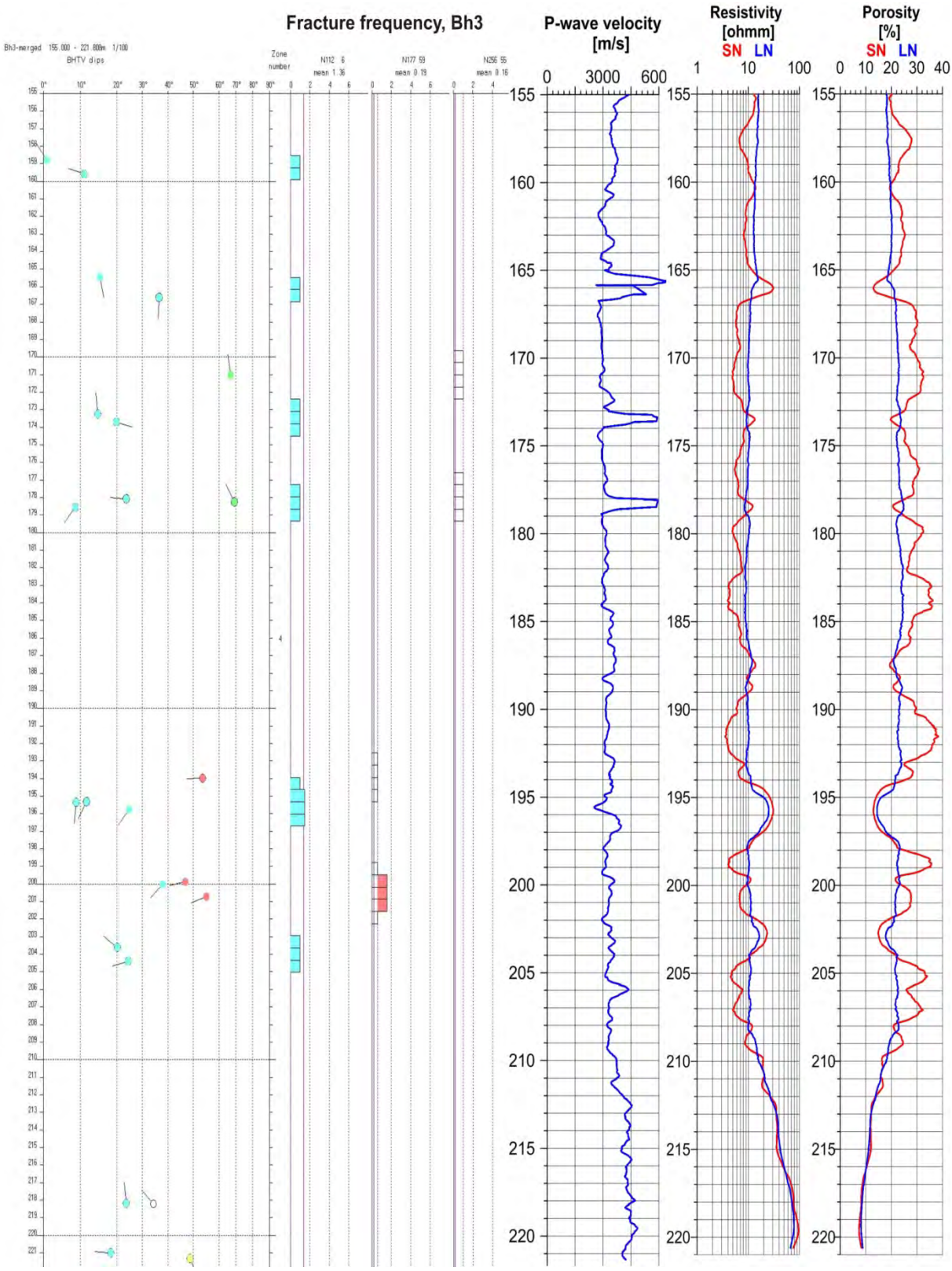

Figure 8.32. BH 3, 155 – 222 m. Fracture frequency, resistivity, porosity and P-wave velocity.

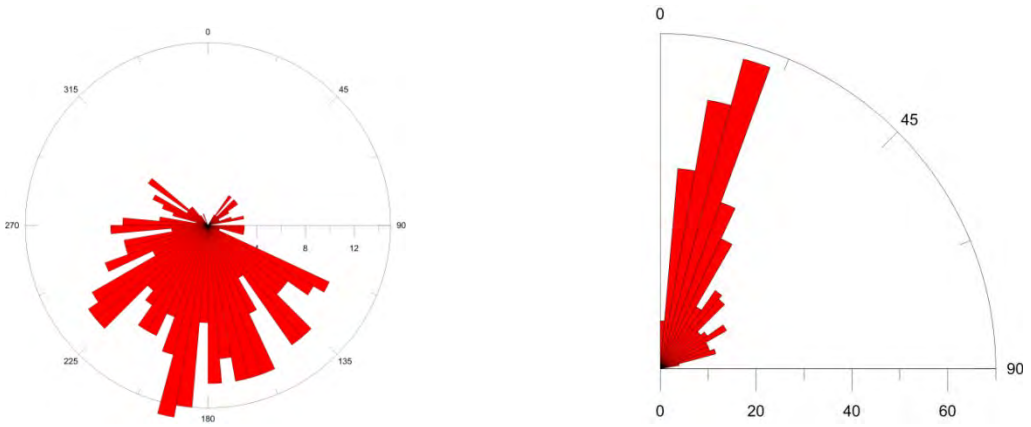

Figure 8.33. BH 3, fracture azimuth (left) and fracture dip angle (right).

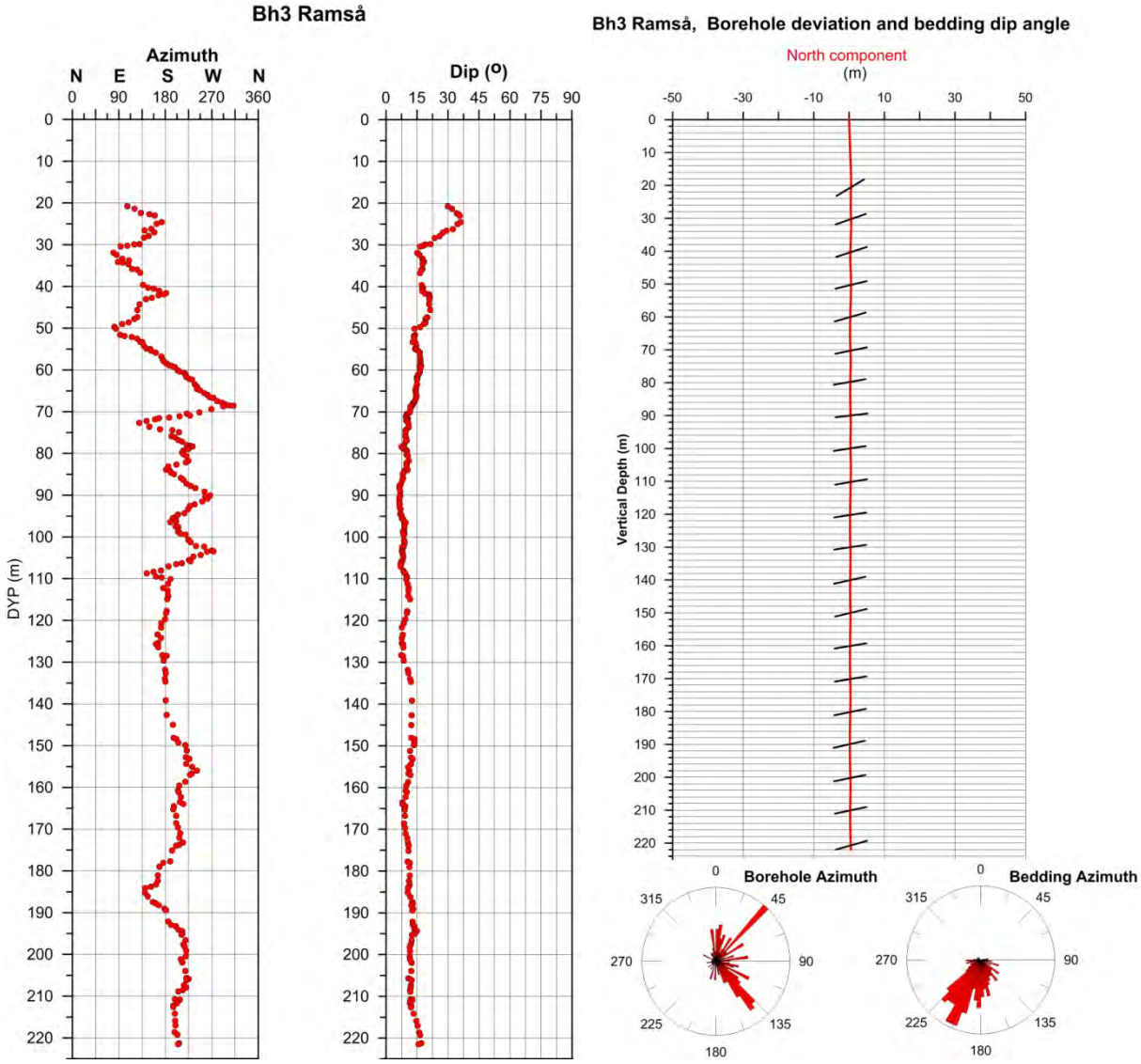

Figure 8.34. BH 3, Azimuth and dip angle of bedding (left), borehole deviation, borehole azimuth and bedding azimuth (right).

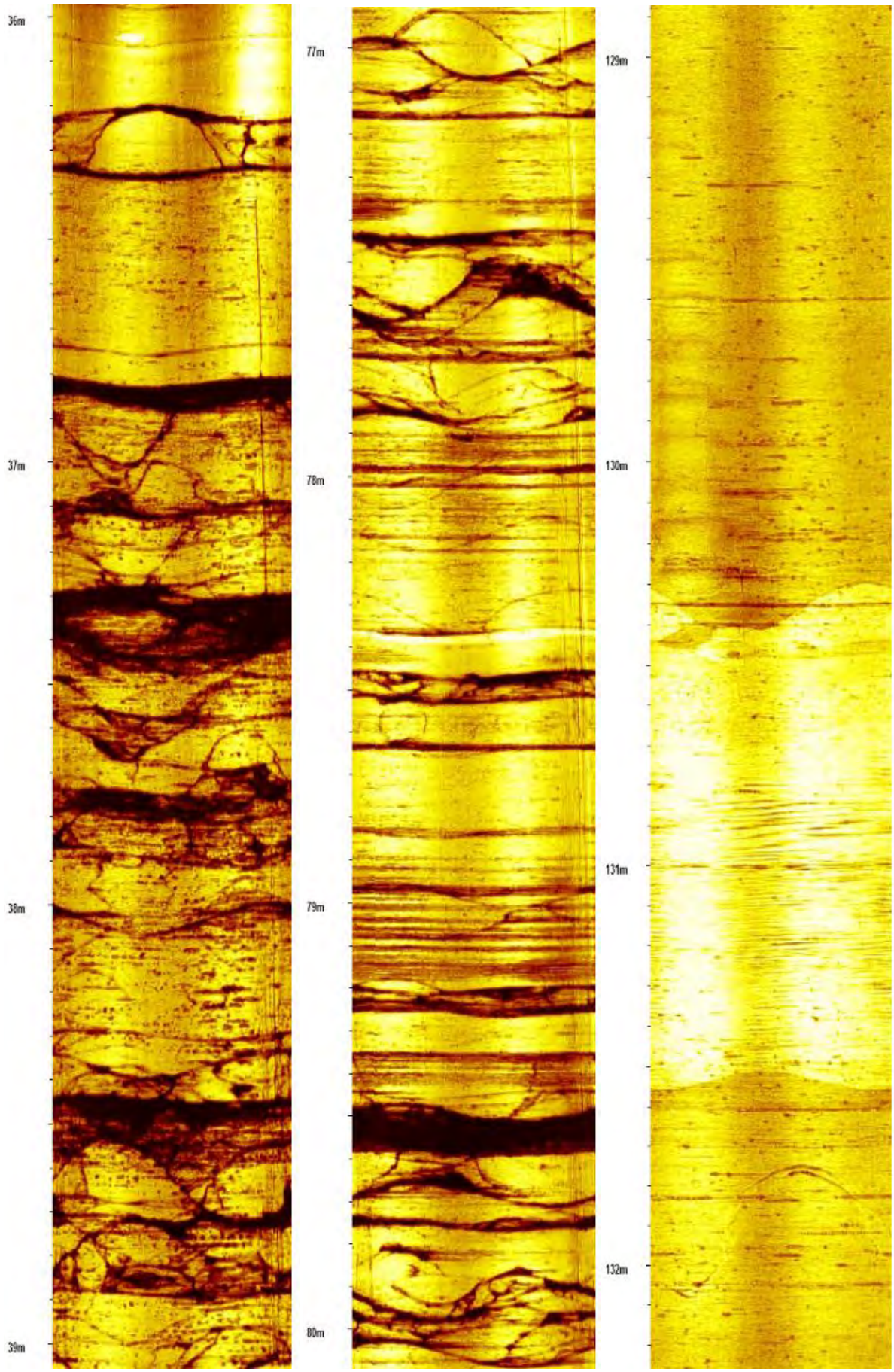

Figure 8.35. BH 3, Acoustic images 36-39m, 77-80m and 129-132m. Calcite vein 130.5-131.5m.

8.5.4 Results BH 4

BH 4 was drilled close to the southern border of the Ramså Basin, about 270 m south of BH 1.The main aim was to map the extension of the Ramså Basin to the south. Close to the BH 1 location deeply weathered rocks were observed at the surface. It was clear that the location was outside the Ramså Basin and drilling was stopped at 53.7 m. Figure 8.36 shows the BH 4 location, south of an old military camp.

Figure 8.36. BH 4 location south of an old military camp.

Logging parameters in BH 4 were temperature, fluid conductivity, total natural gamma and resistivity. The resistivity sonde got stuck in the bottom of the borehole. Several attempts were made to pull the sonde out, but the wire loosened from the cable head on the sonde with the result that the sonde was lost in the borehole at 53 m depth.

The logs from BH 4 are presented in Figure 8.37. The borehole is too short to get a reliable thermal gradient which is calculated to 16 – 22 ^{o}C/km. The bottom hole (51.7 m) temperature is 4.9 ^{o}C.

The conductivity measurements indicate fresh water. The gamma radiation is low. Below 20 m it is quite constant, 25 – 50 API. In the upper part the gamma radiation varies, but it is still low. There seems to be a change in the lithology at 20 m depth. The resistivity is 700 - 1000 ohmm, increasing to 2000-3000 ohmm in the last 5 m to the bottom of the hole. A resistivity below 1000 ohmm with fresh pore-water indicates either fractured rock or a high porosity.

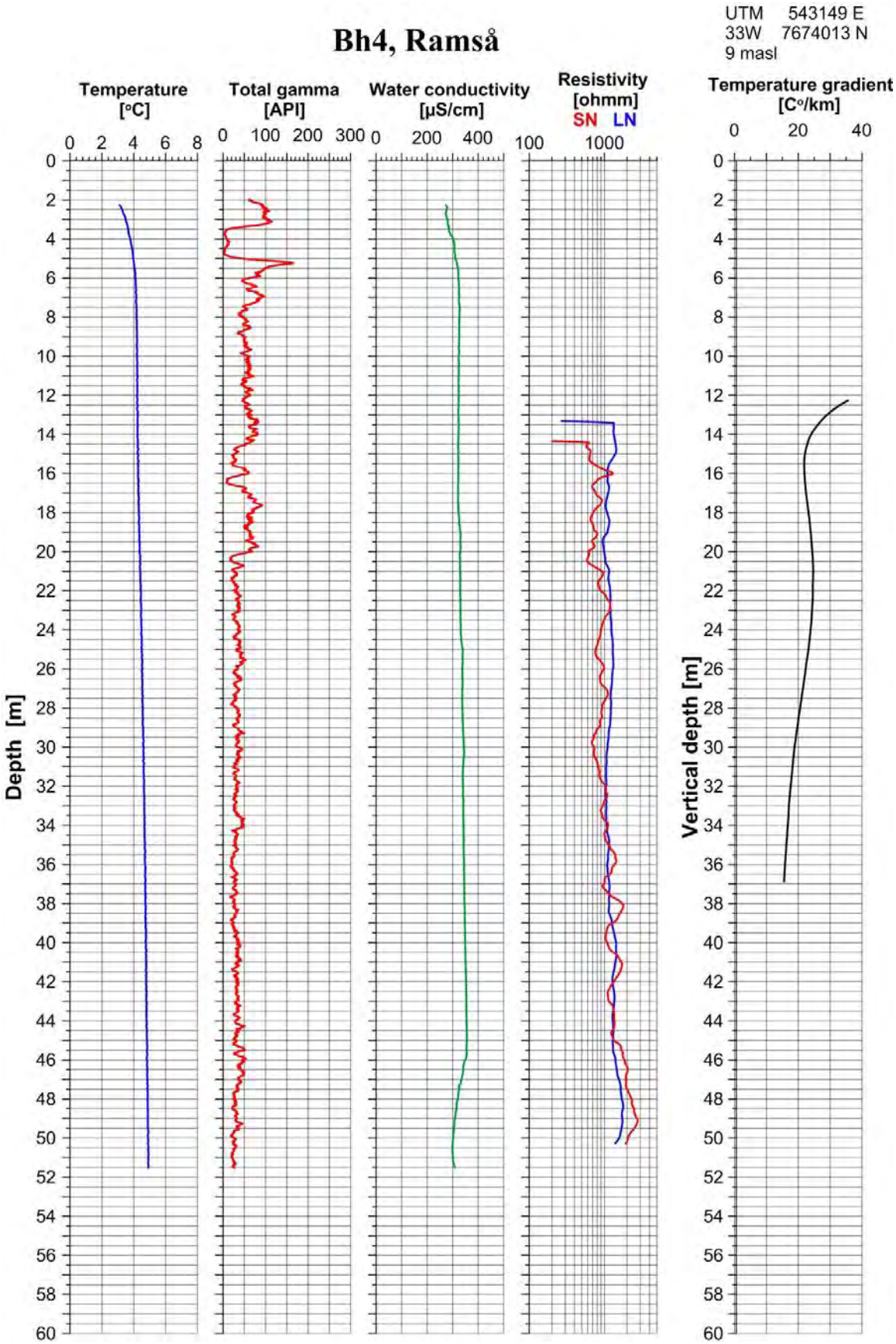

Figure 8.37. BH 4, logs of temperature, temp. gradient, total gamma, water conductivity and resistivity.

8.6 **Ovalisation and breakout logs**

Borehole breakouts are stress-induced enlargements of a wellbore cross-section. When a borehole is drilled the core material removed from the subsurface is no longer supporting the surrounding rock. As a result the stresses become concentrated in the borehole wall. Borehole breakouts occur when stresses around the borehole exceed the strength of the rock. This might cause compressive failure of the borehole wall (Zobak et al. 1985). Development of intersecting conjugate shear planes leads to enlargements of the wellbore. This can be determined by measuring the borehole diameter using a calliper log or acoustic televiewer. The ovalisation of the borehole will indicate breakouts.

Around a vertical borehole stress concentration is greatest in the direction of the minimum horizontal stress S_h. Hence, breakouts are oriented approximately perpendicular to the maximum horizontal stress orientation, $S_{H,}$ (Figure 8.38) (Plumb & Hickman 1985).

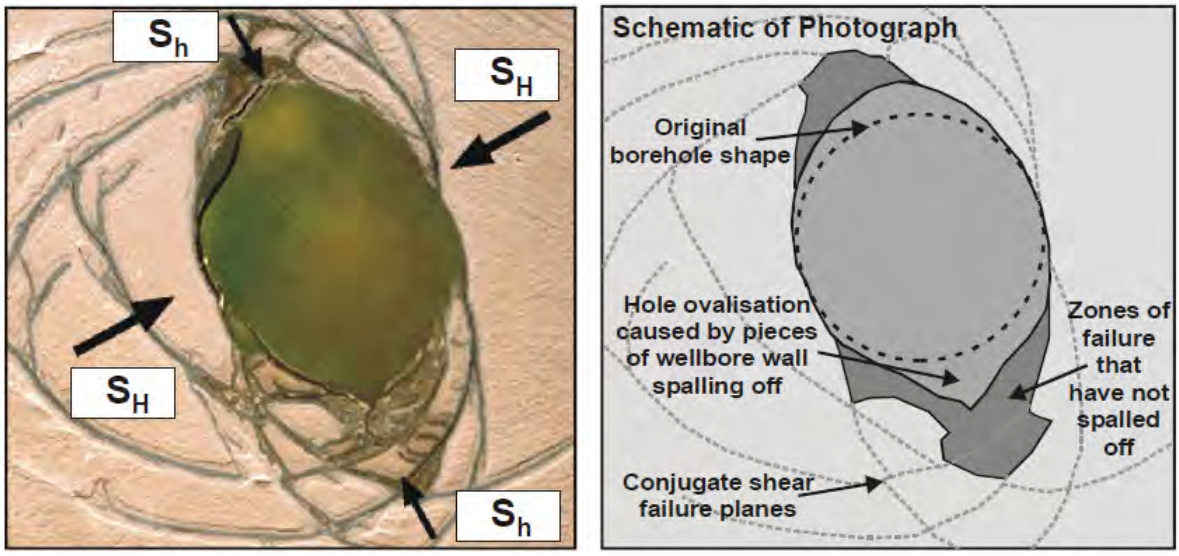

Figure 8.38. Result of a lab test simulating borehole breakout showing that the maximum horizontal stress S_H is perpendicular to the wellbore enlargement caused by intersecting conjugate shear planes. The lab test was performed by CSIRO, Division of Geomechanics (Plumb & Hickman 1985).

By using the acoustic televiewer the normalised maximum (alpha) and minimum (beta) diameters are measured. The ratio alpha/beta will be the ovalisation of the borehole cross-section. Values higher than 1 indicate an oval cross-section (breakouts?). However, all kinds of fractures will have an influence on the measured diameter and thereby the ovalisation ratio. The azimuth of alpha is the azimuth of maximum diameter (breakout) and from this the direction of maximum horizontal stress S_H can be calculated.

The acoustic televiewer is also used to calculate the real radius in N-S and E-W trends to make a caliper4 log.

If breakouts caused by horizontal stress are present in a borehole this will be seen on the borehole image log as vertical dark stripes c. 180^o apart.

8.6.1 BH 1 ovalisation and calliper 4.

Figure 8.39 shows the ovalisation log in BH 1. No real breakouts can be seen on the acoustic image and the 'anomalies' on the ovalisation log are caused by open fractures. In this case the azimuth of alpha has no meaning. At 128 m depth a 1 m-thick fracture zone can be seen on the image log which is also clearly indicated on the ovalisation log. The big ovalisation at about 15 m depth is an artificial effect probably caused by a large decentralisation of the probe.

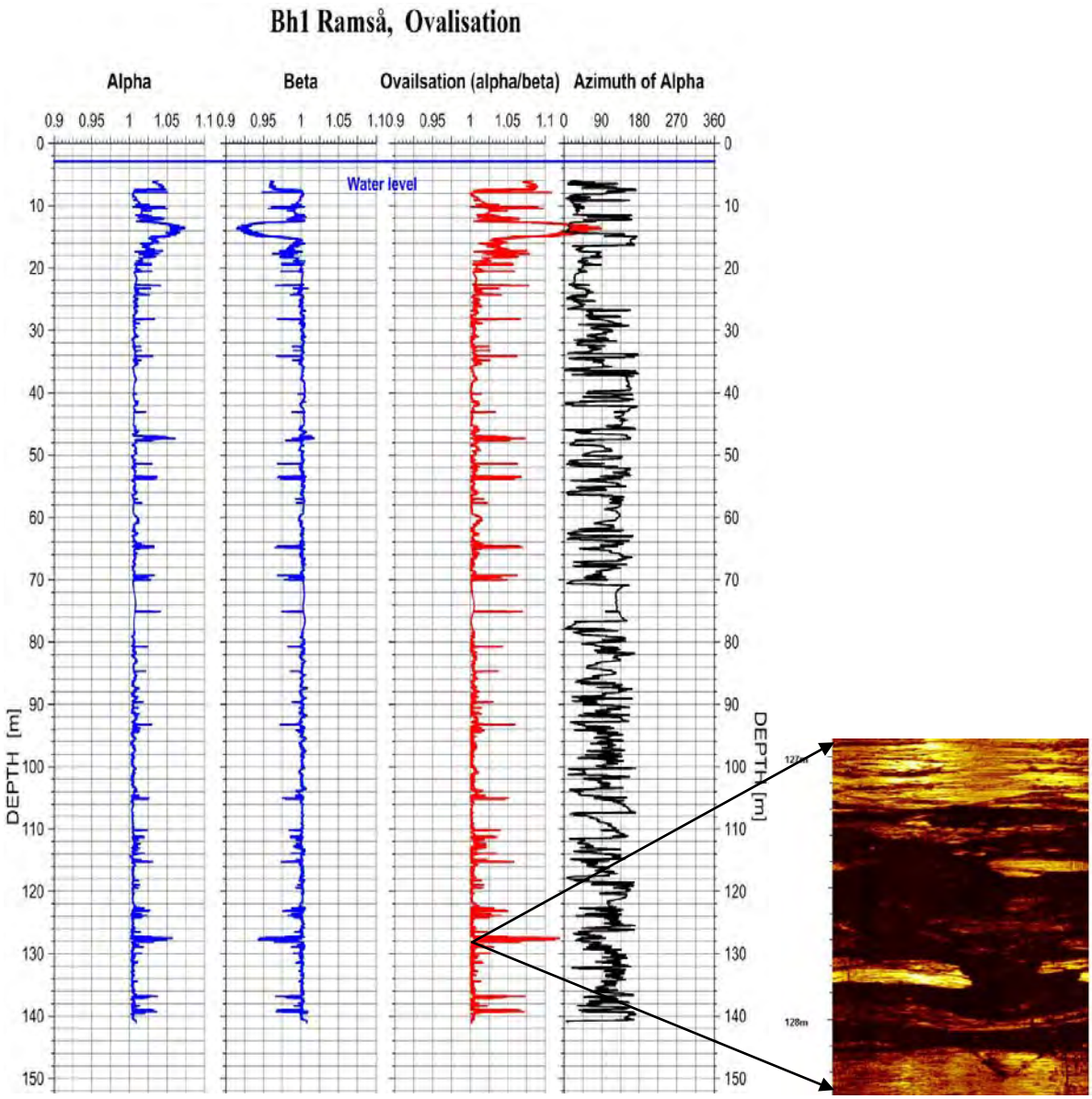

Figure 8.39. Ovalisation log BH 1. Fracture zone at 127 -128 m is can be seen on acoustic image.

The caliper4 log is shown in Figure 8.40 together with the total gamma log. The calculated diameter is about 7 cm. Between 70 and 80 m depth the diameter increases up to almost 8 cm.

This is inside the Kullgrøfta member and it fits well with increased gamma radiation. The increased diameter is probably caused by the drilling ability and hardness of the rock.

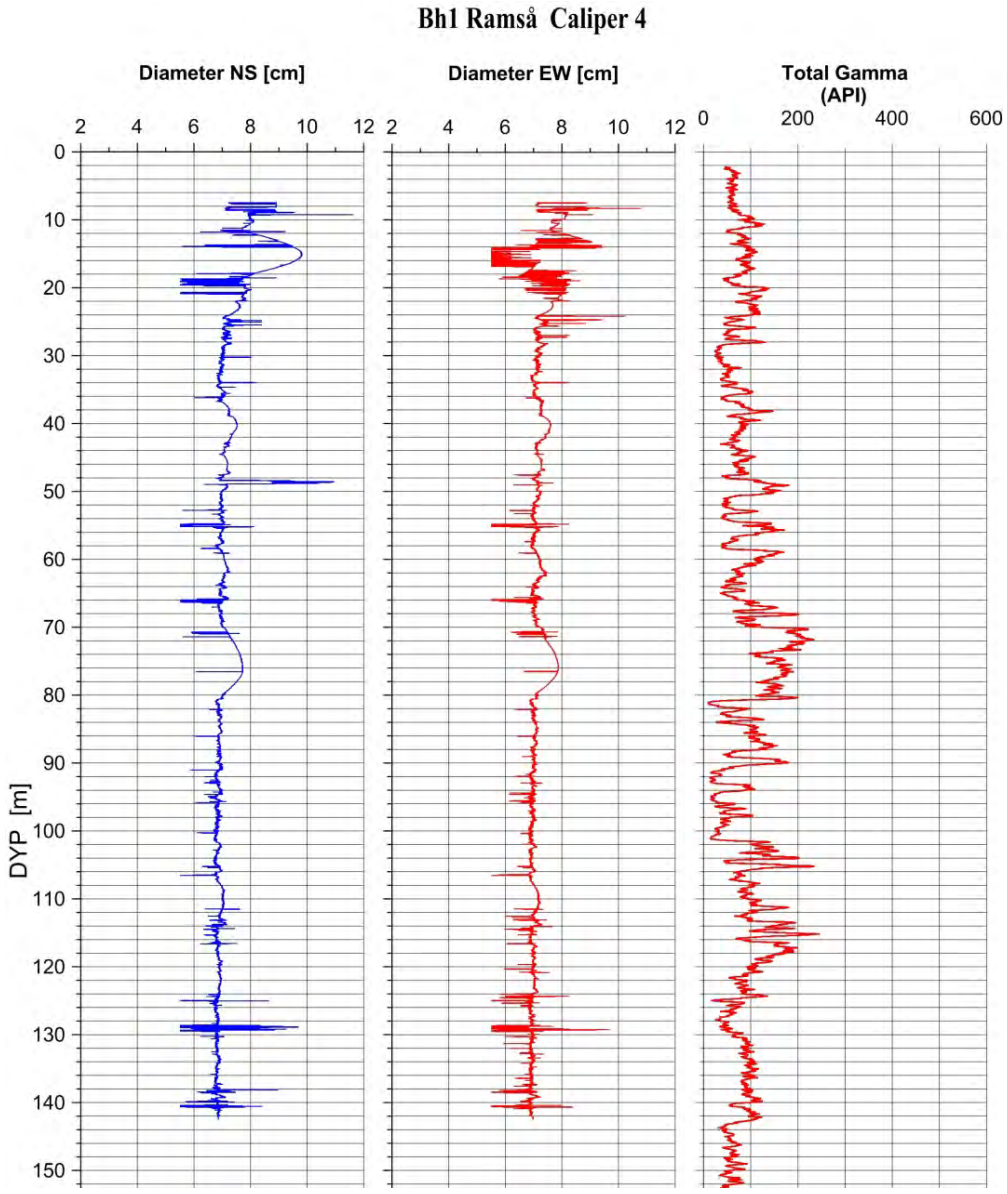

Figure 8.40. BH 1, calliper 4 log (diameter) and gamma log.

8.6.2 BH 2 ovalisation and calliper 4.

The ovalisation log for BH 2 is shown in Figure 8.41. No typical breakout pattern was observed on the acoustic image log. Big variations on the ovalisation log are caused by fracturing of the sediments; it is therefore it is difficult to observe stress directions.

The caliper4 log is shown in Figure 8.42 together with the total gamma log. The calculated diameter is about 7 cm, but this increases slightly below 160 m depth.

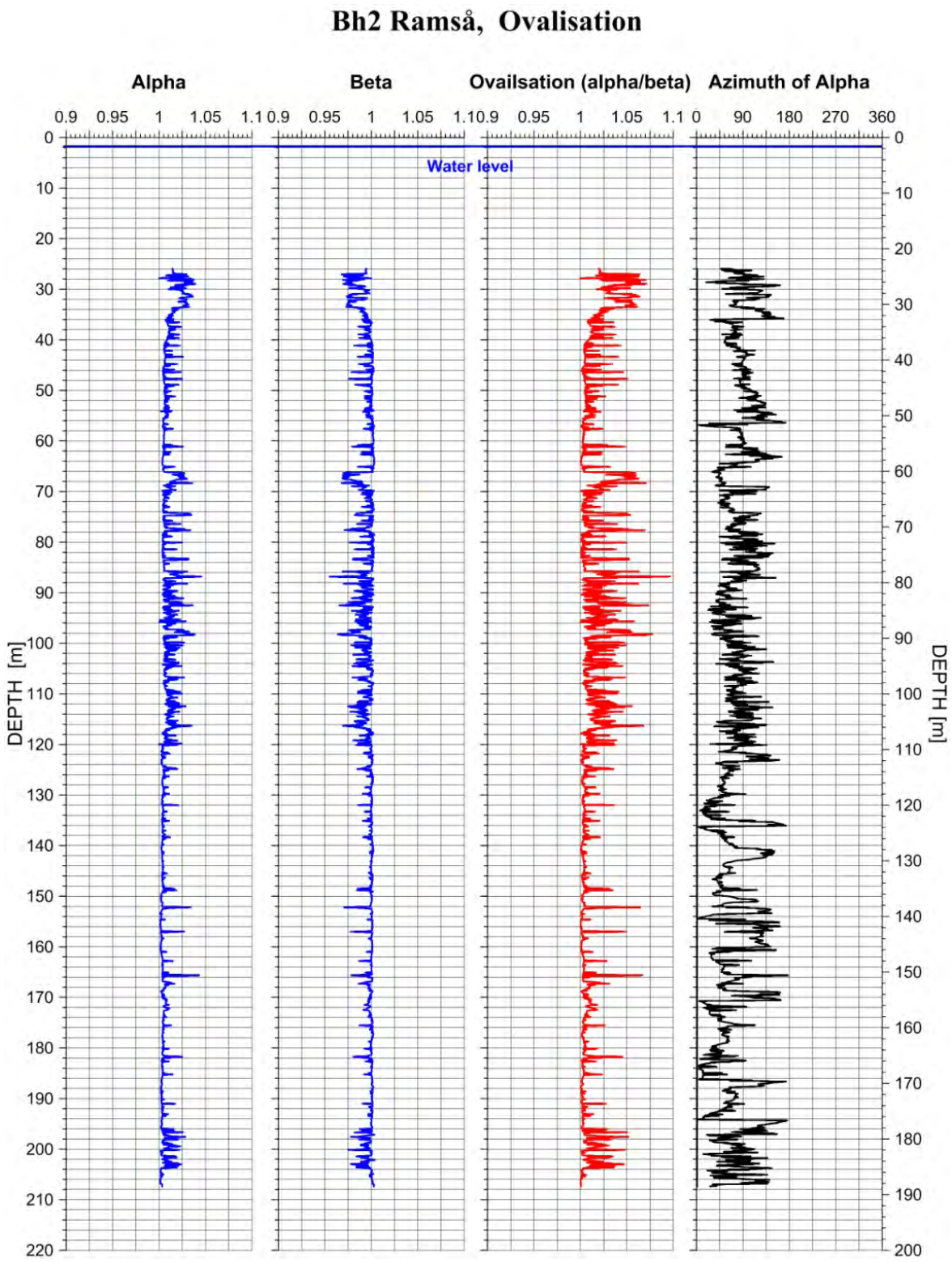

Figure 8.41. Ovalisation log BH 2.

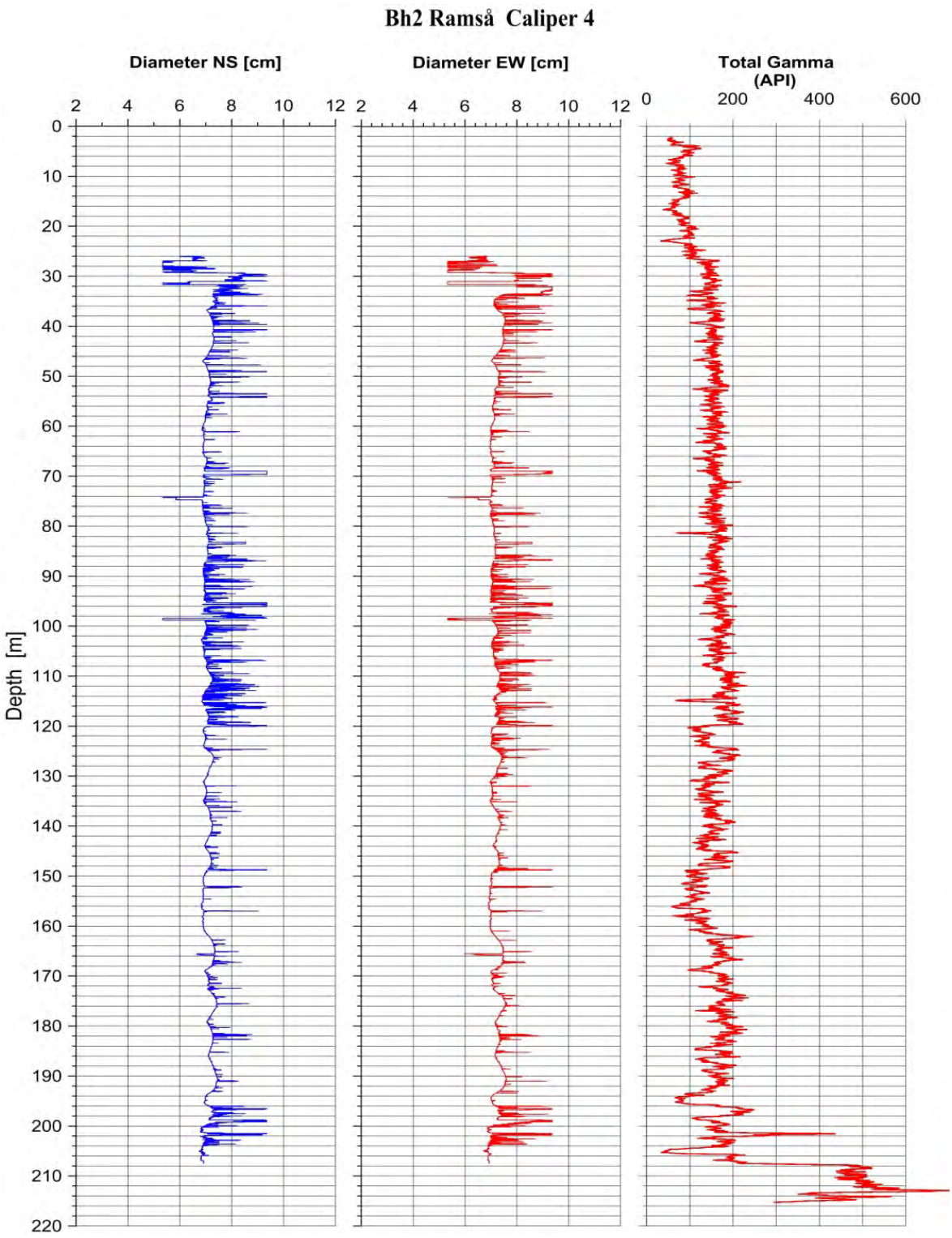

Figure 8.42. BH 2, calliper 4 log (diameter) and gamma log.

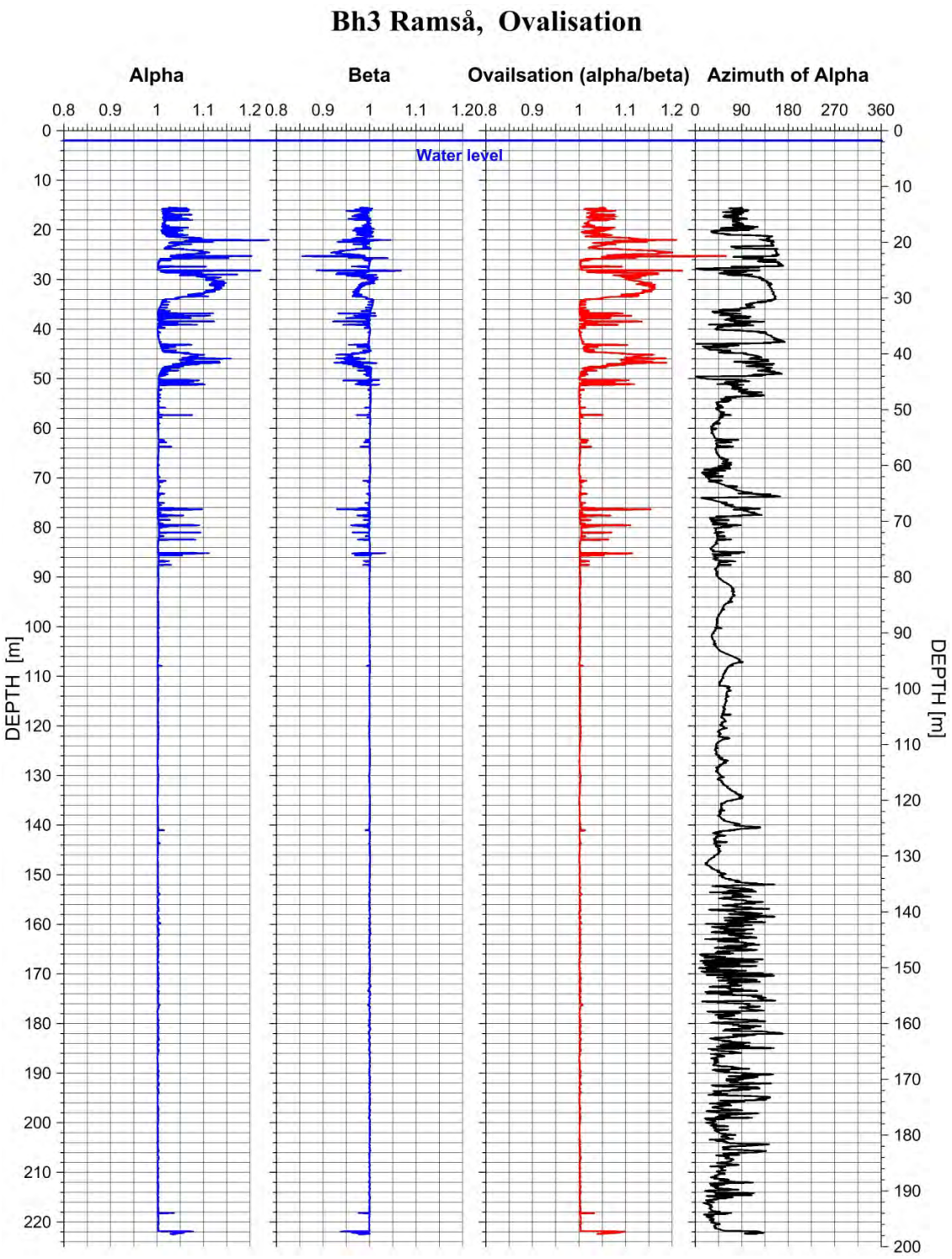

Figure 8.43. Ovalisation log BH 3.

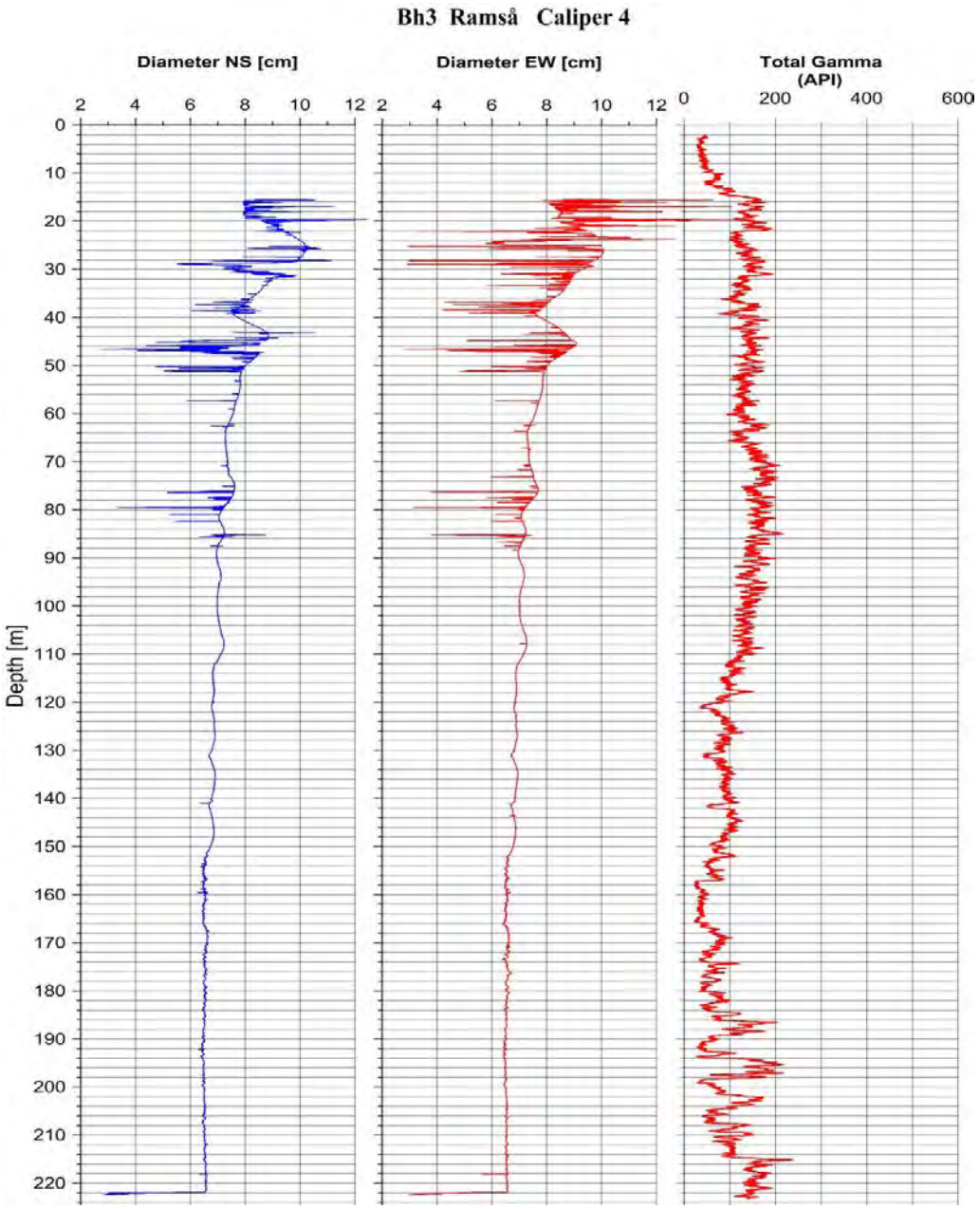

Figure 8.44. BH 3, calliper 4 log (diameter) and gamma log.

8.6.3 BH 3 ovalisation and calliper 4.

The acoustic televiewer image log indicated that the borehole was highly fractured down to c. 90 m depth. This is confirmed by the ovalisation log in Figure 8.44.

In the upper part of BH 3 the borehole diameter is fairly large and variable because of the heavily fractured sediments (see Figure 8.44). Below 90 m there are only few fractures and the diameter is not varying in the same way. However, the diameter decreases towards the bottom of the hole. This could be a result of the increasing temperature. The diameter is measured using a sound pulse travelling through water, and the sound speed increases with increasing temperature and increasing salt content.

8.7 **Summary**

The Ramså Basin is situated between Ramså and Skarstein on the north-eastern side of Andøya in northern Norway. This well-developed strandflat consists of Mesozoic rocks, Lower Cretaceous and Middle-Upper Jurassic, in a 6 km wide and 8.4 km long area known as the only Mesozoic basin onshore Norway. As a part of this NGU project four boreholes were drilled in the Ramså Basin on Andøya during summer 2015 and winter 2016, which were subsequently logged in the autumn 2015 and winter 2016 by NGU with economic support from the Norwegian Public Roads Administration.

The petrophysical logging and the systematic monitoring of fracturing and dip of fractures with an acustic televiewer system was carried out to gain a more detailed understanding of the the tectonic development of the basin and deeply weathered basement rock below the sedimentary strata. Near-surface deeply weathered rocks can be found on the beach and are also reported from old wells drilled (Friis 1903).

Weathering of rocks and particularly deep weathering is an important issue in preliminary investigations for tunnel construction. Geophysical parameters such as seismic velocity, resistivity, magnetic susceptibility and induced polarisation (IP) are often influenced by weathering processes. To gain a better understanding as to how these properties vary in weathered rock geophysical logging were performed in all four boreholes. In situ measurements in boreholes would make it possible to characterise the lithological formations and members. By doing acoustic logs (acoustic televiewer), the azimuth and dip angle in the sediments were mapped. Altogether, including core analysis from the drilling, this would make for a better understanding of the evolution of the Ramså Basin.

Drillcores from BH 1, BH 2 and BH 3 were all highly fractured except the lower half of BH 3. It is not possible, however, to conclude that the geophysical logs have indicated deep weathering in the basement. Only 10 m were logged in the basement in BH 2 and BH 3. The resistivity measurements were highly influenced by the salty pore-water and gave no information about deep weathering and fracturing. Because of the highly fractured rock the P-wave velocity was in general low, also in the basement rock, and it was impossible to differ between ‘ordinary’ fracturing and deep weathering. Normally the magnetic susceptibility will decrease if deep weathering is present. In BH 2 and BH 3 the susceptibility is lowest in the basement, but it is not possible to detect variations in the susceptibility which can indicate deep weathering. This depends on the degree of weathering and the thickness of the weathered zone. Induced Polarisation might indicate clay minerals (from deep weathering?). Several IP anomalies are observed in the sediments probably because of the presence of thin sulphide veins and they fit well with local low-resistivity values. No IP measurements in the basement rock can confirm deep weathering.

Total gamma radiation and gamma spectroscopy (U, Th and K) might be helpful to map the stratigraphy in the boreholes. The different formations and members often have their own signature regarding geophysical parameters such as P-velocity, resistivity, IP, MagSus and

gamma radiation including U, Th and K contents. Table 8.4,Table 8.6 andTable 8.8 show an overview of average values of the measured parameters in each member.

Table 8.9 shows average values of P-velocity, magnetic susceptibility and IP for each member in BH 1, BH 2 and BH 3. BH 1 and BH 3 cut through the same members in the Dragneset and Ramså Formations. The P-velocity is higher in all members in BH 3. One reason for this is that the Ramså Formation is much less fractured in BH 3 (in all members). The magnetic susceptibility is in the range of 10 times lower in BH 3. The IP % is also lower in BH 3. The higher IP% in BH 1 can be caused by the presence of sulphide minerals.

Table 8.9. Average values of P-velocity, magnetic susceptibility and IP in BH 1, BH 2 and BH 3.

Stratigraphic formation	**Stratigraphic member**	**BH 1 P-vel (m/s)**	**BH 2 P-vel (m/s)**	**BH 3 P-vel (m/s)**	**BH 1 Mag (SI 10^{-5})**	**BH 2 Mag (SI 10^{-5})**	**BH 3 Mag (SI 10^{-5})**	**BH 1 IP**	**BH 2 IP**	**BH 3 IP**
Skarstein	Nordelva		3060			911			1.1	
Nybrua			3380			777			0.1	
Dragneset	Ratjønna		3300			679			0.3	
Dragneset	Taumhølet			2700			49.9			0.6
Dragneset	Breisanden	2800		3025	224		24.4	1.8		0.5
Ramså	Bonteigen	2965		3210	224		29.3	2.1		0.8
Ramså	Kullgrøfta	2880		3335	269		2.5	3.0		0.6
Ramså	Hestberget	3290		3515	197		7.2	1.2		0.6
Basal Conglomerate/Basement		4000	3400	4350	231	685	4.3	4.3	0.2	0.5

In Table 8.10, the average content of U, Th and K for different members and BH 1, BH 2 and BH 3 are shown. Both U and Th are high in the Kullgrøfta Member, but the highest Th content is in the Skarstein and Nybrua formations in Cretaceous sediments. High Th-content (7 – 14 ppm) is also found in the basement in all boreholes.

Table 8.10. Average content of U, Th and K in BH 1, BH 2 and BH 3 in different members.

Stratigraphic formation	**Stratigraphic member**	**BH 1 U**	**BH 2**	**BH 3**	**BH 1**	**BH 2**	**BH 3**	**BH 1**	**BH 2**	**BH 3**
Skarstein	Nordelva/Helnesset		4.8			13.5			2.0	
Nybrua			3.9			14.7			2.2	
Dragneset	Ratjønna		6.0			8.4			2.3	
Dragneset	Taumhølet			4.7			7.3			2.5
Dragneset	Breisanden	2.4		2.8	4.7		4.6	1.8		2.3
Ramså	Bonteigen	2.4		1.9	4.8		4.2	1.2		1.2
Ramså	Kullgrøfta	6.8		4.1	10.0		8.7	1.1		1.5
Ramså	Hestberget	3.3		2.0	7.5		6.0	0.2		1.9
Basal Conglomerate/Basement		2.1	8.7	4.5	7.5	9.2	13.8	2.0	2.8	0.6

9. STRATIGRAPHY AND SEDIMENTOLOGY OF THE CORED SECTIONS

Alf Ryseth & Morten Smelror

9.1 Outline of work

Cores from three out of four new boreholes on Andøya (Figure 8.2) were logged macroscopically for lithology and sedimentary features (A. Ryseth) at NGUs facilities during 2016, and plotted at 1:200 scale. A limited number of samples were collected for biostratigraphy during the core description, and have subsequently been dated (M. Smelror).

The logged sections were finally plotted in a 1:500 scale format and interpreted for depositional environments as presented here. Furthermore, the described cores were calibrated to wireline log data, particularly to natural gamma ray data (NGAM). A good match between observed lithology and wireline data was accomplished for boreholes 1 and 2, whereas the calibration was more enigmatic for BH 3. Finally, lithostratigraphic formations were calibrated to results from previous works (Dalland 1979, Smelror et al. 2001). However, new age assignments from the biostratigraphy data will probably require some redefinition of the lithostratigraphy, as will be further addressed below.

BH 1 and 3 generally comprise strata of Jurassic age above basement, and will be discussed first. Sedimentary strata in BH 2 are entirely of Early Cretaceous age, and are consequently discussed separately.

9.2 Jurassic

9.2.1 Introduction

BH 1 (Figure 9.1) is located in close proximity to the beach section at Ramså (Figure 3.2 and 8.5), and is accordingly the most intuitive for direct correlation with the previous work of Dalland (1979). The cored section comprises a basal polymictic conglomerate of Jurassic age overlain by approximately 107 m of sandstone-dominated strata of Mid - Late Jurassic age. A significant Jurassic unconformity is identified at approximately 48 m in BH 1, separating strata of Bajocian age from overlying Late Jurassic (Kimmeridgian) units. This surface also marks a significant change in depositional regime, from essentially lacustine/paralic deposition (below) to open-marine conditions (above), and can be seen as a composite sequence boundary/transgressive surface. Comparison with Dalland (1979) indicates that the surface corresponds to a transgressive level within the Bonteigen Member of the Ramså Formation (Figure 9.1).

BH 3 (Figure 9.2) is located to the west of BH 1, and outside the previously mapped Mesozoic basin on Andøya. The cored sedimentary succession comprises 208 m of presumed Jurassic strata above a basement granodiorite. Based on correlation to Borehole 1, the Mid - Late Jurassic unconformity is located at 176.4 m (Figure 9.2) at a thin conglomerate

separating bioturbated sandstones of interpreted shallow-marine origin from underlying coal-bearing strata (see outline below).

The observation of a significant stratigraphic break within the Ramså Formation as defined in earlier works would probably require a redefinition of the lithostratigraphy. In the following, a division is made from the new biostratigraphywith reference to the established lithostratigraphy.

9.2.2 Basal conglomerate

The section below approximately 114 m in BH 1 (Figure 9.1) was originally described as metamorphic basement. However, observation of likely primary layering and also Jurassic palynomorphs in these strata indicated a sedimentary origin, and a closer examination of the core (Børre Davidsen, NGU) revealed a sandy, conglomeratic/brecciated interval down to 193.8 m, below which indisputable metamorphic basement could be defined. The actual basement lithology, however, comprises a metamorphosed amphibolite, most likely originating from a gabbro. This is in contrast to the other two boreholes where a granodiorite is seen at the base of the sedimentary succession. A thin zone (5 cm) at the sediment contact may indicate some weathering.

Lithologically, the approximately 80 m-thick conglomeratic succession comprises a variety of sandstones and alternating layers of polymict and monomict conglomerates, and sedimentary breccia. Observed clasts comprise common sandstone fragments, but also mafic and ultramafic lithologies. Thin-section microscopy shows abundant feldspars in the sandy background and clasts, with associated opaque minerals and possibly also quartz. Furthermore, unusual minerals including abundant talc and/or Mg-rich chlorite occur in the matrix. Sedimentary features other than layering are rare, but some possible clay-drapes (flaser lamination?) are observed at approximately 127 m.

The unusual composition (ultramafic rock fragments, talc) generally points to an ultramafic parent rock. A possible candidate is represented by mapped ultramafic basement at Steinavær to the east of Andfjorden, but the source could also be represented by an (unknown?) ophiolite complex. Otherwise, the immature texture and mineralogy point to short sediment transport from a local hinterland. It is further suggested that the whole package was deposited from gravitational flow, filling in an underlying palaeotopography.

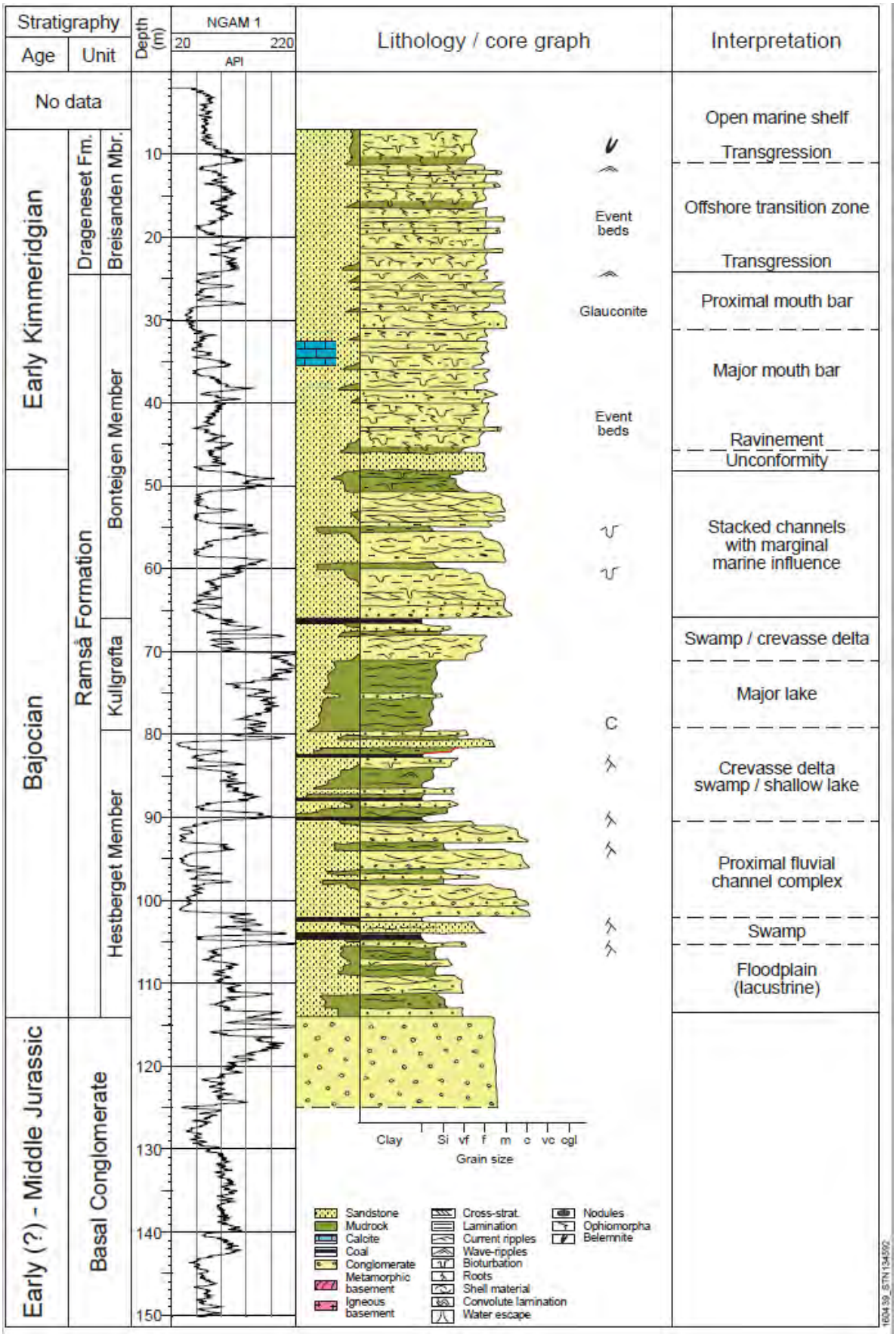

Figure 9.1. Stratigraphic interpretation of the core from BH 1.

9.2.3 Early – Middle Jurassic (lower – middle Ramså Formation)

The cored section from 66 to 114 m in BH 1 (Figure 9.1; Hestberget & Kullgrøfta members) comprises interbedded coals and carbonaceous beds, rooted horizons, laminated mudrocks and sandstones. Major sandstone bodies are sharply based and coarse grained with fining upwards grain size motifs. Furthermore, decimetre-scale cross-stratification is dominant in the lower parts of these units, grading upwards into current ripple lamination and eventually fine-grained facies. Thinner sandstones occur sporadically within associated mudrocks, and also at the top of coarsening upwards facies units. As shown in Figure 9.1, the main sandstone bodies are related to deposition in proximal fluvial channels, whereas the surrounding fine-grained sections record deposition in lakes, crevasse deltas and peat-forming swamps in the adjacent, lacustrine floodplain.

The remaining Middle Jurassic interval (BH 1; 48 - 66m, see Figure 9.1) consists of 3 main medium- to fine-grained sandstone bodies, each with sharp and apparently erosive bases below generally fining-upward facies sequences, separated by thinner fine-grained intervals. Otherwise, the sandstones show common dm-scale cross-stratification and ripple lamination. Also, burrowing traces including *Skolithos* and possible *Ophiomorpha* are recorded from the upper parts of the sandstones and the interbedded finer grained units. Akin to the underlying succession, the main sandstones are related to channellised deposition, although with the observed trace fossils indicating a more marginal marine (paralic) setting than below.

The inferred Middle Jurassic interval in BH 3 (176.4 – 212 m; Figure 9.2) is significantly thinner (35.4m) than in BH 1 where equivalent strata above the basal conglomerate reach up to 48 m. Otherwise, the strata show similar facies characteristics, with two sharply based, cross-bedded and fining upwards sandstone bodies being related to deposition within inferred fluvial channels. Also, interbedded thin coal beds, carbonaceous layers and mudrocks are associated with deposition in shallow lakes and nearby swamps (coal) in the surrounding lacustrine floodplain, and with thinner sandstone units representing crevasses and crevasse deltas spilled from adjacent channels. As in Borehole 1, weak burrowing by *Skolithos* can be observed towards the unconformity, thus possibly indicating more paralic conditions through time.

9.2.4 Late Jurassic (upper Ramså Formation, lower Dragneset Formation)

Above the Mid to Late Jurassic unconformity a major coarsening-upward unit is readily correlated between both boreholes (Figure 9.1, 24 - 48m; Figure 9.2, 148.6 – 176.4m). In both sections, the lower part of the unit comprises moderately bioturbated, fine-grained sandstones punctuated by thin (5 - 20 cm) sharply bounded beds of medium-grained sandstone (event beds). The burrowing assemblage is relatively diverse, including *Schaubsylindichnus*, *Paleophycus*, *Diplocraterion, Ophiomorpha* and *Skolithos*.

In contrast, the upper part (24 - 31m Figure 9.1; 148.6 -164.4m; Figure 9.2) is distinctly coarser grained, also preserving some cross-stratified layers separated by bioturbated units with common *Ophiomorpha* traces. These sandstones also show a pronounced greenish colour, pointing to the possible presence of glauconite (as has also been described from the top of the Ramså Formation by Dalland 1979).

Whereas the observed burrowing assemblage and the possible presence of glauconite indicate open-marine conditions, the relatively coarse-grained nature of the upper parts points to a relatively proximal setting. Accordingly, the facies unit is related to deposition in a marine mouth-bar setting, with the discrete coarse-grained beds recording possible storm/flood events.

In both boreholes, the interpreted mouth bar unit is abruptly replaced vertically (e.g. at 148.6 m; Figure 9.2) by very fine-grained, micaceous and intensively bioturbated sandstones, also with some few thin layers of dark-grey claystone. Calcareous fossils, mainly belemnite tails and more rarely bivalves (Buchia?), are scattered through the section, as are siderite and pyrite nodules.

The burrowing assemblage is diverse, including *Schaubsylindrichnus*, *Paleophycus* and *Chondrites*. Together with the body fossils, the burrowing testifies to an open-marine setting, hence the succession as a whole can be related to deposition in the offshore transition zone and inner shelf environments of a shoreline system.

On the basis of vertical facies/lithology variations the marine strata can be subdivided into a stack of sharply topped coarsening-upward units. Each abrupt transition into fine-grained strata is related to possible flooding events (transgressions), of which the most significant ones are recorded at 105 m and 74 m (Figure 9.2). At these levels, dark-grey shales are preserved, probably reflecting a degree of anoxia immediately following the deepening event. The transgression at 74 m (Figure 9.2) is associated with persistently high gamma ray readings and may constitute a maximum flooding surface (MFS). Above this level, strata are systematically becoming coarser grained, probably reflecting significant shoreline regression.

With reference to the existing lithostratigraphy, it is inferred that the coarsening-upward mouth-bar unit above the unconformity corresponds to the upper half of the Bonteigen Member (Dalland 1979). This accords with the description of coarse-grained, glauconitic sandstones at this level along the beach section at Ramså (Figure 13 in Dalland, 1979). The overlying and deeper marine succession as seen mainly in BH 3 (Figure 9.2) in all likelihood correlates with the lower part of the Dragneset Formation and its two basal members. Specifically, the major marine transgression at 105 m in BH 3 would fit with the top of the Breisanden Member, whereas the still more fine-grained interval would correspond to the Taumhølet Member.

9.3 **Cretaceous**

9.3.1 Introduction

BH 2 (Figure 9.3) is located north of boreholes 1 and 3. Here, approximately 178 m of Early Cretaceous strata were cored above granodioritic basement. Based on lithology and facies a tripartite subdivision of the cored section is proposed, with correlation to the existing lithostratigraphy. The occurrence of reddish and calcareous strata at approximately 120 m (Figure 9.2) is also instrumental in defining the lithostratigraphy of the cored section, as this section could correspond to the Nybrua Formation as defined by Dalland (1979). Smelror et al (2001) correlated this section from Andøya to a condensed offshore section (Klippfisk Formation) of inferred Hauterivian – Valanginian age. Underlying and overlying strata in BH 2 are accordingly correlated with the Dragneset and Skarstein formations, respectively.

9.3.2 Dragneset Formation/Ratjønna Member

The lower section (125 – 200.4 m) is correlated to the Ratjønna Member of the Dragneset Formation. It is dominated by grey to dark-grey siltstone with sandy laminae and more sporadic, thin layers of dark-grey claystone. Soft-sediment deformation features, including convolute laminations and overturned/folded lamina, are common, with a notable 2 m-thick deformed interval immediately below the overlying stratigraphic unit. These fine-grained strata are also bioturbated by *Chondrites* and *Planolites*, and contain scattered macrofossils including belemnite tails and infrequent bivalve shells.

Significant fine-grained sandstones also occur within this interval, typically comprising discrete layers ranging in thickness from a few centimetres to maximum values of approximately 1 metre. Thicker units of stacked sandstone beds also occur, building up to a maximum thickness of 13 metres (149 – 162 m; Figure 9.3). Individual sandstone beds are generally sharply based and fining upwards, commonly with eroded mudclasts (rip-up clasts) concentrated at the base. Otherwise, the sandstones appear to be massive and/or weakly laminated, though with occasional water-escape structures in a few beds. Bed contacts are generally bioturbated to some degree.

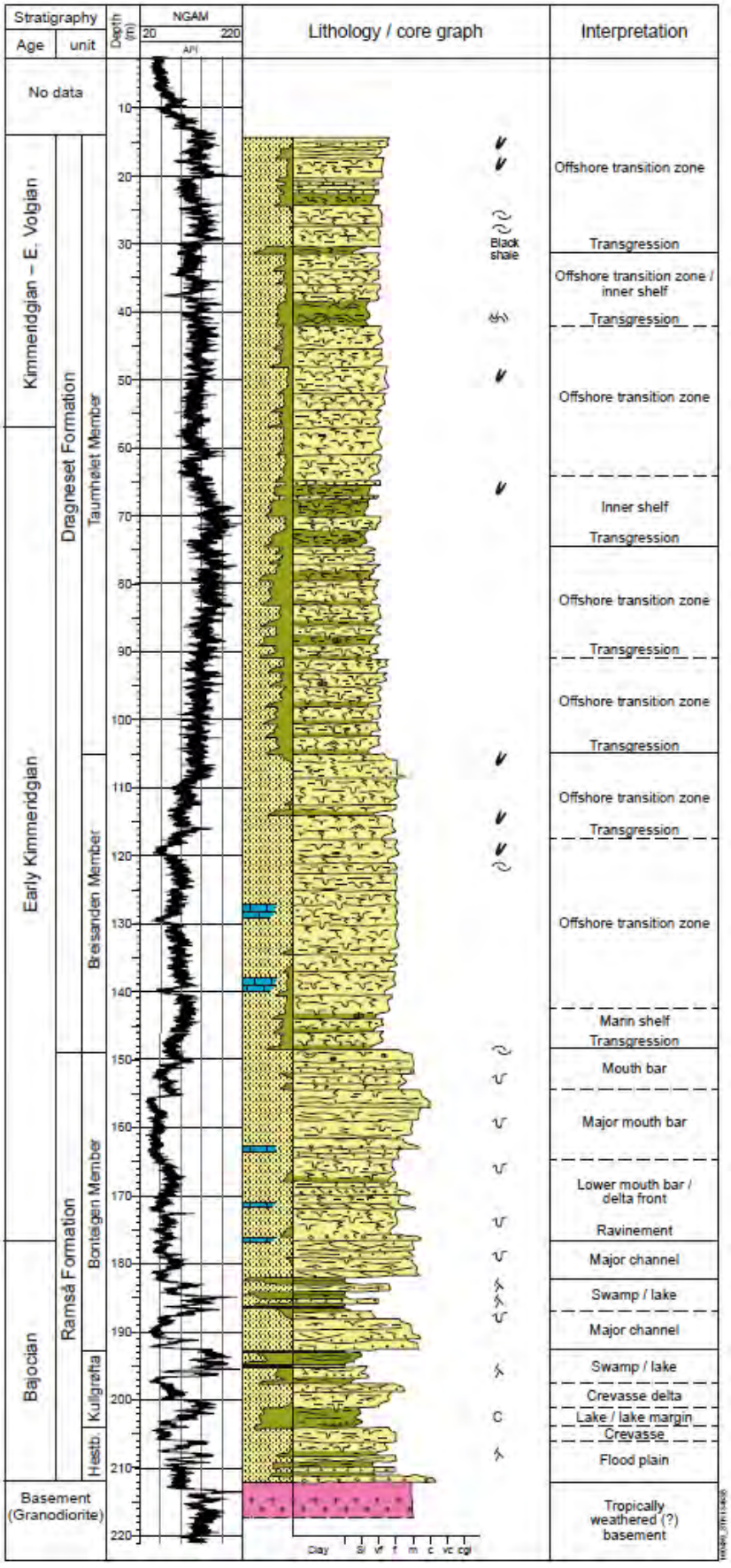

Figure 9.2. Stratigraphic interpretation of the core from BH 3.

A marine origin for the succession, including strata resting directly on crystalline basement, is evident from the fossil material and burrowing styles. Furthermore, the nature of the sandstone beds and stacked units, such as sharp boundaries, rip-up clasts, the massive character and water-escape structures, is generally indicative for deposition from turbid flows, hence a relatively deep-marine setting is inferred. In this context the thicker accumulations are identified as small submarine fan lobes, whereas the thinner, discrete beds are seen as more isolated turbidite beds.

The larger deformed units seem to reflect compression of soft sediment, and slumping is therefore inferred. Accordingly, it is suggested that the deposits accumulated in a lower submarine slope setting.

9.3.3 Nybrua Formation

The section from 114 m to 124.5 m is distinctly different from the underlying strata, particularly by showing strong red colouring as has previously been described from the Nybrua Formation (Dalland, 1979).

At the base, the section comprises a calcite-cemented sandstone layer with abundant shell material. In turn, this sandstone passes upwards into red/brown sandstones with abundant, angular fragments of granodiorite, showing long axes up to 10 cm. Otherwise, these basement clasts seem to 'float' within the sandy matrix, apparently without any preferred orientation. Above 120 m, grey, clay-rich siltstone and fine-grained sandstone dominate, but also thin soapy layers of possible volcanic origin (bentonite?). Finally, the unit is capped by another distinctly red sandstone with floating granodiorite clasts, before passing upwards into dark-grey, laminated and pyritic mudrock of the overlying unit.

Intensive cementation and concentration of macrofossils in the basal interval may indicate a marine hard ground, and accordingly, a stratigraphic break at the base of the section. However, as the strata are of probable marine origin, the surface also marks a transgression and accordingly forms a composite unconformity/transgressive surface.

Other characteristic features, such as the abundant calcite cement and red colouration are related to slow deposition in a partly oxidising environment. Hence, a degree of condensation is inferred (marine condensed section; Figure 9.3). The sandstone layers with clasts of basement rocksare enigmatic, but would generally require some depositional relief for their formation. It is therefore suggested that part of the basin margin was relatively steep, and possibly represented by a fault-related escarpment or basement block, thus forming a local source for the granodiorite clasts. The conglomerate beds may represent debris flows shed off the adjacent basement high(s).

9.3.4 Skarstein Formation

The uppermost part of BH 2 (22 – 114 m; Figure 9.3) is informally assigned to the Skarstein Formation (Dalland, 1979). At the base, the lower contact with the underlying unit is represented by a relatively abrupt transition into approximately 8 m of dark-grey/black, laminated and pyritic claystone. Above this fine-grained unit, the remaining succession is invariably heterolithic, but dominated by a grey – dark grey 'background' lithology of laminated to moderately bioturbated siltstone, occasionally with soft-sediment features including overturned and contorted laminae.

Thin (5 – 100 cm) layers very fine- to fine-grained sandstone are systematically intercalated with the background lithology. These are typically showing sharp lower and upper boundaries with a generally fining-upward grain-size distribution, commonly with small mud-clasts draping sandstone bases. Some beds containing angular basement clasts (granodiorite) occur in the lower part of the section (below 90 m in Figure 9.3). Some thicker and coarser sandstone beds are also recorded from the topmost part of the core.

Less abundant lithologies include scattered layers of black and commonly soft/sticky claystone, rarely reaching more than 5 – 10 cm in thickness. Notably, the section from 39 to 45 m seemingly contains more abundant blackish mudrocks, also with common pyrite nodules. Finally, some discrete, cm-thick layers with a 'soapy' texture, possibly representing volcanic bentonite beds occur throughout, as in the underlying Nybrua Formation. The volcanic origin of these beds needs verification by chemical analyses. However, the observation accords to some degree with previous studies, particularly Dalland & Thusu (1977), who documented some thin ash layers from the Late Jurassic succession on Andøya.

As shown in Figure 9.3, the Skarstein Formation is related to deposition predominantly in a lower submarine slope setting, as represented by the background siltstones. The sandy beds are related to turbid flows, with the conglomeratic beds possibly representing coarse, gravelly debris flows.

However, anoxic basin-floor conditions are inferred for the lowermost black and pyritic mudrock immediately above the condensed strata in the Nybrua Formation. Accordingly, the basal contact (at 144 m in Figure 9.3) may represent another significant marine transgression/deepening. Basin-floor anoxia is also inferred for the uppermost pyrite-bearing section (39 – 45 m; Figure 9.3), and minor 'anoxic' events are probably also represented by the thinner, blackish, claystone beds contained within the lower slope facies.

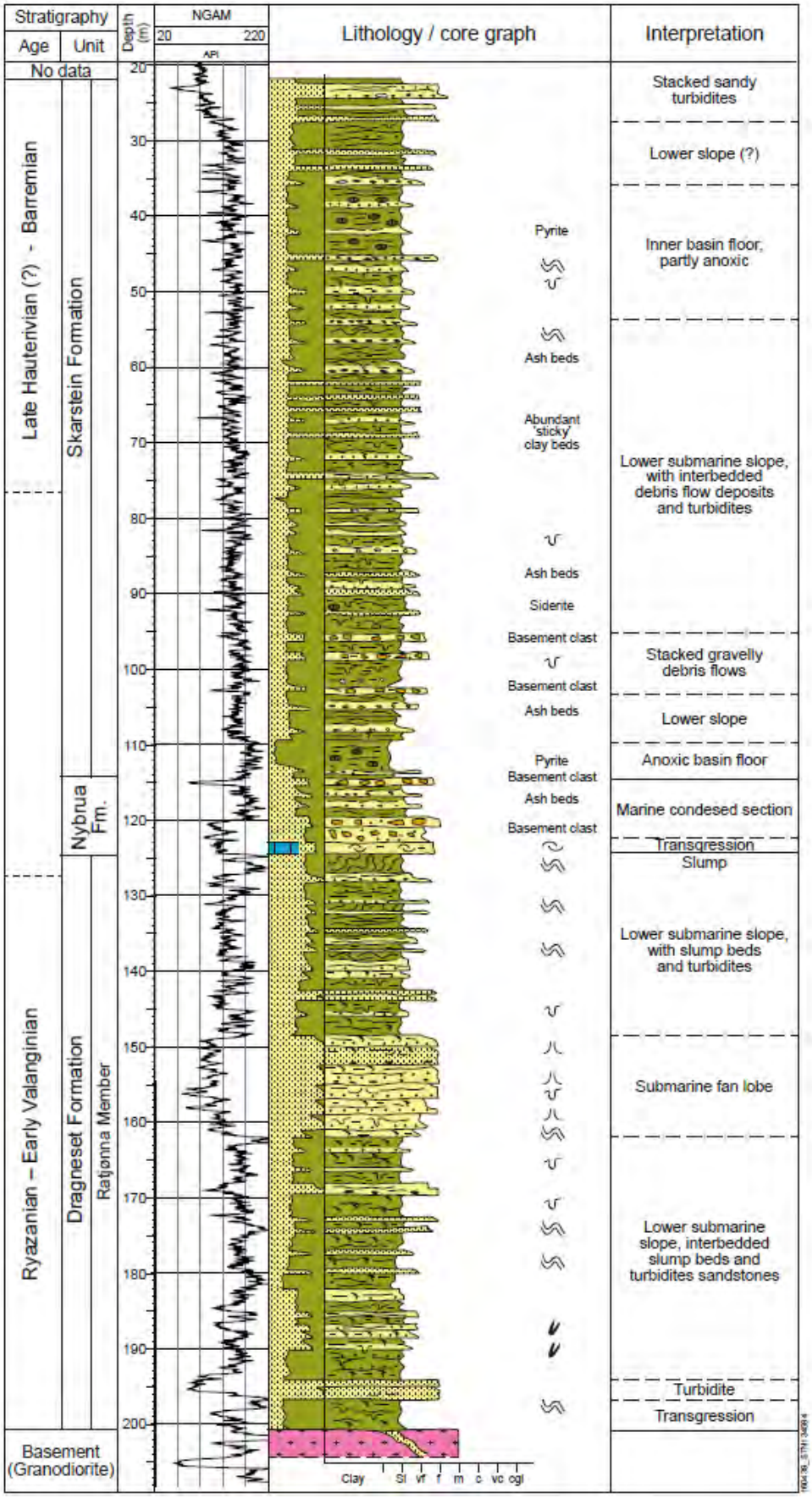

Figure 9.3. Stratigraphic interpretation of the core from BH 2.

10. COMPOSITION OF THE MESOZOIC SEDIMENTS OF THE RAMSÅ BASIN, INCLUDING BASEMENT SAPROLITES

Håkon Rueslåtten, Alenka Črne, Marco Brönner, Annina Margreth, & Jasmin Schönenberger

10.1 Introduction

Sites with deep paleo-weathering of basement rocks are found in several places across Scandinavia (Lidmar-Bergström et al. 1999). In Norway, one of the most well-known locations is Andøya; the northernmost island of Vesterålen (Figure 1.2). Andøya is the only location in Norway with onshore Mesozoic rocks (Jurassic to Cretaceous) deposited onto the Precambrian crystalline basement (Dalland 1974, Sturt et al. 1979, Brönner et al. 2014). According to Dalland (1974) and Sturt et al. (1979), the granodioritic basement is characterised by deep weathering constrained to pre Jurassic time. The overlying Jurassic and Cretaceous sedimentary rocks are also characterised by chemical alteration, with dissolution of feldspars and biotite followed by formation of clay minerals, mainly kaolinite.

The main phase of alteration of Mesozoic siliciclastic sedimentary rocks offshore Norway, from Møre to Troms, has been constrained to be of Upper Triassic to Lower Jurassic age (Fredin et al., 2017). The alteration includes both meteoric weathering; i.e. soil formation, and later diagenetic processes following increased burial. These rocks are characterised by high contents of diagenetically formed kaolinite, and the precursors for the clay mineral formation are mainly feldspars. The clay mineralogy indicates humid continental climate and paralic environments during this period (Mørk et al. 2003, Hammer et al. 2012).

Earlier K-Ar age determinations based on clays from the saprolite horizon of the Precambrian basement rocks at Ramså, Andøya, however, indicated a much older, Early Carboniferous age (Sturt et al. 1979). This led these authors to suggest a Late Palaeozoic weathering phase for the basement saprolite, followed by deep burial of the basement under a 4-5 km-thick sedimentary cover. At present, the maximum thickness of the Mesozoic sediments is in the order of 1-1.5 kilometre (Chapter 2.2).

One of the goals of this project has been to reconstruct the evolution of the Ramså Basin with respect to the basement weathering and the subsequent deposition and diagenesis of the Jurrasic and Cretaceous sedimentary sequence filling up the basin. The present study includes the issue as to whether the chemical alteration of the sedimentary rocks is due to meteoric weathering, and/or diagenetic processes resulting from increased burial and increased temperatures.

In order to reach this goal, we have characterised the petrography, geochemistry and mineralogy of the weathering profiles cropping out on the eastern shore of Andøya. These data are compared with corresponding data from boreholes onshore Andøya, including the

four Norminol wells and the four NGU wells shown in Figure 3.4 Figure 8.5. Data from these wells allow a comparison with the basement contacts at Ramså, and also with the sedimentary strata overlying the Ramså Formation.

Earlier works, including vitrinite reflectance measurements of the sedimentary succession in the Ramså area, are discussed. The correlations between the boreholes and the Ramså profile enable us to discuss the development of the Ramså Basin.

Figure 10.1. Air photography of the Ramså area in the southern part of Andøya (left). Here, ditches were excavated in order to study features related to basement weathering and the overlying Mesozoic sediments. The southern ditch was 26.7 m long, and the northern one 15.6 m. The numbers are referring to the sampling sites. The contact between the weathered basement and Jurassic sediments was interpreted to be between samples 4 and 5.

10.2 Geological setting

The Ramså Basin is located at the western boundary of the Anfjorden Basin (Figure 3.1). The granodioritic basement in the Ramså area was subjected to paleo-weathering processes prior to being overlain by Mesozoic siliciclastic rocks. Dalland (1974) estimated the thickness of the weathering horizon (saprolite) of the basement to be up to 30 m. This estimate was based on observations made in ditches dug out along the shoreline at Ramså, where the dip of the foliation in the basement was estimated to be approximately 20 degrees towards north.

The stratigraphy of the Mesozoic rocks is illustrated in Figure 3.3 and described in detail in Chapter 3.3 with an updated view in Chapter 9.

10.3 Sampling strategy

All of the samples were taken onshore, either from outcrops at the Ramså shoreline or from onshore drill-cores.

Outcrop samples of the saprolite profile were taken in the trenches close to the village of Ramså (Figure 10.1). At each sampling site, the sampling started at the deepest unweathered basement, up throughout the saprolite horizon, and up to the Lower Jurassic siliciclastic rocks (Figure 10.1 and Table 10.1).

Table 10.1 List of samples from the surface profile at Ramså, with sample numbers, positions, and interpreted lithology. See Fig. 2.2 for positions. The geographical position is 0.5 km north of NGU Well BH 1, with coordinates E543036 and N7674280. The samples are ordered according to estimated stratigraphic depths. "Distance' refers to the distance from the previous sampling site (going in a northwards direction).

Sample #	Lab ID	Distance*	Depth**	File name	Lithology
MB 11-3					unweathered granodiorite
MB12-11	98561		0.00	1324011	mildly weathered granodiorite
MB12-12	98562	15	4.04	1324012	mildly weathered granodiorite
MB12-13	98563	11	7.01	1324013	quartz- and clay-rich rocks
MB12-14	98564	12	10.24	1324014	quartz- and clay-rich rocks
	98565			1324015	
MB12-8	98558	5	12.16	1324008	coarse-grained quartz- and clay-rich rock
MB12-1	98551	19	20.02	1324001	coarse-grained quartz- and clay-rich rock
MB12-7	98557	1	20.3	1324007	coarse-grained quartz- and clay-rich rock
MB12-2	98552	0	20.36	1324002	coarse-grained quartz- and clay-rich rock
MB12-3	98553	6	22.42	1324003	coarse-grained quartz- and clay-rich rock
MB12-4	98554	2	23.10	1324004	coarse-grained quartz- and clay-rich rock
MB12-5	98555	2.5	23.96	1324005	quartz sandstone

MB12-6	98556	2.5	24.81	1324006	quartz sandstone
MB12-9	98559	2	25.50	1324009	quartz sandstone
MB12-10	98560	1	25.84	1324010	siltstone
*Distance (m) from the previous sample in the northerly direction of sampling **Stratigraphic depth (m), calculated by assuming a basement dip of 20° towards North					

Sampling of the Norminol boreholes: Four boreholes, numbered from south to north: B, C, A and D (Figure 3.4), were drilled in the northern part of Andøya by the petroleum company Norminol in the early 1970s. In the present study, we have carried out a lithological logging of the deepest part of well B, in the scale 1:100. Eleven samples from wells A, B and C are also taken, and the results of the analysis are included in the present report.

Sampling of NGU boreholes: all four boreholes (Figure 8.5) were investigated by electrical logging, and two of the four boreholes were sampled for this study, namely BH 1 and BH 2. The geographical coordinates for BH 1 are E543036 and N7674280, and for BH 2 E542206 and N7676280. Sampling depths are given in Table 10.2.

Table 10.2 List of samples from two of the four wells drilled by NGU, giving well numbers, sample numbers, sampling depths, and interpreted lithology.

Depths (m)	Borehole No.	Sample No.	Groups:	Lithology and comments
113,4	BH 1	98596	Group 1	Jurassic sediment: «the kaolinite zone»
113,9	BH 1	84002		
115,7	BH 1	98597	Group 2	Transition zone
121,8	BH 1	98598		
132,4	BH 1	98599	Group 3	Altered gabbroic rock: "the plagioclase-biotite-talc-chlorite zone'
134,7	BH 1	98600		
158,2	BH 1	98592		
167,0	BH 1	84001		
185,7	BH 1	98593		
188,5	BH 1	98594		
195,1	BH 1	98595		
200,6	BH 2	98587	Group 4	Non-weathered Precambrian granodioritic gneiss; basement: "Quartz + Feldspar + Mica zone'
201,3	BH 2	98588		
205,3	BH 2	98589		
207,5	BH 2	98590		
212,2	BH 2	98591		

10.4 **Analytical methods**

Several analytical methods were used to characterise the samples:

10.4.1 Light microscope, SEM-BSE and SEM-EDS

Selected polished thin sections were investigated on a light microscope and SEM; both to image interesting textural and diagenetic features and to investigate the chemistry of minerals (SEM-EDS) in order to identify mineral phases correctly.

10.4.2 XRD and XRF analysis

15 surface samples and 8 core samples were analysed for major and trace elements by XRF and for mineralogy by XRD. Major and trace elements were analysed at NGU by X-ray fluorescence spectrometry using a PANalytical Axios at 4 kW.

X-ray diffraction (XRD) analysis was conducted for all of the samples. The samples were prepared according to NGU's standard procedures, and the final milling prior to XRD scanning included micronising in ethanol. The interpretation of the XRD spectra included both identification and semi-quantitative estimates of mineralogy. This was carried out manually due to difficulties of interpreting spectra of clay minerals on computer-based systems.

The quantification of minerals done here is based on measurements of the peak area of selected mineral reflections, multiplied by 'weighed factors' established by running standardised mineral mixtures. The percentages are calculated from the sum of the weighted reflections. A summary of the procedures is given below.

10.5 **Ramså surface profile: lithology, mineralogy, petrography, and chemistry**

10.5.1 Mineralogy from XRD

Sixteen surface samples were collected in the Ramså location, and fifteen of these were along a transect representing an estimated 25 m of stratigraphic depth (Figure 10.1;Table 10.1). This stratigraphic depth is based on the 20 degrees dip of the basement towards east and north, and the excavation strategy. The samples have been grouped into six lithologies from bottom to top, based on their macroscopic and microscopic textures:

1. Granodioritic basement
2. Weathered basement (saprolite)
3. Weathered rock
4. Coarse-grained quartz- and clay-rich rock
5. Quartzitic sediment
6. Mudstone

An additional formation termed the Holen Formation, is supposed to rest upon the the weathered basement. This formation is described as a calcite cemented deposit. No sample of this rock was available and a XRD analysis for this unit is consequently missing.

The interpretation of the X-ray diffractograms of the bulk samples is given in Table 5.1. The table includes stratigraphic depths (calculated), lithologies and mineral compositions of the surface samples from the Ramså sampling sites. Also included are also the ratios between the 10Å/5Å reflections for mica. This ratio is ~2 for muscovite (and dioctahedral illite), and around 10 for biotite (and trioctahedral illite); i.e. the ratio gives extra information about the types of mica and illite present. Also the ratio 7Å/4.45Å for kaolinite is included in Table 10.3. This ratio is a "crystallinity index' for kaolinite, by which the ratio increases with increasing b-axis disorder for the kaolinite.

Petrographically, the surface samples were differentiated into six groups or lithologies. These groups are also recognised on the XRD analysis by their mineral compositions, and are included in Table 10.3. The mineralogy of each of these six groups is commented on below.

Table 10.3. Surface samples from the Ramså surface profile. Mineral composition based on semi-quantitative interpretation in weight-% from XRD data. Estimated 'Stratigraphic depth' (m) and short descriptions of lithologies are included.

Abbreviations: Qtz=quartz; Pla=plagioclase; Kfs=K-feldspar; Am=amphibole; Pyr=pyrite; Kao=kaolinite; Ch=chlorite; V=vermiculite; S=smectite; C=calcite; An=anatase; 10Å/5Å=ratio between the 10Å and 5Å XRD reflections of mica and illite; 7Å/4.45Å=ratio between these two kaolinite reflections (crystallinity index).

Sample #		Strat. Depth	Lithology	Qtz	Pla	Kfs	Mic	Kao	Pyr	S+V +Am	Ch+C +An	10Å/ 5Å	7Å/4 ,45
010	MB12-10	25,8	Mudstone	17	32	9	9	-	3	8S/V 5Am	16Ch	10	-
009	MB12-9	25,5	Quartzitic sediment	85	-	-	2	11	2	-	-	-	3,7
006	MB12-6	24,8		57	-	3	2	35	2	-	-	3,0	3,5
005	MB12-5	24,0		79	-	2	2	12	5	-	-	-	4,5
004	MB12-4	23,1	Coarse-grained quartz- and clay-rich rocks	30	6	-	7	52	5	-	-	2	5,9
003	MB12-3	22,4		31	4	-	7	53	4	-	1C	2	6,2
002	MB12-2	20,4		32	3	-	2	57	3	3S	-	2	5,9
007	MB12-7	20,3		40	-	3	8	46	2	-	1C	1,8	5,7
001	MB12-1	20,0		27	2	-	4	65	2	-	-	1	4,9
008	MB12-8	12,2		37	12	5	3	41	1	-	1C	1	8,3
014	MB12-14	10,2		59	-	-	-	41	tr	-	-	-	6,1
013	MB12-13	7,0	Weathered rock	44	-	-	-	55	-	-	2An	6	6,6
012	MB12-12	4,0	Weathered basement	36	-	36	8	20	-	-	-	3	7
011	MB12-11	0		41	-	31	9	19	-	-	-	4	6
017	MB11-3	0	Basement	27	37	26	9	1	-	-	-	10	-

Granodioritic basement: Sample MB-11-3 shows the composition of the granodioritic basement rock, with quartz, two feldspar, and mica. The mica is mainly a biotite type, seen by the high 10Å/5Å ratio from XRD (Table 10.3). A small content of kaolinite is identified (1 wt %), indicating an initial weathering.

Weathered basement (Saprolite): Samples MB-12-11 and MB-12-12 represent the saprolite developed in the granodioritic basement. The main minerals are quartz, K-feldspar and kaolinite. Mica is still a significant component, but the 10Å/5Å ratio of the XRD reflections

for mica is reduced from 10 to 3-4, indicating dissolution of biotite, while muscovite and sericite is showing a relative increase. All of the plagioclase feldspar is dissolved, and it is suggested that kaolinite is crystallised from the residue of feldspar and biotite.

Holen Formation: Dalland (1974) reported the presence of a thin, calcite cemented formation, referred to as the Holen Formation. This formation is supposed to be sandwiched between the weathered basement and the sediments of the lower Ramså Formation. This formation was not observed during this study and consequently no XRD data exist.

Weathered rock: Sample MB-12-13 is *supposed* to represent the Lower Jurassic sediments deposited upon the carbonaceous Holen Formation, or alternatively, onto the weathered granodioritic basement. These rocks are the lower part of the Ramså Formation, and consist of relatively coarse-grained quartz where the intergranular porses are filled with kaolinite. Some anatase is also identified, which may be a residue of e.g. dissolved biotite. No feldspar is detected, interpreted to be the result of pervasive chemical weathering.

Coarse-grained quartz- and clay-rich rock: This group is represented by 5 samples; MB-12-7,-8, -14, and MB-12-1, -2, -3, and -4. The mineralogy is dominantly quartz and kaolinite, but some mica (mainly muscovite), plagioclase and pyrite are also present.

Quartzitic sediment: The quartzitic rock is represented by samples MB12-5, -6, and -9. These samples show very high quartz contents, but also contain some kaolinite and mica. Pyrite is also found.

Mudstone: The mudstone group is represented by sample MB-12-10, and displays a very diverse mineralogy: quartz, two feldspars, amphibole, pyrite, mica (biotite type with very high 10Å/5Å ratio on XRD) and chlorite; i.e. a rather iron- and magnesium-rich environment. The quartz content may be due to quartz-filled fractures. This sample has no kaolinite and shows no signs of severe weathering, although it contains some smectite and/or vermiculite. However, these minerals may be allochthonous.

10.5.2 Petrographic description

Granodioritic basement: Samples of granodioritic basement from the lower level of the saprolite that contain negligible amounts of clay minerals are referred to as ‘unweathered granodioritic basement’. The samples from the weathered zone above, containing significant amounts of clay minerals are referred to as ‘weathered granodiorite’. The unweathered granodiorite has a medium- to coarse-grained phaneritic texture (Figure 10.2a) and consists of plagioclase, K-feldspars, quartz and biotite (Figure 10.2a, b).

Quartz crystals ranging from a few mm to more than 1 cm in size are either monocrystalline or polycrystalline (Figure 10.3b) with very few fractures. Orthoclase and microcline are found in almost equal amounts, with large crystals up to 1 cm in size.

Weathered granodiorite basement retains the overall macroscopic phaneritic texture of the granodiorite, but plagioclase is hardly found, and the content of phyllosilicates is increased compared to the unweathered granodiorite; either as a macroscopically homogeneous matrix (Figure 10.4b) or as layers enveloping feldspar and quartz crystals (Figure 10.4c).

K-feldspars are heavily fractured and partly replaced by clay minerals. The most abundant phyllosilicate is kaolinite, which occurs as matrix between quartz and feldspars as c. 1.5 mm-long vermicular crystals and as c. 1.5 mm-long fibrous aggregates. The colour indicates iron staining.

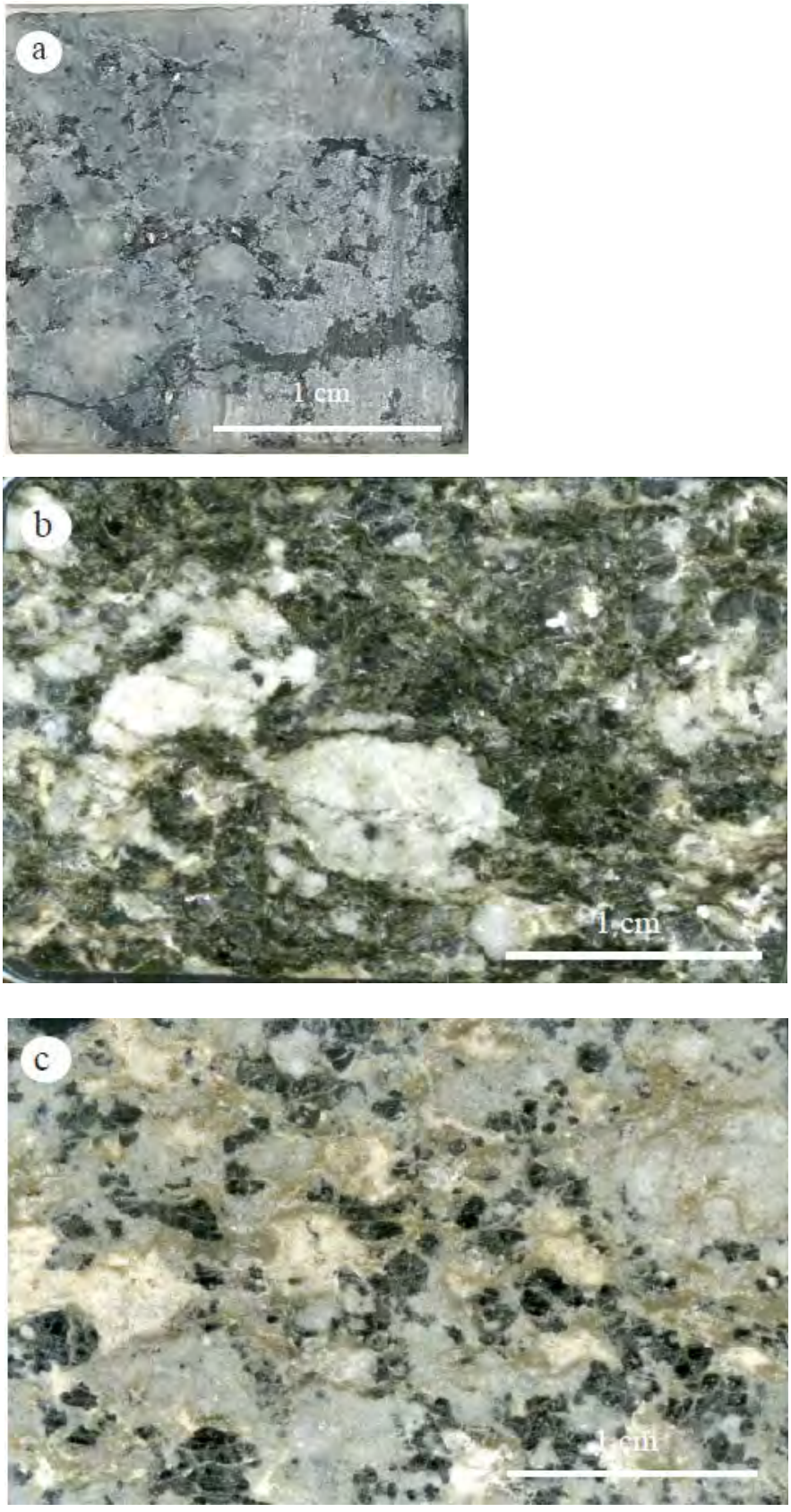

Figure 10.2. Thin-section micrographs of granodioritic basement textures: (a) Medium- to coarse-grained phaneritic texture (sample MB-11-3); (b) large crystals of quartz surrounded by phyllosilicate matrix (black) (sample MB-12-11); (c) medium- to coarse-grained phaneritic texture. Note greenish-brownish layers of phyllosilicates (mainly kaolinite) filling porosity between feldspar crystals (white) and quartz (light grey) (sample MB-12-12).

Weathered rock of the lower Ramså Formation is a fairly homogeneous coarse-grained quartzitic and kaolinite-rich rock (Figure 10.3). Some horizontal fractures are partly filled with quartz. In places some irregular wavy layering is seen, probably caused by variations in the relative abundances of clay.

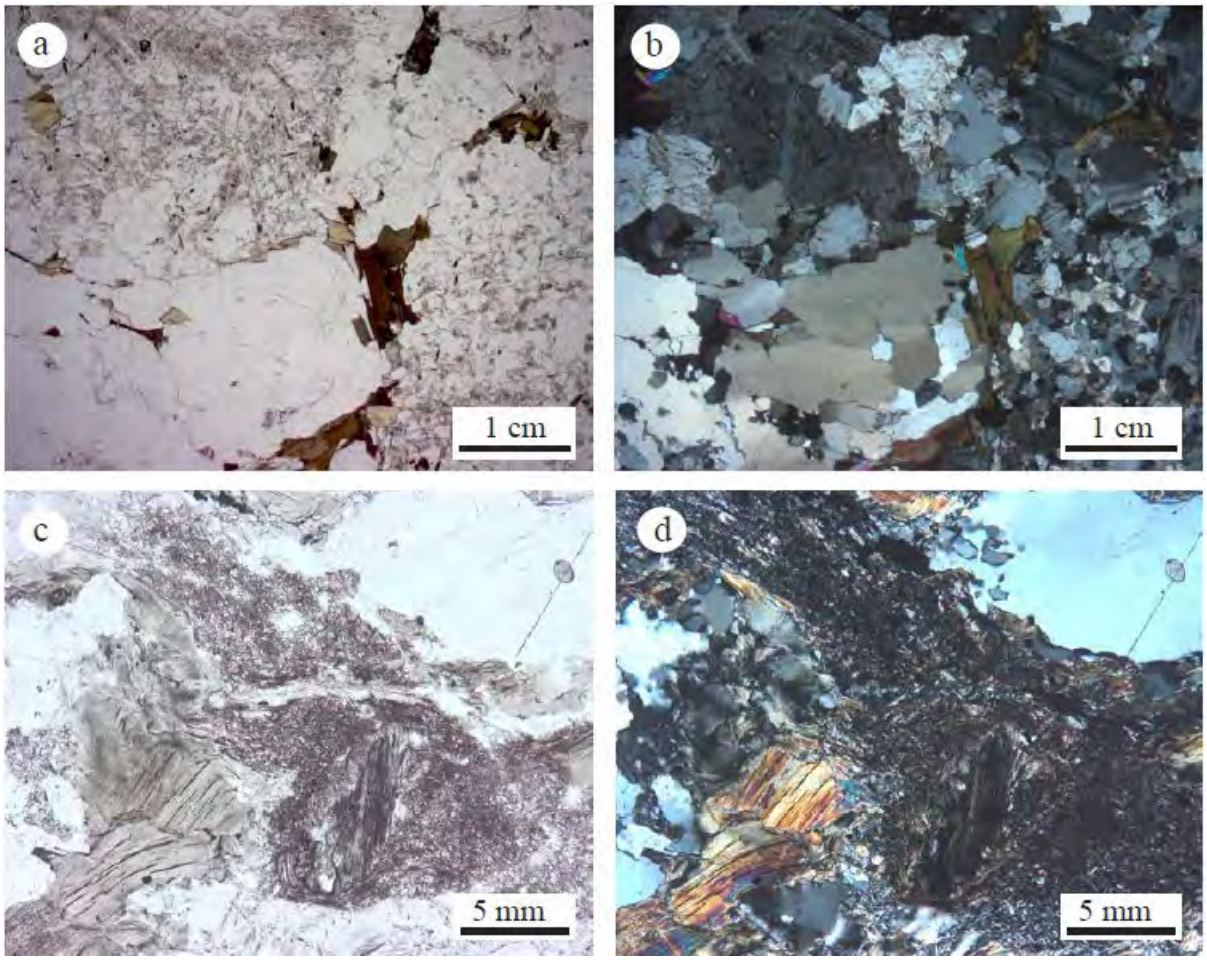

Figure 10.3. Thin-section micrographs of granodioritic basement: (a)'unweathered granodiorite' with phaneritic texture with quartz, plagioclase, K-feldspars, biotite, and small amounts of muscovite (sample MB-11-3). Feldspars in the upper left corner show alteration. The large quartz crystal in the middle is surrounded by 'unweathered' biotite (sample MB-11-3). (b) Same as (a) with crossed nicols. (c)'Mildly weathered granodiorite' showing large quartz crystals surrounded by phyllosilicate matrix (sample MB-12-12). (d) Same as (c) under crossed nicols.

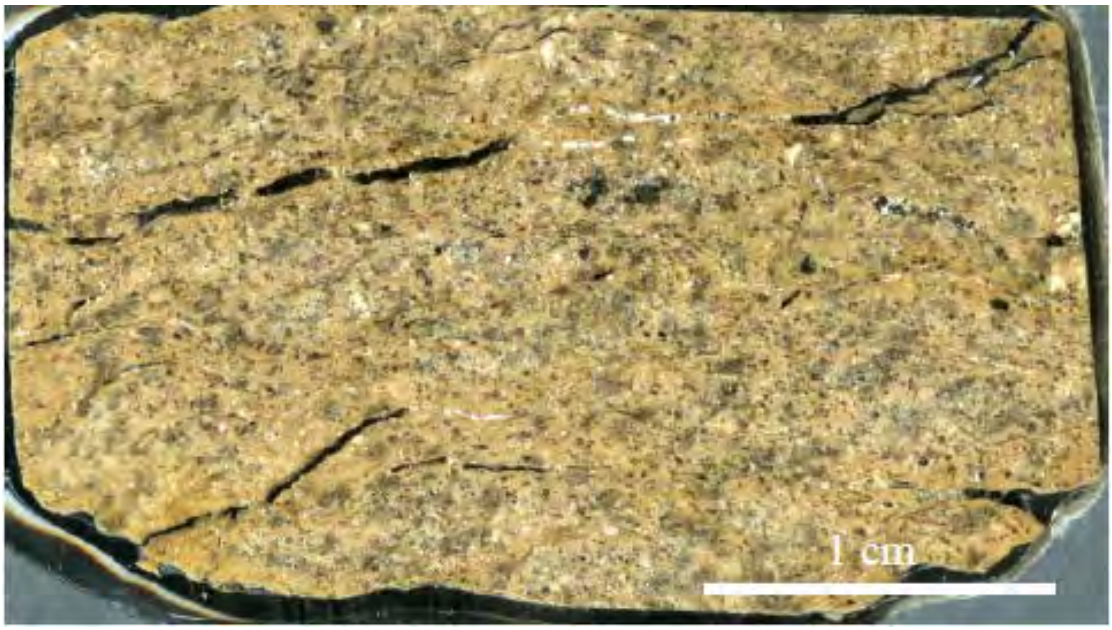

Figure 10.4. Macroscopic texture of the quartz- and clay-rich rock overlying the granodiorite basement. Note the characteristic sub-horizontal fractures partly filled with quartz.

Under the petrographical microscope kaolinite and quartz are recognised as the most abundant minerals (Figure 10.5a, b). Most of the quartz particles are larger than 2 mm; i.e., they belong to the gravel fraction. Also present are a few mm-large pockets filled with titanium oxides (Figure 10.5e and f). This titaniumoxide corresponds to the anatase in Table 10.3.

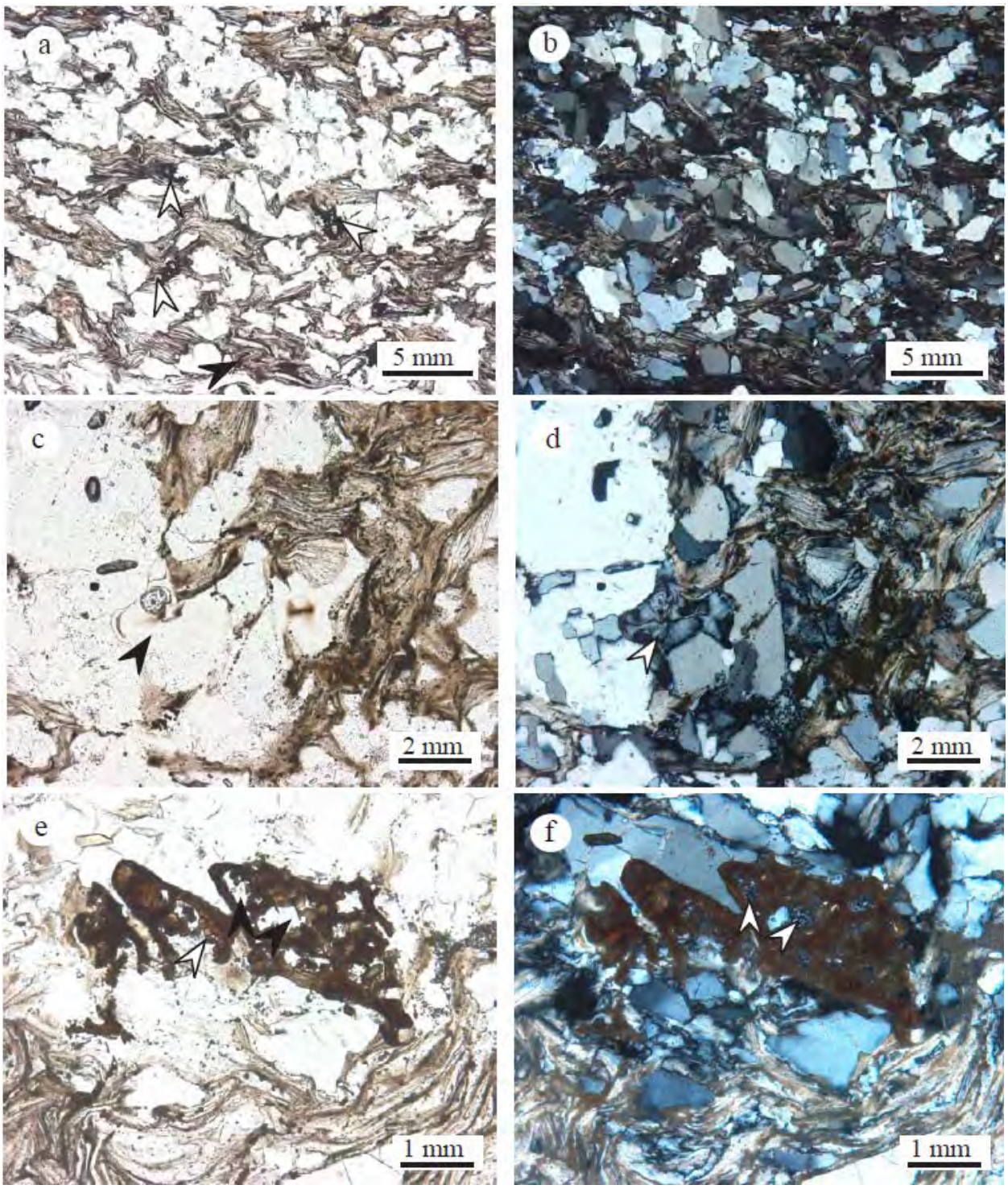

Figure 10.5. Texture of the strongly weathered rock of sample MB-12-13. (a) and (b) Angular quartz grains enveloped in fibrous kaolinite, in a mainly quartz-grain supported texture ((b) with crossed nicols). Micrographs (c) and (d)(crossed nicols) show quartz grains surrounded by booklets of kaolinite (black and white arrows in (d)). Micrographs (e) and (f)(crossed nicols) show 'rods' of titanium oxide (marked by arrows) surrounded by fibrous kaolinite.

Kaolinite occurs as three distinct phases:

- brownish, elongated, twisted, and fibrous crystals up to a few mm in size. The dark colour is supposed to reflect staining by iron-oxides (Figure 10.5a-f);
- c. 1.5 mm-long vermicular crystals that are white in polarised light and show wavy/corrugated extinction under the analyser;
- small (c. 0.1 mm) booklets of kaolinite (Figure 10.5c, d).

Long brown, fibrous kaolinite aggregates form the bulk of the clay matrix and are mostly horizontally oriented; aggregates having different orientations show significant vertical deformation (Figure 10.5c, e). This deformation of kaolinite is suggested to be the result of feldspar dissolution; plagioclase in particular. The dissolution of feldspar grains has caused collapse of the initial feldspar- and quartz-grain supported texture of the rock, followed by compaction of the clay in between the quartz grains. The 1.5 mm-long fibrous kaolinite growing outwards towards the quartz grains does not show any signs of deformation (Figure 10.5c, d). This is interpreted to be a late phase of kaolinite formation, developed after the main compaction of the weathered rock. It is suggested that this growth habit of kaolinite is due to diagenetic processes during deeper burial of the rocks.

The elongated and twisted shape of the kaolinite in this sample (MB12-13) is suggested to be an initial kaolinite formation. The shape and colour of the kaolinite aggregates fits with descriptions of kaolinite in the German 'Tonstein' referred to as 'leverierite' (Millot 1970). This kaolinite was formed in sediments underlying swamps in tropical climates by the transformation of mica and feldspars. The pervasive leaching was caused by percolating water containing organic acids from the overlying swamps, which may be an analogue to the Ramså Formation. The Ramså Formation has several layers of brown coal, which shows the presence of swamps during the formation of the sedimentary succession.

The quartz grains are a few mm in diametre; i.e. gravel size. They are angular and mostly monocrystalline (Figure 10.5a, b). Titanium oxides occur within the kaolinite matrix as pockets of 1-2 mm-long rods (Figure 10.5a, e, f). These minerals are identified as anatase and brookite in the XRD analysis.

An ambiguity exists as to whether this rock is a sediment of the Ramså Formation or a saprolite; i.e. pervasive weathered (granodiorite) basement rock. This is discussed later in this chapter.

Coarse-grained quartz- and clay-rich rocks contain grains and pebbles of quartz enveloped in a phyllosilicate matrix. Macroscopically, the phyllosilicates form a relatively homogeneous matrix (Figure 10.6a and c) consisting of fibrous outward-growing crystals enveloping the quartz grains (Figure 10.6d), and occur as layers, laminae and pockets (Figure 10.6b).

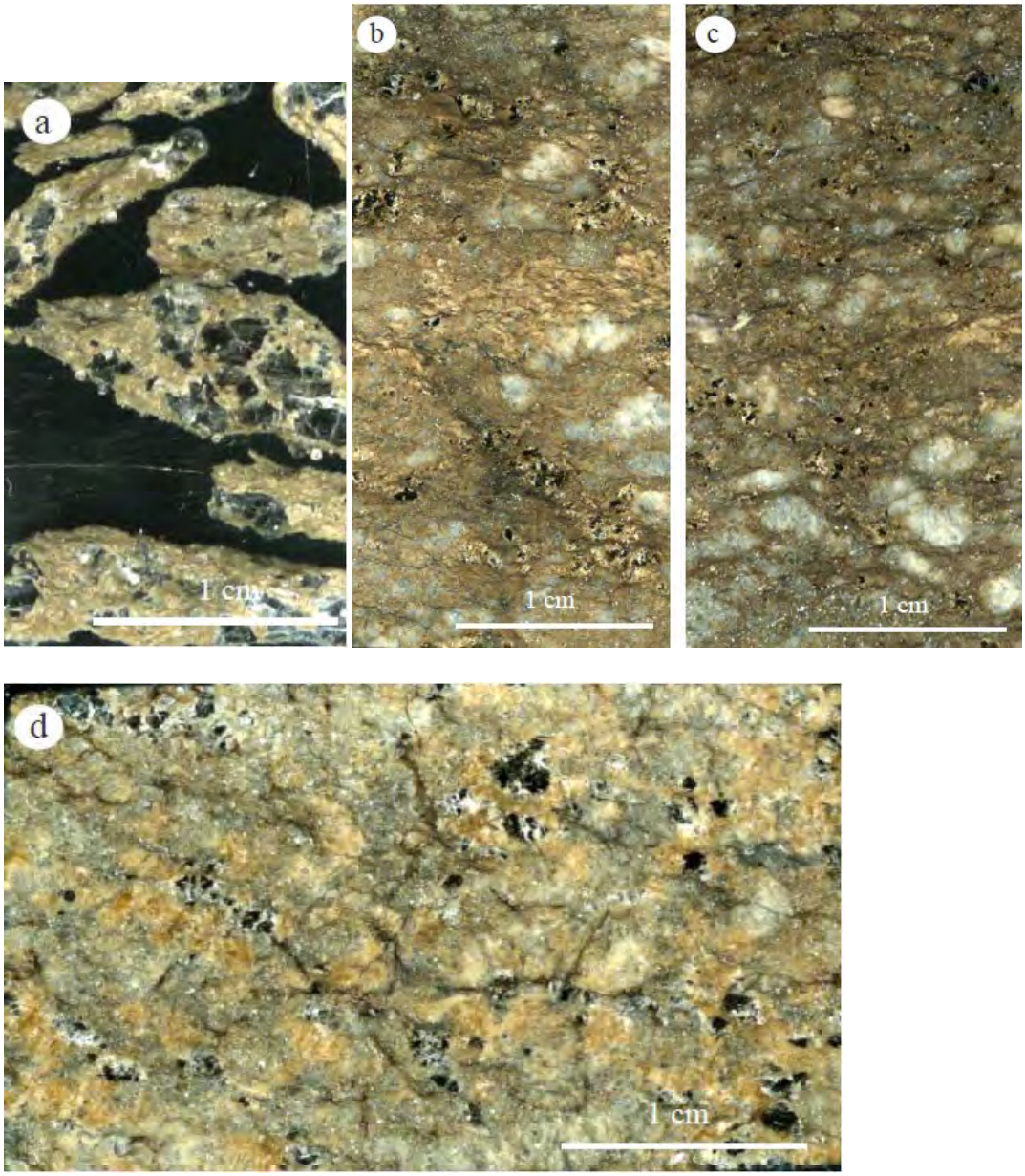

Figure 10.6. Texture of the coarse-grained quartz- and clay-rich rocks of sample MB12-8, -1, and -3. (a) Quartz grains enveloped in clay matrix (sample MB-12-8). Micrographs (b) and (c)(crossed nicols) shows quartz grains 'floating' in clay matrix (MB-12-1). Micrograph (d) shows area with fibrous kaolinite (brown) enveloping quartz grains (sample MB-12-3).

Macroscopically recognisable well-rounded aggregates consisting of quartz and kaolinite may be several cm in size. Under the microscope we have observed that these pebbles of quartz are composed of smaller mm-to-cm-sized quartz grains (Figure 10.7i, j), which are closely packed, mostly arranged in a jigsaw texture and commonly share the optical orientation with their neighbours. The narrow fractures between the quartz grains are filled with kaolinite stained by iron-oxides. Some quartz grains contain fractures which range from thin and short (<0.5 mm; Figure 10.7e, f) to thicker and filled with kaolinite matrix. Kaolinite pebbles, a few cm in size (Figure 10.7k, l), are also well-rounded and consist of both randomly packed clay particles and larger vermicular aggregates of kaolinite a few mm long oriented in all directions.

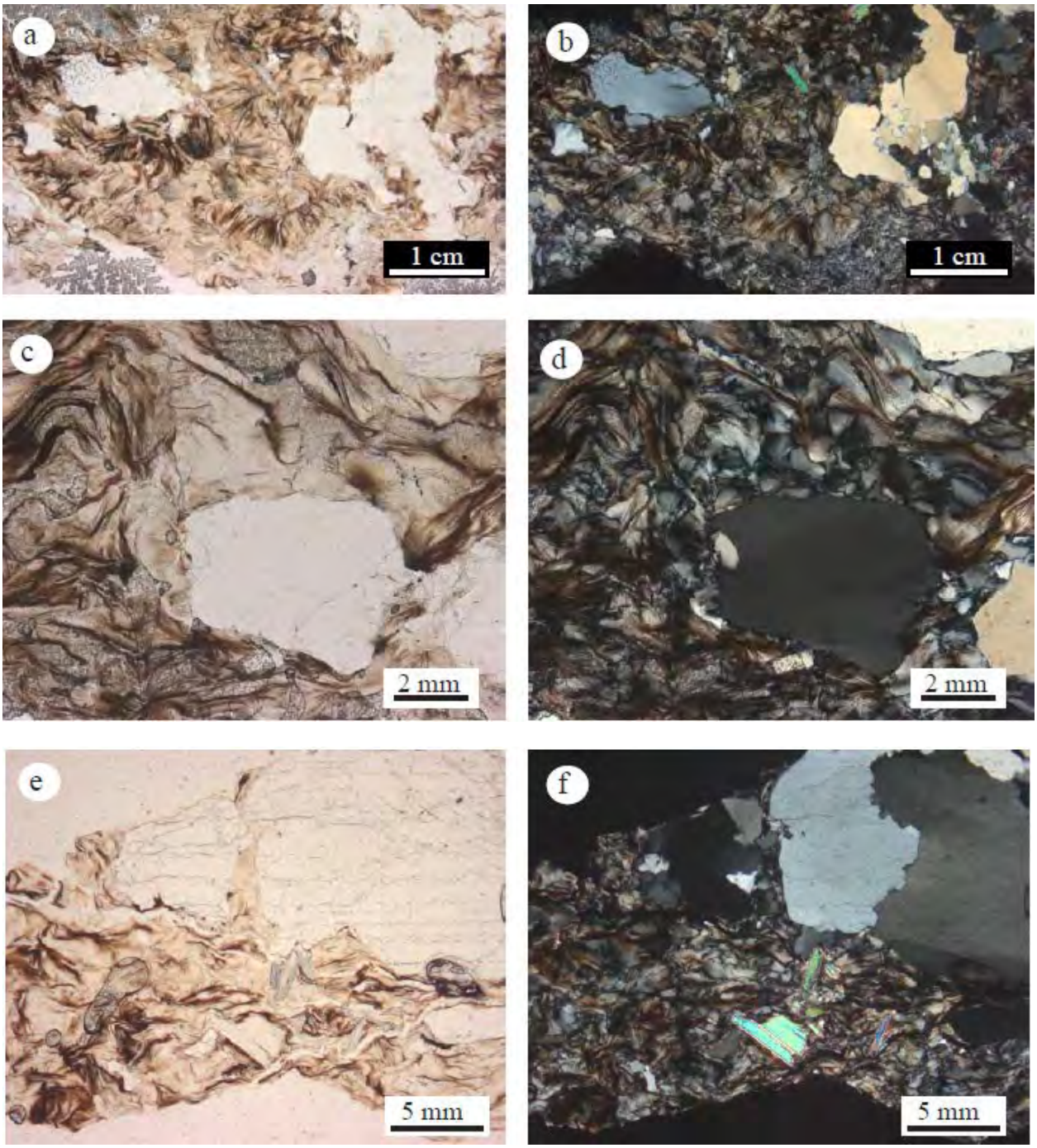

Figure 10.7. Sample MB-12-8: Textures of coarse-grained quartz- and clay-rich rock. a) Angular quartz grains enveloped in kaolinite matrix. Notice the several mm long fibrous kaolinite aggregates, which form concave laminae. b) Site a) under crossed nicols shows quartz grains in kaolinite matrix containing some muscovite. c) Quartz grain enveloped in fibrous kaolinite matrix. d) Fig. 8c under crossed nicols showing monocrystalline quartz grains and fibrous (brownish) kaolinite. e) Quartz grains surrounded by fibrous kaolinite. Note that quartz grains have c. 0.5 mm-long fractures. f) Site e) under crossed nicols showing polycrystalline quartz grains and kaolinite matrix, which also contains some muscovite.

Matrix consists of kaolinite, which occurs as: (i) elongated brownish aggregates a few mm in length (Figure 10.7a, b, c and d); and (ii) clay matrix either between the quartz grains or between vermicular kaolinite aggregates. The fibrous aggregates may form some cm-long discontinuous undulating laminae within the kaolinite matrix (Figure 10.7a, 1), or occur within the clay matrix as vermicular kaolinite aggregates oriented in all directions (Figure 10.7a). Discontinuous laminae recognised macroscopically (Figure 10.7b) are composed of kaolinite containing variable amounts of ironoxides and some framboidal pyrite (Figure 10.7h) or of randomly oriented vermicular aggregates of kaolinite.

An ambiguity exists also for these rocks as to whether they are sediments of the Ramså Formation or a pervasively weathered (granodiorite?) basement rock.

The sedimentary rocks from the upper part of the surface profile are alternating gravelly, coarse- and fine-grained, siliciclastic sandstones, containing sub-rounded to rounded quartz grains, mostly 0.5 to 1 mm, but also up to 1 cm in size. Pyrite occurs either in small nodules or as framboids (Figure 10.8a). Wavy horizontal stylolites occur within the quartz sandstones (Figure 10.8b).

The mudstone sample is green with a cross-cutting quartz vein (Figure 10.8d) and contains silt- to very fine sand-sized quartz grains, biotite laths, chlorite and clays (Figure 10.9c,d). The biotite appears almost unweathered (Figure 10.9c,d).

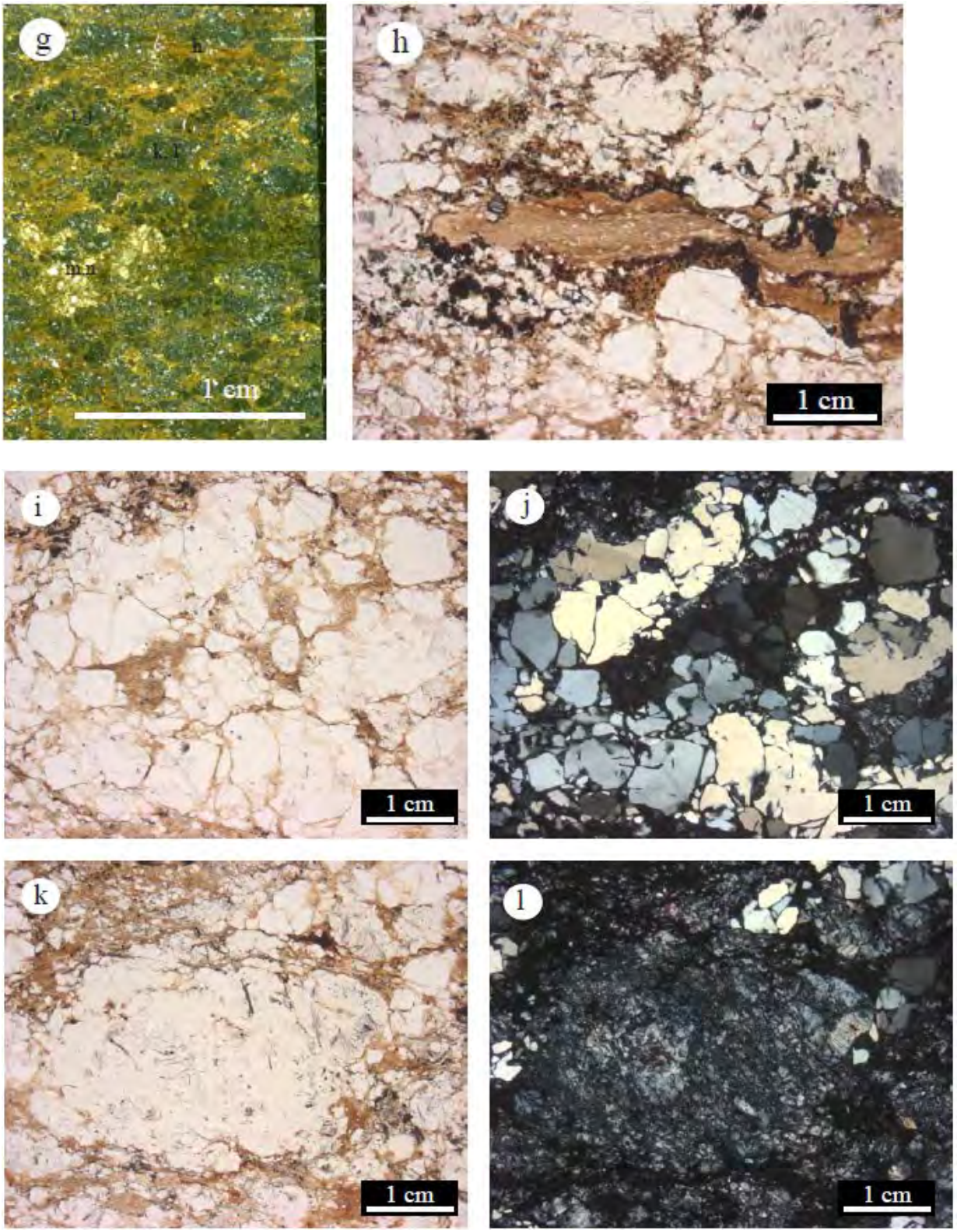

Figure 10.8. (continued). g) Sample MB-12-1: Macroscopic texture of coarse-grained quartz and clay-rich rock. The micrographs h) to n) are magnifications from image g). h) Lamina of kaolinite. Opaque grains of framboidal pyrite are surrounding the lamina. i) Quartz pebble composed of smaller quartz grains, which form a jigsaw texture. j) Site i) under crossed nicols shows that most quartz grains share their optical orientation with their neighbours. k) Kaolinite pebble (or ball) surrounded by kaolinite matrix stained by iron oxides (brown) and some quartz grains. l) Site k) under crossed nicols showing single kaolinite crystals in the kaolinite ball.

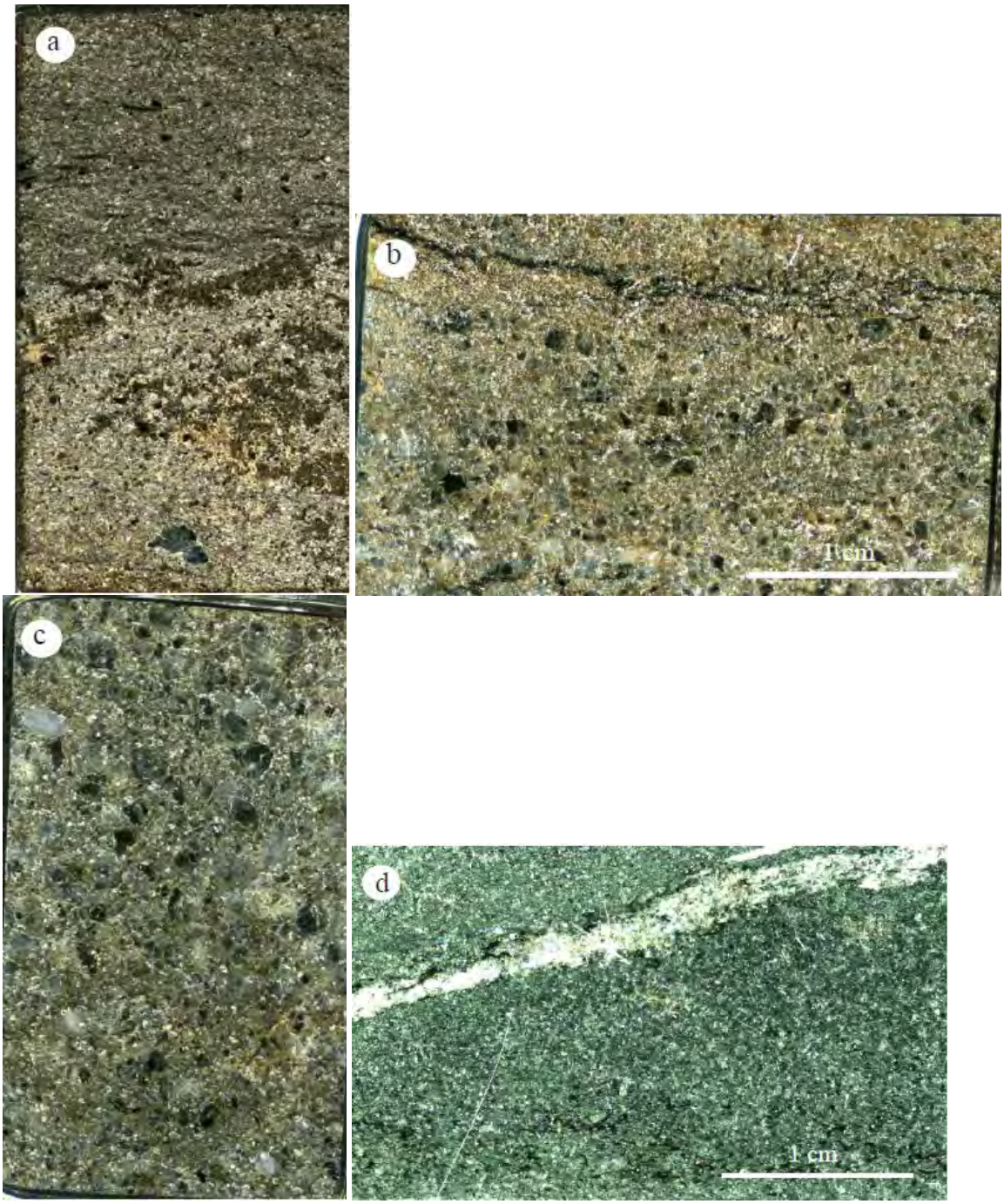

Figure 10.9. Macroscopic textures of samples MB12-6, -9, -5, and -10. a) Medium-grained quartz sandstone containing pyrite; overlain by sandy siltstone (sample MB-12-6). b) Medium-grained quartz sandstone with organic-rich laminae and stylolites (sample: MB-12-9). c) Medium-grained sandstone composed of subrounded quartz grains (sample MB-12-5). d) Green sandy siltstone with a diagonal quartz-filled fracture (sample: MB-12-10).

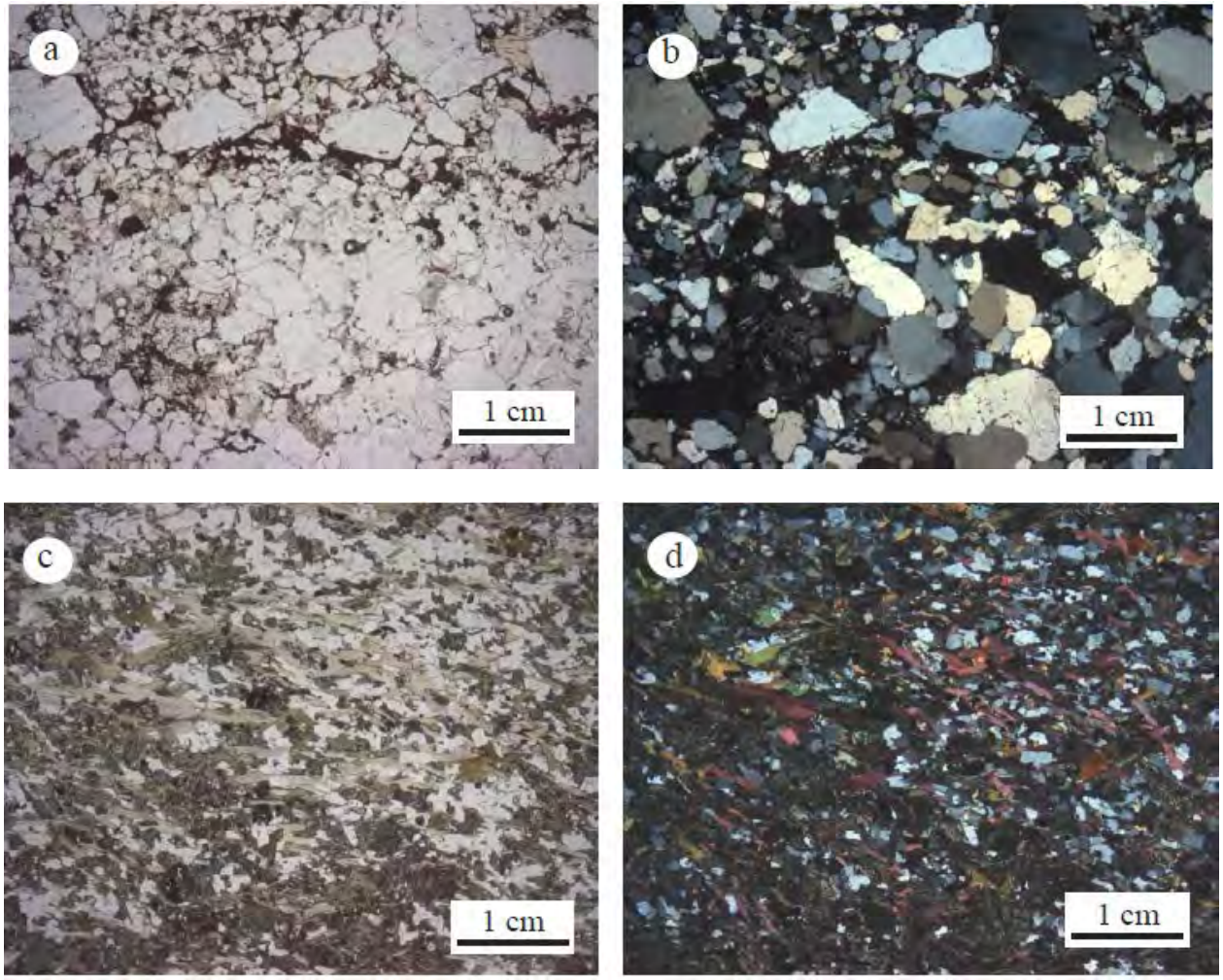

Figure 10.10. Microscopic textures of sedimentary rocks. a) Gravelly sandstone containing subangular to subrounded quartz grains and some pyrite (sample MB-12-5). b) Site a) under crossed nicols shows the tightly packed monocrystal quartz grains. c) Sandy siltstone containing quartz grains surrounded by biotite, chlorite and clays (sample MB-12-10). d) Site c) under crossed nicols.

10.5.3 The lithology and mineralogy of the Ramså surface profile:

The lithologies and mineralogy of the entire Ramså surface profile are illustrated in Figure 10.11. The transition from the clearly defined basement granodiorite and the weathered parts of it to the overlying kaolinite rich rocks is seen by the sudden decline in K-feldspar (from MB12 to MB13). Magnesium and iron is also reduced throughout the basement section.

The lithologies referred to as 'weathered rock', 'coarse-grained quartz and clay-rich rocks' and 'quartz and clay-rich rock' are covering c. 18 m of the interval above the 'weathered basement' (up to the stratigraphic depth of 24 m), and have been difficult to define. Are these rocks weathered sediments or weathered basement rocks?

The rocks are characterised by consisting mainly of quartz and kaolinite. The quartz grains are angular and poorly sorted, having grain-sizes partly in the gravel fraction. This indicates no sorting by transportation and depositional processes. Furthermore, the kaolinite in this sequence is characterised by elongated, twisted and brownish aggregates, an appearance

described in the literature as leverierite, formed in laterite profiles by the percolation of water (containing organic acids) from overlying swamps; i.e., an in-situ formation (Millot, 1970).

Typical shapes of diagenetically formed kaolinite are also seen by the vermicular growth habit and as shorter 'booklets', commonly seen as diagenetically formed kaolinite in deeply buried sandstones in the North Sea (Ehrenberg 1991). These delicate *in-situ* kaolinite structures would not survive an erosion, transportation and deposition cycle. Some of these kaolinite features may, of course, have been formed diagenetically (e.g., kaolinite booklets), but the entire texture of the rock, with quartz grains 'floating' in the authigenic kaolinite structures indicates that all of the clay is formed *in-situ*. Thus, it is suggested that the growth habits of the kaolinite are the result of both meteoric weathering and subsequent diagenetic formation of kaolinite during burial.

Features pointing towards a sedimentary origin are, e.g., rounded pellets of kaolinite and quartz (Figure 10.8k,sample MB12-1), and laminae of kaolinite (Figure 10.8h,sample MB12-1). However, these features may also be explained by tropical weathering; e.g. the short laminae of kaolinite may result from the dissolution of large feldspar crystals and the occurrence of quartz aggregates are described in the literature as a result of tropical weathering (Millot, 1970).

The grain sizes and texture are similar to these of the weathered basement granodiorite, but the mineralogy is different, in that they are without (or are very low in) K-feldspar and plagioclase. However, this dissolution of feldspars may also be a result of tropical weathering.

Based on these observations it is concluded that the 18 m section between the 'weathered basement' and the 'quartzitic sediment' (Table 10.3) represents the upper part of a saprolite developed in the granodiorite basement.

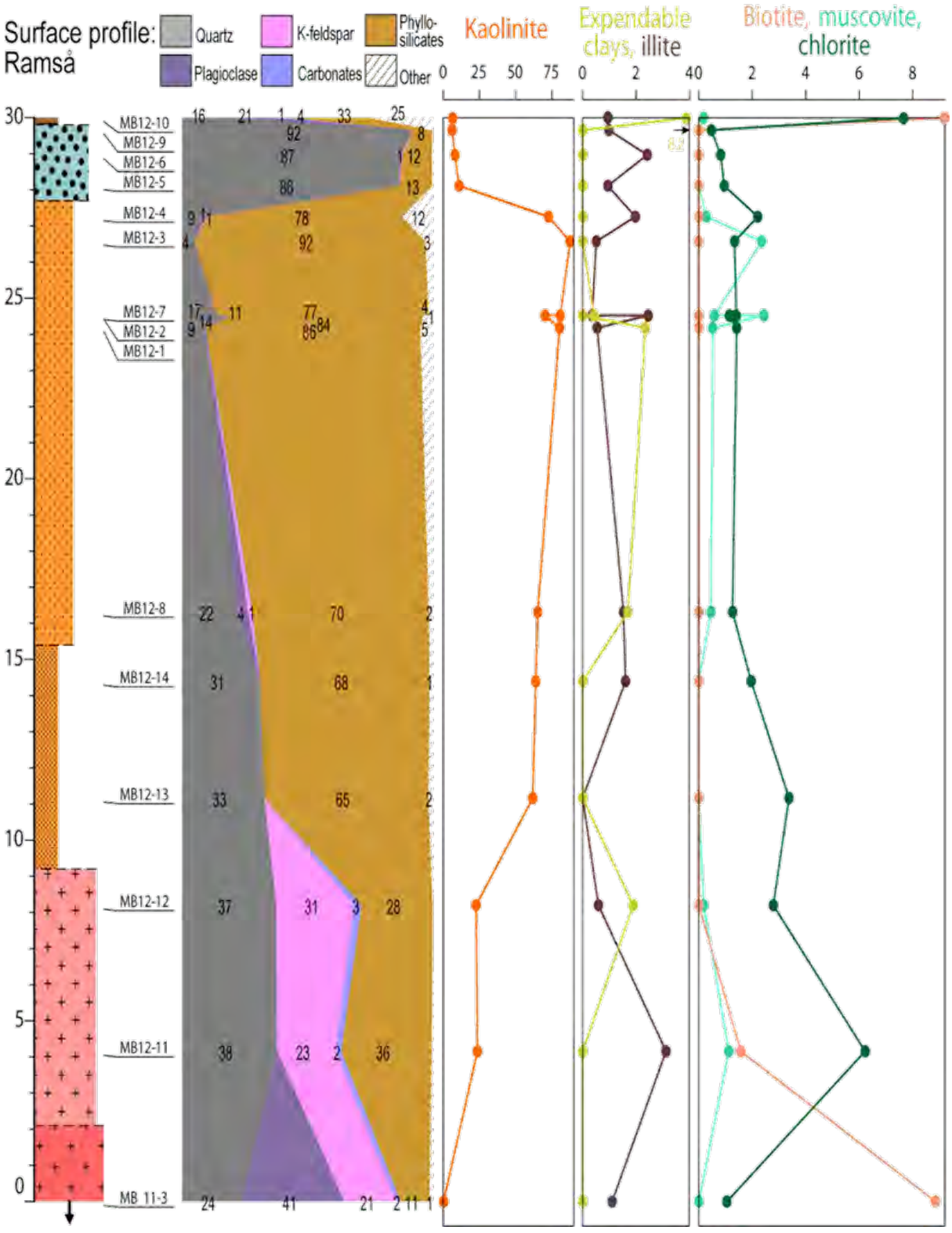

Figure 10.11. Lithostratigraphic column of the 'surface profile' at Ramså. Plot of mineralogy versus depth. Sample MB-11-3 (at depth 0) is from the unweathered granodiorite basement. The lithology legend is shown in Table 10.3.

10.5.4 Chemical composition of samples from the Ramså surface profile

The variations in geochemistry (and lithology) throughout the Ramså surface profile are illustrated in Figure 10.12 and Figure 10.13.

Geochemistry of the samples from the Ramså profile

The laboratory-derived XRF data from the Ramså profile are given in Appendix Tables A3 and A4A. Based on the macroscopic description of the samples and their petrography, the sampled profile consists of unweathered and weathered granodioritic basement at the base, a kaolinite-rich part (including fine- and coarse-grained quartz) in the middle, and sedimentary rocks in the upper part, including sandstones and mudstones.

Generally, the amount of silica decreases from the unweathered basement at the base to the kaolinite-rich sediments at the top of the profile (from c. 70 wt % to 52 wt %). A concomitant increase in phyllosilicates (15 to 30 wt %) and 'loss-of-ignition' (0 to 13 wt %) is seen. The Chemical Index of Alteration, CIA, (CIA= $Al_2O_3/(Al_2O_3 + CaO + Na_2O + K_2O)$) increases from 52 to >85 and is mirrored by the ratio ∑Bases/Al (=(Na+K+Ca+Mg)/Al), which decreases from bottom to top in the profile, an exception being the uppermost sample with a very low CIA value.

Granodiorite basement; MB11-3, MB12-11, MB12-12:

The base cations MgO, CaO, NaO and iron (Fe_2O_3) decrease gradually from unweathered to weathered basement, while the amount of K_2O increases. The CIA increases and ∑Bases/Al decreases from unweathered to weathered basement.

Quartz- and clay-rich rocks; MB12-13, MB12-14:

The quartz and kaolinite-rich rock contains mainly silica and Al_2O_3, while most base cations are absent (MgO, CaO, NaO, K_2O). Fe_2O_3 is present with ≈1 wt %. This interval has the highest values of CIA (99) and the lowest ∑Bases/Al, and also the highest amounts of TiO_2, (4 wt %), and high content of Zr (≈320 ppm).

Coarse-grained quartz- and clay-rich rocks; MB12-1, -2, -3, -4, -7, -8:

In this zone the amounts of silica decrease and Al_2O_3 increase from bottom to top, and the amounts of base cations (MgO, CaO, NaO, K_2O) vary between 0 and 1.1 wt %; i.e. very low. Iron-oxide shows values up to 3.4 wt% (Fe_2O_3). The Ba/Sr ratio in the upper part of this stratigraphic interval is the largest in the entire section; 5-9.

Sedimentary rocks; MB12-5, -6, -9, -10:

The lower part of the sedimentary rocks is represented by quartz sandstones which contain high amounts of silica (80-93 wt %), some Al_2O_3 (2-7wt %) and low amounts (<1.5 wt %) of the other main chemical elements (MgO, CaO, NaO, K_2O, Fe_2O_3). These quartz sandstones show high values of CIA (>85) and low values of ∑Bases/Al (≈0.1). They also contain high amounts of TiO_2 and Zr; 0.9-2.3 wt % and 230-810 ppm respectively. They also have the highest Ti/Al ratio of all studied samples (0.37-0.45).

The variation in the weathering index, CIA, is a good illustration of the degree of weathering throughout the profile, with generally high values above the basement (Figure 10.13).

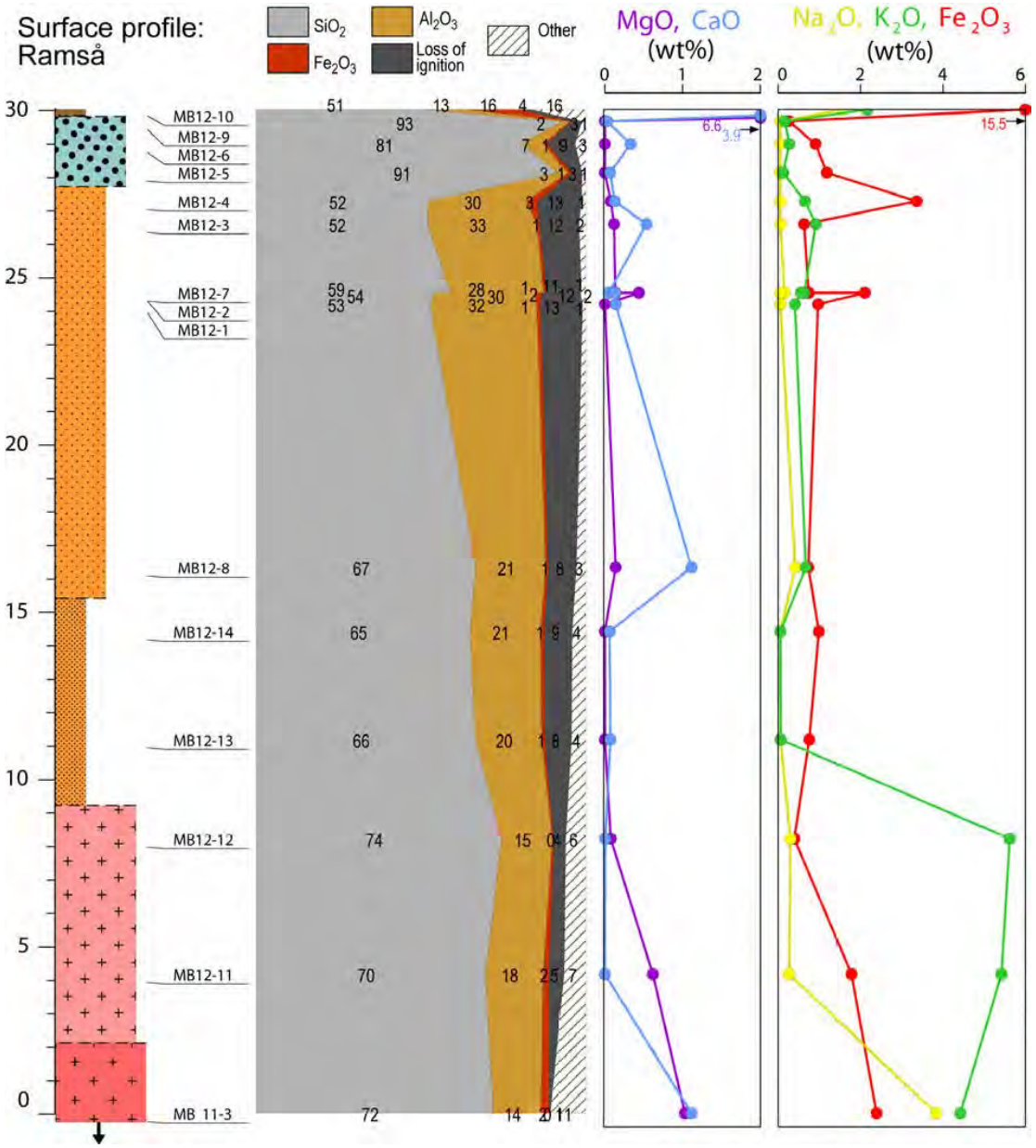

Figure 10.12. Lithostratigraphic column of the 'surface profile' at Ramså showing variations in elements of geological interest throughout the profile.

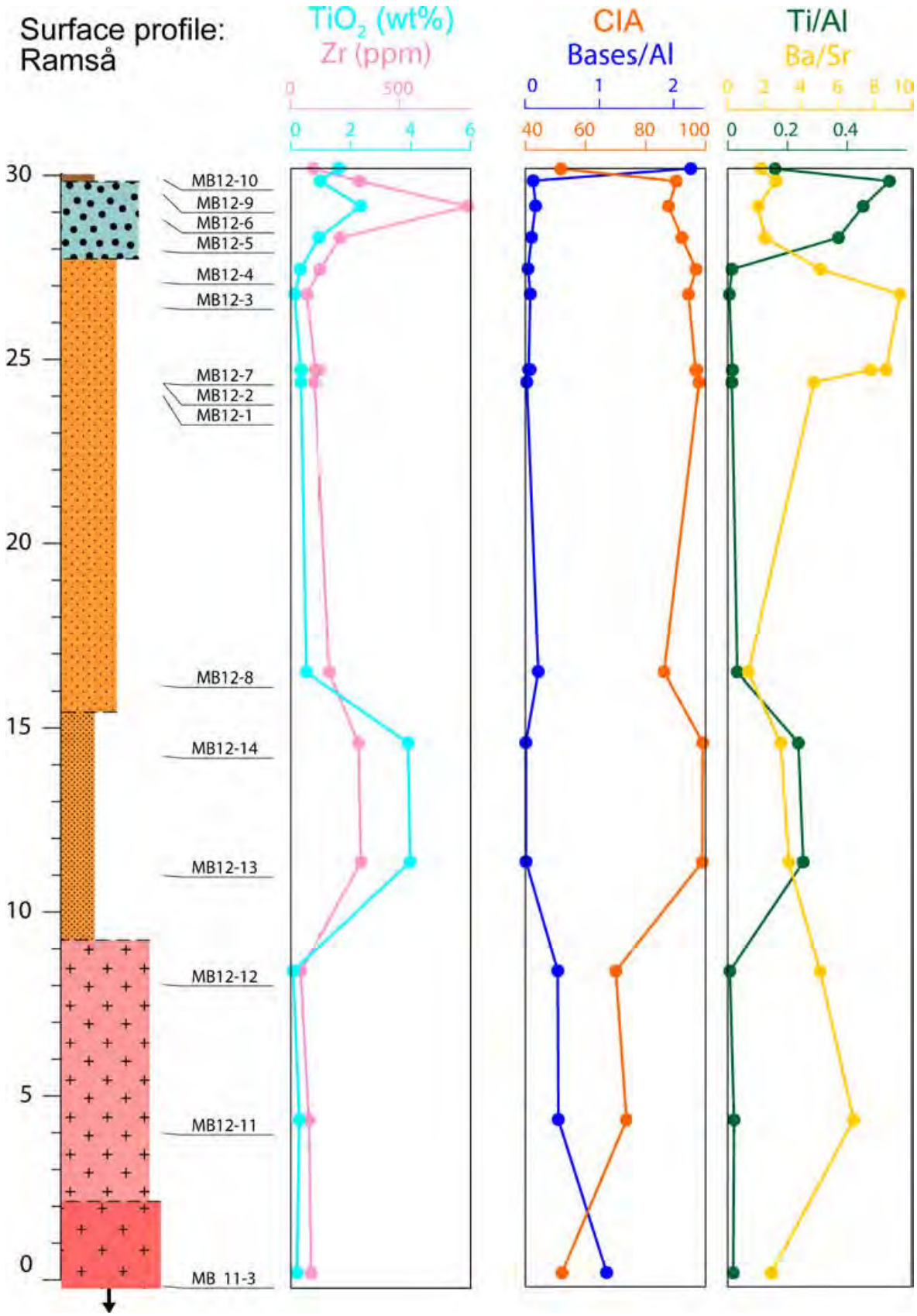

Figure 10.13. Lithostratigraphic column of the 'surface profile' at Ramså. Plot of trace elements Ti and Zr; weathering index CIA (Chemical Index of Alteration); Ti/Al ratios; and Ba/Sr ratios.

10.6 **Cores from Norminol Wells A, B, and C**

Eleven core samples were selected for XRD and XRF analyses from Norminol wells A, B and C. The basement contacts with the overlying rocks were sampled in all three wells: 3 samples from core B, 3 from core C, and 5 from core A.

10.6.1 Mineralogy from XRD

The interpretation of the X-ray diffractograms of the bulk samples is given in Table 6.1. The table includes depths and mineral composition for the samples from Wells A, B and C. The clay minerals smectite, vermiculite and mixed-layered illite/smectite and illite/vermiculite are added together (S+V+M in Table 10.4). This is done because we only have bulk XRD analyses and consequently, no glycol-saturated samples to run on XRD for the identification of smectite. Hematite is identified in sample 239.5, and that is noted under the 'Pyrite' column. Comments on the results are given below.

Table 10.4 Mineral composition of eleven drillcore samples from the Ramså Formation and basement in Norminol wells A, B, and C. Semi-quantitative interpretation in weight-% from XRD data. The basement contact in Well A is at 530.8 m depth; that of Well B is at 530 m depth; and in Well C it is at 235 m depth. Samples from the basement are coloured yellow in the table. Abbreviations: Qtz=quartz; Pla=plagioclase; Kfs=K-feldspar; Kao=kaolinite; Chl=chlorite; S=smectite; V=vermiculite; M=mixed-layered minerals; Cal=calcite; Py=pyrite; He=hematite.

Sample	Qtz	Pla	Kfs	Mica	Kao	Chl	S+V+M	Py+He	Cal
Well A									
527.6	29	13	11	7	15	4	12	9 Py	-
529.2	36	7	13	4	33	7	tr	12 Py	-
532.4	41	23	30	4	2	-	-	-	-
534.7	33	32	33	2	tr	-	-	-	-
543.5	23	55	-	16	4	tr	-	2 Py	-
Well B									
527	5	-	-	-	15	-	80	-	-
539	20	16	11	9	15	3	22	-	4
543	21	16	14	9	13	3	19	-	5
Well C									
234.5	59	12	10	8	11	tr	-	-	-
235.0	75	5	9	2	9	-	-	-	-
239.5	13	27	-	-	tr	21	-	5He	34

Well A; 527.6 m to 543.5 interval: The main minerals in this sequence are quartz and two feldspars; a granodioritic composition. The granodioritic basement was encountered at 530.8 m depth in this well. The two samples above this depth are sediments, with abundant kaolinite and some vermiculite and smectite; i.e. weathered. Below this depth there is less than 4 wt % kaolinite and a granodioritic composition, with quartz, two feldspars and mica; i.e. mildly weathered basement. The deepest sample, 543.5, is a more micaceous sample, and without K-feldspar.

Well B; 527 m to 543 m interval: The granodioritic basement in this well is suggested to be at 530 m depth. The two samples below this point have very similar composition, and the original granodioritic composition is seen by the content of quartz and two feldspars. However, both samples are weathered, seen by the kaolinite contents and mixed layered minerals (ML). The ML minerals are suggested to be illite/vermiculite formed by leaching of potassium from biotite. There is still unweathered mica present, and also some chlorite (3 wt %). The sample collected above the basement is a fine-grained sediment. This is also seen from the mineral composition, by the low quartz content, no feldspars and 95% phyllosilicates. In addition, the X-ray reflections are broad, indicating small particle sizes, which is typical for smectitic clays. The 12Å mineral present is therefore suggested to be a smectitic phase, e.g., smectite/chlorite or an illite/smectite mixed-layered mineral; although this is not confirmed by ethylene glycol treatment. The texture and composition of this rock may indicate a weathered volcanic ash, which is reported by Dalland (1979) at the base of the Kullgrøfta Member.

Well C; 234.5 to 239.5 m interval: The basement contact in this well is at 235 m depth, i.e. higher up than for the other two wells. One of the samples is from this depth, and there is one sample below and one above. Samples 234.5 and 235 have high quartz contents, two feldspars, and mica; i.e., a granodioritic composition, but both are weathered, and contain kaolinite, although in moderate amounts. The deepest sample is very different from the others; without K-feldspar, mica and kaolinite. Instead, it has abundant calcite, chlorite and hematite. This mineral paragenesis indicates an altered, more basic rock.

10.6.2 Petrography and lithology of cores from Wells A, B and C

Well B is the most proximal located well, while wells C and A are more distal. Well B was therefore chosen for more detailed studies of the lower formations, in order to make comparisons with the exposed profiles at Ramså, described above, and the other investigated wells. A lithological column for Well B, including sedimentary structures, was constructed based on the cores studied; Figure 10.15. This column describes the well from 425 m down to 543 m depth, and the basement boundary is at 430 m depth.

10.6.2.1 Cores from Well B

Granodiorite basement (543 – 529.1 m): The lowermost 14 m of the core consists of granodioritic basement, which is texturally heterogeneous (Figure 10.14) and contains (1) pinkish granodiorite with a phaneritic texture (Figure 10.14b, d), (2) fractured granodiorite enriched in clay minerals along the fractures (Figure 10.14.a), and (3) a greenish granodiorite containing higher amounts of chlorite and lower amounts of feldspars (Figure 10.14c) than the pinkish granodiorite.

The feldspars are euhedral to sub-euhedral (Figure 10.14b, d), and in places deformed (Figure 10.14e). The uppermost 30 cm of the granodiorite basement consists of quartz and white feldspars, whereas amphiboles, micas and pink K-feldspars are absent.

Figure 10.14. Photos of cores from Well B: a) fractured granodiorite, enriched in clay along fractures (depth: 541.5 m). b) Granodiorite with phaneritic texture (depth: 539.5 m). c) Greenish granodiorite, with some chlorite and feldspars (depth: 536.4 m). d) Granodiorite with phaneritic texture and diagonal seam poor in feldspars (depth: 535.5 m). e) Granodiorite with deformed feldspars (depth: 533 m). f) Green rock with a texture of fine-grained sandstone (depth: 527.5 m). g) Conglomerate overlain by claystone, containing rootlets and organic matter. The conglomerate contains sub-rounded quartz clasts floating in a sandy matrix (depth: 526,5 m). h) Claystone with rootlets (depth: 526 m).

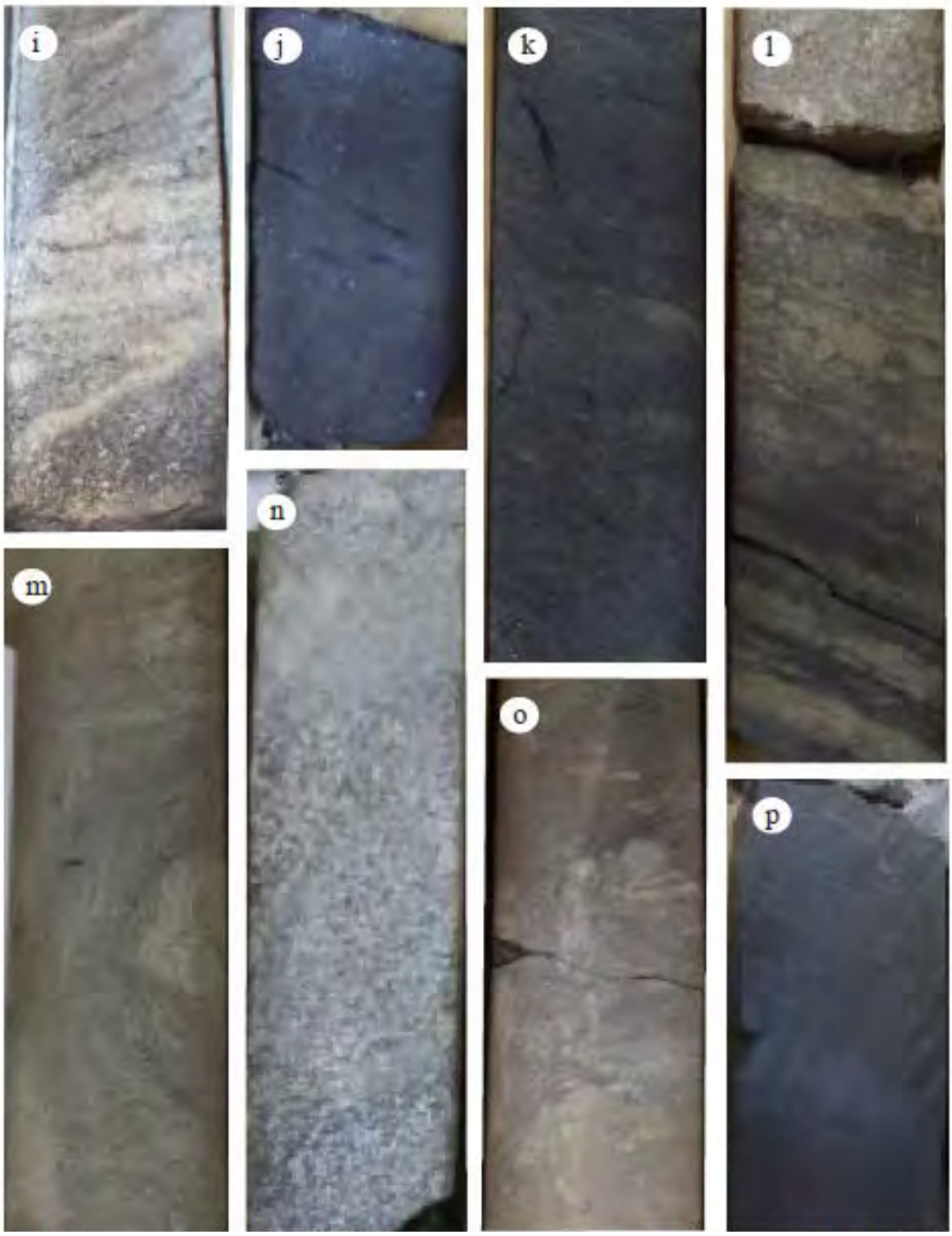

Figure 10.14 cont. Photos of cores from well B. i) Medium-grained sandstone, syn-sedimentary deformed (depth 523 m). j) Coal layer (521.5 m). k) Siltstone with pyrite lenses and rootlets (519.5 m). l) Siltstones interbedded with slumped, fine-grained sandstones (504.8 m). m) Slumped siltstones interbedded with fine sand. n) Quartz sandstones, varying from very coarse to medium-grained (518.2 m). o) Slumped very fine sandstones interbedded with siltstones (517.7 m). p) Coal layer (491.5 m).

Figure 10.14. cont. Photos of cores from Well B. q) Fine-grained sandstone overlain by intra-formational conglomerate with sandstone intra-clasts (depth 503.8 m). r) Very fine- to fine-grained sandstones containing siltstone laminae (depth 501.7 m). s) Syn-sedimentary deformed sandstones with thin laminae of siltstones (depth 485.3 m). t) Cross-laminated sandstones (depth 481.8 m). u) Flat-laminated sandstone laminae. w) Green massive fine- to medium-grained sandstone (depth 459.9 m). x) Grey massive fine- to medium-grained sandstone (depth 457.8 m).

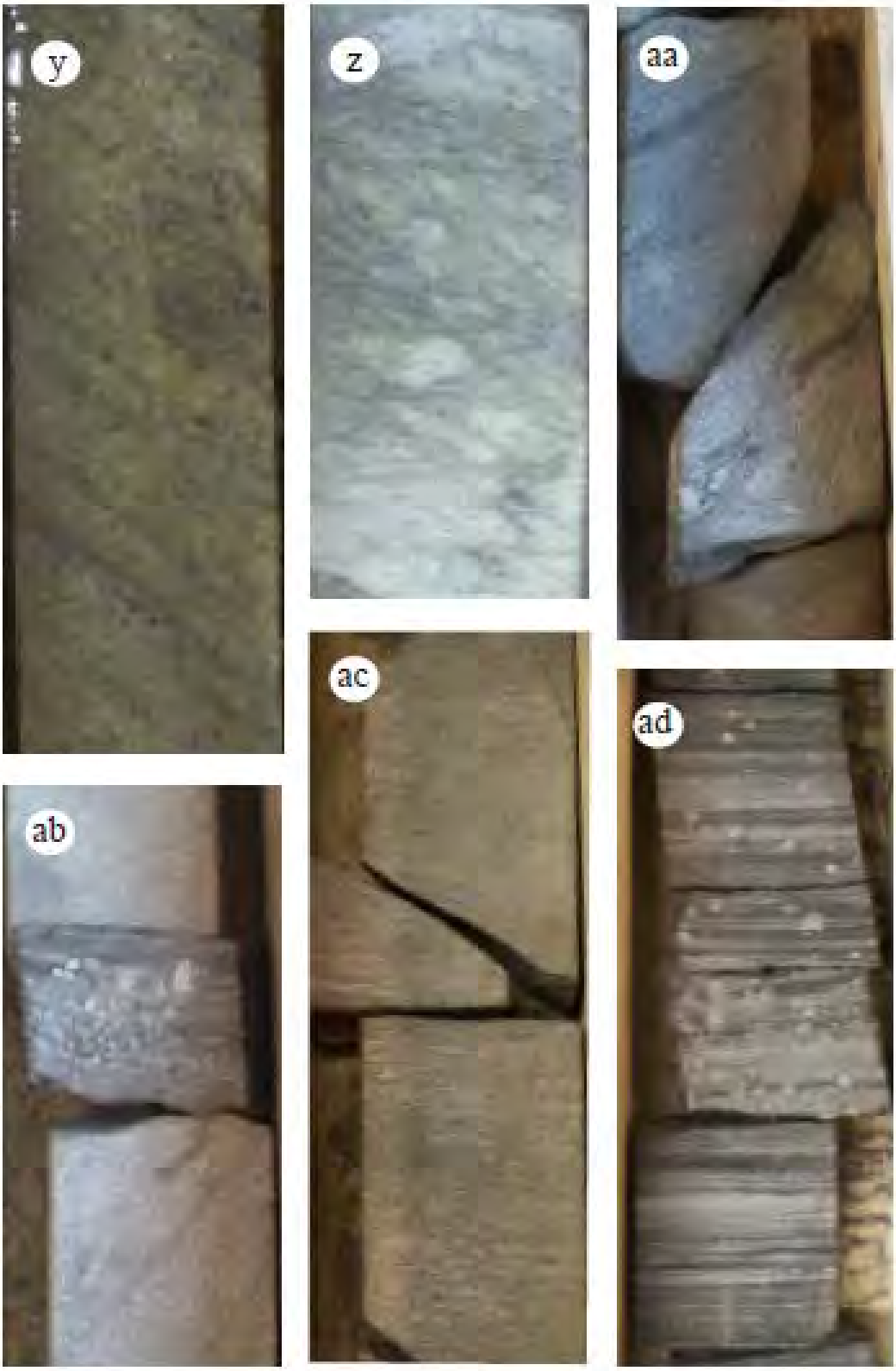

Figure 10.14. cont. Photos of cores from Well B. y) Cross-bedded medium-grained sandstone (470.8 m). z) Syn-sedimentary deformed fine-grained sandstone containing siltstone laminae (468.1 m). aa) Sandstone containing siltstone clasts (439.4 m). ab) Sandstone with pyrite-bearing siltstone interlayers (436.5 m). ac) Lenticular laminated very fine-grained sandstone interbedded with siltstones (432.8 m). ad) Flat-laminated sandstone interlaminated with siltstones containing some pyrite (431 m).

Microscopically, the pinkish granodiorite (seen in Figure 10.14) with the phaneritic texture contains large amounts of quartz, K-feldspars, plagioclase and chloritised biotite, but also minor amounts of muscovite. The greenish granodiorite contains the same minerals, but much less plagioclase than the pinkish variety (Figure 10.16a, b). Calcite overgrowths are extensive (Figure 10.16a, b) and make up a significant part of the rock.

Green rock (529.1 – 527 m): Overlying the granodioritic basement is a 2.1 m-thick interval of green rock that has the texture of fine-grained sandstone (Figure 10.16c, d), but no apparent sedimentary structures (Figure 10.16e,f). The uppermost 5 cm of the interval consists of green, massive quartz sandstone, which has a gradual contact with the underlying green rock.

Microscopically, the sample consists mainly of quartz grains (many of them are fractured (Fig. 6.3e)) and phyllosilicates, the latter commonly chloritised. Fe- and/or Mn-oxides are abundant along the cleavage of the phyllosilicates (Figure 10.16e, f).

Dragneset Formation (435.8 – 296 m): The Dragneset Formation consists of alternating very fine- to fine-grained sandstones and siltstones, laminated on mm-scale. Flat lamination is the most common (Figure 10.14ad), but a few intervals show lenticular laminations (Figure 10.14ac). The contact with the underlying Ramså Formation is gradual; the boundary is defined at the beginning of a several metres thick interval of flat-laminated siltstones and sandstones.

Ramså Formation (527 – 436 m): Sedimentary rocks of the Ramså Formation are recognised by the presence of primary sedimentary structures, particularly lenticular-, flat-, and cross-laminations. The Ramså Formation is subdivided into three members; Hestberget, Kullgrøfta and Bonteigen Members.

In NGU's Well BH 1, the Kullgrøfta Member is defined as the interval 81 - 70 m above basement (Figure 9.1); i.e., a thickness of c. 11 m, characterised by dark grey, bituminous silty mudrock, identified as a lake deposit. From the core material in Well B, however, it is difficult to identify the Kullgrøfta Member. For this reason the Ramså Formation in Well B is subdivided into two lithostratigraphic units; a Lower and an Upper Unit.

The main lithologies of the Lower Unit are sandstones, siltstones (Figure 10.14l), and claystones (Figure 10.14g and h). Also present are a few layers of coal (Figure 10.141,j, p) and some intraformational conglomerates (Figure 10.14q). Two types of sandstones are identified, the most common being a grey, massive, in places laminated, medium- to very coarse-grained sandstone with subrounded quartz grains (Figure 10.14i and n). Less common are very fine- to fine-grained sandstones, often interbedded with siltstones (Figure 10.14r). These alternating sandstones and siltstones show various sedimentary structures; mostly flat-lamination, but also wavy- and lenticular-lamination, and some syn-sedimentary slumping (Figure 10.14l, m and o). Sandstones and siltstones contain organic-rich layers and rootlets in places (Figure 10.14k) and also secondary calcite (Figure 10.14r). Claystone intervals can be more than one m thick, with brownish colour, and may contain organic-rich layers with

rootlets together with pyrite (Figure 10.14g and h). Two coal-rich layers occur; a 15 cm-thick layer at 518 m and a more than one metre-thick layer at 492 to 490.8 m.

The base of the Lower Unit (Hestberget Member; 527 – 486.5 m) is a 10 cm-thick conglomerate layer, containing subrounded quartz clasts up to 3 cm in size, floating in a sandstone matrix (Figure 10.14g). A 10 cm-thick intraformational conglomerate occurs at 503.8 m (Figure 10.14q) consisting of irregularly shaped clasts of sandstone floating in a siltstone matrix (Figure 10.14q).

The Upper Unit (486.5– 435.8 m) consists mainly of sandstones, with subordinate siltstones and some few thin claystone layers. The base of the member is marked by a normally graded sandstone layer. Sandstones are medium- to very coarse-grained, commonly grey, but also green coloration occurs. Within the lower and upper parts of the Upper Unit the sandstones commonly alternate with siltstones. The sandstones are flat- and cross-laminated (Figure 10.14t, u, v, y, ab), and in places syn-sedimentary deformed (Figure 10.14s, z, aa), and sometimes contain siltstone intra-clasts (Figure 10.14aa). The middle part of this unit consists of a several metres-thick sequence of massive grey or green sandstones (Figure 10.14x, w). Thicker siltstone packages occur in the uppermost part of the Upper Unit, while a 10 cm-thick claystone layer and organic-rich layers of sand- and siltstones are present in the lower part of the unit (Figure 10.14u).

Figure 10.16a and b show the texture of the weathered granodiorite at 543 m depth, while Figure 10.16c, d, e, and f show images of the weathered ‘green’ granodiorite at 527 m depth. Details regarding the mineralogy are given in the figure caption.

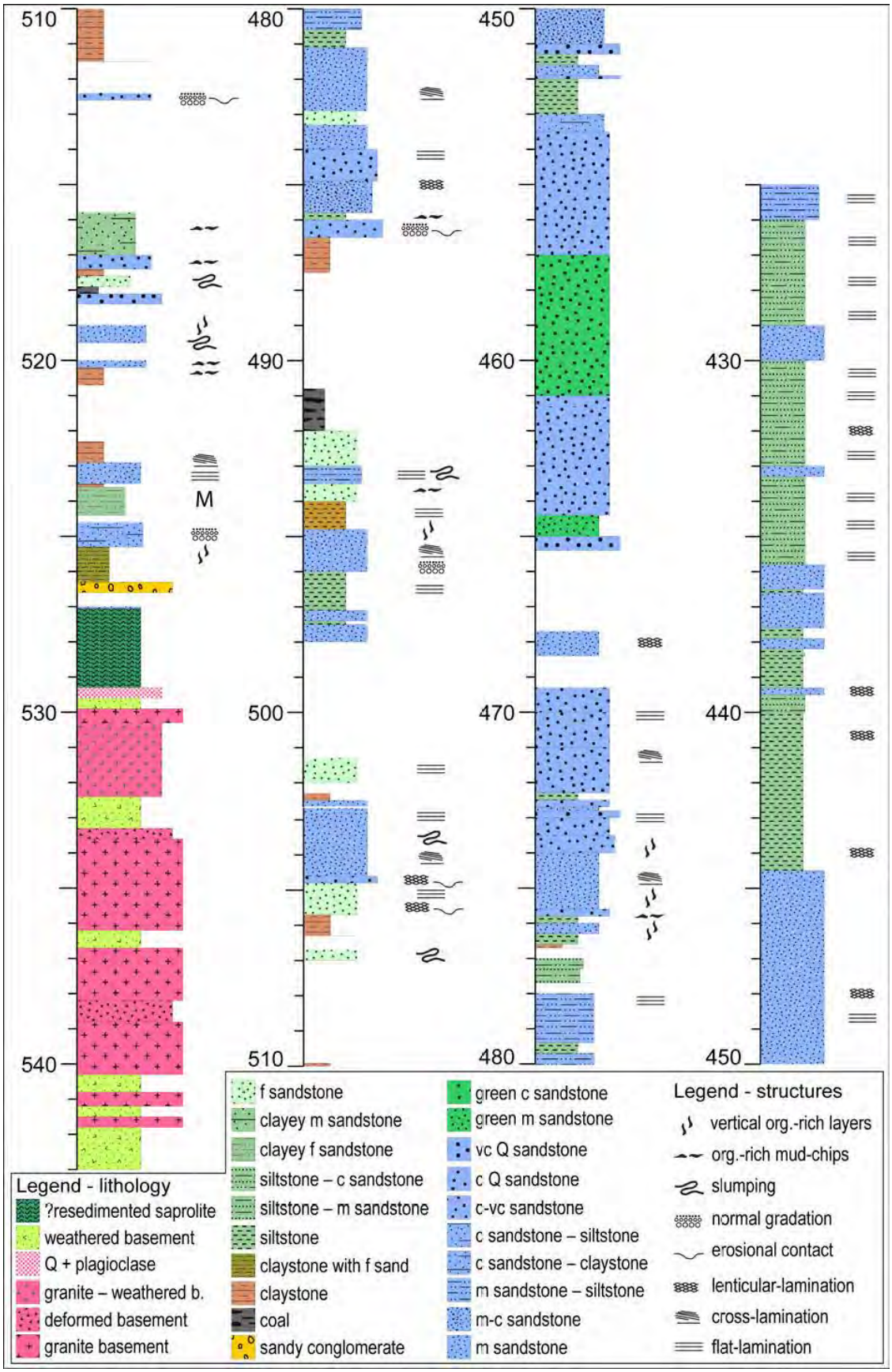

Figure 10.15. Lithological column with sedimentary structures from the lower part of Well B. The interpretations are based on investigations of cores (Fig. 6.1). The term 'granite' in the legend should actually be 'granodiorite'.

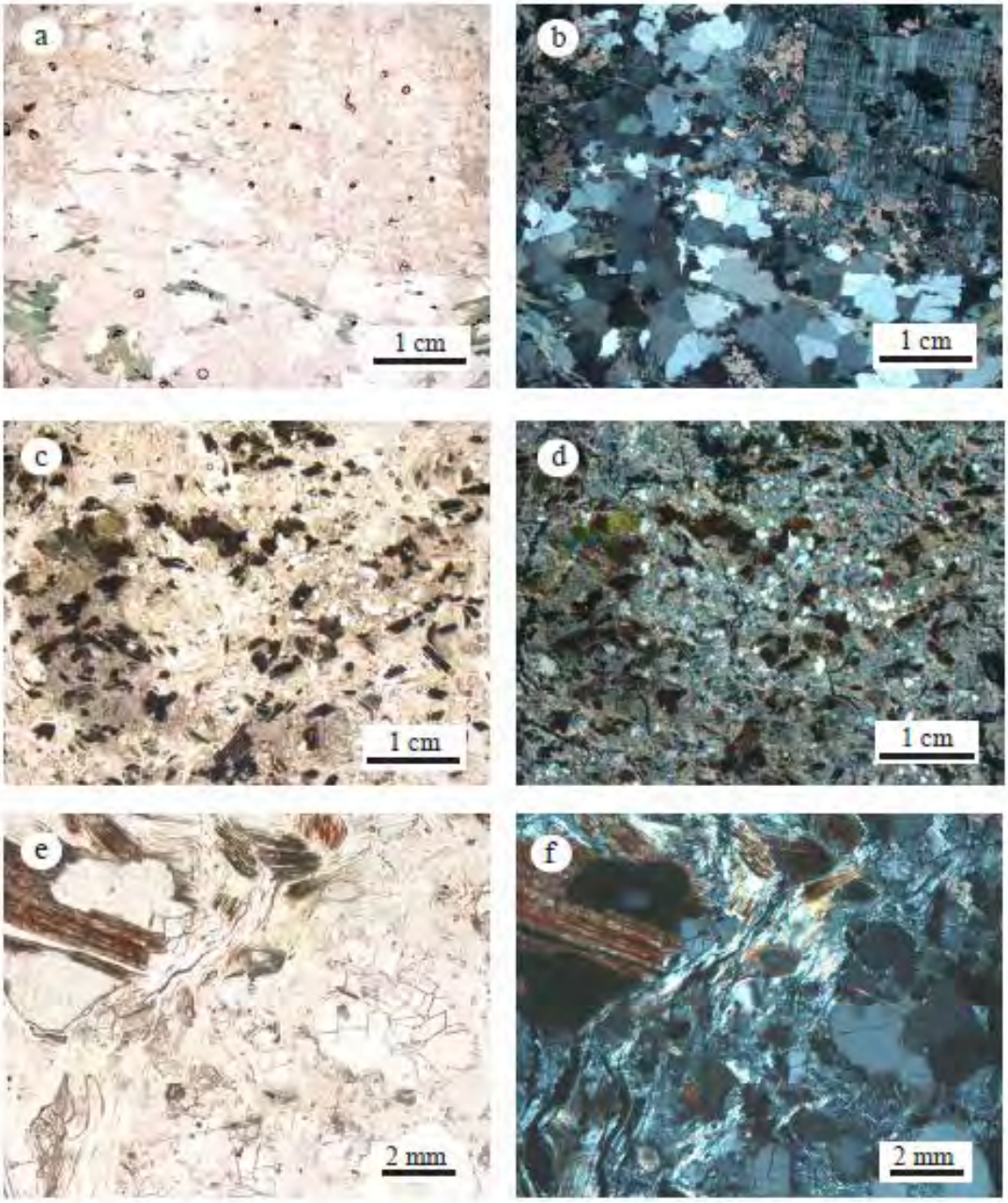

Figure 10.16. Microscopic textures of samples from Well B cores. a) Basement granodiorite containing quartz, microcline, and some chloritised biotite (Sample 543 m). b) Site a) under crossed nicols showing polycrystalline quartz and large microcline crystals overgrown by calcite (Sample 543 m). c) Sedimentary green rock (above basement) with quartz and chloritised phyllosilicate matrix (Sample 527 m). d) Site c) under crossed nicols showing the same. e) Green rock with fractured quartz grains and phyllosilicates containing Fe-oxides (Sample 527 m). f) Site e) under crossed nicols.

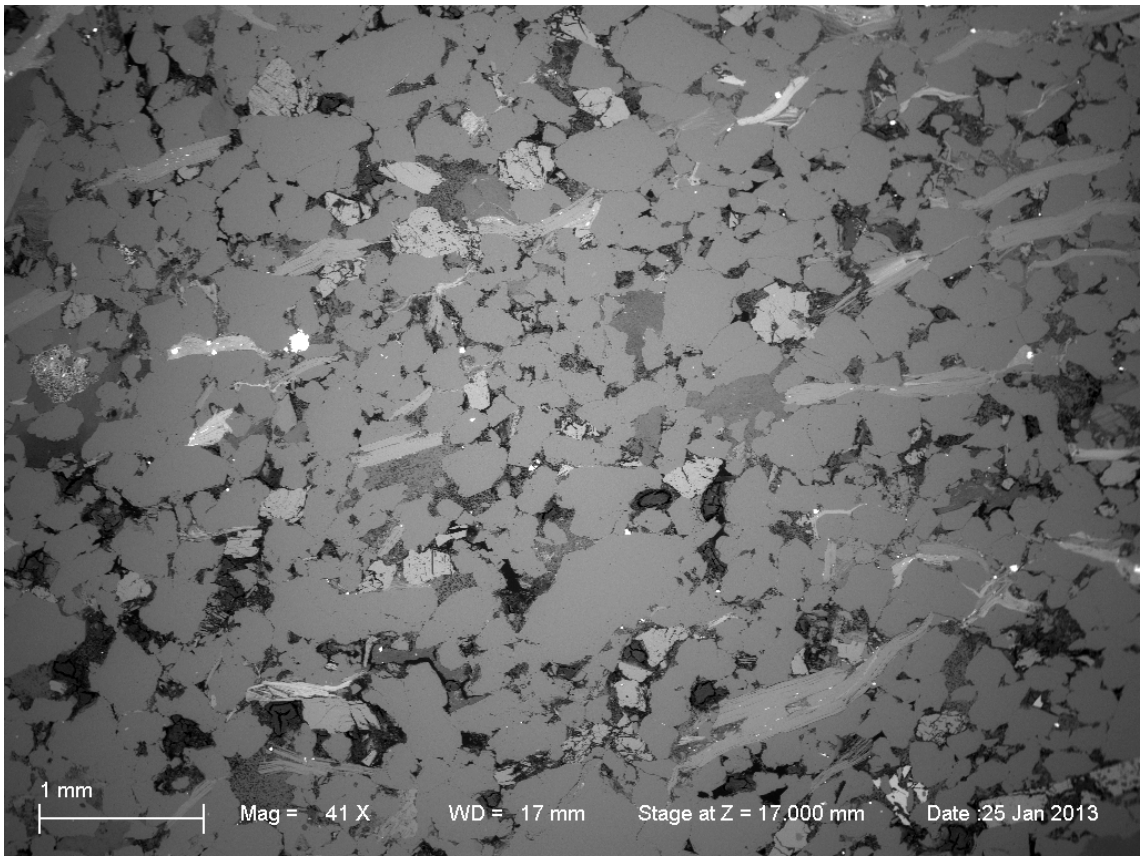

Figure 10.17. SEM BSE image of thin-section showing the quartzitic, poorly sorted sandstone at 234.5 m depth in Well B (see scale bar at left). The 20-25% non-quartz grains include mica, feldspars and kaolinite. The porosity is high, also because the authigenic kaolinite is associated with some 50% micro-porosity, which is protected from compaction by the grain-supported texture. See also how quartz grains have apparently 'melted' and re-shaped along mica grains.

10.6.2.2 Core from Well C

The contact between the basement and the overlying gritstones and sandstones has been macroscopically recognised at c. 235 m (Midbøe, 2011). The sample below the contact contains heavily fractured plagioclase and some phyllosilicates, which are chloritized and contain abundant Fe- and Mn-oxides (Figure 10.18a and b). Above the basement, gritstones contain subrounded grains of quartz, some microcline and very little clay matrix (Figure 10.18c and d).

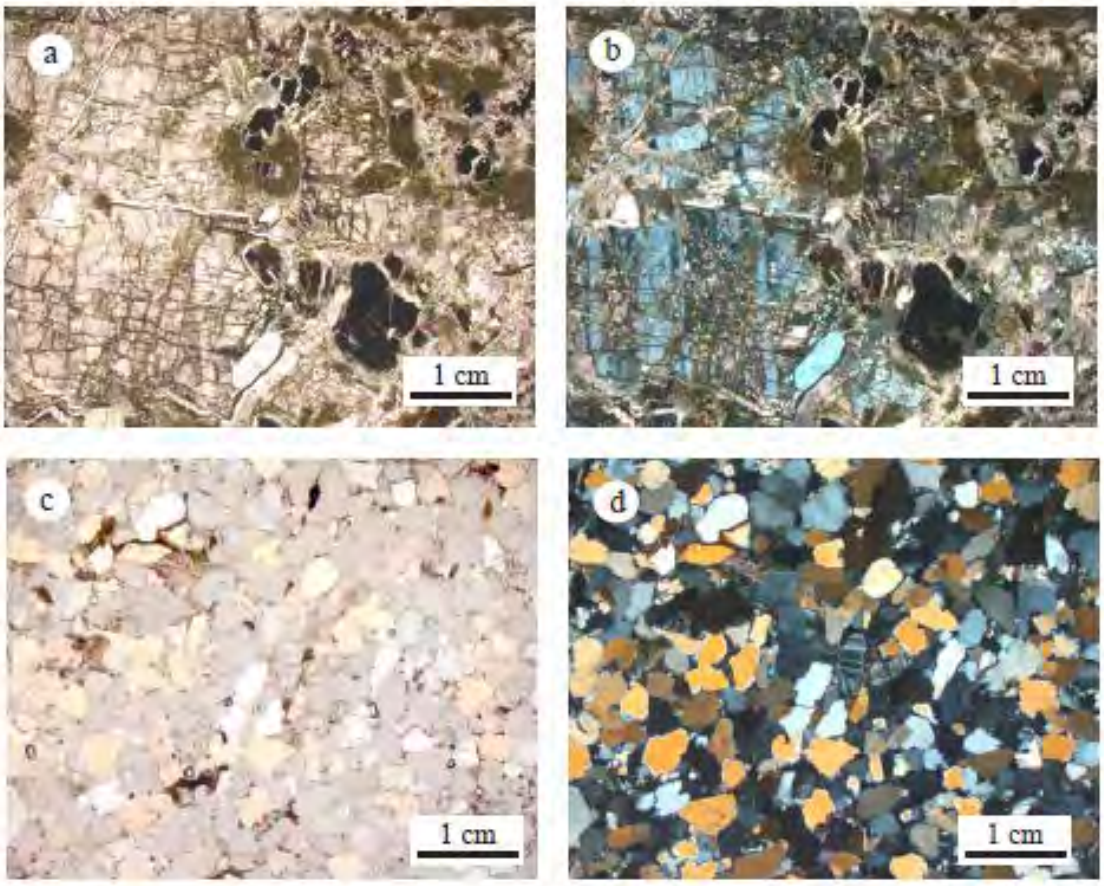

Figure 10.18. Microscopic textures of samples from Well C cores. a) Plagioclase surrounded by phyllosilicates, which are Fe- and Mn-rich and chloritised; fractures within the plagioclase are filled with calcite (239.5 m). b) Site a) under crossed nicols illustrates the same. c) Gritstone containing subrounded quartz and microcline grains and very little kaolinite (235 m). d) Site c) under crossed nicols.

The lower part of the sampled interval contains mostly carbonate (31 wt %), plagioclase (26 wt %), phyllosilicates (18 wt %) and some quartz (7 wt %). The phyllosilicates include expandable clays (5.8 wt %), kaolinite (5.7 wt %), chlorite (4.6 wt %) and biotite (2 wt %). Other minerals include magnetite and Fe-oxides (each 4 wt %) together with pyrite (1 wt %). Also present are serpentine (2.5 wt %), garnet and olivine (1 wt % each).

The upper part of the sampled interval consists of quartz sandstones that mostly contain quartz (78-86 wt %), phyllosilicates (7-15 wt %) and some feldspars (6-7 wt %); the

plagioclase to K-felspar ratio is 1:2. Among phyllosilicates, illite (2.8-6.5 wt %) and kaolinite (3.1-6 wt %) are most abundant, but biotite (0-1.6 wt %) and chlorite (0.6-1.3 wt %) are also present.

10.6.2.3 Core from Well A

The basement contact has been recognized at c. 530.8 m (Midbøe, 2011). The upper part of the sampled basement contains carbonates (2.4-4 wt %) and phyllosilicates (9-11 wt %); mainly illite (2.8-3.7 wt %), expandable clays (2.1-3.5 wt %), kaolinite (0-1.8 wt %), glauconite (0-1.2 wt %), and chlorite (0-3.9 wt %) (Figure 10.19a and b). Also present in minor amounts are magnetite (<1 wt %) and olivine (<0.5wt %).

The lowermost part of the basement has quartz (26 wt %), plagioclase (45 wt %), and phyllosilicates (26 wt %), mainly biotite (20 wt %), while clay minerals occur in minor amounts (<2 wt %). Also present are clinopyroxenes (<1 wt %) and small crystals of pyrite. No K-feldspar is observed (Figure 10.19c and d).

The sedimentary rocks (Figure 10.19e and f) contain mainly phyllosilicates (50-60 wt %), quartz (20 wt %), two feldspars (8 wt %), and carbonate (3-5 wt %). Among phyllosilicates, clay minerals are abundant and include illite (0-23 wt %), expandable clays (3.7-9.3 wt %), and kaolinite (4.5-8.4 wt %). Also present are chlorite (2-16 wt %), muscovite (0.9-17 wt %), and biotite (0-2.8 wt %). These rocks also contain olivine (0-8 wt %), pyrite (3-8 wt %), pyroxenes (1-2.8 wt %), and some Fe-oxides and rutile (each < 1 wt %).

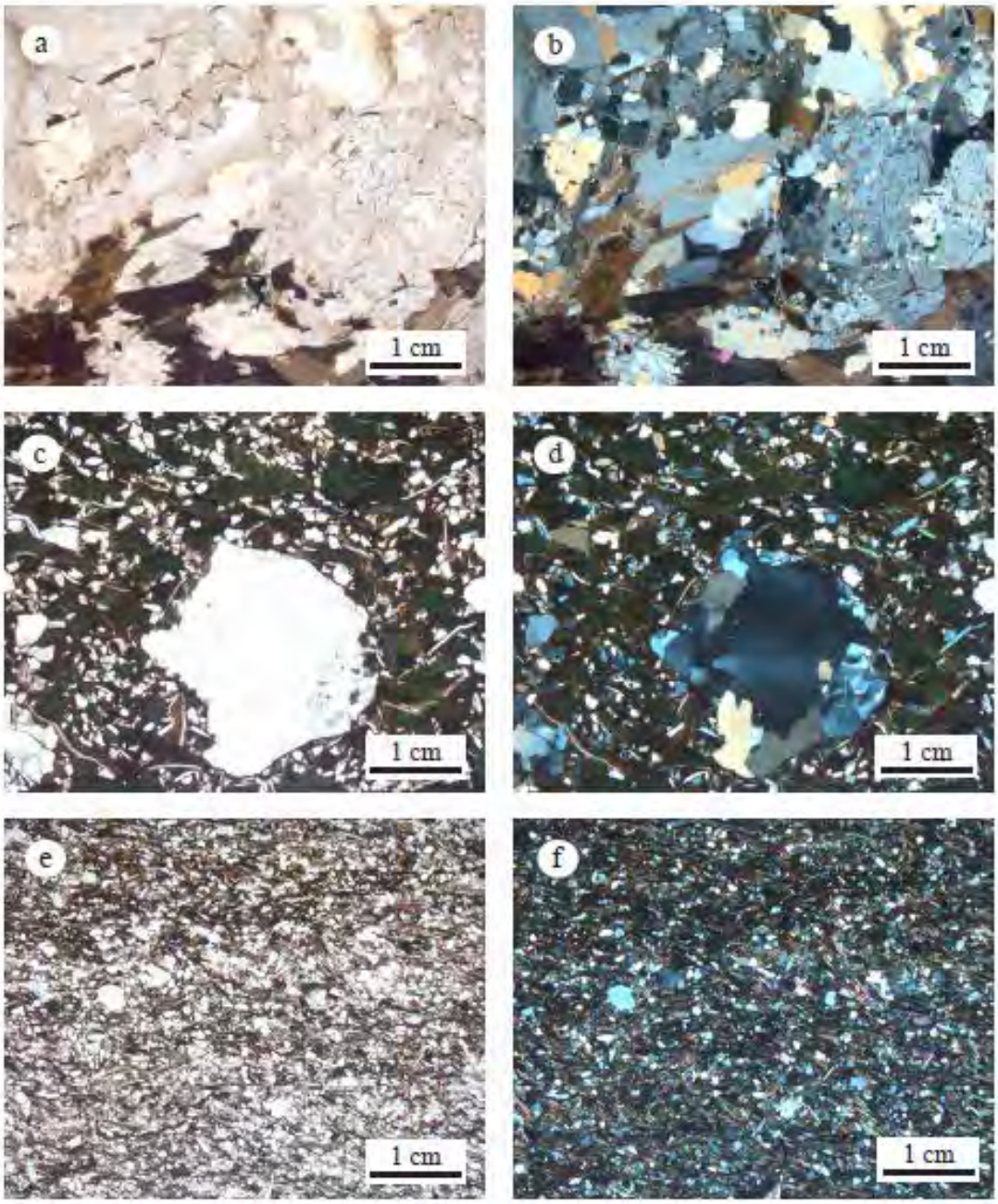

Figure 10.19. Microscopic textures of samples from Well A core. a) Granodiorite containing abundant plagioclase, quartz and unaltered biotite (543.5 m). b) Site a) under crossed nicols shows also a thin calcite vein. c) Fine-grained sandstone containing cm-sized quartz grains (529 m). d) Site c) under crossed nicols illustrates the same. e) Granodiorite with large quartz crystals surrounded by phyllosilicates (527.6 m). f) Site e) under crossed nicols.

Well A and C cores: lithostratigraphy and mineralogy: The mineral compositions of samples from cores Well A and Well C are illustrated in vertical plots in Figure 10.21. Drillcores A and C contain plagioclase throughout the basement profile, but the deepest sample has no K-feldspar. This, and the geochemical and mineralogical composition of the basement from bottom to top, shows no obvious trends that indicate increased weathering

towards the upper part of the basement. This indicates that weathering of the basement in these areas never occurred; or that the saprolite was eroded during later uplift.

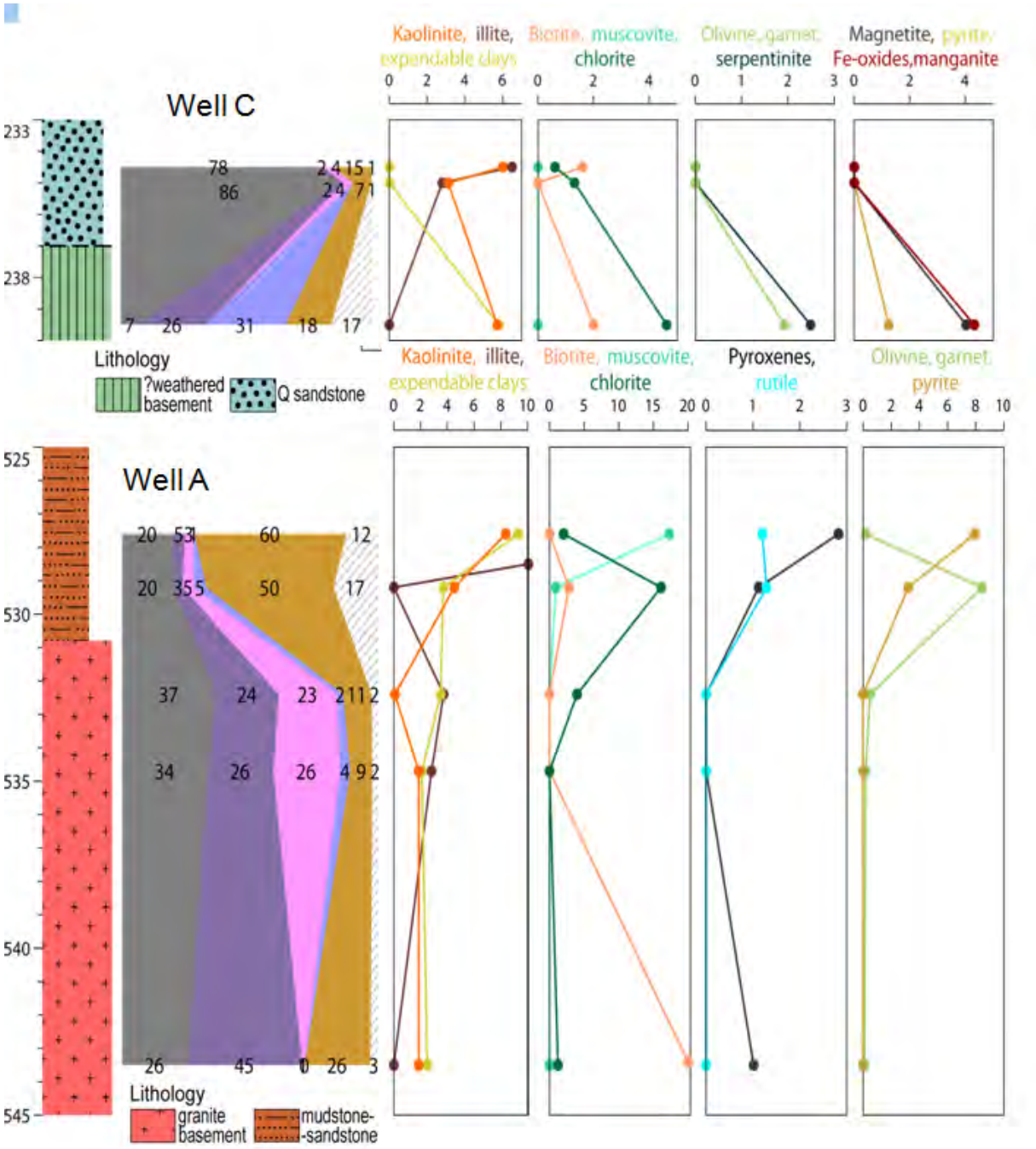

Figure 10.20. Wells C and A: Lithostratigraphic column with plots of mineralogy. Lithology codes are given in Fig. 10.15. The term 'granite' in the legend should be 'granodiorite'.

10.6.3 Cores from Norminol Wells A, B and C: geochemistry

Geochemical compositions of spot-sized parts of the Well B core were measured by a portable XRF analyser. Major elemental ratios versus Al are used in order to interpret the relative amounts. Cores from Wells C and A, however, were sampled and analysed at the NGU lab, and the XRF data are given as absolute values.

10.6.3.1 Well B core: geochemistry

The granodiorite basement: The granodiorite basement (543-529.1 m) shows a quite heterogeneous geochemical composition with Si/Al ratios between 4 and 17 (Figure 10.21). The middle part of the logged granodiorite basement (538-532 m) contains somewhat stable relative amounts of major oxides with elemental ratios vs. Al around or less than 0.5. Compared to the middle part of the granodiorite basement, the lowermost and uppermost parts (543-528 m and 532-529.1 m) contain higher relative amounts of K (higher K/Al ratios), in some samples also increased relative amounts of Ca and Fe (up to 1) and no Mg. These are also the intervals with higher ratios of Mg+Ca+K/Al, which is the best approximation for the parameters ∑Bases/Al and CIA used in other drillcores.

The green rock: The green rock contains much higher relative abundances of Fe than the underlying granodioritic basement. This interval has stable Si/Al ratios of around 4, which is lower than the average of the granodiorite basement.

The Ramså Formation: The lowermost part of the Ramså Formation has high Si/Al ratios and – apart from the lowermost sandy claystone with relative high Fe and K contents – also very low relative contents of all the main geological elements.

Lithostratigraphy and geochemical parameters: Basement in the cores from Well B is texturally (Figure 10.16) and geochemically (Figure 10.21) heterogeneous, without any obvious increase of weathering towards the top part of the basement. The green rock has low Si/Al ratios indicating relatively large amounts of clay minerals: the only lithology having lower Si/Al ratios are claystones. Relatively large amounts of clay minerals together with increased amount of iron, associated with the phyllosilicates, allow us to speculate that the green rock may represent a redeposited saprolite. The conglomeratic bed overlying the green rock contains several cm-large quartz clasts and indicates erosion and redeposition of terrigenous material in a high-energy environment.

The lower member of the Ramså Formation recognised in this study corresponds to the Hestberget and Kullgrøfta members *sensu* Dalland (1974): the Lower Member and the Hestberget Member consist mainly of coarse-grained quartz sandstones, whereas the thickest coal-rich layer near the top of the Lower Member is probably representing the Kullgrøfta Member.

The upper member of the Ramså Formation corresponds to the Bonteigen Member, containing mainly medium- and coarse-grained sandstones (Dalland 1974). The Hestberget Member indicates deposition in paralic, continental to shallow-marine environments. Some claystones and siltstones contain vertical organic-rich layers, interpreted as rootlets or injections of organic-rich mud. The sandstone-siltstone interbeds are commonly cross-laminated, indicating migration of ripples in a shallow–water environment. Quartz sandstones are commonly slumped, indicating steepening of the depositional area, possibly due to tectonic activity. The thick coal layer of the Kullgrøfta Member reflects deposition in peat-forming swamps, which were interpreted to have occurred regionally (Petersen et al. 2013).

The Bonteigen Member was deposited in shallow-water marine environments on the inner shelf and the cross-bedded sandstones are derived from migrating dunes. The upper part of the Bonteigen Member, however, consists of massive green sandstones, probably containing glauconite, and therefore deposited in a middle- to outer-shelf environment.

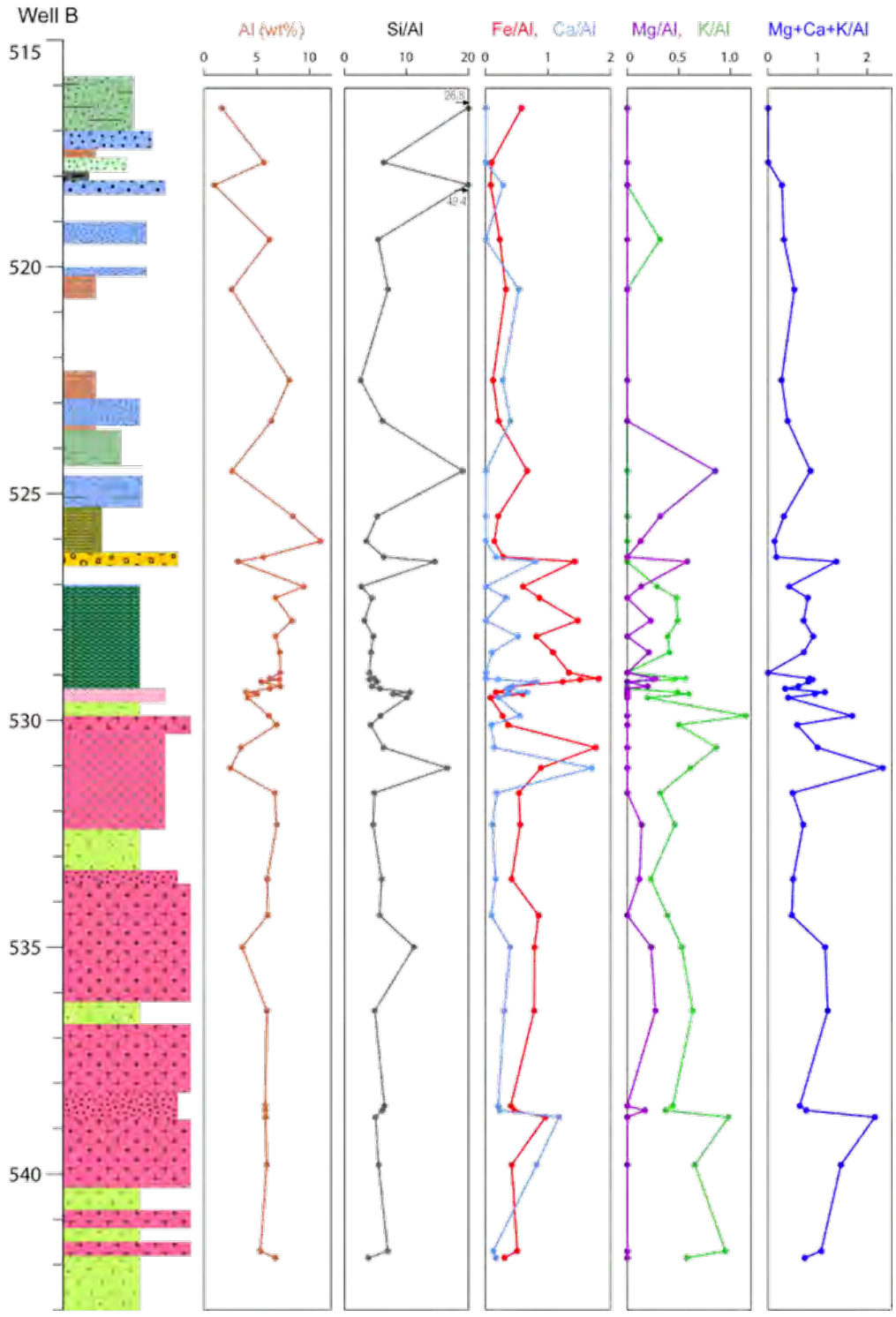

Figure 10.21. Well B: Lithostratigraphic column with plot of geochemical parameters, based on point-analysis with a portable XRF spectrometer. The Si/Al ratio is rather stable up through the basement, with the exception of a point at 535 m depth and another at 531 m depth. The basement boundary is set at 530 m depth, and from this point and upwards the chemical signature changes to a more wiggly pattern, showing the heterogeneity of the sediments. Lithology codes are given in Fig. 10.15. The term 'granite' in the legend should be 'granodiorite'.

10.6.3.2 Well A core: geochemistry

The lowermost samples from the granodioritic basement contain 65 wt % silica and 15 wt % Al_2O_3, while the other main elements range in abundance from 1 to 6 wt %. From bottom to top, the granodioritic basement shows an increase in silica from 65 to 75 wt % and a concomitant decrease in the other major elements (MgO, CaO, NaO and Fe_2O_3). The uppermost part of the granodioritic basement contains Na_2O and K_2O above 2 and 5 wt %, respectively. A slight decrease in TiO_2 and Zr is seen from bottom to top. The values of CIA are stable throughout the granodiorite basement, varying from 52 to 55.

The overlying sedimentary rocks contain less silica (48-54 wt %), similar amounts of Al_2O_3, MgO, CaO and K_2O, higher amounts of Fe_2O_3 (6.5-22.3 wt %), and lower amounts of Na_2O (<1 wt %). TiO_2 and Zr contents are similar to the lowermost sample of the granodiorite basement. The CIA values are higher than for the underlying granodiorite basement, varying from 64 to 73.

10.6.3.3 Well C core: geochemistry

The lowermost sample, most probably from weathered basement, contains high amounts of CaO (22.6 wt %), Fe_2O_3 (13.5 wt %) and some Na_2O. According to the XRD data, this sample contains 34 wt % of carbonate minerals, mainly calcite. This means that 19 wt % of CaO occurs in carbonates and the remaining c. 3.6 wt % of CaO occurs in other minerals, mainly plagioclase. This sample also contains high amounts of Fe_2O_3 (13.5 wt %) and of Ti_2O (3.4 wt %). The CIA is low (30) and the ∑Bases/Al high.

The quartz sandstones overlying the basement contain mainly silica and Al_2O_3; also present is some K_2O and Fe_2O_3, while the amounts of other elements are low (<0.5 wt %). CIA has values of around 70.

The gritstones and coarse-grained sandstones (with subrounded to subangular quartz grains) overlying the basement in core C indicate transportation of quartz grains from a saprolitic source area. The coarse-grained sandstones of drillcore C indicate deposition in high-energy marine environments, whereas siltstones interbedded with sandstones and abundant pyrite in drillcore A indicate a lower energy depositional environment.

10.7 **Cores from NGU boreholes BH 1 and BH 2**

Borehole BH 1 was drilled at Ramså, while BH 2 is located c. 2 km NNW of BH 1.

In the map in Figure 8.5 it can be seen that BH 1 occurs in an area marked as sedimentary rocks (schists and sandstones), while BH 2 is located in an area marked as gabbro and hornblende gneiss. Sixteen core samples were selected from NGU boreholes BH 1 and BH 2; eleven from BH 1 and five from BH 2 (Table 10.2).

A brief description of the cores from BH 1 is given below. Photographs of the core boxes, with more detailed descriptions given in the figure captions, are presented in Appendix 2. The depths are given in metres:

113.50-129.78 m: Variegated, fine-clastic sediment, with abundant kaolinite. Mainly a mafic derived sand, but also some quartz-feldspathic layers. Possibly some chert layers and thin layers of clay (possibly smectite?).

129.78-143.20 m: Biotite, talc and chlorite-rich sediment with talc lenses . Some enigmatic rock fragments were not identified.

143.20-144.30 m: Polymict conglomerate with abundant matrix. Similar composition as above.

144.30-182.16: Monomict sedimentary breccia, with fragments of fine-grained light grey sandstone, also as layers and in matrix with talc and chlorite. Some enigmatic rock fragments were not identified.

182.16-190.55 m: Polymict conglomerate with abundant matrix, interlayered with thin layers of fine-grained light-grey sandstone.

190.55-193.75 m: Talc-rich sediment with talc lenses . Some enigmatic rock fragments were not identified.

193.75-203.80 m: Granodioritic basement. Possibly a weathering zone at 193.75-193.80 m depth.

10.7.1 Mineralogy from XRD analysis

The interpretation of the X-ray diffractograms of the bulk samples is given in Table 10.4. The table includes sampling depths and a classification of the samples given by colour coding. The samples coloured yellow are sediments; the orange colour represent a transition zone from the weathered sediments and down to a gabbroid rock, which is interpreted to be in the greenschist facies and given a green colour. The samples from BH 2 represent unweathered basement and are coloured blue.

10.7.1.1 Samples 113.4 and 113.95:

These are weathered sediments, with high contents of kaolinite. They also have high contents of K-feldspar, but very little plagioclase, which is supposed to be the source for the kaolinite formation. The lack of quartz may indicate either that it is a very fine-grained sediment or that the source area for the sediment did not have quartz; e.g., a basic rock, such as gabbro. This last suggestion was confirmed by SEM investigations of thin-sections cut from these rocks which show that the rocks were initially feldspathic sandstones with medium-sized grains (Figure 10.22).

Table 10.5 Mineral composition of bulk samples from BH 1 based on XRD, in weight %. The amphibole at depth 115.6 m is actinolite, while the amphibole in samples 195.1 m and 205.3 m is hornblende. Abb.: Qtz= quartz; Kf=K-feldspar; Pla=plagioclase; Ill/m=illite and muscovite; Biot=biotite; Kao=kaolinite; Chl=chlorite; Talc=talc; V=vermiculite; S=smectite; M=mixed-layered 10Å/14Å minerals; Am=amphibole; He=hematite; Ca=calcite; Pyx=pyroxene; Py=pyrite; An=anatase; Stil=stilbite;To=tourmaline; tr=trace.

Depth (m)	Sample No.	Qtz	Kf	Pla	Ill/m	Biot	Kao	Chl	Talc	V+S +M	Am	Stil	He+ Ma	Ca	Other
113,4	98596	7	23	11			48			3			2	4	1Py
113,9	84002	8	19		1		38	7		22			2		3An
115,7	98597	29						tr			15	3		47	6Py
121,8	98598	18	1	31	3			36		8					3Py
132,4	98599	2		12	11	32		3	38	1			1		
134,7	98600			6	8	49		5	31	3			4		2Py
158,2	98592	2	2	33	2			23	19	16			3		
167,0	84001	2		45	2	8		5		30			8		trTo
185,7	98593	2			11	30		16	32	3			4		2Py
188,5	98594	6		32	3	5		29	14	7			3		
195,1	98595	3		24	1						64	5			1Pyx
200,6	98587	35	20	37	5			2					tr		1Py
201,3	98588	38	19	31	5			1					tr	6	tr Py
205,3	98589	20	1	10	3			9		4	51	2			
207,5	98590	42	6	41	10			1					tr		tr Py
212,2	98591	36	29	30	1								1		3An

Another question is whether the clay was deposited together with sand (as a slide), or if the clay (kaolinite) was formed *in situ*. Figure 10.23 shows a pore between sand grains, filled with kaolinite. The clay shows two textures, one a homogeneous structureless texture, and another with kaolinite in a worm-like growth habit; i.e., vermicular kaolinite. Such structures would never survive an erosion and transportation process without dispersion of the single kaolinite platelets. Based on this, it is suggested that the kaolinite was formed *in situ*, probably during a diagenetic process. In a profile with meteoric weathering, one would expect to see rootlets and other biogenic structures that would disturb the development of these delicate clay structures. These are not seen here.

The sediment was grain-supported; i.e., the weight of the overburden was carried by the contacts between sand grains. An important effect of this grain-supported sediment texture is that newly formed kaolinite is protected from the lithological compaction pressure exerted by the overlying sediments. Authigenic kaolinite in sandstone pores has typically around 50% porosity; i.e., micro-porosity, and the abundance of desiccation cracks in the clay matrix seen in the thin-sections shows that this micro-porosity was not reduced by compaction (Figure 10.22 and Figure 10.23).

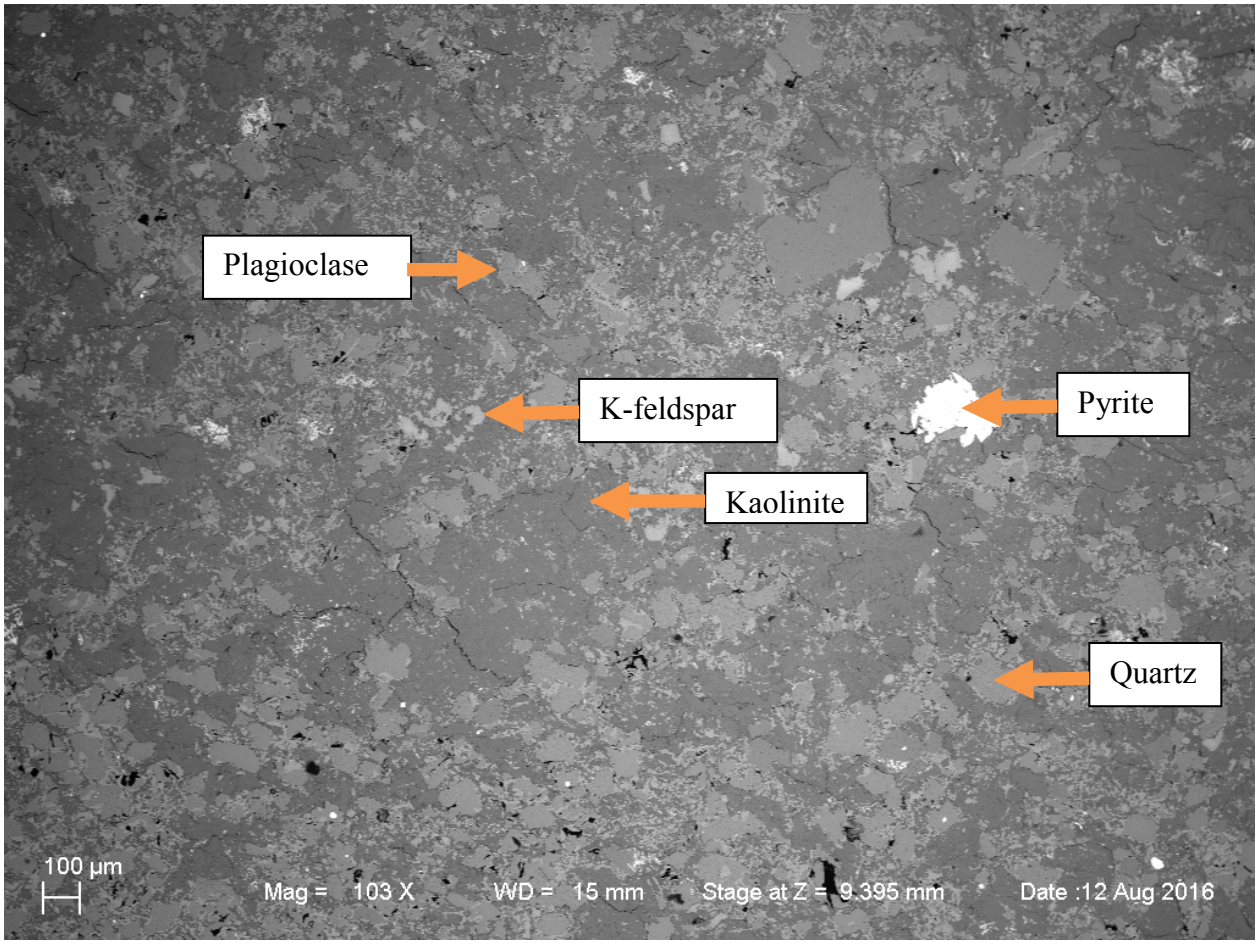

Figure 10.22. SEM-BS micrograph of the texture in sample 113.4. Magnification 103X (scale bar to the left).This was initially a grain-supported sediment of medium sand. But extensive dissolution of feldspar grains has apparently changed this to such an extent that sand grains are 'floating in clay'; i.e. in this 2D image. Authigenic kaolinite has commonly around 50% porosity (i.e. micro-porosity), and this is manifested by desiccation cracks in the clay-filled areas.

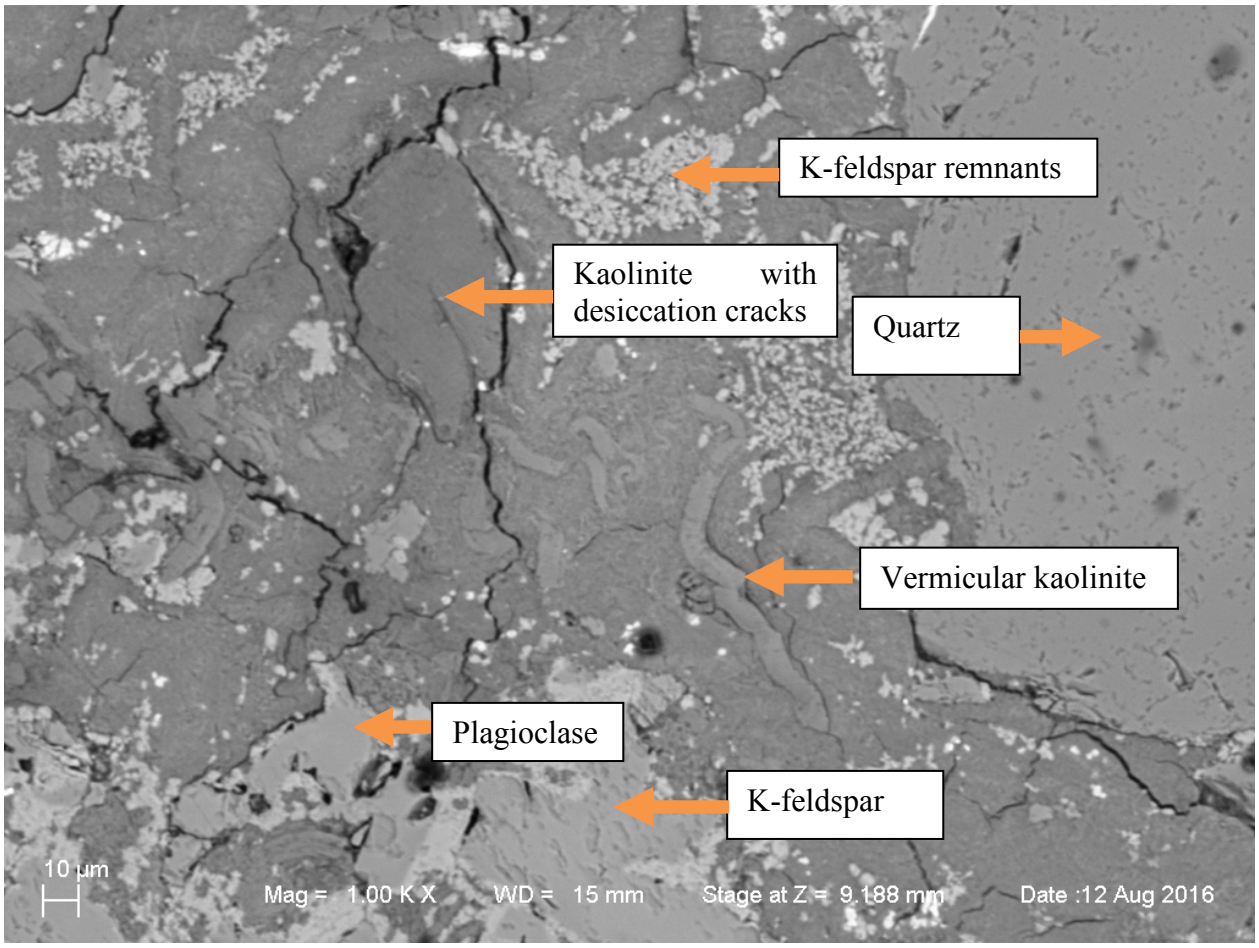

Figure 10.23. SEM-BS micrograph of the texture in sample 113.4 at 1000X magnification (scale bar to the left). The image shows a clay-filled pore between sand grains. Most of the feldspathic sand grains are dissolved, and kaolinite is filling the space of the dissolved grains. The clay has two different textures; one a homogeneous structureless pore filling, and one with vermicular (worm-like) kaolinite. The lighter spots are remnants of K-feldspars. The sand grain to the right is quartz. Note the desiccation cracks in the clay.

10.7.1.2 Sample 115.7:

The correct sampling depth is actually 115.70-115.85 m. It was originally suggested that basement was at 114 m depth in this well, but the well logs (Chapter 8) gave an ambiguous signature just below this depth and observation of likely primary layering and also Jurassic palynomorphs in this basal conglomerate indicated a sedimentary origin (Chapter 9.2.2) and the top basement was finally defined at c. 194 m (Figure 8.7). Sample 115.6 represent a rock from this basal conglomerate. The mineral paragenesis of this rock is strange, by its composition of quartz, actinolite, and calcite. This is illustrated in Figure 10.24 where two of the minerals, quartz and actinolite, are identified chemically by SEM-EDS.

It looks as if actinolite was transformed into calcite and quartz in a diagenetic process and that these 'new' minerals are filling up fractures and pores. Quartz is characterised by ribbons and scabbards, partly with radial structure and zonation growth, marked by entrained dust. These features suggest also that this is a diagenetic process.

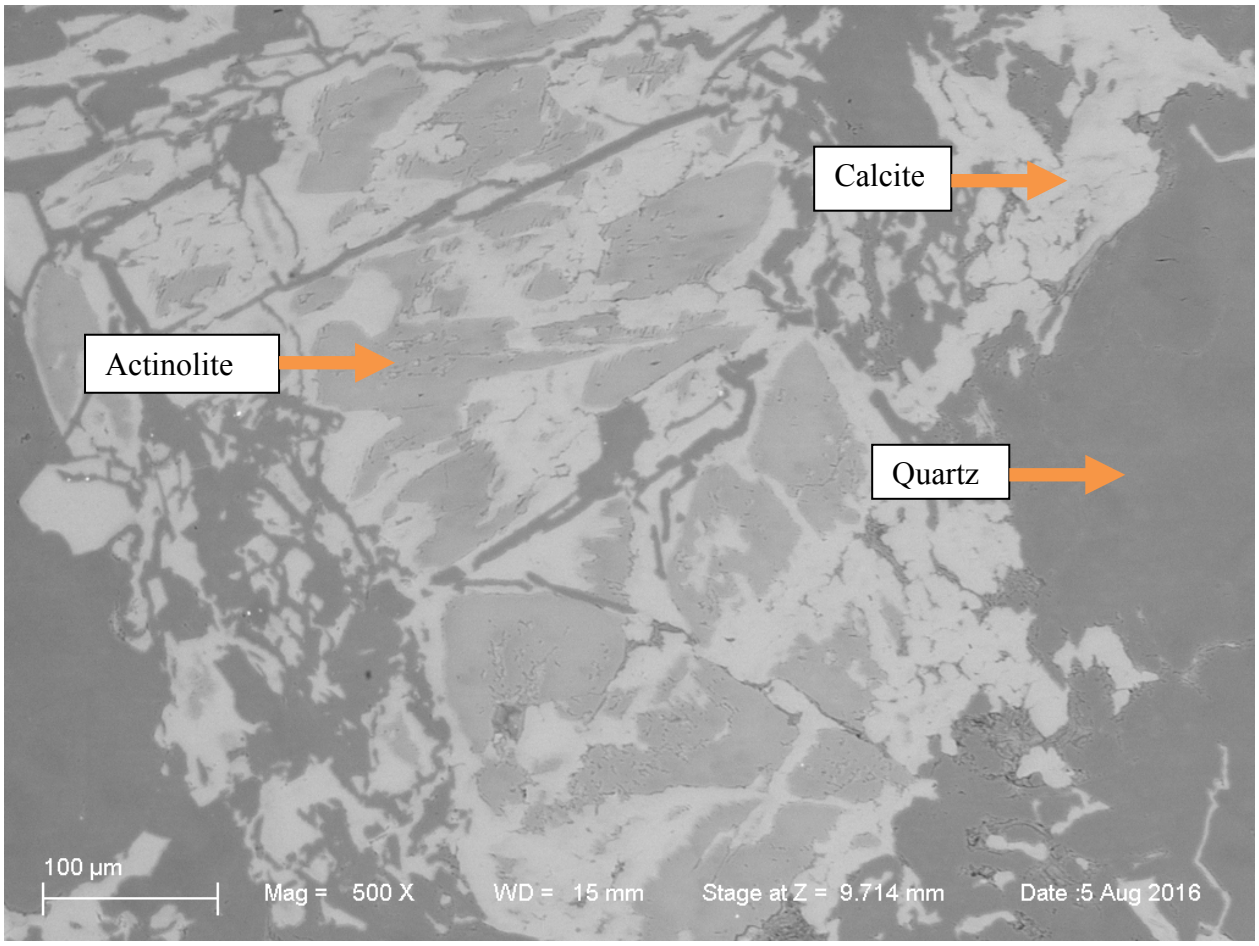

Figure 10.24. SEM-BS image of sample 115.7 at 500X magnification (scale bar to the left). This rock is enigmatic, as it has a strange mineral paragenesis compared to the other lithologies in the profile, with quartz, actinolite, and calcite. The image shows the texture of the rock, with the distribution of the three minerals. The rugged shape of the actinolite and quartz grains gives an impression of a pervasive diagenetic process, where actinolite alters to calcite and quartz.

10.7.1.3 Sample 121.8:

This is the second rock in this transition zone. However, this rock type is more like the rock below it, with abundant plagioclase, chlorite and mica (Figure 10.25), but like the rock above it also contains significant amounts of quartz, i.e., the sediment has more than one source. Thin-section SEM analysis of the rock reveals a texture where the phyllosilicates show some orientation, but there are no identifiable sedimentary structures. Phyllosilicates, quartz and feldspars show a wide range in grain sizes. The ‘random’ grain-size distribution does not fit with sedimentation in water, but rather with a debris flow, where big grains and clasts are supported by the high ‘pseudo density’ of the slurry, thus maintaining grain contacts during flow. Thus, it is suggested that this is an altered rock, with an original gabbroic composition in amphibolite facies. The mineralogy of the underlying rock is similar, with abundant plagioclase, chlorite and biotite (or phlogopite). The distribution of pyrite particles (<50 micron) also indicates that mineral transformations have taken place, including the crystallisation of pyrite.

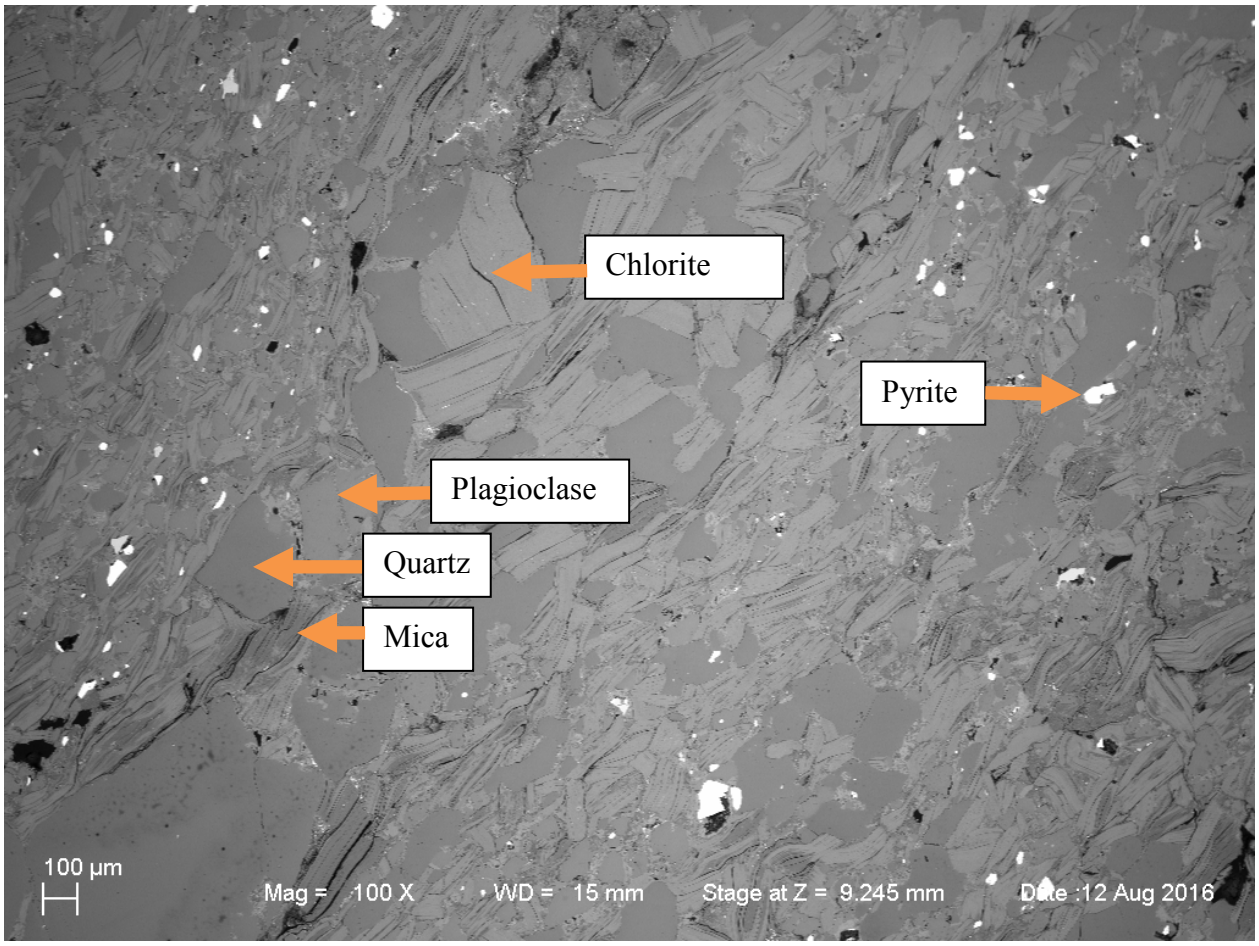

Figure 10.25. SEM-BS micrograph of sample 121.8. Magnification 100X (scale bar to the left). The texture is dominated by phyllosilicates with a wide range of grain size. Quartz and feldspar are also showing large variations in particle size. Some orientation of the phyllosilicates is seen, but the lack of sedimentary structures, and the large spread in grain size suggests that this is a debris flow, just like the rock shown inFigure 10.24. This site on the thin-section shows a number of pyrite crystals; generally finer than 50 micron.

10.7.1.4 Samples 132.4 to 188.5:

These are the Group 3 samples, which are characterised by having plagioclase, talc, biotite, chlorite, muscovite/illite, vermiculite and hematite. The rock is magnesium rich, and the biotite composition (on SEM-EDS analysis) indicates that it is phlogopite rather than biotite. Chloritisation of biotite is also observed. The mineral paragenesis indicates that the rock is an altered gabbroic intrusion.

Inspection of the drillcores shows a brecciated or conglomeratic texture, with a wide range of grain sizes of angular rock fragments. The content of the finer grained matrix is variable. However, some sedimentary features are seen; e.g., sandy layers, which is evidence of transportation in water. Even pebbles of talc are preserved during transportation and sedimentation. These talc pebbles may be clasts from 'talc beds' that have been subsequently eroded and redeposited in these debris flows. The angularity of these rather soft rock fragments (talc, chlorite and biotite) indicates very short distance of transport. Some of the

clasts seem to be plastically deformed by compaction prior to consolidation. The sediments are, therefore, interpreted to represent debris flows arising from transportation down steep slopes, where fluvial and gravitational forces are acting together. Other parts of the sequence seem to be more fluvially dominated, with formation of conglomerates. The texture and mineralogy of these debris flow deposits is shown in Fig. 7.5 and in the core photographs of Appendix III; e.g. Fig. A3-7B.

The provenance of these deposits is suggested to be an elevated block of altered mafic composition, brecciated during tectonic events in Mid Jurassic time, with syn-tectonic erosion and deposition of the short-transported rock debris. This age is confirmed by dating of palynomorphs found in the sediments (Chapter 9). It is suggested that this elevated basement block must have been west of Ramså, and with a transportation direction towards east (and north). Since these rocks are found only in NGU Well BH 1, it is inferred that the deposits have a very limited extension.

Sample 167.0 m represents a 25 cm-thick layer of fine-grained sediments in this sequence, but this sample contains no talc (see Table 10.5). Instead, it contains crystals of diagenetically formed tourmaline up to five mm in size. Tourmaline was hardly detected on XRD, because the big crystals were spread throughout the matrix with some distance between them; i.e. low bulk concentrations. Since seawater is the main source of boron to form tourmaline crystals, it is reasonable to assume that marine conditions (in the pore system) prevailed during this diagenetic event. The porosity of the sediments is still saturated with salt water. The mineralogy of this sediment indicates an altered tuffite composition, with abundant plagioclase, swelling clay minerals, biotite, chlorite and hematite. Some quartz is also found, suggested to be diagenetic from the dissolution of tuffaceous glass and the formation of clay minerals.

The chemical composition of Sample 167.0 m is also indicating a tuffaceous composition, but the diagenetic processes have caused an increased loss-on- ignition (LOI) (due to formation of clay minerals), leaching of calcium, increase in magnesium, and an increase in titanium (Gale et al. 2013). In the text, however, this sample is referred to as ‘light-grey sandstone’.

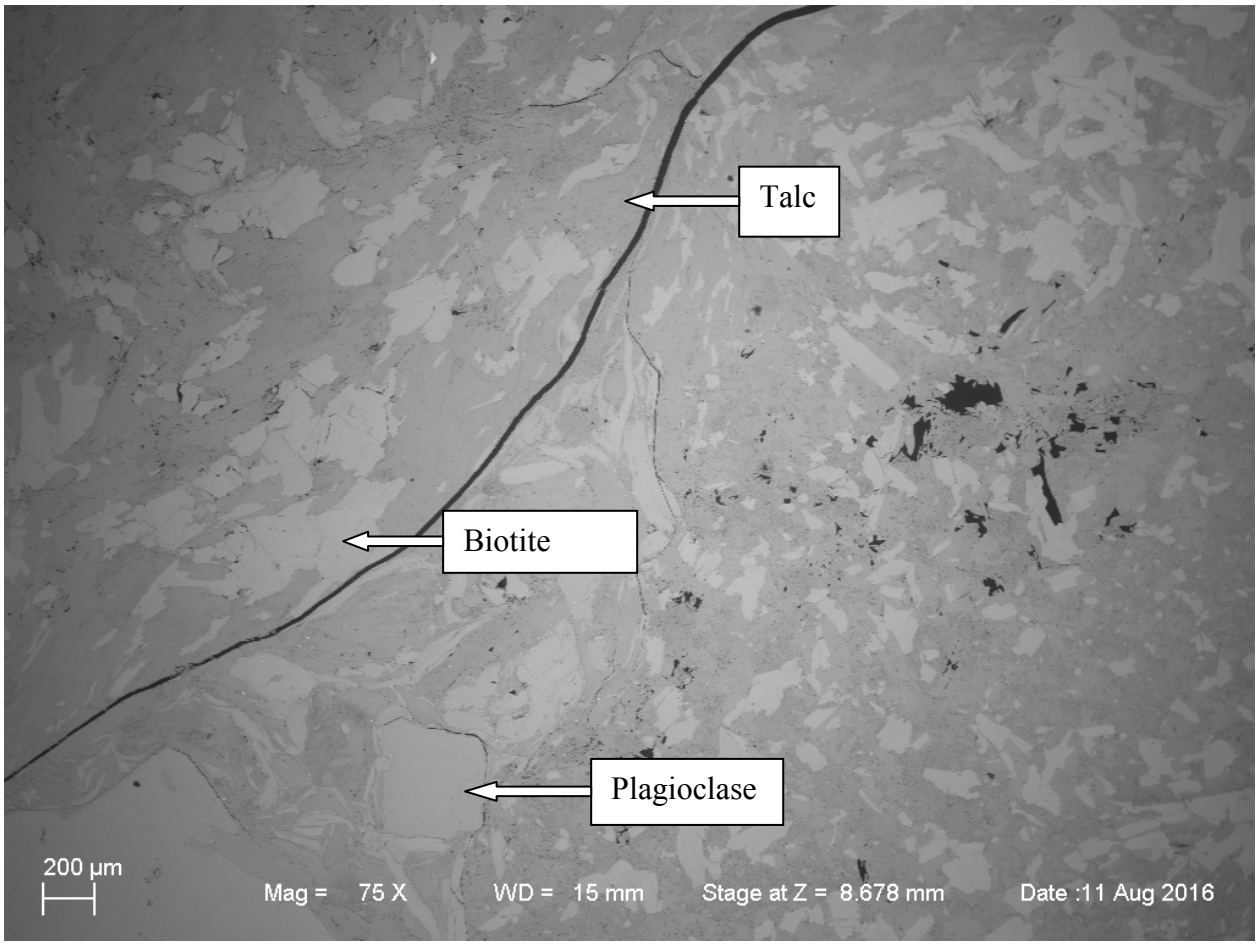

Figure 10.26. SEM-BS micrograph of sample 134.7. Magnification 75X (scale bar to the left). The texture is dominated by phyllosilicates (talc, chlorite, vermiculite and biotite) with a wide range in grain size. Plagioclase is also showing large variations in particle size. Some orientation of the phyllosilicates is seen, but the lack of sedimentary structures in addition to the large spread in grain size suggests that this is a debris flow or talus-fan. This is a magnesium-rich rock, and the biotite is high in magnesium and low in potassium, and may belong to the phlogopite group of mica. The low potassium content makes it difficult to distinguish between phlogopite, vermiculite and chlorite based on SEM-EDS analysis.

10.7.1.5 Sample 195.1:

The basement contact in this well is at 193.7 m, with a thin weathering zone in the basement surface, from 193.75 to 193.80 m. The present sample represents the upper part of the basement (below the weathered zone). The sample shows a magmatic texture with laths of plagioclase and an interstitial phase of mafic minerals that have recrystallised to aggregates of hornblende. The rock is suggested to be an intrusive sill. Trace amounts of rutile and veins of calcite are seen in thin-section.

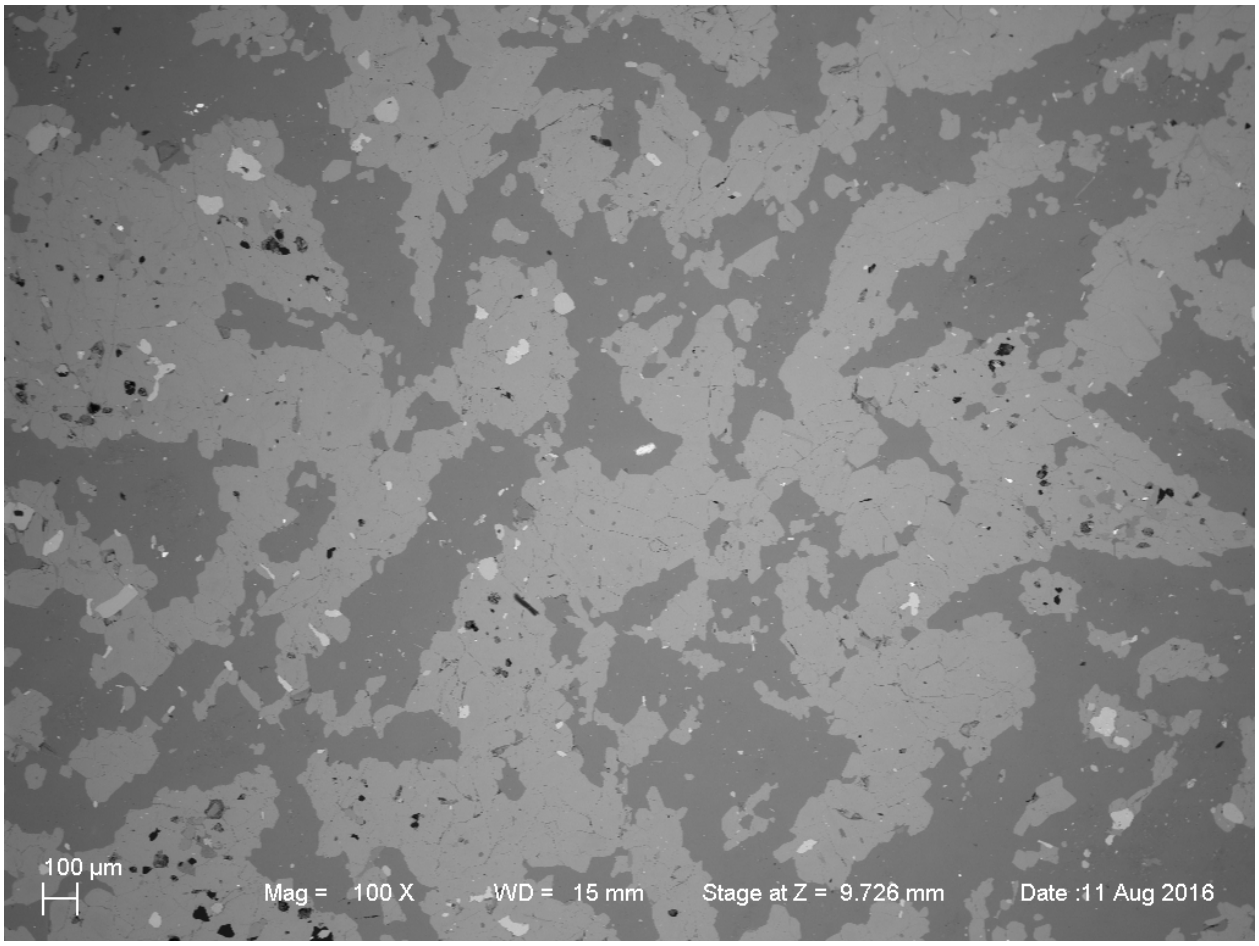

Figure 10.27. SEM-BS micrograph of sample 195.1. Magnification 100X (scale bar to the left). This rock is an intrusive amphibolite, with 65 wt % hornblende (light grey). In addition, it contains abundant plagioclase (dark grey). Minor contents of mica, quartz, pyroxene and apatite are also seen.

10.7.1.6 Sample 200.6 to 212.2:

This is the granodioritic basement from BH 2 at Ramså. Sample 205.3 is an exception, because this is also an intrusive amphibolite in the granodiorite (Table 10.5). The granodioritic basement has a typical granodioritic composition, with quartz, two feldspars and mica. The texture of the rock is illustrated in Figure 10.28 and Figure 10.29. Fractures in the granodiorite are filled with calcite, mica (biotite/phlogopite) and chlorite. SEM-EDS investigation shows very low potassium values for the biotite. This may partly be due to chloritisation. However, the XRD analyses show clearly that it is mica, and not vermiculite.

The texture of the rock is best seen in Figure 10.29, which shows a 500X magnification of the central part of Figure 10.29.

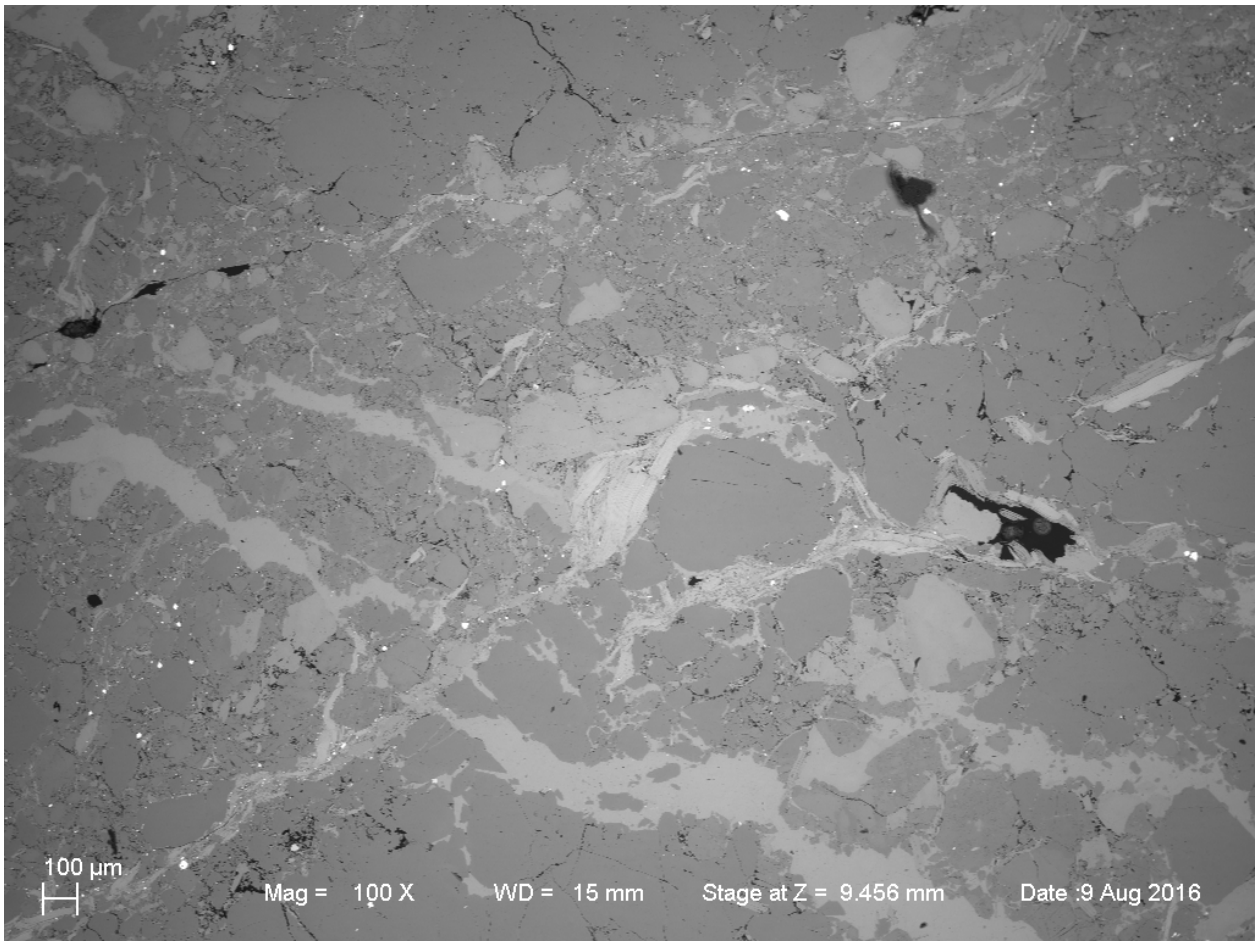

Figure 10.28. SEM micrograph of sample 201.3; 100X magnification. Texture of granodioritic basement rock. Fractures are filled with calcite, chlorite and biotite. SEM-EDS analysis give low K-values for biotite, but XRD-data give no indication on weathering reactions for the biotite. Chloritisation of biotite may explain the low potassium values. Identification of minerals: see Figure 10.29, which is a magnification of the middle part of Figure 10.28.

10.7.1.7 Sample 205.3:

Sample 205.3 is interpreted as an intrusive amphibolite, just like sample 195.1 (Table 10.5). The compositions of these two rocks are actually very similar, with hornblende and plagioclase being the dominant minerals. A certain orientation of lath-like plagioclase and quartz crystals indicate old flow structures. Some characteristic fractures are seen orthogonal to these feldspar lineaments. These fractures are filled with chlorite. Ilmenite and pyrite are also identified in the thin-section.

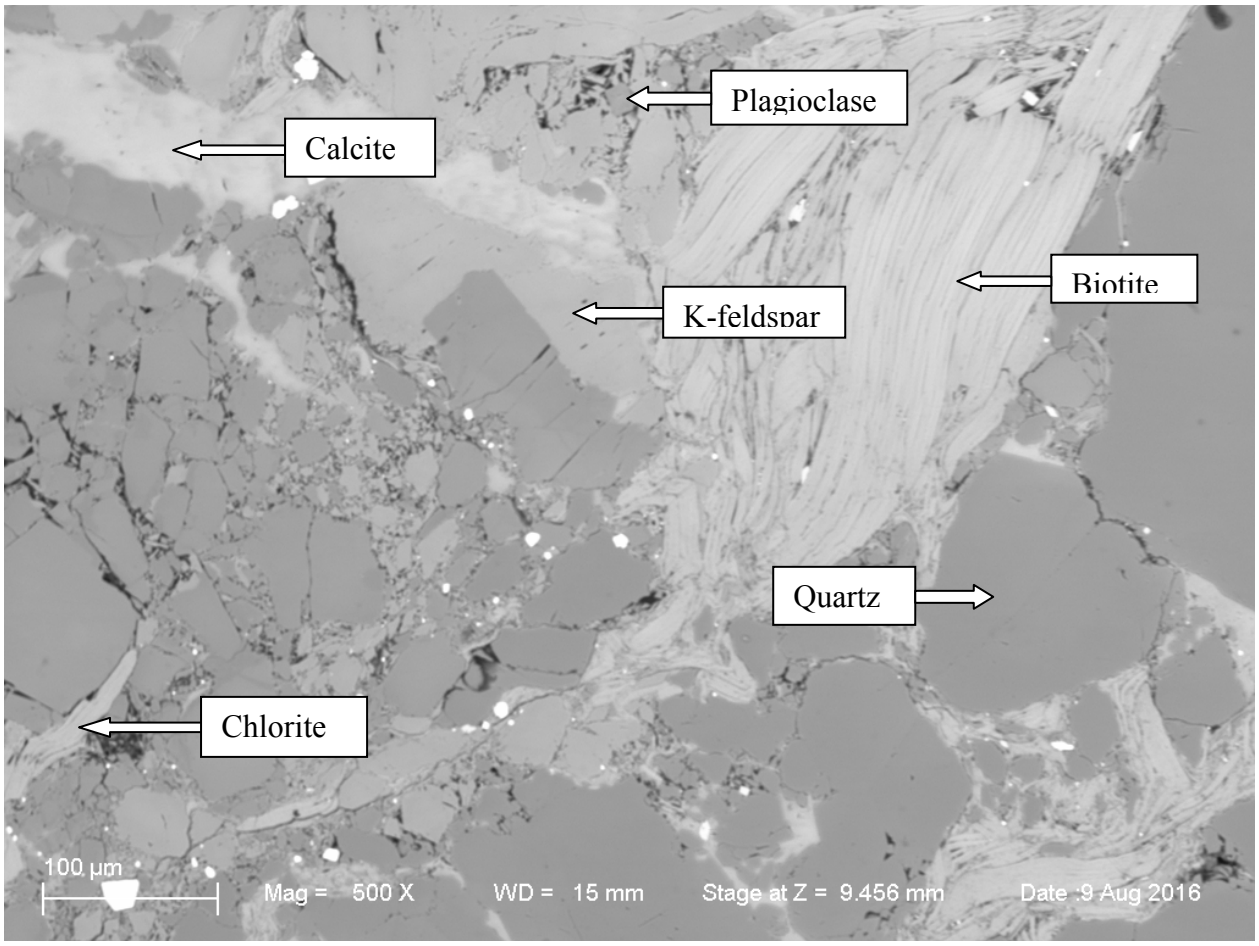

Figure 10.29. SEM micrograph of sample 201.3, 500X magnification of the central part of Figure 10.28. The main minerals; quartz, K-feldspar, plagioclase, biotite and chlorite are identified by SEM-EDS; shown by arrows in image. It is difficult to distinguish properly between biotite and chlorite because of a similar composition and the low potassium values in biotite.

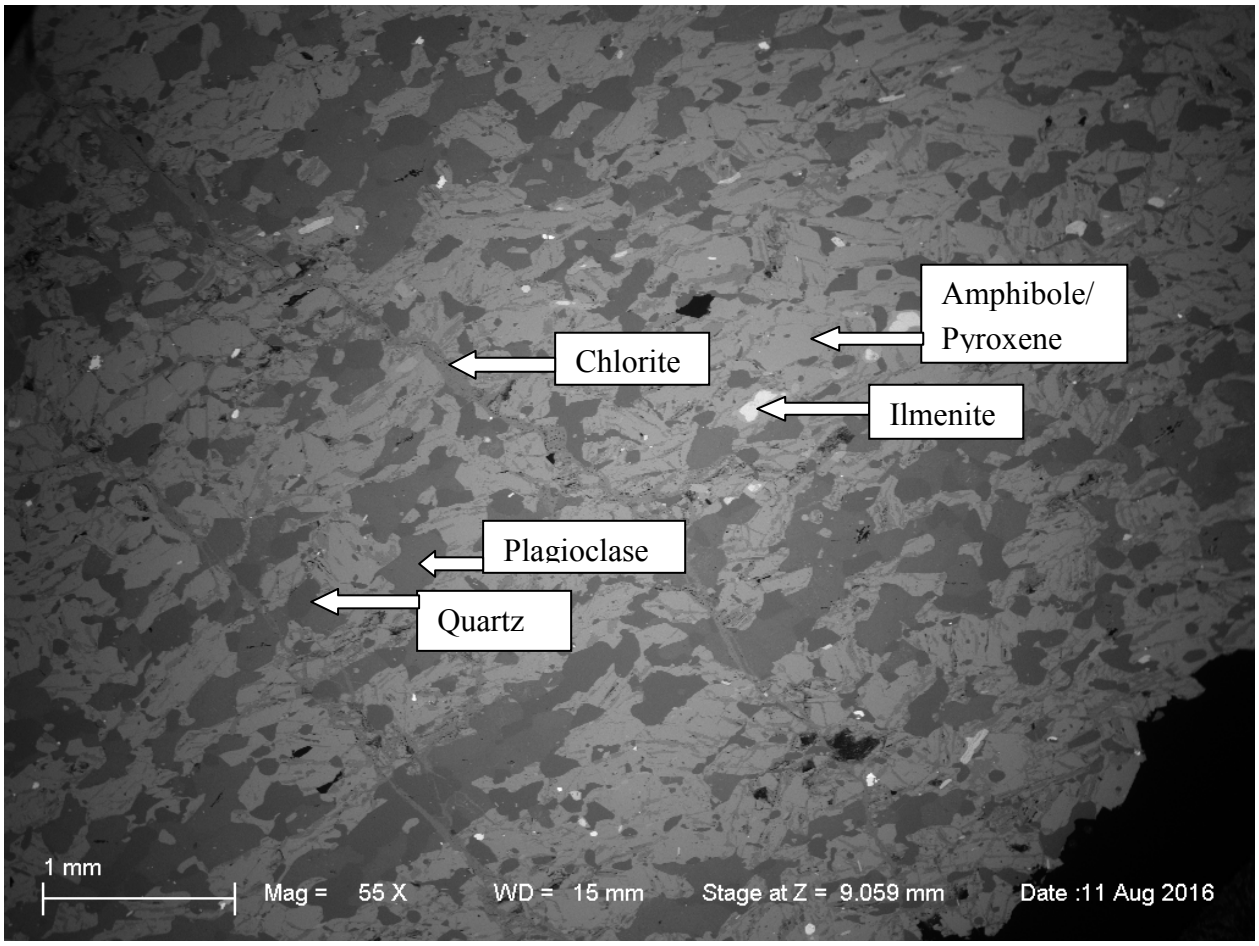

Figure 10.30. SEM micrograph of sample 205.3, 55X magnification. Texture of basement rock; e.g. diabase. Diabase normally has a texture of euhedral lath-shaped plagioclase crystals in a fine matrix of pyroxene, magnetite, hematite and ilmenite. This rock is composed of plagioclase, chlorite, amphibole, pyroxene and quartz. Chlorite-filled fractures are crossing (at nearly right-angles) the lineaments with elongated plagioclase and quartz crystals.

10.7.2 Chemical composition of samples from NGU BH 1 and BH 2

Bulk chemical analyses were carried out on XRF for the samples from NGU wells BH 1 and BH 2 at Ramså (described above). The results of these analyses – both major and trace elements are given in the Appendix, Table A.2 and A.3A, -3B, and -3C. Sample ID and sampling depths (in m) are also given.

The XRF analyses have a higher degree of accuracy than the mineralogical quantification from XRD data. It is therefore very useful to have both datasets in order to study the various mineral types and alteration due to weathering, etc. The mineralogy described above shows a very magnesium-rich environment. This is tested by plotting the magnesium-bearing minerals in the samples versus MgO from the XRF data from Table A.2. A good trend is seen, except for the two amphibolites. Their magnesium values are lower than for the phyllosilicates; consequently they plot above the trend.

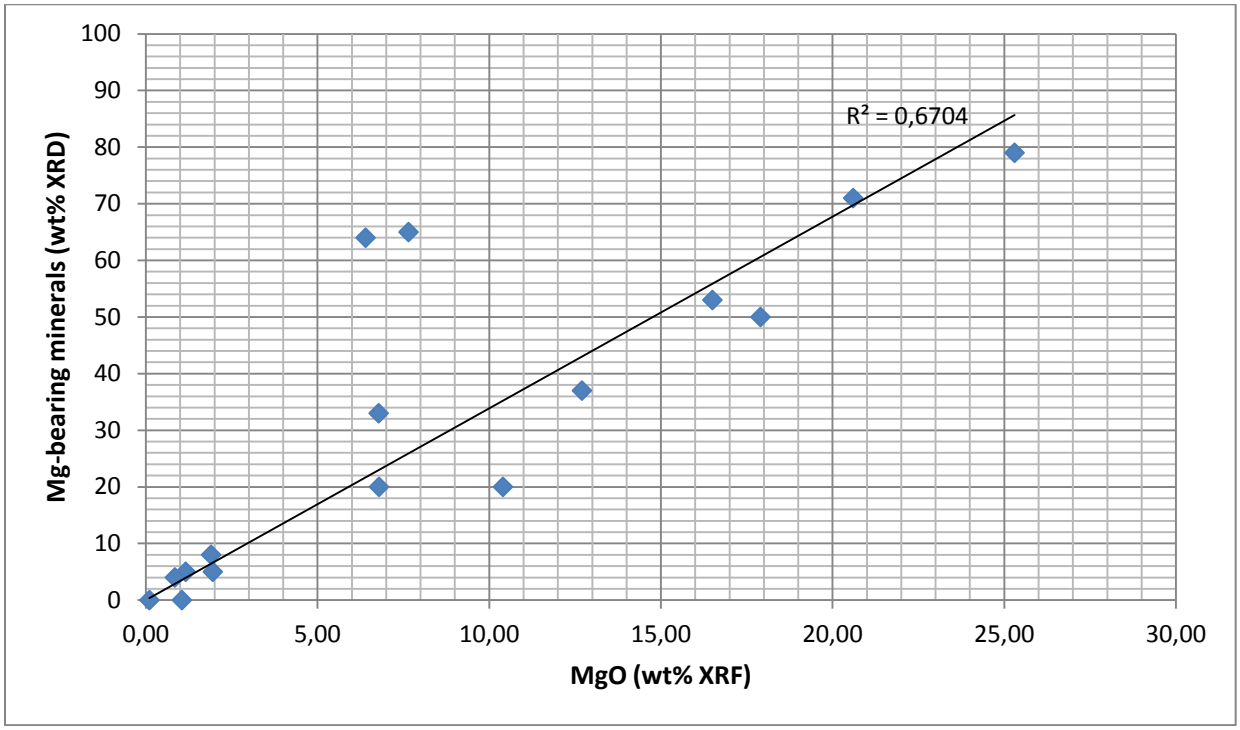

Figure 10.31. NGU Wells BH 1 and BH 2 at Ramså. The phyllosilicates are dominated by magnesium-bearing minerals. In this figure the magnesium-bearing minerals quantified by XRD; chlorite, biotite/phlogopite, talc, vermiculite, mixed-layered minerals and amphibole are plotted versus MgO from XRF analyses. A good trend is seen. The two samples above the trend are the two amphibolites with hornblende, which have lower relative magnesium contents than the phyllosilicates.

The evaluation of weathering is to a large extent resting on the interpretation of the XRD data. When other data are available it is important to use them to test out the robustness of the mineral data interpreted from XRD. In the present test, we have calculated the potassium content in the potassium-bearing minerals quantified from XRD data. This is done by setting the K_2O value of K-feldspar to 17 weight %, and for mica to 10 weight %. These calculated K_2O values are plotted versus the corresponding K_2O values obtained from the XRF analyses (in Table A.2); see Figure 10.32.

Significant uncertainty is associated with the potassium contents in biotite (and phlogopite), also because variable amounts of potassium are lost from these minerals due to leaching. In spite of these uncertainties a good trend is seen in Figure 10.32.

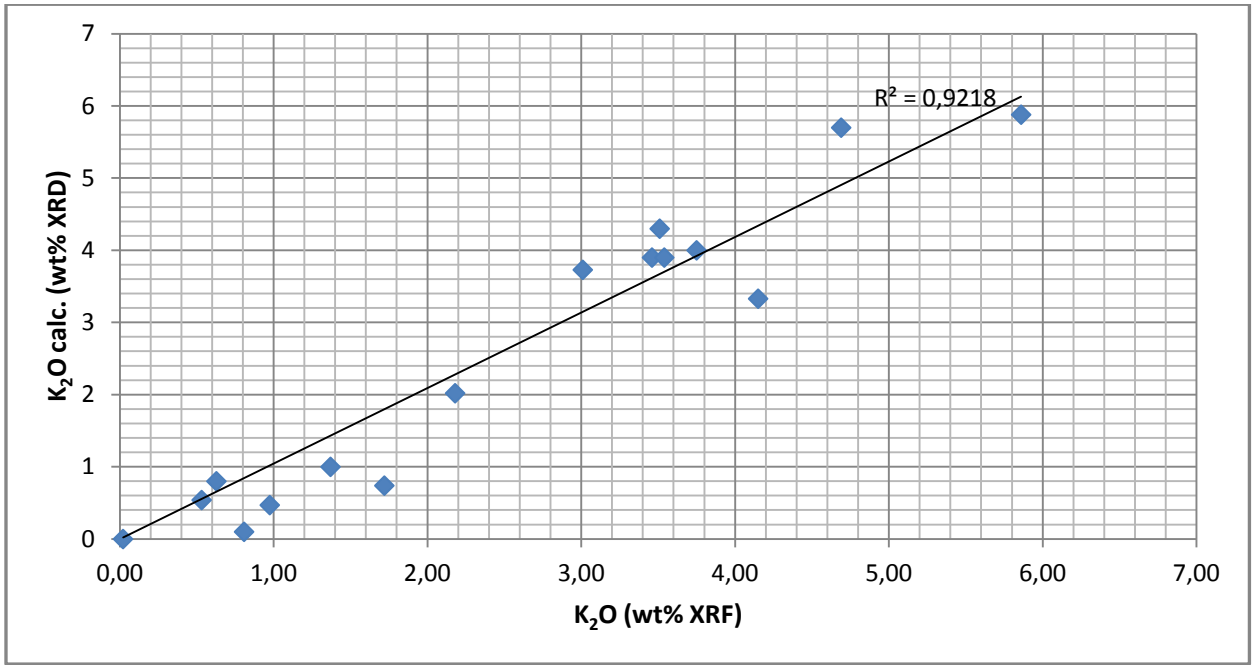

Figure 10.32. BH 1 and BH 2 at Ramså. A plot of K_2O from XRF versus calculated K_2O values from K-bearing minerals quantified by XRD is performed in order to control the consistency between these two datasets. The calculations are based on setting the potassium content of K-feldspar to 17 wt %, and in mica to 10 wt %. Significant uncertainty is associated with potassium contents in biotite (and phlogopite), because variable amounts of potassium are lost due to leaching and chloritisation. In spite of these uncertainties a good trend is seen.

The degree of weathering in a given profile is commonly evaluated by looking at variations in the geochemical data. One 'Weathering Index' is the ratio $Al_2O_3/(CaO+Na_2O+K_2O)$. This is based on the fact that the base cations, Ca, Na and K is leached out in a weathering profile, commonly from dissolution of feldspars, biotite, etc. At the same time, the aluminum content of the dissolved minerals is included in the formation of new clay minerals; e.g., smectite and kaolinite. A similar weathering index is CIA: The Chemical Index of Alteration (CIA= $Al_2O_3/(Al_2O_3 + CaO + Na_2O + K_2O)$. This index is mirrored by the 'inverse'ratio ∑Bases/Al (=(Na+K+Ca+Mg)/Al).

Data from Table A.2 (in Appendix) are used to calculate these ratios, and they are plotted versus sampling depths in Figure 10.33. The sample points are aggregating in separate areas of the diagram, and are recognised as the same groups shown (in colours) in Table 10.2 and Table 10.4. It is only Group 1 that represents really weathered rocks, with their high kaolinite contents. These samples are also the only ones that have substantially higher contents of ZrO_2 and V_2O_5; another clear indication of severe chemical weathering (Table A.2).

The other groups are unweathered or just mildly weathered (slightly leached in potassium, etc.). The two samples in the transition zone; Group 2, are very different from all the others.

One of the samples has a high calcite content and, consequently, a Weathering Index close to zero.

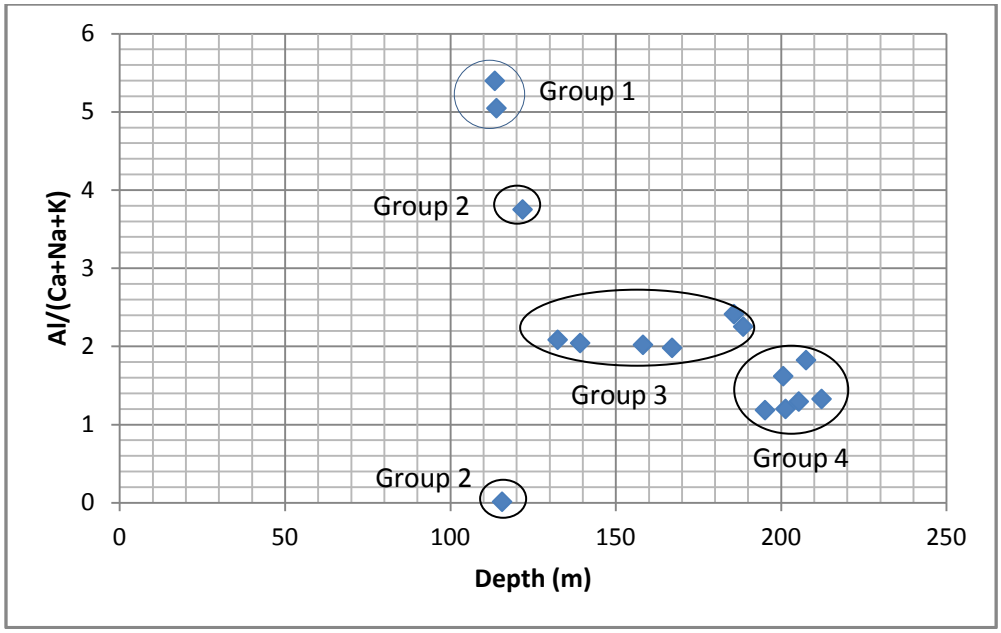

Figure 10.33. BH 1 and BH 2 at Ramså. The degree of weathering is commonly evaluated by looking at geochemical variations down through the weathering profile. One weathering index is the ratio $Al_2O_3/(CaO+Na_2O+K_2O)$. This ratio is plotted versus sampling depths in NGU wells BH 1 and BH 2. The 'Group 1 to 4' is defined in Table 10.2: Group 1 is the weathered sediments; Group 2 is the transition zone, with two different rock types; Group 3 is the plagioclase-chlorite-talc zone interpreted as a debris flow; and Group 4 is the basement granodiorite in BH 2. Only Group 1 is pervasively weathered.

As seen in Fig. A.2 most of the phyllosilicates are rich in magnesium. One interesting question is whether these minerals have the same source. One way to investigate this is to look at variations in trace elements. This is done here by making cross-plots of several elements. A cross-plot of Fe_2O_3 versus TiO_2 (from Table A.2) is shown in Figure 10.34.

A very good correlation is seen for the phyllosilicates, indicating that they are derived from the same source, with the same iron/titanium ratio. The two intruded amphibolites, however, are falling outside the trend of the phyllosilicates, with higher titanium/iron ratios.

The **transition metals** are commonly seen to follow each other, because of similar chemical properties. This is illustrated in Figure 10.35, with a plot of V versus Cr. A relatively good correlation is seen, with the exception of one sample 98589, which has very high V contents. The reason for this is not known. The other amphibolite, sample 98595, has a V/Cr ratio comparable to the other samples.

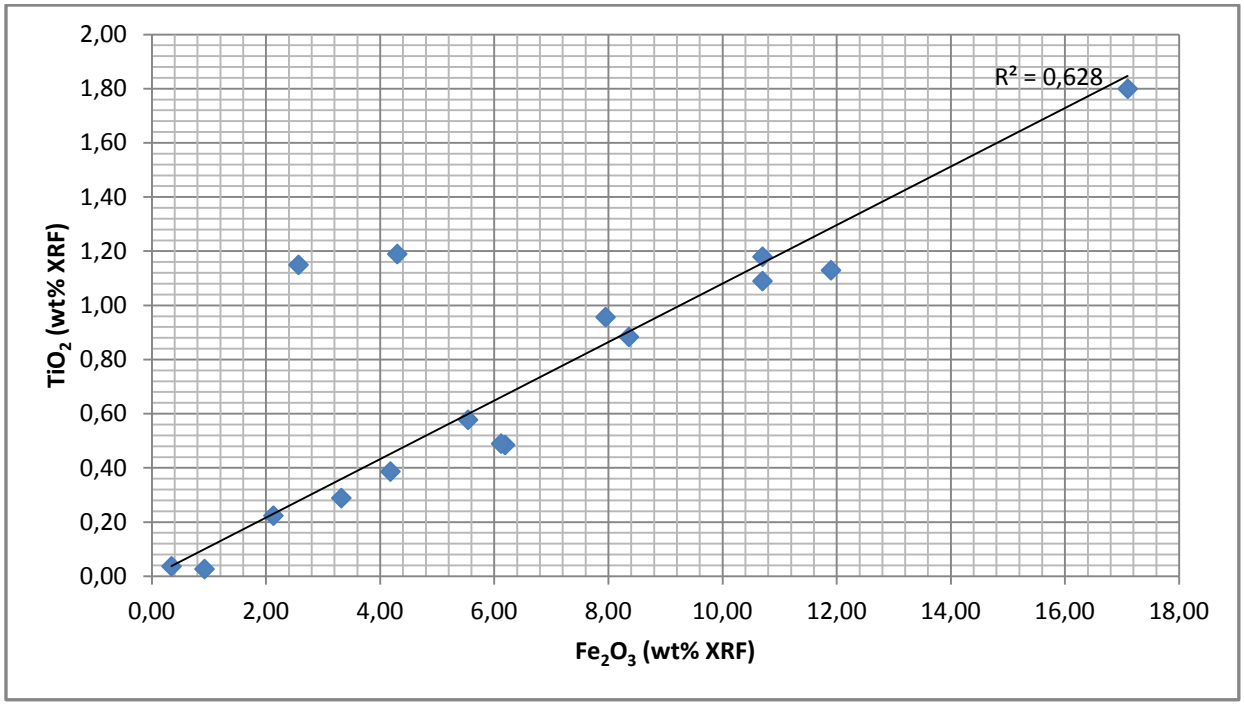

Figure 10.34. BH 1 and BH 2 at Ramså. Iron content versus titanium content in weight % from XRF. A good correlation is seen. The two 'outliers' are the two amphibolite samples, which have much higher titanium/iron ratios than the others. The phyllosilicates are dominating the trend, and indicate that biotite/phlogopite, chlorite, and vermiculite are very similar regarding the iron/titanium ratios; indicating a similar geological provenance.

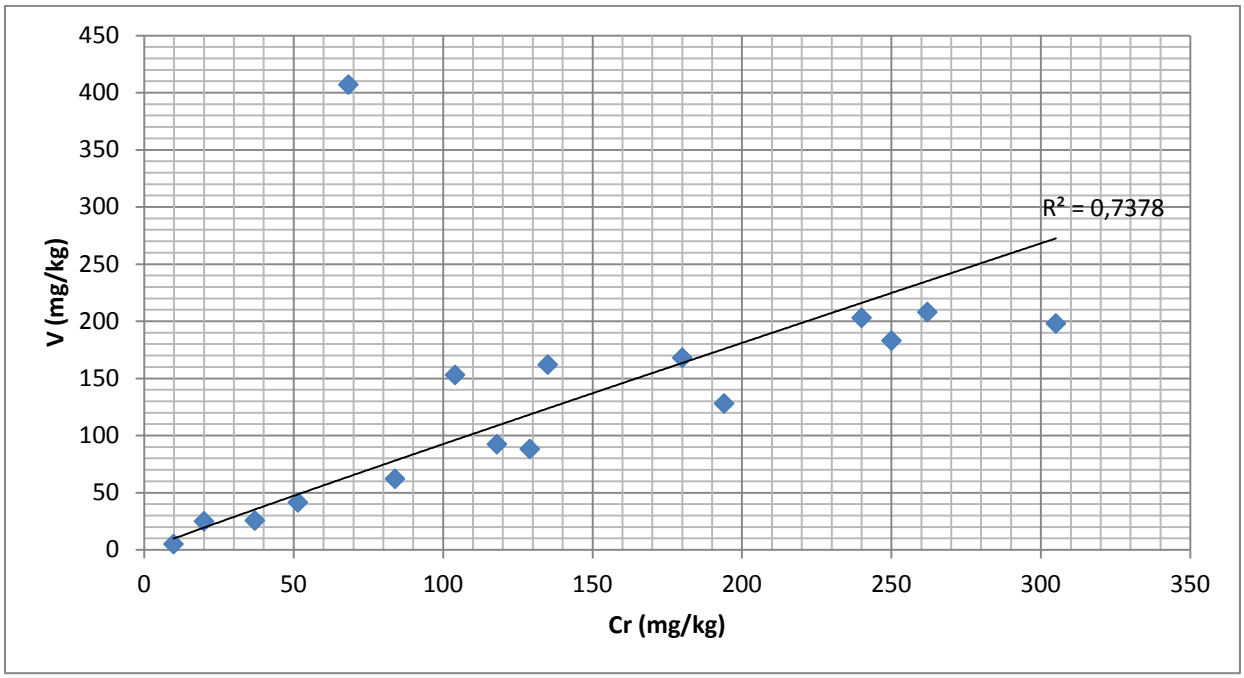

Figure 10.35. BH 1 and BH 2 at Ramså. Trace elements V (mg/kg) plotted versus trace element Cr (mg/kg). A relatively good correlation is seen, with the exception of sample 98589, an amphibolite, with a V content ten times above the trend (407 mg/kg). The other amphibolite, sample 98595, has only half this V value (208 mg/kg).

Also the **rare earth elements** (lanthanides) are commonly seen to follow each other, and they also tend to accumulate in weathering zones. This is illustrated in Figure 10.36, with Nd plotted versus Ce. A relatively good correlation is seen, including both fresh and weathered samples.

All of the cross-plots in Figure 10.34 to Figure 10.36 suggest a similar source for the rocks, maybe with the exception of the intrusive amphibolites. This is not unexpected, since we are dealing with very different rock types; both granodioritic basement and ultrabasic rock fragments in the debris-flow deposits. The sediments above the debris flow contain no talc, but are still showing similar geochemical trends as the rocks below. This indicates that they are derived from similar sources as the basement rocks.

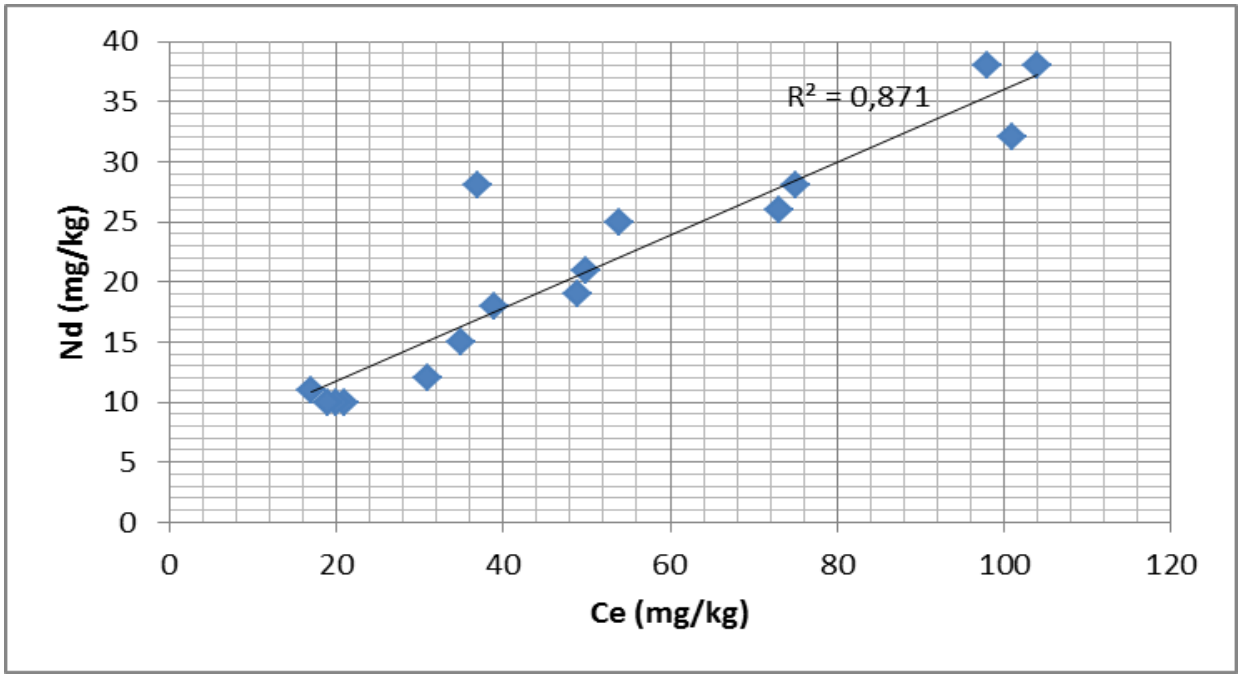

Figure 10.36. NGU Wells BH 1 and BH 2. Trace elements Nd (mg/kg) plotted versus trace element Ce (mg/kg). A relatively good correlation is seen for both weathered and non-weathered samples, with a correlation coefficient of R2=0.87.

10.8 Depositional environments – a summary of the localities

10.8.1 Summary of the surface section at Ramså

The section referred to as 'basement' and "weathered basement' shows a trend from bottom to top, characterised by less plagioclase and biotite and more kaolinite. The weathered part is also containing some Fe-oxides. Based on this, the weathered granodiorite is defined as a saprolite, formed in a tropical climate.

The quartz- and clay-rich rocks overlying the confirmed weathered granodiorite contain the highest amounts of kaolinite and 'immovable elements'; e.g. TiO_2 and ZrO_2, and the highest CIA (Chemical Index of Alteration) value of 99. Furthermore, their biotite and feldspars are nearly completely dissolved; i.e., everything indicates that this interval experienced severe *in-situ* meteoric weathering. The important question is whether the whole 18 m thick profile of these quartz and clay-rich rocks represent *in-situ* weathered basement (i.e. saprolite) or reworked saprolite. Some of the pros and cons are discussed below:

Indications of saprolite:

- Gradual increase in Al_2O_3 and a concomitant reduction in SiO_2 from bottom to top.
- The angular shapes of the gravel-size quartz grains indicate negligible transport lengths.
- The vermicular growth of TiO_2 and kaolinite aggregates suggests *in-situ* formation.

Indications of reworked saprolite:

- The presence of cm-size kaolinite pellets and short laminae within the coarse-grained quartz- and clay-rich rocks supports the idea of redeposition of saprolite.
- Some rounded cm-size pebbles of quartz are seen in thin-sections.
- The upper part of the interval contains more clinopyroxenes and amphiboles than the unweathered granodiorite basement (MB-11-3). This is causing slightly lower CIA values than the thin, quartz- and clay-rich interval below.

Well-rounded pebbles of quartz may result from the pervasive in-situ weathering (McFarlane et al., 2007), and that is also the case for the occurrence of kaolinite pellets and short kaolinite laminae (Millot, 1970). Based on these considerations it is cautiously suggested that *the 18 metre interval above the initially defined 'weathered basement' is also weathered basement; i.e. saprolite, developed in granodiorite.* The precise position of the basement boundary is therefore somewhat dubious.

The quartzitic sandstone above the 18 m-interval may be derived from eroded saprolite from the local granodioritic terrain, where much of the kaolinite was transported further out in the basin, while the coarse-grained quartz particles and remaining feldspar grains were deposited locally. A continued weathering of these deposits took place after deposition, followed by diagenetic processes upon deeper burial. The siltstones above this 18 metre interval are

sediments, containing significant amounts of biotite and clinopyroxenes (more than granodiorite), and are therefore likely derived from different source areas than the local saprolite.

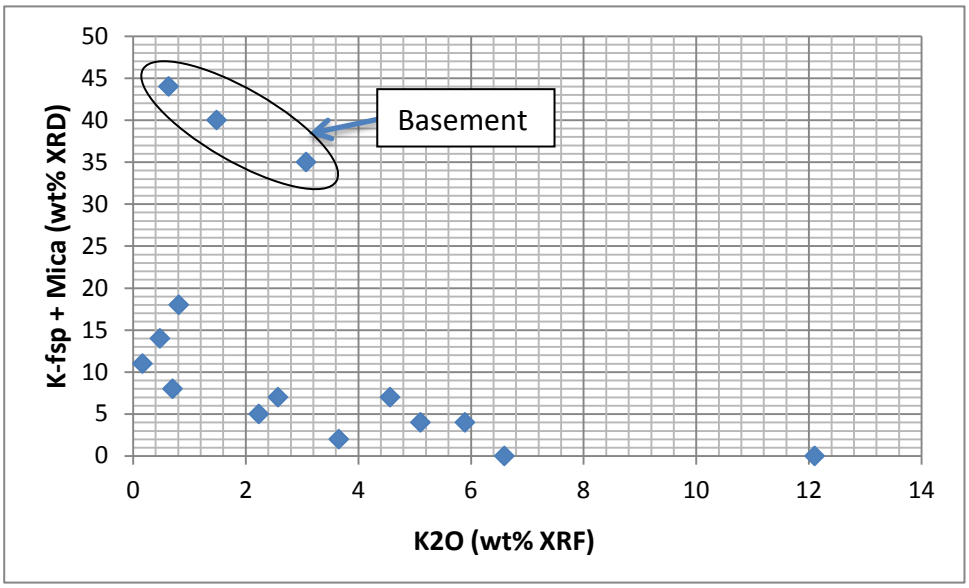

Figure 10.37. Ramså surface profile: K2O (weight % XRF) versus K-feldspar + Mica + illite (weight % XRD). The three basement samples are falling outside the trend for the other samples due to the abundance of K-feldspar in the basement rock.

10.8.2 Summary of data from the NGU Wells BH 1 and BH 2.

All four NGU wells in the Ramså area were logged with petrophysical logging tools, including a full suite of radioactive tools: total gamma, and spectral logs for uranium, thorium and potassium. The result of the spectral gamma logging in BH 1 is shown in Figure 8.8 and discussed inChapter 8.5.1. The boundaries between the various formations and members are commonly identified based on electrical logs. The boundary between the Ramså Formation and Precambrian basement was initially set at 114 m depth. The present investigation shows that this contact marks the boundary between kaolinite-rich sandstones and an underlying debris-flow deposit, composed predominantly of altered mafic rocks.

The sandstone samples from 113 to 114 m depth contain abundant kaolinite, and it is well known from the oil industry that high thorium values are associated with kaolinite (Ehrenberg 1991; Hampson et al. 2005). This is seen on the gamma log responses here, too. However, this zone also contains abundant K-feldspar and, hence, also high potassium readings on the spectral log.

The investigated sample of the rock underlying the weathered sandstone (at 115.7 m in NGU well BH 1) shows a rock consisting of actinolite, calcite and quartz. It is concluded that this is a strongly altered amphibolitic rock, where the diagenetic processes have transformed most of the actinolite into calcite and quartz. Low gamma log readings characterise this rock.

The next sample is from 121.8 m depth, and shows an altered mafic debris flow, with low gamma readings. The next boundary is at 131 m depth, with the transition into the main debris

flow in this interval, which goes all the way down to the basement at 193.8 m depth. These sediments contain biotite, and hence, the spectral gamma log gives responses for potassium, but low readings for thorium and uranium (Figure 8.8). Unfortunately, the logging tool was stuck at 143 m depth, and no more log information is available below this depth.

The age of these debris flows is assumed to be Mid-Jurassic (Chapter 9.2).

The basement in Well BH 1 is amphibolite, characterised by Sample 195.1 m. The mineralcomposition of this rock is dominantly hornblende and plagioclase. This is very different from Well BH 2 (and also the other localities investigated), which has a granodioritic basement, consisting predominantly of quartz, K-feldspar and plagioclase (Table 10.5).

The basement in Well BH 1 show signs of weathering only in the upper 5 cm, while the basement in BH 2 shows no signs of weathering. In this well, an amphibolite intrusion is found in the granodiorite, characterised by Sample 205.3 m in Table 10.5.

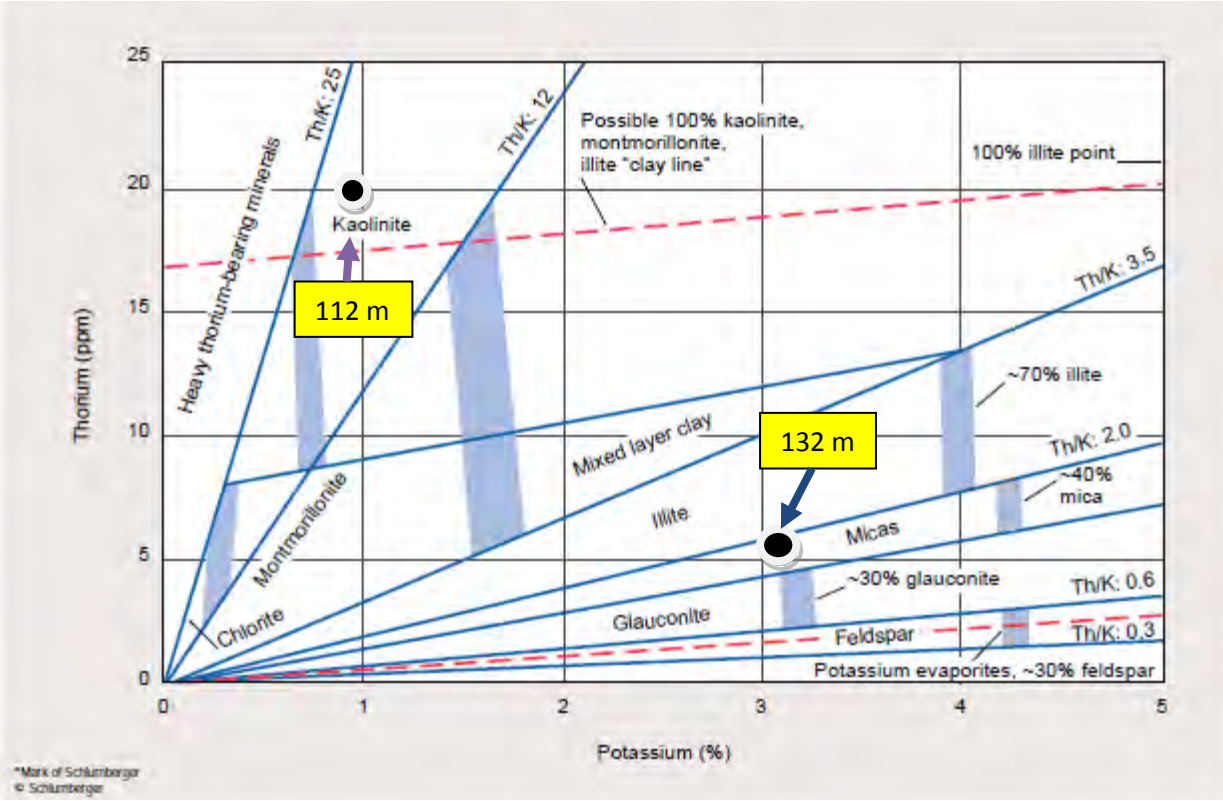

Figure 10.38. Schlumberger's mineral identification chart for natural gamma ray spectroscopy (NGS), CP-19. Cross plot of Th and K logs to identify clay minerals; in this case kaolinite and mica+ illite. Two data points (black dots) from the spectral gamma logging of NGU well BH 1 (shown in Fig. 9.2) plotted in Schlumberger's identification chart CP-19: kaolinite rich zone at 112 m depth plots in the kaolinite field, while the micaceous zone at 132 m depth plots in the mica field. See also Table 10.5for mineral data.*

Schlumberger (2016) has published clay mineral identification cross-plots based on his experience with natural gamma spectral logging tools. Measurements from two zones in BH 1 are plotted in Schlumberger's Th-K cross-plot form in Figure 10.38; one measurement from 112 m depth, characterised by high contents of kaolinite, and one from 132 m depth characterised by high mica contents (40 wt%). The data points plot nicely in their respective fields for kaolinite and mica (Figure 10.38). Thus, the gamma log readings can be calibrated by using the mineralogical and petrographical information from the core samples, and vice-versa; and the logs are giving continuous information regarding the variation in rock composition, in this case confirming the interpretation of the lithological boundaries.

10.8.3 Summary of data from the Norminol Wells A, B and C

Very few samples are analysed from wells A and C, and here there are only signs of initial weathering of the upper granodioritic basement for Wells A and C (Table 10.4 and Figure 10.20). However, a more thorough investigation was conducted on the cores from Well B, including point analysis with a hand-held XRF spectrometer throughout the entire length of the cores (Figure 10.21). The Si/Al ratio seems rather stable throughout the drilled basement zone (530m to 543 m depth), but the two samples from the basement zone at 539 m and 543 m have both 13-15 wt% kaolinite and also swelling minerals; i.e., indicative of significant weathering. However, these samples are taken from weathered zones in the basement, (e.g. fracture zones) and are not representative for the entire upper section. This is illustrated in Figure 10.15.

Wells B and C are drilled on either side of a fault block, and Well B is closest to the NGU Wells BH 1 and BH 2. However, the debris-flow lithology found in BH 1 is not seen in the Norminol wells. There is a conglomerate in Well B at 503.8 metres depth (Figure 10.14q), but it consists of sandstone clasts in a silty matrix; i.e. very different from the debris flows in NGU Well BH 1. It therefore seems that the mafic debris-flow sediments are found only on the fault block where BH 1 was drilled.

10.9 **Burial depths**

The maximum burial depth of the Jurassic and Cretaceous sediments on Andøya has been a matter of discussion during the last three decades (Dalland, 1974; Sturt et al. 1979; Hansen et al., 2012)

10.9.1 Crystallinity of kaolinite

During the evaluation of the data it was observed that the kaolinite crystallinity varied significantly. This is seen by how well defined the XRD reflections are in the range 4.45Å to 4.17Å, and also on the ratio between the 7Å and 4.45Å reflections; i.e., this ratio is increasing with increased b-axis disorder in the kaolinite (Brindley et al., 1963; Bergaya et al. 2005).

The 7Å/4.45Å ratio is a simple and robust parameter for studying the crystallinity of kaolinite, and this ratio is calculated for all of the surface samples from the Ramså surface profiles, see Table 10.3.

It is possible that increased b-axis disorder is caused by contamination with other ions i.e., other than silica and alumina in the pore water during crystallisation of kaolinite. Dissolution of feldspar and crystallisation of kaolinite requires a minimum through-flow of water to remove cations such as Ca^{++}, Na^{+} and K^{+} and silica (Bjørlykke 1988). Permeability and the rate of flow of percolating water through the weathering formation are crucial parameters for the formation of well crystalline kaolinite. It is therefore to be expected that kaolinite formed in well drained soils has better crystallinity than kaolinite formed in low permeable soils with poor drainage. This is seen in Table 10.3, where the lowest crystallinity index (7Å/4.45Å ratio) for kaolinite is found for the sandy sediments MB12-6 and MB12-9. The other samples are characterised by having kaolinite with various degrees of b-axis disorder.

The leaching of base cations is commonly more efficient in the upper part of the weathering profile than in the lower parts; particularly in saprolites. For this reason, the crystallinity ratios are plotted versus depths in Figure 10.39. It is seen that the deeper samples, including the ones from the saprolite itself, give higher 7Å/4.45Å ratios on XRD; i.e., poorer crystallinity.

The samples with well crystalline kaolinite have a 7Å/4.45Å ratio below 5. The samples with ratios higher than 5 are interpreted as having kaolinite with some b-axis disorder. It is notable that almost all kaolinite- and quartz-rich samples, with the exception of sample MB-12-1, show a 7Å/4.45Å ratio above 5 indicating some b-axis disorder. The only samples having the ratio well below 5 and therefore showing no b-axis disorder are the quartz sandstones from the top of the section. As the whole kaolinite-rich part of the profile contains kaolinite with some b-axis disorder, it is most likely that all these rocks –including fine- and coarse-kaolinite- and quartz-rich rocks –formed in-situ. Noteworthy, though, is that the highest b-axis disorder is found within two samples: the fine-grained clay- and quartz-rich rock (MB12-12 with 7Å/4.45Å ratio = 7) and the stratigraphically lowermost sample of the coarse-grained kaolinite- and quartz-rich rock (MB12-8 with 7Å/4.45Å ratio = 8.3).

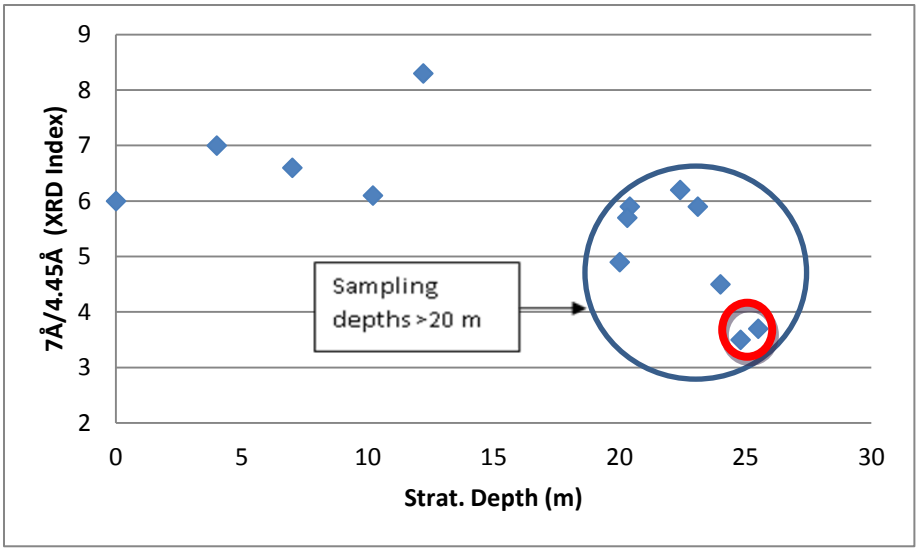

Figure 10.39. Kaolinite crystallinity given by the 7Å/4.45Å ratio versus stratigraphic depths at Ramså (data fromTable 10.3). Note, that depth is measured in the 'opposite direction'; from bottom to top. The granodiorite basement is at zero depth. Kaolinite in the upper parts of the sedimentary sequence is characterised by a better crystallinity than in the deeper parts, including the saprolite. The two samples in the red circle are the two kaolinite-rich sediments at the top of the profile.

It has been questioned whether kaolinite in the sediments is formed *in-situ* or is deposited as a sediment (allochthoneous). The SEM investigations of thin sections of these rocks show clearly that much of the kaolinite has crystallised *in-situ*, with a vermicular growth habit; e.g. Figure 10.23. Such vermicular structures would never develop in a sedimentary depositional process where particles are dispersed in the water phase, and flocculate upon settling in marine environments.

What the situation is for the shales and mudrocks it is more difficult to conclude. It is reasonable to think that erosion of saprolites was an important source for forming the sedimentary rocks, including the fine grained ones. For this reason, it is considerable that kaolinite eroded from the saprolites in the area is a part of (at least some of) the shales and mudrocks. In this case, we would not expect to find vermicular kaolinite in the rock, just a random packing of kaolinite particles. An example of such random packing is shown in Fig. 5.6.k and l, with a pellet of kaolinite. This may be a clay clast from water eroding in a channel (clay lumps falling into the channel from the sides).

Additional processes, which may mask these features, include the development of vegetation and soil profiles. Rootlets are commonly seen in the core samples; e.g., Figure 10.14g and h. Here, soil weathering processes and roots may disturb the texture of diagenetically formed kaolinite.

Another question is whether the kaolinite found in the sediments was formed diagenetically or as a result of tropical weathering. We know that the saprolite in the basement rocks can only develop by the percolation of oxidized meteoric water under tropical climatic conditions. This process can of course also take place in sediments deposited under subaerial conditions. However, experience from the North Sea indicates that diagenetic kaolinite may start forming

at the expense of feldspars, at relatively shallow burial depth . For this reason, we cannot exclude this possibility.

For muscovite the 10Å/5Å ratio is ~2. The kaolinite- and quartz-rich sample MB-12-2 has a 10Å/5Å ratio of 1.6, which indicates that mainly muscovite (and dioctahedral illite) is left, while all of the biotite is transformed to vermiculite by the leaching of potassium and oxidation of iron in the octahedral layers of biotite. This is not the case with the mudstone sample, MB12-10, which still has a high 10Å/5Å, meaning that it contains biotite or phlogopite. In the unweathered basement this ratio is 10; i.e. typical for biotite.

Burial of kaolinite to temperatures of 100 - 120 ^{O}C is causing recrystallisation of kaolinite to dickite (Beaufort et al. 1998). The presence of dickite may therefore give a hint of the maximum burial depths of these rocks.

Parnell et al. (2000) reported that kaolinite and dickite occur widely in Central Scotland and Northern Ireland and that they were formed as a result of weathering of Lower Carboniferous volcanic rocks. The kaolinite crystallisation was focused along the high-permeability Highland Boundary Fault zone (Parnell et al., 2000).

Analysis of hydrogen and oxygen stable isotopes in the kaolinite and dickite showed similar compositions, suggesting that the crystallisation of kaolinite occurred first, as a result of interaction between meteoric water and the volcanic rocks at temperatures <50 ^{O}C. The subsequent recrystallisation of kaolinite to dickite was a result of heating that accompanied intrusions of dykes during Late Carboniferous – Permian times.

The samples from Andøya were also carefully checked for the occurrence of dickite, both by XRD and SEM imagery. However, no indications of the presence of dickite were observed. The burial depths of these sediments and saprolite are discussed further in the next paragraph: Vitrinite reflectance.

10.9.2 Vitrinite reflectance

Bjorøy et al. (1980) measured vitrinite reflectance on 25 samples from the Ramså area, sampled in the ditches shown in Figure 10.1. Most of the samples were of shales and shaly siltstones. Average vitrinite reflectance is calculated for each member of the various formations (Table 10.6). These values are used to estimate the maximum burial temperatures that the rocks were exposed to by applying commonly used relations lies between T_{max} (highest burial temperature) and vitrinite reflectance (Rm) (Barker & Pawlewicz, 2005). Since the majority of reflectance values for these samples are ranging from 0.4 to 0.65, they are indicating a maximum burial temperature interval of 30 to 65 degrees C (Figure 10.39).

Table 10.6. Vitrinite reflectance data for 25 samples collected from the excavated ditches at Ramså. Variations in reflectance and average values for each member are shown. Highest values are obtained for the Leira member. These samples are characterised by having abundant coal fragments. (Data from Bjorøy et al. 1980).

Formations (Dalland 1974)	Members (Dalland 1974)	Number of samples	Ranges of vitrinite reflectance	Average Vitrinite reflectance
Skarstein	Helneset	2	0.63→0.67	0.65
	Nordelva	5	0.26→0.78	0.47
Nybrua	Skjermyrbekken	0	-	-
	Leira	7	0.41→2.14	1.04
Dragneset	Ratjønna	10	0.29→0.61	0.45
	Taumhølet	1	0.45	0.45
	Breisanden	3	0.44→1.11	0.67
Ramså	Bonteigen	0	-	-
	Kullgrøfta	1	0.45	0.45
	Hestberget	6	0.32→0.45	0.41

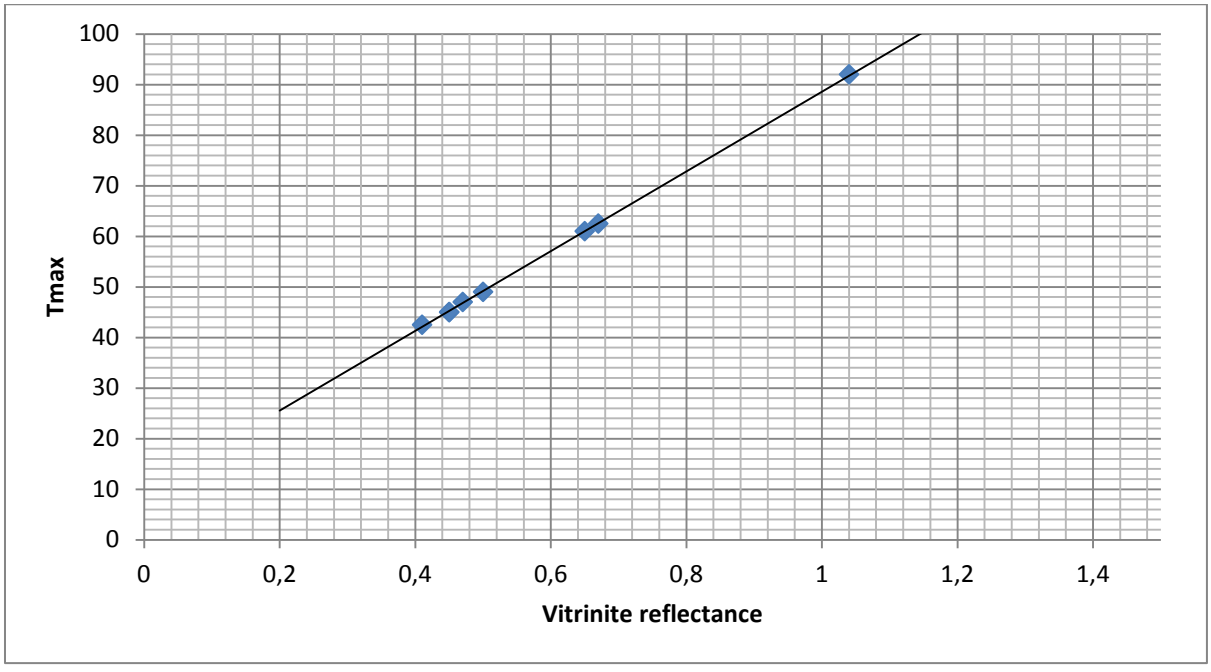

Figure 10.40. Average vitrinite reflectance values versus estimated Tmax for each Member of the sedimentary succession at Ramså. The majority (27 of 33) reflectance values are ranging from 0.26 to 0.67, indicating a temperature interval of 31 to 62 degrees C. However, the seven samples from the Ramså Formation (the lowermost formation) give values from 0.32 to 0.45 with an average of 0.41, indicating a Tmax of 42°C.

The highest reflectance values are obtained for the samples from the Leira Member. This is suggested to be associated with an abundance of coal fragments in these fine-grained silty samples. However, the provenance of these coal fragments is not known. Since the vitrinite reflectance values show lower values below the Leira Member, it is reasonable to suggest that vitrinite values lower than 0.65 – and probably lower than 0.50 are representing the correct T_{max} temperatures (Figure 10.40). This is also the conclusion by Bjorøy et al. (1980).

Bjorøy et al (1980) concluded further that the Cretaceous samples are immature, with a poor potential as source rocks for gas and oil. The Jurassic samples are very different from the Cretaceous ones, both in terms of extractability and of composition of extractable hydrocarbons. However, also the Jurassic samples (including the Ramså Formation) show normal patterns for immature samples, but with a good potential as source rocks for oil and gas.

The estimated temperature interval of 31 to 62°C, also fits well with the mineralogy found in the same sampled interval as the vitrinite samples. From the North Sea sedimentary sequence it is seen that smectite is transformed to illite/smectite mixed-layered minerals and illite at temperatures above 60°C. This smectite transformation is not seen here, hence, it is suggested that the temperature was well below 60°C.

By applying the present vertical temperature gradient for the Norwegian Shelf of ~30°C per km, the reflectance values indicate a maximum burial depth of ~2 km.

Since the thickest sequence of Mesozoic sediments observed at Andøya today is less than 1 km, it indicates that up to 1 km of sediments have been eroded after the deposition of the Cretaceous sediments. If for the northern Ramså Basin, the thickness increased to more than 1 km as proposed by the old seismic line (Figure 2.2) the eroded sedimentary material is accordingly less.

10.10 Tectonic events and depositional environments

According to Steltenpohl et al. (2011) the Lofoten-Vesterålen archipelago was affected both by Caledonian orogenesis in Silurian time and subsequent gravity collapse in the Devonian. The next major tectonic event was associated with the Uralian suturing in Late Permian, which facilitated a southwards transgression through the proto-North Atlantic rift. Another extensional phase took place in the Triassic, but access to the Atlantic rift was restricted due to paleogeographic barriers (Doré 1991).

The following paleogeographic evolution of the area was governed by an interplay between marine transgressions and a sequence of tectonic events leading to the break-up of the Pangean supercontinent. Pangea existed during the Late Palaeozoic and Early Mesozoic, and began to break apart in Early Jurassic time (about 175 Ma). Following Uralian suturing in the Late Permian and Early Triassic the paleogeographic evolution of the area was governed by

an interplay between marine transgression and a sequence of tectonic events leading to the break-up of the Pangean supercontinent. Important extensional events are recorded in the Mid-Permian, Triassic and Late Jurassic-Early Cretaceous. The Mid-Permian faulting facilitated a southwards transgression through the proto-North Atlantic rift in the Later Permian, although this marine tract did not connect to Tethys. During the Triassic, ingressions into the Atlantic rift domain were restricted by paleogeographic barriers and no direct connection existed between marine realms at the extreme north and southeast of the study During the Early Jurassic an open seaway was established between Tethys and the Boreal Sea (Torsvik et al., 2002). However, this seaway was again closed in the Middle Jurassic due to major uplifts in the central North Sea. Later rifting and extensional events took place during the Late Jurassic-Early Cretaceous, which opened up the marine connection and gave rise to marine transgressions in the Lofoten area (Doré 1991).

This sequence of tectonic events may explain the paralic development of the Mesozoic sedimentary strata on Andøya, with deposition of sediments in alternating fresh, brackish and marine environments. The upheaval of the land area in Mid Jurassic time probably caused erosion of the previously deposited sediments and saprolites(?), with redeposition in the deeper parts of the basin. The dip of the basement blocks towards north and east may indicate the transport direction. This is particularly the case with the debris-flow deposits in NGU borehole BH 1.

Generally, the sediments of the Ramså Formation were deposited onto the basement, and the deeper parts are dominated by floodplain deposits, with some crevasse displays, fluvial sand, and swamp deposits with coal; i.e., freshwater environments in the Hestberget Member (lower Ramså Formation). A marine transgression occurred at the transition between Hestberget and Kullgrøfta members, and alternating marine and brackish to freshwater conditions continued upwards in the sedimentary sequence throughout the Bonteigen Member. The above-lying Breisanden Member in the Dragneset Formation shows also alternating marine and freshwater conditions (upper and lower shoreface deposits) with with deposition of silt and sand.

The debris flow deposits found in NGU borehole BH 1 are somewhat enigmatic with respect to this general depositional model. Fossils indicate a Mid Jurassic age for the debris-flow deposits, and from the core descriptions and the wireline logs it looks as if the Ramså Formation is overlying this sedimentary unit (Chapter 9).

10.11 **Local and regional correlations**

The 18 m-thick kaolinite-rich zone exposed close to Ramså village is sandwiched between weathered basement rocks and the overlying Lower Jurassic siliciclastic sediments. A similar kaolinite-rich horizon of comparable thickness is not found in any of the boreholes located farther northwest onshore Andøya. Thus, deeply weathered basement rocks may therefore have developed only locally, or were only locally preserved. Both processes are probably

important for the distribution of saprolite. Saprolites can only develop onshore, and it is not known whether all of the fault blocks were elevated above sea-level during the development of the saprolite at Ramså. Norminol Well B shows some weathered zones with kaolinite and other clay formation in the upper 13 m of the basement, but is not weathered throughout, like the Ramså profile. During later tectonic activity, with the formation of fault blocks, etc., erosion of elevated parts may have removed much of the saprolites there, and the formation of deep saprolites in basement rocks requires long spans of time (Hansen et al. 2012).

Parnell et al. (2000) described the formation of kaolinite in Scotland and Northern Ireland during Late Carboniferous-Permian time, and that the precipitation of kaolinite is focused along high-permeability fault zones. This is because the infiltrating meteoric water needs to leach out most of the dissolved elements (e.g., the base cations) in order to create the right geochemical environment in the pore water for kaolinite crystallisation to occur.

Weathered basement was observed in IKU (Institutt for kontinentalsokkelundersøkelser) well 6814/4-U-1, which was drilled offshore Langøya, approximately 100 km SW from Ramså. The core recovered consists of weathered basement gneisses overlain by Mid Jurassic shallow-water siliciclastic sediments. The basal bed is a conglomerate, which is overlain by bioturbated clays and sandstones deposited in shoreface to foreshore environments (Hansen et al., 2012).

Another IKU core 6710/3-U-3 was drilled further towards the southwest, 260 km SW of Ramså. This core contains unweathered basement gneisses overlain by Early Triassic conglomerates, sandstones and some siltstones, which are interpreted to be immature alluvial-fan deposits of local provenance (Hansen et al. 2012). Due to the absence of weathered basement under Early Triassic siliciclastic rocks, it may be inferred that the weathering process occurred after the Early Triassic, i.e., in Late Triassic time (Mørk et al. 2003; Hansen et al. 2012, Fredin et al. 2017), in humid continental climate and paralic environments. This age (235.2 Ma) is also confirmed by K/Ar dating of a clay fraction (<2 micron) from one of the Ramså samples.

However, an older, Carboniferous age, indicated by the K/Ar analyses of the <0.1 micron fraction, should not be dismissed either, as this is the time interval when an extremely humid climate and large peat formations developed globally (Parrish 1993). Regionally, the geological data support the impression of intense weathering of basement during the Late Palaeozoic. This has been confirmed from the Barents Sea, where weathered basement was found to be overlain by the Lower Carboniferous Soldogg Formation (Larssen et al. 2002). It is therefore likely that two time intervals were important for the development of the deeply weathered basement zones on Andøya:

- (i) a Late Palaeozoic phase, suggested by Sturt et al. (1974), and
- (ii) a Late Triassic phase, suggested by Mørk et al. (2003) and Fredin et al. (2017).

Our data are consistent with both of these weathering phases affecting the basement ont Andøya.

10.12 **Weathering and diagenetic processes**

10.12.1 Development of soil profiles

Meteoric weathering and the formation of saprolites are mostly associated with the development of soil profiles, where plant growth is an instrumental part of the process. The development of soil profiles is a constructive process whereby disintegrated rock material gets converted into a soil body. A soil profile is divided into four main horizons, referred to as horizons O, A, B and C:

- The O horizon is the uppermost organic rich layer, with decomposing and fresh plant material. A wide spectre of insects, bacteria, fungi and viruses are participating in the decomposition processes, and the residue is referred to as humic material. Important products from the decomposition process are fulvic and humic acids, humin, CO_2, oxalic acid, acetic acid, etc.
- The A horizon is the layer with maximum leaching, where iron and aluminum from dissolving silicates are forming complexes and chelates with fulvic and humic acids. These organo-metallic compounds are transported downwards with percolating acidic water, to be precipitated in the horizons below.
- The B horizon is the accumulation zone for clay minerals, organo-metallic complexes, and sesquioxides; commonly forming complexes with fulvic and humic acids.
- C horizon is the horizon below the B horizon, which is relatively less affected by soil forming processes; i.e. below the root zones of the vegetation.

10.12.2 Hydrolysis dominates the initial weathering

The dominant chemical weathering process is hydrolysis (Millot 1970). Consequently, the percolation of acidic meteoric water is accelerating the weathering process. Calculations of the amount of acids needed to dissolve the primary minerals removed from podzol profiles in Southern Norway (sub-arctic climate) during the 10 000 years after deglaciation shows that more than 85% of the acids needed are produced in the soil itself, mainly from the decomposition of organic matter (Rueslåtten 1976). The interaction between meteoric water and feldspars that results in hydrolysis, is initially comparable to a cation exchange process, where the base cation is exchanged with a proton (Rueslåtten & Jørgensen 1977); e.g.:

$$NaAlSi_3O_8 + H_2O \rightarrow HAlSi_3O_8 + Na^+ + OH^-$$

This reaction includes the dissolution of base cations; i.e. the reaction is alkaline, and the pH of the water phase increases if not buffered by acidic percolating meteoric water, containing humic and fulvic acids. Feldspars at equilibrium with pure water will attain a pH close to 10.

Chemical weathering of sericiticised feldspar on a syenite surface near Oslo illustrate this feldspar weathering (Figure 10.41). This SEM image also demonstrates that dioctahedral mica (in this case sericite) is much more resistant to chemical weathering than feldspar.

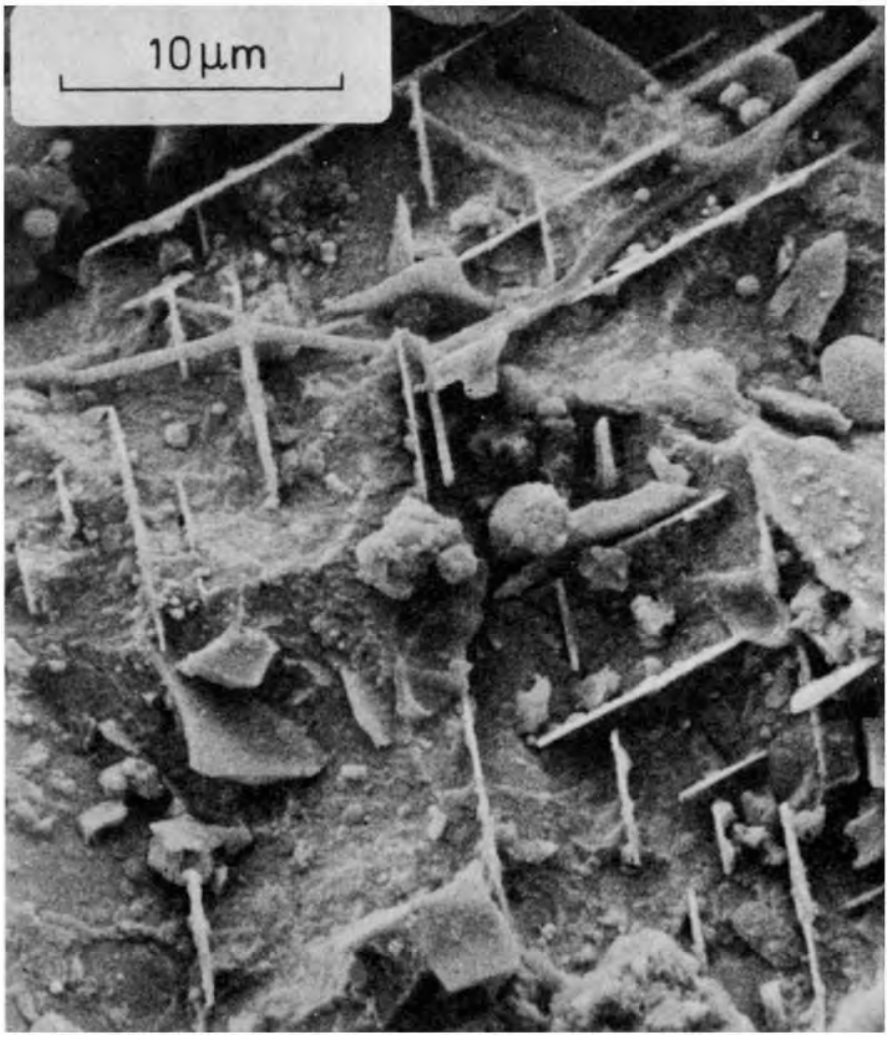

Figure 10.41. Weathering of sericitisised feldspar in the surface of an out-cropping syenite near Oslo. Feldspar is more vulnerable to acid surface water then sericite. This weathering took place during the Holocene. (From Rueslåtten & Jørgensen 1978).

The 'hydrogen feldspar' resulting from the hydrolysis is unstable, and also aluminum and silica will be leached; silica faster than alumina. If the climate is subtropical to tropical, and the weathering zone is well drained, kaolinite may crystallise from the dissolved aluminum and silicon components from the feldspar. If the drainage is poor, smectite may crystallise Millot 1970). This is seen in e.g., the mudstone sample (MB12-10) from the Ramså profile, which contains smectite, while the more permeable sandstones contain abundant kaolinite (Table 10.3).

10.12.3 Lateritisation

A general trend for the development of saprolites is that hydrolysis proceeds, and that silicon and aluminum tend to organise into forming clay minerals, e.g., kaolinite. Lateritic soils are

the subsoils of equatorial forests and savannas in the humid tropical regions, developing on top of the saprolites. They cover most of the land area between the tropics of Cancer and Capricorn; the tropic of Cancer being the latitude 23°26′13.5″ north of the Equator. Its Southern Hemisphere counterpart is the tropic of Capricorn. The zones of lateritisation cover about one-third of the Earth's continental land area (Tardy, 1997).

Laterites occurring outside the present-day humid tropics are considered to be the result of continental drift, climatic changes or a combination of both.

The ultimate lateritisation is that the leaching continues, including the leaching of silica, until only aluminium- and iron-oxi-hydroxides are left *in-situ*. Other 'immobile' elements, like titanium and zirconium oxides, are also accumulated in the laterite profile. At this stage, the main minerals in the laterite profile are gibbsite ($Al(OH)_3$), boehmite (AlO(OH)), hematite (Fe_2O_3) and goethite (FeOOH); i.e. the major components of bauxite. Such laterite horizons are commonly seen overlying saprolites consisting of quartz and kaolinite. This type of laterite profile is not found on Andøya, indicating that the weathering halted before a complete laterite profile was developed. This may be due to either climatic conditions or a limited time span for the development of the weathering profiles before they were submerged by marine transgression and/or covered by sediments.

It has been argued that the upper parts of the weathering profiles may have been eroded, and that this could explain why the lateritic horizons are mising. However, if lateritic minerals existed, they should have been found in the sediments from the eroded laterite profiles. *This is not the case, and it is therefore concluded that the weathering never reach the laterite stage.*

10.12.4 Weathering and climate

Climate is a major factor in the weathering process. In a humid climate with temperatures around 30°C, the weathering is four times faster than in a humid climate at prevailing temperatures of 10°C (Millot 1970). The deep saprolite found in the basement granodiorite at Ramså suggests that humid tropical climatic conditions prevailed during the development of this saprolite profile.

10.12.5 'Retrograde metamorphism

'Retrograde metamorphoism' is commonly seen in the 'fresh' rocks exposed to weathering. This is identified by e.g. sericitisation and sausseritisation of feldspars and chloritisation of biotite; processes that are causing instabilities in the crystal lattices of the rock forming minerals and, thus, making them more vulnerable to weathering. This is also seen in the basement rocks at Ramså.

10.12.6 The source for kaolinite formation

It is well known from North Sea reservoirs that dissolved feldspars are the main source for the formation of kaolinite (Bjørlykke 1998). This is tested here for the samples from the Ramså surface profile, by plotting the amount of kaolinite in the samples versus the sum of feldspars

and quartz in Figure 10.42. A good correlation is seen, indicating that this hypothesis is valid also here.

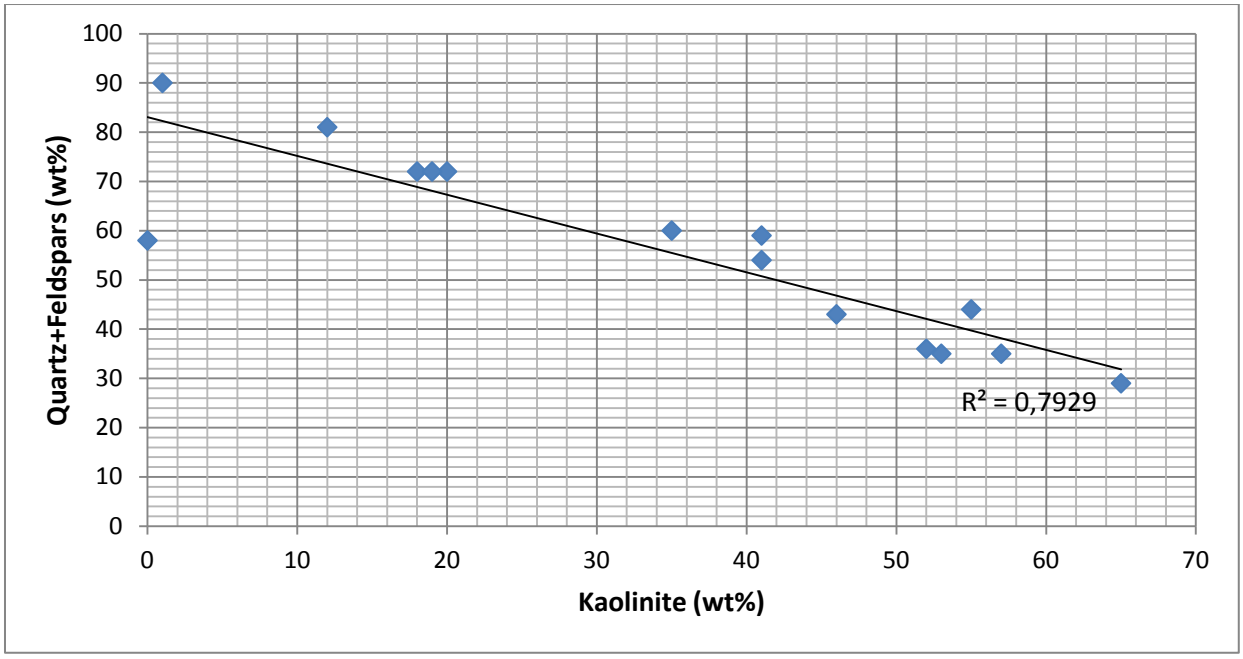

Figure 10.42. The Ramså surface profile: Kaolinite versus quartz + feldspars (XRD analysis Table 10.3). The interpretation of this correlation is that dissolved feldspars are the major source for kaolinite formation.

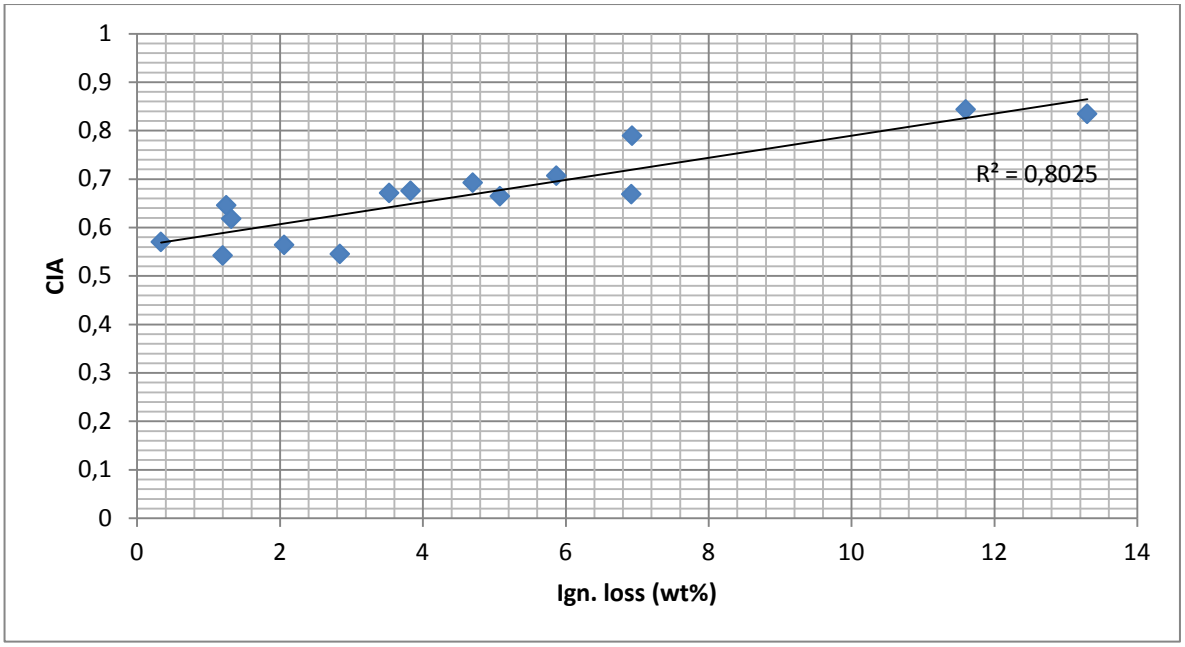

Figure 10.43. NGU's BH 1+BH 2: Chemical Weathering Index, CIA, versus Ignition loss (XRF analysis, Table A.1). The trend seen is explained by the fact that increased weathering leads to the formation of more hydroxyl-bearing minerals; i.e. clay minerals, which have higher Ignition losses and higher CIA.

10.12.7 The Chemical Index of Weathering, CIA

The Chemical Index of Weathering, CIA, is widely used as a proxy for the degree of weathering: CIA= $Al_2O_3/(Al_2O_3 + CaO + Na_2O + K_2O)$. This index is also used in this report; see Figure 10.43. However, the CIA index is also responding to an increased content of phyllosilicates versus quartz and feldspars; not only newly formed clay minerals. This may explain the difference between Figure 10.43 and Figure 10.45. The composition of the sediments in BH 1 is rich in phyllosilicates (mica, chlorite and talc), while the Ramså surface profile is dominated by weathered granodiorite.

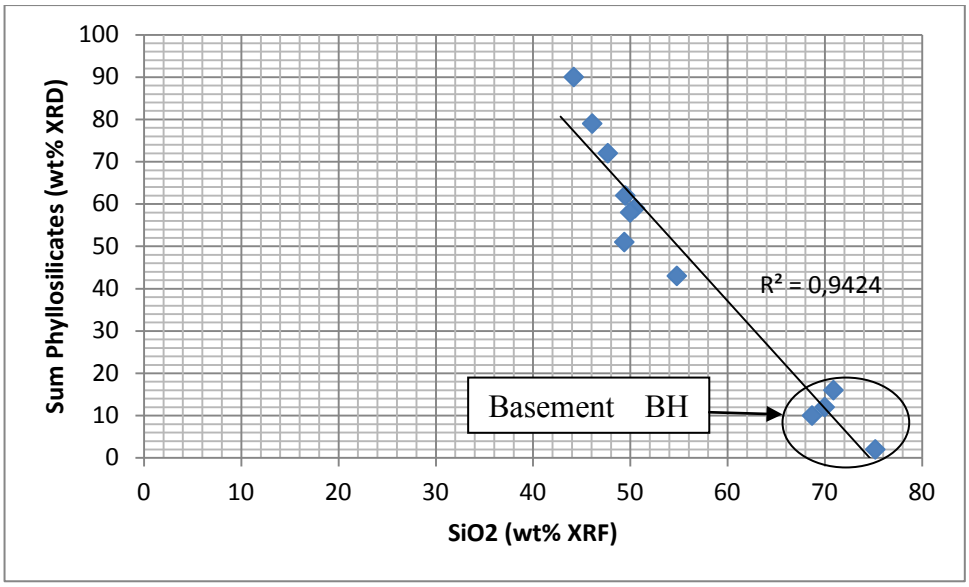

Figure 10.44. NGU's BH 1 + BH 2: SiO_2 (weight % XRF) versus sum phyllosilicates (weight % XRD). The amphibolites are excluded; also sample 167, due to their low quartz contents. The basement samples of BH 2 (unweathered granodiorite) have the highest SiO_2 values (marked) due to their dominating contents of tectosilicates.

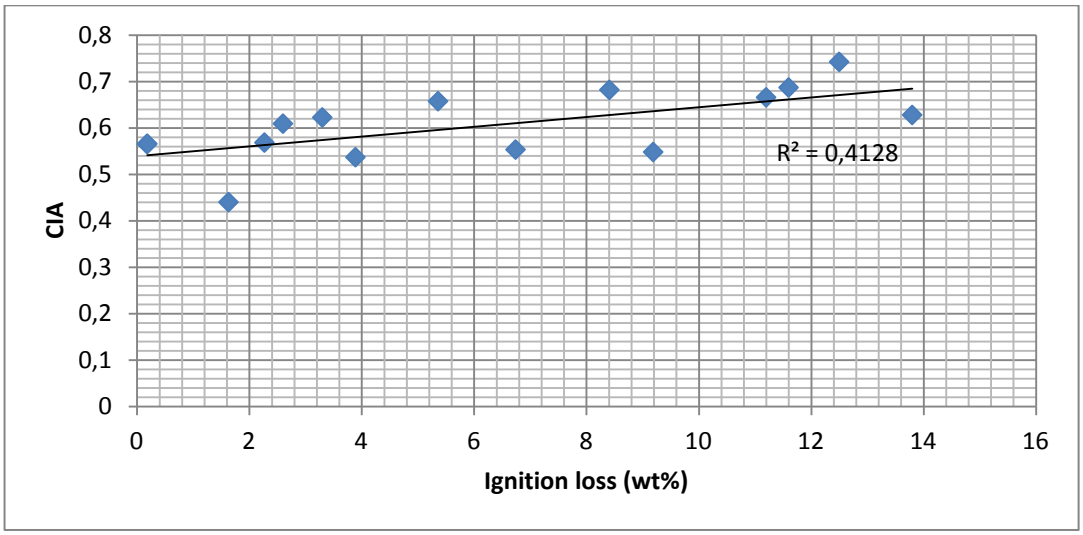

Figure 10.45. Ramså surface profile: Chemical weathering index, CIA, versus Ignition loss. The trend seen is explained by the fact that increased weathering leads to the formation of more hydroxyl bearing minerals; i.e. clay minerals, which have higher Ignition losses and higher CIA. However, the trend for these samples are not as good as that from BH 1 and BH 2 (Figure 10.44).

10.13 Provenance and mineral alterations

10.13.1 Burial depths and mineral alterations

It is well known that kaolinite recrystallises to dickite when exposed to temperatures higher than 100°C (Beaufort et al. 1998). A detailed investigation of kaolinite from the various formations applying both XRD and SEM analysis shows no sign of dickite formation; i.e. the sediments were never exposed to temperatures as high as 100°C.

Furthermore, a detailed investigation of vitrinite reflectance throughout the profile at Ramså was carried out by Bjorøy et al. (1980). The Ramså Formation (the lowermost one) gave reflectance values from 0.32 to 0.45 with an average of 0.41.This indicates a T_{max} of 42°C. By taking the assumption that the thermal gradient was 30°C per km, the burial depth never exceeded 1.5 km. *The maximum thickness of the sediments today is less than one km, indicating that in the order of 0.5 km of sediments were eroded and deposited inside or outside of the Ramså Basin.*

10.13.2 Provenance of the sediments:

Trace element variations in NGU well BH 1 and in the Ramså surface profile indicate that the sediments have a similar provenance, with the exception of the amphibolitic intrusions. Weathered basement (granodioritic) is the main source, but the thick sequence (61 metres) of mafic-dominated debris flows/conglomerates/sedimentary breccia in NGU Well BH 1 is a dominating source in this area. However, such mafic sediments are hardly seen in the other investigated localities. The main minerals in these debris-flow sediments are plagioclase, biotite, chlorite, talc and hematite. Brecciation of fault zones during upheaval of such basic rocks may be the source for these debris-flows, probably deposited from west to east. These debris flows are also detected on seismic profiles in that area (pers. comm. Tormod Henningsen, 2016). In the other areas, it appears as if weathered granodiorite was a major source for the sediments.

10.13.3 Observations on Andøya

Three different alteration processes have influenced on the profiles studied on Andøya:

- Meteoric weathering of basement rocks; e.g., the saprolite developed in the basement granodiorite at Ramså.
- Soil development in the Jurassic and Cretaceous sediments where vegetation was established. This is seen by rootlets and organic layers in the sedimentary strata.
- Diagenetic alteration, which has had an impact on the sediments during their deeper burial; e.g., the formation of vermicular kaolinite from dissolved feldspar in the pore system. These features are formed *in-situ* (Figure 10.23).

All three processes have been identified in the rocks, and some of these processes have been going on for quite some time; e.g. diagenetic processes have altered weathered soils during burial.

Boehmite or gibbsite are not found in the samples from Andøya, indicating that the weathering halted before the laterite profiles were fully developed, in spite of the pervasive weathering of the basement rock at Ramså.

The developments of deep saprolites in basement rocks, like the one at Ramså, are not found in the other wells. *It is therefore concluded that saprolite formation was not covering the entire basin, and/or that most of the saprolites were eroded and transported to the deeper parts of the basin where they were deposited; i.e., towards east and north.*

10.14 **Tectonic events and age determination**

Palaeosols and palaeosaproliths provide information about climate, vegetation and topography that determined their development. Dating of these features is therefore a prioritised task. The K/Ar method was applied for age determination, and the following samples were dated:

- one weathered basement sample from Well A (530.5 m depth);
- three sediment samples from Well A
- two samples from the lower strata at Ramså outcrop profile.

The clay fractions (<2 micron) were separated out for the analysis, and also the fractions <0.1 micron (fine clay).

The <2 micron fractions gave two different ages: 485.9 ± 10 Ma (Early Ordovician-Tremadocian) and 235.2 Ma (Mid Triassic-Ladinian). This is consistent with the formation of the Triassic-Jurassic rift basins flanking the Lofoten Ridge (Steltenpohl et al. 2013).

Earlier apatite fission-track data indicate Triassic to Early Jurassic ages; i.e., that most of the tectonic (faulting) activity took place prior to the Late Triassic (Davids et al. 2013). The Mid Triassic (235 Ma) pulses of E-W-directed post-orogenic continental rifting may also have had an influence on the structural evolution of the Ramså Basin and exposed the basement rocks to atmospheric weathering. Thus, the Mid to Late Triassic can be interpreted as one possible age for the saprolite formation at Ramså.

The <2 micron fraction from the weathered basement in Well A at 530.5 m depth, gave a K/Ar age of 111.1 ± 2.4 Ma, or Early Cretaceous (Albian) age. A regional tectonic activity is recognised in central and northern Norway during the Lower Cretaceous, and a resetting of the K/Ar system may be due to infiltration of meteoric water in fault systems during these tectonic events, which may explain the K/Ar age obtained.

It is generally accepted that the finest authigenic mineral particles in the clay fraction; e.g. the fraction <0.1 micron, are the latest particles to have crystallised *in-situ*; i.e. this fraction (<0.1 micron) should give the youngest age in K/Ar dating. However, this is not the case for one of the surface samples at Ramså. The <0.1 micron fraction of this sample gave an age of 333.6 ±

70 Ma, i.e. Carboniferous, an age between the two ages obtained for the <2 micron fractions. However, this age is consistent with the age span obtained by Sturt et al. (1979), who obtained ages from 342 Ma (Early Carboniferous) to 207 Ma (Late Triassic). The fact that our results are similar to the ones of Sturt et al. (1979) is not surprising, because the surface samples most probably came from the same location. Our data may therefore be looked upon as supportive to the conclusions reached by Sturt et al. (1979). Thus, the age dating seems to give two reasonable time intervals for the formation of the basement saprolites, which are also consistent with earlier dating:

- Late Palaeozoic; e.g. Permian (suggested by Sturt et al. 1979)
- Late Triassic (suggested by Mørk et al. 2003, Fredin et al. 2017).

Sturt et al. (1979) also suggested that a deep burial of the Ramså Basin subsequent to the saprolite formation had given a strong impact on the K/Ar ratios. However, we cannot see any signs of such a deep burial (deeper than 2 km); neither on vitrinite reflectance nor by kaolinite-to-dickite recrystallisation.

A similar study of saprolites developed on Devonian monzogranite in the South Mountain Batholith, Canada, came out with three different ages; pre-Carboniferous (i.e. Devonian), pre-Triassic (e.g. Permian), and pre-Pleistocene (O'Beirne-Ryan 2006). These findings demonstrate that saprolites developed also on the American continent during the Palaeozoic and Mesozoic eras. However, the ages deviate significantly from our findings, except for the pre-Triassic (e.g. Permian) dating, which seems to coincide with ours.

11. INTEGRATED INTERPRETATION

Marco Brönner, Tormod Henningsen, Håkon Rueslåtten, Bent Ole Ruud & Tor Arne Johansen

The Ramså Basin is a small basin at the western boundary of Andfjorden which is mostly known because it is the only recorded Mesozoic sedimentary basin onshore Norway. In actual fact there is so much more to study and we can learn a great deal from a thorough investigation of the basin and the surroundings. The occurrence of deeply weathered basement (Chapter 3.3) underneath Mid-Jurassic sedimentary strata gave a minimum age for the disintegrated bedrock, similar to the situation at Ivö, Sweden, where Late Cretaceous rocks overlie a clay-type weathering (Lidmar-Bergström et al. 1997). However, for a long time it was generally accepted that the clay-type weathering was rather old, possibly of Mesozoic age, whilst the grusy type was relatively young and thought to be of Plio-Pleistocene age (Hall et al. 2015). This is in contradiction with what one can observe at the southern edge of the Ramså Basin, where c. 30 m of weathered basement is exposed at the beach (Figure 10.1) and a gradual transition from unweathered over grusy weathering to clay-rich weathering is observed. This also reflects the classical understanding of a regolith (Figure 8.4). Sturt et al (1979) dated the weathered basement and obtained Permian-Carboniferous to Jurassic-Triassic ages and concluded that the major period of weathering could have been in the Jurassic-Triassic. This is in good agreement with a recent paper by Fredin et al. (2017) where weathering was dated from different places in Norway, using the K-Ar method.

Furthermore, the basin is part of the strandflat on Andøya, which suggests a possible close connection between this peculiar landscape and deep weathering processes (Brönner et al. 2017 (subm.), Olesen et al. 2013). The remains of Mesozoic sedimentary rocks with physical and chemically disintegrated basement rock underneath indicate that the strandflat could represent a paleic surface, an old weathering front where the existence of weathered bedrock can have favoured the erosion of large amounts of material, both sedimentary rocks and dissolved, soft basement, which could also explain the high uplift rates still being regarded across the Lofoten-Vesterålen region.

This is an important objective we wanted to address in the present study and to investigate the characteristics and setting of the deeply weathered rocks within the basin and whether geophysics can aid in mapping this phenomenon.

The close position to Andfjorden would suggest that the Ramså Basin is a kind of sub-basin and its development can thus be closely connected to the development of the Andfjorden Basin. Structural studies have been carried out onshore and existing well cores were studied to better understand the connection between, and the tectonic development of these two basins (Forthun, 2014; Dalland, 1975), but very little geophysical data had been acquired since 1975. A few, rather short refraction seismic lines exist and three c. N-S-trending seismic lines were acquired in the fjord, where two are from 1988 and rather modern (Figure 5.16). To investigate the connection between the Ramså Basin and the Andfjorden Basin and develop a

tectonic concept of the area can contribute to a better understanding of the development of the Lofoten-Vesterålen margin and can throw light upon the question as to where and how basement weathering developed and can be preserved beneath sedimentary strata.

11.1 Geophysical interpretation

In addition to airborne acquisition of magnetic, gravity and EM data , reflection seismic data were collected onshore and offshore (Chapters 4, 5 and 6), which together provide a comprehensive database of geophysical data to help achieve the objectives in this project. Bedrock mapping (Chapter 7) and petrophysical measurements (Chapter 4.4), as well as stratigraphic, mineralogical and geochemical analyses from well cores and surface observations (Chapters 8, 9 and 10), have revealed heterogeneous bedrock settings and a complex structural development of the study area, which underline the complexity in the development of the Ramså Basin and the adjacent Andfjorden.

We have combined the achieved observations and analyses in a joint modelling and interpretation to better realise the objectives of this project.

The airborne and seismic data were subsequently interpreted as is much of this presented in the Chapters 4, 5 and 6.

11.1.1 Airborne geophysical interpretation

The airborne magnetic and gravity data were used to identify linear structures which represent faults and bedrock contacts. Variations in amplitude and gravity and magnetic highs and lows indicate sedimentary basins and basement highs or a change in the basement domain. We applied a set of wavelength filters to separate the residual field from the regional to highlight lineaments and the basin-related settings.

From the magnetic data, the Ramså Basin is not very prominent (Figure 11.1), which is to a large extent due to an overprint of a high-magnetic NW-SE-striking gabbro body. From the filtered data the gabbro dyke appears as a set of irregular small, high-magnetic anomalies surrounded by deep magnetic lows, which points to a significant segmentation of this rock and a limited depth extension. Farther south, the Skogsvoll group (Figure 7.3) has a similar signature to the magnetic, but the anomalies here are linked to layers with magnetic minerals embedded in a matrix of supracrustal metasedimentary rocks organised in a folded structure (Chapter 7.2.2), which explains the horse-shoe structure in both the gravity and the magnetic data.

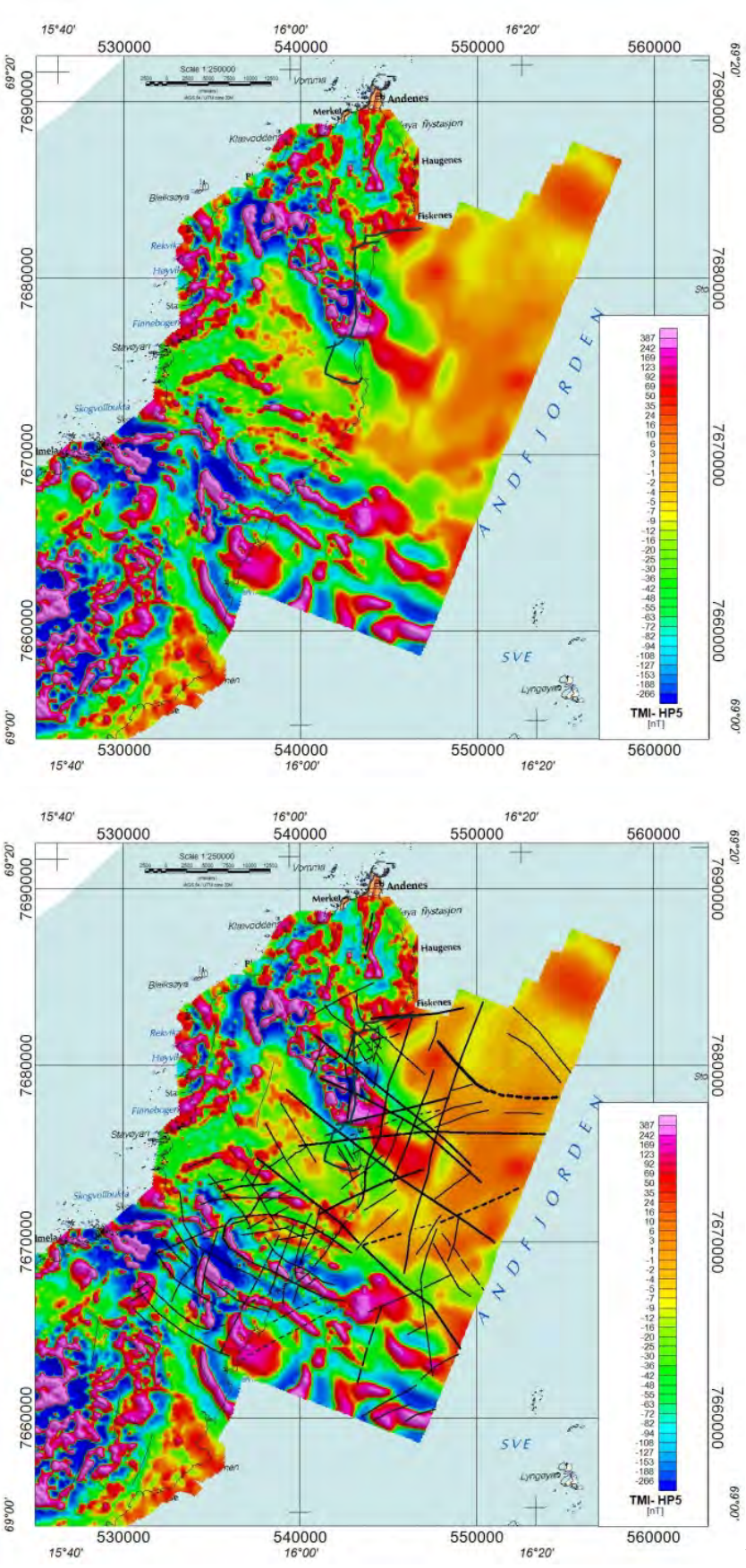

Figure 11.1. a) 5 km high-pass filter of the magnetic data and b) with interpreted lineaments.

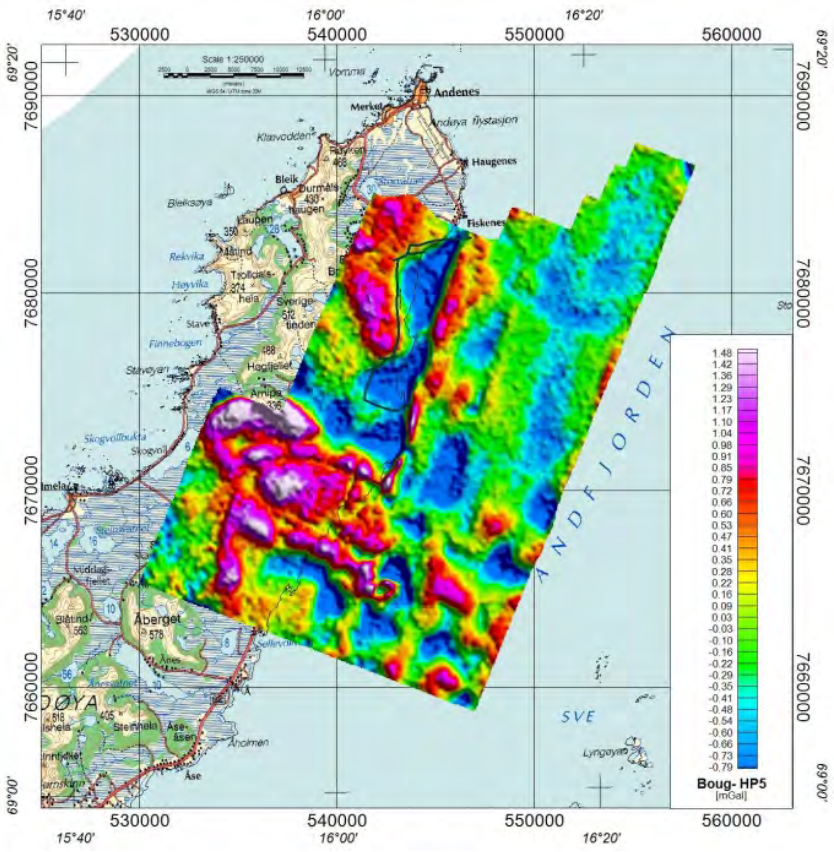

a)

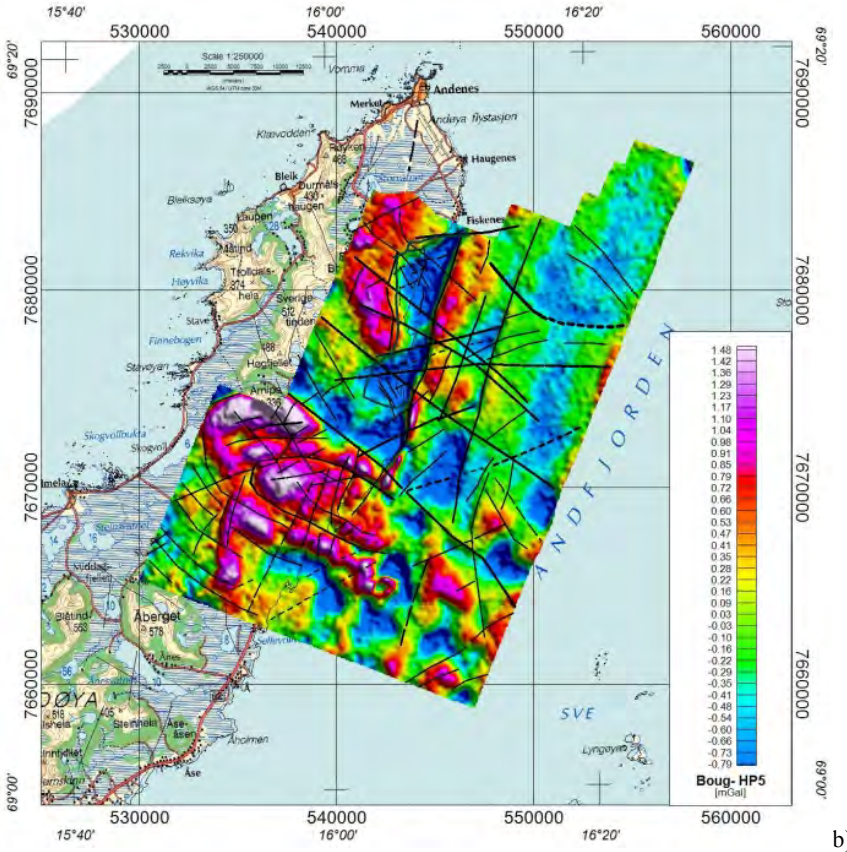

b)

Figure 11.2 a) 5 km high-pass filter of the gravity data and b) with interpreted lineaments.

In the gravity data the Ramså Basin is a prominent gravity low, which reflects the character of two sub-basins separated by a basement horst as was inferred earlier (Figure 3.2). However, the gravity data indicate an extension of the Ramså Basin offshore, bordered by a fairly sharp narrow, N-S-striking gravity high. In addition, there are a few more isolated gravity lows observed, where at least two of them are onshore to the south of the Ramså Basin, which was a decisive factor in extending the seismic lines 2 and 3 to the south beyond the original basin boundary. The amplitude and appearance of these two magnetic lows is very similar to the one in the Ramså Basin. The westernmost of these two anomalies is also indicated by the helicopter EM data (Figure 6.2Figure 6.3), but the EM data rather suggest an extension and not an isolated sub-basin, although there is a prominent basement outcrop observed (Figure 7.3).

In general we identified three major trends from the gravity and magnetic data: NW-SE, NE-SW and N-S. Furthermore, we observed a northward arc-shaped lineament SW of Fiskenes, which is visible from both gravity and magnetics. Especially the N-S trend, but also this arcuate trend is also reflected in the bathymetry data (Figure 5.1).

The E-W extension of the gravity lows seems to be to a large extent linked to the N-S trend, whereas cross-cutting NW-SE and NE-SW-striking lineaments control the limits in a N-S direction. The prominent NW-SE-striking magnetic anomaly, which can be related to the gabbro onshore, also shows an abrupt change in amplitude and width at one of the N-S-striking lineaments, which indicates the fault nature of these lineaments and suggests a complex tectonic setting for the Andfjorden.

11.1.2 Seismic interpretation

The quality of the seismic data reflects to a large extent the complexity of the study area, but it also accommodates the adjustment of the acquisition to minimise possible environmental effects. We therefore applied gravity and magnetic data during the seismic interpretation to support in particular the top-basement interpretation. Furthermore, we used the reprocessed regional NPD profiles to tie our interpretation on the new seismic lines and the existing well interpretations (Figure 3.5). We identified the top basement, BCU and locally two intra-Cretaceous reflectors, which we interpreted as 'near base Barremian' and 'near base Aptian' units in accordance with our experience from the Norwegian shelf and the Lofoten-Vesterålen area in particular, where these two units are relatively good markers in the seismic data.

Line 1 crosses the Ramså Basin along the basin's N-S axis and confirms the general geometry with a central basement horst and two deeper basins in the south and the north (Chapter 11.1.1 and Figure 3.2). The seismic data show downfaulted and rotated blocks with a major border fault at the southern basin boundary. The Jurassic strata were drilled and observed to show a c. 200 m thickness. This is in good correlation with our interpretation of the BCU, which infers a rather thin layer with Jurassic sedimentary strata. The sedimentary strata are dipping northwards within the southern basin, whilst for the shallower Cretaceous sediments no predominant dip could be identified. For the northern basin the dip seems to point towards the

deepest part of the basin with an apparent dip change from north to south, whilst in the shallower part some flat-lying reflectors are observed which could confirm that the lower Andøya sequence is onlapping (Figure 2.2).

The horst appears to be significantly fractured and faulted and to have a rough surface, which also correlates with the interpretation from the magnetic signature of this block. It is bounded by southward-dipping normal faults. An intra-basement reflector, which could indicate the depth of this body, could not be identified.

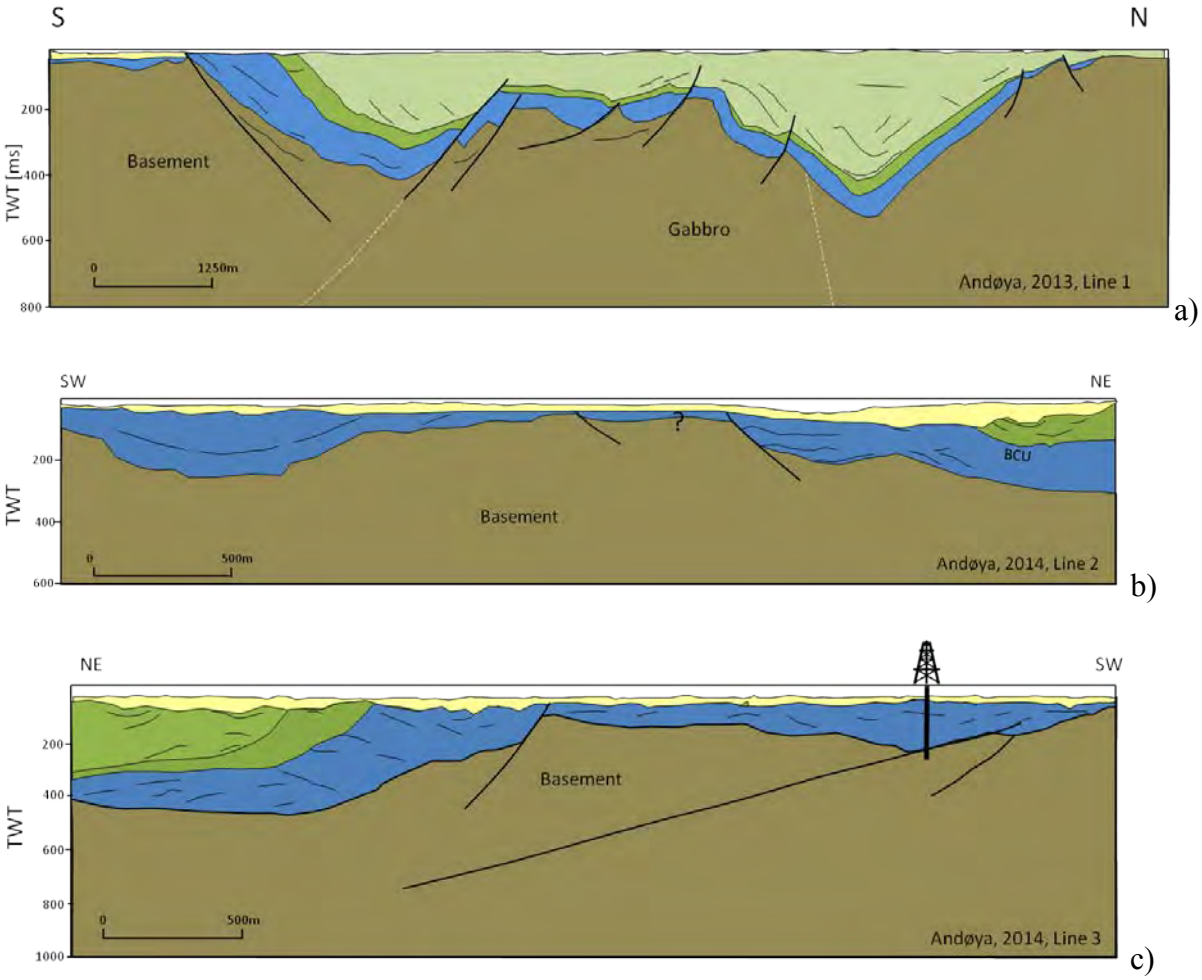

Figure 11.3. Interpretation of the land seismic lines a) Line 1, b) Line 2 and c) Line 3 with BH 3. For positions of the profiles, see Figure 5.1.

The line 2 (Figure 11.3b) runs across the eastern gravity anomaly, which is south of the Ramså Basin, and identifies a sub-basin. The infill remains unclear, but we assume a similar setting for both the new sub-basins and postulate the presence of Jurassic sedimentary strata since these were drilled in the western sub-basin (Line 3). It is noteworthy that the EM data do not indicate a basin, but show high resistivity in this area.

The seismic data suggest a basement high in the transition to the Ramså Basin, which can also be overlain by some sediments. However, we observed in the field a significant amount of moraine sands in this area and cannot distinguish whether the sediments observed from seismic are Quaternary deposits or Mesozoic sedimentary rocks. The profile also maps parts of the southern Ramså Basin and it indicates that the southern boundary to be rather a normal faulted setting with rotated blocks rather than a pure onlap as it has been suggested earlier (Chapter 3.3).

Line 3 (Figure 11.3c) crosses the western new sub-basin, observed from gravity and EM data and covers the southern Ramså Basin. It confirms the Ramså Basin rim to be a normal faulted rotated block. An intra-Cretaceous reflector could be estimated locally and was extrapolated based on the surface observation, taken from Henningsen & Tveten (1997). The new western sub-basin was confirmed by drilling to be c. 200 m deep and filled with Jurassic sedimentary rocks. The transition between the basins remains uncertain. From the gravity data a basement horst is indicated and confirmed by a basement outcrop. However, the seismic data indicate a deeper basement along the profile with sediments on top. The age of the sediments is unknown and they could also be Quaternary moraine sands, but such a setting is actually in good correlation with the EM data which do not indicate a clear and continuous boundary between these two basins.

Due to shallow water between the onshore seismic and the marine seismic data a gap exists which was not accessible with the seismic vessel. However, the western end of the marine seismic lines coincides with the eastern boundary of the Ramså Basin, inferred from gravity data by a noticeable N-S-trending narrow gravity high (Figure 11.2). The offshore part of the Ramså Basin is consequently not imaged with seismic data, but is modelled on composite lines (11.2).

The interpretation of the marine seismic lines is consistent with observations onshore regarding the sedimentary strata although an accurate age for the marine strata remains uncertain. The lowermost sediments are possibly older than what is observed in the Ramså Basin and are referred to as Triassic-Jurassic, which should not exclude the possibility of thin layers with Late Palaeozoic sedimentary rocks. However, the sedimentary strata are relatively thin compared to other basins on the Norwegian shelf like the Vestfjorden Basin or the Nordkapp Basin, which thus indicate a fairly late development of the Andfjorden area. Thick packages with Cretaceous sedimentary rocks, however, are common for all the interpreted seismic lines, suggesting major rifting phases and basin development in the Early and/or Late Cretaceous.

For the new seismic lines which are oriented mostly E-W, the major N-S faults inferred from gravity and magnetic interpretation were interpreted as normal faults with a sub-parallel east-dipping major border fault sytem in the west and a large west-dipping fault in the east, referred to as the Senja fault.

As can be observed from the bathymetry map the Andfjorden is getting wider in the north and this is also well reflected in the seismic data. The seismic shows the Andfjorden to be a half-graben, or more precisely a set of half-grabens controlled by N-S-trending faults. Profile M7 shows a set of three basins which are separated by basement highs. The westernmost basin shows very steep west-dipping reflectors resting on a rotated basement block, which also has a noticeable expression in the bathymetry. The central basin is a graben-like downfaulted basin, with border faults on both sides, but with an asymmetric east-dipping setting.

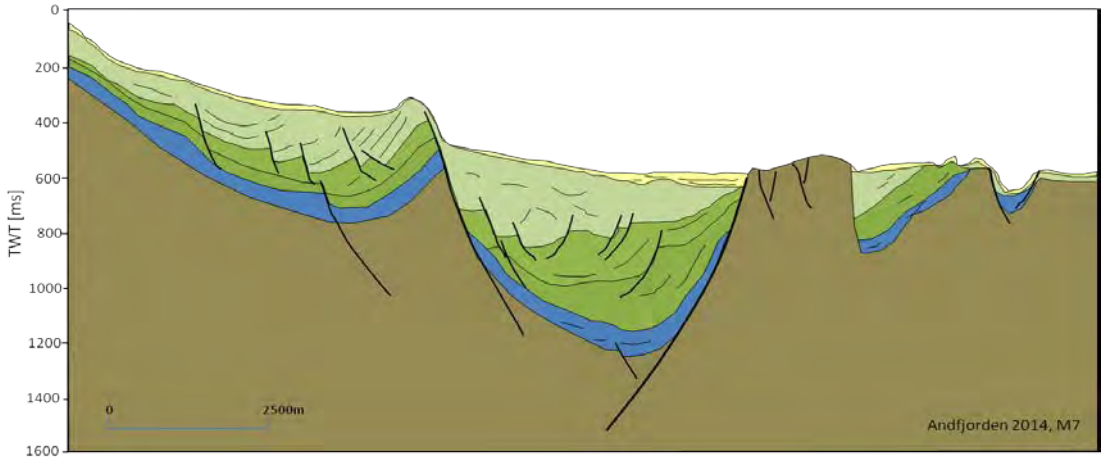

Figure 11.4. Seismic interpretation of profile M7. For positioning see Figure 5.1.

The easternmost basin is one of the smaller sub-basins, as they can be observed from the gravity data (Figure 11.2). The basin is downfaulted to the NW and connected to a larger basin to the north as can also be seen from the bathymetry map.

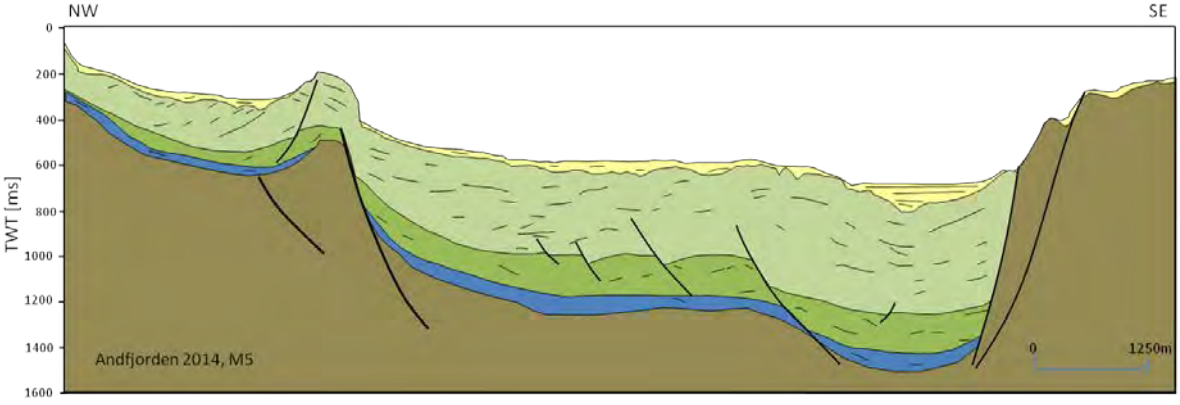

Figure 11.5. Seismic interpretation of profile M5. For positioning see Figure 5.1.

On profile M5 farther north, the eastern border fault evidently became the controlling structure for the development of the Andfjorden Basin. West-dipping normal faults exist, but are of minor relevance and show significantly smaller vertical offsets. However, the western basement high with its expression in the seafloor and interpreted as a rotated fault block separates another basin to the west and the Ramså Basin even farther west from the main Andfjorden Basin. Very steep reflections on top of this basement high indicate a significant

tilting of this basement block and with pre-tectonic sediments on top (Figure 11.4). Later sediments onlap these layers, indicating syn- and post-rift sedimentation during Early to Late Cretaceous time.

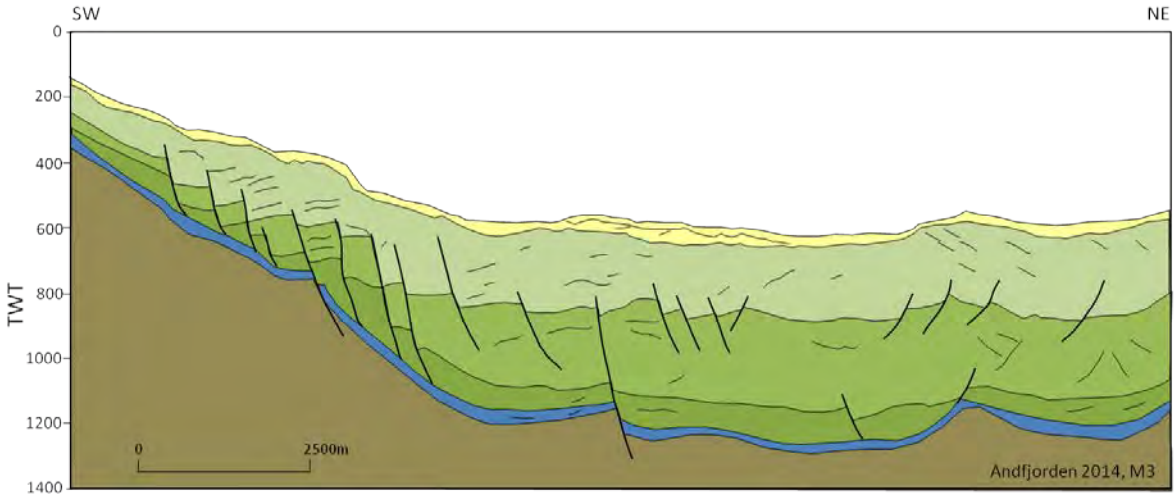

Figure 11.6. Seismic interpretation of profile M3. For positioning see Figure 5.1.

To the north the angle of the rotated sediments becomes less and the basement high fades out as can also be seen from the seafloor map but also in the seismic data (Profiles M3 & M6, Figure 11.6 &Figure 11.7) and an east-dipping border fault and the migration of the deepest part of the Andforden Basin from east to west (Profile M8, Figure 11.8) indicates a shift in the tectonic settings. Furthermore, the basement depth increases significantly between M6 and M8 from c. 1250 ms to 1800 ms TWT.

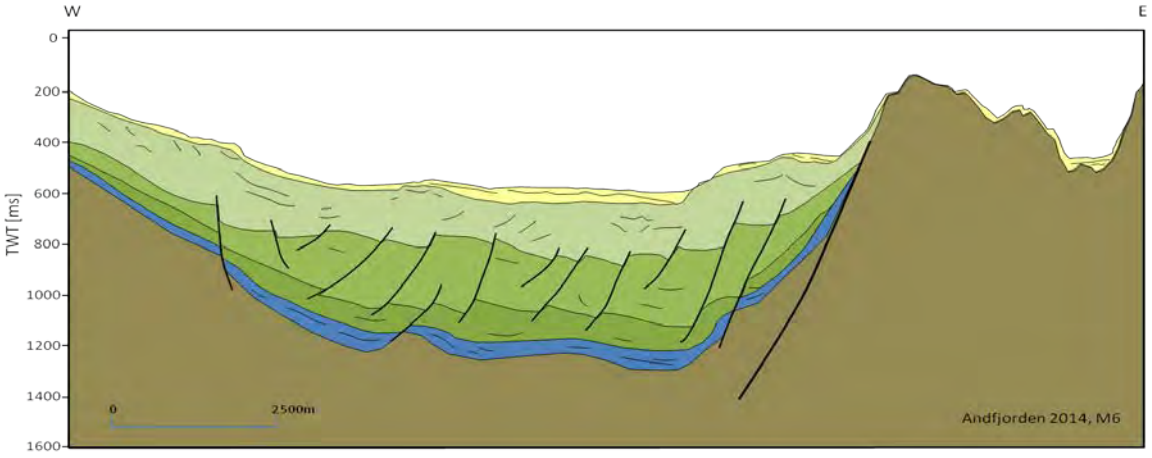

Figure 11.7. Seismic interpretation of profile M6. For positioning see Figure 5.1.

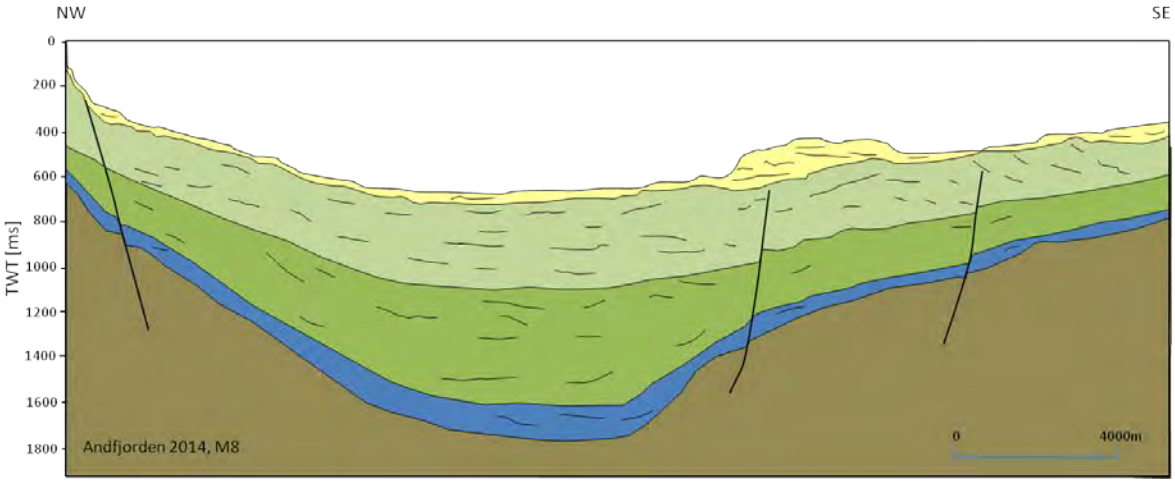

Figure 11.8. Seismic interpretation of profile M8. For positioning see Figure 5.1.

Between M6 and M8 the arcuate lineament is observed from the gravity and magnetic data, which can be linked on LO-88-11 and -13 (Figure 11.9 a and b) to a major normal fault and downfaulting of the sedimentary strata to the north. The change in the stress field happened most likely in Early to Late Cretaceous times and was coupled to a major rifting phase in the Harstad Basin and possibly also in the Tromsø Basin, with the development of a large-scale detachment farther north at the transition of the Andfjorden to the Harstad Basin. LO-88-52 crosses this detachment surface and is observed as an almost horizontal concave fault, east of the Andøya basement horst.

Detachments and normal faulting as observed from LO-88-11 and -13 are common expressions of extensional phases. However, from the reprocessed seismic lines especially on line LO-88-11 in the Upper Cretaceous strata (<1000 ms TWT) folding is noticeable, which indicates a compressional phase, a feature which is peculiar in the context of the extensional geometries, observed elsewhere on this seismic section.

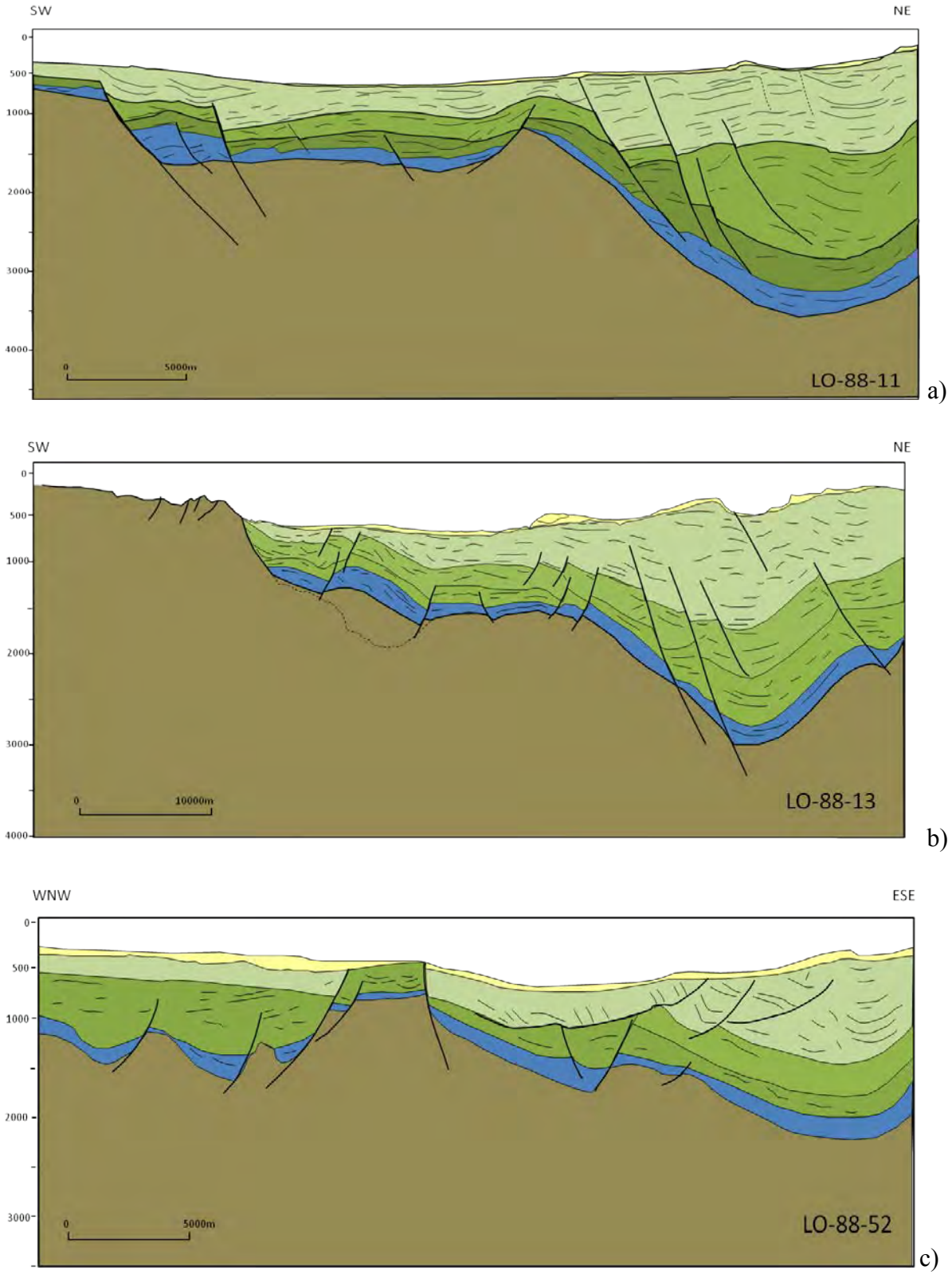

Figure 11.9. Interpreted NPD seismic lines. Three seismic lines, acquired by NPD in 1988, were interpreted a) LO-88-11, b) LO-88-11-13 and c) LO-88-52. LO-88-11 and -13 were reprocessed by UiB (See Chapter 5). All lines are in TWT (ms). For positioning see Figure 5.1.

The interpreted basement from the seismic data was gridded and interpolated (Figure 11.10 &Figure 11.11) to achieve a first order view of the basement settings in the Ramså and Andfjorden basins. The distribution of the seismic lines and the large distance between the lines hamper a detailed interpretation and some artefacts are introduced due to the interpolation. However, the Andfjorden Basin in the south up to the level of the arcuate lineament is a complex hoalf graben with several sub- basins and basement highs in between, mostly dominated by N-S-trending normal faults. North of the arcuate lineament, the Andfjorden Basin is significantly deeper and has a stepwise deepening and transition into the Harstad Basin and a major north-dipping detachment. The Ramså Basin can thus be confirmed as two basins separated by a basement horst in the central part. Two new sub-basins were found onshore south of the Ramså Basin where one was drilled and proved to be filled with Mid Jurassic sedimentary rocks.

Between the onshore and offshore seismic lines a gap exists and the offshore extension of the Ramså Basin and its eastern boundary cannot be directly derived from the seismic data. Potential field modelling of some key lines was used to fill this gap and provide a hint of the possible geometry of the Ramså Basin offshore (Chapter 11.2).

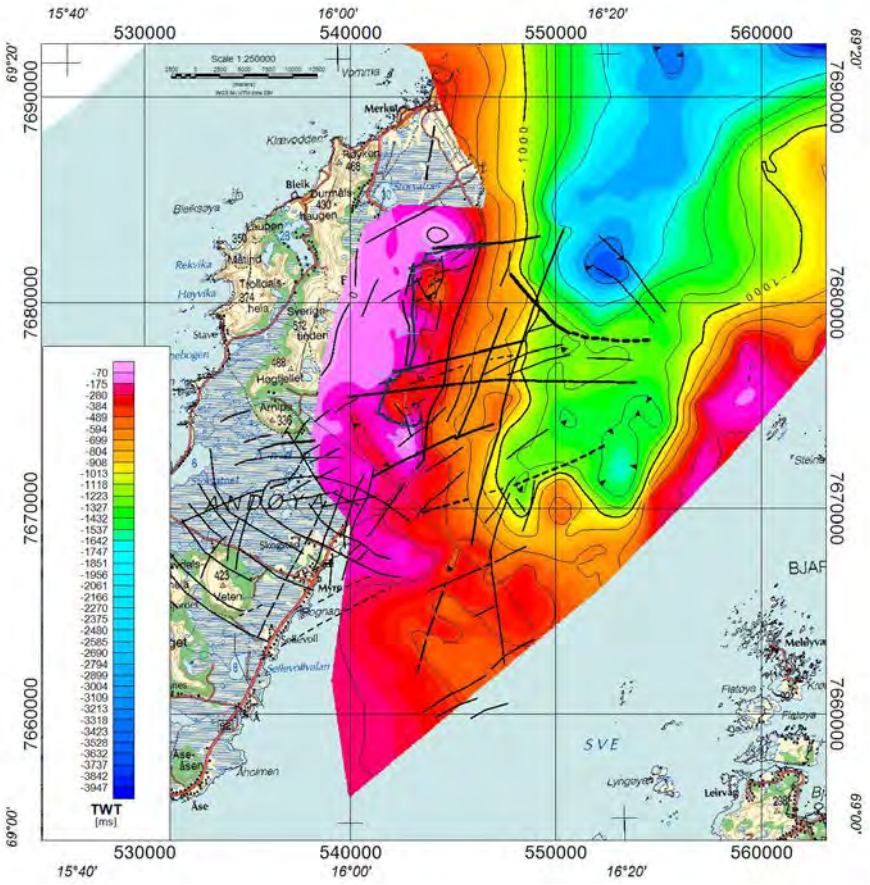

Figure 11.10. Top-basement map interpolated from 2D seismic profiles. The map is overlain by the interpreted N-S and NE-SW-striking faults derived from the gravity and magnetic interpretation. The observed arcuate anomaly marks the transition to a significantly deeper basement in the Andfjorden Basin.

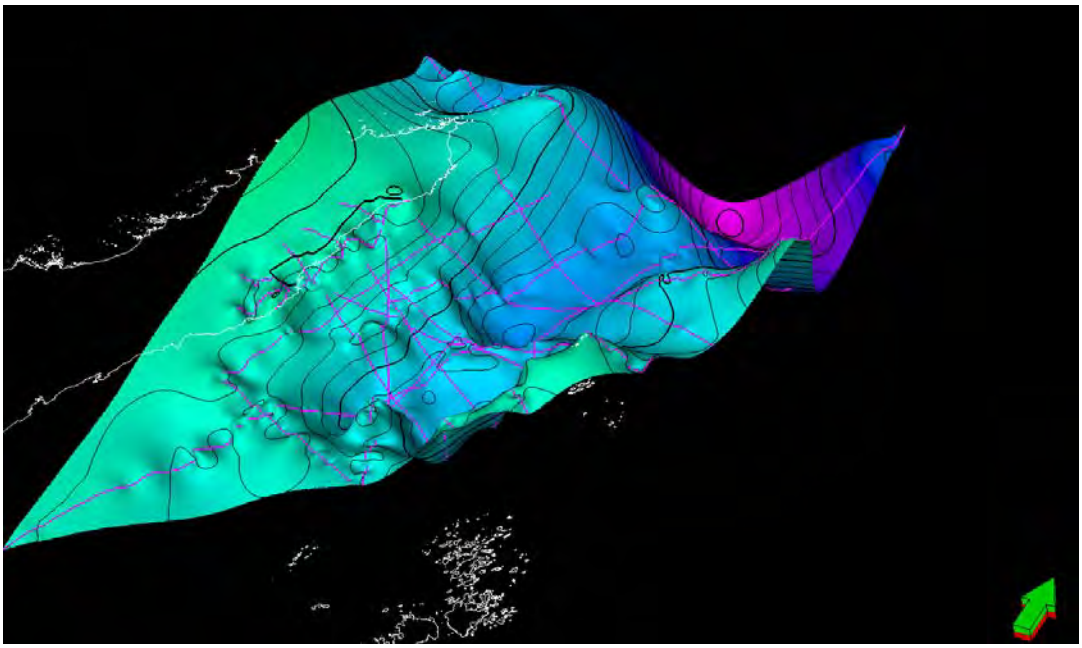

Figure 11.11. 3D display of the interpolated top-basement interpretation, overlain by the position of the interpreted seismic profiles.

11.2 **Potential field modelling**

To test the seismic intepretation and to derive more details about the character of the basement we carried out a 2D gravity and magnetic modelling along some key profiles.

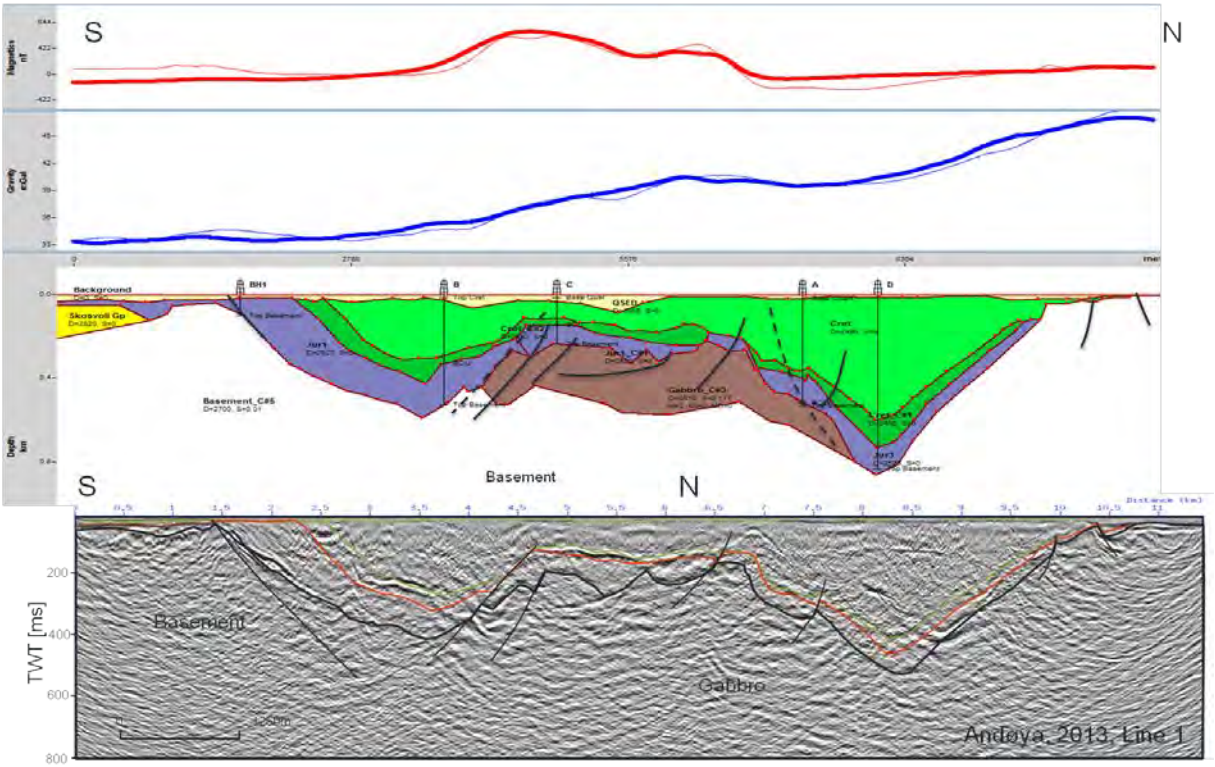

Figure 11.12. Grav/mag modelling result for Line 1 onshore Andøya. The thinner lines for gravity and magnetics represent the model response whilst the thicker ones are the observed field data.

For the gravity modelling the seismic sections had to be depth converted and filled with appropriate densities for each unit. Depth conversion was carried out using the observed velocity values from the measured core material. The values were adjusted to fit the interpreted stratigraphy of the Norminol wells but also the new NGU wells. Densities and magnetisations for the sedimentary rocks and the basement were taken from the petrophysical studies and varied with certain ranges during the modelling.

The modelling result for Line 1 (Figure 11.12) supports the seismic interpretation. Gabbro specimens were measured for density and susceptibility and revealed a significantly higher magnetisation, both induced and remanent magnetisation and higher density for this unit. This explains the noticeable magnetic high as it was already inferred from the magnetic map interpretation. The gabbro's rugged surface observed from seismic is only partly resolved in the magnetic data but could fit with the observed magnetics. The gabbro appears to be no thicker than 300 to 400 m, which is even more than observed from the core of Well C. Other rocks such as peridotite observed in the drillcores are likely to have a similar high magnetisation and are also high in density and were not differenciated further during this modelling. The southern basin was modelled to a maximum depth of c. 700 m, which is in good correlation with Well B. For the northern basin, however, basement was not reached and a basin depth of up to 1500 m was suggested (Chapter 2). Based on our modelling this seems to be unlikely. We modeled the basement at c. 800 m and at that depth already recorded a deficiency in the magnetics.

The magnetic data are mostly sensitive to the depth-to-basement since the sedimentary rocks are commonly low magnetic. To compensate for an even larger deficiency with the basement at greater depth, we would need to infers a higher magnetic basement like the gabbro, but there is so far no indication for this.

The modelling of line LO-88-13 in Andfjorden has some challenges as it is clearly disturbed due to 3D effects. The line is striking SSW-NNE partly in between basement highs and sedimentary basins. Consequently some significant misfits remain, which could not be explained by the derived geometries from seismic interpretation. For the depth conversion we applied similar parameters as for Line 1 and the basement depth varies between seafloor in the south, c. 3 km in the central part and up to 6 km in the north. Both the gravity response and the magnetics fit fairly well with some exceptions as mentioned above. Densities for the sediments in the north were slightly increased, indicating a higher compaction rate due to greater burial depth, but they still could be increased a bit more to get a better fit. For the magnetics a surplus is observed in the central part, which could be corrected with a slightly lower basement magnetisation. The gabbro as inferred from seismic, however, fits quite well, but could extend farther south, where a magnetic deficiency still exists, Since an intra-basement reflection here might indicate the limit of the gabbro we rather assume 3D effects in this context.

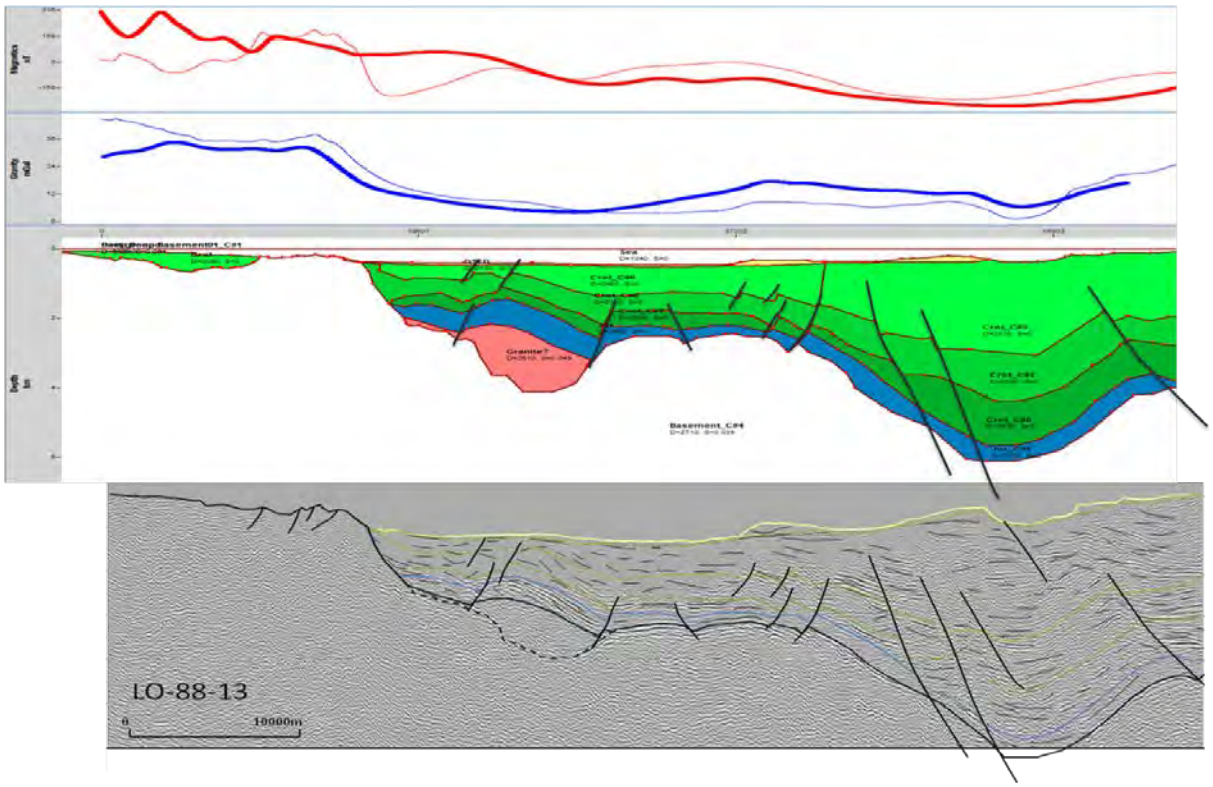

Figure 11.13. Grav/mag modelling result for Line LO-88-13. The thinner lines for gravity and magnetics represent the model response whilst the thicker ones are the observed field data.

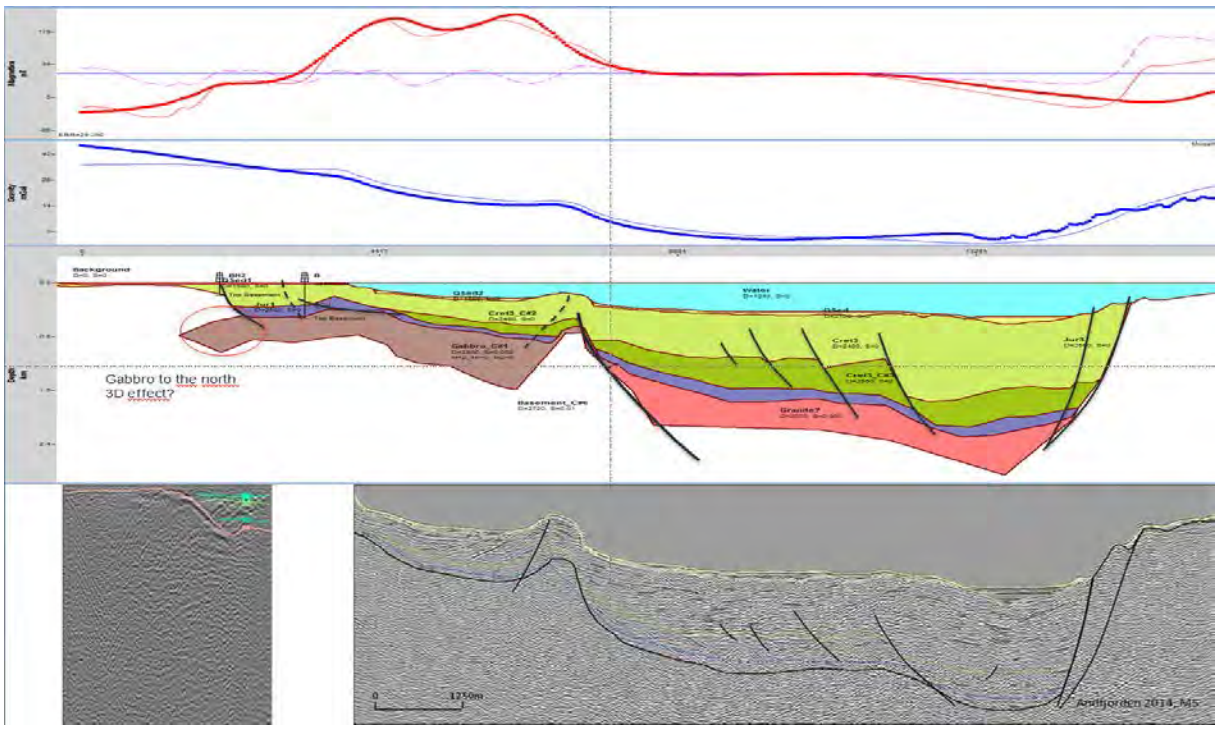

Figure 11.14. Grav/mag modelling result for the composite line onshore- offshore L5-M5. The thinner lines for gravity and magnetics represent the model response whilst the thicker ones are the observed field data.

The composite profile of the onshore line 5 and the offshore line M5 is displayed in Figure 11.14. The data were depth-converted as before and densities and magnetisation were addressed accordingly to the different layers. Well B is not located directly on the profile but a bit to the north and was projected into the profile to provide a hint of the basement depth. The fit between observed and modelled data is very good, although we suspect that ther are also 3D effects from the gabbro to the north of the profile. The prominent basement high on M5 separates the two basins in Andfjorden where the western one is underlain by a gabbro, whilst the eastern one seems to be more like a granite with high magnetisation but lower density. This interpretation, however, remains uncertain, since any other observations are missing and a similar setting was not observed from any other modelled line.

Farther west the Ramså Basin was modelled with its offshore extension. The basin is deepening towards the east and its eastern boundary. However, the basement complexity and the interaction with the gabbro makes it difficult to determine the structure in more detail.

The 2D gravity and magnetic modelling in general supports the intepretation from seismic with basement depth and morphology. Some more information regarding variations in the basement are indicated and need to be followed up.

11.3 **Discussion**

11.3.1 Tectonic development of the Ramså Basin and the adjacent Andfjorden

The joint interpretation of the existing data reveals a very complex tectonic setting for the Ramså Basin and the adjacent Andfjorden. Three main trends were observed which can be related to different times and different tectonic developments of the area. The NW-SE trend is parallel to the the trend of the gabbro dyke, but is not limited to it. Lineaments, subparallel to the gabbro are observed especially to the south, what might indicate a very old regional trend, possibly Palaeoproterozoic with later reactivation due to segmentation as has been proposed before (Chapter 3). The gabbro was dated to 1.8 billion years and was therefore in place before the development of Andfjorden. An abrupt change in the magnetic anomaly and downfaulting of the gabbro along a N-S-trending normal fault in Andfjorden confirms that the gabbro is older than the N-S-trending faults.

Although we cannot exclude tectonic activity already during the Late Palaeozoic, significant rifting probably did not happen before Late Triassic time. Dalland (1979) suggested an uplift and erosion in the Triassic, where all the sedimentary succession was eroded and only the Holen Fm. (Late Palaeozoic?) was locally preserved. The terrestrial sedimentation dated to Mid Jurassic in the Ramså Basin indicates that the area had been stable in a rather high position in Late Triassic –Mid Jurassic time before the onset of the E-W opening of the Andfjorden and significant downfaulting along a N-S-trending fault system was initiated. Analysis of the cored sedimentary strata (Chapter 9) shows that significant transgression and the submarine setting did not occur before the Early Kimmeridgian. Hendriks et al. (2010) suggested significant uplift in the Early Cretaceous, which could have been coeval with the onset of major rifting phases in the region, as has been shown from seismic data.

The geometry of Andfjorden is V-shaped and much narrower in the south. Here, the Andfjorden Basin is still a half-graben (Figure 11.5) with a set of normal faults in the west and a major border fault in the east, termed the Senja Fault (Figure 3.1), that controlled the rifting. The normal faults in the west gave rise to an E-W segmentation of the Andfjorden Basin with N-S-striking basins (Figure 11.15) seperated by tilted basement blocks and further segmented by cross-cutting NE-SW and NW-SE striking faults, developing several sub-basins. This setting fades out to the north where the Andfjorden Basin appears as a continuous basin with east dipping normal faulting, distributed over a larger area and accommodated by several smaller normal faults (see Figure 11.6). The Ramså Basin, however, remains separated from the Andfjorden Basin also in the north. Gravity and magnetic modelling were applied to estimate the geometry and indicate a deepening of the basin to the east with a tilted basement block as the eastern basin boundary.

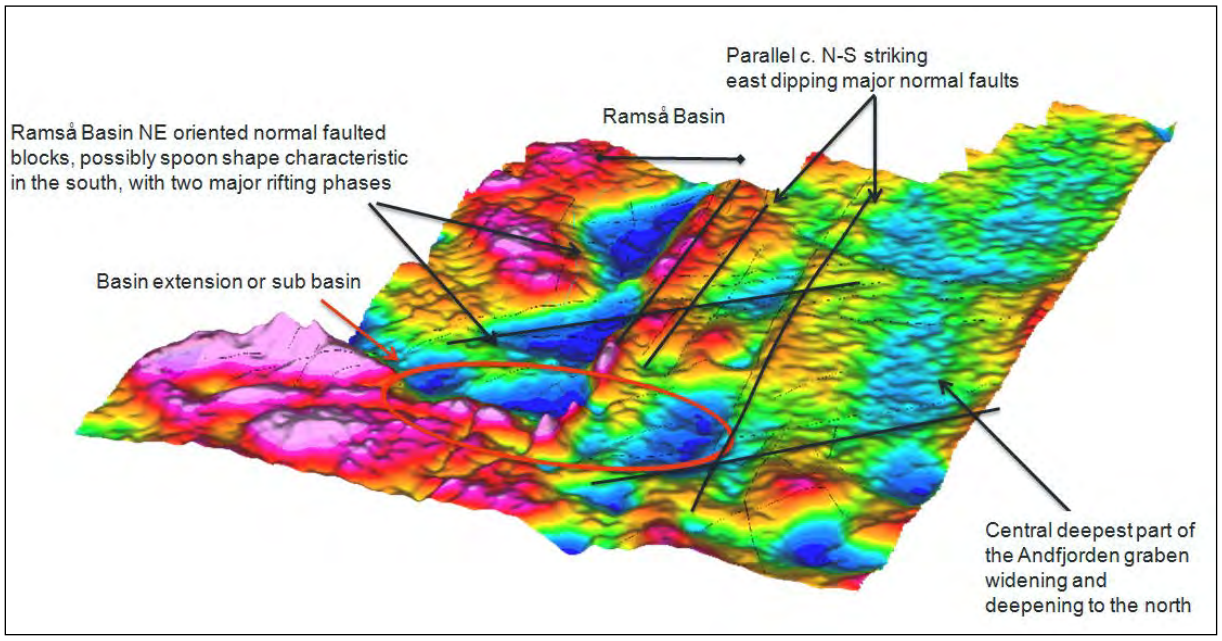

Figure 11.15. 5km gravity high-pass overlain by the tectonic setting derived from the joint interpretation of airborne data and seismic.

In Early Cretaceous time the Harstad and Tromsø basins experienced major rifting phases (Brekke & Riis 1987), which obviously resulted in a stress domain change in Andfjorden and extension in a predominantly N-S direction with fault block rotation and an arcuate detachment to the north. Hendriks (2003) suggested based on fission track dating an uplift and exumation of the Andøya horst c. 140 My ago, which affirms a major tectonic phase accombined with a substantial change in the stress field. Due to this domain change, the western border faults were reactivated with signifcant downfaulting. As a consequence, also the Ramså Basin experienced a major rifting most likely in a NE-SW direction, starting with normal faulting and subsequent detachment along reactivated faults and rotation of downfaulted basement wedges (Figure 11.16b). The rotated basement wedges form the eastern boundary of the Ramså Basin and separate it from the Andfjorden Basin. This concept was tested with 2D grav/mag modelling and is in accordance with the steep seismic reflectors

overlying a basement high farther east, where the same concept is valid (Figure 11.6,Figure 11.5Figure 11.4).

It remains unclear, however, to what extent the new sub-basins south of the Ramså Basin were affected by tectonic activity. It seems likely that they were originally developed during the E-W extension and the onset of development of the Andfjorden Basin in most likely latest Trassic-Jurassic times. However, a fracture analysis of the Jurassic strata in BH 3 (Figure 8.33) indicates horizontal layering without any noticeable sign of tectonism, which is also suggested from the seismic (Figure 5.13) where seismic reflections only show undisturbed sedimentation and subsidence.

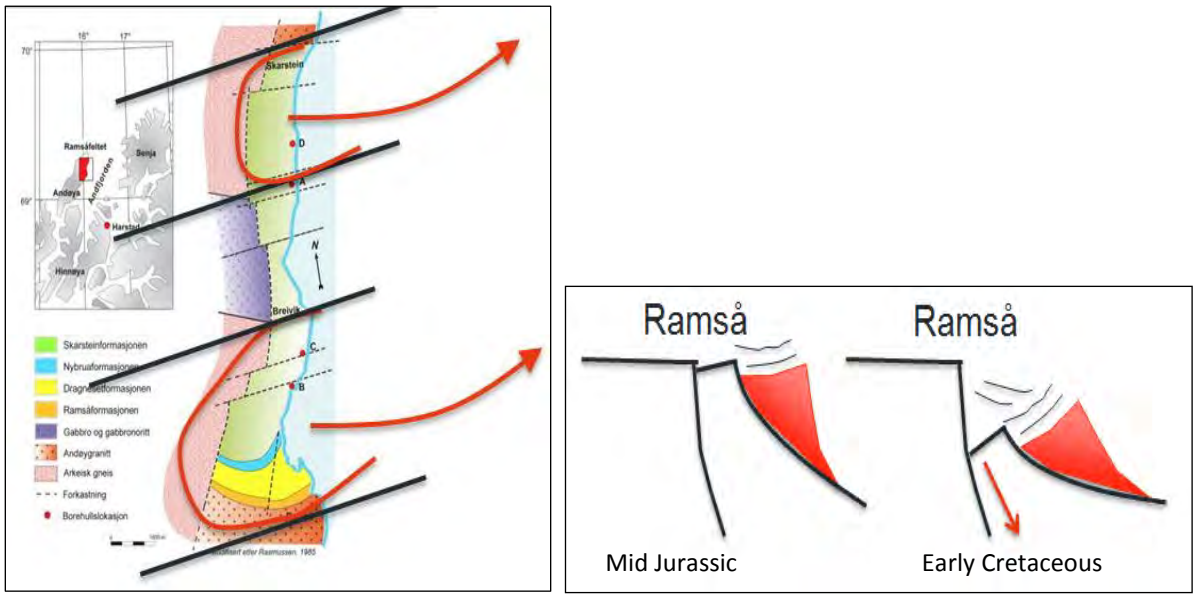

Figure 11.16. a) Late Jurassic-Early Cretaceous development of the Ramså Basin. Initiated due to major rifting in the Harstad Basin and northwards extension in the Andfjorden, normal faulting and tilting in a NW direction developed the Ramså Basin. b) a conceptual figure for a possible scenario, inferred from seismic interpretation and grav/mag modelling suggests normal faulting and rotation towards NE at the onset, followed by a detachment along a major border fault and rotation of basement wedges.

The Andfjorden Basin and the Ramså Basin in particular are consequently relatively young basins, which experienced a complex tectonic development, originally controlled by the opening of the North Atlantic with westward crustal extension and faulting and tilting of downfaulted blocks. However, the proximity to the NW-SE-trending Senja Fracture Zone (SFZ) and the development of the Harstad Basin with the NE-SW-striking Troms-Finnmark Fault Complex (TFFC) along the eastern basin boundary and deep steep basin flanks exposed the Andfjorden area to a complex and high degree of tectonism. Several episodes of uplift and burial have been suggested (Bergh et al. 2007) and were inferred from the well cores (Chapter 9), but chemical and mineralogical data show that burial depth has never been more than 2 km for the Ramså Basin (Chapter 10.13.1) and also for the southern Andfjorden Basin, which change significantly at the level of Fiskenes, where downfaulting and an abrupt increase in basement depth was observed.

The NE-SW trend, is observed elsewhere in the Lofoten-Vesterålen area (Bergh et al. 2007, Hansen et al. 2009) and probably has a regional impact. However, we propose that the vicinity to the Harstad Basin within the complex stress field of the Senja Fault Complex and the Troms Finnmark Fault Zone are the major factors which controlled and caused the collapse in the outer Andfjorden and the Ramså Basin.

This downfaulting points to a close connection of the development between the Andfjorden and the Harstad Basin. The regional magnetic data indicate a spoon-shape detachment or downfaulting, both for the Andfjorden and for the southernmost part of the Harstad Basin, which confirms the observation from the reprocessed NPD seismic data (Figure 5.16) and the arc-shaped lineaments from the high-resolution gravity and magnetic data. This magnetic structure has a continuous transition into a predominant magnetic low, characterizing the southern Harstad Basin. The angular form of the magnetic low anomaly likely indicates a fault bounded deeper basin here, which is mainly controlled by the SFZ and the TFFC.

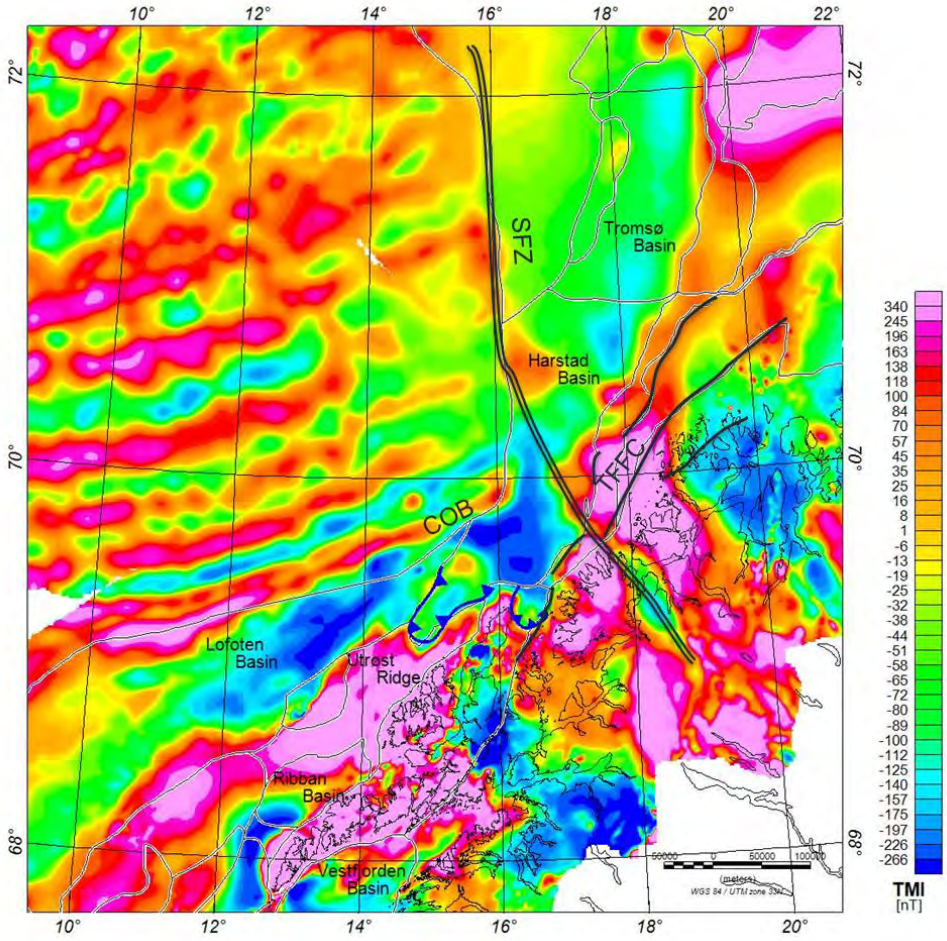

Figure 11.17. Regional magnetic map with structural elements showing the setting between the Andfjorden and the Harstad Basin. The southern Harstad Basin is a noticeable magnetic low, bounded by the Senja Fracture Zone (SFZ) to the east and the Troms-Finnmark Fault Complex (TFFC) to the south.

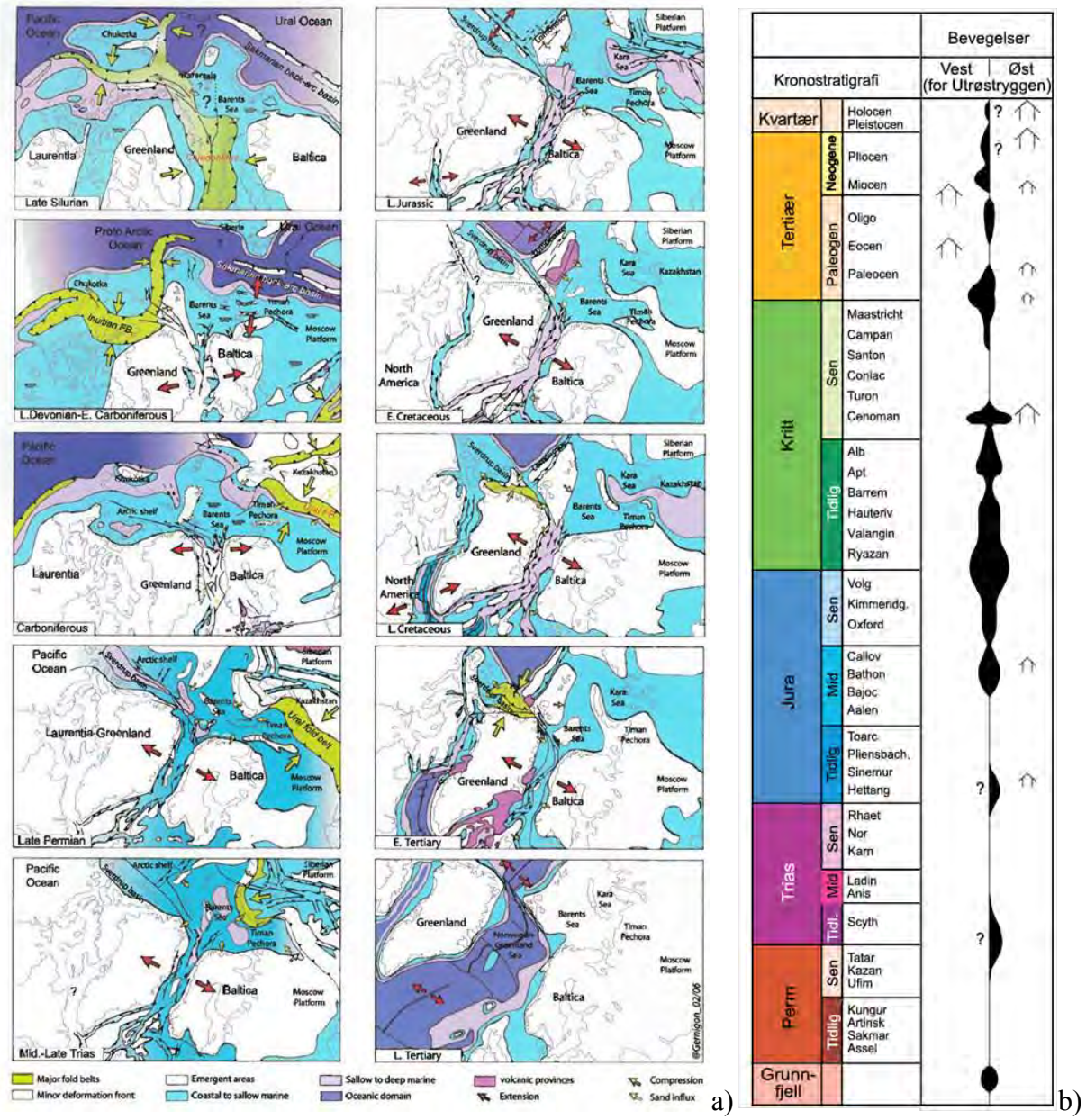

Figure 11.18. a) Schematic cartoon of the geodynamic evolution of the North Atlantic and arctic region (in Smelror et al. 2009). b) Rift phase and uplift history of the Lofoten Margin (internal Statoil report, 2012)

The Harstad Basin is general considered being developed together with the Tromsø and the Lofoten basins during the opening of the North Atlantic. The onset of the rifting most likely started in Late Permian -Triassic times or earlier, but major rifting did not appear before Early Cretaceous. Considering the Andfjorden Basin, we suggest in accordance with Bergh et al. (2007) that the area has been in a rather high position during Mid-Late Jurassic with repeated episodes of uplift and erosion (Figure 11.18b). Rifting was moderate and subsidence much less than e.g. in the Vestfjorden.

However, further uplift combined with crustal thinning in Early Cretaceous yielded extensive rifting of the basins and normal faulting (Figure 5.16). The stress field was still dominated by

a NW-SE extension between Baltica and Laurentia when it triggered the activation of the SFZ and the development of a dextral shear zone in Early Tertiary (Figure 11.18a), possibly inherited from existing old crustal weakness zones, which have an onshore extension in the Bothnian-Kvænangen Fault Complex. This activation must have changed the stress field significantly and possibly reactivated the TFFC and sinistral NE-SW shearing, which favoured a NE-SW extension of the Harstad Basin, whilst the Vesterålen underwent compression as indicated from seismic data in the Andfjorden (Figure 5.15b). The southern part of the Harstad Basin marks therefore the transition between the Barents Sea and the Lofoten-Vesterålen margin with extensional features in both NW-SE and NE-SW direction. With the break-up in Eocene, the stress pattern changed again and with the ridge push the SFZ at some stage changed direction and became a sinistral strike-slip fault zone. To what extend this anew stress domain change affected the Harstad Basin is beyond the topic of this study. The seismic data from Andfjorden Basin, however, did not indicate compression in NW-SE direction.

11.3.2 The Ramså Basin and deep weathering

The Ramså Basin was always associated with an onshore Mesozoic basin underlain by deeply weathered basement, which is exposed at the southern boundary of the basin (Dalland 1974, Sturt et al. 1979) and core descriptions by Friis (1903) suggest that the weathering horizon continues northwards as an apparently continuous layer. Consequently, one of the main objectives in the present study was to gain better knowledge about the weathering of the basement and to test how and to what extent geophysics can be applied to map deep weathering underneath sedimentary rocks. However, starting with the analysis of the Norminol cores, Wells A-C (Chapter 9) showed that the amount of weathering is very little and far from the 30 m-thick layer inferred from the surface observations. From the four new wells, drilled during this study (BH 1 - BH 4), only two showed signs of weathering and only BH 3 drilled c. 10 m of weathered bedrock. Core recovery was almost 99 % and even if the lost cores were of weathered basement, this means that the thickness was hardly more than 1 metre.

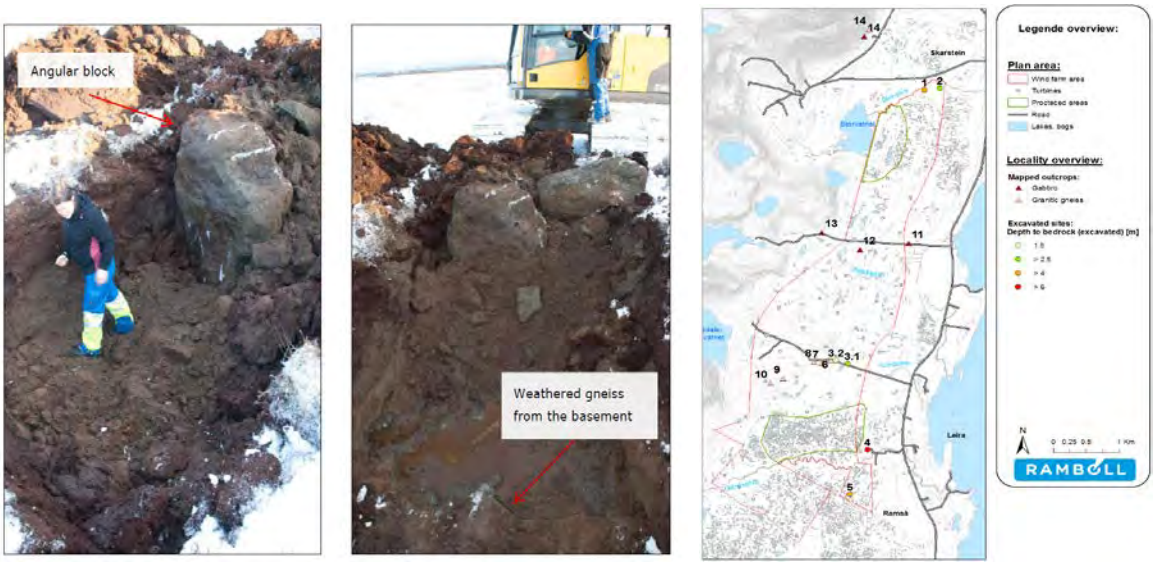

Figure 11.19. Excavating on Andøya at location 3.1 on behalf of Rambøll and in context with a wind mill foundation study reveals flat angular blocks with fractures filled with weathered basement material of the grussy type.

The drilled weathering in BH 3, however, was not comparable with that exposed on the surface at Ramså, nor was it the grussy type of weathering as can be observed commonly elsewhere in Nordland. The weathered bedrock was clay-rich (c. 40% clay minerals), which also indicates an advanced stage of chemical weathering, but the material is consolidated and actually very hard and density measurements revealed densities of c. 2.7 g/cm^3, which is comparable with basement rock density. For the IKU well 6814/4-U-1 deeply weathered bedrock was also reported with a similar high clay content and very high density (J. Knies, pers. comm. 2015). The age of the weathering in BH 3 has not yet been determined, but could be an explanation since the burial depth was obviously not very great. Further studies are also necessary to investigate for possible hydrothermal processes, although indications of this have not been detected so far.

However, deep weathering has played an important role for the development of the landscape of Andøya. As suggested by Brönner et al. (2017) and Olesen et al. (2013) the development of the strandflat along the Norwegian coast is to a large extent related to deep weathering. Excavations on the strandflat of Andøya (Figure 11.19) showed large amounts of blocks of weathered bedrock in moraine sands and underneath flat angular blocks were found with fractures in between which were filled with grussy type weathered basement.

The surfaces of the blocks can be related to an edged surface, where former saprolite was eroded at latest by glaciers during the Quaternary ice ages. The angular appearance of the rock is common for the deepest part of a weathering profile, commonly referred to as saprorock and close to the unweathered basement (Figure 11.20b). Especially in Nordland most of the weathering remains are related to the deeper part of a formerly much thicker layer with weathered basement (Olesen et al. 2012), where the upper part has subsequently been eroded.

Figure 11.20. a) Photo by Rambøll with reconstruction of how the angular blocks were lying in the pit before they were moved by the excavator. b) An example from Eiavatnet in Nordland for such angular blocks. The angular blocks are a common appearance in the deepest part of a weathering profile, close to the front with unweathered basement, commonly referred to as sapro-rock.

The edged surface of the blocks not only confirms that the strandflat was to a large extent formed by basement weathering, it also provides a minimum age for the weathering which must be older than the overlying Mid Jurassic sedimentary rocks. This fits well with the age dating by Sturt et al. (1979) who even dated weathering samples from Andøya to Carboniferous and Permian ages, similar to the ages reported in the present study (Chapter 10).

However, regarding the question whether a continuous layer with deeply weathered basement (areal weathering) can be preserved underneath the sedimentary strata, the timing of the erosion of the saprolite is of importance.

We can assume that there were various phases of erosion and the thicker the sedimentary cover was the more likely it would appear that weathering remains from the Palaeozoic could be preserved. Hansen et al. (2012) suggested that the Vesterålen Margin could have been the western flank of a large graben which covered the Vesterålen islands, which infers that the sedimentary cover was quite extensive. However, from our study the burial depth for the existing Mesozoic strata on Andøya cannot have been more than 2 km (Chapter 10.9) and consequently not more than 1 km of sedimentary strata has been removed, considering a basin depth of c. 1 km, as inferred from Well D. This erosion must not have been earlier than late Early Cretaceous - Late Cretaceous and subsequently led to the removal of the entire sedimentary strata and existing weathering remains onshore Andøya. On the other hand, in BH 2 Early Cretaceous sedimentary rocks rest upon unweathered, possible etched bedrock, a feature that indicates erosion during the Early Cretaceous which does not fit into a simple concept with fairly regular erosion of deeply weathered basement.

The first erosion phase, however, is connected tightly to the age of the weathering and can already have started in the Late Palaeozoic, suggesting that the very old ages from the K-Ar dating represent weathering ages. However, it appears logical that one major erosion phase

must have been in the Mid Jurassic, when older sedimentary strata and possibly large parts of the saprolite were removed. In between, extensive areal weathering rahter than linear weathering along existing fracutres could have developed a thick layer of regolith, which contributed to preserve such old weathering remains until today.

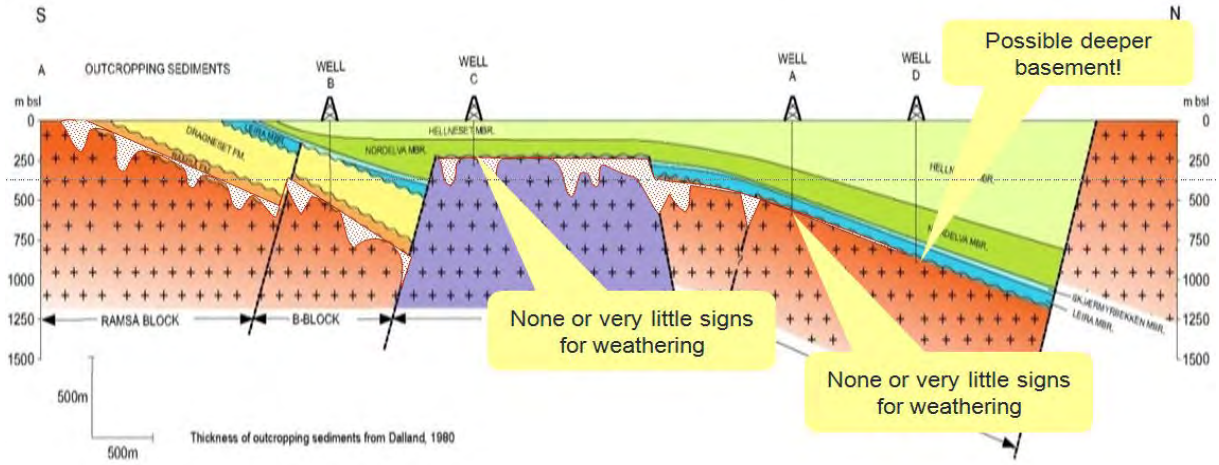

Figure 11.21. Concept for the setting of deep weathering as it is today in the Ramså Basin. Modified from Dalland (1980)

Based on our results, and no matter what are the odds, we must conclude that during the erosional phase in the Mid-Jurassic a former existing layer of weathered basement was entirely removed and weathering remains underneath the sedimentary strata as of today are only preserved in joints and fractures. The exposed weathering at Ramså today represents such a joint at the edge on a downfaulted and rotated fault block (Figure 11.21), and Norminol simply managed not to drill into as such.

To image such joints and fractures with geophysics was one major objective in the present project. The specimens of weathered bedrock observed from the surface nicely show the gradual disintegration of the bedrock (Table 10.1) The weathered basement, which were observed from the Norminol cores showed a similar characteristics and density, magnetisation and seismic velocity obviously decrease with increasing degree of alteration (Figure 4.2 - 4.4). The weathering remain in the cores, however, were too thin to be resolved in the geophysical data. However, ERT profiling (Olesen et al. 2012) resolved resistivity variations in the sub-surface down to c. 100-150 m and registered fractures zones and a rugose basement surface, which indicate fracturing and a basemetn surface which was formed most likely by weathering. The seismic Line 1 is parallel to the ERT line and observes a dipping basement to the south, but cannot comfirm rugose top basement geometry (Figure 11.22). However, from our seismic interpretation (Figure 5.10), both data indicate a deeping of the basement overlain by undefined material. An attempt to drill this basement low failed unfortunately due the inaccessibility of the location when the drilling rig was on site.

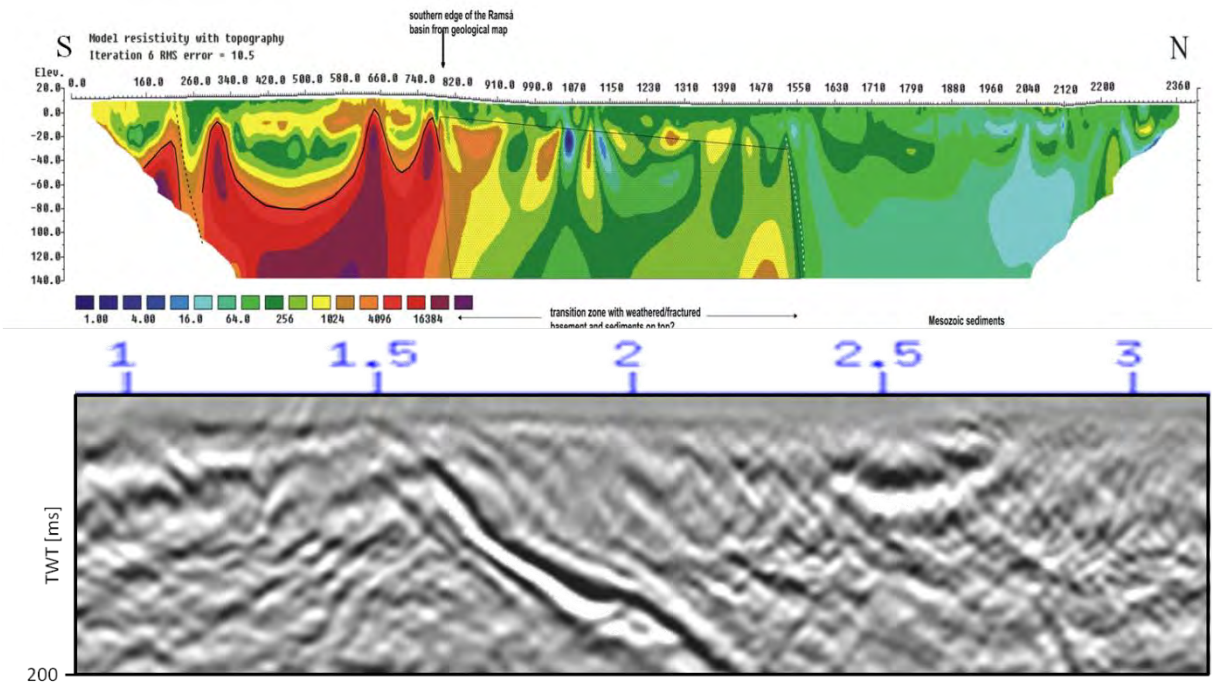

Figure 11.22. ERT profile 1 (Olesen et al. 2012) runs in N-S direction parallel to the onshore seismic profile Line 1 (below). The ERT line shows a rugose basement surface and fracture zones in the southern part, outside the Ramså Basin, which could indicate an etched basement with possible remains of deeply weathered basement.

BH 3 drilled weathered basement at about 200 m. Considering the petrophysical characteristics of this cored material, the weathered basement in the deeper part of the Ramså Basin and most likely also in the Andfjorden Basin appears difficult if not impossible to map from geophysical data since the petrophysical parameters resemble compacted sedimentary rocks or even unweathered basement.

Examples from e.g. the Utsira, Mandal and Frøya highs on the Norwegian shelf show that weathered basement can be fairly unconsolidated at depths of e.g. 1000 or even more (Lie et al. 2016), having low density and low seismic velocity, which is also in agreement with on- and offshore studies from other parts of the world (Kitschka et al. 2016). The geochemical and mineralogical analysis of the weathered rock samples in this project indicate a burial depth not more than 2 km (Chapter 10), and consequently other processes must be responsible for the re-consolidation of the saprolitic rocks. The lithology of the bedrock and size of the altered minerals are surely an important factor, but also changing conditions with repeated compaction over a rather long time could be an explanation and would correlate well with the Palaeozoic ages of the weathered material. In this context the concepts of either linear or areal weathering can also be of relevance, as it is discussed above. Further studies of the core material and comparison with the cores from the IKU well 6814/4-U-1 are necessary and planed in the BASE II project to better understand the processes necessary to re-consolidate saprolitic rocks.

12. CONCLUSIONS

- Comprehensive geophysical data were acquired around and across the Ramså Basin and the adjacent area in the Andfjorden. The data contribute to a more detailed imaging of the Ramså Basin settings and verified and updated the setting for this basin.
- EM inversion detected significantly higher conductivity as it is commonly the case for fresh bedrock, which was related to intense fracturing of the bedrock in the sourroundings of the Ramså Basin. Weathered basin underneath the sedimentary strata could not be detected from this method in such a marine setting.
- From the airborne gravity and magnetic data, three major linear trends were observed and related to different epochs in the development of the margin in general and the Ramså and Andfjorden basins in particular. Furthermore the gravity and EM infered an extension of the Ramså Basin or sub-basins to the south, which were confirmed by seismic data end one of them was confirmed to be filled with Jurassic sedimentary rocks.
- Seismic data were interpreted together with airborne geophysical data to derive a depth-to-basement map and tectonic model for the Ramså and Andfjorden basins. Both are relatively young basins, which experienced various phases with complex tectonism. The Andfjorden Basin developed not before the Late Palaeozoic and experienced major rifting not before in Early Cretaceous. It is a V-shaped half-graben system with a set of rather shallow N-S trending basins and with a close link to the southern Harstad Basin. Northwards on the level of Fiskenes an arcuate detachment marks a noticable deeping of the Andfjorden Basin and a significant change in the vertical displacement to the west. The SFZ in the NW and the TFFC in the E changed the stress field signifcantly in Early Tertiary and leaded to compression and folding in the Andfjorden.
- Bedrock mapping was carried out around the Ramså Basin and the bedrock map for northern Andøya was refined and updated accordingly regarding the new geological and geophysical observations. Regarding the basement, the Fiskenes granite north of the basin and the gabbro could be confirmed and were refined regarding the geophysical maps. The granite, which was suggested earlier to the south of the Ramså Basin does not exist and here the same granodiorite is the principal bedrock as it is know for the area west of the Ramså Basin. BH 4 also drilled an ultra-mafic dyke at the edge of the Ramså Basin, which fits with the conglomerate in BH 1 and has an affinity with mafic rocks observed at some of the islets within Andfjorden, indicating significant faulting and mafic intrusion of the crust most likely in the Proterozoic.
- Four wells were drilled onshore Andøya and petrophysical and fracture logging was carried out. The gamma logging shows a very good correlation with the identified stratigraphic boundaries, whilst the dip and strike of the observed fractures indicate the

tectonics and rotation of fault blocks within the Ramså Basin. For the sub-basin, however, the impact of tectonic events appears much less.

- Mineralogical and geochemical analysis of three Norminol well cores was carried out for deeply weathered basement. The results show that barely any weathered bedrock was drilled underneath the sedimentary strata, which is in contrast to the reports by Friis (1903) and Vogt (1905) and the surface observations, where up to 30 metres with disintegrated bedrock was reported. The burial depth was not more than 2 km for the sediments in the Ramså Basin and consequently not more than c. 1 km thick packages of sedimentary rocks were removed in post Aptian times.
- Imaging of deeply weathered bedrock from the geophysical data could not be achieved, which can be due to an actually limited amount of weathering remains preserved under the sedimentary rocks in the Ramså and Andfjorden basins. The remains are mostly concentrated in fractures and joints which were however not resolved on the geophysical data but were, however, reported from the early drillings. Furthermore the drilled weathering remains in BH 3 actually resemble the physical characteristics of unweathered basement, which makes them indistinguishable from basement by geophysics.
- The Holen Fm. is extensively described by Dalland (1974) and Aslagsen (1981) both from the old wells I, II and V (Friis (1903) and from surface samples. Within this study, we could not identify any rocks which would fit the description in the literature. A rock sample provided by Harald Brekke and which was supposed to be Holen Fm. was analysed and identified as a quartz sandstone with more than 80 % quartz, which corresponds with the deeper Ramså Fm. rather than Holen.

13. ACKNOWLEDGEMENT

Fugro Airborne Services from South Africa carried out the fix wing airborne services. Helge Johnsen was planning and organising the onshore seismic acquisition. Marte Louise Strømme, Alf Nilsen, Geir Viken, Nils Per Nilsen Sara, Isak Anders Nilsen Eira and Ottar Isaksen helped to carry out the seismic surveys. GeoDrilling was responsible for the successful core drilling on Andøya. Bjørn Wissing at NGU assisted the XRF and XRD analysis and Roelant van der Lelij did the K-Ar dating. The sample preparation was done by Wieslawa Koziel and Ann Elisabeth Karlsen. Dag Bering and Christian Magnus did additional P-wave velocity measurements on the Norminol cores at NPD. Thank you all for all your effort. We also want to thank the crew of the Håkon Mosby for the good cooperation during the seismic acquisition in the Andfjorden. Aker BP, Lundin Norway, Wintershall Norge, Mærsk Oil, NGU, NPD, and Statoil financed this project. Norwegian Public Road administration supported financially the logging of the four wells. We express our thanks to these companies. We further wish to thank in particular Arne Grønlie, Hans Konrad Johnsen, Dag Bering, Inger Flesland Strass, Hans Martin Helset, Nils E. Bakke and Jan Strømmen for following the project and giving valuable advice during different stages of the work tasks. David Roberts and Odleiv Olesen are acknowledged for the thoroughly detection and correction of the errors in the text and the fine tuning of the English.

14. REFERENCES

AarhusInv, 2013. Manual for inversion program, ver. 6.1, HydroGeophysics Group (HGG), University of Aarhus, Denmark, 71. http://www.hgg.geo.au.dk/HGGsoftware/em1dinv/em1dinv_manual.pdf

Advanced Logic Technology, 2006. WellCAD, FWS processing, version 4.1.

Anschütz H., Bazin S. & Pfaffhuber A.A., 2014. AEM method description & project examples, *NGI report 20130058-02-R_ENG*, 59.

Archie, G.E., 1942. The electrical resistivity log as an aid in determining some reservoir characteristics. *Petroleum Technology, 5*, 1422 – 1430.

Asch T.H., Deszcz-Pan M., Burton B.L. & Ball L.B., 2008. Geophysical characterization of American River levees, Sacramento, California, using electromagnetics, capacitively coupled resistivity, and dc resistivity, *U.S. Geological Survey Open-File Report 2008-1109*, 12.

Aslagsen, M., 1981. Studier av kjemisk forvitrt grunnfjell, rekrystallisert Paleozoisk (?) kalkstein og Mesozoiske sandsteiner fra Andøy, Nord-Norge, Hovedoppgave i petroleumsbeologi, avd A, Uinversitet i Bergen, 182 pp.

Auken, E. and Christiansen A.V. 2004. Layered and laterally constrained 2D inversion of resistivity data, *Geophysics, 69*, 752-761.

Barker, C. E. & Pawlewicz, M. J., 2005. The correlation of vitrinite reflectance with maximum temperature in humic organic matter. *Paleogeothermics, Vol. 5* pp79-93.

Beaufort A., Cassagnabere, A., Petit, S.,Lanson, B., Berger, G., Lacharpagne, J.C., & Johansen, H., 1998. Kaolinite-to-dickite reaction in sandstone reservoirs. *Clay Minerals 33*.

Bell, D. G., 1985. Palynology of well D from Andøya, Northern Norway. Stratlab A. S.

Bergaya, F., Theng, B. and Lagaly, G. (Eds.), 2005. *Handbook of clay science*, Elsevier Ltd.

Bergh, S. G., Eig, K., Kløvjan, O. S., Henningsen, T., Olesen, O., & Hansen, J. A., 2007. The Lofoten-Vesterålen continental margin: a multiphase Mesozoic-Paleogene rifted shelf as shown by offshore-onshore brittle fault-fracture analysis. *Norwegian Journal of Geology, 87*, 29-58.

Birkelund, T., Thusu B. & Vigran, J. O., 1978. Jurassic-Cretaceous biostratigraphy of Norway, with comments on the British Rasenia cymodoce zone. *Paleontology, 21*, 31-63.

Bjorøy, B., Hall, K. , & Vigran, J.O., 1980. An organic geochemical study of Mesozoic shales from Andoya, North Norway. P*hysics and Chemistry of the Earth, Volume 12*.

Bjørlykke, K., 1998. Clay mineral diagenesis in sedimentary basins, a key to the prediction of rock properties. Examples from the North Sea Basin. *Clay Minerals 33*, 15-34.

Blystad, P., Brekke, H., Færseth, R. B., Larsen, B. T., Skogseid, J., & Tørudbakken, B., 1995. Structural elements of the Norwegian Continental Shelf, Part II: The Norwegian Sea region. Norwegian Petroleum Directorate Bulletin, 8, 45 pp.

Bose, L. I. 1960. Leaf cuticle and other plant microfossils from the Mesozoic rocks of Andøya, *Norway. Paleobotanist, 8 (1-2)*, 1-7.

Brekke, H., & Riis, F., 1987. Tectonics and basin evolution of the Norwegian shelf between 62°N and 72°N. Norwegian Journal of Geology, 67, 295-321.

Brown, G. (Ed.), 1961. The X-ray identification and crystal structures of clay minerals. Mineral Soc. London.

Brönner, M., Olesen, O., Dalsegg, E., Larsen, B.E. & Rønning, J.S., 2017. Deeply weathered basement along the Norwegian coast and implications for the strandflat formation. Norwegian Journal of Geology, submit.

Brönner M., Dalsegg E., Fabian K., Rønning J.S. & Tønnesen J.F., 2012. Geophysical methods, In Olesen O., Bering D., Brönner M., Dalsegg E., Fabian K., Fredin O., Gellein J., Husteli B., Magnus C., Rønning J.S., Solbakk T., Tønnesen J.F. & Øverland J.A. (eds.): Tropical Weathering In Norway, TWIN Final Report, NGU Report 2012.005, 19–26.

Brönner, M., Knies, J., Fredin, O., Olesen, O., & Viola, G., 2014. Deeply weathered basement rocks in Norway. *NASA Astrophysics Data System (ADS)*

Bøe, R., Fossen, H., & Smelror, M., 2010. Mesozoic sediments and structures onshore Norway and in the coastal zone. *Norges geologiske undersøkelse Bulletin, 450*, 15- 32.

Chun, J.H. & Jacewitz, C.A., 1981. The first arrival time surface and estimation of statics. Presented at the 51st Annual Meeting of the Society of Exploration Geophysicists, Los Angeles.

Christensen C.W., Pfaffhuber A.A., Anschutz H. & Smaavik T.F., 2015. Combining airborne electromagnetic and geotechnical data for automated depth to bedrock tracking, *Journal of Applied Geophysics 119*, 178-191.

Corfu, F. 2004a: U-Pb age, Setting and tectonic significance of the Anorthosite-Mangerite-Charnockite-Granite suite, Lofoten-Vesterålen, Norway. Journal of Petrology, Vol. 45, No. 9, 1799-1819.

Corfu, F., 2004b. U-Pb geochronology of the Leknes Group: an Early Caledonian metasedimentary assemplage stranded on lofoten besement, northern Norway. *Journal of the Geological Society, London, 161*, 619-627.

Corfu, F., 2007. Multistage metamorphic evolution and nature of the amphibolite-granulite facies transition in Lofoten-Vesterålen, Norway, revealed by U-Pb in accessory minerals. *Chemical Geology, 241*, 108-128.

Cox L.H, Wilson G.A. & Zhdanov M.S., 2012. 3D inversion of airborne electromagnetic data, *Geophysics, 77*, WB59–WB69

Dobrin M.B. 1960. Introduction to geophysical prospecting, McGraw-Hill, p. 446. v. 8, p. 19.

Dahll, T. 1891. Kulforekomsten paa Andøen. *Norges geologiske undersøkelse 4*: 131-138.

Dalland, A., Hansen, R. & Sellevoll, M., 1973. Geologiske og geofysiske undersøkelser av jura-krittfeltet på Andøya utført av Universitetet i Bergen 1969-1971 - foreløpig meddelelse. Upublisert Universitetet i Bergen rapport, 35s

Dalland, A., 1974. Geologisk undersøking av den mesozoiske lagrekkja på Andøy, Nord-Noreg. Hovudfagsoppgåve i mineralogi/petrografi, Universitetet i Bergen, pp. 223, 6 appendices.

Dalland, A., 1975. The Mesozoic rocks of Andøy, northern Norway. *Norges geologiske undersøkelse 316*, 271-287.

Dalland, A. & Thusu, B., 1977. Kimmeridgian volcanic ash in Andøya, north Norway. Mesozoic Northern North Sea Symposium, Oslo. 12pp.

Dalland, A., 1979. The sedimentary sequence on Andøy, northern Norway – depositional and structural history. Norwegian Sea Symposium. *Norwegian Petroleum Society.* NNS/26, 1-31.

Dalland, A., 1981. Mesozoic sedimentary succession at Andøy, northern Norway, and relation to structural development of the North Atlantic area. In Kerr, J. W. and Ferguson, A. J. (eds.) Geology of the North Atlantic Borderlands. *Canadian Society of Petroleum Geologists, Memoir, 7*, 563-584.

Davids, C., Wemmer, K., Zwingmann, H. & Bergh, S.G., 2013. K–Ar illite and apatite fission track constraints on brittle faulting and the evolution of the northern Norwegian passive margin. *Tectonophysics 608*, 196-211.

Davids, C., Benowitz, J. A., & Layer, P., 2012a. Constraining the Caledonian tectonic overprint in a Precambrian gneiss terrane in northern Norway. *Thermo 2012, 13th* International Conference on Thermochronology, 2012-08-24 - 2012-08-28.

Davids, C., Kohlmann, F., Hansen, J. A., Benowitz, J. A., Layer, P., & Jacobs, J., 2012b. Post-Caledonian onshore exhumation history of Troms, northern Norway, as constrained by K-feldspar 40Ar/39Ar and appatite fission track thermochronology. Abstract and proceedings of the Geological Society of Norway. Onshore-Offshore relationship on the North Atlantic margin, Trondheim, October 17-18, 2012. NGF. Number 2.

Davids, C., Bergh, S. G., Wemmer, K., & Layer, P., 2010. K-Ar and 40Ar/39Ar dating of post Caledonian brittle faults in northern Norway. Thermo 2010, 12th International Conference on Thermochronology, Glasgow, UK, 16-20 August 2010.

Davidsen, B. & Smelror, M., 2000. Finnes det et mesozoisk basseng i Sortlandsundet, Vesterålen. Poster at Seminar: Biostratigraphy and paleoecology of the Norwegian continental shelf and coastal areas. 13th and 14th September, 2000. NGU, Trondheim. Page 27.

Davidsen, B., Smelror, M. and Ottesen, D., 2001a. Et nyoppdaget mesozoisk basseng i Sortlandsundet, Vesterålen. Abstract, Norsk Geologisk Forenings XVII. Vinterkonferanse, Oslo, 8.-10. januar 2001. Geonytt 2001, 42-43.

Davidsen, B., Sommaruga, A. and Bøe, R., 2001b. Final Report: Sedimentation, tectonics and uplift in Vesterålen. Phase 1 – Localizing near-shore faults and Mesozoic sediment basins. *NGU-rapport 2001.111*. 16 s + vedlegg.

Davidsen, B. & Skår, Ø., 2004. Lofoten and Vesterålen: A Precambrian puzzle. (Abstract). The 26th Nordic Geological Winter Meeting, January 6th – 9th 2004, Uppsala, Sweden. GFF, vol 126, 20-21.

Doré, A.G., 1991. The structural foundation and evolution of Mesozoic seaways between Europe and the Arctic. Palaeogeography, Palaeoclimatology, *Palaeoecology Volume 87, Issues 1–4*, pp 441-492

Doré, A. G., Cartwright, J. A., Stoker, M. S., Turner, J. P., & White, N. E., 2002. Exhumation of the North Atlantic Margin: Timing, Mechanisms and Implications for Petroleum Exploration. *Special Publications - Geological Society of London, 196*, 45-65.

Ehrenberg, S.N., Aagaard, P., Wilson, M.J., Fraser, A.R. & Duthie, D.M.L., 1993. Depth-dependent transformation of kaolinite to dickite in sandstones of the Norwegian continental shelf. *Clay Minerals 28*, 325–352.

Ehrenberg, S.N., 1991. Kaolinized, potassium-leached zones at the contacts of the Garn Formation, Haltenbanken mid-Norwegian continental shelf: *Marine and Petroleum Geology, 8(3)*, 250-269

Elvebakk, H., Brønner., M. og Gellein, J., 2016: Geofysisk logging av 4 borehull i Ramså feltet, Andøya, Nordland. NGU report.

Eig, K., 2008. Onshore and offshore tectonic evolution of the Lofoten passive margin, north Norway. (PhD), University of Tromsø, Unpublished.

Eig, K., & Bergh, S. G., 2011. Late Cretaceous-Cenozoic fracturing in Lofoten, North Norway: Tectonic significance, fracture mechanisms and controlling factors. *Tectonophysics, 499*, 190-205.

Eldholm, O., E. Sundvor, and A. Myhre, 1979. Continental margin off Lofoten-Vesterålen, northern Norway, *Mar. Geophys. Res., 4*, 3-35.

Elvebakk, H., 2011. Sammenstilling av resistivitet, seismiske hastigheter og naturlig gammastråling i norske bergarter. *NGU Rapport 2011.042*.

Elvebakk, H., 2013. Geofysisk logging av borehull ved Geologisk Museum, Tøyen, Oslo. *NGU Rapport 2013.040*.

Engvik A.K., Davidsen B., Coint N., Lutro O., Tveten E. and Schiellerup H., 2016. High-grade metamorphism of the Archean to Palaeoproterozoic gneiss complex in Vesterålen, North Norway. *31st Nordic Geological Winter Meeting 2016*, Helsinki

Fabricius, I.L., Dahlerup Fazladic, L., Steinholm, A., and Korsbech, U., 2003. The use of spectral natural gamma-ray analysis in reservoir evaluation of siliciclastic sediments: a case study from the Middle Jurassic of the Harald Field, Danish Central Graben. *Geological Survey of Denmark and Greenland Bulletin 1*, 349–366 (2003).

Forthun, T., 2014. Onshore-offshore correlation in the Andfjorden area and the structural controls on the opening and evolution of the Mesozoic sedimentary basins on Andøya and Andfjorden, northern Norway. Unpublished Master thesis, Univerity of Tromsø, pp.122

Fredin, O., G. Viola, et al., 2017.The inheritance of a Mesozoic landscape in western Scandinavia. *Nature Communications 8*: 14879.

Friis, J. P., 1903. Andøens kullfelt. *Norges geologiske Undersøkelse, 36*, 1, 1-38

Fürsich, F. and Thomsen, E., 2005. Jurassic biofacies in erratics from the Sortland area, northern Norway. *Norges geologiske undersøkelse Bulletin, 443*, 37-53.

Gabrielsen, R. H., Færseth, R. B., Jensen, L. N., Kalheim, J. E., & Riis, F., 1990. Structural elements of the Norwegian continental shelf - Part I: The Barents Sea region. *Norwegian Petroleum Directorate Bulletin 6*, 33.

Gautneb, H. and Tveten, E., 2000. The geology, exploration and characterisation of graphite deposits in the Jennestad area, Vesterålen, northern Norway. *Norges geologiske undersøkelse Bulletin, 436*, 67-74.

Geosoft, 2005. Helicopter electromagnetic data processing, analysis and presentattion System for Oasis montaj v6.2: tutorial and user guide manual, Geosoft Incorporated, Canada.

Geosoft, 2012. Oasis montaj How-to-guide: 3D gridding- create voxels using 3D gridding methods, Geosoft Incorporated, Canada.

Geotech, 1997. Hummingbird Electromagnetic System. User's manual. Geotech Ltd., Canada.

Griffin, W. L., Taylor, P. N., Hakkinen, J. W., Heier, K. S., Iden, I. K., Krogh, E. J., Malm, O., Olsen, K. I., Ormaasen, D. E. and Tveten, E., 1978. Archaean and Proterozoic crustal evolution in Lofoten-Vesterålen, N Norway. *Journal of the Geological Society, London, 135*, 629-647.

Grønlie, A., Nilsen, B., & Roberts, D., 1991. Brittle deformation history of fault rocks on the Fosen Peninsula, Trøndelag, Central Norway. *Norges geologiske undersøkelse Bulletin, 421*, pp. 39-57.

Hampson, G.J., Davies, W., Davies, S.J., Howell, J.A., and Adamson, K.R., 2005. Use of spectral gamma-ray data to refine subsurface fluvial stratigraphy: late Cretaceous strata in the Book Cliffs, Utah, USA: J*ournal of the Geological Society, London, 162,* p. 18.

Hansen, J. A., Bergh, S. G. & Henningsen, T., 2012. Mesozoic rifting and basin evolution on the Lofoten and Vesterålen Margin, North-Norway; time constraints and regional implications. *Norwegian Journal of Geology, v. 91*, p. 203-228.

Hansen, J. A., Bergh, S. G., & Henningsen, T., 2012. Mesozoic rifting and basin evolution on the Lofoten and Vesterålen Margin, North-Norway; time constraints and regional implications. *Norwegian Journal of Geology, 91*,203-228.

Hansen, J.W., Bakke, S., Løseth, H., Mørk, A., Mørk, M.B.E., Rise,L., Smelror, M.,Verdenius, J.G., Vigran, J.O. & Weiss, H.M., 1992. Shallow drilling Nordland VI and VII 1991. *Main report.Continental Shelf and Petroleum Technology Research Institute (IKU) Report 23*.1594.00/02/92, 390 pp.

Heier, K. S. & Compston, W., 1969. Rb—Sr isotopic studies of the plutonic rocks of the Oslo Region. *Lithos 2*, 133-145.

Henningsen T. & Tveten E., 1998. Berggrunnskart ANDØYA, M 1:250 000. Norges geologiske undersøkelse, Trondheim, Norway.

Hendriks, B.W.H., Osmundsen, P.T. and Redfield, T.F., 2010. Normal faulting and block tilting in Lofoten and Vesterålen constrained by Apatite Fission Track data. *Tectonophysics, 485*, 154-163.

Hendriks, B. W. H. 2003. Cooling and denudation of the Norwegian and Barents Sea Margins, Northern Scandinavia. Constrained by appatite fission track and (U-Th)/He thermochronology. PhD thesis, Vrije Universiteit Amsterdam, 192pp.

Heer, O., 1877. Über die Pflanzen-Versteinerungen von Andø in Norwegen. *Flora Fossilis Artica, 4*, 1-4.

Heier, K. S.. 1960. Petrology and geochemistry of high grade metamorphic and igneous rocks on Langøy, northern Norway. *Norges geologiske undersøkelse, 207*, 1-246.

Hinckley D.N., 1963. "Variability in 'crystallinity' values among the kaolin deposits of the coastal plain of Georgia and South Carolina'. *Clays and Clay Minerals, II*, 229-235.

Høyer A.S., Jørgensen F., Foged N., He X. & Christiansen A.V., 2015. Three-dimensional geological modelling of AEM resistivity data–A comparison of three methods, *Journal of Applied Geophysics 115*, 65–78.

Indrevær, K., Bergh, S. G., Koehl, J. B., Hansen, J. A., Schermer, E. R., & Ingebrigtsen, A., 2014. Post-Caledonian brittle fault zones on the hyper-extended SW Barents Sea Margin: New insights into onshore and offshore margin architecture. *Norwegian Journal of Geology, 93,* pp. 167–188.

Johanson, N., 1920. Neue mesozoische Pflanzen aus Andö in Norwegwn. *Svensk Botanisk Tidsskrift, 14*, 249-257.

Kitchka A.A., Kuzmanenko G.O., Shnyukova K.Ye., Solomyanyi A.R., Kozar M.O., Shurko M.M., Kutas R.I., Petrovskyy O.P., Fedchenko T.O. & DEPROIL Ltd. Team, 2016. Multidisciplinary Research of the Weathered Crystalline Crust (WCC) in Ukraine. *NGU Report 2016.051, 309 pp.*

Klemperer, S., 1987. Seismic-noise-reduction techniques for use with vertical stacking: An empirical comparison. *Geophysics, 52 (No 3)*, 322-334.

Korenaga, J., Holbrook, W.S., Kent, G.M., Kelemen, P.B., Detrick, R.S., Larsen, H.-C., Hopper, J.H. and Dahl-Jensen, T., 2000. Crustal structure of southeast Greenland margin from joint reflection and refraction tomography. *Journal of Geophysical Research, 105 (B9),* 21591-21614.

Lambrecht, J.L., Miller, R.D. and Rademacker, T.R. 2004. Advantages and disadvantages of pre-correlation stack processing on near-surface, high-resolution Vibroseis data. Extended abstract, *SEG Int. Exposition and 74th Annual Meeting*, Denver, CO.

Lanson et al., 2002. Authigenic kaolin and illitic minerals during burial diagenesis of sandstones: a review, *Clay Minerals, v. 37,* 1–22.

Larssen, G. B., Elvebakk, G., Henriksen, L. B., Kristiensen, S.-E., Nilsson, I., Samuelsberg, T.J., Svånå, T. A., Stemmerik, L., Worsley, D., 2002. Upper Palaeozoic lithostratigraphy of the southern Norwegian Barents Sea. *NPD Bulletin, v. 9,* 76 pp.

Ley-Cooper Y., Macnae J. & Tweed S., 2008. Estimating subsurface porosity and salt loads using airborne geophysical data. *Near Surface Geophysics 6*, 31-37.

Li W.-B., Zeng Z.-F., Li J., Chen X., Wang K. & Xia Z., 2016. 2.5D forward modeling and inversion of frequency-domain airborne electromagnetic data. *Applied Geophysics, 13*, pp. 37-47.

Lidmar-Bergström, K., Olsson, C.D. & Roaldset, E., 1999: Relief features and palaeoweathering remnants in formerly glaciated Scandinavian basement areas. In: Thiry, M. & SimonCoinçon, R. (eds.), Palaeoweathering, palaeosurfaces and Related Continental Deposits. *International Association of Sedimentologists, Special Publications 27*, 275-301.

Lindahl, I., 1978. Dverberg kisfelt, Andøya, Nordland. Undersøkelse av Statens bergrettigheter 1976. *NGU-rapport. 1430/12A*. 7s + appendices.

Liu Y. & Yin C., 2016: 3D inversion for multipulse airborne transient electromagnetic data, *Geophysics, 81*, 1–8.

Løfaldli, M., & Thusu, B., 1979. Micropalaeontological studies of the Upper Jurassic and Lower Cretaceous of Andøya, northern Norway. *Palaeontology, 22*, 413-425.

Løseth, H., & Tveten, E., 1996. Post-Caledonian structural evolution of the Lofoten and Vesterålen offshore and onshore areas. *Norsk Geologisk Tidsskrift, 76*, 215-230.

Manum, S., 1968. A new Jurassic species of Pseudotorellia Florin from the Jurassic of Andøya, northern Norway. *Linnean Society of London Botanical journal, 61 (348*), 197-200.

Manum, S. B., Bose, M. N., & Vigran, J. O., 1991. The Jurassic flora of Andøya, northern Norway. *Review of Palaeobotany and Palynology, 68*, 233-256.

Markl, G., Frost, B. R. and Bucher, K., 1998. The origin of anorthosites and related rocks from the Lofoten Islands, Northern Norway. I. Field relations and estimation of intrinsic variables. *Journal of Petrology, 39,* 1425–1452

McFarlane, M. J., Coetezee, S. H., Kuhn, J. R., Vanderpost, C. H. M., Exkardt, F. D., 2007. In situ rounding of quartz grains within an African surface weathering profile in North West Nngamiland, Botswana. *Z. Geomorph. N. E., 51*, 269-286.

Midbøe, P., 2007. Geologiske innføring til Ramsåfeltet, Andøya og Sortlandsundetbassenget, *Internal Statoil report,* pp. 22

Midbøe, P., 2011. Geologisk introduksjon til Ramsåfeltet, Andøya og Sortlandsundetbassenget Vesterålen, 4 utgave. Rapport Statoil.

Midbøe, P., 2008: Sokkelbergarter på land. *Geoforskning 2008/3*.

Millot, G., 1970: Geology of clays. Textbook. Springer Verlag.

Miller, R., Black, W., Miele, M., Morgan, T., Ivanov, J., Shelby, P. and Wang, Y., 2016. *The Leading Edge, 35 (9)*, 760–769.

Mjelde, R., Sellevoll, M.A., Shimamura, H., Iwasaki, T. & Kanazawa, T., 1993. Crustal structure beneath Lofoten, N. Norway, from vertical incidence and wide-angle seismic data. *Geophysical Journal Internationa1 14*, 116–126.

Mokhtari, M., & Pegrum, R. M., 1992. Structure and evolution of the Lofoten continental margin, offshore Norway. *Norsk Geologisk Tidsskrift, 72*, 339-355.

Mosar, J., Eide, E. A., Osmundsen, P. T., Sommaruga, A., & Torsvik, T. H., 2002. Greenland-Norway separation: A geodynamic model for the North Atlantic. *Norwegian Journal of Geology, 82*, 281-298.

Myhre, A.M., Eldholm, O., Faleide, J.I., Skogseid, J., Gudlaugsson, S.T., Planke, S., Stuevold, I.M. & Vågnes, E., 1992. Norway-Svalbard continental margin: Structural and stratigraphic style: Poag, W.C. & de Graciansky, P.C. (eds.) *Geological evolution of Atlantic continental rises, New York: Van Nostrand Reinhold*, 157-185.

Mørk, M.B.E., McEnroe, S.A. & Olesen O., 1996. OSRAM - Origin of Sediment-Related AeroMagentics. *IKU report 96.133*, pp. 115

Mørk, M.B.E.,Vigran, J.O., Smelror, M., Fjerdingstad,V. & Bøe, R., 2003. Mesozoic mudstone compositions and the role of kaolinite weathering – shallow cores in the Norwegian Sea (Møre to Troms). *Norwegian Journal of Geology, v. 83*, 61-78.

Nilssen, O. 2005: Ramsafeltet på Andøya. Bergverksaktivitet gjennom tidene. http://www.vesteraalen.info/andoy_hovedside.htm

Often, M. 1980. Diamantboring, Dverberg kisfelt, Andøya, Nordland. Undersøkelse av Statens bergrettigheter 1980. *NGU-rapport nr. 1650*/12C, 11s + appendices.

Okazaki, K., Mogi, T., Utsugi, M., Ito, Y., Kunishima, H., Yamazaki, T., Takahashi, Y., Hashimoto, T., Yamamaya, Y., Ito, H., Kaieda, H., Tsukuda, K., Yuuki, Y. & Jomori, A., 2011. Airborne electromagnetic and magnetic surveys for long tunnel construction design. *Physics and Chemistry of the Earth 36*, 1237-1246.

Olesen, O., Torsvik, T. H., Tveten, E., Zwaan, K. B., Løseth, H., & Henningsen, T., 1997. Basement structure of the continental margin in the Lofoten-Lopphavet area, northern Norway: Constraints from potential field data, on-land structural mapping and paleomagnetic data. *Norsk Geologisk Tidsskrift, 77*, 15-30.

Olesen, O., Lundin, E., Nordgulen, O., Osmundsen, P.T., Skilbrei, J.R., Smethurst, M.A., Solli, A., Bugge, T. & Fichler, C., 2002. Bridging the gap between the onshore and offshore geology in Nordland, northern Norway. *Norwegian Journal of Geology 82*, 243-262.

Olesen, O. 2006: Aktsomhetskart for tunnelplanlegging, Østlandsområdet, Geofysisk tolkning av dypforvitring, Scale 1:100,000. Norges geologiske undersøkelse, Trondheim.

Olesen, O. & Rønning, J.S., 2008. Deep weathering: Past climates cause tunnel problems. *Gråsteinen no. 12*. Geological Survey of Norway, Trondheim.

Olesen O., Bering D., Brönner M., Dalsegg E., Fabian K., Fredin O., Gellein J., Husteli B., Magnus C., Rønning J.S., Solbakk T., Tønnesen J.F. & Øverland J.A. 2012. Tropical Weathering In Norway, TWIN Final Report, *NGU Report 2012.005*, pp.188.

Olesen, O., Kierulf, H.P., Brönner, M., Dalsegg, E., Fredin, O. & Solbakk, T. 2013. Deep weathering, neotectonics and strandflat formation in Nordland, northern Norway. *Norwegian Journal of Geology, Vol 93*, pp. 189–213.

Osmundsen, P. T., Redfield, T. F., Hendriks, B. W. H., Bergh, S. G., Hansen, J. A., Henderson, I. H. C., Davidsen, B., 2010. Fault-controlled alpine topography in Norway. *Journal of the Geological Society, 167*, 83-98.

Paasche, Ø., Strømsøe, J.R, Dahl, S.O. & Linge, H., 2006. Weathering characteristics of arctic islands in northern Norway. *Geomorphology 82*, 430–452.

Parnell, J., Baron, M., Boyce, A., 2000. Controls on kaolinite and dickite distribution, Highland Boundary Fault Zone, Scotland and Northern Ireland. *J. Geol. Soc., London, Vol. 157*, pp. 635-640.

Parrish, J.T., 1993. Climate of the Supercontinent Pangea. *The Journal of Geology, 101*, p. 215-233.

Park, C.B., Miller, R. D., Steeples, D. W. & Black, R.A. 1996. Swept impact seismic technique. *Geophysics, 61*, 1789 – 1903.

Petersen, H. I., Øverland, J. A., Solbakk, T., Bojesen-Koefoed, J. A., Bjerager, M., 2013. Unusual resinite-rich coals found in northeastern Greenland and along the Norwegian coast: Petrographic and geochemical composition. *International Journal of Coal Geology, v. 109-110*, 58-76.

Peulvast, J. P., 1986. Structural geomorphology and morphological development in the Lofoten – Vesterålen area, Norway. *Norsk geografisk Tidsskrift, vol. 40*, s. 135–161.

Plumb, R.A., and Hickman, S.H., 1985. Stress-induced borehole enlargement: a comparison between the four-arm dipmeter and the borehole televiewer in the Auburn geothermal well. - *J. Geophys. Res., 90*, 5513-5521.

Rasmussen. E., 1985. Summary of the Mesozoic Rocks on Andøya, northern Norway, with emphasis on reservoir geology, source rock potential and dating of unconformities. *Norsk Hydro Report.*

READ, 1987. Mesozoic Rocks of Andøya. An interpreted data package from four wells. Palynology and sedimentology. Unpublished industry report prepared by READ Production Geology Services A/S, July 1987

Redfield, T. F., & Osmundsen, P. T., 2013. The long-term topographic response of a continent adjacent to a hyperextended margin: A case study from Scandinavia. *Geological Society of America Bulletin, 125(1-2)*, 184-200.

Rueslåtten, H.G. and Jørgensen, P., 1978. Interaction between bedrock and precipitation at Temperatures Close to 0°C. *Nordic Hydrology, 9,* 1-6.

Reinecker, J., Tingay, M. & Müller, B. 2003: Borehole breakout analysis from four-arm caliper logs. University of Karlsruhe, Geophysical Institute. World Stress Map Project.

Roach I.C., Jaireth S. & Costelloe M.T. 2014. Applying regional airborne electromagnetic (AEM) surveying to understand the architecture of sandstone-hosted uranium mineral systems in the Callabonna Sub-basin, Lake Frome region, South Australia, Australian *Journal of Earth Sciences, 61*, 659-688.

Rodionov, A., Ofstad, F. & Tassis, G. 2012. Helicopter-borne magnetic, electromagnetic and radiometric geophysical survey at Andøya, Nordland County. *NGU Report no.: 2012.056*.

Rodionov, A., Ofstad, F. & Tassis, G. 2013a: Helicopter-borne magnetic, electromagnetic and radiometric geophysical survey in the western part of Austvågøya, Lofoten archipelago, Nordland. *Norges geologiske undersøkelse Report 2013.045,* 26 pp.

Rodionov, A., Ofstad, F., Stampolidis, A. & Tassis, G. 2013b. Helicopter-borne magnetic, electromagnetic and radiometric geophysical survey in at Langøya in Vesterålen, Nordland. *Norges geologiske undersøkelse Report 2013.044*, 26 pp.

Robertson Geologging Ltd. 2004. Interpretation manual. RGLDIP version 6.2.

Russell, B.H. 1989. Statics corrections – A tutorial. *CSEG Recorder, 14 (No 3)*, 16-30.

Rückemann, C.-P. 2012. Comparison of stacking methods regarding processing and Computing of geoscientific depth data. *GEOProcessing,* 35 – 40.

Siemon B., Christiansen A.V. & Auken E., 2009: A review of helicopter-borne electromagnetic methods for groundwater exploration. *Near Surface Geophysics 7*, 629-646.

Siemon B., Steuer A., Ullmann A., Vasterling M., & Voß W. 2011: Application of frequency-domain helicopter-borne electromagnetic for groundwater exploration in urban areas, *Physics and Chemistry of the Earth, 36*, 1373–1385.

Smelror, M., Mørk, A., Mørk, M.B., Weiss, H.M. and Løseth. H., 2001. Middle Jurassic – Lower Cretaceous transgressive – regressive sequences and facies distribution off northern Nordland and Troms, Norway. In O.J. Martinsen and T. Dreyer (eds.), Sedimentary Environments Offshore Norway – Paleozoic to Recent. *Norwegian Petroleum Society Special Publications, 10*, 211 – 232.

Scheunert M., Ullmann A., Afanasjew M., Börner R.-U., Siemon B. & Spitzer K., 2016: A cut-&-paste strategy for the 3-D inversion of helicopter-borne electromagnetic data - I. 3-D inversion using the explicit Jacobian and a tensor-based formulation, *Journal of Applied Geophysics, 129*, 209–221.

Schlumberger, 2016: Mineral Identification from NGS* Natural Gamma Ray Spectrometry Log CP-19. Internet version.

Smelror, M., Petrov, O., Larssen, G.B. & Werner, S.C. 2009: Atlas: geological history of the Barents Sea. Norges geologiske undersøkelse, Trondheim, 135 pp.

Smith R.S., Rodney K., Hodges G. & Lemieux J. 2011: A comparison of airborne electromagnetic data with ground resistivity data over the Midwest deposit in the Athabasca basin, *Near Surface Geophysics 9*, 319-330.

Sokolov, N., 1912. Fauna der mesozoischen Ablagerungen von Andø. Vitenskapsselskapet i Kristianias Skrifter, Matematisk-Naturvitenskaplig klasse, 6, 1-16.

Stampolidis, A., Ofstad, F. and Baranwal, V. 2014: Helicopter-borne magnetic and radiometric geophysical survey at Austvågøya, Hinnøya, Tjeldøya and Hadseløya areas, in Troms and Nordland counties. *Norges geologiske undersøkelse Report 2014.007*, 36 pp.

Steltenpohl, M.G., Andresen, A., Prouty, J., Augland, L.E., 2013. Late-and-post Caledonian tectonic exhumation of middle- and lower-crustal rocks exposed in the region between Bodø and the Lofoten Islands, north Norway Latitudes 67.5-69°, *EGU General Assembly 2013, held 7-12 April, 2013 in Vienna, Austria*, id. EGU2013-6328

Steltenpohl, M. G., Moecher, D., Andresen, A., Ball, J., Mager, S. & Hames, W., 2011. The Eidsfjord shear zone, Lofoten-Vesteralen, north Norway: An Early Devonian,

paleoseismogenic low-angle normal fault. *Journal of Structural Geology 33(5)*, pp 1023-1043.

Stemmerik, L., Dalhoff, F., Larsen, B. D., Lyck, J., Mathiesen, A., & Nilsson, I., 1998. Wandel Sea Basin, eastern North Greenland. *Geology of Greenland Survey Bulletin, 180*, 55-62.

Sturt, B.A., Dalland, A. & Mitchell, J.L. 1979. The age of the sub mid Jurassic tropical weathering profile on Andøya, Northern Norway, and the implications for the Late Palaeozoic palaeography in the North Atlantic Region. *Geologische Rundschau 68*, 523-542.

Sundvor, E. and Sellevoll, M. A. 1969. Seismiske undersøkelser av den norske kontinentalsokkel Andøya – Fugløybanken. Jordskjelvstasjonen, Universitetet i Bergen, Teknisk rapport, nr. 4. 26 pp.

Torsvik, T.H., Carlos, D., Mosar, M., Cocks, L.R.M., Malme, T. In Eide, E.A. coordinator, 2002, *BATLAS – Mid-Norway plate reconstruction atlas with global and Atlantic perspectives.* Geological Survey of Norway.

Thunehead, H. & Olsson, O. 2005. Borehole Corrections for a Thick Resistivity Probe. *Journal of Environmental & Engineering Geophysics, Vol. 9, Issue 4,* pp. 217- 224.

Tsikalas, F., Eldholm, O. & Faleide, J.I. 2005. Crustal structure of the Lofoten-Vesteralen continental margin off Norway. *Tectonophysics, 404*, 151-174.

Tsikalas, F., Faleide, J. I., & Eldholm, O., 2001. Lateral variations in tectono-magmatic style along the Lofoten-Vesterålen volcanic margin off Norway. *Marine and Petroleum Geology, 18*, 807-832.

Tull, J. F. 1977. Geology and Structure of Vestvågøy, Lofoten, North Norway. *Norges geologiske undersøkelse, 333*, 1-59.

Tveten, E. 1978. Geologisk kart over Norge, berggrunnskart Svolvær i 1:250.000. *Norges geologiske undersøkelse.*

Tveten, E. 1990. Sortland 1232 III, Foreløpig berggrunnskart. *Norges geologiske undersøkelse*.

Valleau N.C. 2000. HEM data processing - a practical overview, *Exploration Geophysics, 31*, 584-594.

Viezzoli A., Munday T., Auken E. & Christiansen, A.V. 2010. Accurate quasi-3D versus practical full 3D inversion of AEM data – the Bookpurnong case study, Preview 149, 23–31.

Viezzoli A., Christiansen A.V., Auken E. & Sørensen K., 2008. Quasi-3D modeling of airborne TEM data by spatially constrained inversion: *Geophysics, 73*, F105–F113.

Vigrand, J. and Thusu, B., 1975. Illustration and distribution of Jurassic Palynomorphs of Norway. *Roy. Norw. Coun. Ind. Res. Cont. Shelf Div. Publ. 65*, 56pp.

Vogt, C., Lauterjung, J., Fischer, R.X., 2002. Investigation of the clay fraction (<2 micron) of the Clay Minerals Society Reference Clays. *Clays and Clay Minerals, v. 50*, 388-400.

Vogt, J. H. L., 1905. Om Andøens jurafelt, navnlig om landets langsomme nedsynken under juratiden og den senere hævning samt gravforkastning. *Norges Geologiske Undersøkelse, 43*. 5, 1-67.

Whitehead N. 2005: Helicopter electromagnetic data processing, analysis and presentation system for Oasis montaj v6.2, *Geosoft HEM system tutorial and user guide*, 54.

Wilson, R. W., McCaffrey, K. J. W., Holdsworth, R. E., Imber, J., Jones, R. R., Welbon, A. I. F., & Roberts, D. (2006). Complex fault patterns, transtension and structural segmentation of the Lofoten Ridge, Norwegian margin: Using digital mapping to link onshore and offshore geology. *Tectonics, 25*(TC4018).

Zoback, M.D., D. Moos, L.G. Mastin & Anderson, R.N. 1985. Well bore breakouts and in situ stress. - *J. Geophys. Res., 90*, 5523-5530.

Zwaan, K. B., & Grogan, P. W. (Cartographer). (1998). Geologiske Kart over Norge, Berggrunnskart TROMSØ, M: 1:250000.

Ørvig, T., 1953. On the Mesozoic field of Andøya. 1. Notes on the Ichthyosaurian remains collected in 1952, with remarks on the age of the vertebrate bearing beds. *Acta Borealia, A. Scientia, 4*, 1-32.

Ørvig, T., 1960. The Jurassic and Cretaceous of Andøya in northern Norway. *Norges Geologiske Undersøkelse, 208*, 344-350.

Åm, K., 1975. Aeromagnetic basement complex mapping north of latitude 62 N, Norway. *Norges geol. Unders. 316*,

Appendix I

Procedure for static corrections of seismic data

Statics are preferably determined from reflections, but since clear reflections are missing in pre-stack data for most of our lines, we had to use first breaks instead. By inspection of the shot records, we found that first arrivals in the offset interval 70 to 400 m were refracted waves, propagating along the upper part of the solid rocks below the low velocity surface materials (sanddunes, peats, moraine, etc). A well-known method used for computing surface consistent refraction statics is the time-term method (Russell 1989, Chun & Jacewitz, 1981). In this method it is assumed that the refraction velocity is constant, which is obviously not the case for much of our data where the lines cross over the boundary between the sediment basin and the basement rock. In order to account for the lateral velocity variations we computed the travel time of the first arrival as:

$$T_{ij} = \int_{Xi}^{Xj} \frac{dx}{v(x)} + t_S(x_i) + t_R(x_j)$$

where T_{ij} is the traveltime from source i to receiver j, x_i is the source position, x_j is the receiver position, v(x) is the laterally varying refraction velocity, $t_s(x_i)$ is the time delay of the source, and $t_r(x_j)$ is the time delay of the receiver. If v(x) is constant, this equation reduces to that of the original time-term method. We used a piecewise linear function for v(x) with 150 m between the velocity nodes. Since the contribution of the horizontal part of the ray to the traveltime is an integral over the inverse velocity, the traveltimes will be smooth functions of the horizontal coordinate. More irregular variations in the traveltimes must be accounted for by the time-terms. An automatic first break picker was used to pick arrival times within a guided time window. This resulted in thousands of traveltimes for each line, which were then used to compute the hundreds of unknowns (velocities and time-terms) in a damped linear inversion. The time delays, as shown in Figure 5.8 for Line 1, and in Figure A.1 for lines 2-6, indicate the depth to the bedrock (the depth increases with increasing delays). However, in order the convert the time delays to depths one must know the velocites in the weathered layer, which in our case cannot be determined accurately since we are using geophone strings (and not single geophones). The static corrections were set to the computed time delays minus 10 ms (as seen from the figures the smallest values are around 10 ms). The computed bedrock

velocities clearly define the boundary of the Mesozoic sediments near the surface even when the boundary is too steep to be imaged by seismic reflections.

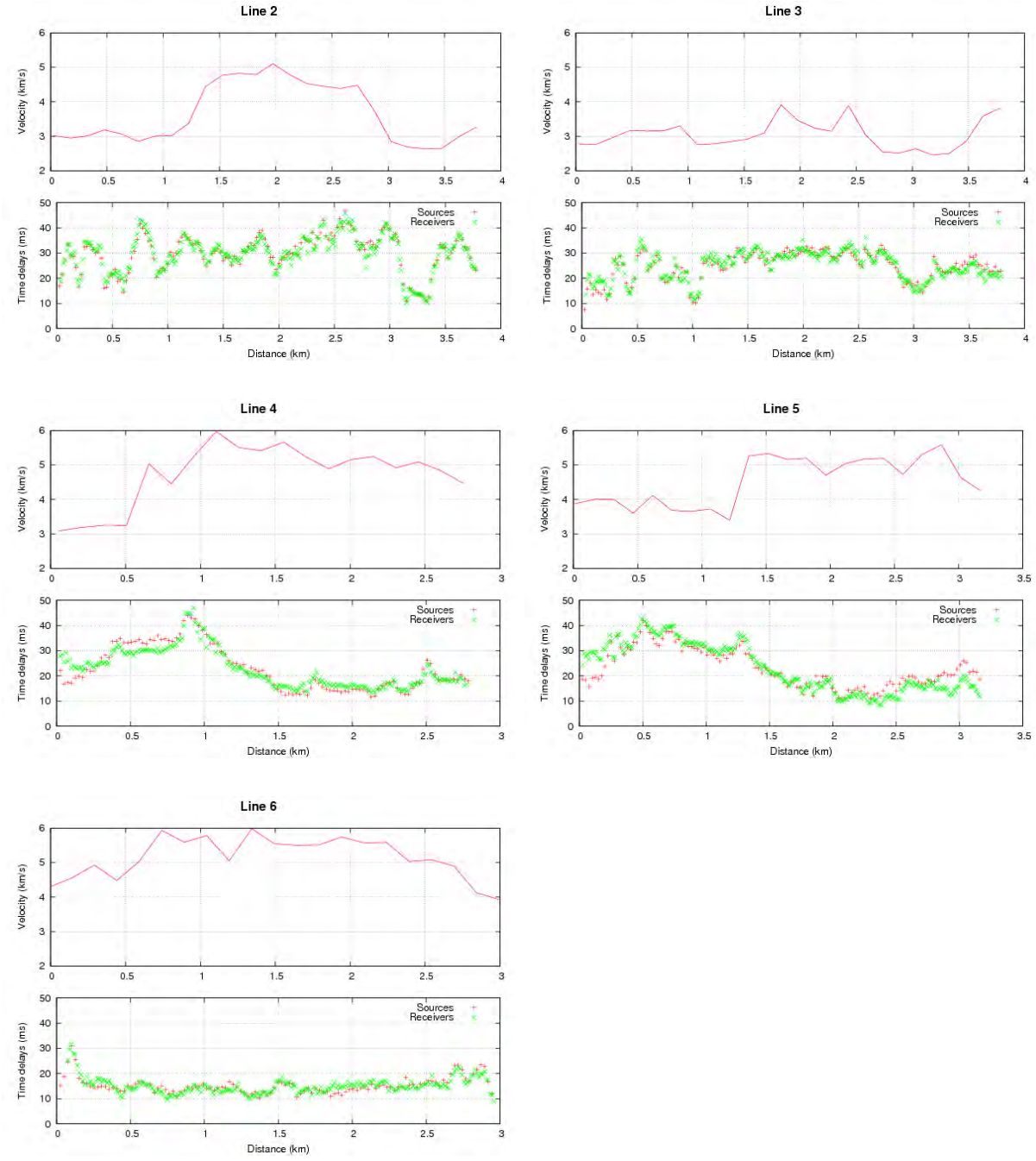

Figure A1.1. Time delays (statics) and upper bedrock velocities for land lines 2-6.

Appendix II

Chemical analyses of samples from NGU BH 1 and BH 2

Table A2.1. Main elements of samples from NGU BH 1 and basement of BH 2; given as weight % from XRF. Also shown is sampling depths (m) and samples Id. Ign.l.=ignition loss (weight %).

Sample	Depth	SiO2	Al2O3	Fe2O3	TiO2	MgO	CaO	Na2O	K2O	MnO	P2O5	Ign. l
Id.	(m)	[%]	[%]	[%]	[%]	[%]	[%]	[%]	[%]	[%]	[%]	[%]
98596	113,4	50,5	27,3	2,57	1,15	1,05	0,559	1,04	3,46	<0.01	0,021	11,6
84002	113,9	47,7	25,5	4,30	1,19	1,90	0,573	0,33	4,15	<0.01	0,016	13,3
98597	115,6	42,8	0,340	0,923	0,027	6,79	26,9	0	0,021	0,346	0,016	20,1
98598	121,8	49,4	18,6	11,9	1,13	6,78	0,899	2,34	1,72	0,041	0,012	6,93
98599	132,4	49,5	13,3	8,36	0,884	16,5	0,111	2,76	3,51	0,041	0,039	3,83
98600	134,7	46,1	13,1	7,95	0,957	20,6	0,063	1,66	4,69	0,048	0,028	3,53
98592	158,2	50,0	11,8	5,54	0,578	17,9	1,69	3,62	0,532	0,094	0,814	6,92
84001	167	48,4	15,3	10,7	1,09	10,4	0,542	5,81	1,37	0,063	0,068	5,08
98593	185,7	44,2	11,4	6,19	0,485	25,3	0,345	0,63	3,75	0,101	0,056	5,87
98594	188,5	54,8	14,1	6,12	0,490	12,7	0,381	5,25	0,628	0,081	0,060	4,70
98595	195,1	48,5	15,8	10,7	1,18	7,65	8,99	3,54	0,808	0,154	0,191	1,20
98587	200,6	70,0	14,1	3,32	0,289	1,16	1,26	3,91	3,54	0,024	0,058	1,32
98588	201,3	68,7	13,2	2,13	0,224	0,845	3,95	4,04	3,01	0,050	0,073	2,84
98589	205,3	48,3	12,6	17,1	1,80	6,40	6,76	2,00	0,975	0,233	0,243	2,06
98590	207,5	70,9	13,3	4,18	0,387	1,95	1,23	3,88	2,18	0,057	0,058	1,25
98591	212,2	75,2	13,1	0,345	0,037	0,104	0,760	3,25	5,86	<0.01	0,018	0,335

Table A2.2A. Trace elements in samples from NGU BH 1 and basement in BH 2; weight % from XRF. Values obtained from melted specimens. Also shown is sampling depths (m) and samples Id. Most values are below the detection limits. ZrO_2 is highest in the two deeply weathered sediment samples, 98596 and 84002.

Depth	Sample	BaO	Cr2O3	CuO	NiO	PbO	SrO	ZnO	V2O5	ZrO2	SO3
(m)	Id.	[%]	[%]	[%]	[%]	[%]	[%]	[%]	[%]	[%]	[%]
113,4	98596	0,029	0,036	<0.01	<0.01	<0.01	<0.04	<0.01	0,034	0,033	<0.1
113,9	84002	<0.025	0,042	<0.01	<0.01	<0.01	<0.04	<0.01	0,031	0,033	0,18
115,6	98597	<0.025	<0.02	<0.01	<0.01	<0.01	<0.04	<0.01	<0.02	<0.02	0,63
121,8	98598	<0.025	0,025	<0.01	0,011	<0.01	<0.04	<0.01	0,030	<0.02	<0.1
132,4	98599	<0.025	<0.02	<0.01	<0.01	<0.01	<0.04	<0.01	0,027	<0.02	<0.1
134,7	98600	<0.025	0,023	<0.01	<0.01	<0.01	<0.04	<0.01	0,031	<0.02	<0.1
158,2	98592	<0.025	<0.02	<0.01	<0.01	<0.01	<0.04	0,011	<0.02	<0.02	<0.1
167	84001	<0.025	0,041	<0.01	<0.01	<0.01	<0.04	0,010	0,042	<0.02	<0.1
185,7	98593	<0.025	0,030	<0.01	<0.01	<0.01	<0.04	0,014	0,024	<0.02	<0.1
188,5	98594	<0.025	<0.02	<0.01	<0.01	<0.01	<0.04	0,011	<0.02	<0.02	<0.1
195,1	98595	<0.025	0,044	<0.01	<0.01	<0.01	<0.04	<0.01	0,038	<0.02	<0.1
200,6	98587	0,092	<0.02	<0.01	<0.01	<0.01	<0.04	<0.01	<0.02	<0.02	0,54
201,3	98588	0,070	<0.02	<0.01	<0.01	<0.01	<0.04	<0.01	<0.02	<0.02	0,62
205,3	98589	0,057	<0.02	0,020	<0.01	<0.01	<0.04	0,018	0,077	<0.02	0,15
207,5	98590	0,062	<0.02	<0.01	<0.01	<0.01	<0.04	<0.01	<0.02	<0.02	<0.1
212,2	98591	<0.025	<0.02	<0.01	<0.01	<0.01	<0.04	<0.01	<0.02	<0.02	0,15

Table A2.2B. NGU BH 1 and basement in BH 2. Trace elements in mg/kg. Analysis of compacted powder specimens. Elements with values below the detection limits are excluded from the table. Sampling depths in meter and corresponding sample numbers.

Sample depth m	Sample id.	Ba	Ce	Co	Cr	Cu	Ga	La	Nb	Nd	Ni
113.4	98596	221	54	<4	250	<5	33,5	28	15,5	25	17,4
113.9	84002	142	37	<4	305	<5	28,8	21	17,1	28	34,1
115.6	98597	10	31	5,5	20	<5	<3	<15	2,7	12	5,6
121.8	98598	135	20	39,9	180	<5	25,1	<15	8,3	<10	110
132.4	98599	168	49	29,3	104	<5	17,8	23	7,9	19	79,3
134.7	98600	185	75	32,6	135	<5	21,9	46	11,2	28	89,6
158.2	98592	45	101	25,6	129	<5	17	51	7	32	86,0
167.0	84001	35	19	25,7	240	<5	17,3	<15	6,3	10	83,0
185.7	98593	97	73	28,4	194	<5	15,3	40	7,8	26	81,5
188.5	98594	25	35	19,9	118	<5	18,7	20	7,2	15	61,4
195.1	98595	141	17	39,1	262	15,8	15,9	<15	5,2	11	71,0
200.6	98587	676	50	7,2	51,4	12,5	15,8	21	8,6	21	18,8
201.3	98588	612	104	6,6	37	23,8	13,9	50	7,5	38	13,0
205.3	98589	438	39	53,2	68,3	142	17,8	17	9,6	18	57,5
207.5	98590	480	98	9,3	83,9	21,8	18,2	50	9,3	38	29,6
212.2	98591	93	21	<4	9,8	<5	18,1	<15	4,4	<10	<5

Table A2.2C. NGU BH 1 and basement in BH 2. Trace elements in mg/kg, with the exception of Cl, which is in weight %. Elements with values below the detection limits are excluded from the table. Analysis of compacted powder specimens. Sampling depths in meter and corresponding sample numbers.

Sample depth m	Sample id.	Pb	Rb	Sc	Sr	Th	V	Y	Zn	Zr	Cl
113.4	98596	<5	91,4	39,7	120	20,7	183	29,0	8,7	253	0,029
113.9	84002	<5	157	46,5	230	22,2	198	8,4	17,8	263	0,030
115.6	98597	<5	<5	<5	79,2	9,6	24,9	22,9	7,3	8,2	<0.02
121.8	98598	<5	73,1	40,1	145	<3	168	16,9	43,7	89,0	0,028
132.4	98599	<5	96,6	31,5	13,3	4,4	153	12,1	45,8	78,6	0,045
134.7	98600	<5	149	16,4	<5	9,3	162	17,9	64,4	87,7	0,036
158.2	98592	<5	19,7	23,9	78,9	3,3	88,2	24,8	92,0	88,1	0,025
167.0	84001	<5	45,5	27,7	62,5	<3	203	7,4	84,2	56,7	<0.02
185.7	98593	<5	113	14,5	29,6	11,0	128	13,5	118	63,8	<0.02
188.5	98594	<5	20,7	12,5	28,4	4,3	92,4	11,5	96,6	69,6	0,024
195.1	98595	<5	34,9	24,5	199	<3	208	20,8	29,7	63,4	0,105
200.6	98587	19,3	91,1	8,5	224	14,4	41,5	<3	18,4	121	0,030
201.3	98588	17,9	74,1	8,1	240	9,6	25,6	17,1	24,2	86,2	<0.02
205.3	98589	<5	28,7	39,1	198	<3	407	35,6	139	126	0,027
207.5	98590	15,9	97,1	7,8	296	21,8	62,1	11,2	50,1	127	0,021
212.2	98591	55,9	186	<5	50,1	16,6	<5	45,7	<5	67,5	<0.02

Chemical analyses of samples from Ramså surface profile

Table A2.3. Main elements of the samples from the Ramså surface excavation (in weight %).

Sample No	Sample Id	SiO2	Al2O3	Fe2O3	TiO2	MgO	CaO	Na2O	K2O	MnO	P2O5	Ign.loss	Sum Main elem.
		[%]	[%]	[%]	[%]	[%]	[%]	[%]	[%]	[%]	[%]	[%]	[%]
MB12-10	108510	36	15,3	19	1,12	8,95	2,73	1,78	0,809	0,45	0,181	12,5	98,8
MB12-9	108509	53,9	16,1	7,85	0,893	6,69	4,31	5,55	0,474	0,098	0,109	2,6	98,5
MB12-6	108506	39	11,4	23	2,02	0,868	2,11	2,42	2,23	0,667	0,356	13,8	97,8
MB12-5	108505	74,2	11,8	2,95	0,347	0,06	0,529	3,45	5,1	0,085	0,028	0,18	98,7
MB12-4	108504	40,4	12,1	15,7	2,4	6,34	4,91	2,5	2,57	0,319	1,45	9,19	97,9
MB12-3	108503	46,3	11,2	10,6	1,03	11,4	8,14	1,55	4,56	0,183	1,07	1,63	97,6
MB12-2	108502	49,4	13,2	13	1,77	0,331	3,81	3,2	3,65	0,518	0,72	6,74	96,4
MB12-7	108507	49,9	15,8	11,2	0,828	7,91	4,95	4,47	0,164	0,171	0,075	3,3	98,8
MB12-1	108501	68,2	14,7	3,7	0,335	0,113	1,27	4,12	5,89	0,081	0,05	0,185	98,7
MB12-8	108508	36,6	13	20,6	0,866	8,99	5,14	0,69	0,699	0,476	0,12	11,2	98,3
MB12-14	108514	41,8	17,9	11,9	1,24	4,64	1,27	0,3	6,59	0,296	0,441	11,6	98
MB12-13	108513	61,7	17,5	1,76	0,506	0,975	0,432	0,76	12,1	0,06	0,099	2,27	98,2
MB12-12	108512	47,5	15,4	11,4	1,32	9,72	3,76	3,64	0,628	0,26	0,081	5,36	99,1
MB12-11	108511	47,1	15,9	9,81	1,15	6,8	8,05	4,19	1,48	0,149	0,063	3,89	98,7
MB11-3	108517	50,6	16,2	10,7	0,97	2,06	2,02	2,47	3,07	0,121	0,628	8,41	97,2

Table A2.4A. Trace elements of the samples from the Ramså surface excavation (in weight %).

Sample No	Sample Id	BaO	Cr2O3	CuO	NiO	PbO	SrO	ZnO	V2O5	ZrO2	SO3
		[%]	[%]	[%]	[%]	[%]	[%]	[%]	[%]	[%]	[%]
MB12-10	108510	0,029	0,036	<0.01	<0.01	<0.01	<0.04	<0.01	0,034	0,033	<0.1
MB12-9	108509	<0.025	0,044	<0.01	<0.01	<0.01	<0.04	<0.01	0,038	<0.02	<0.1
MB12-6	108506	<0.025	<0.02	<0.01	<0.01	<0.01	<0.04	0,011	<0.02	<0.02	<0.1
MB12-5	108505	<0.025	<0.02	<0.01	<0.01	<0.01	<0.04	<0.01	<0.02	<0.02	0,15
MB12-4	108504	0,062	<0.02	<0.01	<0.01	<0.01	<0.04	<0.01	<0.02	<0.02	<0.1
MB12-3	108503	0,057	<0.02	0,020	<0.01	<0.01	<0.04	0,018	0,077	<0.02	0,15
MB12-2	108502	0,070	<0.02	<0.01	<0.01	<0.01	<0.04	<0.01	<0.02	<0.02	0,62
MB12-7	108507	<0.025	0,030	<0.01	<0.01	<0.01	<0.04	0,014	0,024	<0.02	<0.1
MB12-1	108501	0,092	<0.02	<0.01	<0.01	<0.01	<0.04	<0.01	<0.02	<0.02	0,54
MB12-8	108508	<0.025	<0.02	<0.01	<0.01	<0.01	<0.04	0,011	<0.02	<0.02	<0.1
MB12-14	108514	<0.025	0,023	<0.01	<0.01	<0.01	<0.04	<0.01	0,031	<0.02	<0.1
MB12-13	108513	<0.025	<0.02	<0.01	<0.01	<0.01	<0.04	<0.01	0,027	<0.02	<0.1
MB12-12	108512	<0.025	0,025	<0.01	0,011	<0.01	<0.04	<0.01	0,030	<0.02	<0.1
MB12-11	108511	<0.025	<0.02	<0.01	<0.01	<0.01	<0.04	<0.01	<0.02	<0.02	0,63
MB11-3	108517	<0.025	<0.02	<0.01	<0.01	<0.01	<0.04	0,025	<0.02	0,059	0,59

Appendix III

Pictures of relevant core boxes from NGU BH 1.

The cores are photographed in wet conditions to improve the contrast between lithologies. A brief description of the cores is given in the figure captions for each core box. The start and the end of each core box are marked with the correct drillers' depths in meters.

Figure A3-1. NGU BH 1; cores from 112-119 m depth. Three samples are selected from this core box: 113.4 m (marked with white label), 113.9 m (marked with arrow), and 115.6 m (marked with white label). From 112 to 114 m: Motley, fine clastic sediment, consisting of mainly feldspars, quartz and kaolinite (Table 7.1). Sample 115.6 represent an altered conglomeratic rock consisting of actinolite, calcite and quartz. The rocks further down to 129.8 are sediments derived mainly from mafic rocks (dark grains), but also some quartz-feldspatic layers. Possibly also some thin layers of chert and clay (smectitic clay?). The top and bottom of the first and last core in the box are marked with correct depth. (The scale bar is divided into dm and cm).

Figure A3-2: NGU BH 1; cores from 119-126 m depth. Site of Sample 121.8 m is marked with white label. XRD data for this sample shows mainly quartz, plagioclase, and chlorite (no talc) (Table 7.1).The cores represent sediments derived mainly from mafic rocks (dark grains), but also some quartz-feldspatic layers. Possibly also some thin layers of chert and clay (smectitic clay?).

Figure A3-3: NGU BH 1; cores from 126-133 m depth. Sample from 132.4 m is marked with white label. The cores represent mainly mafic derived sand (dark grains), but also some quartz-feldspatic layers. Lenticular lenses and also some thin layers of possibly chert and clay (smectitic clay?). Sample 132.4 m consists mainly of talc, biotite, illite, plagioclase, and some chlorite (Table 7.1). The cores from 130-132 m show conglomeratic intervals, with angular rock clasts: may be debris flows?

Figure A3-4. NGU BH 1; cores from 133-140 m depth. Sediment derived mainly from mafic rocks, also with quartz-feldspatic layers and lenticular lenses. Some conglomeratic layers with angular rock clasts; maybe debris flow? Sample 134.7 m is from this core box. XRD data for this sample shows mainly talc, biotite, illite, plagioclase, and some chlorite (Table 7.1).

Figure A3-5. NGU BH 1; cores from 140- 147 m depth. 129.78-143.20 m: Some conglomeratic layers with angular-to-rounded rock clasts; maybe debris flow? Similar composition as the previous core interval.

Figure A3-6. NGU BH 1; cores from 147-154 m depth. Similar lithologies as the previous core interval. Several conglomeratic layers, with angular to sub-rounded clasts; commonly in a light grey matrix.

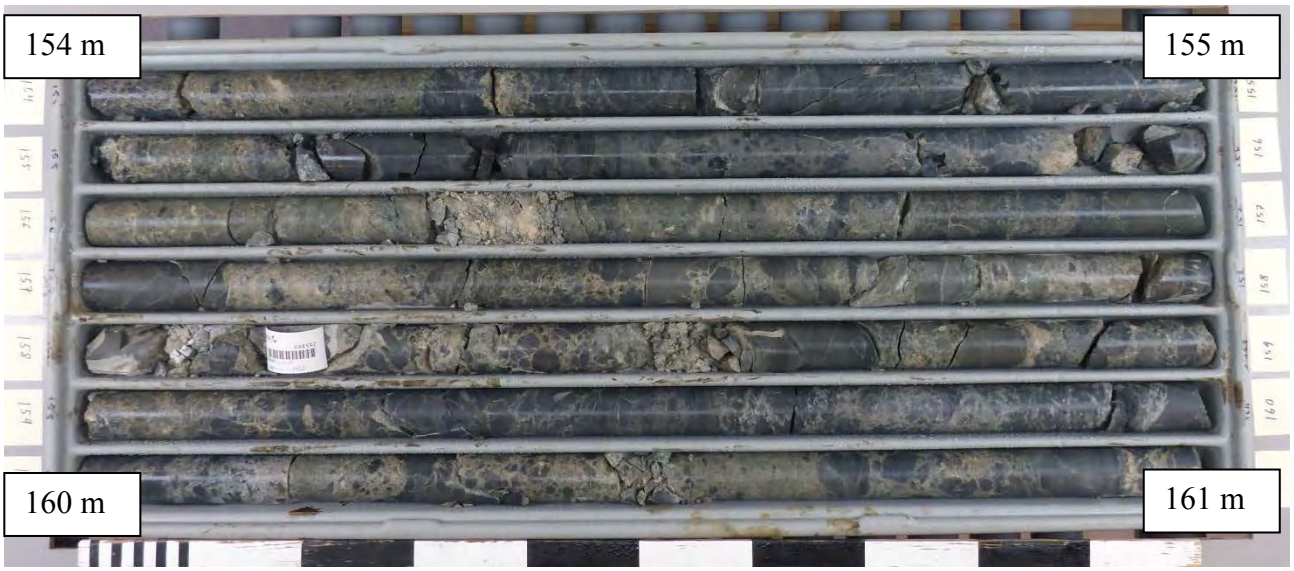

Figure A3-7A: NGU BH 1; cores from 154-161 m depth. Sample 158.2 m is from this core box (white label). The entire interval is dominated by conglomerates, with angular to sub-rounded dark mafic rock clasts in lighter matrix. These sediments are described as sedimentary breccia or debris flows. The dominating minerals in Sample 158.2 m are plagioclase, chlorite, talc, and smectitic clay (Table 7.1).

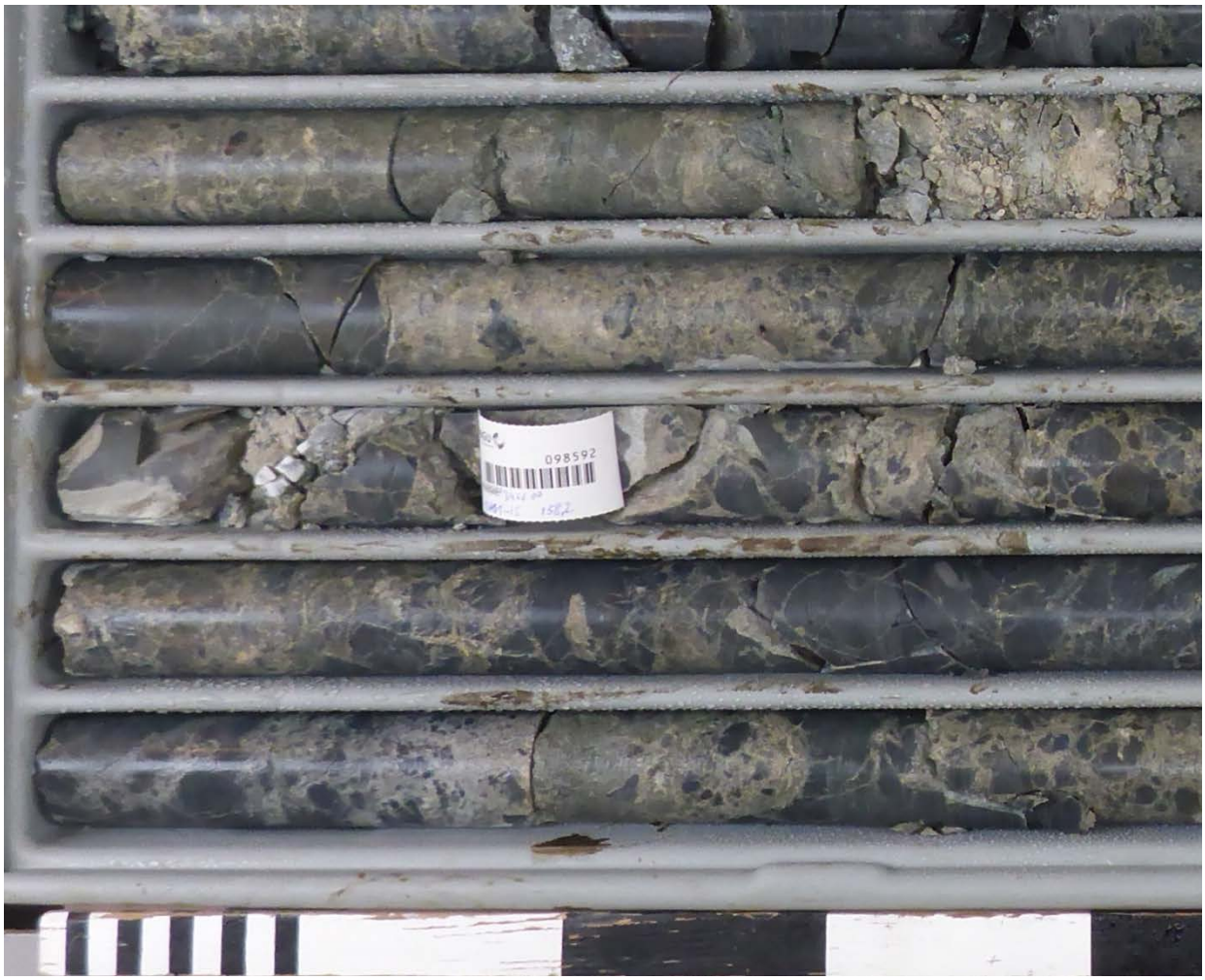

Figure A3-7B: NGU BH 1; cores from 154-161 m depth. Sample 158.2 m is shown with a white label. A magnified view from the previous picture (Fig. A2-7A), showing lithologies and textures of the sediments.

Figure A3-8: NGU BH 1; cores from 161-168 m depth. Sample 167.0 is from this core box (white label). These sediments are characterized as sedimentary breccia or debris flow, partly with large clasts of altered mafic rocks. Fragments of fine-grained light grey sandstone are also seen, partly as layers and in the matrix, together with talc and chlorite. The mineralogy of this fine sandstone (Sample 167.0 m) indicates that it is actually an altered tuffite; the dominating minerals being plagioclase, smectitic clay minerals, biotite and hematite. Furthermore, this is the only sample between 129.8 m and 193.75 m depth that is without talc, which further indicates an origin different from the debris flows/sedimentary breccias.

Figure A3-9: Cores from 161-168 m depth in NGU BH 1. This core interval is also characterized as sedimentary breccias or debris flows, partly with large (several cm) clasts of altered mafic rocks. Fragments of fine-grained light grey sandstone are also seen, partly as layers and in the matrix, together with talc and chlorite.

Figure A3-10: Cores from 175-182 m depth in NGU BH 1. The sediments in this interval are described as polymict conglomerates of dark angular mafic rock clasts with abundant (lighter) matrix; probably debris flows. Some interlayering with thin layers of fine-grained light grey sandstone.

Figure A3-11: Cores from 182-189 m depth in NGU BH 1. Samples 185.7 m and 188.5 m are from this core box (white label for sample 185.7 m). The core interval is described as mainly polymict conglomerates with abundant matrix The dominating minerals in Samples 185.7m and 188.5 m are talc, biotite, illite, plagioclase, and chlorite (Table 7.1).

Figure A3-12A: Cores from 189-196 m depth in NGU BH 1. Sample 195.1m is from this core box (white label). The sediments from 189 to 190.55 m are described as a polymict conglomerate with abundant matrix, interlayered with thin layers of fine-grained light grey sandstone, while the interval from 190.55 m to 193.75 m are described as a sedimentary breccia or debris flow, partly with lenticular lenses and large clasts of talc-rich altered mafic rocks. The dominating minerals in Sample 195.1 m are plagioclase and hornblende; i.e. an amphibolite intrusion (Table 7.1). The boundary to the granodioritic basement is at 193.75 m, and a c. 5 cm thick fossil weathering zone seem to have developed in the upper rim of the granodiorite.

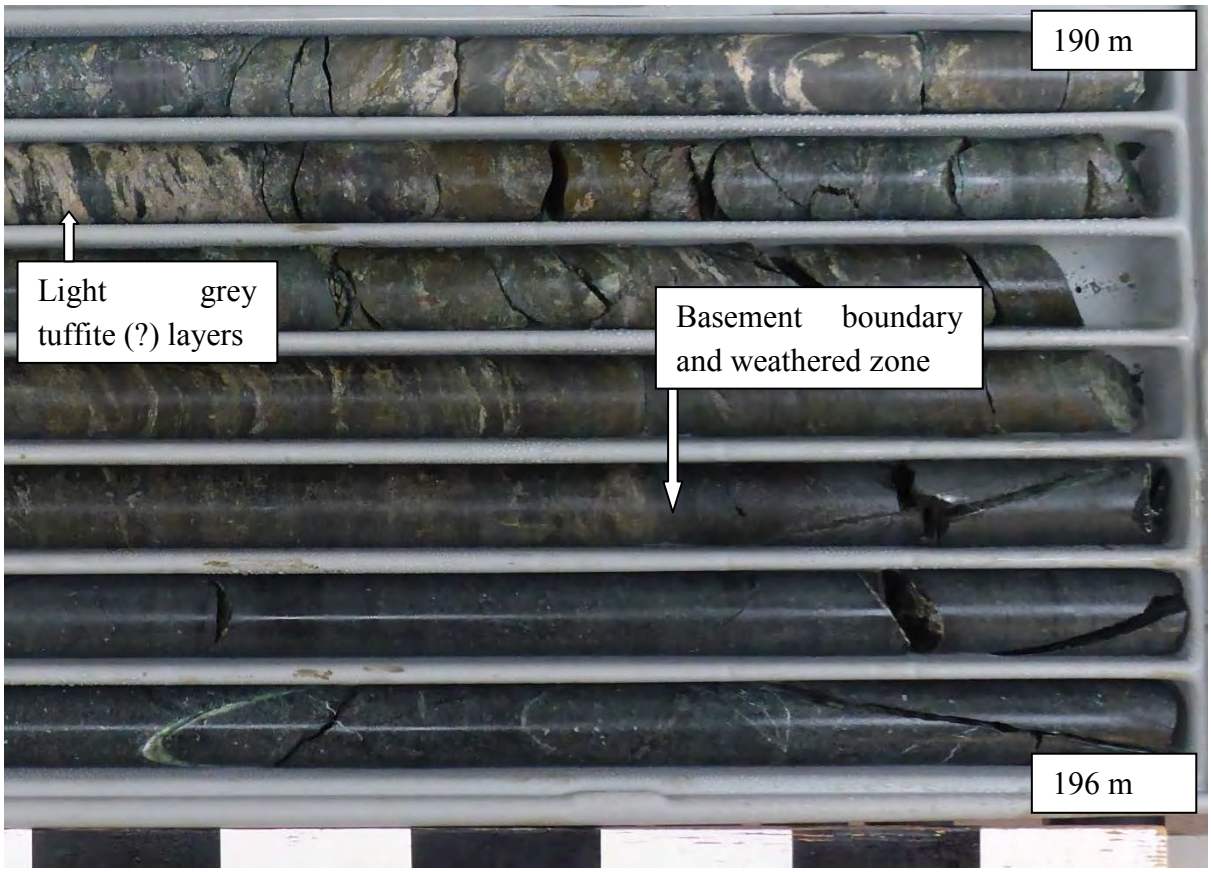

Figure A3-12B: NGU BH 1: Cores from 189-196 m depth in NGU BH 1. A magnified view of the right hand side of the previous picture (Fig. A2-12A), showing lithologies and textures of the sediments. Also the basement boundary with its weathered zone (in granodiorite) is marked.

GEOLOGICAL
SURVEY OF
NORWAY

· NGU ·

Geological Survey of Norway
PO Box 6315, Sluppen
N-7491 Trondheim, Norway

Visitor address
Leiv Eirikssons vei 39
7040 Trondheim

Tel (+ 47) 73 90 40 00
E-mail ngu@ngu.no
Web www.ngu.no/en-gb/